ADVANCES IN POLYMER SCIENCE 230

Polymer Characterization

Rheology, Laser Interferometry, Electrooptics

Springer

230
Advances in Polymer Science

Advances in Polymer Science

Recently Published and Forthcoming Volumes

Polymer Characterization
Vol. 230, 2010

Modern Techniques for Nano- and Microreactors/-reactions
Volume Editor: Caruso, F.
Vol. 229, 2010

Complex Macromolecular Systems II
Volume Editors: Müller, A.H.E., Schmidt, H.-W.
Vol. 228, 2010

Complex Macromolecular Systems I
Volume Editors: Müller, A.H.E., Schmidt, H.-W.
Vol. 227, 2010

Shape-Memory Polymers
Volume Editor: Lendlein, A.
Vol. 226, 2010

Polymer Libraries
Volume Editors: Meier, M.A.R., Webster, D.C.
Vol. 225, 2010

Polymer Membranes/Biomembranes
Volume Editors: Meier, W.P., Knoll, W.
Vol. 224, 2010

Organic Electronics
Volume Editors: Meller, G., Grasser, T.
Vol. 223, 2010

Inclusion Polymers
Volume Editor: Wenz, G.
Vol. 222, 2009

Advanced Computer Simulation Approaches for Soft Matter Sciences III
Volume Editors: Holm, C., Kremer, K.
Vol. 221, 2009

Self-Assembled Nanomaterials II
Nanotubes
Volume Editor: Shimizu, T.
Vol. 220, 2008

Self-Assembled Nanomaterials I
Nanofibers
Volume Editor: Shimizu, T.
Vol. 219, 2008

Interfacial Processes and Molecular Aggregation of Surfactants
Volume Editor: Narayanan, R.
Vol. 218, 2008

New Frontiers in Polymer Synthesis
Volume Editor: Kobayashi, S.
Vol. 217, 2008

Polymers for Fuel Cells II
Volume Editor: Scherer, G.G.
Vol. 216, 2008

Polymers for Fuel Cells I
Volume Editor: Scherer, G.G.
Vol. 215, 2008

Photoresponsive Polymers II
Volume Editors: Marder, S.R., Lee, K.-S.
Vol. 214, 2008

Photoresponsive Polymers I
Volume Editors: Marder, S.R., Lee, K.-S.
Vol. 213, 2008

Polyfluorenes
Volume Editors: Scherf, U., Neher, D.
Vol. 212, 2008

Chromatography for Sustainable Polymeric Materials
Renewable, Degradable and Recyclable
Volume Editors: Albertsson, A.-C., Hakkarainen, M.
Vol. 211, 2008

Wax Crystal Control · Nanocomposites Stimuli-Responsive Polymers
Vol. 210, 2008

Functional Materials and Biomaterials
Vol. 209, 2007

Polymer Characterization

Rheology, Laser Interferometry, Electrooptics

Volume Editors: Karel Dušek
Jean-François Joanny

With contributions by

J.-F. Berret · V.A. Bershtein · D. Bogdal · S. Lerouge
K. Matras-Postolek · P.N. Yakushev

Springer

Editors
Karel Dušek
Institute of Macromolecular Chemistry
Czech Academy of Sciences
of the Czech Republic
Heyrovský Sq. 2
16206 Prague 6, Czech Republic
dusek@imc.cas.cz

Jean-François Joanny
Institut Curie
Physiochimie Curie
Rue d'Ulm 26
75248 Paris Cedex 05
France
jean-francois.joanny@curie.fr

ISSN 0065-3195 e-ISSN 1436-5030
ISBN 978-3-642-13531-6 e-ISBN 978-3-642-13532-3
DOI 10.1007/978-3-642-13532-3
Springer Heidelberg Dordrecht London New York

Library of Congress Control Number: 2010930980

Cover design: WMXDesign GmbH, Heidelberg

Printed on acid-free paper

Springer is part of Springer Science+Business Media (www.springer.com)

Volume Editors

Karel Dušek

Institute of Macromolecular Chemistry
Czech Academy of Sciences
of the Czech Republic
Heyrovský Sq. 2
16206 Prague 6, Czech Republic
dusek@imc.cas.cz

Jean-François Joanny

Institut Curie
Physiochimie Curie
Rue d'Ulm 26
75248 Paris Cedex 05
France
jean-francois.joanny@curie.fr

Editorial Board

Advances in Polymer Sciences Also Available Electronically

Advances in Polymer Sciences is included in Springer's eBook package *Chemistry and Materials Science*. If a library does not opt for the whole package, the book series may be bought on a subscription basis. Also, all back volumes are available electronically.

For all customers who have a standing order to the print version of *Advances in Polymer Sciences*, we offer the electronic version via SpringerLink free of charge.

If you do not have access, you can still view the table of contents of each volume and the abstract of each article by going to the SpringerLink homepage, clicking on "Browse by Online Libraries", then "Chemical Sciences", and finally choose *Advances in Polymer Science*.

You will find information about the

- Editorial Board
- Aims and Scope
- Instructions for Authors
- Sample Contribution

at springer.com using the search function by typing in *Advances in Polymer Sciences*.

Color figures are published in full color in the electronic version on SpringerLink.

Aims and Scope

The series *Advances in Polymer Science* presents critical reviews of the present and future trends in polymer and biopolymer science including chemistry, physical chemistry, physics and material science. It is addressed to all scientists at universities and in industry who wish to keep abreast of advances in the topics covered.

Review articles for the topical volumes are invited by the volume editors. As a rule, single contributions are also specially commissioned. The editors and publishers will, however, always be pleased to receive suggestions and supplementary information. Papers are accepted for *Advances in Polymer Science* in English.

In references *Advances in Polymer Sciences* is abbreviated as *Adv Polym Sci* and is cited as a journal.

Special volumes are edited by well known guest editors who invite reputed authors for the review articles in their volumes.

Impact Factor in 2009: 4.600; Section "Polymer Science": Rank 4 of 73

Publisher's Note for Volumes with Independent Contributions

This volume was not originally planned as a topical volume by the stated Volume Editors. It contains substantial review articles on interesting and valuable subjects which were invited and reviewed by the stated Editors on an independent basis and then – upon receipt – put together in one volume by the Publisher.

Marion Hertel
Executive Editor Chemistry, Springer

Contents

Adv Polym Sci (2010) 230: 1–71
DOI:10.1007/12_2009_13

Published online: 26 August 2009

Shear-Induced Transitions and Instabilities in Surfactant Wormlike Micelles

Sandra Lerouge and Jean-François Berret

Abstract In this review, we report recent developments on the shear-induced transitions and instabilities found in surfactant wormlike micelles. The survey focuses on the nonlinear shear rheology and covers a broad range of surfactant concentrations, from the dilute to the liquid-crystalline states and including the semidilute and concentrated regimes. Based on a systematic analysis of many surfactant systems, the present approach aims to identify the essential features of the transitions. It is suggested that these features define classes of behaviors. The review describes three types of transitions and/or instabilities: the shear-thickening found in the dilute regime, the shear-banding which is linked in some systems to the isotropic-to-nematic transition, and the flow-aligning and tumbling instabilities characteristic of nematic structures. In these three classes of behaviors, the shear-induced transitions are the result of a coupling between the internal structure of the fluid and the flow, resulting in a new mesoscopic organization under shear. This survey finally highlights the potential use of wormlike micelles as model systems for complex fluids and for applications.

Keywords Instabilities under shear · Lyotropic mesophases · Shear-banding · Shear-thickening · Surfactant · Viscoelasticity · Wormlike micelles

Contents

S. Lerouge and J.-F. Berret (✉)
Laboratoire Matière et Systèmes Complexes (MSC), UMR 7057 CNRS-Université Paris-Diderot, 10 rue Alice Domon et Léonie Duquet, F-75205 Paris Cedex 13, France
e-mail: sandra.lerouge@univ-paris-diderot.fr; jean-francois.berret@univ-paris-diderot.fr

Abbreviations and Notations

$Al(NO_3)_3$	Aluminum nitrate
$AlCl_3$	Aluminum chloride
CP/Sal	Cetylpyridinium salicylate
CPCl	Cetylpyridinium chloride
$CPClO_3$	Cetylpyridinium chlorate
C_8F_{17}	Perfluorooctyl butane trimethylammonium bromide
$C_{12}E_5$	Penta(ethylene glycol) monododecyl ether
C_{12}TAB	Dodecyltrimethylammonium bromide
C_{14}TAB	Tetradecyltrimethylammonium bromide
C_{14}DMAO	Tetradecyldimethylamine oxide
C_{16}TAB	Hexadecyltrimethylammonium bromide
C_{16}TAC	Hexadecyltrimethylammonium chloride
C_{18}TAB	Octadecyltrimethylammonium bromide
C_{18}-C_8DAB	Hexadecyloctyldimethylammonium bromide
C_nTAB	Alkyltrimethylammonium bromide
CTAHNC	Cetyltrimethylammonium 3-hydroxy-2-naphthalenecarboxylate
CTAT	Hexadecyltrimethylammonium *p*-toluenesulfonate
CTAVB	Cetyltrimethylammonium benzoate
Dec	Decanol
DJS	Diffusive Johnson–Segalman
DLS	Dynamic light scattering
DR	Drag reduction
EHAC	Erucyl bis(hydroxyethyl)methylammonium chloride
FB	Flow birefringence
FI	Faraday instability
Gemini 12-2-12	Ethane diyl-1,2-bis-(dodecyl dimethylammonium bromide)

Hex	Hexanol
HPC	Hydroxypropyl cellulose
I/N	Isotropic-to-nematic
KBr	Potassium bromide
LAPB	Laurylamidopropyl betaine
LSI	Light scattering imaging
LCP	Liquid crystalline polymer
NaCl	Sodium chloride
NaClBz	Sodium chlorobenzoate
$NaClO_3$	Sodium chlorate
$NaNO_3$	Sodium nitrate
NaSal	Sodium salicylate
NaTos	Sodium *p*-toluenesulfonate or sodium tosylate
NH_4Cl	Ammonium chloride
NMR	Nuclear magnetic resonance
PBLG	Poly(benzyl-L-glutamate)
PEO	Poly(ethylene oxide)
PIV	Particle image velocimetry
PTV	Particle tracking velocimetry
SANS	Small-angle neutron scattering
SALS	Small-angle light scattering
SAXS	Small-angle X-ray scattering
SDBS	Sodium dodecyl benzyl sulfonate
SDES	Sodium dodecyl trioxyethylene sulfate
SdS	Sodium decylsulfate
SDS	Sodium dodecyl sulfate
SIP	Shear-induced phase
SIS	Shear-induced structure
TTAA	*Tris*(2-hydroxyethyl)-tallowalkyl ammonium acetate
USV	Ultrasonic velocimetry

1 Introduction

Wormlike micelles are elongated and semiflexible aggregates resulting from the self-assembly of surfactant molecules in aqueous solutions. Wormlike micellar solutions have received considerable attention during the past few decades because of their remarkable structural and rheological properties.

Sixty years ago, Debye and his group in Cornell undertook an extensive study of surfactant solutions using the light scattering technique. The goal of these investigations was to measure the dissymmetry of scattered light in order to gain information regarding the molecular weight and thereby the shape of surfactant aggregates. The dissymmetry of scattered light was defined as the intensity ratio at two scattering angles far apart from each other. If this ratio was one, the micelles were assumed to

be spherical; if it increased, the micelles were assumed to grow in size. In a famous paper, Debye and Anacker had discovered that the addition of an inorganic salt, potassium bromide, to aqueous solutions of hexadecyltrimethylammonium bromide caused the colloidal aggregates to increase in size [1]. Based on these dissymmetry experiments, it was suggested that the micelles undergo a morphological transition, from spherical aggregates at low salt content to rodlike aggregates at high salt content. More than half a century later, the very same systems, now known as wormlike micelles, continue to attract interest from a broad scientific community.

Going from the structure to the rheology was not a straightforward path. One important contribution after that of Debye was that of Nash who mapped viscoelastic regions of surfactant solutions again using hexadecyltrimethylammonium bromide and various naphthalene derivatives. The viscoelasticity was determined visually by looking at how fast a swirl applied by hand to a solution decayed with time [2]. Some years later, Gravsholt established that other additives, such as salicylate or chlorobenzoate counterions, could be solubilized by the micelles and efficiently promote their uniaxial growth [3]. It was proposed that the viscoelasticity of these solutions had the same origin as that of polymer solutions, namely entanglements and reptation.

In the early 1980s, as more and more groups were involved in this research, discoveries were made at a faster pace. By a combination of light scattering, rheology and magnetic birefringence, it was first shown that, under certain conditions, cylindrical micelles could be very long, up to 1 μm in contour length, and flexible [4–10]. The terminology introduced was that of giant [5, 11, 12] or wormlike [6, 8–10] micelles, instead of rodlike aggregates some years before. For several surfactants, Ikeda and collaborators reported electron microscopy images showing thread-like and tortuous filaments, later referred to as worms [8, 9]. Again, using light scattering experiments, Candau and his group demonstrated the existence of a cross-over between dilute and semidilute regimes and of scaling laws as a function of the concentration, two features that were known from polymers [7, 13, 14]. These authors pointed out a formal analogy between surfactant wormlike micelles and polymer solutions. This analogy was completed by the extensive investigations of phase behaviors of surfactant aqueous solutions, and the evidence of isotropic-to-nematic and a nematic-to-hexagonal transitions at high concentrations [12, 15–18]. Figure 1 provides a schematic illustration of the different concentration regimes that will be surveyed in the present review. The analogy with polymers, as well as a marked viscoelasticity, attracted attention from rheologists, who were at first interested in the linear mechanical response of these fluids.

A decisive step towards the description of the micellar dynamics was taken with the first quantitative measurements of the linear viscoelastic response of these solutions. The pioneering works were those of Rehage, Hoffmann, Shikata, and Candau and their coworkers [14, 19–33]. The most fascinating result was that the viscoelasticity of entangled wormlike micelles was characterized by a single exponential in the response function. The stress relaxation function $G(t)$ was found of the form $G(t) = G_0 \exp(-t/\tau_R)$ over a broad temporal range, where G_0 denotes the elastic modulus and τ_R is the relaxation time. Since then, this property was found repeatedly

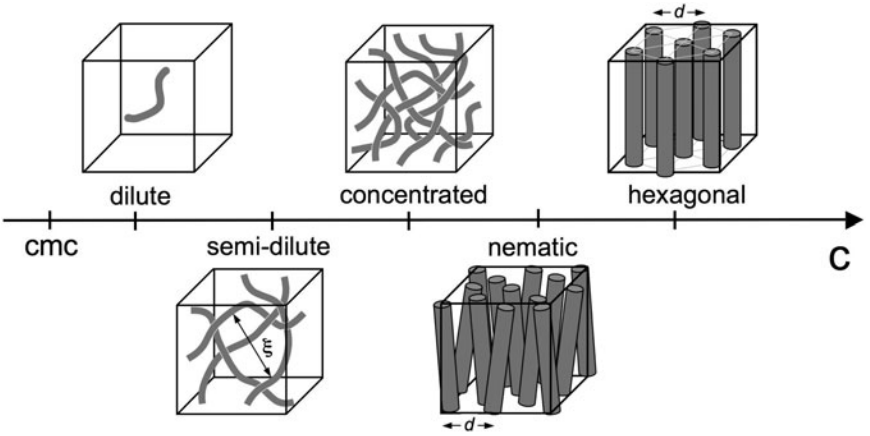

Fig. 1 Illustrations of the different concentrations regimes encountered in wormlike micellar solutions with increasing concentration. ξ is the mesh size of the entangled network in the semidilute regime and d denotes the average distance between colinear micelles in the concentrated isotropic, nematic and hexagonal phases. An estimate of d can be gained from the position of the structure peak in the scattering function

in semidilute wormlike micellar solutions. This rule has become so general that it is now recognized that a single relaxation time in the linear rheology is a strong indication of the wormlike character of self-assembled structures. A simple viscoelastic behavior, together with the fact that micellar solutions are easy to prepare and not susceptible to aging or degradation, have incited several groups to utilize wormlike micelles as reference for the testing of new rheological techniques [34–39].

On the theoretical side, the challenge was to account for this unique time of the mechanical response. This was done by Cates and coworkers in the late 1980s with the reptation-reaction kinetics model [40]. The reptation-reaction kinetics model is based on the assumption that the breaking and recombination events of the chains are coupled to the reptation [41], and as such accelerate the overall relaxation of the stress. In the fast breaking limit, a given micelle undergoes several scission and recombination reactions on the time scale of the reptation. Thus, all initial deformations of the tube segments relax at the same rate, this rate being driven by the reversible scission.

In the present review, we focus on the shear-induced transitions and instabilities that were disclosed in wormlike micellar systems during the last decade or so. The thermodynamics, structure, and rheology of the aggregates at rest or under small deformation have been reviewed many times in the past [19, 25, 28, 42–44], and they will not be treated here. Our survey of the nonlinear rheology now covers all concentration regimes, from the dilute to the liquid-crystalline states, including the semidilute and concentrated regimes (Fig. 1). The present approach aims to demonstrate that the features of the shear instabilities are specific to a concentration regime. Sometimes, the characteristics of a transition extend over a broader concentration

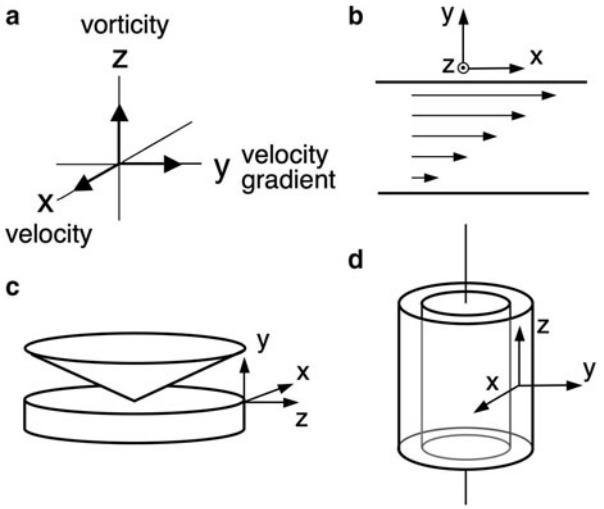

Fig. 2 (**a**) Conventions adopted in this review for the velocity, velocity gradient and vorticity axes characterizing shear flows. Most common geometries of shearing devices producing shear flows: (**b**) planar Couette, (**c**) cone-and-plate, (**d**) cylindrical Couette

range. This is the case for the shear-thickening that was evidenced in the dilute and semidilute regimes. Another goal is to establish correspondences between the shear-induced and the equilibrium phases. A good illustration is that of the isotropic-to-nematic transition, for which the induced nematic exhibits the same orientation and rheological properties as the nematic phase found in the equilibrium phase diagram at high volume fraction.

Although elongational flows have also been imposed on semidilute solutions [45–49], the review will focus essentially on shear flows. The most common devices for shear are the cylindrical Couette and the cone-and-plate geometries (Fig. 2). In a cylindrical Couette system, the sample is contained between two concentric cylinders and the shear is applied by rotating the inner or outer cylinder. If the inner cylinder is rotated, inertia effects may cause a transition from laminar flow to Taylor vortex flow at high shear rates [50]. As for the results discussed in the review, the Reynolds numbers remained below or even much below than that of the Taylor instability. Compared to Couette systems, cone-and-plate devices have more uniform stress, provided the cone angle is small. Figure 2 also specifies the geometrical conventions used throughout the review for the velocity, velocity gradient, and vorticity directions. Another convention concerns the surfactant concentrations. Due to the fact that wormlike micelles were studied by scientists from various research fields, the surfactant concentrations appear in the literature with different units, including molar concentration, volume fraction, weight percent, or weight per volume. In order to allow comparison between different surfactant systems, we have adopted the following rule. We have kept the units used by the authors in reference to their work, and we have added, when necessary, the value of the weight percent concentration

c (units wt). For ternary systems made of a surfactant and an additive (this additive being a hydrotope, a cosurfactant, or an alcohol molecule), c denotes the total surfactant and additive concentration. The molar ratio between additive and surfactant is expressed as R.

The review is organized as follows: Sect. 2 deals with the shear-thickening behavior found in dilute and very dilute surfactant solutions. Section 3 examines the shear-banding instability and the isotropic-to-nematic transition revealed in the semidilute and concentrated regimes, respectively. The last part focuses on the wormlike micellar nematics under shear, and emphasizes the analogy with liquid-crystalline polymers.

2 Shear-Thickening in Dilute Micellar Solutions

2.1 Introduction

Among the rich variety of shear-induced instabilities and transitions encountered in surfactant systems, one of the most puzzling is the shear-thickening effect observed in dilute or very dilute solutions. This transition was first noticed by Rehage and Hoffmann [52] in 1981 for the system cetylpyridinium salicylate (CP/Sal) at a molar concentration of 0.9 mM ($c = 0.04$ wt. %). In their original work, the shear stress was recorded as a function of time over several minutes, and it revealed an unexpected behavior. Above a critical shear rate, the transient stress exhibited a period of induction during which the viscosity increased and then stabilized around 10 times the viscosity of water. This early evidence of the shear-thickening has been reproduced in Fig. 3. The phenomenon was explained by postulating the formation of a supramolecular structure during flow [51, 52].

In the same decade, shear-thickening solutions have attracted much interest because of their potential applications in fluid mechanics. In a number of practical

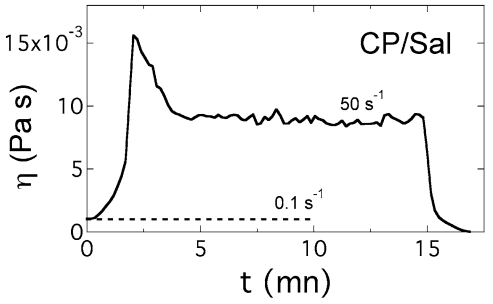

Fig. 3 Shear viscosity as a function of time for equimolar cetylpyridinium salicylate (CP/Sal) at 0.9 mM ($c = 0.04$ wt. %) and temperature $T = 20\,^{\circ}\mathrm{C}$. The transient response at $\dot{\gamma} = 0.1\,\mathrm{s}^{-1}$ exhibits a regular steady behavior for such dilute solution, whereas the response at $50\,\mathrm{s}^{-1}$ shows a period of induction during which the viscosity increases and then stabilizes around ten times the viscosity of water. Figure reprinted with permission from [51]

situations such as fire-fighting operations and transportation of fluids along cylindrical pipes, turbulence occurs near the solid surface and increases the energy losses associated to the flow. It was suggested that additives dispersed in water, e.g., polymers or surfactant, could diminish considerably the turbulent skin friction [53]. Bewerdorff and coworkers have shown that some surfactants reduced effectively the friction factor in turbulent pipe flows [54–56]. Using tetradecyltrimethylammonium with salicylate counterions at concentrations as low as 0.1 wt. %, these authors were able to correlate the drag reduction to the increase of viscosity at high shear rates. Since these early studies, the interest in this transition has increased, especially in the context of the study of complex fluids under shear flow.

In this part, we are dealing with the shear-thickening transition in dilute surfactant solutions. Only solutions with zero-shear viscosity close to that of the solvent and for which no apparent viscoelasticity is observed at rest will be considered. Systems showing both viscoelasticity and shear-thickening have also been found and will be evoked in the part devoted to the semidilute regime.

The features of the shear-thickening transition are summarized as follows:

1. Shear-thickening occurs for surfactants that self-assemble into cylindrical micelles.
2. Under steady shear, above a critical shear rate, the shear viscosity increases as a new and more viscous phase develops. This shear-induced state is called SIS for shear-induced structure [55] or SIP for shear-induced phase [57] in the literature.
3. An induction time is necessary to induce the SIS. At steady state, the stress displays fluctuations that are larger than the instrumental noise response.
4. In the shear-induced state, the solutions are birefringent and exhibit a strongly anisotropic scattering in light and neutron experiments. This anisotropy is compatible with a strong alignment of the shear-induced structures in the flow.
5. The shear stress vs shear rate curve depends on the geometry of shearing cells, and also of the thermal and shear histories experienced by the fluid prior to rheological testing.

In the following (Sect. 2.2) we will first provide a list of surfactant molecules that exhibit shear-induced structures in accordance with points 1–5 and then describe the phenomenology of the transition. The rheology (Sect. 2.3), the orientation properties (Sect. 2.4), and the structure of the flow field (Sect. 2.5) for these fluids will then be examined.

2.2 Shear-Thickening Surfactants

In comparison with the total number of surfactants available by now, only a few of them exhibit a shear-thickening transition in accordance with points 1–5 above. Table 1 lists these systems, with their counterions and/or their hydrotopes. In Table 1 it can be seen that all the surfactants are cationic and that the number of carbon atoms ranges from 13 to 18 per elementary charge. Most of the rheological

Table 1 List of surfactants and additives found to exhibit shear-thickening described by points 1–5. Column 4 makes an inventory of the experimental techniques employed to investigate the SIS

Surfactant	Additive	Salt	Experiment	References
CPCl	NaSal		FB	(a)
C_{14}TAB	NaSal		SANS, FB, DR	(b)
C_{16}TAB	NaSal		FI, FB, DR, SALS, PIV	(c)
C_{16}TAB	NaTos (*)		SANS, FB	(d)
C_{16}TAC	NaClBz		DR	(e)
C_{18}TAB	NaSal			(f)
C_{14}DMAO	SDS		SANS, FB, SALS	(g)
Gemini 12-2-12		Br^-	SANS, FB, SALS	(h)
TTAA	NaSal		LSI, PIV, DR	(i)
C_8F_{17}		Br^-		(j)

(*) For the system hexadecyltrimethylammonium *p*-toluenesulfonate without monovalent counterions, the notation CTAT is prefered to C_{16}TAB/Tos. (a) [51, 52, 58], (b) [54–56, 59–61], (c) [55, 60, 62–74], (d) [68, 71, 75–82], (e) [83, 84], (f) [61], (g) [85–87], (h) [88–95], (i) [57, 96–99], (j) [93]

studies have been performed on systems of the alkyltrimethylammonium bromide class (C_nTAB), using strongly binding counterions or hydrotopes. Well-known examples of hydrotopes are salicylate, *p*-toluenesulfonate, and chlorobenzoate, which all contain an aromatic phenyl group.

In Table 1, for the sake of simplicity, we have given the abbreviations of the surfactants and hydrotopes with their monovalent counterions. Tetradecyltrimethylammonium bromide with sodium salicylate thus becomes in short C_{14}TAB/NaSal. In some cases [51, 52, 59, 60], the small monovalent counterions have been removed by ion exchange procedures, yielding a surfactant salt that is now abbreviated C_{14}TA/Sal [59]. In the following, the abbreviations will take into account these variations. Systems with hydrotopes were generally prepared at equimolar 1:1 conditions. It is interesting to note that, according to Lu et al. [83], only chlorobenzoate isomers with the chlorine in the para-position yields significant shear-thickening and drag reduction, when put in combination with alkytrimethylammonium surfactants (in contrast to the ortho- and meta-isomers). More recently, surfactant systems without hydrotopes were uncovered. The double tail gemini 12-2-12 (ethanediyl-1,2-bis(dodecyl dimethylammonium bromide)) [88–92] and the partially fluorinated surfactant (perfluorooctyl butane trimethylammonium bromide) [93] are among the most surveyed systems of this kind. Concerning the class of gemini surfactants, some molecules with specific architecture were also shown to self-assemble into micelles with more complex topologies, such as ring-like [100] and branched [101] structures. Note finally a system made from oppositely charged surfactants, tetradecyl dimethylamine oxide (C_{14}DMAO) and dodecyl sulfate (SDS), which displays the above properties only for mole fractions [C_{14}DMAO]/([C_{14}DMAO] + [SDS]) between 0.5 and 0.8 [85–87]. In Table 1, again for simplicity, we have omitted commercial surfactants showing a polydispersity of the aliphatic tails, or chemical structures that are less well characterized [102].

2.3 Rheology

The shear-thickening transition in dilute surfactant solutions was investigated using both strain- and stress-controlled rheometry. Due to the low viscosity of the solutions, Couette geometries either with single or double Couette walls were preferred (Fig. 2). Due to the long transients in the kinetics of the SIS formation, the shear stress vs shear rate curves were determined by measuring the time dependence of the stress, and by recording its stationary value. The flow curves were then constructed point by point so as to ensure that they corresponded to the stationary state of flow.

2.3.1 Strain-Controlled Rheometry

Figure 4 displays the general behavior of the shear-thickening transition observed with imposed shear rate. The steady shear stress $\sigma(\dot{\gamma})$ and the steady apparent shear viscosity $\eta(\dot{\gamma})$ are shown as a function of the applied shear rate for the hexadecyltrimethylammonium *p*-toluenesulfonate (CTAT) at $c = 0.41$ wt. %. For this system, the overlap concentration was estimated at $c^* = 0.5$ wt. % and the shear-thickening to be present over the range 0.05–0.8 wt. % [75, 103].

In Fig. 4, three flow regimes can be distinguished:

- *Regime I*. At low shear rates, the stress increases linearly with the rate, indicating a Newtonian behavior.
- *Regime II*. At $\dot{\gamma}_c$, the viscosity increases and deviates progressively from the Newtonian behavior. The transition toward the shear-thickened state is continuous.
- *Regime III*. The apparent viscosity passes through a maximum, at a level that is several times that of the solvent viscosity, and then shear-thinning is observed.

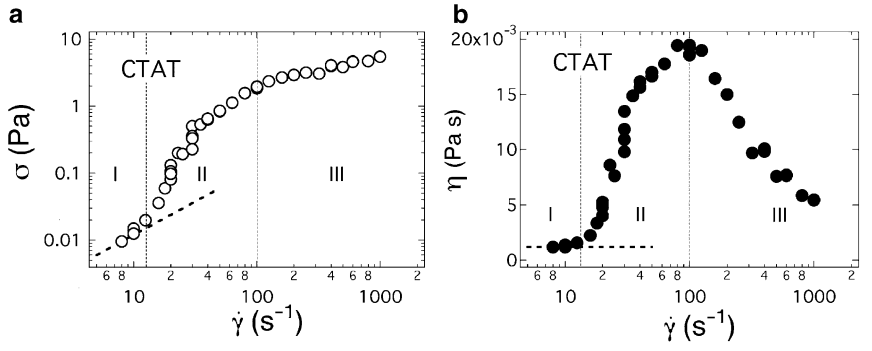

Fig. 4 Steady state shear stress (**a**) and viscosity (**b**) vs shear rate for hexadecyltrimetylammonium *p*-toluenesulfonate (CTAT) at $c = 0.41$ wt. % and $T = 23\,^{\circ}$C. With increasing shear rates, three flow regimes are encountered. At low shear rates (Regime I), the stress increases linearly with the rate with a constant slope η_0, indicating a Newtonian behavior (*dashed lines*). At $\dot{\gamma}_c = 14 \pm 2\ s^{-1}$, the viscosity increases and deviates progressively from the Newtonian behavior. In Regime III, the viscosity passes through a maximum, and shear-thinning is observed. Figure adapted from [75]

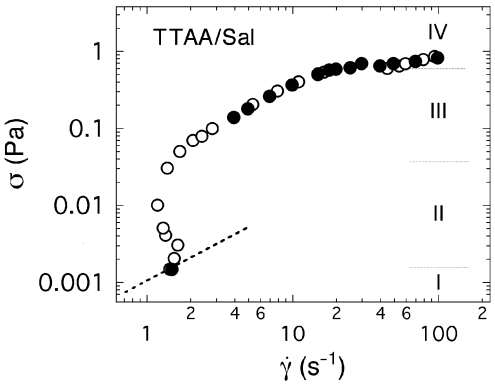

Fig. 5 Steady state rheological behavior of 1.7/1.7 mM *tris*(2-hydroxyethyl)-tallowalkyl-ammoniumacetate/sodium salicylate (TTAA/Sal), corresponding to a total weight concentration $c = 0.10$ wt. %. For this system, four flow regimes were reported, as indicated. Note the re-entrant shear stress vs shear rate curve for the stress-controlled data (*open symbols*), and the discontinuity for the strain-controlled data (*closed symbols*). Figure reprinted with permission from [99]

The three regimes are indicated in the figures by dashed vertical lines. Similar data, and in particular the observation of a continuous viscosity increase in Regime II, were obtained on various systems of Table 1, namely on C_{16}TA/NaSal [62–65, 104] gemini 12-2-12 [88, 89]. Note that, for TTAA/Sal, a discontinuous transition between Regime I and Regime III was reported with controlled strain rates, as illustrated in Fig. 5 and discussed in details below [99].

2.3.2 Stress-Controlled Rheometry

Stress-controlled rheometry has been operated on fewer systems, as compared to strain-controlled rheometry. In C_{16}TAB with salicylate and *p*-toluenesulfonate counterions, Hartmann et al. observed a phenomenology close to that reported in Fig. 4, that is the occurrence of the sequence Newtonian (I) – shear-thickening (II) – shear-thinning (III) [68]. Pine and coworkers were the first to notice the existence of a re-entrant flow curve above the critical shear rate (Fig. 5). These results were obtained on a 1.7/1.7 mM *tris*(2-hydroxyethyl)-tallowalkyl ammonium acetate/sodium salicylate (TTAA/Sal), in which TTAA represents a mixture of C_{16} and C_{18} alkyl chain surfactants [57, 96–99, 105]. The total weight concentration of this sample was $c = 0.10$ wt. %. Careful transient measurements allowed to confirm the existence of stationary flows at shear rate below $\dot{\gamma}_c$ (re-entrant behavior). These findings were interpreted as strong evidence that a more viscous phase was building up under constant stress. With increasing shear stress, the $\sigma(\dot{\gamma})$-flow curve of TTAA/Sal was found similar to that of most compounds, showing a transition toward a shear-thinning at high shear stress. Unlike most rheological characterizations, Pine and coworkers reported four flow regimes, noted I to IV on the figure. There, Regimes I, II, and IV correspond to the three regimes of Fig. 4, whereas Regime III sets the

limits of a range where the viscosity stays constant as a function of $\dot{\gamma}$. Using stress-controlled rheometry, Walker and coworkers also observed a slightly re-entrant behavior above the critical stress in the CTAT dilute solutions [76].

2.3.3 Transient Rheology

As already mentioned, considerable care was taken by experimentalists in order to ensure the actual determination of the steady state. Most procedures used start-up experiments, which consisted of imposing the shear rate (respectively, stress) on freshly poured solutions and measuring the stress (respectively, rate) as a function of time. This approach had already been suggested by the work of Hoffmann and Rehage (see Fig. 3). Start-up experiments have revealed two major results that were later corroborated on most systems:

- In Regimes II and III, the shear-thickening state was reached after an induction time noted $t_{\rm ind}$.
- As noticed by most of the earlier reports, this induction time varied as $1/(\dot{\gamma}-\dot{\gamma}_c)$ [77], or as $1/\dot{\gamma}$ far from the critical conditions [86,87,89,98,106]. In other words, the closer the shear rate was from the critical value, the longer was the time to reach stationary state. This result was interpreted as an indication that the relevant quantity for the induction of the SIS was the total deformation $\dot{\gamma}t_{\rm ind}$ applied. These findings were observed for CP/Sal [51,52], C_{16}TAB/NaSal [63] and TTAA/NaSal [98].

More recently, a closer inspection of the transient stress rheology for thickening systems has revealed more complicated patterns, such as structural memory effects. Berret et al. [78] and Oeschlager et al. [93, 107] have observed that the transient mechanical response also depended on the thermal and shear histories. Samples having been treated thermally, e.g., heated up to 90 °C for 2 h, behaved very differently from samples freshly prepared or already sheared. The induction time could last several hours, and was not proportional to the inverse shear rate, as mentioned previously. It was concluded that the lack of reproducibility under certain thermal and shear conditions might indicate that these surfactant solutions were characterized by long-lived metastable states.

Other transient experiments commonly carried out on these solutions were stop-flow measurements. When sheared in the thickening regime, at the abrupt arrest of the shearing cell, the shear stress was found to relax via a double exponential decay, the shortest time being of the order of 1 s (associated to the reorientation dynamics) [89], and the longest time being of the order of seconds or minutes. Concerning this longer time, values in the range 1–1000, 5–500, and 5–40 s were observed for C_{14}TA/Sal [55], gemini 12-2-12 [89], and CTAT [108] dilute solutions respectively. The above ranges correspond to different conditions of temperature and/or concentration. Because of the monoexponential character of the long-time relaxation, and also because semidilute micellar solutions respond to stop-flow similarly [21], the

vanishing of the stress was ascribed to the relaxation of entangled wormlike micelles. Such a conclusion implicitly assumes that the micelles have grown under shear, although this was not formulated in such terms in the literature. We will come back to this point later.

2.3.4 Concentration and Temperature Dependence

With increasing concentrations, all the reported surfactants exhibit a transition between a dilute and a semidilute regime at c^*. Below c^*, micelles are short and do not overlap, whereas above c^*, chain entanglements slow down considerably the dynamics of the network and the zero-shear viscosity increases sharply [59,61,65,66,75,96,99,103]. The shear-thickening transition has been observed for concentrations below and above the overlap concentration. Shear-thickening in solutions with viscosities up to 1000 times that of water were reported [99]. Concerning the concentration dependence of the critical shear rate $\dot{\gamma}_c$, no universal behavior could be evidenced. $\dot{\gamma}_c$ was found to increase in CTAT (with D_2O as a solvent) [75] and in TTAA/NaSal [99], and to decrease in C_{14}DMAO/SDS [85], in gemini 12-2-12 [89] and in C_{16}TAB/NaSal [67]. In some other systems, it was found to remain concentration independent [75].

Much stronger dependences were observed as a function of the temperature. All systems investigated exhibited an Arrhenius-type behavior for the critical shear rate $\dot{\gamma}_c$, i.e.:

$$\dot{\gamma}_c(T) \sim \exp\left(-\frac{E_a}{k_B T}\right), \tag{1}$$

where E_a is an activation energy, k_B the Boltzmann constant, and T the absolute temperature. Activation energies E_a were found in the range 20–120 $k_B T$ ($T = 300\,K$), or equivalently between 50 and 300 kJ mol^{-1}. Concomitant to the shift of $\dot{\gamma}_c$ to larger values, the amplitude of the shear-thickening effect diminished with increasing temperature [55,62,63,75,89]. Ultimately, above 50 °C, the shear-thickening vanished. The origin of the underlying activated process in shear-thickening systems has not yet been identified.

In addition to concentration and temperature, other parameters capable of modifying the transition have been studied. These were (i) the shearing cell geometry, and in particular the gap of the Couette cell [55,58,62,96,99,104], (ii) the ionic strength [68, 85], and (iii) the addition of polymeric additives, such as PEO (poly(ethylene oxide)) or HPC (hydroxypropyl cellulose) [103]. Among these parameters, the geometry effect is certainly the most intriguing. Already present in the work by Ohlendorf and Wunderlich [55,62], it was noticed that smaller gaps shifted the critical shear rate towards higher values, and reduced the amplitude of the viscosity jumps. The gap effects were later interpreted by Pine and coworkers as a consequence of the slipping of the SIS along the walls, through the presence of a thin lubricating layer (see Fig. 8 for details) [96].

2.4 Structure and Orientation Under Shear

2.4.1 Small-Angle Scattering Under Shear

Thanks to an excellent neutron scattering contrast of hydrogenated surfactants in deuterated water (D_2O), small-angle neutron scattering (SANS) has become a privileged tool for the investigation of dilute shear-thickening solutions. Most of the systems in Table 1 have been investigated by SANS in quiescent conditions [54, 56, 75, 76, 85, 90, 103, 108]. All these studies have revealed a unique behavior: the surfactants self-assemble into cylindrical micelles. The radius of the micelles was also determined, and found to be around 2 nm [54, 56, 75, 76, 85, 90, 103, 108]. The other feature revealed by SANS was the occurrence of a structure factor indicative of strong repulsive interactions between the micellar threads. These interactions were attributed to the electrostatic charges at the surfaces of the rods. Electrostatic structure factors were observed on salt-free solutions of C_{14}DMAO/SDS [85], gemini 12-2-12 [88, 90], and CTAT [75, 79, 108]. During the last two decades, neutron [54, 56, 75, 76, 79, 85, 88, 90, 103, 108] and light [87, 91–93, 106, 107] scattering under shear were performed repeatedly on dilute thickening systems. As early as 1986, Bewersdorff and coworkers set up a Couette cell on a neutron spectrometer in order to detect the anisotropy of the scattering induced by the shearing [54]. In a series of runs performed on C_{14}TA/Sal, it was shown that, under shear, the scattered intensity collected on a two-dimensional detector was highly anisotropic, the scattering being predominantly in the direction perpendicular of the velocity. It was concluded that the shear-induced phase corresponded to a highly aligned state of cylindrical micelles [54]. An illustration of this anisotropy shown in Fig. 6a for

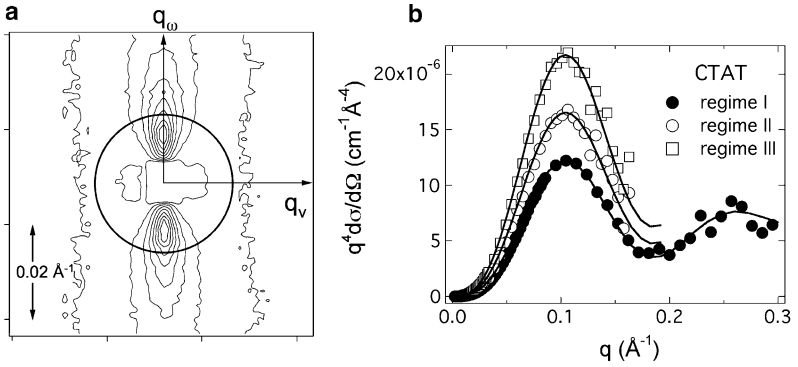

Fig. 6 (**a**) Two-dimensional neutron scattering pattern characteristic of the shear-induced phase in hexadecyltrimethylammonium *p*-toluenesulfonate dilute solutions. The solvent here is D_2O, the concentration $c = 0.26$ wt. %, and the shear rate $\dot{\gamma} = 188\,s^{-1}$ (Regime III in Fig. 4). $\mathbf{q}_v$ and $\mathbf{q}_w$ are, respectively, parallel to the velocity and vorticity directions of the flow. The ring shows the wave-vector at which the scattering cross-section is maximum in the quiescent state. (**b**) Porod representation of the neutron scattering intensities in Regimes I, II, and III (intensity in the vorticity direction). The oscillations in the form factors for the three set of data are in agreement with a morphology of cylindrical micelles with radius $R_c = 1.95$ nm, with a standard deviation of 0.2 nm (*continuous lines*). Figure adapted from [79]

CTAT ($c = 0.26$ wt. %, $\dot{\gamma} = 188\,s^{-1}$ corresponding to Regime III) is representative for this class of materials. An approach in terms of orientation distribution function was performed on the neutron spectra by analogy with the data analysis of nematic phases [109] (see Sect. 4). The order parameter of the micellar orientations was then derived and found to be 0.8. This value is close to unity, which designates a perfect alignment. On the same CTAT specimen, additional information could be gained from the study of the position of the structure factor as functions of surfactant concentration and shear rate. Below c^*, the structure factor peak of the SIS was found to shift to lower wave-vectors by 30% as compared to its value in the Newtonian regime (Fig. 6a). It actually moved down to the semidilute $q^{1/2}$-scaling law that was determined from solutions above c^*. This shift was interpreted as an indication of a shear-induced growth of the micelles, from short rodlike to wormlike aggregates. Similar shifts of the structure factor were observed for the gemini 12-2-12 surfactants [88, 90].

Concerning the shear-thickening transition, the question was raised about a possible transition of morphology, a transition where the original microstructure would be changed into heterogeneous patterns showing stippled or sponge-like textures [105]. It was also suggested by others that the micellar threads would eventually undergo a transition towards a bundle state [110]. Figure 6b shows the scattering intensities in the direction perpendicular to the flow velocity in Regimes I, II (shear-thickening), and III (shear-thinning), again for the CTAT system [79]. There, the Porod representation ($q^4 \times d\sigma(q)/d\Omega$ vs q) has been used in order to emphasize the local morphology at rest and under shear. As a result, all three data sets exhibit oscillations consistent with a cylindrical micelles with radius $R_c = 1.95$ nm. Qualitatively, the fact that the position of the first maximum remains unchanged under shear supports the conclusion that the local morphology remains rodlike. Similar rodlike. Similar results were found in gemini 12-2-12 dilute they were not interpreted using the Porod representation [111].

More recently, on gemini surfactants Weber and Schosseler have investigated the light scattering properties under shear, in order to probe the sheared fluid at length scales larger than those accessible by SANS [91]. For a 18.3 mM solution ($c = 1.0$ wt. %), an intense streak pattern perpendicular to the velocity direction was observed in the shear-thickening regime. The patterns exhibited strong fluctuations in amplitude, as well as a spatial modulation along the vorticity axis. A correlation length of the order of 30 µm was derived from this modulation. It was finally argued that these 30 µm were not compatible with the intermicellar distance, estimated in this solution at a few tens of nm. The light scattering data were interpreted in terms of a strongly aligned and heterogeneous gel-like layers in the gap of the Couette cell.

2.4.2 Flow Birefringence

A remarkable property of the shear-induced phase is its flow birefringence. Flow birefringence experiments on shear-thickening surfactant solutions were introduced

by Hoffmann and coworkers more than two decades ago [55, 59]. Wunderlich et al. have shown, for instance, that, for C_{14}TA/Sal [59], the onset of flow birefringence coincided with the increase of viscosity. Such results were found on all shear-thickening systems studied by this technique. Flow birefringence was measured by transmission using a Couette geometry. With this configuration, the polarized light propagates along the vorticity direction and the transmitted light reads

$$I = \frac{I_0}{2} \sin^2 \frac{\delta}{2} \sin^2(2(\chi - \theta)), \tag{2}$$

where I_0 is the incident light intensity, $\delta = 2\pi h \Delta n/\lambda$ the phase angle, χ the extinction angle, and θ the angle made by the polarization of the incident beam with the flow velocity (in the expression of the phase angle, h is the height of the Couette cell and λ the wavelength of light). The values of the birefringence Δn were found to be negative, lying between -10^{-5} and -10^{-7}, depending on the weight concentration. The flow birefringence was essentially measured at steady state as a function of the shear rate and under various conditions of temperature, concentration, and ionic strength [59, 61, 77, 78, 85, 89, 106].

The two main results of birefringence are illustrated in Fig. 7 for the 3/3 mM C_{14}TAB/NaSal solution ($c = 0.15$ wt. %) [61]. They are:

- An increase of Δn in Regime II, followed by saturation in Regime III.
- An abrupt decrease of the extinction angle at the onset of thickening toward a value close to 0°, both in Regimes II and III.

Figure 7 illustrates that, as soon as the new phase is induced, it is strongly oriented by the flow. In some reports, χ-data shown as a function of the shear rate have revealed that the extinction angle undergoes a discontinuity from $\chi = 45°$ to $\chi \sim 0°$

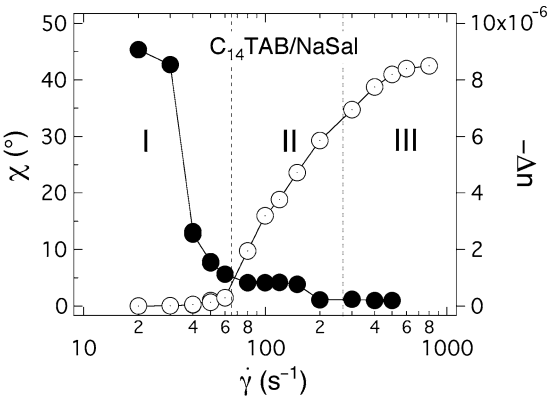

Fig. 7 Shear rate dependences of the flow birefringence Δn (*right scale*, *open symbols*) and of the alignment angle χ (*closed symbols*, *left scale*) for 3/3 mM tetradecyltrimethylammonium bromide and sodium salicylate (C_{14}TAB/NaSal), corresponding to a total weight concentration $c = 0.15$ wt. %. Regimes I, II, and III were determined from steady shear viscosity. Figure adapted from [61], courtesy J.P. Decruppe

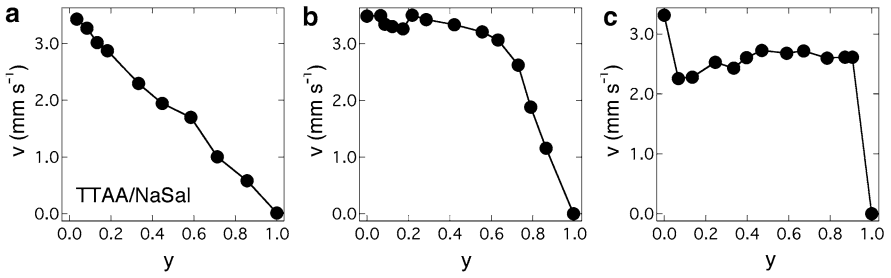

Fig. 8 Time development of the velocity profile in a 4-mm gap Couette cell for a 1.7/1.7 mM TTAA/NaSal solution. The time frames (**a**), (**b**), and (**c**) correspond to 6, 438, and 3,071 s, respectively, after the inception of shear ($\dot{\gamma} = 1\ s^{-1}$). The coordinates are referenced with respect to the inner cylinder (gap position 0) and to the outer cylinder (gap position 1). Figure adapted from [96]

at $\dot{\gamma}_c$ [77]. Recent measurements have confirmed this feature [61]. Time- and space-resolved studies of the flow birefringence were also attempted [77]. In CTAT, these studies have revealed that, once the SIS was initiated, it spread over the whole gap of the cell, and no regime of coexisting states (such as birefringent and nonbirefringent) could be detected.

2.4.3 Particle Image Velocimetry

Flow velocimetry measurements on shear-thickening include works by Koch and coworkers on C_{14}TA/Sal and C_{16}TA/Sal [60] and by Hu et al. on TTAA/NaSal micelles [96], both using particle image velocimetry (PIV). One of the reasons for the few PIV studies lies in the fact that the critical shear rates are high (in general some tens of s^{-1}) and that under such conditions, measurements of flow velocities using seeding particles remain challenging. Figure 8 shows three cartoons of the velocity profiles determined at different times during a start-up experiment. The system placed under scrutiny was TTAA/NaSal at 1.7 mM and at 1:1 ratio between surfactant and aromatic counterions (weight concentration 0.10 wt. %) [96]. The gap of the Couette cell was 4 mm and the inner cylinder (gap position 0) was moving. After the inception of shear (Fig. 8a), the linear velocity profile for a homogeneous shear flow was observed. As the SIS began to grow from the inner wall (Fig. 8b), a progressively thicker region of uniform velocity developed, with a steeper velocity gradient near the outer cylinder. For long times (Fig. 8c) the velocity field remained uniform over most of the gap, with two thin and fast layers near the walls. Hu and coworkers concluded that, at steady state, the SIS fills most of the center of the gap and behaves as a "solid" body in rotation (plug flow) [96]. Although less documented than Hu et al.'s paper, the data from Koch et al. displayed typically the same effect, namely that the shear-induced structure was associated with a highly nonhomogeneous flow, with slippage at the walls [60]. Convincing evidence of wall slip was also reported by Sung et al. [58] in CPCl/NaSal solutions from direct rheological measurements.

2.5 Conclusion

In the preceding sections, we have shown that the surfactants listed in Table 1 share identical properties when submitted to shear: above a critical shear rate, a structure that is more viscous than the suspending solvent is induced, yielding an increase in the apparent viscosity of the fluid. In the following, we recapitulate the milestones that are important in the present experimental context, and suggest a minimal scenario for the transition.

1. *The local micellar structure does not change under shear*
   By restricting ourselves to the dilute case, it can be concluded that the rodlike micelles are unentangled at rest and in the Newtonian domain. There, the viscosity is close to, or a few times, that of water. Small-angle neutron scattering shows conclusive evidence that the cylindrical structure of the rods is preserved at all shear rates. The hypothesis suggested in the past, according to which the shear-thickening could originate from a modification of the local structure of the surfactant assemblies, can reasonably be ruled out [105, 110].
2. *Shear-thickening is associated with micellar growth*
   The structural modifications of the aggregates occur in contrast at a larger scale, namely at the scale of their length. Using light and neutron scattering, it was demonstrated that the shear-thickening transition is accompanied by a uniaxial growth of the micelles, which hence undergo a transition from rodlike to wormlike aggregates [79, 87, 90].
3. *The shear-induced structure is viscoelastic*
   The second indication of the wormlike micellar character of the SIS is its viscoelasticity. The viscoelasticity of the shear-induced phase was observed in stop flow experiments in a series of systems [52, 55, 59, 78, 85, 89, 108]. According to the definition of viscoelasticity [112], the long time seen in these experiments can be ascribed to the intrinsic relaxation of the shear-induced state. With this in mind, the Weissenberg number (the product of the shear rate and relaxation time) for these micellar fluids can be estimated. In Regimes II and III, the Weissenberg numbers reach values lying between 10 (at $\dot{\gamma}_c$) and 1000. Depending on the system, this range can go even higher, as in gemini 12-2-12 [89] or CTAT [108]. Hence, once the micelles have grown in size, they are directly brought to a state that is strongly sheared on the time scale of the fluid. At high Weissenberg numbers, the sheared solutions could undergo elastic instabilities, that could then generate more complex flows such as flows along the vorticity direction [113]. Three-dimensional flows associated with the shear-thickening in dilute regime have not been reported so far.

In Fig. 9, a schematic diagram accounts for a possible scenario of the shear-thickening transition. There, curve A denotes the apparent viscosity of a dilute surfactant solution containing nonoverlapping rodlike micelles (Newtonian), whereas curve B corresponds to the flow curve of the same solution, but for which the micelles are long and entangled (shear-thinning). At the transition rate, the fluid jumps from branch A to branch B. With decreasing shear rate, starting from the induced phase, the SIS vanishes reversibly as the micelles disassemble into short rodlike

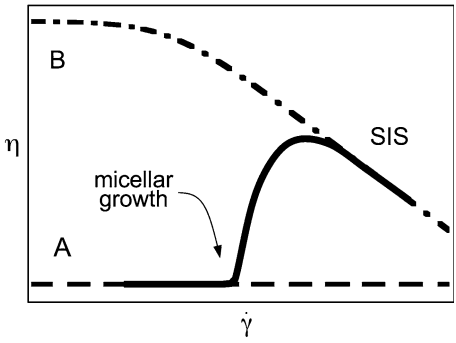

Fig. 9 Schematic diagram accounting for the shear-thickening transition in dilute surfactant solutions

aggregates. From this minimal scenario, it can be understood that the micelles are strongly aligned in the flow, or that the flow becomes nonhomogeneous [60, 96, 99] or turbulent in the shear-thinning regime [96, 98]. The hydrodynamic instabilities of dilute wormlike micelles and in turbulent flows remain one of the most promising issues of this field.

Concerning the mechanism of growth induced by shear, many theories and models were developed during the last three decades, and none of them were fully satisfactory. Most models were based on the assumption that the increase of viscosity was related to a shear-induced "gelation." Many phenomenological models were constructed assuming a banded state of coexisting gel and fluid phases [114, 115]. Some microscopic theoretical attempts had anticipated that "gelation" could be connected to a shear-induced micellar growth [116–118]. Concerning these earlier models, however, the predicted critical shear rates were too large as compared to the experimental values [108]. It is out of the scope of the present review to survey the theoretical treatments of the shear-thickening transition. We rather refer to recent and exhaustive reviews by Cates and Fielding [119] and by Olmsted [120].

The structural memory effects found in different systems (such as CTAT, gemini 12-2-12 and in the fluorocarbon surfactant C_8F_{17}), and discussed in the transient rheology section, suggest that the aggregation in the quiescent state and the thickening transition are interrelated. It is certainly not easy to conceive that dilute and very dilute solutions could exhibit exotic behaviors, in particular in reference to the self-assembly mechanism. One possible explanation would be that the surfactant solutions are in a metastable self-assembled state, due, for instance, to the long range electrostatic interactions. This metastable state could then be described as a coexistence state of of short rodlike aggregates and slowly evolving supramolecular structures, such as huge micelles or pieces of entangled network. This additional and unexpected populations of large micelles have been recently observed in two systems, again the gemini 12-2-12 studied by Schosseler and coworkers and in the fluorcarbon surfactant by Oehlschager et al. [93]. Light scattering performed on quiescent solutions have shown the coexistence of short, intermediate, and very large micelles, which respective populations varied with the thermal and shear histories. It remains now to demonstrate that these large structures are playing the role of initiators for the shear-thickening transition, as well as to understand the metastability of the different self-assemblies.

3 Shear Banding Transition in Semidilute and Concentrated Giant Micelles

3.1 Introduction

This part is devoted to the nonlinear rheology of semidilute and concentrated giant micelles systems. In the semidilute regime, characterized by concentrations ranging typically from 0.1 to $\simeq$10 wt. %, wormlike micelles form a viscoelastic network and, are supposed, by analogy with polymers, to follow simple scaling laws [25, 40]. In the concentrated regime, corresponding typically to weight concentrations between $\simeq$10 wt. % and c_{I-N}, the isotropic-to-nematic phase boundary, the mesh size of the entangled micellar network becomes of the order of or shorter than the persistence length (see Fig. 1).

When submitted to simple shear flow, giant semidilute and concentrated micelles show original nonlinear responses. A number of experimental publications suggest that micellar solutions undergo a shear-banding transition. This transition, due to the coupling between the internal structure of the fluid and the flow, is usually associated with a new mesoscopic organization of the system. In turn, the modification of the supramolecular architecture of the fluid affects the flow itself and generates shear localization effects generally characterized by a splitting of the system into two macroscopic layers bearing different shear rates and stacked along the velocity gradient direction.

This transition from a homogeneous towards a nonhomogeneous flow has been reported in complex fluids of various microstructure such as lyotropic micellar and lamellar phases [44, 121, 122], triblock copolymers solutions [123, 124], viral suspensions [125], thermotropic liquid crystal polymers [126], electro-rheological fluids [127], soft glassy materials [128], granular materials [129, 130], or foams [131–133].

Among these systems, the shear banding flow of reversible wormlike micelles is particularly well documented [44]. The rheological signature of this type of flow has been observed for the first time in the pioneering work of Rehage et al. [28]: the measured flow curve $\sigma(\dot{\gamma})$ is composed of two stable branches respectively of high and low viscosities separated by a stress plateau at $\sigma = \sigma_p$ extending between two critical shear rates $\dot{\gamma}_1$ and $\dot{\gamma}_2$ (see Fig. 10a). When the imposed shear rate $\dot{\gamma}$ is lower than $\dot{\gamma}_1$, the state of the system is described by the high viscosity branch which is generally shear-thinning: the micellar threads are slightly oriented with respect to the flow direction and the flow is homogeneous. For macroscopic shear rates above $\dot{\gamma}_1$, the flow becomes unstable and evolves towards a banded state where the viscous and fluid phases coexist at constant stress σ_p (see Fig. 10b). The modification of the control parameter is only supposed to affect the relative proportions f and $1-f$ of each band according to a simple lever rule that results from the continuity of the velocity at the interface:

$$\dot{\gamma} = f\dot{\gamma}_1 + (1-f)\dot{\gamma}_2. \tag{3}$$

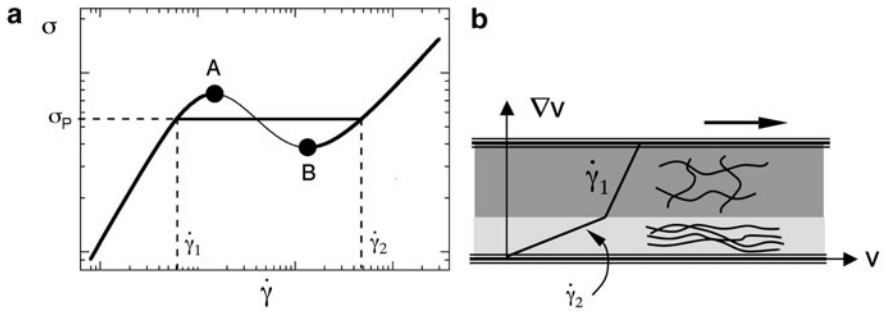

Fig. 10 (**a**) Nonmonotonic constitutive relation for giant micelles composed of two stable branches separated by an unstable region AB. The corresponding steady-state flow curve presents a stress plateau at $\sigma = \sigma_p$, extending between two critical shear rates $\dot{\gamma}_1$ and $\dot{\gamma}_2$, and associated with the shear-banding transition. (**b**) Scheme of the shear-banding scenario in giant micelles systems

Above $\dot{\gamma}_2$, the system is entirely converted into the fluid phase: the induced structures are strongly aligned along the flow direction and the homogeneity of the flow is recovered. This scenario, due to the existence of a nonmonotonic relation between the shear stress and the shear rate as schematized in Fig. 10, was predicted by Cates and coworkers more than 15 years ago [134]. Since then, it has been the subject of intense experimental and theoretical studies. From an experimental point of view, shear banding has been identified unambiguously in wormlike micelles using various techniques probing either the local flow field or the structure of the system.

In the following, we review the phenomenology of shear banding flow in semidilute and concentrated wormlike micelles. This part is organized as follows. In Sect. 3.2, we describe the mechanical signature of the shear-banding transition. Section 3.3 is devoted to the characterization of the local flow field, while in Sect. 3.4, we focus on the structural properties of the banded state.

3.2 Nonlinear Rheology

3.2.1 Steady-State Rheology

Standard Behavior

In order to illustrate the typical nonlinear mechanical response of wormlike micelles under steady shear flow, we chose to focus on the cetylpyridinium (CPCl)/sodium salicylate (NaSal) system. It is often considered as a model system since it follows the right scaling laws for the concentration dependence of the static viscosity and plateau modulus [32]. Moreover, for concentrations ranging from 1 to 30 wt. %, the samples behave, in the linear regime, as almost perfect Maxwellian elements with a single relaxation time τ_R and a plateau modulus G_0. This system has been

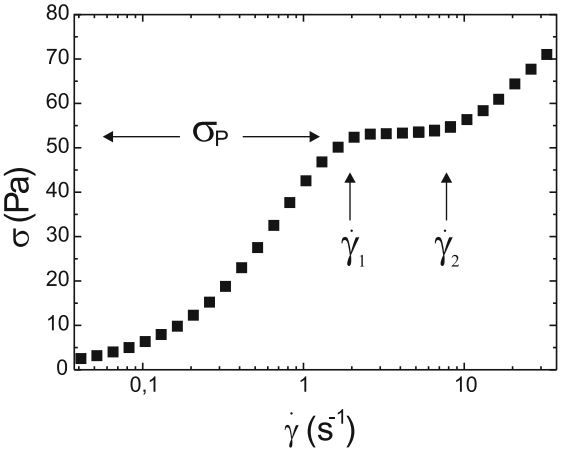

Fig. 11 Experimental steady-state flow curve of a semidilute binary mixture made of cetylpyridinium chloride/sodium salicylate diluted in 0.5 M NaCl brine at a temperature of 25 °C. The total weight fraction is 6.3 wt. % and the molar ratio R =[Sal]/[CPCl]= 0.5. The shear stress is measured under strain-controlled conditions in a cone and plate geometry

extensively studied during the last two decades [28,33,135–141] and the description of its mechanical behavior is certainly one of the most complete.

Figure 11 displays, on a semilogarithmic plot, the evolution of the shear stress σ as a function of the shear rate $\dot{\gamma}$ for a sample at a total weight fraction $c = 6.3$ wt. % obtained under strain-controlled conditions in a cone and plate geometry [33]. This flow curve is made up of two increasing branches separated by a stress plateau extending between two critical shear rates $\dot{\gamma}_1$ and $\dot{\gamma}_2$. The high viscosity branch is Newtonian at very low shear rates and becomes shear-thinning when approaching the first threshold $\dot{\gamma}_1$, whereas the low viscosity branch above the second critical shear rate $\dot{\gamma}_2$ is usually purely shear-thinning, indicating that the constitutive behavior of the induced structures is non-Newtonian. At the critical shear rate $\dot{\gamma}_1$, the shear stress reaches a value $\sigma = \sigma_p$ and the flow curve exhibits a strong change of slope followed by a stress plateau that can extend over several decades in shear rates, depending on the composition of the sample. In some cases, the stress plateau presents a significant slope and is generally well fitted by a power-law $\sigma \sim \dot{\gamma}^{\alpha}$ with exponent α between 0.1 and 0.3. This shear rate dependence is usually explained by the coupling between flow and concentration fluctuations [142, 143].

Various shear histories have been applied in order to test the robustness of the stress plateau. The latter has been found to be unique and history independent. This reproducibility is a crucial feature of the nonlinear rheology of wormlike micellar systems [33, 138, 140, 144].

The mechanical behavior described above concerns most semidilute wormlike micelles. The situation for concentrated samples is analogous with minor changes: the low shear rate branch is purely Newtonian and the transition towards the stress plateau is more abrupt [137].

Table 2 Systems of wormlike micelles known to exhibit a stress plateau in their steady flow curve

Surfactant	Additive	Salt	Conc. regime	Experiment	References
CPCl	NaSal		sd	NMR, FB, PIV, SANS, SALS	(a)
CPCl	NaSal	NaCl	sd/c	NMR, FB, DLS, PTV, PIV, USV, FI	(b)
C_{16}TAB			c	NMR, FB, USV, SANS	(c)
$CPClO_3$		$NaClO_3$	c	SANS	(d)
C_{16}TAB	NaSal		sd	FB, USV, SANS, LSI, SALS	(e)
C_{16}TAB		KBr	sd/c	FB	(f)
C_{16}TAB		$NaNO_3$	sd/c	FB, LSI, SALS	(g)
CPCl	Hex	NaCl	c	SANS, FB	(h)
CTAT			sd/c	...	(i)
CTAT		NaCl	sd	...	(j)
C_{16}TAC	NaSal		sd/c	FB	(k)
C_{12}TAB	NaSal		sd	...	(l)
SDS		$Al(NO_3)_3$	sd	...	(m)
EHAC		NH_4Cl	sd	...	(n)
EHAC		NaCl	sd	FB, SANS, SALS	(o)
EHAC	NaSal		sd	FB, SANS, SALS	(p)
CTAHNC			sd	...	(q)
CTAT	SDBS		sd	FB, SANS	(r)
SDES		$AlCl_3$	sd	...	(s)
SDS	LAPB	NaCl	sd	...	(t)
CTAVB			sd	...	(u)

Column 5 lists the experimental techniques that were used to study shear-banding. The abbreviations are "sd" for semidilute and "c" for concentrated. The letters in the last column denote sets of references detailed below. (a) [28, 135, 136, 140, 141, 145–154], (b) [33, 137–139, 150, 151, 155–165], (c) [166–172], (d) [173], (e) [23, 30, 72, 154, 174–187], (f) [30, 188–191], (g) [144, 165, 192–196], (h) [197–199], (i) [80, 200–205], (j) [200, 206, 207], (k) [208–211], (l) [212], (m) [213], (n) [49], (o) [214], (p) [214, 215], (q) [95, 216], (r) [217, 218], (s) [219], (t) [220], (u) [221]

Hence, the stress plateau in the flow curve $\sigma(\dot{\gamma})$ is the central feature of the nonlinear rheology semidilute and concentrated giant micelles systems and appears as the mechanical signature of the shear-banding transition. The first experimental evidence for such a behavior is due to Rehage and Hoffmann [28] on the semidilute CPCl (100 mM)/NaSal (60 mM) ($c = 4.5$ wt. %) solution. From that time, the stress plateau in wormlike micelles has generated an abundant literature. It is now reported, using various flow geometries such as cylindrical Couette, cone and plate, plate and plate or vane-bob and capillary rheometer, in many other surfactant systems with or without additive and/or salt as illustrated in Table 2.

If normalized shear stress σ/G_0 and shear rate $\dot{\gamma}\tau_R$ are introduced, it is possible to summarize the overall nonlinear rheological behavior measured at different concentrations and temperatures on a master dynamic phase diagram as shown in Fig. 12 [137]. The flow curve at 21 wt. %, a concentration close to the I–N transition, makes the link with the concentrated regime. As concentration decreases, stress

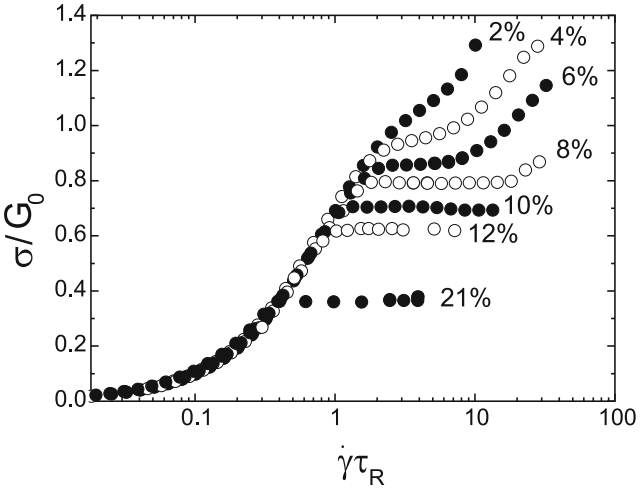

Fig. 12 Generalized "flow phase diagram" obtained for CPCl/NaSal system derived from a superimposition between flow curves at different concentrations and temperatures, using normalized coordinates σ/G_0 and $\dot{\gamma}\tau_R$. No stress plateau is observed beyond the critical conditions $\sigma_p/G_0 > 0.9$ and $\dot{\gamma}\tau_R \simeq 3 \pm 0.5$. From Berret et al. [137]

plateaus are still observed, but the normalized stress and shear rate at which the discontinuity occurs are shifted to larger values. At 6 wt. % and below, the transition between the high viscosity branch and the stress plateau becomes much smoother and the shear stress levels off without discontinuity. Beyond the following critical conditions $\sigma_p/G_0 > 0.9$ and $\dot{\gamma}\tau_R \simeq 3 \pm 0.5$, the stress plateau is replaced by an inflexion point. In other words, the above critical conditions suggest that, by choosing the concentration, temperature or salt content adequately, it is possible to find a stress plateau comprised between $\sigma_p/G_0 \simeq 0$ and 0.9, and of onset $\dot{\gamma}\tau_R$ between 0 and 3. A striking point in Fig. 12 is that the set of normalized flow curves is strongly reminiscent of the phase diagram of a system undergoing an equilibrium phase transition.

All the data presented and discussed until now have been gathered with the shear rate as control parameter. However, numerous studies dealing with the effect of an imposed shear stress have been performed both on semidilute and concentrated wormlike micellar systems [30, 140, 166, 188, 192, 208, 215, 217, 219, 222]. Steady-state flow curves obtained in stress-controlled mode have been found to coincide with flow curves measured under strain-controlled conditions. However, there is a major difference for systems with flat plateaus: it is not possible to reach a stationary coexistence state at imposed stress, since the system directly switches from the low to the high shear rate branch.

Finally, it is also important to emphasize that the nonlinear rheology of viscoelastic surfactant solutions is characterized by the existence of normal stresses of nonnegligible magnitude. In steady-state flow, a nonzero first normal stress difference N_1 has been detected once the first stable branch becomes shear-thinning. N_1 was found to increase with $\dot{\gamma}$ and a slight change of slope was observed at the

onset of the banding regime ($\dot{\gamma} > \dot{\gamma}_1$) [28, 149, 161, 220]. Normal stresses in shear-banded flows are much less documented than their shear counterpart. However, they are well-known to drive elastic instabilities for sufficiently high shear rates [113]. Their role is probably essential to explain some fluctuating behaviors observed in shear-banded flows of wormlike micelles [223–225].

The steady-state mechanical behavior described in this paragraph is representative for entangled wormlike micelles solutions. In the semidilute concentration range, however, a few exceptions to this standard behavior have been reported, as briefly discussed below.

Nonstandard Behaviors

In this paragraph, we mention some marginal rheological behaviors encountered in semidilute wormlike micelles. This list is not exhaustive but allows the illustration of the rheological diversity in these systems.

If the stress plateau is the most encountered feature in the rheology of giant micelles, it is also possible to find solutions for which the Newtonian branch is followed by shear-thinning where the flexible chains simply align along the flow direction as in the case of classical polymer solutions. Such a phenomenology has been reported for samples with low or high concentrations of strongly binding counterions [28, 149, 211].

Another system showing a nonstandard behavior is the equimolar solution made of cetylpyridinium chloride and sodium salicylate, the concentration of each component being fixed at 40 mM. This corresponds to a total weight fraction of 2.1 wt. %. This peculiar system has been extensively studied, especially by Fischer's group during the last few years [169, 222, 226–229] and more recently by Marin-Santibanez et al. [230]. Its nonlinear rheology has been investigated in various flow geometries: at very low shear rates, the solution is Newtonian and then shear-thins, the stress smoothly reaching a pseudo-plateau but without evidence of shear-banding. This regime is followed by a pronounced shear-thickening behavior above a reduced shear rate $\dot{\gamma}\tau_R \simeq 3$ associated with vorticity banding and complex dynamics. We will come back on that point in the section dedicated to time-dependent evolutions.

At the lowest concentrations in the class of semidilute systems, typically ranging from 0.1 to 1 wt. %, a simple shear flow can lead to strong thickening above a critical stress [57, 96, 98, 99]. This is the case of the TTAA/NaSal solutions, already discussed in the part devoted to the shear-thickening transition (Sect. 2). The overall rheological behavior of such systems resembles in some respect that of the equimolar CPCl/NaSal 40 mM solution just evoked above. At concentrations around 10 mM, the micellar network is entangled and the static viscosity is larger than that of the solvent by a factor of 10–1000. As the shear rate is increased, there is first shear-thinning and an abrupt shear-thickening at the critical stress. In addition, concomitantly with the shear-thickening transition, shear-induced structures grow from the inner cylinder, as in the shear-banding transition.

Finally, Hoffmann and coworkers [231] have investigated a binary mixture of hexadecyloctyldimethylammonium bromide (C_{18}–C_8DAB) in water at a concentration of 2.3 wt. %. The flow curve of this solution does not present a stress plateau. However, using small angle neutron scattering experiments under simple shear flow, the authors argued that this system undergoes an isotropic-to-hexagonal transition, where cylindrical micelles of different lengths coexist. The short ones contribute to the isotropic phase, while the long ones ensure the long range hexagonal order. This flow-induced transition presents strong similarities with the I/N transition under shear in concentrated wormlike micelles but without the mechanical signature described in Sect. 3.2.1

3.2.2 Time-Dependent Rheology

During the past decade, many authors have paid close attention to the evolution of the shear stress as a function of time in systems exhibiting a stress plateau. The aim was to identify the mechanisms responsible for the shear-banding transition. In most cases, shear stress time series in response to steady shear rate consists of a slow transient (compared to the relaxation time of the system) before reaching steady state. Nonetheless, more complex fluctuating behaviors such as erratic oscillations suggestive of chaos or periodic sustained oscillations of large amplitude have been observed in peculiar systems.

Standard Transient Behavior

The time-dependent mechanical response is collected from start-up of flow experiments: at $t = 0$, a step-like shear rate is suddenly applied to the sample at rest and the evolution of the shear stress as a function of time is recorded until steady-state is achieved. For imposed shear rates below $\dot{\gamma}_1$ and belonging to the Newtonian part of the high viscosity branch, the shear stress follows a monoexponential growth towards steady-state, with a characteristic time corresponding to the Maxwell time of the system [28, 138]. When the applied shear rate lies in the shear-thinning region of the high viscosity branch, the stress response shows an overshoot at short time before reaching steady-state, a feature classically observed in concentrated solutions of entangled polymers [232, 233].

The start-up curves for various imposed shear rates in the plateau region are displayed in Fig. 13. For all investigated shear rates, the shear stress exhibits an overshoot at short times, the amplitude (σ_{os}) of which increases significantly with $\dot{\gamma}$, followed by a slow relaxation towards a stationary value σ_{st}. This relaxation process comprises a latency period during which the stress remains practically constant at a value $\sigma = \sigma_M$ and then, a decay of sigmoidal shape whose time scale greatly exceeds the terminal relaxation time of the solution (Fig. 13a). The characteristic time τ_N of this slow relaxation diminishes with $\dot{\gamma}$ while σ_M increases (Fig. 13b). When the mean

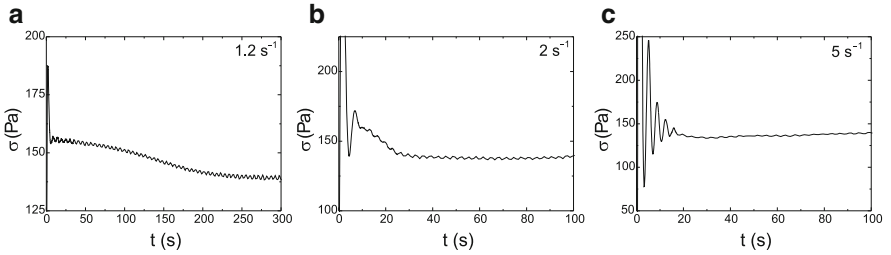

Fig. 13 Transient shear stress recorded after different step shear rates (**a**) $\dot{\gamma} = 1.2\ \mathrm{s}^{-1}$, (**b**) $2\ \mathrm{s}^{-1}$, and (**c**) $5\ \mathrm{s}^{-1}$ for a semidilute sample of CPCl/NaSal (12 wt. %) in 0.5 M NaCl brine at a temperature of $T = 20.3\,^{\circ}\mathrm{C}$. All the applied shear rates belong to the plateau region. Reprinted from Berret [138]

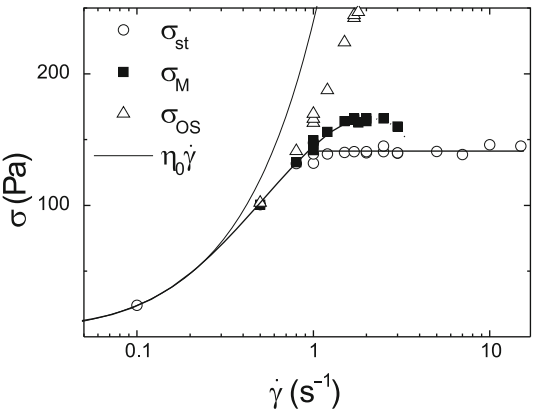

Fig. 14 Stress overshoot σ_{os}, initial shear stress before the onset of the long-time sigmoidal relaxation σ_M and steady-state shear stress σ_{st} gathered from start-up of flow experiments on the semidilute sample of CPCl/NaSal (12 wt. %) in 0.5 M NaCl brine. The purely Newtonian behavior ($\eta_0\dot{\gamma}$) has been added for comparison. Reprinted from Berret [138]

shear rate is incremented, $\sigma(t)$ shows oscillations at short times that precede the long sigmoidal decay. The variations of σ_{os}, σ_{st}, and σ_M with the mean shear rate are given in Fig. 14. The $\sigma_M(\dot{\gamma})$ curve provides evidence for the existence of a metastable branch in which the system is trapped on time scales much longer than the relaxation time τ_R. At higher strain rates, the stress response is dominated by damped oscillations (Fig. 13c). The period of the oscillations has been found to decrease with $\dot{\gamma}$ but, in contrast to nematic wormlike micelles, it does not scale with the inverse shear rate (see Sect. 4). For concentrated samples, a purely monoexponential decay has been observed [199]. Note that such transients are often prolonged by a small undershoot before the steady-state is achieved [33, 140, 144, 157, 191, 194–196].

This type of time-dependent behavior has been observed in various semidilute [23, 33, 138, 140, 144, 150, 157, 161, 174, 177, 180, 191, 195, 196, 203, 220] and

concentrated systems [33, 171, 172, 199]. The sigmoidal decay has been modeled by a stretched exponential of the form [33, 138, 199]:

$$\sigma(t) = \sigma_{st} + (\sigma_M - \sigma_{st}) \exp\left[-\left(\frac{t}{\tau_N}\right)^{\alpha}\right] \tag{4}$$

Depending on the system and on the applied shear rate, α has been found to vary between 1 and 4 [33, 138, 140, 144, 191, 199]. Such kinetics suggests metastability reminiscent of equilibrium first-order phase transitions and has been originally interpreted by Berret and coworkers [33,138] in terms of nucleation and one-dimensional growth of a fluid phase containing highly ordered entities. Other mechanisms involving the slow drift of a sharp interface to a fixed position in the gap of the cell have also been advanced to explain this slow kinetics [190, 234, 235].

Up to now, we have described the time-dependent behavior of the shear stress as a transient towards a steady-state value σ_{st}. However, the notion of steady-state shear stress has to be made clear. Strictly speaking, at long times, $\sigma(t)$ is not rigorously stationary since it presents fluctuations around an average value defined as σ_{st}. The relative amplitude of the fluctuations never exceeds 1% in most of cases. However, some authors have reported fluctuations of stronger amplitude (typically between 5% and 25% of the steady-state signal), revealing complex stress dynamics [80, 159, 169] that we address in the following paragraphs.

Rheochaos

Bandyopadhyay et al. focused on the time-dependent behavior of semidilute solutions of hexadecyltrimethylammonium *p*-toluenesulfonate (CTAT) at weight fractions around 2 wt. % in water, with and without addition of sodium chloride (NaCl). This system is well known to exhibit stress plateau or pseudo-plateau in the flow curve for concentrations ranging between 1.3 and 20 wt. % [80, 203, 206, 207, 236].

Typical time sequences observed in this system are illustrated in Fig. 15. In this data set, the shear rate is kept fixed and the shear stress is recorded as a function of time with the temperature as the control parameter. From the highest temperatures, the stress temporal patterns appear successively periodic and then quasi-periodic with two dominant frequencies (Fig. 15b, c). At lower temperature, the time series still present quasi-periodicity but disrupted by chaotic bursts, typical of intermittency (Fig. 15d). If the temperature is further decreased, the signal becomes finally chaotic (Fig. 15e). The existence of deterministic low-dimensional chaos generating erratic fluctuations in the time series is proved by positive Lyapunov exponent [237] and fractal correlation dimension greater than 2. The route to rheochaos is via type-II temporal intermittency with a Hopf bifurcation [207]. Similar time sequences for the shear rate have been gathered by decreasing the temperature at fixed stress. In that case, the route to rheochaos was found to be of type-III intermittency with period doubling bifurcation [207].

The route to rheochaos can thus be tuned by varying the temperature and consequently the mean micellar length at fixed stress or shear rate [207]. These results

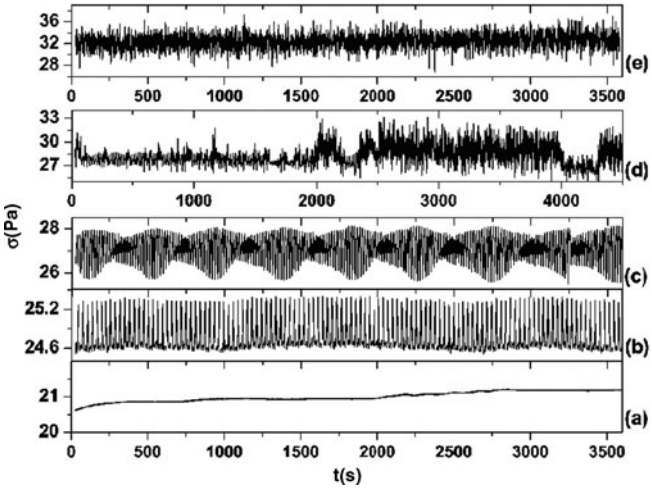

Fig. 15 Stress time series recorded after start-up of flow experiment at a fixed shear rate $\dot{\gamma} = 25\,s^{-1}$ for different temperatures (**a**) $T = 31.5\,°C$, (**b**) $T = 28.8\,°C$, (**c**) $T = 27.2\,°C$, (**d**) $T = 26.5\,°C$, (**e**) $T = 26\,°C$. The sample under scrutiny is made of hexadecyltrimethylammonium *p*-toluenesulfonate (CTAT) at 2 wt. % mixed with 100 mM NaCl in water. The time sequences are found to be (**a**) time-independent, (**b**) periodic, (**c**) quasi-periodic, (**d**) intermittent and (**e**) chaotic. Reprinted with permission from R. Ganapathy and A.K. Sood [207]

agree with recent theoretical predictions due to Fielding et al. [238] using the Diffusive Johnson Segalman (DJS) model and adding a coupling of the flow variables with the mean micellar length. Coupling between flow and concentration fluctuations is also supposed to play a major role in the observed complex dynamics [200, 236].

The same type of irregular time variations of the shear stress (respectively shear rate) at imposed shear rate (respectively shear stress) have been reported for a given temperature. In both cases, the sequence of Fig. 15 has been reproduced by increasing the control parameter [80, 203, 206].

Note that rheochaos has also been observed in solutions of mixed anionic-zwitterionic surfactants [220] and in other systems including shear-thickening wormlike micelles [239], lamellar, onion, and sponge surfactant phases [156, 240–243] and dense colloidal suspensions [244].

Case of the Vorticity Banding

In Sect. 3.2.1, we made reference to a complex constitutive behavior for an equimolar solution of CPCl/NaSal experiencing a shear-thinning to shear-thickening transition. The dynamics of this system has been extensively studied both in strain- and stress-controlled modes. Huge sustained oscillations of the measured quantities (shear and normal stresses or shear rate) as a function of time have been observed in

the shear-thickening regime [169, 227]. The authors showed that these oscillations are correlated with the existence of a banding pattern organized along the vorticity direction and exhibiting a complex dynamics (see Sect. 3.4.2). Note that, unlike the classical shear-thickening transition encountered in dilute surfactant systems and discussed previously, there is no induction time for the shear-induced structures to grow.

Similar stress dynamics has been observed in a semidilute solution of C_{16}TAB (50 mM) and NaSal (100 mM) ($c = 3.4$ wt. %) that also exhibits apparent shear-thickening [183]. However, for this system, the phenomenology is different insofar as the shear-thinning region preceding the apparent thickening transition is characterized by a stress plateau and gradient shear-banding. Besides, Decruppe et al. did not observe vorticity structuring in that case, the flow remaining homogeneous [187].

3.3 Structure of the Flow Field: Velocimetry

To elucidate the shear-banding scenario in wormlike micelles, different velocimetry techniques with high spatial resolution, typically between 10 and 50 µm, such as nuclear magnetic resonance (NMR) velocimetry, particle image velocimetry (PIV), particle tracking velocimetry (PTV), photon correlation spectroscopy (DLS), and ultrasonic velocimetry (USV) have been developed. All provide the velocity component along the flow direction taken from a one-dimensional slice across the gap. For details on these techniques, the reader is invited to refer to [245, 246].

3.3.1 Long-Time Response: Time-Averaged Velocity Profiles

Semidilute Systems

The early velocimetry studies of shear-banding flow in wormlike micellar systems have been performed by Callaghan's group using NMR imaging of the semidilute CPCl (100 mM)/NaSal (60 mM) ($c = 4.5$ wt. %) solution in different flow geometries [135, 145–148, 150]. The method is based on a combination of magnetic field gradient pulses and resonant radio-frequency pulses to encode the NMR signal both from the nuclear spin position as well as translational displacement. The typical spatial resolution is 30 µm. The acquisition times typically vary from 30 min to 4 h, the observed banding structures resulting from long time averages. In addition, the use of a specific encoding method allows the determination of pointwise velocity distribution [246].

In millimetric pipe flow, the increase of the flow rate from the Newtonian to the plateau regime was characterized by a transition from a nearly parabolic Poiseuille profile to an almost flat velocity profile with high shear bands near the tube walls, clearly distinguishable from slip [135]. The thickness of this high shear rate band

was found to grow with the apparent shear rate [139]. Broadening of the velocity distribution revealed fluctuations of the flow field on time scales larger than the encoding time (50 ms) and shorter than the total duration of the experiment [139,146]. Similar velocity profiles were also obtained from PIV measurements in capillary flow [152]. From this local description, the authors were able to reconstruct a complete macroscopic flow curve, consistent with that gathered from bulk rheology. Note that, for the PIV technique, a radial laser sheet illuminates a cross section of the sample in a plane $(\mathbf{v}, \nabla v)$. Images are taken from 90° to the laser sheet and velocity profiles are extracted from spatial correlation between pairs of images.

In cone-and-plate geometry, where the stress distribution is homogeneous in the small gap approximation, Britton et al. showed that the flow field along the plateau region was organized in three bands as displayed in Fig. 16 [150]. The gray scale images clearly show the presence of a central high shear band flanked by two adjacent low shear regions for all applied shear rates. Shear rate profiles computed along the white line point out the mid-gap position of the high shear band. As the mean applied shear rate is incremented, the high shear band expands in width at a constant maximum shear rate around $60\,\mathrm{s}^{-1}$. This value is not consistent with the critical shear rate $\dot{\gamma}_2 \simeq 100\,\mathrm{s}^{-1}$ at the upper limit of the stress plateau. This discrepancy has been ascribed to local fluctuations of the flow field. Velocity fluctuations of different time constants have been observed, depending on sample composition [139].

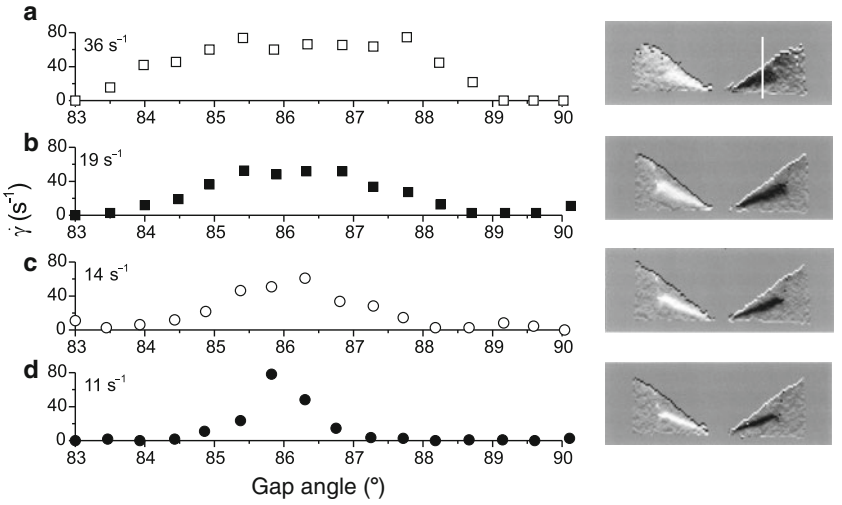

Fig. 16 Time-averaged shear rate profiles and corresponding gray scale images for the CPCl (100 mM)/NaSal (60 mM) ($c = 4.5$ wt. %) solution at $T = 25°$C, measured using NMR velocimetry in a 7° cone-and-plate at different applied macroscopic shear rates (**a**) $11\,\mathrm{s}^{-1}$, (**b**) $14\,\mathrm{s}^{-1}$, (**c**) $19\,\mathrm{s}^{-1}$, and (**d**) $36\,\mathrm{s}^{-1}$. The profiles are extracted along a line (*in white*) at fixed radius from the cone axis as illustrated on the images at *right*. The gray scale indicates the shear rate in arbitrary units. Note the opposite sign shear for the receding and advancing segments of fluid on opposite sides of the gap. The "free" surface of the fluid is in contact with a containment jacket in Teflon, leading to vanishing of the gradient banding structure beyond a critical radius. Each measurement requires an acquisition time of about 2 h. Reprinted with permission from Britton et al. [150]

In Couette geometry, a thin high-shear band ($\simeq$30 μm) near the inner cylinder but in the bulk of the fluid as well as wall slip have been detected [145, 146]. A different picture emerged from the NMR-study of the 10 wt. % CPCl/NaSal in brine [159]: the shear-banding structure was composed of two macroscopic layers bearing different shear rates, the lower one being compatible with the $\dot{\gamma}_1$ value. The width of the high shear rate band was found to increase significantly with the applied shear rate while wall slip was observed at the moving wall. Enhanced local velocity fluctuations have been reported in the high shear rate region at the vicinity of the inner rotating cylinder.

Very similar time-averaged velocity profiles in Couette geometry have also been determined using heterodyne dynamic light scattering (DLS). This technique, developed by Salmon and coworkers, is based on the analysis of the correlation function of the interference signal generated by the mixing of a reference beam and the light scattered by a small volume of sample (typically $(50\,\mu m)^3$) [247]. The scattering signal is enhanced by nanoparticles embedded in the fluid. A few seconds are required to yield the mean velocity for each scanned scattering volume, the total duration for the acquisition of a complete profile reaching a few minutes. This technique has been implemented to examine the precise local structure of the flow in the much-studied 6 wt. % CPCl/NaSal in brine [155, 156]. Figure 17 summarizes the typical velocity profiles gathered for various applied shear rates all along the flow curve, the latter being recorded in a simultaneous way. For $\dot{\gamma} < \dot{\gamma}_1$, the velocity profile is continuous and nearly linear, with a slight curvature typical of a weakly shear-thinning fluid, consistent with the evolution of the high-viscosity branch. For $\dot{\gamma}_1 < \dot{\gamma} < \dot{\gamma}_2$, the velocity profiles become discontinuous, and are composed of two linear regions of well-distinct slopes. The flow is then nonhomogeneous with two coexisting layers supporting very differing local shear rates, the values of which are compatible with $\dot{\gamma}_1$ and $\dot{\gamma}_2$. Note that rapid temporal fluctuations of the flow field in the high shear

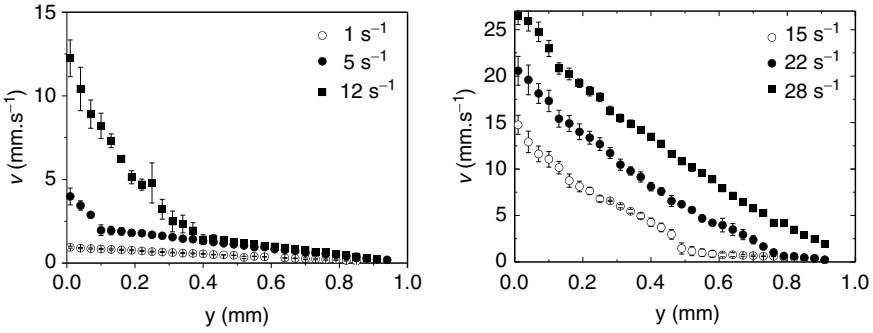

Fig. 17 Velocity profiles obtained using heterodyne dynamic light scattering for different mean shear rates along the flow curve: $\dot{\gamma} = 1\,s^{-1}$, $\dot{\gamma} = 5\,s^{-1}$, $\dot{\gamma} = 12\,s^{-1}$, $\dot{\gamma} = 15\,s^{-1}$, $\dot{\gamma} = 22\,s^{-1}$, and $\dot{\gamma} = 28\,s^{-1}$. For reference, the stress plateau extends from $\dot{\gamma}_1 \simeq 2.5\,s^{-1}$, and $\dot{\gamma}_2 \simeq 26\,s^{-1}$. The sample is 6 wt. % CPCl/NaSal in brine and is sheared in a Couette device at a temperature of 21.5 °C. The inner rotating and outer cylinders are marked, respectively by the positions $y = 0$ and $y = 1$ mm. The *errors bars* are representative of temporal fluctuations. Reprinted with permission from Salmon et al. [156]

rate band were reported. The increase of the applied shear rate $\dot{\gamma}$ along the stress plateau only affects the relative proportions f and $1-f$ of both bands: $1-f$ was found to increase linearly with $\dot{\gamma}$, hence satisfying the classical lever rule (Eq. 3). Finally, for $\dot{\gamma} > \dot{\gamma}_2$, the flow appears homogeneous again: the velocity profiles are characteristic of a strongly shear-thinning fluid, consistent with the evolution of the low viscosity branch. These experiments provided evidence for the classical shear-banding scenario invoked in the introduction (Sect. 3.1).

This type of velocity profiles, showing the coexistence of two differently sheared regions, the relative proportions of which vary with the applied shear rate, has also been measured using PIV and USV in Couette geometry on CPCl/NaSal in brine [157, 158] and C_{16}TAB/NaSal [187]. However, other features have sometimes been reported, including organization of the high shear band into multiple bands, variation of the local shear rate in each band with the control parameter, and wall slip at the moving inner wall.

Concentrated Systems

The structure of the flow field has also been explored in the concentrated regime. Fischer et al. carried out NMR velocimetry experiments in Couette geometry on a sample of C_{16}TAB/D_2O at 20 wt. %, a concentration just below c_{I-N}. For the investigated mean shear rates in the plateau region, the authors identified wall slip at the inner moving wall together with the following banding sequence: low-high-low shear rate bands stacked from the inner to the outer cylinder [169, 170]. The shape of the velocity profile near the moving inner cylinder was interpreted as evidence for near rigid body motion. As we shall see later in the section devoted to the microstructure of the coexisting phases, the comparison of these velocity profiles with ordering profiles simultaneously gathered from NMR spectroscopy experiments led the authors to argue that, surprisingly, the induced nematic state is a state of high viscosity, possibly associated with mesoscale ordering. In addition, local fluctuations of the flow field were suggested from the analysis of the velocity distribution at each pixel across the gap.

Bécu et al. studied the same system using high-frequency USV. This technique, developed by Manneville and coworkers [248], is based on cross-correlation of high frequency ultrasonic signals backscattered by the moving fluid. The signals consist of ultrasonic speckles resulting from the interferences of echoes from micrometric scatterers suspended in the fluid. The displacement of the scatterers is estimated from the time shift between two successive echoes. Full velocity profiles are recorded every 0.02–2 s, depending on the shear rate, with a spatial resolution of 40 µm. By averaging velocity profiles over 100 s, the authors observed a similar banding sequence, with an apparently unsheared region at the vicinity of the inner moving cylinder where the fluid velocity is slightly larger than the rotor velocity [172]. Their interpretation of these peculiar profiles differed somewhat from the previous one, incriminating a three-dimensional flow instability. We will come back on that point in Sect. 3.3.2.

Thereby, all these experiments confirm that the stress plateau in semidilute and concentrated micellar solutions is effectively associated with nonhomogeneous flow. They also reveal the existence of fluctuations of the flow field and address the question of the role played by wall slip. However, a unified picture of shear-banding has not emerged from the measurement of these time-averaged velocity profiles. A spatio-temporal approach with enhanced resolution is then required to get a better description of the shear-banding transition. Taking into account this need for high temporal resolution to follow the dynamics of the flow field, some groups have improved their velocimetry technique [249], while others have developed new powerful probes [157, 158, 248].

3.3.2 Time-Resolved Velocity Profiles

Transient Behavior

The early stages of banded-state formation have been studied on different solutions of CPCl/NaSal in brine [157, 158]. Using a PTV method, Hu et al. investigated the kinetics of shear-banding on the CPCl/NaSal (6.3 wt. %) in 0.5 M NaCl brine [157]. PTV only differs from PIV by the image processing, which is based on particle tracking rather than spatial correlation. This yields an improved spatial resolution ($\simeq$10 µm). Interestingly, the time evolutions of the velocity profiles and the shear stress have been monitored simultaneously, providing information on the correlation between local and global rheology. The transient stress response after start-up of flow of this system has been discussed in Sect. 3.2.2.

Figure 18 illustrates the corresponding transient velocity profiles. For $t < \tau_R$, the velocity profiles are linear across the gap of the Couette device: the flow is homogeneous with no wall slip at the walls (see Fig. 18a). When the stress overshoot occurs, the local behavior is found to depend on the applied shear rate. For huge overshoots, significant wall slip is detected at the inner wall, and the velocity profile takes an abnormal shape ($t = 0.9$ s). During the short-time relaxation of the stress overshoot, the homogeneous flow is restored. The velocity profile appears then slightly curved ($t = 2$ s), the local shear rate increasing towards the inner wall and decreasing towards the outer wall. This process has been ascribed to coupling between stress gradient inherent to the flow geometry and chain disentanglement. When the local shear rate at the outer wall reached the critical value $\dot{\gamma}_1$ ($t \simeq 3.6$ s), the low shear band begins to grow. The expansion of the low shear band towards the inner cylinder together with the increase of the local shear rate in the high shear band are linked to the slow stress relaxation towards steady state including the small undershoot (Fig. 18b). The stationary state is characterized by two well-defined shear bands with a relatively broad interface, the position of which fluctuates as a function of time. Contrary to the observations of [156], the local shear rates in each band varies with the imposed shear rate. Under stress-controlled conditions, the development of the banding structure was somewhat different: the kinetics was much slower and the curvature of the initial linear profile was followed by the nucleation and growth of

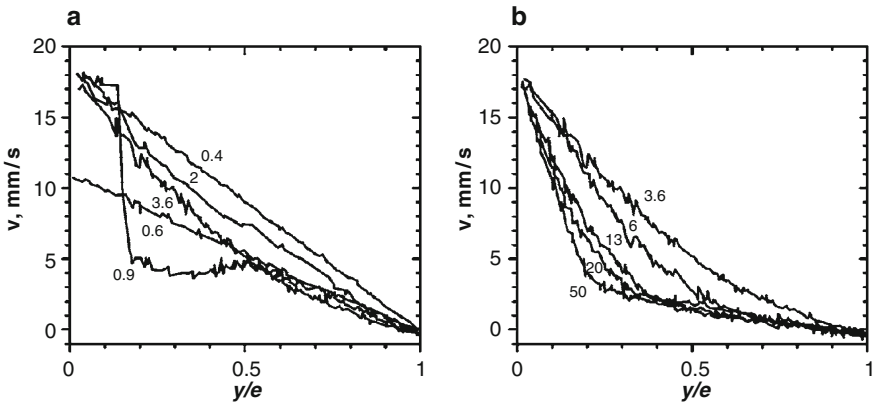

Fig. 18 Velocity profiles as a function of time at $\dot{\gamma} = 10\ s^{-1}$ obtained in a Couette device of gap e using PTV. The spatial resolution is 10 µm. The micellar system is the 6.3% w/v CPCl and NaSal at molar ratio $R = [Sal]/[CPCl] = 0.5$, in 0.5 M H_2O NaCl brine at $T = 23\,°C$. The kinetics of formation of the banding structure is composed of two main stages. (**a**) A short-time response where the flow stays homogeneous most of the time with increasing and decreasing local shear rates respectively at the inner and outer walls. (**b**) Growth of the low shear rate band from the outer wall. Reprinted with permission from Hu et al. [157]

the high shear rate band from the inner rotating cylinder. Note that, using PIV with a high-speed camera, Miller et al. also identified multi-stages development of the banding structure [158].

Fluctuating Behaviors

Using fast NMR velocimetry imaging, Lopez-Gonzalez et al. gathered two-dimensional full velocity profiles every second for a semidilute sample of CPCl/NaSal in 0.5 NaCl brine [161, 250]. The usable extension of the velocity map along the flow and the gradient directions was 5 mm and the data were averaged over 5 mm along the vorticity direction. The long-times flow dynamics was studied for a fixed applied shear rate $\dot{\gamma} = 37\,s^{-1}$. The corresponding stress time series, recorded independently, exhibited fluctuations of about 5% around its mean value. Time-resolved velocity profiles across the 1-mm gap extracted from a one-dimensional slice of the velocity map are displayed in Fig. 19. In addition to the banding structure described for this system in Sect. 3.3.1, the authors demonstrated that the position of the interface between bands strongly fluctuates as a function of time. The high shear rate band (light gray zone in Fig. 19) supports a roughly constant shear rate ($\dot{\gamma} \simeq 70\,s^{-1}$) and its width is strongly correlated to the degree of slip at the inner moving wall. The fluctuations are quasi-random or periodic, depending on sample preparation, and seem then to be driven by wall slip. A frequency analysis revealed that the correlation time ($\simeq$10 s) is of the same order of

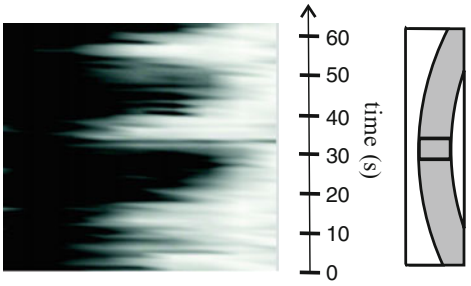

Fig. 19 Velocity profiles as a function of time, recorded at 1-s intervals using rapid NMR imaging in Couette device for an imposed shear rate $\dot{\gamma} = 37\,\mathrm{s}^{-1}$. The left and right sides of the gray scale map correspond respectively to the outer and inner cylinders. The gray levels give the magnitude of the velocity, ranging from 0 to $25\,\mathrm{mm\,s}^{-1}$. The spatial resolution is $100\,\mu\mathrm{m}$. The micellar system placed in the 1 mm gap is made of 10% w/v CPCl and NaSal at molar ratio $R = [\mathrm{Sal}]/[\mathrm{CPCl}] = 0.5$, in0.5 M H_2O/NaCl brine. The temperature is kept at 25 °C. Reprinted with permission from Lopez-Gonzalez et al. [160]

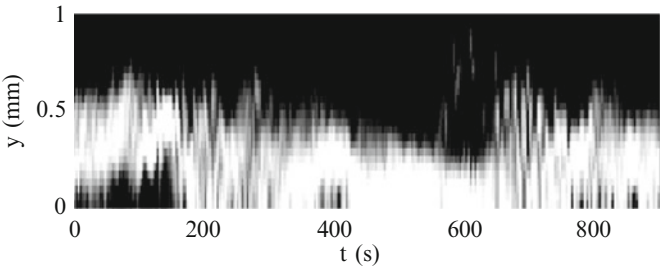

Fig. 20 Map of the local shear rate $\dot{\gamma}(y,t)$ determined using USV, for a 20 wt. % C_{16}TAB/D_2O concentrated micellar system after start-up of flow at a fixed shear rate $\dot{\gamma} = 50\,\mathrm{s}^{-1}$ in the banding regime. The extremum values of the gray scale are associated with $\dot{\gamma} = 0\,\mathrm{s}^{-1}$ (*black*) and $\dot{\gamma} > 120\,\mathrm{s}^{-1}$ (*white*). The positions $y = 0$ and $y = 1$ correspond, respectively, to the inner moving and outer fixed cylinders. The temperature is kept at 41 °C. Reprinted with permission from Bécu et al. [172]

magnitude as that observed in stress fluctuations. Moreover, along the 5 mm of the observation window in the velocity direction, the velocity profiles did not change.

Similar fluctuations of the banding structure have been observed on the C_{16}TAB/D_2O (20 wt. %) concentrated system using high frequency USV [171, 172]. The typical features of the flow dynamics in response to a step shear rate are illustrated in the gray scale map of $\dot{\gamma}(y,t)$ in Fig. 20. First, strong erratic fluctuations of the interface position between the two shear bands from $y \simeq 0.3$ to $y \simeq 0.5$ mm occur on time scales ranging from 3 to 200 s. They are correlated to the dynamics of the slip velocities. Second, an unsheared zone appears intermittently in the vicinity of the inner cylinder, with a spatial extension between 200 and 400 µm. During this process, the time-dependent velocity profiles are highly unstable and composed of three distinct shear bands. The authors emphasized that the local velocity in the unsheared region passes through a maximum that overcomes the rotor

velocity, a feature also observable in [170]. Taking into account their experimental configuration, they interpreted this particular shape of velocity profiles as the signature of three-dimensional flow. This assumption was reinforced by the organization of the ultrasonic tracers into patterns along the vorticity direction.

Vorticity Banding

Herle et al. [229] investigated the equimolar solution CPCl (40 mM) and NaSal (40 mM) ($c = 2.1$ wt. %) that exhibits a complex flow curve with successively Newtonian, shear-thinning, and shear-thickening regimes (see Sects. 3.2.1 and 3.2.2). They performed pointwise USV velocimetry measurements in Couette geometry with the stress as the control parameter. In the shear-thinning region, the flow was homogeneous. At the onset of the shear-thickening regime, the authors observed the presence of two radial bands supporting different shear rates. At higher imposed shear stresses, coexistence of both radial and vorticity bands has been identified. Large temporal oscillations of the velocity profiles have been reported, related to periodic appearance and disappearance of the vorticity bands.

Note that the same system has been explored using PIV in capillary flow [230]. The flow curve built from the local velocity profiles was consistent with that obtained from the bulk rheology. Above the critical wall stress, shear-thickening zones characterized by convexity in the velocity profiles were observed, extending roughly on half of the capillary diameter. Spatio-temporal oscillations of these profiles together with stick-slip were mentioned, leading to continuous creation and breakage of the induced structures. Similar coupling between changes in the microstructure and stick-slip has been also suggested to explain the "apparent" shear-thickening branch of the C_{16}TAB (50 mM)/NaSal (100 mM) ($c = 3.4$ wt. %) solution [187].

3.4 Structural Characterization of the Banded State: Rheo-Optics, Scattering, and Spectroscopy

In Sect. 3.3.2, the existence of shear bands at constant stress has been demonstrated. The shear bands have differing viscosities and consequently different internal structures. A way to collect additional information is then to probe the microstructural organization of the system. Different tools have been used to study the shear-banding transition in wormlike micelles, including flow birefringence (FB), small angle neutron and light scattering (SANS and SALS), and NMR spectroscopy. As in the case of the velocimetry, most of these experimental techniques have been improved to give a space- and time-resolved description of the transition. In the following, we focus on the local structure of the banded state and on the potential connections with the bulk rheology and the local flow field.

3.4.1 Characterization of the Shear-bands Under Steady Flow

Direct Observation Using Flow Birefringence

The first evidence for band separation in wormlike micellar solutions came from flow birefringence experiments performed on a concentrated solution by Decruppe and coworkers [167]. The experimental configuration was as follows: the sample, placed in the gap of a Couette geometry, was illuminated with a white light source and visualized between crossed polarizers. The transmitted intensity was recorded on a digital camera, the spatial resolution reaching 15 µm. Figure 21 shows six photographs of a 1-mm gap filled with a system CPCl/Hex in 0.2 M brine, illustrating the typical scenario observed in concentrated giant micelles [44]. Figure 21a is representative of the optical behavior along the high viscosity branch: the gap of the Couette cell appears dark and the birefringence intensity and the average orientation of the micellar medium are homogeneous. Once the first critical shear rate $\dot{\gamma}_1$ is reached, a highly birefringent bright band nucleates against the moving inner cylinder and coexists with a dark band of differing optical properties. The location of the induced band at the inner cylinder is explained by the stress gradient inherent to the Couette geometry [251, 252]. The stress varies as $1/r^2$ in the gap, implying that the state of higher stress is reached at the inner wall. When the applied shear rate is further increased along the stress plateau, the bright band broadens (see Fig. 21b–e), the orientation state of the system remaining unchanged in each band as demonstrated by pointwise FB [153, 158, 191]. Finally, above $\dot{\gamma}_2$ the gap is entirely filled by the highly birefringent and oriented shear-induced structures (Fig. 21f).

This scenario was originally interpreted as evidence of the shear-banding transition, the states of low and high shear rates being deduced from the molecular

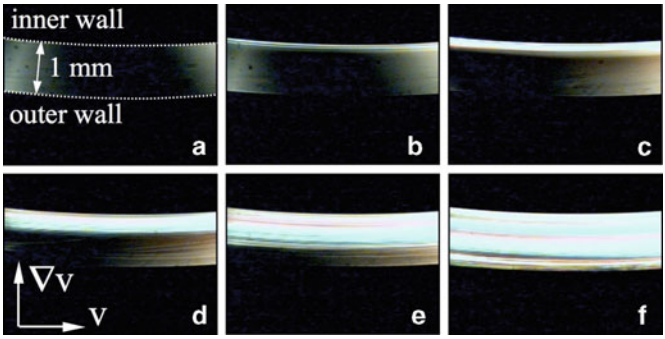

Fig. 21 Snapshots of the 1-mm gap of a Couette cell containing a concentrated solution of CPCl-Hex at respective concentrations $c_{CPCl} = 28$ wt. % and $c_{Hex} = 3.9$ wt. % for different applied shear rates along the flow curve. The sample is illuminated with white light and observed between crossed polarizer and analyser. The orientation of the polarizer is chosen to match the mean orientation of the micelles in the band adjacent to the fixed cylinder. This configuration makes the latter dark and improves the contrast between bands. Exposure times are typically of the order of milliseconds. With increasing shear rates (from **a** to **f**), the bright induced band fills up the gap progressively. Reprinted from Berret [44]

alignment in each band. From a general point of view, it has been observed in concentrated solutions such as C_{16}TAB in water and C_{16}TAB/D_2O [167, 168] and in several semidilute samples, e.g., in C_{16}TAC/NaSal [208, 211], C_{16}TAB/KBr/H_2O and –D_2O [188, 190, 191], CPCl/NaSal [137, 157], C_{16}TAB/NaSal [177, 186], and C_{16}TAB/$NaNO_3$ [144, 194]. Notwithstanding, careful examination of the "steady-state" banding structure revealed important differences in the spatial organization from a sample to another with, for example, heterogeneities of the induced bright band or multiple bands [137, 144, 153, 157, 158, 177, 188, 191].

In this context, the question of the correspondence between shear and birefringence bands has been raised by some authors [169, 170]. In recent studies of semidilute CPCl/NaSal solutions, simultaneous measurements of velocity profiles and optical visualizations were performed, showing a good agreement between shear and birefringence bands [157, 253]. However, this correlation did not seem so obvious for other systems [169, 170]. We will see later (Sect. 3.4.2) using time-resolved birefringence measurements that all these features could certainly be explained by the existence of fluctuations already revealed by velocimetry experiments.

Quantitative measurements of the birefringence intensity Δn and extinction angle χ (Eq. 2) carried out with convenient arrangements of optical components [254] have shown a general steady evolution compatible with that of the shear stress: the absolute value of Δn first increases linearly with $\dot{\gamma}$ while, in the same time, χ decreases smoothly from 45°, indicating a gradual alignment of the micelles with respect to flow direction. Above $\dot{\gamma}_1$, both quantities exhibit a discontinuity of slope followed by a plateau, characteristic of the coexistence of the dark and bright bands [144, 153, 158, 167, 174, 179, 191, 208]. Typically, dark and bright bands have birefringence intensity of the order of -10^{-5} and -10^{-3} (the negative sign of Δn is due to the anisotropy of the polarisability tensor associated with the monomeric surfactant chain [174, 255]), and extinction angle ranging from 20° to 40° for the dark band and of the order of a few degrees for the bright band. This indicates that the induced structures are strongly aligned with respect to the flow direction. Note that the stress-optical law, which establishes a linear relationship between stress and refractive index tensors, does not hold in the shear-banding regime [174, 189, 211, 255].

Nature of the Induced Phases

Concentrated Systems

Various micellar solutions, at a concentration close to the isotropic-to-nematic transition at rest, have been studied using SANS [168, 173, 197, 198] and NMR spectroscopy [169, 170].

SANS gives information on the orientational degrees of freedom of a fluid subjected to flow and has been used to probe the structure of these systems for shear rates all along the flow curve. The sample was placed in a Couette device and two-dimensional scattering patterns were collected in radial configuration, the incident neutron beam passing through the cell along the velocity-gradient direction. For

shear rates along the high viscosity branch, the scattering consists of an isotropic ring and exhibits a broad maximum resulting from strong translational correlations between the micellar threads. The order of magnitude of the distance between micelles, estimated from the position of this maximum, is typically 6–9 nm. In the plateau regime, the scattering function becomes anisotropic, with crescent-like peaks in the vorticity direction. Finally, along the low viscosity branch, at high shear rates, the ring-like structure vanishes and the scattering is dominated by anisotropic pattern, qualitatively analogous to that obtained from a micellar solution which is nematic at rest and subjected to a moderate shearing. These results, showing that the macroscopic phase separation observed in flow birefringence corresponds to shear-induced isotropic-to-nematic transition, have been reported in several systems such as $CPClO_3/NaClO_3$ [173], CPCl/Hex [197, 198], and $C_{16}TAB/D_2O$ [168]. In addition, the nematic order parameter and the proportions and concentrations of each phase as a function of shear rate in the plateau regime could be derived from the SANS spectra. Breakdown of the simple lever rule has been observed [168, 198], and for the CPCl-Hex system the I-N transition was supposed to result from flow-concentration coupling [198].

NMR spectroscopy is also useful to probe the local microstructure. It allows one to resolve spatially the spectral splitting associated with the quadrupolar interactions of the deuteron nuclei with the local electric-field gradient. This splitting is actually proportional to the order parameter of the phase that is initiated. Should this splitting be zero, the phase is disordered; should it be nonzero, the phase is nematic. The splitting is actually due to the fact that, in an oriented nematic phase of micelles, the D_2O molecules of the solvent inherit the alignment of the cylindrical structures. For a detailed description of this technique, the reader can refer to [249, 256]. NMR spectroscopy brought confirmation about the nematic order of the induced phase in the $C_{16}TAB/D_2O$ concentrated sample (20 wt. %) as illustrated in Fig. 22 [169, 170]. At a given shear rate, the splitting characteristic of an ordered phase is clearly visible near the inner moving cylinder, while the spectra at the fixed wall are composed of a single peak, indicative of isotropic phase. The completely ordered and isotropic phases are separated by a mixed region. The existence of broad isotropic and nematic bands is compatible with birefringence observations on the same system [168]. Note that, in contrast, the corresponding NMR velocity profiles do not seem to be correlated in an obvious way with this simple picture (see Sect. 3.3.1). Notwithstanding, velocity profiles measured using USV seem in reasonable agreement with ordering profiles [172].

Relative volume fractions of each phase could be computed from the NMR spectra and were found in remarkable agreement with the SANS data.

Semidilute Systems

For semidilute micellar solutions at concentrations far from the isotropic-to-nematic boundary at rest, the situation is less clear, insofar as the set of structural data on different standard systems available in the literature is reduced, making a definite conclusion about the nature of the induced structures difficult.

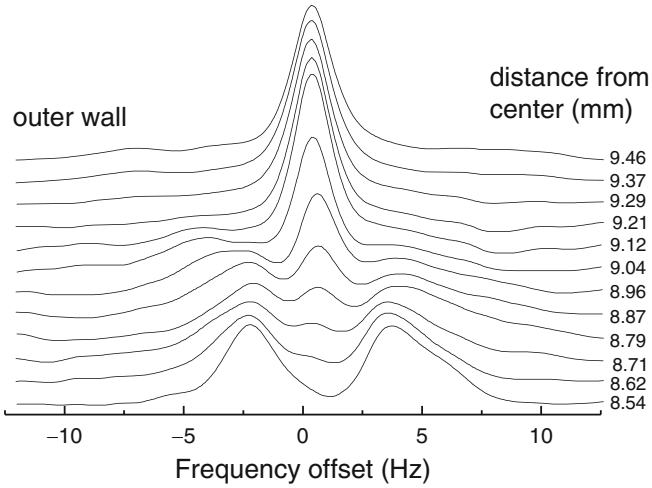

Fig. 22 ^{2}H NMR spectra obtained from 20 wt. % $C_{16}TAB/D_2O$ (41 °C) at different positions across the gap of a cylindrical Couette cell. The applied shear rate is 20 s^{-1}. Near the inner wall, a quadrupole splitting is observed, consistent with a nematic phase, while near the outer wall the single peak of an isotropic phase is seen. Both regions are separated by a mixed phase. Reprinted with permission from Fischer et al. [169]

NMR spectroscopy has been used to investigate the local structure of the 10 wt. % CPCl/NaSal (molar ratio 2:1) in 0.5 M NaCl brine [161, 250]. The shear-induced alignment of the micelles was measured by introducing a deuterated dodecane probe molecule into the micellar core. For applied shear rates belonging to the plateau region, splitting of the NMR spectra were observed, indicating a nonzero order parameter, strongly suggestive of nematic order. The volume fraction of the shear-induced nematic phase was found to increase linearly with the mean shear rate and seemed then to follow a simple lever rule. Moreover, proton NMR spectroscopy revealed a strong correlation between molecular orientational dynamics and shear stress.

Shear-induced isotropic to nematic phase transition has also been reported in semidilute wormlike micelles solutions with excess of salt or strongly binding counterions, forming multiconnected networks [182, 214]. Such a string-like phase has been observed using polarized SALS under shear and manifests itself by anisotropic SALS patterns characterized by butterfly or tulip-like shapes with enhanced scattering in the flow direction superimposed to bright streak perpendicular to the flow direction [178–181]. These features of the scattering patterns indicate shear-enhanced concentration fluctuations [257] at different length scales and are usually accompanied by turbidity and flow dichroism [214]. Recent pointwise SANS experiments on these systems suggested that the high shear rate band, which was turbid and appears strongly striated, was composed of a highly branched concentrated micellar solution coexisting with a nearly isotropic, brine phase [258].

Such SALS patterns and shear-induced turbidity have been highlighted in the equimolar CPCl/NaSal system exhibiting vorticity banding (see Sect. 3.2.2) [222, 226,227], but also in more classical semidilute systems [144,157,177,194–196,200, 236, 253]. In those cases, these phenomena are strongly time- and space-dependent and will be addressed in the following section.

3.4.2 Time-Dependent Behaviors

Transient Behaviors

The formation of the banding structure has been explored using FB, direct visualisations, SALS and turbidity measurements in various semidilute wormlike micelles systems including C_{16}TAB/NaSal, C_{16}TAB/KBr, C_{16}TAB/$NaNO_3$, CPCl/NaSal in brine [144, 153, 157, 158, 177, 191, 194–196]. Note that, in each case, the transient rheology after a sudden step shear rate in the coexistence zone followed the "standard behavior" evoked in Sect. 3.2.2. Interestingly, the temporal evolution of the birefringence intensity and extinction angle, averaged over the gap thickness, showed strong quantitative analogies with that of the shear stress.

The short-time response was dominated by an overshoot and was followed by a stretched exponential or damped oscillations depending on the applied shear rate. The subsequent behavior was a slow variation towards steady state that could be related to the small undershoot observed in $\sigma(t)$ [144, 191].

Figure 23 illustrates the main stages of formation of the banding state for a semidilute mixture of C_{16}TAB (0.3 M) with $NaNO_3$ (0.405 M) ($c = 11$ wt. %) under controlled shear rate.

- *Step 1*: At the onset of the simple shear flow, the entire gap becomes turbid (photo 2). The maximum of scattered intensity is reached when the overshoot in σ, Δn, and χ occurs. The observed turbidity is then supposed to result from the orientation and the stretching of the micellar network [144, 177, 191, 194], generating concentration fluctuations along the flow direction [257] as suggested by butterfly patterns observed using two-dimensional SALS experiments under shear [157, 194]. At this time, all the new phase is nucleated but not arranged into a macroscopic band.
- *Step 2*: The building of the banding structure starts with the relaxation of the stress overshoot. One can observe the formation of a diffuse interface that migrates from the fixed wall towards its stationary position in the gap and progressively sharpens (see photos 3–5). The corresponding behavior in the shear stress response is the sigmoidal relaxation or the damped oscillations depending on the magnitude of the averaged shear rate.
- *Step 3*: When the front is sharp and has reached its equilibrium position, first signs of interface destabilization along the vorticity direction are observed (photo 6). The instability grows with time and finally saturates (photos 7–9). The final state corresponds to the coexistence of a turbid band with a nonturbid band, separated by an undulating interface with well-defined wavelength and finite

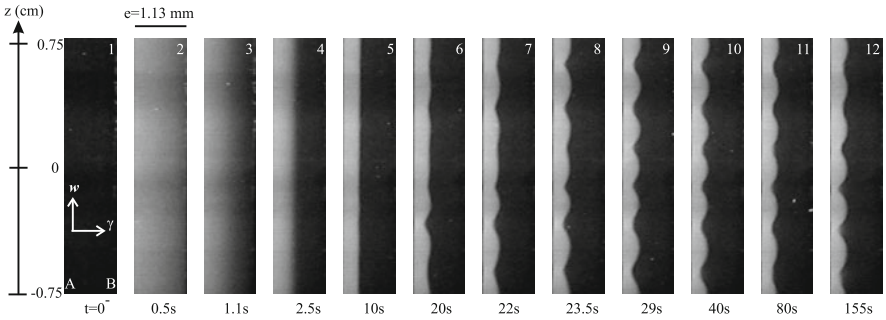

Fig. 23 Views of the 1.13-mm gap in the plane velocity gradient/vorticity taken out from the recording of the scattered intensity at different times during the formation of the induced band at a shear rate of $30\,s^{-1}$. The sample made of $C_{16}TAB$ (0.3 M) and $NaNO_3$ (0.405 M) ($c = 11$ wt. %) at $T = 30°C$ is initially at rest and does not scatter the laser light (photo 1). The experimental configuration is as follows: a transparent Couette cell is illuminated with a thin laser sheet propagating along the velocity gradient direction and the intensity scattered at 90° of the incident beam is recorded on a digital camera. The scattering signal is gathered simultaneously with the temporal stress evolution allowing precise correlation of the structural and mechanical responses. The left and right sides of each picture correspond respectively to the inner and the outer cylinders. Due to the compromise between the spatial resolution and the size of the field of observation, this latter is limited to 1.5 cm in height (the total height of the inner cylinder is 4 cm) and centered at halfway of the cell. Reprinted from Lerouge et al. [195]

amplitude (photo 12). Note that such different scattering properties in each band have also been reported in [153,157] using polarized SALS. The part of the stress dynamics corresponding to the appearance and the development of the interface instability is the small undershoot that precedes steady-state [195,196].

A crucial point in this time sequence is that the small undershoot in the $\sigma(t)$ curve appears as the mechanical signature of the interface instability. Since the undershoot has been detected on other semidilute systems (see Sect. 3.2.2), this suggests that the interfacial instability is presumably not inherent to this particular solution.

Dynamics of the Banding Structure

If the early stages of formation of the banding structure seem to be common to various semidilute solutions, the space and long-time responses strongly differ from one sample to another.

Figure 24 displays, for example, the long-time dynamics of a $C_{16}TAB/NaNO_3$ solution ($c = 11$ wt. %) sheared at $\dot{\gamma} = 8\,s^{-1}$ in a 1.5-mm gap of a Couette cell and observed between crossed polarizers. For reference, the critical shear rates for this sample are $\dot{\gamma}_1 = 5\,s^{-1}$ and $\dot{\gamma}_2 \simeq 110\,s^{-1}$. As expected along the stress plateau, the fluid is split into two bands of strongly differing optical properties. The band located against the fixed cylinder is homogeneous. However, a careful examination of the induced band reveals additional features: the latter appears striated and is composed of

Fig. 24 Illustration of fluctuating behavior of the banding structure on long time scale. The sample, made of C_{16}TAB (0.3 M) and $NaNO_3$ (1.79 M) ($c = 11$ wt. %) is sheared at $\dot{\gamma} = 8\ s^{-1}$ in the annular gap of a Couette cell placed between crossed polarizers and illuminated by a source of white light. The temperature is fixed at 30 °C. The observation is realized in the $(\mathbf{v}, \nabla v)$-plane. The inner rotating cylinder and the outer fixed wall of the Couette cell are indicated by the letters **a** and **b**, respectively. Reprinted from Lerouge et al. [144]

fine sub-bands, the typical thickness of which is estimated to be 100–150 µm. These sub-bands are characterized by differing refraction index. They continuously nucleate from the inner rotating cylinder and migrate towards the outer fixed wall. The interface between the two macroscopic bands seems unstable and shows fluctuations of position, reminiscent of the pictures observed in velocimetry (see Sect. 3.3.2). Note that the striations extend over approximately half of the gap width. Taking into account the boundaries of the stress plateau, the birefringence bands observed here do not follow a simple lever rule.

This type of dynamical behavior has also been reported in various CPCl/NaSal solutions using FB and SALS [138, 153, 157]. Hu and Lips [157] also brought new insights about the fine structuring of the induced band. The simultaneous recording of the velocity profiles showed that the sub-bands support the same local shear rate. Besides, cessation of flow experiments suggested that the sub-bands relaxation time was larger than the macroscopic shear bands lifetime.

The fluctuating character of the interface between bands highlighted from space- and time-resolved velocimetry and optical experiments, appears then as a robust feature of the shear-banding flow in giant micelles systems. With regard to one-dimensional velocimetry measurements, the experimental configuration of Fig. 23 enables to follow the spatiotemporal dynamics of the interface using two-dimensional scattering in the velocity gradient-vorticity plane.

Three main regimes of dynamics have been highlighted along the stress plateau as illustrated in Fig. 25 where the gray levels materialize the position of the interface in the gap. Figure 25a displays a typical spatiotemporal sequence at low shear rates. After a transient including construction, sharpening and migration of the interface, the pattern exhibits, on large scale, a well-defined wavelength of approximately half of the gap width. At smaller scale the dynamics is more complex: the pattern oscillates along the vertical direction of the cell and waves propagate towards the bottom and the top of the cell. At intermediate imposed shear rates in the coexistence zone, the interface keeps a spatially stable profile over very long times. The wavelength of the interface undulation is about three times the gap width (Fig. 25b). The amplitude of the interface profile is modulated in course of time.

For the highest shear rates in the plateau region, emergence of complex dynamics of the interface is observed (cf. Fig. 25c). After a transient slightly under 200 s,

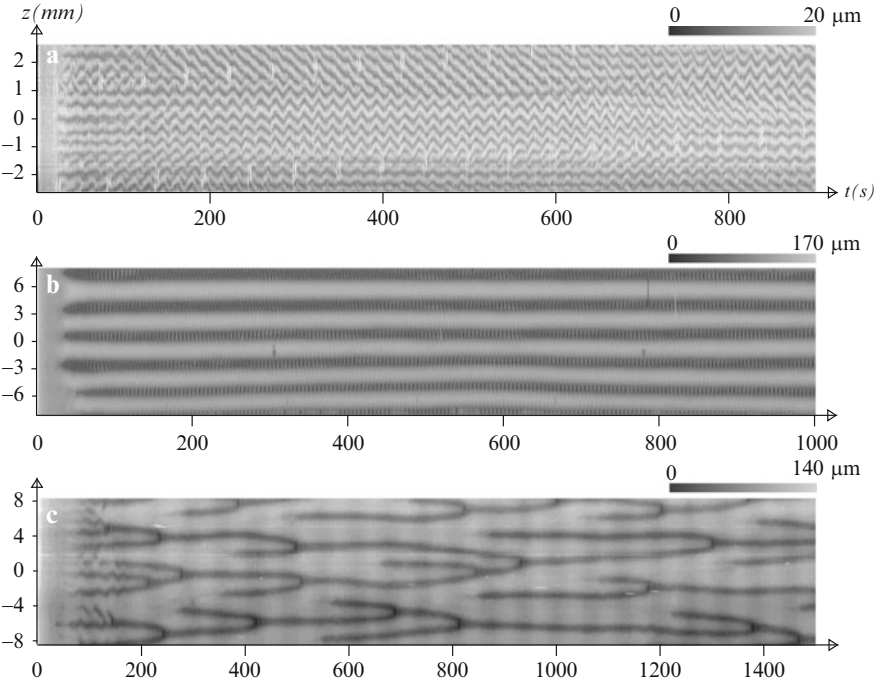

Fig. 25 Spatiotemporal evolution of the interface position in the gap of the Couette cell during a step shear rate from rest to (**a**) $\dot{\gamma} = 6.5\,s^{-1}$, (**b**) $\dot{\gamma} = 30\,s^{-1}$, (**c**) $\dot{\gamma} = 70\,s^{-1}$. The position of the interface in the gap is given in *gray scale*, the origin being taken at the inner moving wall so that *dark gray regions* correspond to positions of the interface nearer to the inner cylinder than *light gray regions*. The z-axis represents the spatial coordinate along the cylinder axis. The sample is made of C_{16}TAB (0.3 M) and $NaNO_3$ (0.405 M) ($c = 11$ wt. %) at $T = 28°C$. Reprinted from Lerouge et al. [196]

the amplitude of the interface profile saturates while the wavelength continuously evolves over time: two neighboring minima have a tendency to merge and when the distance between a pair of minima increases, several other minima close to this pair nucleate and finally merge again with a minimum of longer lifetime. The system does not seem to tend toward a stationary situation and the spatiotemporal diagram strongly suggests chaotic dynamics.

Case of Vorticity Banding

In Sect. 3.2.2, we mentioned the particular time-dependent rheological behavior of an equimolar solution of CPCl/NaSal ($c = 2.1$ wt. %). The shear-thickening transition was characterized by strong oscillations as a function of time in the shear and normal stresses at fixed shear rate (or vice versa). Using direct visualizations and SALS experiments, the authors showed that these oscillations were correlated

with the existence of a pattern made of clear and turbid rings stacked along the vorticity direction, the position and intensity of which alternate in course of time [169, 222, 226, 227]. This complex dynamics, where formation and destruction of shear-induced structures couple with flow instabilities, has been observed in parallel plate, cone and plate and Taylor–Couette cells. Although the development of these spatiotemporal patterns was robust in reference to the flow geometry, the frequency and the amplitude of the oscillations in the bulk rheology were found to depend on the gap width [227], suggesting that the shear induced structures need some space to develop fully. Recent pointwise SANS and video imaging experiments revealed that both clear and turbid bands contain strongly aligned structures [228]. Note that vorticity structuring has also been observed in shear-thickening polymer solutions [259] and in shear-thinning viral suspensions [125, 260, 261].

3.5 Conclusion

In this part we have described the nonlinear behavior of semidilute and concentrated wormlike micelles under simple shear flow. Taking into account the list established in Table 2, we can argue that most surfactant wormlike micelles present a "standard rheological behavior" at steady state, characterized by the existence of a stress plateau in the flow curve. The results accumulated during the last two decades using different velocimetry and optical techniques show unambiguously that the stress plateau is associated with a shear-banding transition. Probing the flow field and the local structure in the $(\mathbf{v}, \nabla v)$-plane leads to a minimal one-dimensional scenario for the base flow, at least when time-averaged measurements are considered: all the velocimetry techniques (NMR imaging, DLS, PIV, PTV, and USV) show that, once the stress plateau is reached, the sample splits into two macroscopic layers bearing different shear rates and stacked along the velocity gradient direction. When the control parameter is increased, the high shear rate band progressively invades the gap of the shearing cell. Birefringence experiments also support this basic picture. The degree of orientation in each layer is very different and the induced structures in the high shear rate band are strongly aligned along the flow direction. For concentrated samples, SANS and NMR spectroscopy under shear indicate that the new phase exhibits long range orientational order of nematic type.

In addition to this simple picture, strongly fluctuating behaviors have been reported in many semidilute and concentrated surfactant systems, including irregular time variations of the bulk rheological signals indicative of chaotic dynamics and fluctuations of the flow field, mainly localized in the high shear rate band. New insights recently emerged from the development of rheo-optical and velocimetry tools with improved spatial and temporal resolution. One-dimensional NMR and USV velocimetry measurements in the $(\mathbf{v}, \nabla v)$-plane have evidenced, on some well-known systems, that the position of the interface between bands exhibits periodic or erratic fluctuations as a function of time, correlated with the slip at the moving wall. Two-dimensional optical visualizations in the $(\mathbf{v}, \omega)$-plane of one particular

semidilute sample revealed that the interface between bands is unstable with respect to wave-vector in the vorticity direction. Interestingly, this behavior is associated with a time-dependent mechanical signature shared by a great number of semidilute and concentrated systems, suggesting that such interfacial instability is potentially common to different wormlike micellar systems.

Note that, in a more marginal way, vorticity structuring has also been observed in semidilute giant micelles showing a shear-thinning to shear-thickening transition. This particular spatial organization also presents a complex dynamics.

From a theoretical point of view, the shear-banded base flow is a consequence of a non-monotonic constitutive relation between the shear stress and the shear rate. Such a relation has been formulated by Cates using a microscopic approach more than 15 years ago [262]. Substantial advances in the understanding of the shear-banding transition have been realized using phenomenological models. Such models derived with inclusion of non-local (or spatial gradient) terms in the equation of motion of the viscoelastic stress lead to a unique stress plateau, independent of flow history. They also allow a more realistic description of the interface between bands, taking into account its finite width [234, 235, 252, 263–269]. In the framework of such models, other issues have been addressed, such as the impact of the flow geometry [252, 269] and its interplay with the boundary conditions [270] on the banding structure, the role of flow-concentration coupling [142, 143, 271], and the effect of the control parameter [143, 264, 271].

Recently, a strong effort has also been made to rationalize the complex time-dependent behaviors observed experimentally. Using the diffusive Johnson-Segalman (DJS) model, Fielding et al. demonstrated that a coupling between mechanical and structural variables such as the concentration or the micellar length can qualitatively reproduce the irregular time-variations of the stress (or shear rate) leading to rheochaos [225, 238]. Note that complex dynamics and rheochaos have also been predicted in phenomenological models of vorticity banding [272, 273].

The stability of the one-dimensional planar shear-banding flow has also been examined within the DJS model. The interface between bands is found to be unstable with respect to small perturbations with wave-vector in the plane made by the flow and the vorticity directions [223, 224, 274]. In the asymptotic state, the interface presents undulations along the velocity and vorticity directions. Jumps in normal stresses and shear rate across the interface are supposed to be the parameters driving the instability. The nonlinear analysis reveals a complex spatio temporal dynamics of the interface with a transition from traveling to rippling waves depending on the ratio between the thickness of the interface and the length of the cell [275].

For details on the theoretical state of the art and exhaustive bibliography, the reader is invited to refer to recent reviews on shear-banding [119, 120, 225].

To conclude, the shear-banding transition in wormlike micelles exhibits complex features beyond the basic one-dimensional scenario. The recent results brought a large amount of new information and also opened promising perspectives that will require strong experimental and theoretical efforts to elucidate fully the underlying mechanisms. The open issues concern, among other things, the organization of the induced structures in the semidilute case, the origin of the turbidity and

consequently of microscopic length scales in these systems, the role of wall slip in the complex dynamics, the effect of the cell geometry and boundary conditions, the microscopic origin of non-local terms, and the mechanisms driving the interfacial instability. Determination of the complete three-dimensional velocity profiles is also a very challenging but exciting task for the near future.

4 Nematic Phases of Wormlike Micelles

4.1 Introduction

At surfactant concentrations above 20–30 wt. %, wormlike micellar solutions undergo equilibrium transitions from an isotropic state to nematic and hexagonal liquid crystalline states. Nematic phases exhibit long-range orientational order with no positional order, whereas hexagonal phases show both orientational and translational long range orders of the centers of mass of the micelles. From their orientation and texture properties, these lyotropic phases bear strong similarities to thermotropic liquid crystals [276]. However, with lyotropics the concentration remains the control parameter for the transitions between the orientationally disordered and ordered states. The nematic phase is characterized by a non-zero order parameter noted S, which describes the orientation state of the director [276–278]:

$$S = \left\langle \frac{1}{2}\left(3\cos^2\psi - 1\right)\right\rangle \tag{5}$$

In Eq. 5, the brackets indicate the averaging over the orientational distribution function, and ψ is the angle between the orientation of a micelle and that of the director. The order parameter is zero in the isotropic phase and equals unity in the fully aligned state. In contrast to the isotropic state, nematic and hexagonal phases are birefringent. Observed by optical microscopy between crossed polarizers, solutions exhibit a strong static birefringence associated with Schlieren (nematic) and fan-like (hexagonal) textures.

Since the work by Lawson and Flaut on sodium decylsulfate/decanol/water (SdS/Dec) [279], numerous surfactant solutions were found to display long range orientational order at high concentrations [12, 16–18, 166, 172, 173, 197, 280–286]. From magnetic susceptibility measurements [287], two different nematic phases were evidenced. One phase, called N_C for *nematic calamitic*, was found to be made of rodlike aggregates, whereas the second phase, called N_D for *discostic nematic*, displayed disk-like aggregates. As shown by structural studies on SdS/Dec, the anisotropy ratio in the N_C phase was estimated to be around 3, yielding a micellar length around 10 nm [288, 289]. Interestingly, Porte and coworkers mentioned that the nematic phases could also be obtained with long and flexible aggregates, such as in the system cetylpyridinium chloride/hexanol/brine 0.2 M NaCl (CPCl/Hex) [12, 16]. There, for a fixed cosurfactant/surfactant ratio, the

nematic phase formed a small island located between large isotropic and hexagonal areas. Hexadecyltrimethylammonium bromide (C_{16}TAB) and sodium dodecylsulfate/decanol (SDS/Dec) were also shown to display nematic wormlike micelles. These phases were later investigated by rheology [166, 168, 172, 284, 290].

For semiflexible chains characterized by contour length much larger than persistence length, Semenov and Kokhlov demonstrated that the values of the phase boundaries between the isotropic and nematic states, as well as the order parameter of the nematic phase could be predicted [291]. Following Onsager [277], it was shown that the boundary c_{I-N} depends only on the ratio between the radius and the persistence length [277, 291, 292]. For nematic wormlike micelles, this limit was found to vary between 20 and 45 wt. %, in fair agreement with the theoretical values [44].

At still higher concentration, around 40 wt. %, hexagonal phases occur. In hexagonal phases, the surfactant aggregates are assumed to be very long and arranged according to a sixfold symmetry structure. The translational order confers to these phases a property that is not present in isotropic and nematic phases. Hexagonal phases are strong elastic gels, and as such possess a yield stress [112]. The rheology of hexagonal phases will not be presented in the present review. One reason is the relative low number of papers dealing with shear-induced instabilities and transitions in hexagonal phases. The second reason concerns the nature of the surfactant systems that were examined. These were on the one hand nonionic surfactants such as penta(ethylene glycol) monododecyl ether ($C_{12}E_5$) [293–297], and on the other microemulsions in which the cylinders are swollen with an apolar solvent [298–300]. In terms of size, charge, and microstructure, these systems are different from those discussed so far. Moreover, the rheology of their dilute or semidilute phases was not extensively addressed. We refer to the above citations for details.

4.2 Rheology

4.2.1 Steady-State

Figure 26 displays the shear rate dependence of the viscosity at the stationary state for a CPCl/Hex nematic sample at concentration $c = 36$ wt. % and at molar ratio $R = [\text{Hex}]/[\text{CPCl}] = 0.49$ [283, 301]. Up to a shear rate of $1\,\text{s}^{-1}$ in Fig. 26, $\eta(\dot{\gamma})$ exhibits a "Newtonian" plateau around 6 Pa s, followed by a shear-thinning regime. This shear-thinning behavior is representative for this class of materials [166, 284, 285, 290]. From the early surveys, it was noted that the viscosity of the nematic phase was lower than that of the isotropic solutions located below the transition concentration, a result which is in agreement with theory [41]. In Fig. 26, the shear-thinning behavior was found to be weaker than that of the isotropic solutions. In its asymptotic high shear rate range, the continuous line in Fig. 26 corresponds to a shear-thinning behavior of the form $\eta \sim \dot{\gamma}^{-0.73}$ [301].

4.2.2 Transients, Flow Reversals, and Scaling Laws

Shearing nematic surfactant solutions has revealed complex transient responses [172,283,284,301,302]. When submitted to a step shear rate, nematic samples usually exhibit a transient regime characterized by oscillations of the stress, this regime being followed by a stationary state. The viscosity data in Fig. 26 were obtained from these steady state stress values. The main results were obtained on CPCl/Hex [283,301,302], C_{16}TAB [172], and on SDS/Dec [284,290,303] nematics. They can be summarized as follows:

1. The transient regime depends on the history experienced by the solution prior to the actual measurement. The stationary stress on the contrary is history independent. A convenient way to control the sample history consists in applying a shearing to the sample for a time that is long enough. History controlled procedures made use of preshearing rate $\dot{\gamma}_{Presh}$.
2. The time needed to reach the stationary state, t_{st}, varies inversely with the shear rate, indicating that whatever $\dot{\gamma}$, steady state is reached after a constant deformation. For both CPCl/Hex and SDS/Dec this deformation was of the order of 300 strain units [284,301]. Nematic surfactant solutions of micelles can be considered to have forgotten their shear history after having been sheared for more than a few hundreds strain units.

The transient responses of nematic wormlike micelles were examined by Berret and coworkers as functions of $\dot{\gamma}$ and $\dot{\gamma}_{\mathrm{Presh}}$ in the "Newtonian" and shear-thinning

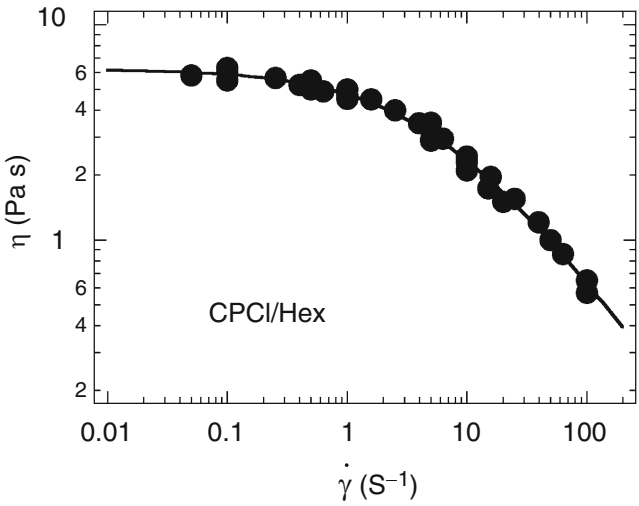

Fig. 26 Variation of the apparent shear viscosity $\eta = \sigma_{st}(\dot{\gamma})/\dot{\gamma}$ as a function of the shear rate for a solution of CPCl/Hex wormlike micelles in 0.2 M NaCl brine. The total concentration is $c = 36$ wt. % and the molar ratio [Hex]/[CPCl] = 0.49. The continuous line between the data points is a guide for the eyes. At high shear rates, the viscosity decreases according to a power law with exponent −0.73

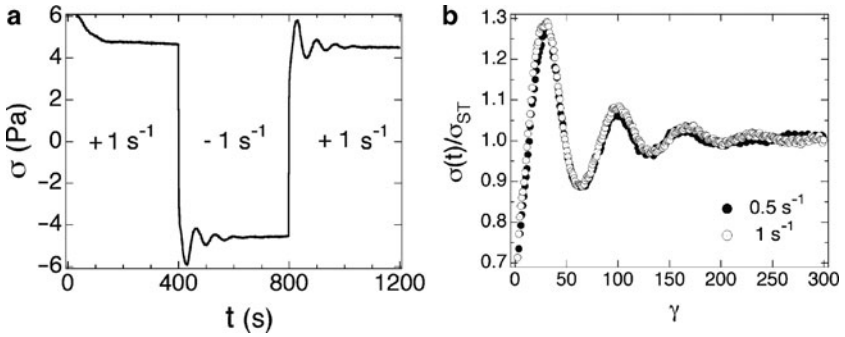

Fig. 27 (**a**) Shear stress response obtained from a flow reversal experiment in CPCl/Hex nematic wormlike micelles at total concentration $c = 37$ wt. % and molar ratio [Hex]/[CPCl]=0.49 [302]. In the flow reversal, the shear rate is changed stepwise from $+1\,s^{-1}$ (after sample loading) to -1 s^{-1} and then to $+1\,s^{-1}$. (**b**) Variation of the normalized shear stress $\sigma(t)/\sigma_{st}$ as a function of the total applied deformation for the same solution. Flow reversal experiments were carried out at $\dot{\gamma} = 0.5\,s^{-1}$ (*close circles*) and $1\,s^{-1}$ (*open circles*) and were found to be superimposed

regimes. In this context, flow reversal [302] and step shear rate [283] experiments were evaluated. In a flow reversal, the sample is first presheared at fixed rate $\dot{\gamma}_{Presh} = \dot{\gamma}_0$ until the steady state condition are reached. The direction of the shear flow is then switched abruptly from $+\dot{\gamma}_0$ to $-\dot{\gamma}_0$. In step shear rate experiments, only the amplitude of the shearing is changed, not the sense of rotation. Raw data of two consecutive flow reversals obtained on CPCl/Hex nematic solutions ($c = 37$ wt. % and [Hex]/[CPCl]=0.49) are displayed as a function of time in Fig. 27a ($\dot{\gamma}_0 = 1 s^{-1}$). Upon flow inception, for a freshly loaded sample, the shear stress exhibited a large overshoot, then decreasing monotonously toward its stationary value. After reversing the flow direction, damped oscillations were observed in the stress responses, either in the negative or in the positive torque ranges. Similar oscillations were found in step shear rates [283].

The approach consisting of preshearing the solutions was actually inspired from the research on liquid crystalline polymers (LCP) [304, 305]. LCPs have attracted much attention during the past few decades because of their remarkable flow and mechanical properties. In LCPs, the competition between the local molecular relaxation of the polymers and the structure and orientations predicted by classical nematodynamics results in a very complex rheology, for which only mesoscopic theories exist [306]. It is out the scope of the present review to enter into the details of the mesoscopic approaches developed for LCPs, and the reader should refer to the seminal papers by Larson and Doi [306] and Srinivasarao [307]. The first experimental evidence of damped oscillations in the transient shear stress was due to Moldenaers et al. on poly(benzyl-L-glutamate solutions) (PBLG) of high molecular weights [305]. PBLG is a lyotropic liquid crystal, where nematogens arise from the hydrogen bonding helix conformation of the backbone. The stress oscillations were related by Larson and Doi to the tumbling instability of the nematic director in the flow [305]. A major property of the constitutive equations derived by Larson and

Doi was their scaling behavior. The model predicted that the time evolution of the shear stress is a function of only two parameters, the strain $\dot{\gamma}t$ applied to the sample and the ratio $\dot{\gamma}/\dot{\gamma}_{Presh}$ [306, 308], i.e.:

$$\frac{\sigma(t,\dot{\gamma},\dot{\gamma}_{\rm Presh})}{\sigma_{\rm st}} = F\left(\dot{\gamma}t, \frac{\dot{\gamma}}{\dot{\gamma}_{\rm Presh}}\right), \tag{6}$$

where $\dot{\gamma}/\dot{\gamma}_{\rm Presh} = -1$ for flow reversals.

Figure 27b displays the results of flow reversals obtained at two different shear rates ($\dot{\gamma} = 0.5$ and $\dot{\gamma} = 1\ s^{-1}$), where, to obey Eq. 6, the stress has been divided by the stationary value, and the time replaced by the deformation. The data at 0.5 and $1\ s^{-1}$ are found to be superimposed, demonstrating the scaling of the stress responses. Scaling laws were also obtained with nematic calamitic and discotic phases of SDS/Dec, although, with more complex patterns [284, 290, 309]. It is important to realize that the mechanical responses in Fig. 27 are very different from those of the isotropic phases, for which the scaling with deformation or the dependence on the shear history have not been observed [138].

As for CPCl/Hex, the conclusions are twofold:

1. Although polymers and wormlike micelles are very different in nature, the flow properties of their nematic phases are similar. This property was ascribed to the existence of textures at a mesoscopic scale, and to the fact that the dynamics of the textures dominate the mechanical responses of these fluids [310].
2. One of these similarities concerns the possibility for the nematic director to tumble in the flow. This tumbling is associated with the periodic oscillations of the stress, as seen in Fig. 27.

For tumbling nematics, the director is assumed to find no preferred orientation and hence to rotate indefinitely in the flow. Tumbling conditions are met for Ericksen numbers larger than a critical value of about 10 (the Ericksen number is defined as the ratio between the viscous and elastic torques) [311].

A second requirement for this instability to occur is that the two Leslie viscosity coefficients α_2 and α_3 are of opposite signs [276, 312]. If the ratio between the two viscosities is positive, the director exhibits different dynamics: it aligns with respect to the velocity at an angle θ_0 such that $\tan^2(\theta_0) = \alpha_2/\alpha_3$. Note finally that, despite a complex microstructure, the classification in terms of flow-aligning and tumbling nematics, as defined for low molecular weight liquid-crystals, still applied to lyotropic systems.

4.3 Textures and Microscopy

A great amount of experimental data using optical microscopy has shown the existence of textures in thermotropic, as well as in lyotropic liquid crystals [304, 313, 314]. These textures are in the micrometer range and are interpreted in terms of

spatial variations of the nematic director through the sample. At rest, the textures translate into a polydomain structure where the distribution of nematic directors remains constant within each domain. Few optical data have been gathered on surfactant nematics however. For the calamitic phase at rest, Schlieren textures with characteristic line and point defects were observed in various systems [12,15,16,172,284,288,301]. As samples were allowed to relax for some hours, the Schlieren textures coarsened and an alignment resulted due to the interactions with the glass surfaces of the cell.

Under shear, texture refinement was predicted, and observed for LCPs as resulting from the competition between the viscoelastic and the elastic Frank stresses. Here, the Frank stresses arise from the orientational heterogeneities of the director occurring at the transitions or walls from domain to domain. The balance between the elastic and viscous energy density allowed Marrucci to show that the texture lengths should decrease with the shear rate as $\dot{\gamma}^{-1/2}$. Roux et al. have performed rheo-optical measurements on CPCl/Hex nematics in order to assess these predictions [301]. At low shear rates, striped textures parallel to the flow could be identified. The texture lengths were estimated to be of the order of 5–10 µm, depending on the applied rate. A refinement of the stripes was also observed with increasing shear rate, but not estimated quantitatively. Stop-flow experiments on the same system were also carried out and allowed to confirm the predictions of the mesoscopic domain theory [306]. At the cessation of the flow, dark and bright stripes perpendicular to the flow velocity were found, with a band spacing growing as $\sim t^{1/2}$. Similar results were observed in LCPs [314]. In conclusion of this section, the rheo-optical data confirm a polydomain structure, the coupling of the textures to the flow, and the close analogy with liquid crystalline polymers.

4.4 Director Orientations Under Shear: Scattering and NMR

Small-angle neutron and X-ray scattering were undertaken in order to retrieve the local orientation of the micellar threads at rest and under shear. As shown on thermotropic [278] and lyotropic [12, 16, 288, 289] liquid crystals at rest, these two techniques provide unambiguous signatures of nematic long-range orientational order through the generation of a diffuse scattering patterns. For experiments at rest, the alignment of the nematic director was achieved using an externally applied magnetic field.

Under shear, Couette or cone-and-plate cells specifically designed for small-angle scattering [56, 315] were used at large scale facilities by many authors. With the help of two-dimensional detectors, the anisotropy in the forward scattering was targeted. This combined configuration of shearing and detection allowed one to observe the scattering in the three planes of the reciprocal space, ($\mathbf{q}_v$,$\mathbf{q}_{\nabla v}$), ($\mathbf{q}_v$,$\mathbf{q}_\omega$), and ($\mathbf{q}_{\nabla v}$,$\mathbf{q}_\omega$), where we recall that $\mathbf{q}_v$, $\mathbf{q}_{\nabla v}$, and $\mathbf{q}_\omega$ are the wavevectors parallel to the velocity, velocity gradient, and vorticity. Most of the data on nematic wormlike micelles were collected in the ($\mathbf{q}_v$,$\mathbf{q}_\omega$)- and ($\mathbf{q}_v$,$\mathbf{q}_{\nabla v}$)-planes

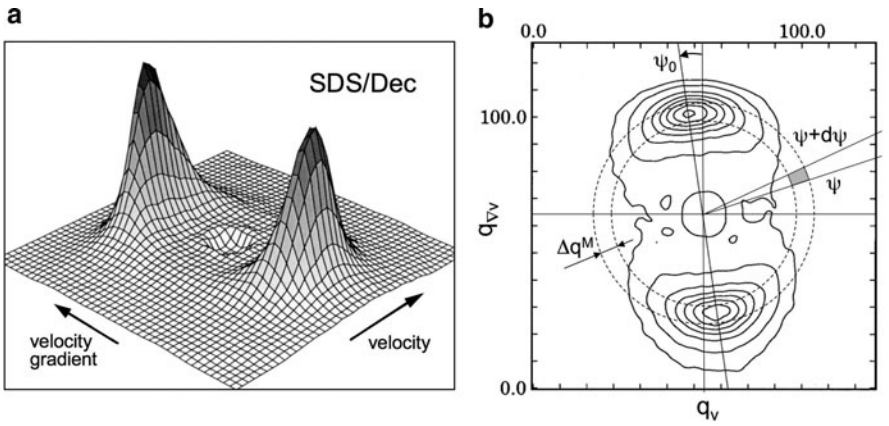

Fig. 28 (**a**) 3D-plot of the neutron scattering cross-section measured in the $(\mathbf{q}_v, \mathbf{q}_{\nabla v})$-vorticity plane for the SDS–Dec nematic calamitic phase. The SDS/Dec solution was prepared in D_2O for contrast reasons at total concentration $c = 29.5$ wt. % and molar ratio [Dec]/[SDS] = 0.33 [317]. The shear rate of the experiment was $\dot{\gamma} = 50\ s^{-1}$. (**b**) Iso-intensity contours obtained for the same conditions as in (**a**). Along the $\mathbf{q}_v$- and $\mathbf{q}_{\nabla v}$-axis, the wave-vector ranges from -0.16 to $+0.16\ Å^{-1}$. The *dashed circles* set the limits of the domain of integration for the data treatment (see text)

[33, 168, 172, 173, 301–303, 316]. Figure 28a displays a typical three-dimensional plot of the neutron intensity scattered by a nematic lyotropic solution in the $(\mathbf{q}_v,\mathbf{q}_{\nabla v})$-plane. The data were obtained on the SDS/Dec calamitic phase at $50\ s^{-1}$ (concentration $c = 29.5$ wt. % and $R = [\text{Dec}]/[\text{SDS}] = 0.33$). As shown in the iso-intensity contour plot (Fig. 28b), the patterns are characterized by two crescent-like peaks aside from the velocity axis. The maximum scattering corresponds to the first order of the structure factor, from which the distance between the center-of-mass of the micelles can be estimated (here 6 nm for a radius of $\sim$2 nm). The modulation of the azimuthal intensity is also of interest since it reflects the distribution of micellar orientations. The spectra were analyzed in terms of angular distribution of the scattered intensity. The scattering was integrated over an elementary surface $\mathrm{d}q_v\,\mathrm{d}q_{\nabla v} = q^{\mathrm{M}}\Delta q^{\mathrm{M}}\Delta\psi$, where Δq^{M} corresponds typically to the half width at half maximum of the peak. Plotted as a function of the azimuthal angle ψ, two parameters could be retrieved:

- The order parameter S of the nematic phase under shear (Eq. 5). The analytical technique to transform the azimuthal intensity into an orientational distribution has been quoted in several papers [109, 276, 278].
- The tilt angle ψ_0 of the scattering pattern with respect to the vertical axis. It was shown that the tilt angle angle ψ_0 was actually the orientation angle between the nematic director and the flow. By symmetry, it is zero in the $(\mathbf{q}_v,\mathbf{q}_\omega)$-plane, nonzero in $(\mathbf{q}_v,\mathbf{q}_{\nabla v})$-plane [290, 318], and changes sign by flow reversal [317].

In Fig. 29, the order parameter $S^{v,\omega}$ is shown as a function of the shear rate, together with characteristic SANS spectra obtained on CPCl/Hex nematic solution.

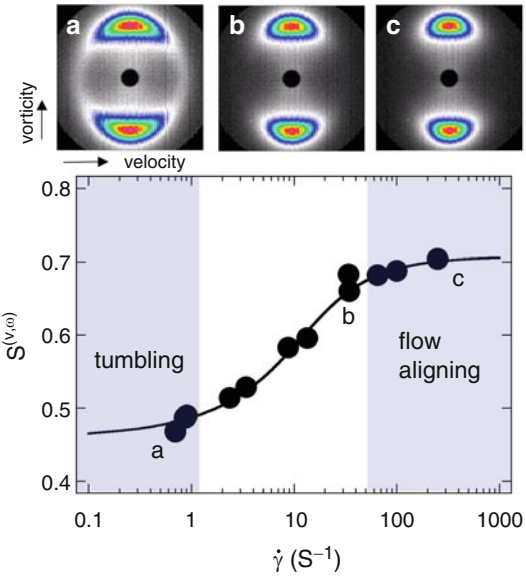

Fig. 29 *Upper panels*: Neutron scattering intensities obtained from a CPCl/Hex nematic micellar solution in the $(\mathbf{q}_v, \mathbf{q}_{\nabla v})$-plane at different shear rates: (**a**) $\dot{\gamma} = 0.94\ s^{-1}$, (**b**) $\dot{\gamma} = 34.5\ s^{-1}$, and (**c**) $\dot{\gamma} = 250\ s^{-1}$. The nematic phase was made in deuterated water at concentration $c = 35.2$ wt. % and molar ratio [Hex]/[CPCl] = 0.49 [301]. *Lower panel*: Shear rate dependence of the orientational order parameter $S^{v,\omega}$ (Eq. 5) obtained from the SANS cross-sections shown in the *upper panel*. The *continuous line* is a guide for the eyes. The increase of the order parameter was interpreted in terms of a transition between the tumbling and the flow-alignment regimes [290, 303]

It illustrates that shear orients the nematic phase steadily and that this process is concomitant to the shear-thinning behavior (Fig. 26). As recognized by Burghardt and coworkers [290, 303], bulk measurements of S reflect the distribution of micellar orientations around the local director as well as the distribution of director orientations in the polydomain sample. The progressive increase from $S^{v,\omega} = 0.45$ to $S^{v,\omega} = 0.70$ in Fig. 29 was ascribed to the transition between the polydomain tumbling regime toward the flow-alignment monodomain regime [290, 301, 303]. Using synchroton X-ray radiation, Caputo et al. reported the time dependence of the order parameter $S^{v,\nabla v}$ in the $(\mathbf{q}_v, \mathbf{q}_{\nabla v})$-plane [290, 303]. SAXS spectra were collected every second during step shear rate and flow reversal testing. It was shown by these authors that the orientational response of CPCl/Hex nematics was consistent with the Doi–Larson model developed for the LCPs, i.e. that the order parameter decreased after reversing the flow, a result that was not seen on classical LCPs.

The second surfactant nematics that was studied thoroughly, SDS/Dec, shows a different behavior. Although it is a textured material with a bulk shear-thinning rheology similar to CPCl/Hex or C_{16}TAB, this system exhibits what appears to be common characteristics of aligning nematics: (i) a constant orientation state and order parameter in steady shear, (ii) a single undershoot of long duration in average orientation upon flow reversal, and (iii) no significant orientation change upon step increase or decrease in shear rate or upon flow cessation [284, 290, 309, 317].

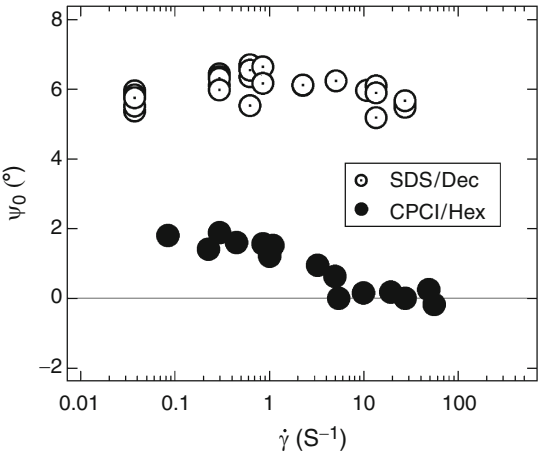

Fig. 30 Evolution of the orientation angle ψ_0 as a function of the shear rate for the SDS/Dec and CPCl/Hex nematics. Samples characteristics are those of Fig. 28 [317]

Caputo et al. concluded that this system followed the polydomain model predictions of transient orientation for aligning nematics [290]. As an illustration, Fig. 30 displays the evolution of the orientation angle ψ_0 as a function of the shear rate for both SDS/Dec and for CPCl/Hex [317]. For SDS/Dec, the orientation of the director with respect to the velocity remains unchanged at $\psi_0 = 6^\circ$ over three decades in shear rates. For the tumbling nematic micelles, the tilt angle has a nonzero value at low shear rates, $\psi_0 = 1.8^\circ$, but decreases to zero with increasing shear rates. The shear rates at which ψ_0 deviates from its low shear rate value corresponds to the upper limit of the tumbling regime. As the system enters into the flow alignment regime, the orientation angle ψ_0 decreases to zero, yielding a fully symmetric scattering pattern. These results are in qualitative agreement with those obtained on tumbling LCPs by flow birefringence [319].

Using ^{2}H NMR-spectroscopy under shear, the flow-aligning properties of SDS/Dec calamitic phase prepared in D_2O could be confirmed. In this experiment, the anisotropic motions of the D_2O molecules in contact with the micellar surfaces result in a small residual quadrupole coupling, which is related to the angle between the nematic director and the magnetic field [320]. The line splitting $\Delta\nu$ corresponding to this coupling is given by $\Delta\nu$=3/4 $\delta(3\cos^2\theta - 1)$ where δ is the quadrupole coupling constant. In the configuration adopted, the magnetic field was parallel to the velocity gradient, i.e. $\theta = \pi/2 - \psi$, where ψ is the tilt angle defined in Fig. 28b. Figure 31a illustrates a series of spectra obtained for the nematic calamitic sample at $\dot{\gamma} = 0.32\ s^{-1}$ and at different deformations γ after inception of shear. With increasing deformation, a decrease of the splitting is first observed. At $\gamma \sim 1.4$, the two resonance lines overlap at the magic angle ($\theta = 54.7^\circ$). When the deformation is further increased, the splitting stabilizes at the steady state value, which is slightly lower than half of the initial splitting. Beyond $\gamma = 15$, no change is observed, neither in the splitting nor in the line shape. The strain evolution in Fig. 31b shows an increase and a saturation at θ_0 = 78 $\pm$ 2°. This result is again a strong indication that the SDS/Dec nematic is flow-aligning. The flow-alignment behavior can be checked by

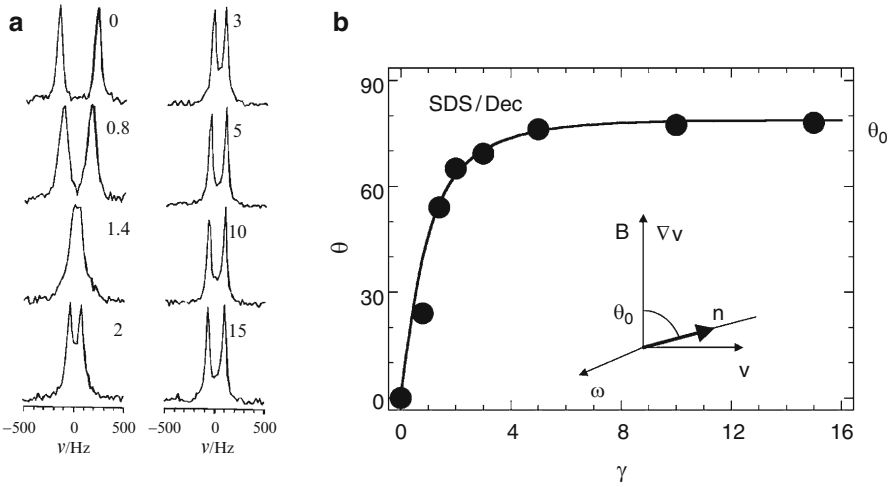

Fig. 31 (**a**) Transient behavior of the NMR splitting for an SDS/Dec nematic calamitic solution at concentration $c = 29.5$ wt. % and molar ratio [Dec]/[SDS] = 0.33 and sheared at $\dot{\gamma} = 0.32\,\mathrm{s}^{-1}$ [284]. (**b**) Evolution of the orientation angle of the nematic director with respect to the magnetic field as function of the strain. The symbols correspond to the spectra in (**a**), and the continuous line is determined from Eq. 7, yielding an asymptotic angle of $\theta_0 = 78 \pm 2°$. *Inset*: Orientation of the nematic director in presence of the flow and of the magnetic field

comparing the director orientation as a function of strain, $\theta(\dot{\gamma})$ as predicted by the Leslie–Ericksen continuum theory [112, 276]. Neglecting the effect of the magnetic field [321], the evolution of the director angle reads

$$\theta(\gamma) = \arctan\left[\sqrt{\frac{\alpha_2}{\alpha_3}}\tanh\left(\frac{\sqrt{\alpha_2\alpha_3}}{\alpha_3 - \alpha_2}\gamma\right)\right] \quad \text{with} \quad \alpha_2, \alpha_3 < 0 \tag{7}$$

where α_2 and α_3 are Leslie coefficients. The continuous line in Fig. 31b has been calculated using Eq. 7 with $\alpha_2/\alpha_3 = \tan^2(\theta_0) = 25$ as unique fitting parameter. The good agreement between the experimental and the calculated $\theta(\gamma)$ is a further indication of the flow-alignment character of the N_C phase. For a tumbling system a more complex transient evolution of the director orientation is expected, and was indeed observed for the tumbling PBLG [297].

4.5 Conclusion

Using scattering and spectroscopy experiments, it has been shown that the physical quantities characterizing the wormlike micellar nematics such as the order parameter, Leslie viscosities ratio, or alignment angles can be determined. The main result of this section is the analogy between the wormlike micelles and the liquid-crystalline polymers, as far as their nematic states are concerned. Because these

fluids are textured, their rheology is unique. This rheology is determined by the coupling between the spatial heterogeneities in the nematic director and the flow. Another interesting result concerns the evidence of the director tumbling instability found for CPCl/Hex or C_{16}TAB nematics. For a better description of these systems under shear, additional experiments should be performed, such as those on the texture dynamics, and on the measurements of the Franck (elastic) and Leslie (viscosity) coefficients.

5 Summary

In this review, we provided an overview of the nonlinear rheology of surfactant wormlike micelles, from dilute to liquid crystal states. The equilibrium phase diagram of these systems is extremely rich. We showed that this leads, under steady shear flow, to different rheological signatures such as shear-thickening, shear-thinning or a combination of the two. These nonlinear behaviors are associated with strong modifications both of the flow field and of the internal structure of the fluid. The dilute phases of wormlike micelles thicken under shear due to the growth of a viscous shear-induced structure. The semidilute and concentrated phases of giant micelles undergo a shear-banding transition, where phases of different fluidities, spatially organized, coexist. Finally, nematic phases of micelles present a tumbling instability of the director. All these transitions and instabilities share a common feature: they are characterized by extremely long transients compared to the intrinsic relaxation time of the system. These specific behaviors are related to rearrangements of the internal structure at the mesoscopic scale. Another crucial point that emerged from recent experiments is that these transitions result in a complex spatiotemporal dynamics of the flow, involving either bulk or interfacial instabilities, the driving parameters of which remain to determine.

Besides their practical interest in today's life, giant micelles are attractive, notably because of the accurate knowledge of their phase behavior and dynamical properties, the simplicity of their linear response, and their analogy with conventional polymers. The major interest comes from the large diversity of their flow behaviors that continue to fascinate lots of experimentalists and theoreticians, especially because they are representative of many phenomena encountered in other complex fluids.

Acknowledgements The present review would not have been possible without the extended network of colleagues and friends being, as we are, fascinated by this subject. It is a pleasure to acknowledge the collaborations and the fruitful discussions we had over the years with Jacqueline Appell, Wesley Burghardt, Olivier Cardoso, Jean-Louis Counord, Jean-Paul Decruppe, Marc-Antoine Fardin, Olivier Greffier, Guillaume Grégoire, Heinz Hoffmann, Sébastien Manneville, François Molino, Julian Oberdisse, Peter Olmsted, Grégoire Porte, Ovidiu Radulescu, Jean-Baptiste Salmon, Claudia Schmidt, Jean-François Tassin, and Lynn Walker. The Laboratoire Léon Brillouin (CEA, Saclay, France), the Institute Laue-Langevin, and the European Synchrotron Radiation Facilities (Grenoble, France) are also acknowledged for their technical and financial supports. We have also benefited from research organizations and fundings, such as the GDR

1081 “Rhéophysique des Colloides et Suspensions”, European TMR-Network “Rheology of Liquid Crystals” contract number FMRX-CT96-0003 (DG 12 - ORGS), Agence Nationale pour la Recherche (ANR JCJC-0020). We are finally very grateful to Sébastien Manneville for his comments on the first version of the manuscript.

References

1. Debye P, Anacker E (1951) Micelle shape from dissymetry measurements. J Phys Chem 55:644–655
2. Nash T (1958) The interaction of some naphtalene derivatives with a cationic soap below the critical micelle concentration. J Colloid Sci 13:134–139
3. Gravsholt S (1976) Viscoelasticity in highly dilute aqueous solutions of pure cationic detergents. J Colloid Interface Sci 57:575–577
4. Porte G, Appell J, Poggi Y (1980) Experimental investigations on the flexibility of elongated cetylpyridinium bromide micelles. J Phys Chem 84:3105–3110
5. Porte G, Appell J (1981) Growth and size distributions of cetylpyridinium bromide micelles in high ionic strength aqueous solutions. J Phys Chem 85:2511–2519
6. Ikeda S (1984) Sphere-rod transition of surfactant micelles and size distribution of rodlike micelles. J Phys Chem 88:2144–2149
7. Candau S, Hirsch E, Zana R (1985) Light scattering investigations of the behavior of semidilute aqueous micellar solutions of cetyltrimethylammonium bromide: analogy with semidilute polymer solutions. J Colloid Interface Sci 105:521–528
8. Imae T, Kamiya R, Ikeda S (1984) Electron microscopic observation of rodlike micelles of dimethyloleylamine oxide regenerated from its aqueous solutions. J Colloid Interface Sci 99(1):300–301
9. Imae T, Kamiya R, Ikeda S (1985) Formation of spherical and rodlike micelles of cetyltrimethylammonium bromide in aqueous nabr solutions. J Colloid Interface Sci 108(1):215–225
10. Imae T, Ikeda S (1986) Sphere-rod transition in micelles of tetradecyltrimethylammonium halides in aqueous sodium halide solutions and flexibility and entanglement of long rodlike micelles. J Phys Chem 90(1):5216–5223
11. Porte G, Poggi Y, Appell J, Maret G (1984) Large micelles in concentrated solutions. The second critical micellar concentration. J Phys Chem 88:5713–5720
12. Porte G, Gomati R, Elhaitamy O, Appell J, Marignan J (1986) Morphological transformations of the primary surfactant structures in brine-rich mixtures of ternary-systems (surfactant alcohol brine). J Phys Chem 90(22):5746–5751
13. Candau S, Hirsch E, Zana R (1984) New aspects of the behaviour of alkyltrimethylammonium bromide micelles: light scattering and viscometric studies. J Phys 45:1263–1270
14. Candau S, Hirsch E, Zana R, Adam M (1988) Network properties of semidilute kbr solutions of cetyltrimetylammonium bromide. J Colloid Interface Sci 122:430–440
15. Amaral L, Helene M, Bittencourt D, Itri R (1987) New nematic lyomesophase of sodium dodecyl sulfate. J Phys Chem 91:5949–5953
16. Gomati R, Appell J, Bassereau P, Marignan J, Porte G (1987) Influence of the nature of the counterion and of hexanol on the phase behavior of the dilute ternary systems: cetylpyridinium bromide or chloride-hexanol-brine. J Phys Chem 91:6203–6210
17. Amaral L, Helene MM (1988) Nematic domain in the sodium lauryl sulfate/water/decanol system. J Phys Chem 92:6094–6098
18. Hertel G, Hoffmann H (1988) Lyotropic nematic phases of double chain surfactants. Trends Colloid Interface Sci 4:123–131
19. Hoffmann H, Löbl H, Rehage H, Wunderlich I (1985) Rheology of surfactant solutions. Tenside Detergents 22:290–298

20. Shikata T, Hirata K, Kotaka T (1987) Micelle formation of detergent molecules in aqueous media. 1. viscoelastic properties of aqueous cetyltrimethylammonium bromide solutions. Langmuir 3:1081–1086
21. Rehage H, Hoffmann H (1988a) Rheological properties of viscoelastic surfactant systems. J Phys Chem 92:4712–4719
22. Shikata T, Hirata K, Kotaka T (1988b) Micelle formation of detergent molecules in aqueous media. 2. role of free salicylate ions on viscoelastic properties of aqueous cetyltrimethylammonium bromide-sodium salicylate solutions. Langmuir 4:354–359
23. Shikata T, Hirata H, Takatori E, Osaki K (1988a) Nonlinear viscoelastic behavior of aqueous detergent solutions. J Non-Newt Fluid Mech 28(2):171–182
24. Shikata T, Hirata K, Kotaka T (1989) Micelle formation of detergent molecules in aqueous media. 3. viscoelastic properties of aqueous cetyltrimethylammonium bromide-salicylic acid solutions. Langmuir 5:398–405
25. Cates ME, Candau SJ (1990) Statics and dynamics of wormlike surfactant micelles. J Phys Cond Matt 2(33):6869–6892
26. Shikata T, Hirata K, Kotaka T (1990) Micelle formation of detergent molecules in aqueous media. 4. electrostatic features and phase behavior of cetyltrimethylammonium bromide:salicylic acid micellar solutions. J Phys Chem 94:3702–3706
27. Kern F, Zana R, Candau SJ (1991) Rheological properties of semidilute and concentrated aqueous-solutions of cetyltrimethylammonium chloride in the presence of sodium-salicylate and sodium-chloride. Langmuir 7(7):1344–1351
28. Rehage H, Hoffmann H (1991) Viscoelastic surfactant solutions – model systems for rheological research. Mol Phys 74(5):933–973
29. Clausen TM, Vinson PK, Minter JR, Davis HT, Talmon Y, Miller WG (1992) Viscoelastic micellar solutions – microscopy and rheology. J Phys Chem 96(1):474–484
30. Khatory A, Lequeux F, Kern F, Candau SJ (1993b) Linear and nonlinear viscoelasticity of semidilute solutions of wormlike micelles at high-salt content. Langmuir 9(6):1456–1464
31. Khatory A, Kern F, Lequeux F, Appell J, Porte G, Morie N, Ott A, Urbach W (1993a) Entangled versus multiconnected network of wormlike micelles. Langmuir 9(4):933–939
32. Berret JF, Appell J, Porte G (1993) Linear rheology of entangled wormlike micelles. Langmuir 9(11):2851–2854
33. Berret JF, Roux DC, Porte G (1994a) Isotropic-to-nematic transition in wormlike micelles under shear. J Phys II (France) 4(8):1261–1279
34. Smolka LB, Belmonte A (2003) Drop pinch-off and filament dynamics of wormlike micellar fluids. J Non-Newt Fluid Mech 115(1):1–25
35. Bellour M, Skouri M, Munch JP, Hébraud P (2002) Brownian motion of particles embedded in a solution of giant micelles. Eur Phys J E 8:431–436
36. Buchanan M, Atakhorrami M, Palierne JF, MacKintosh FC, Schmidt CF (2005) High-frequency microrheology of wormlike micelles. Phys Rev E 72(1):011,504
37. Willenbacher N, Oelschlaeger C, Schopferer M, Fischer P, Cardinaux F, Scheffold F (2007) Broad bandwidth optical and mechanical rheometry of wormlike micelle solutions. Phys Rev Lett 99(6):068,302
38. Cappallo N, Lapointe C, Reich DH, Leheny RL (2007) Nonlinear microrheology of wormlike micelle solutions using ferromagnetic nanowire probes. Phys Rev E 76(3)
39. Raudsepp A, Callaghan P, Hemar Y (2008) A study of the nonlinear rheology of complex fluids using diffusing wave spectroscopy. J Rheol 52(5):1113–1129
40. Cates ME (1988) Dynamics of living polymers and flexible surfactant micelles – scaling laws for dilution. J Phys 49(9):1593–1600
41. Doi M, Edwards S (1986) The theory of polymer dynamics. Oxford, Clarendon
42. Lequeux F, Candau S (1994) Dynamical properties of wormlike micelles. In: Herb C, Prud'homme R (eds) Structure and flow in surfactant solutions. ACS Symposium Series 578. American Chemical Society, Washington, DC, pp 51–62
43. Walker LM (2001) Rheology and structure of wormlike micelles. Curr Opin Colloid Inter Sci 6(5–6):451–456

44. Berret JF (2005) Rheology of wormlike micelles: equilibrium properties and shear-banding transition. In: Molecular gels, Elsevier, Dordrecht
45. Prudhomme RK, Warr GG (1994) Elongational flow of solutions of rodlike micelles. Langmuir 10(10):3419–3426
46. Walker LM, Moldenaers P, Berret JF (1996) Macroscopic response of wormlike micelles to elongational flow. Langmuir 12(26):6309–6314
47. Chen CM, Warr GG (1997) Light scattering from wormlike micelles in an elongational field. Langmuir 13(6):1374–1376
48. Rothstein JP (2003) Transient extensional rheology of wormlike micelle solutions. J Rheol 47(5):1227–1247
49. Yesilata B, Clasen C, McKinley GH (2006) Nonlinear shear and extensional flow dynamics of wormlike surfactant solutions. J Non-Newt Fluid Mech 133(2–3):73–90
50. Andereck D, Liu S, Swinney H (1986) Flow regimes in a circular Couette system with independently rotating cylinders. J Fluid Mech 164:155–183
51. Rehage H, Hoffmann H (1982) Shear induced phase transitions in highly dilute aqueous detergent solutions. Rheol Acta 21:561–563
52. Hoffmann H, Platz G, Rehage H, Schorr W, Ulbricht W (1981b) Viskoelastische tensidlösungen. Ber Bunsenges Phys Chem 85:255–266
53. Shenoy A (1984) A review on drag reduction with special reference to micellar systems. Colloid Polym Sci 262:319–337
54. Bewersdorff HW, Frings B, Lindner P, Oberthür RC (1986) The conformation of drag reducing micelles from small-angle-neutron-scattering experiments. Rheol Acta 25(6):642–646
55. Ohlendorf D, Interthal W, Hoffmann H (1986) Surfactant systems for drag reduction: physicochemical properties and rheological behaviour. Rheol Acta 25(5):468–486
56. Lindner P, Bewersdorff H, Heen R, Sittart P, Thiel H, Langowski J, Oberthür R (1990) Drag-reducing surfactant solutions in laminar and turbulent flow investigated by small-angle neutron scattering and light scattering. Trends Colloid Interface Sci 4:107–112
57. Boltenhagen P, Hu YT, Matthys EF, Pine DJ (1997b) Observation of bulk phase separation and coexistence in a sheared micellar solution. Phys Rev Lett 79(12):2359–2362
58. Sung K, Han MS, Kim C (2003) Rheological behavior and wall slip of dilute and semidilute CPyCl/NaSal surfactant solutions. Korea-Australia Rheol J 15(3):151–156
59. Wunderlich I, Hoffmann H, Rehage H (1987) Flow birefringence and rheological measurements on shear induced micellar structures. Rheol Acta 26(6):532–542
60. Koch S, Schneider T, Küter W (1998) The velocity field of dilute cationic surfactant solutions in a couette-viscometer. J Non-Newtonian Fluid Mech 78(1):47–59
61. Dehmoune J, Decruppe J, Greffier O, Xu H (2007) Rheometric and rheo-optical investigation on the effect of the aliphatic chain length of the surfactant on the shear thickening of dilute wormlike micellar solutions. Rheol Acta 46(8):1121–1129
62. Wunderlich A, Brunn P (1989) The complex rheological behavior of an aqueous cationic surfactant solution investigated in a couette-type viscosimeter. Colloid Polym Sci 267:627–636
63. Hu YT, Wang SQ, Jamieson AM (1993b) Rheological and flow birefringence studies of a shear-thickening complex fluid – a surfactant model system. J Rheol 37(3):531–546
64. Liu CH, Pine DJ (1996) Shear-induced gelation and fracture in micellar solutions. Phys Rev Lett 77(10):2121–2124
65. Vasudevan M, Shen A, Khomami B, Sureshkumar R (2008) Self-similar shear thickening behavior in ctab/nasal surfactant solutions. J Rheol 52(2):527–550
66. Cressely R, Hartmann V (1998) Rheological behaviour and shear thickening exhibited by aqueous ctab micellar solutions. Eur Phys J B 6(1):57–62
67. Hartmann V, Cressely R (1998) Occurrence of shear thickening in aqueous micellar solutions of CTAB with some added organic counterions. Colloid Polym Sci 276(2):169–175
68. Hartmann V, Cressely R (1997b) Simple salts effects on the characteristics of the shear thickening exhibited by an aqueous micellar solution of CTAT/NaSal. Europhys Lett 40:691–696
69. Rose GD, Foster KL (1989) Drag reduction and rheological properties of cationic viscoelastic surfactant formulations. J Non-Newt Fluid Mech 31(1):59–85

70. Hu Y, Rajaram CV, Wang SQ, Jamieson AM (1994) Shear thickening behavior of a rheopectic micellar solution – salt effects. Langmuir 10(1):80–85
71. Hartmann V, Cressely R (1997a) Shear-thickening of an aqueous micellar solution of cetyltrimethylammonium bromide and sodium tosylate. J Phys II France 7:1087–1098
72. Kim WJ, Yang SM (2000) Effects of sodium salicylate on the microstructure of an aqueous micellar solution and its rheological responses. J Colloid Interface Sci 232(2):225–234
73. Kim WJ, Yang SM (2001) Flow-induced microstructure in aqueous cationic surfactant solution in the presence of structure-enhancing additives. J Chem Eng Jpn 34(2):227–231
74. Hu H, Larson RG, Magda JJ (2002) Measurement of wall-slip-layer rheology in shear-thickening wormy micelle solutions. J Rheol 46(4):1001–1021
75. Gamez-Corrales R, Berret JF, Walker L, Oberdisse J (1999) Shear-thickening dilute surfactant solutions: the equilibrium structure as studied by small-angle neutron scattering. Langmuir 15:6755–6763
76. Truong M, Walker L (2002) Quantifying the importance of micellar microstructure and electrostatic interactions on the shear-induced structural transition of cylindrical micelles. Langmuir 18(6):2024–2031
77. Berret JF, Lerouge S, Decruppe J (2002) Kinetics of the shear-thickening transition observed in dilute surfactant solutions and investigated by flow birefringence. Langmuir 18:7279–7286
78. Berret JF, Gamez-Corrales R, Lerouge S, Decruppe J (2000a) Shear-thickening transition in surfactant solutions: new experimental features from rheology and flow birefringence. Eur Phys J E 2:343–350
79. Berret JF, Gamez-Corrales R, Séréro Y, Molino F, Lindner P (2001) Shear-induced micellar growth in dilute surfactant solutions. Europhys Lett 54:605–611
80. Bandyopadhyay R, Basappa G, Sood AK (2000) Observation of chaotic dynamics in dilute sheared aqueous solutions of ctat. Phys Rev Lett 84(9):2022–2025
81. Macias ER, Bautista F, Soltero JFA, Puig JE, Attane P, Manero O (2003) On the shear thickening flow of dilute ctat wormlike micellar solutions. J Rheol 47(3):643–658
82. Torres MF, Gonzalez JM, Rojas MR, Muller AJ, Saez AE, Lof D, Schillen K (2007) Effect of ionic strength on the rheological behavior of aqueous cetyltrimethylammonium p-toluene sulfonate solutions. J Colloid Interface Sci 307(1):221–228
83. Lu B, Li X, Scriven L, Davis H, Talmon Y, Zakin J (1998) Effect of chemical structure on viscoelasticity and extensional viscosity of drag-reducing cationic surfactant solutions. Langmuir 14:8–16
84. Qi Y, Zakin J (2002) Chemical and rheological characterization of drag-reducing cationic surfactant systems. Ind Eng Chem Res 41(25):6326–6336
85. Hofmann S, Rauscher A, Hoffmann H (1991) Shear induced micellar structures. Ber Bunsenges Phys Chem 95(2):153–164
86. Hu Y, Wang S, Jamieson A (1993a) Kinetic studies of a shear thickening micellar solution. J Colloid Interface Sci 156(1):31–37
87. Prötzl B, Springer J (1997) Light scattering experiments on shear induced structures of micellar solutions. J Colloid Interface Sci 190:327–333
88. Schmitt V, Schosseler F, Lequeux F (1995b) Structure of salt-free wormlike micelles – signature by sans at rest and under shear. Europhys Lett 30(1):31–36
89. Oda R, Panizzza P, Schmutz M, Lequeux F (1997) Direct evidence of the shear-induced structure of wormlike micelles: gemini 12-2-12. Langmuir 13:6407–6412
90. Oda R, Weber V, Lindner P, Pine D, Mendes E, Schloesser F (2000) Time-resolved small-angle neutron scattering study of shear-thickening surfactant solutions after the cessation of flow. Langmuir 14:4859–4863
91. Weber V, Schosseler F (2002) Shear-thickening in salt-free aqueous solutions of a gemini cationic surfactant: A study by small angle light scattering. Langmuir 18(25):9705–9712
92. Weber V, Narayanan T, Mendes E, Schosseler F (2003) Micellar growth in salt-free aqueous solutions of a gemini cationic surfactant: evidence for a multimodal population of aggregates. Langmuir 19(4):992–1000

93. Oelschlaeger C, Waton G, Candau SJ, Cates ME (2002b) Structural, kinetics, and rheological properties of low ionic strength dilute solutions of a dimeric (gemini) surfactant. Langmuir 18(20):7265–7271
94. Oda R, Lequeux F, Mendes E (1996) Evidence for local orientational order in salt-free wormlike micelles: a transient electric birefingence study. J Phys II France 6:1429–1439
95. Oda R, Narayanan J, Hassan P, Manohar C, Salkar R, Kern F, Candau S (1998) Effect of the lipophilicity of the counterion on the viscoelasticity of micellar solutions of cationic surfactant. Langmuir 14:4364–4372
96. Hu YT, Boltenhagen P, Pine DJ (1998b) Shear thickening in low-concentration solutions of wormlike micelles. i. direct visualization of transient behavior and phase transitions. J Rheol 42(5):1185–1208
97. Myska J, Stern P (1994) Properties of drag reducing micelle system. Colloid Polym Sci 272:542–547
98. Boltenhagen P, Hu YT, Matthys EF, Pine DJ (1997a) Inhomogeneous structure formation and shear-thickening in wormlike micellar solutions. Eur Phys Lett 38(5):389–394
99. Hu YT, Boltenhagen P, Matthys E, Pine DJ (1998a) Shear thickening in low-concentration solutions of wormlike micelles. ii. slip, fracture, and stability of the shear-induced phase. J Rheol 42(5):1209–1226
100. In M, Aguerre-Chariol O, Zana R (1999a) Closed-looped micelles in surfactant tetramer solutions. J Phys Chem B 103:7747–7750
101. In M, Aguerre-Chariol O, Zana R (1999b) Dynamics of branched threadlike micelles. Phys Rev lett 83:2278–2281
102. Lin Z, Zheng Y, Davis H, Scriven L, Talmon Y, Zakin J (2000) Unusual effects of counterion to surfactant concentration ratio on viscoelasticity of a cationic surfactant drag reducer. J Non-Newt Fluid Mech 93:363–373
103. Truong M, Walker L (2000) Controlling the shear-induced structural transition of rodlike micelles using nonionic polymer. Langmuir 16:7991–7998
104. Lee JY, Magda JJ, Hu H, Larson RG (2002) Cone angle effects, radial pressure profile, and second normal stress difference for shear-thickening wormlike micelles. J Rheol 46(1):195–208
105. Keller S, Boltenhagen P, Pine D, Zasadzinski J (1997) Direct observation of shear-induced structures in wormlike micellar solutions by freeze-fracture electron microscopy. Phys Rev Lett 80:2725–2728
106. Hoffmann H, Platz G, Rehage H, Schorr W (1981a) The influence of counter-ion concentration on the aggregation behaviour of viscoelastic detergents. Ber Bunsenges Phys Chem 85:877–882
107. Oelschlaeger C, Waton G, Candau S, Cates M (2002a) Structural, kinetics, and rheological properties of low ionic strength dilute solutions of a dimeric (gemini) surfactant. Langmuir 18(20):7265–7271
108. Berret JF, Gamez-Corrales R, Oberdisse J, Walker LM, Lindner P (1998a) Flow-structure relationship of shear-thickening surfactant solutions. Europhys Lett 41:677–682
109. Deutsch M (1991) Orientational order determination in liquid crystals by X-ray diffraction. Phys Rev A 44:8264–8270
110. Barentin C, Liu AJ (2001) Shear thickening in dilute solutions of wormlike micelles. Europhys Lett 55:432–438
111. Schmitt V, Lequeux F (1995) SANS spectra and elastic plateau modulus in a charged wormlike micelles solution – effect of salt. J Phys II (France) 5(2):193–197
112. Larson R (1999) The Structure and rheology of complex fluids. New York University press, New York
113. Larson R (1992) Instabilities in viscoelastic flows. Rheol Acta 31:213–263
114. Ajdari A (1998) Rheological behavior of a solution of particles aggregating on the containing walls. Phys Rev E 58(4):6294–6298
115. Goveas JL, Pine D (1999) A phenomenological model for shear-thickening in wormlike micelle solutions. Europhys Lett 48:706–712

116. Cates M, Turner M (1990) Flow-induced gelation of rodlike micelles. Europhys Lett 7: 681–686
117. Bruinsma R, Gelbart W, Ben-Shaul A (1992) Flow-induced gelation of living (micellar) polymers. J Chem Phys 96:7710–7727
118. Turner M, Cates M (1992) Flow-induced phase transition in rodlike micelles. J Phys Condens Matter 4:3719–3741
119. Cates ME, Fielding SM (2006) Rheology of giant micelles. Adv Phys 55(7–8):799–879
120. Olmsted PD (2008) Perspectives on shear-banding in complex fluids. Rheol Acta 47(3):283–300
121. Salmon JB, Manneville S, Colin A (2003b) Shear banding in a lyotropic lamellar phase. I. Time-averaged velocity profiles. Phys Rev E 68(5):051503
122. Salmon JB, Manneville S, Colin A (2003c) Shear banding in a lyotropic lamellar phase. II. Temporal fluctuations. Phys Rev E 68(5):051504
123. Berret JF, Serero Y (2001) Evidence of shear-induced fluid fracture in telechelic polymer networks. Phys Rev Lett 87(4):048303
124. Manneville S, Colin A, Waton G, Schosseler F (2007) Wall slip, shear banding, and instability in the flow of a triblock copolymer micellar solution. Phys Rev E 75(6):061502
125. Lettinga MP, Dhont JKG (2004) Non-equilibrium phase behaviour of rodlike viruses under shear flow. J Phys Cond Matt 16(38):S3929–S3939
126. Pujolle-Robic C, Noirez L (2001) Observation of shear-induced nematic-isotropic transition in side-chain liquid crystal polymers. Nature 409(6817):167–171
127. Volkova O, Cutillas S, Bossis G (1999) Shear banded flows and nematic-to-isotropic transition in ER and MR fluids. Phys Rev Lett 82(1):233–236
128. Coussot P, Raynaud JS, Bertrand F, Moucheront P, Guilbaud JP, Huynh HT, Jarny S, Lesueur D (2002) Coexistence of liquid and solid phases in flowing soft-glassy materials. Phys Rev Lett 88(21):218301
129. Losert W, Bocquet L, Lubensky TC, Gollub JP (2000) Particle dynamics in sheared granular matter. Phys Rev Lett 85(7):1428–1431
130. Mueth DM, Debregeas GF, Karczmar GS, Eng PJ, Nagel SR, Jaeger HM (2000) Signatures of granular microstructure in dense shear flows. Nature 406(6794):385–389
131. Debregeas G, Tabuteau H, di Meglio JM (2001) Deformation and flow of a two-dimensional foam under continuous shear. Phys Rev Lett 87(17):178305
132. Lauridsen J, Chanan G, Dennin M (2004) Velocity profiles in slowly sheared bubble rafts. Phys Rev Lett 93(1):018303
133. Gilbreth C, Sullivan S, Dennin M (2006) Flow transitions in two-dimensional foams. Phys Rev E 74(5):051406
134. Cates ME, McLeish TCB, Marrucci G (1993) The rheology of entangled polymers at very high shear rates. Europhys Lett 21(4):451–456
135. Callaghan PT, Cates ME, Rofe CJ, Smeulders J (1996) A study of the "spurt effect" in wormlike micelles using nuclear magnetic resonance microscopy. J Phys II 6(3):375–393
136. Rehage H, Hoffmann H (1988b) Rheological properties of viscoelastic surfactant systems. J Phys Chem 92(16):4712–4719
137. Berret JF, Porte G, Decruppe JP (1997) Inhomogeneous shear flows of wormlike micelles: a master dynamic phase diagram. Phys Rev E 55(2):1668–1676
138. Berret JF (1997) Transient rheology of wormlike micelles. Langmuir 13(8):2227–2234
139. Britton MM, Mair RW, Lambert RK, Callaghan PT (1999) Transition to shear banding in pipe and couette flow of wormlike micellar solutions. J Rheol 43(4):897–909
140. Grand C, Arrault J, Cates ME (1997) Slow transients and metastability in wormlike micelle rheology. J Phys II 7(8):1071–1086
141. Mendez-Sanchez AF, Lopez-Gonzalez MR, Rolon-Garrido VH, Perez-Gonzalez J, de Vargas L (2003a) Instabilities of micellar systems under homogeneous and non-homogeneous flow conditions. Rheol Acta 42(1–2):56–63
142. Schmitt V, Marques CM, Lequeux F (1995a) Shear-induced phase-separation of complex fluids – the role of flow-concentration coupling. Phys Rev E 52(4):4009–4015

143. Fielding SM, Olmsted PD (2003) Flow phase diagrams for concentration-coupled shear banding. Eur Phys J E 11(1):65–83
144. Lerouge S, Decruppe JP, Berret JF (2000) Correlations between rheological and optical properties of a micellar solution under shear banding flow. Langmuir 16(16):6464–6474
145. Mair RW, Callaghan PT (1996) Observation of shear banding in wormlike micelles by nmr velocity imaging. Eur Phys Lett 36(9):719–724
146. Mair RW, Callaghan PT (1997) Shear flow of wormlike micelles in pipe and cylindrical Couette geometries as studied by nuclear magnetic resonance microscopy. J Rheol 41(4):901–924
147. Britton MM, Callaghan PT (1997a) Nuclear magnetic resonance visualization of anomalous flow in cone-and-plate rheometry. J Rheol 41(6):1365–1386
148. Britton MM, Callaghan PT (1997b) Two-phase shear band structures at uniform stress. Phys Rev Lett 78(26):4930–4933
149. Fischer P, Rehage H (1997) Non-linear flow properties of viscoelastic surfactant solutions. Rheol Acta 36(1):13–27
150. Britton MM, Callaghan PT (1999) Shear banding instability in wormlike micellar solutions. Eur Phys J B 7(2):237–249
151. Porte G, Berret JF, Harden JL (1997) Inhomogeneous flows of complex fluids: mechanical instability versus non-equilibrium phase transition. J Phys II 7(3):459–472
152. Mendez-Sanchez AF, Perez-Gonzalez J, de Vargas L, Castrejon-Pita JR, Castrejon-Pita AA, Huelsz G (2003b) Particle image velocimetry of the unstable capillary flow of a micellar solution. J Rheol 47(6):1455–1466
153. Lee JY, Fuller GG, Hudson NE, Yuan XF (2005) Investigation of shear-banding structure in wormlike micellar solution by point-wise flow-induced birefringence measurements. J Rheol 49(2):537–550
154. Forster S, Konrad M, Lindner P (2005) Shear thinning and orientational ordering of wormlike micelles. Phys Rev Lett 94(1)
155. Manneville S, Salmon JB, Bécu L, Colin A, Molino F (2004b) Inhomogeneous flows in sheared complex fluids. Rheol Acta 43(5):408–416
156. Salmon JB, Colin A, Manneville S, Molino F (2003a) Velocity profiles in shear-banding wormlike micelles. Phys Rev Lett 90(22):228303
157. Hu YT, Lips A (2005) Kinetics and mechanism of shear banding in an entangled micellar solution. J Rheol 49(5):1001–1027
158. Miller E, Rothstein JP (2007) Transient evolution of shear-banding wormlike micellar solutions. J Non-Newt Fluid Mech 143(1):22–37
159. Holmes WM, Lopez-Gonzalez MR, Callaghan PT (2003) Fluctuations in shear-banded flow seen by nmr velocimetry. Eur Phys Lett 64(2):274–280
160. Lopez-Gonzalez MR, Holmes WM, Callaghan PT, Photinos PJ (2004) Shear banding fluctuations and nematic order in wormlike micelles. Phys Rev Lett 93(26):268302
161. Lopez-Gonzalez MR, Holmes WM, Callaghan PT (2006) Rheo-nmr phenomena of wormlike micelles. Soft Matter 2(10):855–869
162. Ballesta P, Lettinga MP, Manneville S (2007) Superposition rheology of shear-banding wormlike micelles. J Rheol 51(5):1047–1072
163. Ballesta P, Manneville S (2005) Signature of elasticity in the faraday instability. Phys Rev E 71:026308
164. Ballesta P, Manneville S (2007) The faraday instability in wormlike micelle solutions. J Non-Newt Fluid Mech 147(1–2):23–34
165. Masselon C, Salmon JB, Colin A (2008) Nonlocal effects in flows of wormlike micellar solutions. Phys Rev Lett 1(3):38301
166. Cappelaere E, Cressely R, Decruppe JP (1995) Linear and nonlinear rheological behavior of salt-free aqueous ctab solutions. Colloids Surf A Physicochem Eng Asp 104(2-3):353–374
167. Decruppe JP, Cressely R, Makhloufi R, Cappelaere E (1995) Flow birefringence experiments showing a shear-banding structure in a CTAB solution. Coll and Polym Sci 273(4):346–351
168. Cappelaere E, Berret JF, Decruppe JP, Cressely R, Lindner P (1997) Rheology, birefringence, and small-angle neutron scattering in a charged micellar system: evidence of a shear-induced phase transition. Phys Rev E 56(2):1869–1878

169. Fischer E, Callaghan PT (2000) Is a birefringence band a shear band? Europhys Lett 50(6):803–809
170. Fischer E, Callaghan PT (2001) Shear banding and the isotropic-to-nematic transition in wormlike micelles. Phys Rev E 64(1):011501
171. Bécu L, Manneville S, Colin A (2004) Spatiotemporal dynamics of wormlike micelles under shear. Phys Rev Lett 93(1):018301
172. Bécu L, Anache D, Manneville S, Colin A (2007) Evidence for three-dimensional unstable flows in shear-banding wormlike micelles. Phys Rev E 76(1):011503
173. Schmitt V, Lequeux F, Pousse A, Roux D (1994) Flow behavior and shear-induced transition near an isotropic-nematic transition in equilibrium polymers. Langmuir 10(3):955–961
174. Shikata T, Dahman SJ, Pearson DS (1994) Rheooptical behavior of wormlike micelles. Langmuir 10(10):3470–3476
175. Shikata T, Pearson DS (1994) Phase-transitions in entanglement networks of wormlike micelles. Langmuir 10(11):4027–4030
176. Fischer P, Fuller GG, Lin ZC (1997) Branched viscoelastic surfactant solutions and their response to elongational flow. Rheol Acta 36(6):632–638
177. Lerouge S, Decruppe JP, Humbert C (1998) Shear banding in a micellar solution under transient flow. Phys Rev Lett 81(24):5457–5460
178. Kadoma IA, vanEgmond JW (1996) "Tuliplike" scattering patterns in wormlike micelles under shear flow. Phys Rev Lett 76(23):4432–4435
179. Wheeler EK, Izu P, Fuller GG (1996) Structure and rheology of wormlike micelles. Rheol Acta 35(2):139–149
180. Kadoma IA, vanEgmond JW (1997) Shear-enhanced orientation and concentration fluctuations in wormlike micelles: effect of salt. Langmuir 13(17):4551–4561
181. Kadoma IA, Ylitalo C, vanEgmond JW (1997) Structural transitions in wormlike micelles. Rheol Acta 36(1):1–12
182. Kadoma IA, van Egmond JW (1998) Flow-induced nematic string phase in semidilute wormlike micelle solutions. Phys Rev Lett 80(25):5679–5682
183. Azzouzi H, Decruppe JP, Lerouge S, Greffier O (2005) Temporal oscillations of the shear stress and scattered light in a shear-banding-shear-thickening micellar solution. Eur Phys J E 17(4):507–514
184. Hashimoto T, Turukawa T, Mori N (2005) Flow property and micellar structures in capillary flows of surfactant solutions. Nihon Reoroji Gakkaishi 33(1):1–8
185. Inoue T, Inoue Y, Watanabe H (2005) Nonlinear rheology of ctab/nasal aqueous solutions: finite extensibility of a network of wormlike micelles. Langmuir 21(4):1201–1208
186. Drappier J, Bonn D, Meunier J, Lerouge S, Decruppe JP, Bertrand F (2006) Correlation between birefringent bands and shear bands in surfactant solutions. J Stat Mech-Theory Exp P04003
187. Decruppe JP, Greffier O, Manneville S, Lerouge S (2006) Local velocity measurements in heterogeneous and time-dependent flows of a micellar solution. Phys Rev E 73(6):061509
188. Decruppe JP, Cappelaere E, Cressely R (1997) Optical and rheological properties of a semidiluted equimolar solution of cetyltrimethylammonium bromide and potassium bromide. J Phys II (France) 7(2):257–270
189. Humbert C, Decruppe JP (1998b) Stress optical coefficient of viscoelastic solutions of cetyltrimethylammonium bromide and potassium bromide. Colloid Polym Sci 276(2):160–168
190. Radulescu O, Olmsted PD, Decruppe JP, Lerouge S, Berret JF, Porte G (2003) Time scales in shear banding of wormlike micelles. Europhys Lett 62(2):230–236
191. Lerouge S, Decruppe JP, Olmsted P (2004) Birefringence banding in a micellar solution or the complexity of heterogeneous flows. Langmuir 20(26):11,355–11,365
192. Cappelaere E, Cressely R (1997) Shear banding structure in viscoelastic micellar solutions. Colloid Polym Sci 275(5):407–418
193. Cappelaere E, Cressely R (1998) Rheological behavior of an elongated micellar solution at low and high salt concentrations. Colloid Polym Sci 276(11):1050–1056

194. Decruppe JP, Lerouge S, Berret JF (2001) Insight in shear banding under transient flow. Phys Rev E 63(2):022501
195. Lerouge S, Argentina M, Decruppe JP (2006) Interface instability in shear-banding flow. Phys Rev Lett 96(8):088301
196. Lerouge S, Fardin M, Argentina M, Gregoire G, Cardoso O (2008) Interface dynamics in shear-banding flow of giant micelles. Soft Matter 4(9):1808–1819
197. Berret JF, Roux DC, Porte G, Lindner P (1994b) Shear-induced isotropic-to-nematic phase-transition in equilibrium polymers. Europhys Lett 25(7):521–526
198. Berret JF, Roux DC, Lindner P (1998b) Structure and rheology of concentrated wormlike micelles at the shear-induced isotropic-to-nematic transition. Eur Phys J B 5(1):67–77
199. Berret JF, Porte G (1999) Metastable versus unstable transients at the onset of a shear-induced phase transition. Phys Rev E 60(4):4268–4271
200. Ganapathy R, Sood AK (2006a) Intermittency route to rheochaos in wormlike micelles with flow-concentration coupling. Phys Rev Lett 96(10):108301
201. Soltero JFA, Puig JE, Manero O, Schulz PC (1995) Rheology of cetyltrimethylammonium tosilate-water system .1. relation to phase-behavior. Langmuir 11(9):3337–3346
202. Soltero JFA, Puig JE, Manero O (1996) Rheology of cetyltrimethylammonium tosylate-water system .2. linear viscoelastic regime. Langmuir 12(9):2654–2662
203. Soltero JFA, Bautista F, Puig JE, Manero O (1999) Rheology of cetyltrimethylammonium p-toluenesulfonate-water system. 3. nonlinear viscoelasticity. Langmuir 15(5):1604–1612
204. Hernandez-Acosta S, Gonzalez-Alvarez A, Manero O, Sanchez AFM, Perez-Gonzalez J, de Vargas L (1999) Capillary rheometry of micellar aqueous solutions. J Non-Newt Fluid Mech 85(2–3):229–247
205. Bautista F, Soltero JFA, Macias ER, Puig JE, Manero O (2002) Irreversible thermodynamics approach and modeling of shear-banding flow of wormlike micelles. J Phys Chem B 106(50):13018–13026
206. Bandyopadhyay R, Sood AK (2003) Effect of screening of intermicellar interactions on the linear and nonlinear rheology of a viscoelastic gel. Langmuir 19(8):3121–3127
207. Ganapathy R, Sood AK (2006b) Tuning rheochaos by temperature in wormlike micelles. Langmuir 22(26):11,016–11,021
208. Makhloufi R, Decruppe JP, Aït-Ali A, Cressely R (1995) Rheooptical study of wormlike micelles undergoing a shear banding flow. Europhys Lett 32(3):253–258
209. Aït-Ali A, Makhloufi R (1997a) Linear and nonlinear rheology of an aqueous concentrated system of cetyltrimethylammonium chloride and sodium salicylate. Phys Rev E 56(4):4474–4478
210. Aït-Ali A, Makhloufi R (1997b) On the nonlinear rheology of wormlike micellar system in the presence of sodium salicylate salt. J Rheol 41(2):307–318
211. Decruppe JP, Ponton A (2003) Flow birefringence, stress optical rule and rheology of four micellar solutions with the same low shear viscosity. Eur Phys J E 10(3):201–207
212. Escalante JI, Macias ER, Bautista F, Perez-Lopez JH, Soltero JFA, Puig JE, Manero O (2003) Shear-banded flow and transient rheology of cationic wormlike micellar solutions. Langmuir 19(17):6620–6626
213. Angelescu D, Khan A, Caldararu H (2003) Viscoelastic properties of sodium dodecyl sulfate with aluminum salt in aqueous solution. Langmuir 19(22):9155–9161
214. Schubert BA, Wagner NJ, Kaler EW, Raghavan SR (2004) Shear-induced phase separation in solutions of wormlike micelles. Langmuir 20(9):3564–3573
215. Raghavan SR, Kaler EW (2001) Highly viscoelastic wormlike micellar solutions formed by cationic surfactants with long unsaturated tails. Langmuir 17(2):300–306
216. Hassan PA, Valaulikar BS, Manohar C, Kern F, Bourdieu L, Candau SJ (1996) Vesicle to micelle transition: rheological investigations. Langmuir 12(18):4350–4357
217. Koehler RD, Raghavan SR, Kaler EW (2000) Microstructure and dynamics of wormlike micellar solutions formed by mixing cationic and anionic surfactants. J Phys Chem B 104(47):11,035–11,044
218. Schubert BA, Kaler EW, Wagner NJ (2003) The microstructure and rheology of mixed cationic/anionic wormlike micelles. Langmuir 19(10):4079–4089

219. Mu JH, Li GZ, Jia XL, Wang HX, Zhang GY (2002) Rheological properties and microstructures of anionic micellar solutions in the presence of different inorganic salts. J Phys Chem B 106(44):11,685–11,693
220. Pimenta P, Pashkovski EE (2006) Rheology of viscoelastic mixed surfactant solutions: effect of scission on nonlinear flow and rheochaos. Langmuir 22(9):3980–3987
221. Soltero JFA, Alvarez-Ramirez JG, Fernandez VVA, Tepale N, Bautista F, Macias ER, Perez-Lopez JH, Schulz PC, Manero O, Solans C, Puig JE (2007) Phase and rheological behavior of the polymerizable surfactant CTAVB and water. J Colloid Interface Sci 312(1):130–138
222. Wheeler EK, Fischer P, Fuller GG (1998) Time-periodic flow induced structures and instabilities in a viscoelastic surfactant solution. J Non-Newt Fluid Mech 75(2–3):193–208
223. Fielding SM (2005) Linear instability of planar shear banded flow. Phys Rev Lett 95(13):134501
224. Fielding SM (2007b) Vorticity structuring and velocity rolls triggered by gradient shear bands. Phys Rev E 76(1):016311
225. Fielding SM (2007a) Complex dynamics of shear-banding flows. Soft Matter 3(1):1262–1279
226. Fischer P, Wheeler EK, Fuller GG (2002) Shear-banding structure orientated in the vorticity direction observed for equimolar micellar solution. Rheol Acta 41(1–2):35–44
227. Herle V, Fischer P, Windhab EJ (2005) Stress driven shear bands and the effect of confinement on their structures – a rheological, flow visualization, and rheo-sals study. Langmuir 21(20):9051–9057
228. Herle V, Kohlbrecher J, Pfister B, Fischer P, Windhab EJ (2007) Alternating vorticity bands in a solution of wormlike micelles. Phys Rev Lett 99(15):158,302
229. Herle V, Manneville S, Fischer P (2008) Alternating vorticity bands in a solution of wormlike micelles. Eur Phys J E 26(1):3–12
230. Marin-Santibanez BM, Perez-Gonzalez J, de Vargas L, Rodriguez-Gonzalez F, Huelsz G (2006) Rheometry – piv of shear-thickening wormlike micelles. Langmuir 22(9):4015–4026
231. Jindal V, Kalus J, Pilsl H, Hoffmann H, Lindner P (1990) Dynamic small angle neutron scattering study of rodlike micelles in surfactant solutions. J Phys Chem 94(7):3129–3138
232. Larson R (1988) Constitutive equations for polymer melt and solutions. Butterworth-Heinemann, UK
233. Menezes E, Graessley W (1982) Nonlinear rheological behavior of polymer systems for several shear-flow histories. J Polym Sci 20(10):1817–1833
234. Spenley NA, Yuan XF, Cates ME (1996) Nonmonotonic constitutive laws and the formation of shear-banded flows. J Phys II 6(4):551–571
235. Olmsted PD, Lu CYD (1997) Coexistence and phase separation in sheared complex fluids. Phys Rev E 56(1):R55–R58
236. Ganapathy R, Sood AK (2008) Nonlinear flow of wormlike micellar gels: regular and chaotic time-dependence of stress, normal force and nematic ordering. J Non-Newt Fluid Mech 149(1–3):78–86
237. Ott E (1993) Chaos in dynamical systems. Cambridge University Press, England
238. Fielding SM, Olmsted PD (2004) Spatiotemporal oscillations and rheochaos in a simple model of shear banding. Phys Rev Lett 92(8):084502
239. Bandyopadhyay R, Sood AK (2001) Chaotic dynamics in shear-thickening surfactant solutions. Europhys Lett 56(3):447–453
240. Salmon JB, Colin A, Roux D (2002) Dynamical behavior of a complex fluid near an out-of-equilibrium transition: approaching simple rheological chaos. Phys Rev E 66(3):031505
241. Manneville S, Salmon JB, Colin A (2004c) A spatio-temporal study of rheo-oscillations in a sheared lamellar phase using ultrasound. Eur Phys J E 13(2):197–212
242. Wunenburger AS, Colin A, Leng J, Arneodo A, Roux D (2001) Oscillating viscosity in a lyotropic lamellar phase under shear flow. Phys Rev Lett 86(7):1374–1377
243. Courbin L, Panizza P, Salmon JB (2004) Observation of droplet size oscillations in a two-phase fluid under shear flow. Phys Rev Lett 92(1):018305
244. Lootens D, Van Damme H, Hebraud P (2003) Giant stress fluctuations at the jamming transition. Phys Rev Lett 90(17):178301

245. Manneville S (2008) Recent experimental probes of shear banding. Rheol Acta 47(3): 301–318
246. Callaghan PT (2008) Rheo nmr and shear banding. Rheol Acta 47(3):243–255
247. Salmon JB, Manneville S, Colin A, Pouligny B (2003d) An optical fiber based interferometer to measure velocity profiles in sheared complex fluids. Eur Phys J Appl Phys 22(2):143–154
248. Manneville S, Bécu L, Colin A (2004a) High-frequency ultrasonic speckle velocimetry in sheared complex fluids. Eur Phys J Appl Phys 28(3):361–373
249. Callaghan PT (2006) Rheo-nmr and velocity imaging. Curr Opin Colloid Interface Sci 11(1):13–18
250. Holmes WM, Lopez-Gonzalez MR, Callaghan PT (2004) Shear-induced constraint to amphiphile chain dynamics in wormlike micelles. Eur Phys Lett 66(1):132–138
251. Greco F, Ball RC (1997) Shear-band formation in a non-newtonian fluid model with a constitutive instability. J Non-Newt Fluid Mech 69(2–3):195–206
252. Olmsted PD, Radulescu O, Lu CYD (2000) Johnson-Segalman model with a diffusion term in cylindrical couette flow. J Rheol 44(2):257–275
253. Raudsepp A, Callaghan PT (2008) A rheo-optical study of shear rate and optical anisotropy in wormlike micelles solutions. Soft Matter 4(4):784–796
254. Fuller G (1995) Rheology of wormlike micelles: equilibrium properties and shear-banding transition In: Optical rheometry of complex fluids, Oxford University Press, New York
255. Humbert C, Decruppe JP (1998a) Flow birefringence and stress optical law of viscoelastic solutions of cationic surfactants and sodium salicylate. Eur Phys J B 6(4):511–518
256. Callaghan PT (1999) Rheo-nm nuclear magnetic resonance and the rheology of complex fluids. Rep on Prog in Phys 62(4):599–670
257. Helfand E, Fredrickson GH (1989) Large fluctuations in polymer-solutions under shear. Phys Rev Lett 62(21):2468–2471
258. Liberatore MW, Nettesheim F, Wagner NJ, Porcar L (2006) Spatially resolved small-angle neutron scattering in the 1-2 plane: a study of shear-induced phase-separating wormlike micelles. Phys Rev E 73(2):020504
259. Hilliou L, Vlassopoulos D (2002) Time-periodic structures and instabilities in shear-thickening polymer solutions. Ind Eng Chem Res 41(25):6246–6255
260. Dhont JKG, Lettinga MP, Dogic Z, Lenstra TAJ, Wang H, Rathgeber S, Carletto P, Willner L, Frielinghaus H, Lindner P (2003) Shear-banding and microstructure of colloids in shear flow. Faraday Discuss 123:157–172
261. Kang KG, Lettinga MP, Dogic Z, Dhont JKG (2006) Vorticity banding in rodlike virus suspensions. Phys Rev E 74(2):026307
262. Cates ME (1990) Nonlinear viscoelasticity of wormlike micelles (and other reversibly breakable polymers). J Phys Chem 94(1):371–375
263. Olmsted PD, Goldbart P (1990) Theory of the nonequilibrium phase-transition for nematic liquid-crystals under shear-flow. Phys Rev A 41(8):4578–4581
264. Dhont JKG (1999) A constitutive relation describing the shear-banding transition. Phys Rev E 60(4):4534–4544
265. Olmsted PD (1999a) Dynamics and flow-induced phase separation in polymeric fluids. Curr Opin Colloid Inter Sci 4(2):95–100
266. Radulescu O, Olmsted PD, Lu CYD (1999) Shear banding in reaction-diffusion models. Rheol Acta 38(6):606–613
267. Yuan XF (1999) Dynamics of a mechanical interface in shear-banded flow. Eur Phys Lett 46(4):542–548
268. Lu CYD, Olmsted PD, Ball RC (2000) Effects of nonlocal stress on the determination of shear banding flow. Phys Rev Lett 84(4):642–645
269. Radulescu O, Olmsted PD (2000) Matched asymptotic solutions for the steady banded flow of the diffusive johnson-segalman model in various geometries. J Non-Newt Fluid Mech 91(2–3):143–164
270. Adams J, Fielding S, Olmsted PD (2008) The interplay between boundary conditions and flow geometries in shear banding : hysteresis, band configurations, and surface transitions. J Non-Newt Fluid Mech 151(3):101–118

271. Olmsted PD (1999b) Two-state shear diagrams for complex fluids in shear flow. Europhys Lett 48(3):339–345
272. Aradian A, Cates ME (2005) Instability and spatiotemporal rheochaos in a shear-thickening fluid model. Eur Phys Lett 70(3):397–403
273. Aradian A, Cates ME (2006) Minimal model for chaotic shear banding in shear thickening fluids. Phys Rev E 73(4):041508
274. Wilson HJ (2006) Instabilities and constitutive modelling. Philos Trans R Soc A 364(1849):3267–3283
275. Fielding SM, Olmsted PD (2006) Nonlinear dynamics of an interface between shear bands. Phys Rev Lett 96(10):104502
276. Oswald P, Pieranski P (2000) Les cristaux liquides. Gordon and Breach, Amsterdam
277. Onsager L (1949) The effects of shape on the interaction of colloidal particles. Ann NY Acad Sci 51:627–649
278. Leadbetter A, Wrighton P (1979) Order parameters in sa, sc and n phases by X-ray diffraction. J Phys C3 40:234–242
279. Lawson K, Flautt T (1967) Magnetically oriented lyotropic liquid crystalline phase. J Am Chem Soc 89:5489–5491
280. Itri R, Amaral L (1990) Study of the isotropic-hexagonal transition in the system SLS/H2O. J Phys Chem 94:2198–2202
281. Quist PO, Halle B, Furo I (1992) Micelle size and order in lyotropic nematic phases from nuclear spin relaxation. J Chem Phys 96:3875–3891
282. Itri R, Amaral L (1993) Micellar-shape anisometry near isotropic-liquid-crystal phase transition. Phys Rev E 47:2551–2557
283. Berret JF, Roux DC (1995) Rheology of nematic wormlike micelles. J Rheol 39(4):725–741
284. Thiele T, Berret JF, Muller S, Schmidt C (2001) Rheology and nuclear magnetic resonance measurements under shear of sodium dodecyl sulfate/decanol/water nematics. J Rheol 45(1):29–48
285. Clawson JS, Holland GP, Alam TM (2006) Magnetic alignment of aqueous ctab in nematic and hexagonal liquid crystalline phases investigated by spin-1 nmr. Phys Chem Chem Phys 8(22):2635–2641
286. De Melo Filho AA, Amadeu NS, Fujiwara FY (2007) The phase diagram of the lyotropic nematic mesophase in the ttab/nabr/water system. Liq Crys 34(6):683–691
287. Chen DM, Fujiwara FY, Reeves LW (1977) Studies of behavior in magnetic-fields of some lyomesophase systems with respect to electrolyte additions. Can J Chem-Rev Can Chim 55(12):2396–2403
288. Hendrikx Y, Charvolin J (1981) Structural relations between lyotropic phases in the vicinity of the nematic phases. J Phys 42:1427–1440
289. Hendrikx Y, Charvolin J, Rawiso M, Liebert L, Holmes M (1983) Anisotropic aggregates of amphiphilic molecules in lyotropic nematic phases. J Phys Chem 87:3991–3999
290. Caputo FE, Ugaz VM, Burghardt WR, Berret JF (2002) Transient 1-2 plane small-angle X-ray scattering measurements of micellar orientation in aligning and tumbling nematic surfactant solutions. J Rheol 46(4):927–946
291. Semenov A, Khokhlov A (1988) Statistical physics of liquid-crystalline polymers. Sov Phys Usp 31:988–1014
292. Khokhlov A, Semenov A (1981) Liquid-crystalline ordering in the solution of long persistent chains. Physica A 108:546–556
293. Richtering W, Laeuger J, Linemann R (1994) Shear orientation of a micellar hexagonal liquid crystalline phase: a rheo and small angle light scattering study. Langmuir 10(11):4374–4379
294. Lukaschek M, Grabowski D, Schmidt C (1995) Shear-induced alignment of a hexagonal lyotropic liquid crystal as studied by rheo-nmr. Langmuir 11(9):3590–3594
295. Muller S, Fischer P, Schmidt C (1997) Solid-like director reorientation in sheared hexagonal lyotropic liquid crystals as studied by nuclear magnetic resonance. J Phys II France 7:421–432
296. Schmidt G, Muller S, Lindner P, Schmidt C, Richtering W (1998) Shear orientation of lyotropic hexagonal phases. J Phys Chem B 102(3):507–513

297. Schmidt C (2008) Rheo-nmr spectroscopy. Modern Magnetic Resonance 3:1515–1521
298. Ramos L, Molino F, Porte G (2000) Shear melting in lyotropic hexagonal phases. Langmuir 16(14):5846–5848
299. Ramos L (2001) Scaling with temperature and concentration of the nonlinear rheology of a soft hexagonal phase. Phys Rev E 64(6):061502
300. Ramos L, Molino F (2004) Shear melting of a hexagonal columnar crystal by proliferation of dislocations. Phys Rev Lett 92(1):018301
301. Roux DC, Berret JF, Porte G, Peuvrel-Disdier E, Lindner P (1995) Shear-induced orientations and textures of nematic wormlike micelles. Macromolecules 28(5):1681–1687
302. Berret JF, Roux DC, Porte G, Lindner P (1995) Tumbling behavior of nematic wormlike micelles under shear-flow. Europhys Lett 32(2):137–142
303. Caputo FE, Burghardt WR, Berret JF (1999) Tumbling dynamics in a nematic surfactant solution in transient shear flows. J Rheol 43(3):765–779
304. Burghardt W, Fuller G (1991) Role of director tumbling in the rheology of polymer liquid crystal solutions. Macromolecules 24(9):2546–2555
305. Moldenaers P, Yanase H, Mewis J (1991) Flow-induced anisotropy and its decay in polymeric liquid crystals. J Rheol 35(8):1681–1699
306. Larson R, Doi M (1991) Mesoscopic domain theory for textured liquid crystalline polymers. J Rheol 35:539–563
307. Srinivasarao M (1992) Rheology and rheo-optics of polymer liquid crystals: an overview of theory and experiment. Chemtracts Macromol Chem 3:149–178
308. Takahashi Y, Kurashima N, Noda I, Doi M (1994) Experimental tests of the scaling relation for textured materials in mixtures of two immiscible fluids. J Rheol 38(3):699–712
309. Thiele T, Berret JF, Mueller S, Schmidt C (1998) Rheology and nmr measurements on sds/decanol/water. In: 5th European Rheology Conference, Portoroz (Slovenia)
310. Doi M, Ohta T (1991) Dynamics and rheology of complex interfaces. I. J Chem Phys 95(2):1242–1248
311. Larson RG, Mead DW (1993) The ericksen number and deborah number cascades in sheared polymeric nematics. Liq Crys 15(2):151–169
312. Marrucci G (1985) Rheology of liquid crystalline polymers. Pure and Appl Chem 57:1545–1552
313. Larson R, Mead D (1992) Development of orientation and texture during shearing of liquid-crystalline polymers. Liq Cryst 12:751–768
314. Vermant J, Moldenaers P, Mewis J, Picken S (1994) Band formation upon cessation of flow in liquid-crystalline polymers. J Rheol 38:1571–1589
315. Noirez L, Lapp A (1997) Shear flow induced transition from liquid-crystalline to polymer behavior in side-chain liquid crystal polymers. Phys Rev lett 78:70–73
316. Zipfel J, Berghausen J, Lindner P, Richtering W (1999) Influence of shear on lyotropic lamellar phases with different membranes defects. J Phys Chem B 103:2841–2849
317. Berret JF, Vermant J, Noirez L (2000b) Lyotropic surfactant nematics under shear: neutron scattering in the vorticity plane. In: XIIIth international Congress on Rheology, Cambridge (UK), vol 3, pp 273–275
318. Ekwall P, Mandell L, Fontell K (1969) The cetyltrimethylammonium bromide-hexanol-water system. J Colloid Interface Sci 29(4):639–646
319. Hongladarom K, Burghardt W (1994) Measurements of the full refractive index tensor in sheared liquid-crystalline polymer solutions. Macromolecules 27:483–489
320. Grabowski D, Schmidt C (1994) Simultaneous measurements of shear viscosity and director orientation of a side-chain liquid crystalline polymer by rheo-NMR. Macromolecules 27:2632–2640
321. Siebert H, Grabowski D, Schmidt C (1997) Rheo-nmr study of non-flow-aligning side-chain liquid crystal polymer in nematic solution. Rheol Acta 36:618–627

Editor: J.-F. Joanny

Adv Polym Sci (2010) 230: 73–219
DOI:10.1007/12_2009_36

Published online: 18 February 2010

Laser-Interferometric Creep Rate Spectroscopy of Polymers

Vladimir A. Bershtein and Pavel N. Yakushev

Abstract Laser-interferometric creep rate meter (LICRM) and creep rate spectroscopy (CRS), as an original high-resolution method for discrete relaxation spectrometry and thermal analysis, were developed in the authors' Materials Dynamics Laboratory at Ioffe Physical-Technical Institute of the Russian Academy of Sciences (Saint-Petersburg). In the last few decades they have been successfully applied to solving various problems of polymer physics and materials science, especially being combined with DSC, structural, and other techniques. CRS involves measuring ultra-precisely a creep rate at small tensile or compressive stress, typically much lower than the yield stress, as a function of temperature, over the range from 100 to 800 K. LICRM setup allows one to register precisely creep rates on the basis of deformation increment of 150–300 nm. The survey describes this method and summarizes the results of numerous studies performed with the LICRM setup and CRS technique for different bulk polymeric materials, films, or thin fibers. This approach provided new experimental possibilities superior in resolution and sensitivity compared to the conventional relaxation spectrometry techniques. Among such possibilities are discrete analysis of dynamics; creep on submicro-, micro- and meso-scales; revealing relations between stepwise microplasticity and morphology; kinetic information on creep at any temperature and deformation; polymer dynamics at interfaces; analysis of microplasticity, relaxations, and phase transitions in brittle materials; using creep rate spectra for non-destructive prediction of temperature anomalies in mechanical behavior of materials, etc. Considerable attention has been paid to combined CRS/DSC analysis of the peculiarities of segmental dynamics, nanoscale dynamic, and compositional heterogeneity in different kinds of complex polymer systems and nanocomposites.

V.A. Bershtein (✉) and P.N. Yakushev
Ioffe Physical-Technical Institute of the Russian Academy of Sciences,
26 Polytechnicheskaya str., 194021 Saint-Petersburg, Russia
e-mail: vbersht@polmater.ioffe.ru; yak@pav.ioffe.ru

Keywords Complex polymer systems · Deformation kinetics · Dynamic heterogeneity · Glass transition anomalies · Laser interferometry · Microplasticity vs morphology · Polymer creep · Relaxation dynamics

Contents

Abbreviations

BCP	Block copolymer
BLS	Brilllouin light scattering
CNT	Carbon nanotube
CR	Creep rate (spectra, peaks)
CRS	Laser-interferometric creep rate spectroscopy
DBP	Dibutyl phthalate
DMA	Dynamic mechanical analysis
DMA(σ)	Dynamic mechanical analysis of the statically loaded solids
DRS	Dielectric relaxation spectrometry
DSC	Differential scanning calorimetry
FIRS	Far-infrared spectroscopy
FT-IR	Fourier-transform infrared spectroscopy
HDPE	High-density polyethylene
HEMA	2-Hydroxyethyl methacrylate
IPN	Interpenetrating polymer network
IRS	Infrared spectroscopy
LI	Laser interferometer; Laser interferometry
LICRM	Laser-interferometric creep rate meter
MAA	Methacrylic acid
MDS	Molecular-dynamics simulations
MMT	Montmorillonite (silicate nanolayers)
ND	Nanodiamond
NMR	Nuclear magnetic resonance
ODA	Oxydianiline
PAN	Polyacrylonitrile
PB	Polybutadiene
PBMA	Poly(*n*-butyl methacrylate)
PC	Polycarbonate
PCN	Polycyanurate
PDMS	Poly(dimethyl siloxane)
PE	Polyethylene
PEA	Poly(ethylene adipate)
PEG	Poly(ethylene glycol)
PEO	Poly(ethylene oxide)
PET	Poly(ethylene terephthalate)
PHEMA	Poly(2-hydroxyethyl methacrylate)
PI	Polyimide
PIA	Poly(imide-amide)
PMDA	Pyromellitic dianhydride
PMMA	Poly(methyl methacrylate)
PMPS	Poly(methylphenylsiloxane)
PMS	Poly(α-methylstyrene)
POM	Poly(oxymethylene)

PS	Polystyrene
PTFE	Poly(tetrafluoroethylene)
PTMG	Poly(tetramethylene glycol)
PU	Polyurethane
PVB	Poly(vinyl butyral)
PVC	Poly(vinyl chloride)
PVME	Poly(vinyl methyl ether)
PVP	Poly(vinyl pyrrolidone)
QENS	Quasi-elastic neutron scattering
RAF	Rigid amorphous fraction
SANS	Small-angle neutron scaterring
SAXS	Small-angle X-ray scattering
SEM	Scanning electron microscopy
TDI	Toluene diisocyanate
TEM	Transmission electron microscopy
TMP	Trimethylolpropane
TSDC	Thermally stimulated depolarization currents
UHMWPE	Ultrahigh-molecular-weight polyethylene
WAXD	Wide-angle X-ray diffraction

Symbols

E, Q	Activation energy
Q_0	Activation energy of deformation
Q_α	Activation energy of α-relaxation (glass transition)
Q_β	Activation energy of β-relaxation
ΔS	Activation entropy
v_{act}	Activation volume
α	Activation volume of deformation
v_α	Activation volume of α-relaxation (glass transition)
v_β	Activation volume of β-relaxation
R_{EE}	Average end-to-end distance for unperturbed macromolecule (random coil size)
T_β	Beta-relaxation temperature
E_{coh}	Cohesion energy
T_g''	Completion glass transition temperature
$\dot{\varepsilon}$	Creep rate (velocity of the moving mirror)
T_c	Crossover temperature in the Mode Coupling Theory
L	Deformation step in jump-like creep
v_{CRR}	Donth's cooperatively rearranging region
$\Delta\omega$	Doppler shift
ν_{eq}	Equivalent frequency
Q_η	Flow activation energy

T_f	Flow temperature
ν	Frequency, Beat frequency
R	Gas constant
ΔT_g	Glass transition range
T_g	Glass transition temperature
ΔC_p	Heat capacity step
ω_1	Incident laser beam frequency
I_1	Incident laser beam intensity
Q_i', Q_i'', Q_i'''	"Intermediate" relaxations activation energies
T_i', T_i'', T_i'''	"Intermediate" relaxations temperatures
E_{IMI}	Intermolecular interactions energy
Q_0^{-1}	Internal friction (DMA)
Q_τ^{-1}	Internal friction under static loading [DMA(σ)]
B	Internal rotation barrier in chains
H	Jump sharpness in stepwise creep, Film thickness
A	Kuhn segment length
λ	Laser wavelength
C	Light velocity
T_{ll}	"Liquid–liquid" transition temperature
t_m	Maximal tangential stress
T_m	Melting point
C_m	Mobile fraction (NMR)
V_M	Molar volume
σ	Normal stress
N_k	Number of monomer units in Kuhn segment
m	Number of monomer units per a kinetic unit (activation volume) of deformation
N	Number of oscillations (beats) in the interferogram
M_n	Number-average molecular mass
T_g'	Onset glass transition temperature
Z	Parameter of cooperativity in segmental motion
q_i	Partial energy barrier (per mole of monomer units) in deformation kinetics
$\dot{\varepsilon}_0$	Pre-exponential factor (deformation kinetics)
R_g	Radius of gyration
ω_2	Reflected laser beam frequency
I_2	Reflected laser beam intensity
I	Resultant laser beam intensity
τ_{sh}	Shear stress
δ	Solubility parameter
T_s	Splitting (bifurcation) point
T	Temperature
t	Time
ε	Total creep value
V	Volume of monomer unit, Heating rate

M_w	Weight-average molecular mass
ε_y	Yield point deformation
σ_y	Yield stress (point)

1 Introduction

In the surrounding world, physical objects, such as various solids, industrial materials, constructions, buildings, and natural substances, are subjected to continuous or periodical impact of a constant mechanical stress that may lead to their creep. For this reason, scientists have widely studied the problems of the creep resistance of metals at ultrahigh temperatures and polymeric and other materials under normal conditions, as well as slow creep processes occurring in some areas of earth crust. These studies have been particularly extensive in the last few decades.

An increase in the accuracy of creep measurements has always been of importance but recently it has become a focal research problem for two reasons. First, the development of novel highly precise instruments for measuring creep rates is necessary in the context of increased interest in studies being performed on the micro-, submicro-, and even nano-levels. Second, it may a priori be assumed that creep behavior of polymeric materials is associated intimately with their basic physical characteristics, namely, molecular dynamics and supermolecular structure. However, the common widespread methods of the deformation measurements provide a rather "smoothed" picture and often allow no discerning of the fine effects depending on the changes in dynamics and structure of materials.

In this survey, the novel Laser-Interferometric Creep Rate Meter (LICRM) setup and the original method of Creep Rate Spectroscopy (CRS) are described. We present the results of the numerous applications, in particular the new CRS possibilities as the high resolution method for the relaxation spectroscopy and thermal analysis of polymer systems. Furthermore, this method contributes to general progress in studying the deformation properties of polymers and other solids, especially at the micro- and submicrolevels.

The method being described is based on the high-precision measurement of the parameters of the extremely small linear displacements, aided by a laser interferometer in combination with the devices for mechanical tests.

Since the nineteenth century, interferometers have been known as tools for the measurement of small linear displacements. Until the last few decades, this kind of measurement had a limited application and did not expand beyond laboratories since it required significant labor expenses, was complicated by the separation of coherent light source and its exploitation, and used a "hands-on" approach to the interference fringes calculation.

Thanks to the invention of lasers, the revolutionary breakthrough in this field occurred in the 1960s. Since then, lasers have become ubiquitous, utilized in thousands of highly varied applications in every section of modern society, including consumer electronics, information technology, science, medicine, industry, entertainment, and

the military. Since the early period of laser history, laser research has produced a variety of improved and specialized laser types including solid-state lasers, gas lasers, semiconductor lasers, as well as chemical, liquid, eximer, fiber-hosted, and many other types of lasers [1].

In recent decades, Laser Interferometer (LI) systems based on the Michelson interferometer have been used in a very wide range of applications, first of all in non-contact measurements of distance or small displacement with high accuracy and nearly unlimited resolution. Laser interferometer application has proved itself successful in various technical applications as well as in physics, geophysics, biology, medicine, and other fields [2]. For instance, different problems such as plasma diagnostics, measuring distances in cosmic studies, or vibratory displacement measuring have been solved with help of the LI systems. The results of numerous laser interferometry studies have been presented regularly for many years at the International Conferences in San Diego (USA).

For the design of LI the lasers were used which emitted radiation over the spectral range of the visible region. In this case, it is easy to adjust the optical part of a measuring device and to control its state in the course of experiment. As a rule, the lasers of continuous work (*cw*) regime are used for deformation measurements. Among them, He–Ne lasers with the wavelength $\lambda = 623.8\,\text{nm}$ are most representative because of their reasonable cost, despite the fact that they have an exceptionally low gain and efficiency, and their *cw* output does not exceed 100 mW. Their applications are typically limited to low-power tasks which include interferometric measurements.

In recent years, however, semiconductor lasers have been greatly improved, which has led to their increased advantage over gas lasers. The strength of semiconductor lasers consists in compactness, simplicity, and the convenience of operation. The devices that use laser diodes are comparable with systems based on a typical He–Ne laser. Gas lasers are facing stiff competition from semiconductor lasers but they are still powerful tools in many scientific, medical, and industrial applications.

The prehistory of the method which we describe in the survey began in 1968 when Barker developed a new scheme for a Michelson interferometer with a He–Ne laser looking for the measurement of the high-speed displacements of ca. 10^2–$10^3\,\text{m}\,\text{s}^{-1}$ [3]. It was made because the frequency of the Michelson interferometer output at such velocities was too high to be registered. In order to overcome this limitation, Barker developed an original velocity interferometer by introducing, additionally, the "delay line" into the Michelson interferometer. As a result, the signal frequencies became proportional instead of displacement to displacement velocity. This simplified significantly the high-speed registration, and in fact the new kind of interferometers has found a wide range of application [4, 5].

In the same years, our Materials Dynamics Laboratory at the A.F. Ioffe Physical-Technical Institute of the Russian Academy of Sciences in Saint-Petersburg carried out investigations of the stress-wave propagation in solids, and Barker's idea was realized in the original high-speed interferometer designed for measuring both the shock-transit time and a profile of the transmitted stress wave [6, 7]. This setup allowed a variety of shock-wave studies to be performed for polymers, glass-fiber-reinforced plastics, ceramics and metals.

In the late 1970s, a new, opposite idea was born in our laboratory, to measure precisely the ultralow creep rates in materials using the solutions found for high-speed measurements. This task was successfully solved by integration of a laser interferometer with the home-made setup for mechanical testing of solids. As a result, Pugachev, Peschanskaya, and Yakushev [8, 9] developed a new type of the research equipment: laser interferometers combined with the setup for mechanical testing of materials under compression or tension. Later, such a setup was called LICRM. It provided the possibilities for the high-precision measurement of creep rates in the range from 10^{-10} to $10^{-3}\,\mathrm{m\,s^{-1}}$, over wide ranges of stresses and temperatures, and at the limit on the basis of a deformation increment of only 150 nm. This created a qualitatively new experimental level for measuring deformation rates and performing the respective studies.

Using both gas and semiconductor lasers in the different modifications of these instruments, the new LICRM apparatus made it possible to develop a new way for the studies of relaxation dynamics and thermal characterization of polymers and other solids. This new method was later named the laser-interferometric Creep Rate Spectroscopy (CRS). The first publication on this topic appeared in 1984 [10], and the short survey of the earlier studies, performed with the LICRM setup and the CRS technique, was published in 1994 [11].

2 Laser-Interferometric Creep Rate Spectroscopy

2.1 Laser-Interferometric Creep Rate Meter: A Scheme of the Setup and the Principle of Operation

Laser interferometry represents the most perfect up-to-date trend in the high-precision measurements of displacements (creep rates or creep values, in our case) using an optical approach to recording the deformation characteristics, while transforming an optical signal into an electrical one convenient for registering and following processing. The LICRM setups, developed in our laboratory, are optical-electronic devices combined with the setups for mechanical loading, under uniaxial tension or compression, of solid samples.

The main point is as follows. When a beam from the stabilized laser is reflected from a moving surface, motion of this target induces a slight frequency shift in the beam due to the Doppler effect. This frequency shift may be measured and converted into the displacement characteristics.

The LICRM setup is based on utilizing a Michelson interferometer, in which the continuously operating laser (as highly stabilized coherent light source) is applied to recording the deformation characteristics. A plane mirror or corner reflector is rigidly connected with the moving clamp (under extension) or the puncheon (under compression) following the deformation of a loaded specimen.

If this reflector is moved in the direction normal to its face, the laser beam reflected off this mirror undergoes a “longitudinal” Doppler effect (a Doppler shift

$\Delta\omega$) when the beam frequency is shifted from an incident beam frequency ω_1 to a frequency ω_2:

$$\Delta\omega = \pm\,(\omega_2 - \omega_1). \tag{1}$$

The frequency of the reflected beam is determined by the formula

$$\omega_2 = \omega_1 \frac{1 + \frac{u}{c}}{\sqrt{1 - \frac{u^2}{c^2}}}, \tag{2}$$

where the light velocity $c = 3 \times 10^8\,\mathrm{m\,s^{-1}}$, and u is a velocity of the light source in the mirror (virtual image), that is, $u = 2\dot{\varepsilon}$ where $\dot{\varepsilon}$ is a velocity of the moving mirror. Since $u^2 \ll c$, (2) can be rewritten as

$$\omega_2 = \omega_1(1 + 2\dot{\varepsilon}/c) \quad \text{or} \tag{3}$$

$$\Delta\omega = 2\dot{\varepsilon}\omega_1/c. \tag{4}$$

In the interferometer, two laser beams with close frequencies, a beam of changed frequency ω_2 and an initial incident beam with frequency ω_1, are superposed. Their interference results in low-frequency beats arising in a resultant beam with the intensity oscillating with the "beat frequency" $\Delta\omega = \omega_2 - \omega_1$; this intensity is transformed by the photocells into an electric signal of the same "Doppler frequency" ν (Fig. 1).

If the intensities of incident and reflected laser beams are designated as I_1 and I_2, the intensity of the resultant beam I may be expressed by the formula

$$I = I_1 + I_2 + 2\sqrt{(I_1 I_2)\cos\Delta\omega\mathrm{t}}. \tag{5}$$

The maximum intensity $I_{\max}$ of the beat wave is attained at $\cos\,\Delta\omega t = 1$. Therefore, the intensity of the resultant light beam varies from zero to $I_{\max} = 4I_1$ with

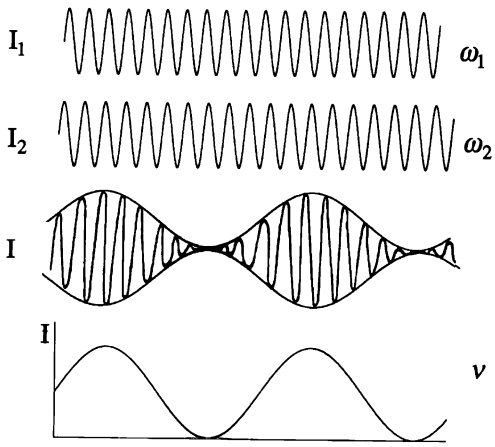

Fig. 1 Formation of low-frequency Doppler beats

a frequency designated below as a beat frequency ν. Taking into account that $\nu = \Delta\omega/2\pi$ and $\omega_1 = 2\pi c/\lambda$, (4) gives

$$\nu = 2\dot{\varepsilon}/\lambda, \tag{6}$$

where $\lambda \approx 650\,\text{nm}$ is the wavelength for a semiconductor laser being used. Since the rate $\dot{\varepsilon}$ to be measured could vary in our experiments in the range from 10^{-10} to $10^{-3}\,\text{m}\,\text{s}^{-1}$, Doppler frequency $\nu \approx (10^{-4} - 10^{3})\,\text{s}^{-1}$. These frequencies are attainable for measuring with the up-to-date instruments.

Thus, the time evolution of the creep process is registered as an interferogram. A displacement velocity $\dot{\varepsilon}$ of the mirror rigidly connected with the moving clamp, that is, a specimen creep rate, and its total displacement (total specimen deformation) ε may be determined using the relations

$$\dot{\varepsilon} = \frac{\lambda}{2}\nu \quad \text{and} \tag{7}$$

$$\varepsilon = \frac{\lambda}{2}N, \tag{8}$$

where N is a number of oscillations of the intensity (beats) in the interferogram sector chosen for the measurements.

Figure 2 shows three variants of the optical schemes utilized in the LICRM setups. Each of these schemes has inherent advantages and disadvantages. The scheme "**a**" is the simplest regarding its adjustment and the control regulation in the course of an experiment, but the coefficient of light efficiency of this scheme is relatively low due to substantially different intensities of interfering beams c and b. This disadvantage is practically absent in the scheme "**b**"; however, it is more difficult for the adjustment. The scheme "**c**" incorporating the corner reflectors turned out to be optimal regarding both light utilizing and the convenience of the adjustment.

The principle of operating the optical schemes in the LICRM systems is as follows (Fig. 2a). The beam a from the laser light source 1 is split by the semi-transparent mirror ("50% beam splitter") 6 into sub-beams b and c. The latter transmitted beam attains the semi-transparent mirror 7 with the unchangeable frequency, whereas the beam b undergoes to Doppler frequency shift $\Delta\omega$ after reflection from the moving reflector 2. Then both beams are superposed at mirror 7. Due to interference of beams b and c, light flux Φ_1 with periodically changing intensity (beat frequency ν) reaches photocell 5. Simultaneously, light flux Φ_2 with invariable intensity reaches photocell 4. Further, the signal from photocell 4 is subtracted from the signal of photocell 5, and only the variable component of light flux, caused by the displacement of moving reflector 2, is registered as an electric signal with varying beat frequency ν.

On the basis of these measurements and using (7) and (8), a displacement velocity of the moving reflector 2, i.e., creep rate $\dot{\varepsilon}$ of a specimen, and a total displacement of this reflector, i.e., deformation ε of a specimen, are recorded.

The LICRM setups have been built and successfully used for studying bulk samples, films, or thin fibers operating under uniaxial compression or extension.

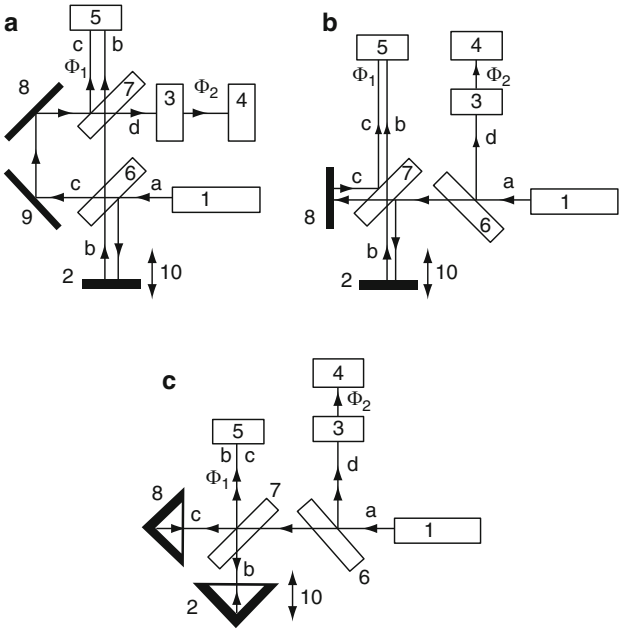

Fig. 2 Schemes of the optical part in the LICRM system. 1, Laser light source; 2, movable plane mirror or corner reflector; 3, polarizer; 4 and 5, photocells; 6 and 7, semi-transparent (half-silvered) mirrors; 8 and 9, stationary mirrors; 10, the directions for the reflector 2 displacement

Figure 3 shows the scheme of the LICRM setup that operates under compressive stress. Cylindrical specimen 9, with typically 6 mm height and 3 mm in diameter, is set between immobile support 10 and mobile puncheon 11. Loading is performed via the lever system. Figured lever 14 allows a stress in the specimen to be unchanged irrespective of a degree of its deformation. Corner reflector 2, as the element of the optical part of the setup, is rigidly attached to mobile puncheon 11. Besides interferometric recording, total deformation of a specimen is also controlled by clock-like micrometer 12. The temperature conditions of an experiment are assigned by heater 18 that is operated by programmed automatic temperature regulator 19/20.

In short-time experiments, an electric signal on the way out of the interferometer after amplifying 21 is registered by recorder 22. Figure 4 gives an example of such registration and the respective creep rate vs time plot. Moreover, computer processing of the data being obtained is typically performed. For this purpose the initial analog signal of sinusoidal form (Fig. 1) is converted by Schmitt trigger 24 into the meander, and then it can be recognized by the interface board that is built into the computer 25 (Fig. 3). As a result, automatic plotting of $\dot{\varepsilon} = f(t)$, $\dot{\varepsilon} = f(\varepsilon)$, and $\varepsilon = f(t)$ curves may be performed during the course of experiment. Figure 5 represents schematically three lines of deformation information, including a typical stress–strain $\sigma(\varepsilon)$ curve (dotted line), for a glassy polymer; the yield point with parameters σ_y and ε_y is also indicated.

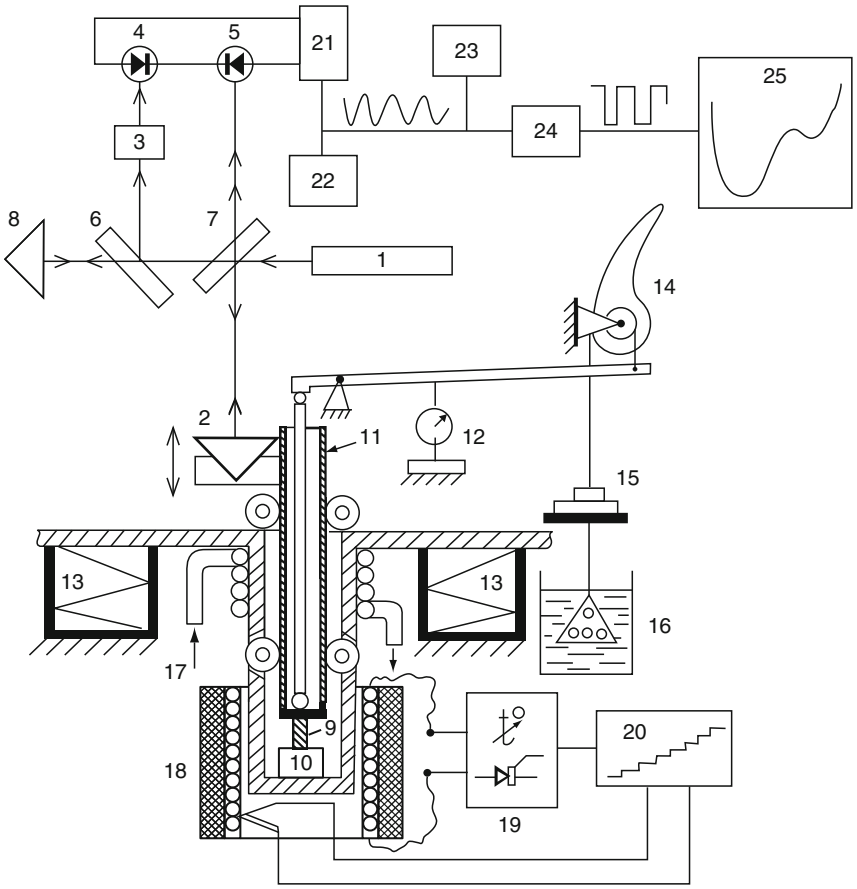

Fig. 3 A scheme of the LICRM setup operating under compressive stress. 1, Laser light source; 2, movable corner reflector; 3, polarizer; 4 and 5, photocells; 6 and 7, semi-transparent mirrors; 8, stationary corner reflector; 9, specimen; 10, support; 11, puncheon; 12, clock-like scale micrometer for rough controlling deformation; 13, dampers; 14, figured lever providing a stress constancy; 15, load; 16, oil damper; 17, cooling unit; 18, heater; 19 and 20, programmable temperature regulator; 21, amplifier; 22, tape recorder; 23, oscillograph; 24, shaper of a meander (Schmitt trigger); 25, computer with the interface board imbedded

Taking (7) and (8) into account, the relative values of creep rate and total creep value are calculated by formulas

$$\dot{\varepsilon} = \frac{\lambda}{2L_0} v \ (\mathrm{s}^{-1}) \quad \text{and} \tag{9}$$

$$\varepsilon = \frac{\lambda}{2L_0} N \times 100 \ (\%), \tag{10}$$

where L_0 is the initial length of a specimen.

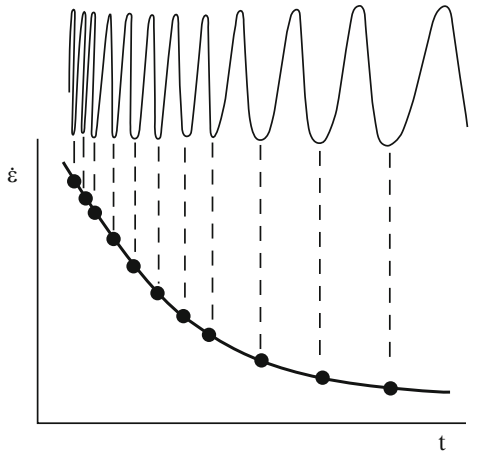

Fig. 4 A scheme of the interferogram/creep rate vs time plots obtained using the LICRM setup

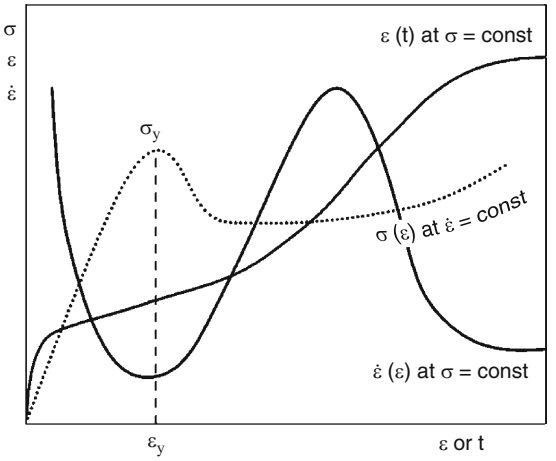

Fig. 5 Schematic representation of deformation information types being obtained using the LICRM setup

The most obvious merit of the technique being described is that the interferometer has great inherent accuracy combined with the high sensitivity and resolution (see below). Additionally, a few other advantages of this method must be mentioned. Thus, LICRM needs no calibration, and the mechanical contact of a specimen with the measuring scheme is excluded. It means that the measurement process itself does not affect the result obtained. LICRM is an inertia-less instrument. The linear dependence between deformation and signal characteristics is retained at any displacement (deformation), and the continuous information of the indicated types can be obtained in the course of the experiment. Insensitivity of a laser beam to the external influence, such as electric and magnetic fields, irradiation, etc., is also essential in some cases.

2.2 *Creep Rate Spectrum: Scheme of the Experiment, Optimal Experimental Conditions, Spectral Resolution, and Reproducibility*

One of the main purposes of utilizing the LICRM setup is registering the Creep Rate (CR) spectra of solids, i.e., measuring creep rate at applying the small stress as a function of temperature ($\dot{\varepsilon}$ vs T plot). A scheme in Fig. 6 illustrates the sequence of actions in the CRS experiment (1); the regular changes in the process parameters (σ, ε, T) with time (2), and gives an example of forming the CR spectrum (3).

CRS experiment starts from cooling a specimen down to the lowest point of the experimental temperature range and holding it at this temperature for stabilizing its thermal state; this procedure takes typically 1 h at -150°C. When background rate becomes less than $10^{-6}\,s^{-1}$, a small stress chosen from the trial experiment, much less than 10% of the yield stress or fracture stress at room temperature (typically of about 5–20 MPa) is applied. A load is usually chosen to attain about 1 μm creep at minimum temperature for 1 min. Within or in the vicinity of the temperature region of glass transition, the chosen stress is decreased by an order of magnitude, down to 1–2 MPa or less.

The specimen is held under stress for $\sim$1 min, and the deformation process is recorded in the interferogram. Then a specimen is unloaded, heated at the rate of 1 K min^{-1} to a temperature ΔT higher and loaded again with the same stress; again, the interferogram is registered, the sample is unloaded and so on. The choice of ΔT "step" determines the number of experimental points in a CR spectrum; its value may be 4–5 K for studying the broad relaxation regions but 1–2 K only for the transitions occurring in the narrow temperature regions.

Figure 6 shows that a small deformation of the sample accumulated for 1 min loading is totally reversible after unloading since creep at a low stress was predominantly associated with local shear strains (micro- or even submicro-plasticity).

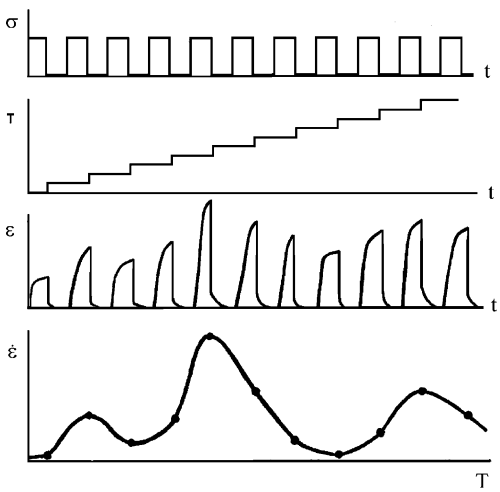

Fig. 6 A scheme of the CRS experiment (see text)

Moreover, a total recovery of an initial creep rate was observed after a reverse jump in temperature. This assumed that the structural state of a specimen remained unchanged during the measuring process. In addition, in the extension experiments a specimen was set into the special clamps providing high friction and preventing the errors from a slip; the latter was confirmed by a full recovery after unloading.

At low-stress loading of the samples, the creep rate typically decreases as the creep process proceeds (Fig. 4). Therefore, besides a stress value, the time t from a moment of loading to an onset of measurement, as the second important experimental parameter, was taken unchanged while measuring creep rates at different temperatures. Time $t = 10\,\mathrm{s}$ or sometimes 30 s, corresponding to a bend in the $\dot{\varepsilon} = f(t)$ dependence (Fig. 4), has typically been chosen in the CRS experiments.

In the case of the hand data treatment, Doppler frequency ν is determined for the certain time t by measuring a distance S between the first and last beats of a chosen interferogram sector with N beats (a chosen deformation increment) by the formula

$$\nu = \frac{N}{S} v_{\mathrm{t}}, \tag{11}$$

where v_{t} is a velocity of the recorder tape.

Figure 7 shows the example of the computerized measurement with construction of creep rate vs compressive strain plot obtained for polycarbonate (PC) near the yield point (deformation $\varepsilon_{\mathrm{y}} = 6.5\%$) [12]. The data are presented on the different scales. Each point corresponds to the deformation increment of 300 nm (0.005%). Figure 7 displays continuous changing of a creep rate even within the narrow deformation ranges, with minimum at ε_{y}. It should also be stressed that the variance of the creep rate for neighboring experimental points is not scattering but reflects the jump-like development of deformation (see Sect. 5).

The LICRM setup could be used for measuring creep rates with constant resolution and high accuracy in any point of the deformation process over the temperature range from 100 to 800 K. This technique allows yielding creep rates $\dot{\varepsilon} = (10^{-6}\text{–}10^{1})\,\mathrm{s}^{-1}$ on the basis of deformation increment of ca. 0.003–0.005%. The minimum deformation increment allowing the determination of a creep rate is equal to 150 nm (half of one beat) or 300 nm (one beat). The instrumental accuracy of computerized $\dot{\varepsilon}$ estimation, predetermined by precision of the beat frequency estimation, may not exceed 1%, although the influence of other (mechanical) factors increases the scattering in the CR spectra (see below). The equivalent frequency of the CRS experiments is equal to $\nu_{\mathrm{eq}} = (2\pi t)^{-1} \approx 10^{-2}\,\mathrm{Hz}$, i.e., time conditions of these experiments are virtually identical to those in the DSC measurements.

This survey gives many examples of the CR spectra obtained for various polymer systems, especially with complex structures. At the beginning, we present here five examples of the spectra illustrating four important points: (1) their surprisingly discrete character; (2) the importance of a proper choice of the experimental parameters (σ, t) to register successfully the CR spectra; (3) a degree of spectral reproducibility in the CRS; and (4) the CRS superiority in resolution to other relaxation spectrometry and thermal analysis techniques.

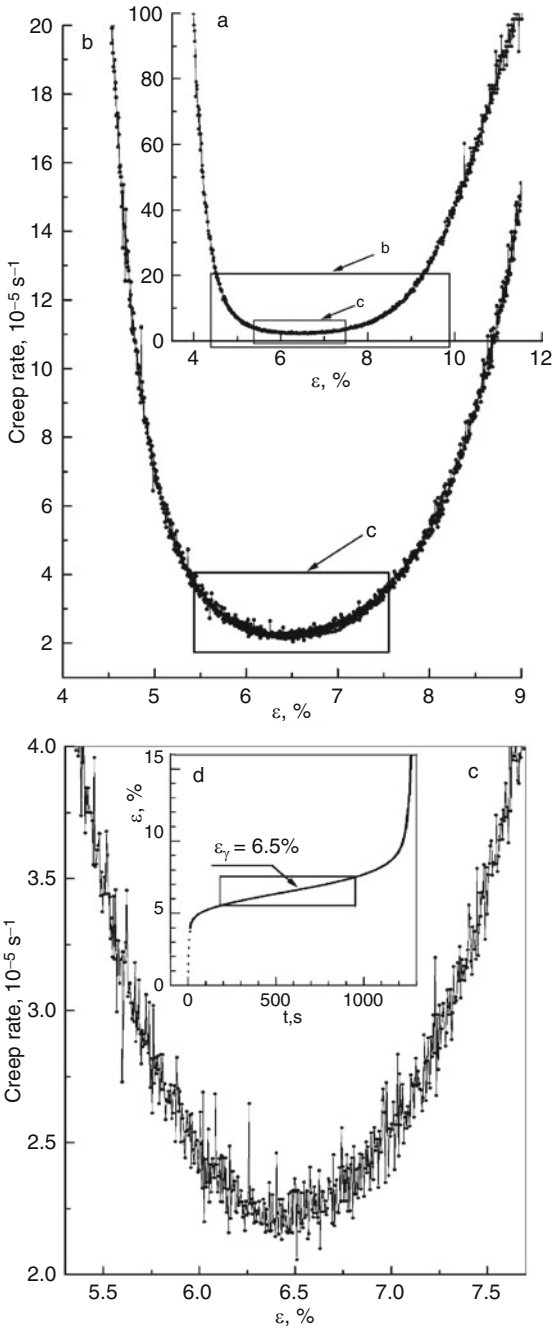

Fig. 7 Computerized measurement and the creep rate vs compressive strain plot obtained for polycarbonate near the yield point $\varepsilon_y = 6.5\%$ [12]. Each point corresponds to a deformation increment of 300 nm (0.005%). The variance of the creep rate reflects the jump-like development of deformation (see Sect. 5). *Inset*: stationary creep in the strain-time coordinates, at 70 MPa and room temperature

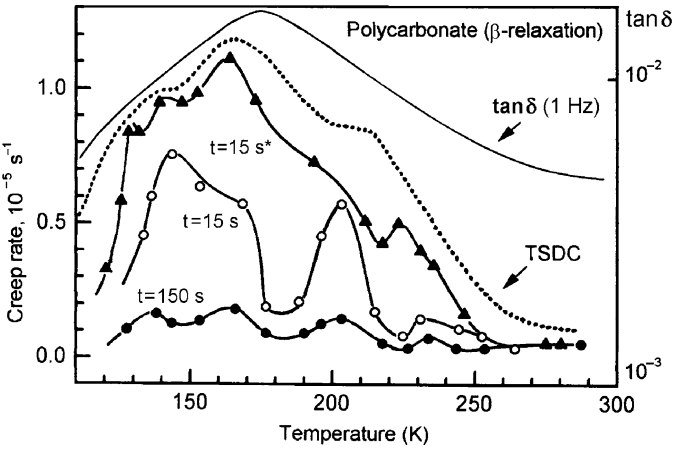

Fig. 8 The β-relaxation dynamics in polycarbonate [13]: the CR spectra (*three bold lines*), DMA spectral contour (*thin line*), and TSDC spectral contour (*dotted line* [14]). CR spectra were obtained at the compressive stress of 30 MPa and $t = 15$ or 150 s. The spectrum for $t = 15\,s^*$ was measured after the low-temperature training (10 cycles from -196°C to 20°C with the rate of 80°C min^{-1})

Figure 8 compares the relaxation spectra of bisphenol A PC characterizing dynamics in the low-temperature region of β-relaxation, as estimated by dynamic mechanical analysis (DMA), thermally stimulated depolarization currents (TSDC), and CRS techniques. The presence of two oxygen atoms as "hinges" in each repeat monomer unit of this polymer predetermines the low thermodynamic rigidity of PC chains (Kuhn segment length $A = 1.4$ nm or $N_k = 1$–1.5 monomer units [15]), and the pronounced, broad β-transition covering the temperature region from ~100 to 250 K; this results in the enhanced low-temperature plasticity of PC. The nuclear magnetic resonance (NMR) [16], quasi-elastic neutron scattering (QENS) studies [16, 17], and the molecular-dynamics simulations (MDS) [18] have indicated a rather complicated PC dynamics in this sub-T_g region. As found, this is associated with the presence of several dynamic modes such as large-amplitude rotations of diphenylene propane and carbonate units; their correlated (synchronous) rotational motions in chain; a broad distribution of rotational angles (about 80°) depending on the local packing, as well as phenylene "flips."

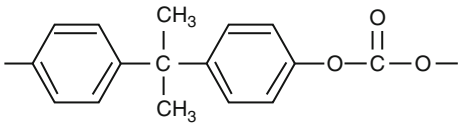

Figure 8 shows the smoothed mechanical loss (DMA) peak of β-relaxation. A tendency only to the appearance of three constituents in this temperature region may be seen from the TSDC spectrum. Unlike that, four partly overlapping peaks are distinctly registered in the CR spectrum of PC. One can see that the peak intensities strongly decrease with increasing time from the moment of loading to an onset

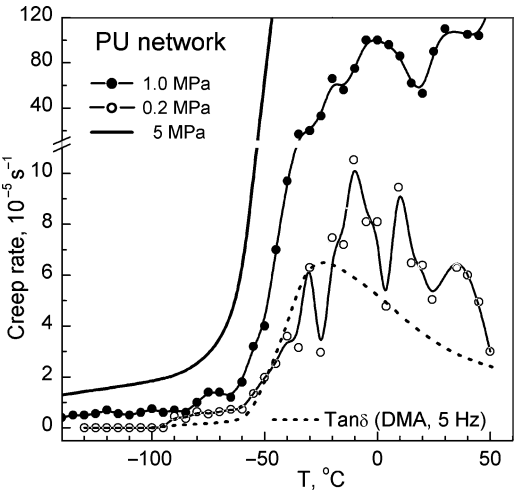

Fig. 9 Polyurethane network: creep rate spectra obtained at tensile stresses of 0.2, 1.0, or 5.0 MPa, and the mechanical loss spectral contour (1 Hz) [19]

of measuring, namely, at $t = 150$ s. This figure also demonstrates a high sensitivity of CR spectrum to fine changes in structure (molecular packing)/dynamics of PC caused by the low-temperature cyclic treatment. Overall increase in the creep rates, the displacement of peaks to lower temperatures, and the redistribution of their intensities are observed. Hence it follows that such treatment can provide an additional increase in the low-temperature plasticity of PC.

Figure 9 shows the CR spectra obtained at different tensile stresses for a polyurethane (PU) network. These spectra will be analyzed in Sect. 3.2. DMA shows again a single broad glass transition peak. We emphasize so far the significance of the appropriate choice of stress for the successful registration of the spectra. The spectrum could not be obtained at all at the stress of 5 MPa when the steep acceleration of a creep rate with temperature occurred. Meanwhile, the complicated spectra are observed at 1 or 0.2 MPa; the former is characterized with large overlapping of four CR peaks whereas the distinct four-peak spectral contour is observed if the stress of 0.2 MPa is applied. This stress was enough for inducing sufficient creep rates to be reliably measured provided a high spectral resolution was also maintained. The spectrum indicates the large dynamic heterogeneity: a few modes constitute dynamics within the PU glass transition.

Figures 10 and 11 illustrate the level of reproducibility in the CR spectra. The former was obtained in the temperature range of sub-T_g (β and γ) relaxations, for two samples of the model epoxy-amine network taken from two separate batches. Figure 11 shows the spectra for semi-crystalline poly(oxymethylene) (POM) with an extremely complicated crystalline structure [22]. Simultaneously, the contours of their DMA spectra are also given. These materials and their spectra are discussed in Sects. 3.2 and 3.6.1, respectively.

Two points must be noted at a glance: very complex, multi-modal dynamics in these systems instead of the smoothed, broadened DMA peaks, and a satisfactory (within certain limitations) reproducibility of this complexity in the experiments

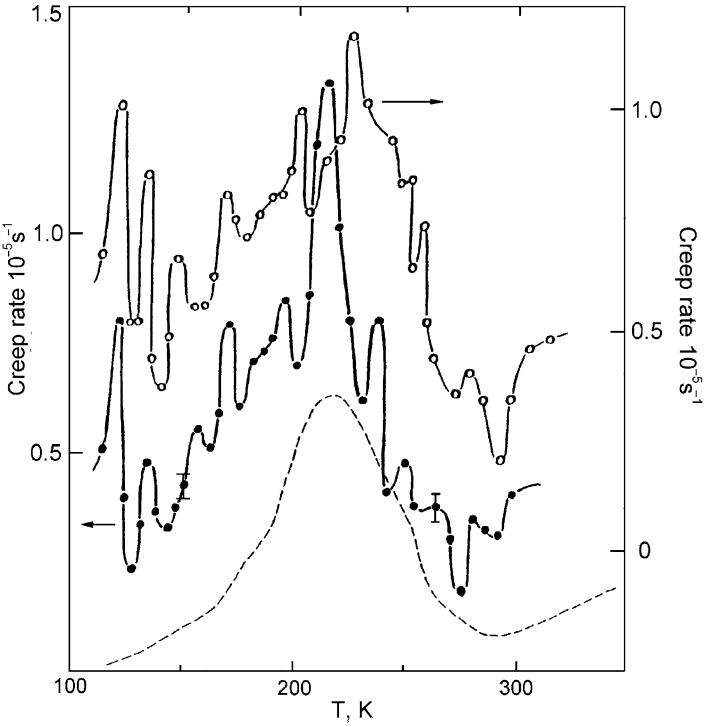

Fig. 10 Reproducibility of the CR spectra obtained at sub-T_g temperatures and compressive stress of 20 MPa for two samples of the model epoxy-amine network (DGEBA-DDM/60BAN, see Sect. 3.2) coming from two separate batches [20]. The *dotted line* corresponds to its contour of DMA spectrum (1 Hz)

performed for two specimens. Some scattering and incomplete coincidence of the spectra, in both amplitude and temperature location of peaks is observed. This may probably be the result of cumulative effects of small differences in molecular architecture (for the epoxy samples coming from different batches), and non-identity in the experimental conditions of mechanical experiments. Rather high reproducibility is observed, however, for two identical POM samples cut from one piece. The complex structure of the spectrum and the relative contributions of constituent peaks to the spectral contour are satisfactorily reproduced, being rather stable in position along the temperature axis.

There are a few factors resulting in CR peak multiplicity in polymer systems although it is difficult to achieve the total assignment of the multiple CR peaks from these mechanical data only. Using additional data coming from the complementary techniques allows us to do it in some cases. Of great interest is the fact that the CR spectrum can respond in a very discrete way to "unfreezing" of different constituent motions in a polymer. This phenomenon is inherent to CRS to a much larger extent than to the other relaxation spectrometry/thermal analysis techniques (DSC, DMA, TSDC, DRS, etc.).

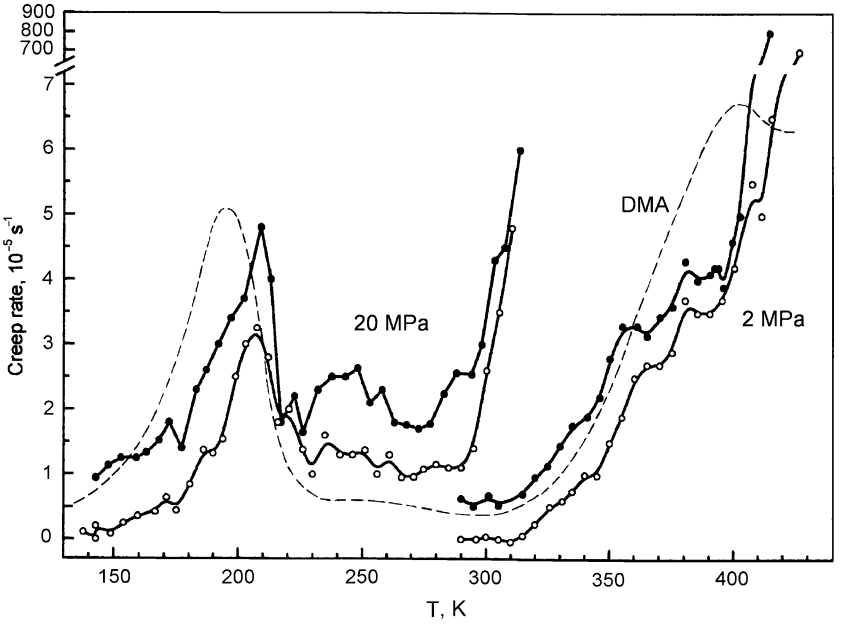

Fig. 11 Creep rate spectra obtained at tensile stress of 20 MPa (at low temperatures) or 2 MPa (at elevated temperatures) for two identical commercial POM (Delrin®, Du Pont) samples [21]. The spectra with white circles were displaced by 0.5 unit downwards. *Dashed line* corresponds to the contour of POM mechanical loss spectrum (DMA, 1 Hz)

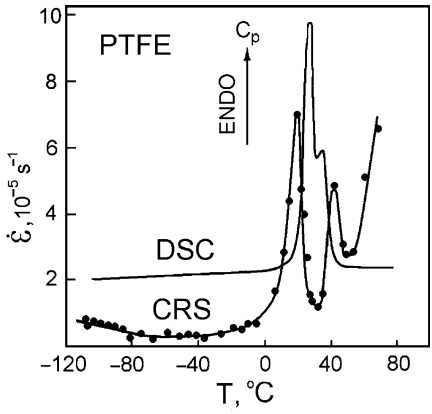

Fig. 12 Solid-state phase transitions in PTFE [13]: the CR spectrum (tensile stress of 2 MPa, $t = 30$ s), and the DSC curve (heating rate 20°C min^{-1})

Finally, CR spectra of semi-crystalline polymers may characterize not only the relaxation transitions in the disordered regions but also the transformations occurring in the crystalline regions, namely solid–solid transitions. Figure 12 shows the DSC curve and the CR spectrum of poly(tetrafluoroethylene) (PTFE). Strongly overlapping endothermic peaks I and II at ~25°C and 32°C are observed in the DSC curve. Meantime, distinctly separated peaks I and II at ~20°C and 40°C, with

approximately the same ratio of peak heights, and additionally slight increasing creep rates at temperatures below −80°C (obviously, in the region of small-scale vibrations [23]), and a steep acceleration of creep over 50°C may be seen in the CR spectrum. The latter result can be understood since peak I characterizes triclinic crystallites → trigonal crystallites transformation, and peak II corresponds to the formation of pseudo-hexagonal condis (conformationally disordered) crystallites in PTFE [24]. Transition II is considered, in fact, as a solid-mesophase one; this results in strong creep acceleration.

2.3 Polymer Physics and Materials Science Problems Being Solved by CRS

This survey shows that the LICRM instrument and the CRS technique have been successfully utilized in our laboratory for solving a number of physical and materials science problems. These application possibilities are as follows:

1. Discrete analysis of segmental dynamics in polymers and the superiority in resolution to the conventional relaxation spectrometry techniques. CR spectra may respond discretely to unfreezing constituent dynamic modes within one relaxation region, e.g., of the glass transition or the β-relaxation, with a reproducible recording of the nanoscale dynamic heterogeneity.
2. Discrete analysis of the complicated dynamics in complex polymer systems and nanocomposites, especially of the "anomalies" of the glass transition behavior in these materials, including the interfacial dynamics. Characterization of the dynamic modes within a broad glass transition range caused by the nanoconfinement and constrained dynamics effects.
3. The possibility to probe in some cases a compositional heterogeneity, e.g., the miscibility degree on the nanoscale level in single-phase materials such as miscible blends, or a local heterogeneity of cross-linking in the hybrid polymer networks.
4. New possibilities for a comprehensive, precise analysis of the kinetics of polymer deformation under different experimental conditions, taking into account the changeability of kinetics under different temperature/deformation conditions. The LICRM setup made it possible not only to increase sharply the accuracy of the measurements, but also to study the deformation kinetics under formerly inaccessible conditions, namely (a) to obtain the complete kinetic information on polymer deformation in any temperature point and at any stage of the deformation process and (b) to determine activation parameters under conditions of practically unchangeable polymer structure and mobility.
5. Revealing of the regular relations of polymer kinetics to the potential barriers of intermolecular interactions (IMI) and the parameters of main relaxation transitions.
6. Reliable detection and detailed studying of the jump-like character of polymer creep on the submicro-, micro-, and meso-scale levels, and the successful looking

for the correlations between the parameters of micro-plasticity and the structural characteristics and morphology of isotropic and highly oriented polymers.
7. Detection of fine changes in the temperature dependencies of creep, relaxation dynamics, and elastic modulus values in polymers caused by different treatments or external influences. The latter include various thermal treatments; pre-straining or another mechanical actions; the impact of irradiation or magnetic field, etc.
8. Using CRS as the tool for non-destructive testing and prediction (more distinctly compared to DMA) of the temperature anomalies in mechanical behavior of polymeric materials. This includes the determination of the temperatures of non-linear changes in fracture stress, and precise combined measurements of the elastic properties, together with relaxation (creep) properties, over the broad temperature range in one experiment.
9. Reliable revealing micro- and submicro-plasticity, relaxation and solid–solid phase transitions in brittle and ultra-brittle materials. Some correlations between conductivity (electronic processes) and micro-plasticity, and between the creep rate peaks and brittle–ductile transition could be detected. On this basis, the method for predicting the comparable inclination of materials towards the brittle fracture has been developed. In addition, the kinetic analysis of microplasticity in brittle solids could be performed.

3 Creep Rate Spectroscopy for a Discrete Analysis of the Glass Transition Anomalies and Dynamic/Compositional Heterogeneity in Complex Polymer Systems and Nanocomposites

This chapter presents the experimental data obtained for different types of complex polymer systems by CRS combined with the complementary techniques, first of all DSC.

The numerous studies of the peculiarities of glass transition dynamics in complex polymer systems have been performed in detail for last two decades, starting probably from the works on block copolymers (BCP) [15, 25, 26] and graft copolymers [15, 27]. Their results could be treated in terms of some general notions, also taking the numerous experimental studies of dynamics in polymer nanolayers into account; the latter have been performed during the same time period. These knowledge and experimental results may strongly facilitate understanding of the results obtained for complex polymer systems.

Therefore, it is a reasonable approach to consider at first very concisely the physical basis for the interpretation of the glass transition “anomalies” in complex systems. This relates basically to three topical problems: (1) polymer dynamics in nanoscale-confining geometries or at free surface; (2) constrained polymer dynamics; and (3) the notion of the common segmental nature of the α- and β-relaxations in flexible-chain polymers.

3.1 Physical Origins of the Anomalies and Dynamic Heterogeneity in the Glass Transition: A Brief Outline

3.1.1 Dynamics in Nanoscale-Confining Geometries, at Free Surface and Constrained Dynamics

Beginning from the pioneer works of McKenna [28,29], Keddie [30,31], van Zanten [32–34], and Forrest with co-workers [35–37], a very large series of experimental studies of dynamics has been performed for polymers in ultrathin films, adsorbed on solid substrates, or in the freely standing state, and for polymers and low-molecular-weight substances confined to nanovolumes (nanopores, nanoslits, and so on) [38–65]. The results of these studies have been summarized in particular in the reviews [40, 52, 53].

It has been revealed that glass transition dynamics under these conditions may dramatically differ from that in a bulk polymer in two respects.

On the one hand, the polymer confinement in nanoscale geometries (without strong interaction of confined substance with a restricting surface), or the location of polymer chains at free surface (polymer–air interface), resulted in accelerating dynamics and T_g reduction in polymer nanolayers [30, 35–37, 39, 41, 46, 47, 54]. Sometimes two glass transitions have been observed when the second T_g was lower than that for bulk polymer. For instance, the considerably decreased T_g values were found for freely standing PS films with thickness $h \approx 5$–$10\,\text{nm}$ [35–37, 63] or at the same depth from the surface of the thicker PS samples [64, 65]. The T_g depression depended on the film thickness and molecular weight, and was observed at $h < R_{EE} \approx 2.45 R_g$, where R_{EE} is an average end-to-end distance for unperturbed macromolecule (random coil size), and R_g is the radius of gyration. It was supposed that lesser overlapping of macromolecular coils occurred in such cases that resulted in an increase in free volume and mobility.

On the other hand, an enhanced interaction of thin films with a substrate or a substance in nanoconfined geometries with a limiting surface resulted in the opposite effect of constrained dynamics. Then, "anomalous" slowing down segmental dynamics, with increasing T_g and broadening of the glass transition towards higher temperatures [31–34, 44, 49, 58], up to the total suppression of glass transition dynamics, have been observed.

Thus, the distinct evidence for the dynamic anomalies of both opposite kinds have been obtained by many authors; however, the experimental results depended to some extent on a method used and details of the experiments [52].

One more point must be mentioned here. In the studies of adsorbed ultrathin polymer films by computer simulations [66–68], FT-IR spectroscopy [69], and small-angle neutron scattering (SANS) [70] techniques, it was shown that strongly adsorbed chains acquired the quasi-2D (flattened, "pancake") conformations instead of 3D conformations peculiar to a bulk polymer. Initially polymer chains were adsorbed onto a substrate in a flat configuration ("trains" formation from segments) but at the higher surface coverage adsorbed nanolayers had more chain loops and "tails."

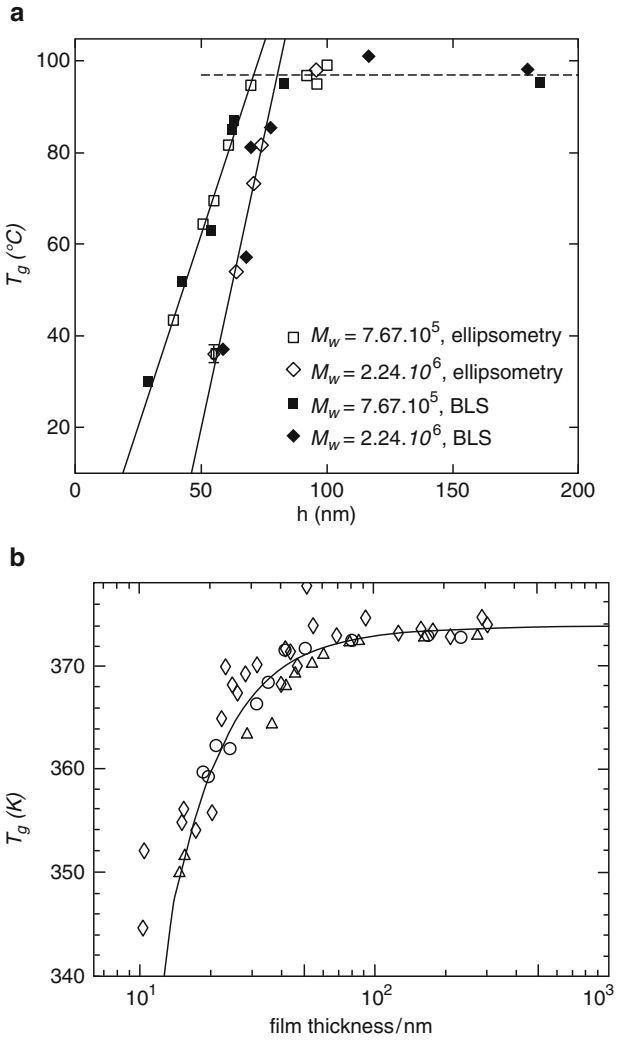

Fig. 13 T_g of PS film as a function of its thickness. (**a**) Freely standing films with two different molecular weights. The experiments were carried out using Brillouin light scattering (BLS) and ellipsometry [35, 37]. (**b**) Films on the native oxide covered silicon surface (ellipsometry measurements) [31]. PS samples with $M_w = 1.2 \times 10^5$, 5×10^5, and 2.9×10^6 were taken

Figures 13 and 14 demonstrate how the state of a substrate surface and a peculiar interfacial (polymer–substrate and/or polymer–air) dynamics affect the thermal behavior of thin polymer films.

Figure 13a shows the T_g values of freely standing PS films measured by ellipsometry and BLS techniques [35, 37]. Its dramatic decrease, from 100°C to 30–40°C, was observed for the 30–50 nm thick films; the critical film thickness (bend in the

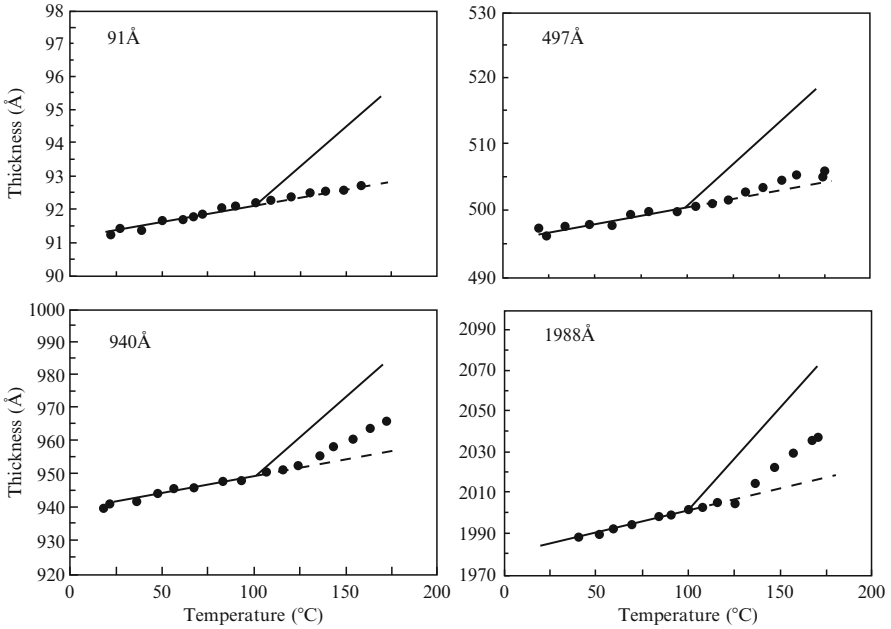

Fig. 14 Thickness vs temperature plots for PS films with different initial thicknesses, as measured by X-ray reflectivity technique during heating the sample with the rate of $10°C\,h^{-1}$ [34]. $M_w{}^{PS} = 2.3 \times 10^5$. Hydrogen passivated silicon surface was used as the substrate. The dependencies are depicted by the *dotted lines. The solid lines* correspond to predictions for glass transition behavior in bulk. *PS*: the break in the lines corresponds to $T_g = 100°C$

curves) decreased with decreasing chain length. An almost "softened" state of PS surface may be attained at normal temperatures. Due to increased mobility at the surface of glassy polymers, the possibility for diffusion-controlled bonding of two PS films at their contact at temperatures much below the bulk T_g was revealed [71]. Depending on the technique used, different authors observed the same or less pronounced effects (see review [52]); however, increased mobility of polymer surface compared with that in a bulk polymer has been proved.

Figure 13b shows the T_g values measured for the adsorbed PS films with three different molecular weights and plotted against the film thickness. The authors [31] spin-cast narrow molecular-weight fractions of PS from toluene solutions onto oxide covered silicon surface. When the films were thinner than a few tens of nanometers, the substantial T_g reduction was obvious. Dependence of this effect on molecular weight, if any, was weak, in particular much weaker than the dependence of radius of gyration R_g on molecular weight. It was concluded that increased mobility of free polymer surface contributed to a large extent to this T_g reduction.

At the same time, PS films on the hydrogen passivated silicon surface showed the very different thermal behavior due to the stronger polymer–substrate interaction [34]. Figure 14 shows that, unlike bulk PS with $T_g = 100°C$, the films with

the initial thicknesses of 497, 940, and 1,988 Å indicate an upturn of the thermal expansion coefficient at ~120°C, and this upturn becomes less evident as the initial film thickness decreases. The PS film with 91 Å initial thickness showed no deviation from a straight line to a temperature of 165°C which was the instrumental limit. It assumes the total glass transition suppression (immobilization of segmental dynamics) at least below 165°C. The impact of substrate-restricted mobility outweighed the effect of free surface in this case. It is noteworthy that the bulk radius of gyration equals 135 Å for this polymer sample ($M_w^{PS} = 2.3 \times 10^5$).

Further, DeGennes has assumed [51] that "future experiments should aim not at the determination of a single T_g but a distribution of the T_gs in thin polymer films." Really, a coexistence of both anomalously fast and ultra-slow segmental dynamics modes in the glass transition could sometimes be observed [40, 45, 47, 50, 59, 60]. Manias and Torkelson et al. published the first MD simulations / NMR [46, 48] and fluorescence data [50] confirming this idea experimentally.

Up to now, the sign, magnitude, and cause of T_g anomalies on the nanometer size scale are still under discussion [52]. Many model approaches have been developed for treating the above-mentioned effects, including comparison of film thickness h or confined nanovolume value with the scale of cooperative motion act or molecular coil size (molecular end-to-end distance R_{EE}). The free volume theory; the percolation model; the manifestation of intrinsic size effect; and a supposition about segregation of chain ends to the free surface, etc., were applied (see reviews [40, 52, 53]).

In our opinion, along with the obvious importance of enhanced polymer/substrate interactions (constrained dynamics), the problem of heterogeneity in molecular packing plays the cardinal role in the glass transition "anomalies." This heterogeneity must result in the differences in intermolecular cooperativity of segmental dynamics, that is, in *the contributions of normal "slow" (cooperative, Vogel-like), as well as less cooperative and "fast" non-cooperative (Arrhenius-like) motional events to glass transition dynamics.*

In this relation, a series of Molecular-Dynamics (MD) computer simulations, performed by Manias et al. for 2 nm wide PS films or 1 nm wide poly(ethylene oxide) (PEO) films confined in slit pores [45–48], is worth mentioning separately. Generally, a very rich dynamic picture was unveiled in the glass transition of these intercalated polymer nanolayers with a thickness equal to a Kuhn segment length. The intercalated polymers exhibited a very wide distribution of segmental relaxation times over a wide range of temperatures. Two points are noteworthy herein. First, a coexistence of fast liquid-like and slow solid-like segmental dynamics was shown in the temperature range close to, below, and above T_g of the bulk polymer. The temperature affected only the relative population of fast/slow segmental motions. Second, a strong correlation between a local density and segmental dynamics was shown: just long-lived density inhomogeneities gave rise to a very wide distribution of segmental processes, with the fast relaxing moieties being located in the low local density regions, basically in the middle part of nanolayers. At lower temperatures, the strong correlation between segmental dynamics and local density in the vicinity of each segment was recorded.

3.1.2 Common Segmental Nature of the α- and β-Relaxations in Flexible-Chain Polymers: The Physical Limit for Anomalous Glass Transition Dynamics

The increase in T_g, up to the total immobilization of the glass transition dynamics, is explainable in terms of strong non-chemical or chemical interactions of a substance with "rigid wall." Meanwhile, the problems of a decrease in T_g, large broadening of the glass transition range ΔT_g towards lower temperatures, as well as the dynamic heterogeneity within this range, still remain disputable. The question is discussed whether the latter effects, in particular T_g reduction, is due to an intrinsic size effect or other reasons. It is believed that there is no clear understanding for the largest T_g reduction [35], that is, the origin of "the physical limit" for T_g reduction observed in ultra-thin films, nanoconfined polymers, as well as in complex polymer systems and nanocomposites; the latter will be described in detail in Sects. 3.2–3.9.

In our opinion, this problem may be resolved proceeding from the notion on the common segmental nature of the α- and β-relaxations.

Figure 15 shows schematically the Arrhenius diagram ("relaxation map") for the frequency dependencies of the α- (glass) transition and β-relaxation temperatures (T_g, T_β), as well as for the temperatures of γ- and δ-relaxations in the frequency range $\nu = 10^{-3}$–10^{13} Hz [15, 72–76]. The straight lines for sub-T_g relaxations, with the intercept $\log \nu_0 \approx 13$ for $T^{-1}(\mathrm{K}^{-1}) = 0$, indicate their obeying the kinetically simple, non-cooperative Arrhenius-like mechanism of motion when the frequency $\nu \approx 10^{13} \exp(-E/RT)$. For these relaxations, the activation energy E may be determined from the temperature location of relaxation peak by the formula [77]

$$E(\mathrm{kJ\,mol^{-1}}) = (0.25 - 0.019 \log \nu)\, T(\mathrm{K}). \tag{12}$$

Cooperative glass (α) transition does not obey (12) over the broad range of frequencies; the curvature of its Arrhenius plot is most pronounced over the range from 10^3

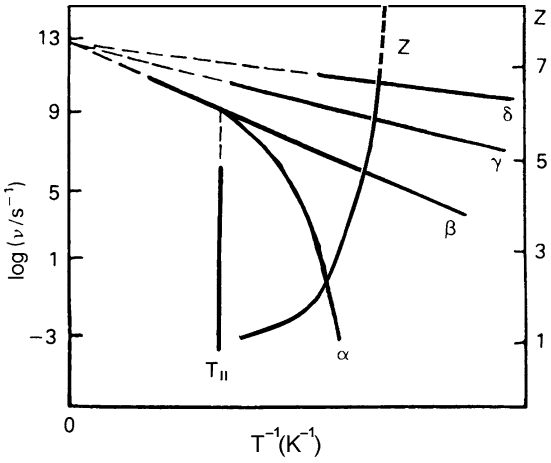

Fig. 15 Arrhenius diagram ("relaxation map") for transitions in flexible-chain polymers. The parameter of intermolecular cooperativity of segmental motion as a function of temperature (Z vs T^{-1} plot) is also shown (see text)

to 10^6–10^8 Hz. At higher frequencies this transition degenerates, merging into the β-relaxation plot. The temperature of merging (on heating) or splitting (on cooling a melt) of the α- and β-relaxations in the Arrhenius diagram determines the quasi-thermodynamic [78] boundary between the rubber-like and fluid states of polymers. This temperature is named differently: as the splitting or bifurcation point T_s [74] or the crossover temperature T_c in the Mode Coupling Theory (MCT) [79, 80], or as the temperature of "liquid–liquid" transition T_{ll} [81–83] or flow temperature T_f [74].

The solid-state β-transition, as the closest to T_g Arrhenius-like relaxation satisfying (12), is usually much less intense than the α-transition. However, the activation barriers of deformation, flow, diffusion, physical ageing, and solid-phase reactions have often turned out to be approximately equal just to the activation energy of the β-transition Q_β [15].

The common picture of changing segmental dynamics in polymers with temperature may be considered in brief as follows. Only quasi-independent motion of chain segments occurs at $T > T_s$ in a polymer melt having a high concentration of "holes" (free volume points). On cooling, free volume gradually decreases, and at T_s the centers of short-range order arise, that is, the relatively stable associates of more-or-less parallel segments. This generates the high-density nanodomains that results locally in intermolecularly cooperative motion. The latter is due to interaction with the neighboring segments within a "cage" when the cooperative rearrangement in a cage is required for motion of a segment ("overcrowded bus" model [74]). Further, with decreasing temperature, the dissipative process of the formation of amorphous structure occurs when the content of these solid-like clusters and the respective contribution of slow cooperative modes to dynamics increase, whereas the contribution of fluid-like nanodomains (fast local modes) to dynamics sharply decreases. Generally, it means that "glassy clusters" and liquid-like regions coexist in different ratios at temperatures T where $T_s > T > T_g$. The curvature of the Arrhenius plot for α-transition over the frequency range from 10^8 to 10^3 Hz (Fig. 15) reflects this process of enhancing the solid-like behavior and increasing activation barriers to segmental motion on cooling.

Moreover, below T_g segmental motion freezes-in not at once but only gradually, and around T_β the segmental motion is retained as the liquid-like loosely packed "islets of mobility" in glassy solid, i.e., the localized events of Johari–Goldstein β-relaxation [73, 76]. The simultaneous appearance of α- and β-relaxation modes in the vicinity of T_g was registered experimentally [75, 84]. Finally, below β-relaxation region segmental motion is totally suppressed, and only small-scale low-amplitude vibrations (γ- and δ-relaxations) [23] take place.

Despite the interrelationship between two basic (α, β) relaxation transitions, the fundamental problems regarding their general molecular mechanisms, kinetic units' scale, and the relations between transitions' parameters and the molecular characteristics of polymers remained to a large extent unclear until the 1980s. Thus, β-relaxation has been presumably associated with vibrations of one or two monomer units, side groups, short chain fragments, or even with the impurities (see references in the book [15]). It was unclear whether the common β-relaxation mechanism was

absent for flexible-chain polymers varying in structure, or the lack of understanding of this phenomenon was caused by the paucity of direct experimental data. Therefore, many problems regarding the connection between the α- and β-relaxations have remained in dispute until recently.

We believe the understanding of this problem came from the notion of the common nature of glass transition and β-relaxation based on a series of systematical experimental studies on this problem performed, basically in the 80th, in our laboratory [85–103]. Three techniques have been used in these studies: differential scanning calorimetry (DSC) [85–90], DMA of statically loaded polymers [DMA(σ)] [91–94], and far-infrared spectroscopy (FIRS) in the 10–400 cm^{-1} region including spectral measurements over the broad temperature range [23, 95–101]. The results obtained have been summarized in the reviews [15, 23, 103], and, therefore, we present below only a very brief outline of this matter.

DSC has been used [85–90] for characterization of α- and β-relaxation modes, and so-called "intermediate relaxations" at temperatures T_i where $T_g > T_i > T_\beta$. Many glassy polymers as well as the oligomer series and low molecular weight glasses have been studied. Special thermal treatments allowed us to manifest a set of endothermic peaks at temperatures $T_\beta \ldots T_i' \ldots T_i'' \ldots T_i''' \ldots T_g$ in the DSC curves. The effective activation energies of these relaxations, $Q_\beta \ldots Q_i' \ldots Q_i'' \ldots Q_i''' \ldots Q_\alpha$, were determined by the displacement of the peak maxima temperatures when varying a heating rate V and using the equation [15, 104]

$$Q = -R\mathrm{d}\ln V / \mathrm{d}\left(T^{-1}\right). \tag{13}$$

Although the β-relaxation is typically absent in the DSC curves, the procedures offered allowed revealing and characterization of the β-relaxation by this technique [15, 86, 88, 90, 103]. As an example, Fig. 16 shows the endothermic peaks within the T_β–T_g range for PMMA, "developed" in the DSC curves due to annealing under different conditions, and the activation energy of segmental dynamics as a function of temperature. One can see the gradual transition from Arrhenius mechanism to cooperative dynamic processes with a fourfold increasing Q value.

Additionally, the Donth's volumes of cooperatively rearranging regions v_{CRR} at T_g, as the characteristics of the motional event scale, were determined from DSC curves using the formula [74, 105]

$$v_{CRR} = kT_g^2 \Delta C_p^{-1} / \rho (\delta T)^2, \tag{14}$$

where $\Delta C_p^{-1} = \Delta C_p / C_{p(T<T_g)} C_{p(T>T_g)}$, ρ is the density, $C_{p(T<Tg)}$ and $C_{p(T>Tg)}$ are the heat capacities before and after the ΔC_p step at T_g, and δT is the half-width of the glass transition range.

The original DMA(σ) technique and the relevant analytical description [91–94] allowed us to estimate experimentally the activation volumes of α- and β-relaxations in polymers. As an example, Fig. 17 shows the mechanical spectra of poly(vinyl chloride) (PVC) obtained without and under different static loading (maximal shear stresses τ_{sh}).

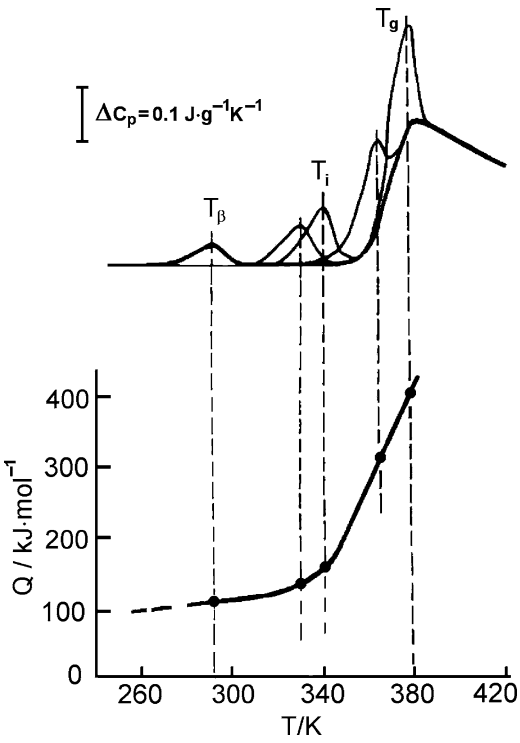

Fig. 16 DSC curves of atactic PMMA samples with different degrees of annealing and the respective activation energy of segmental motion vs temperature plot [89, 103]

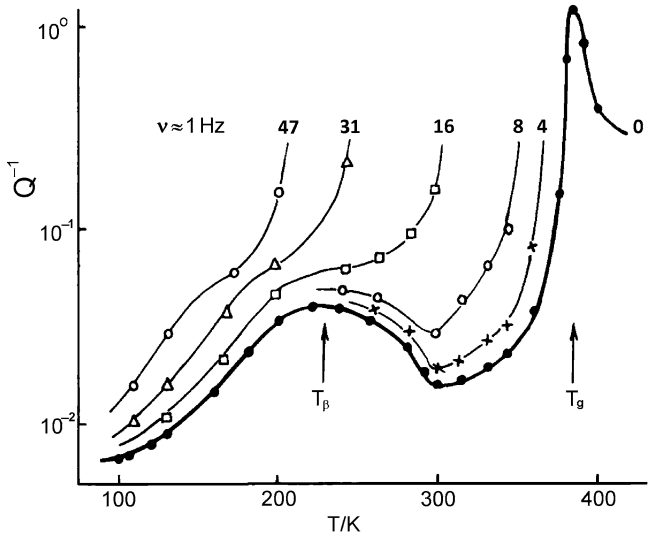

Fig. 17 Temperature dependencies of internal friction in PVC obtained at 1 Hz without (*bold line*) and under static loading with maximal shear stresses of 4, 8, 16, 31, and 47 MPa (DMA of statically loaded samples) [94]

One can see the mechanical activation of relaxation processes, i.e., the shifts of relaxation peaks to lower temperatures due to static loading. According to the performed analysis [91], the activation volumes v_{act} of relaxations (v_α and v_β) at temperatures $T \leq T_{max}$, where T_{max} is the temperature of the relaxation maximum, may be estimated by the formula [94]

$$v_{act} = kT/\tau_{sh}\left[12\left(Q_\tau^{-1}/Q_0^{-1} - 1\right)\right]^{1/2}, \tag{15}$$

where Q_0^{-1} and Q_τ^{-1} are the internal friction values without or with static loading, respectively.

FIRS studies [23, 95–101] allowed us to reveal the molecular nature of sub-T_g (β-, γ- and δ-) relaxations in flexible-chain polymers. Their potential barriers and the motional unit sizes, and the temperatures of the onset of trans–gauche (T–G) rotations in chains, i.e., conformational mobility in glassy polymers, have been estimated. Additionally, the scale of the denser nanoregions, as a feature of solid-state behavior, was estimated by studying the low-frequency "boson" peak; this latter work has been performed in the combined FIRS/Raman spectroscopy measurements [106–108].

As a result, the experiments [85–103] allowed us: (1) to reveal the common nature of β-relaxation in flexible-chain polymers; (2) to find the relations between its parameters and molecular characteristics of polymers; and (3) to prove the common segmental nature of α- and β-relaxations.

According to Eyring et al. [109], a relationship exists between the flow activation energy Q_η and cohesion energy E_{coh} for simple liquids composed of small molecules:

$$Q_\eta = (0.30 \pm 0.05)E_{coh}. \tag{16}$$

We found experimentally (Fig. 18a) practically the same relation (taking into account much lower temperatures and therefore higher cohesive IMI) for solid-state β-relaxation in vitrified low-molecular weight organic liquids and short-chain oligomers [88, 103]:

$$Q_\beta = (0.40 \pm 0.1)\,E_{coh} \quad \text{or} \quad Q_\beta \approx Q_\eta. \tag{17}$$

Remarkably, a similar approximate equality of Q_β and Q_η was also shown for different flexible-chain polymers [15]. This coincidence was one of the pieces of evidence in favor of the "liquid-like" and segmental nature of the solid-state β-relaxation event in polymers.

Further, no regular relation of Q_β to E_{coh} per mole of monomer units was observed in polymers. At the same time, a relationship

$$Q_\beta = (0.30 \pm 0.05)\,E_{coh}N_k + B \tag{18}$$

was obtained for 26 polymers studied (Fig. 18b). Here N_k is the number of monomer units in a Kuhn statistical segment, Q_β is represented in kJ per mole of segments, and a supplement $B = 10 \pm 5$ kJ mol^{-1} coincides with the internal rotation barrier

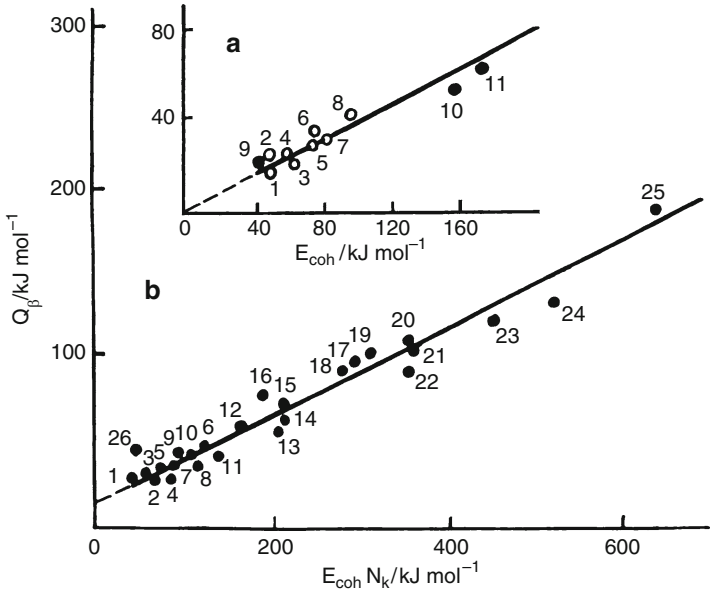

Fig. 18 Activation energy of β-relaxation in (**a**) low-molecular weight glasses and (**b**) linear polymers vs the cohesion energy or cohesion energy of Kuhn statistical segment, respectively [86, 88, 103]. (**a**) (1) Pentanol; (2) isopropylbenzene; (3) 5-methyl-3-heptanol; (4) decalin; (5) 1,1-diphenylpropane; (6) diethyl phthalate; (7) glycerol; (8) *o*-terphenyl; (9) hexamethyl disoloxane; (10) tetra-α-methylstyrene; (11) pentastyrene. (**b**) (1) Polyethylene; (2) polyisoprene; (3) poly(dimethylsiloxane); (4) poly(diethylsiloxane); (5) poly(phenylene oxide); (6) poly(ethylene terephthalate); (7) polytetrafluoroethylene; (8) polycarbonate; (9) polyamide; (10) polypropylene; (11) polymethacrylate; (12) poly(vinyl fluoride); (13) poly(vinyl acetate); (14) poly(vinyl chloride); (15) poly(vinyl alcohol); (16) poly(methyl methacrylate); (17) poly(diphenyl oxyphenylene); (18) poly(butyl methacrylate); (19) polystyrene; (20) polyacrylonitrile; (21) poly(α-methylstyrene); (22) poly(cyclohexyl methacrylate); (23) polyimide I; (24) polyimide II; (25) poly(metaphenylene isophthalamide); (26) polyisobutylene

in chains. N_k values were taken as obtained by the other authors experimentally from the undisturbed dimensions of macromolecules in dilute Θ-solutions at Θ-temperatures.

Thus, the potential barriers Q_β are controlled in polymers by (1) the energy of IMI and (2) the thermodynamic chain rigidity (Kuhn segment size). Additionally, the small term B assumes the participation of T–G transition in an event of the β-transition.

The experimental dependencies of Q_β on the polymerization degree n have been obtained for a few oligomeric series. As found, the Q_β values increased with chain lengthening only up to a definite limit (a critical size close to Kuhn segment length), and then remained invariable [86, 88, 103]. Figure 19 shows such a plot for polystyrene (PS) and poly(α-methylstyrene) (PMS): a critical size was about ten monomer units whereas $N_k = 8$ for these polymers. Moreover, the DMA(σ) experiments showed that the values of activation volume v_β practically coincided with the volumes of Kuhn segment v_k in several polymers (Table 1).

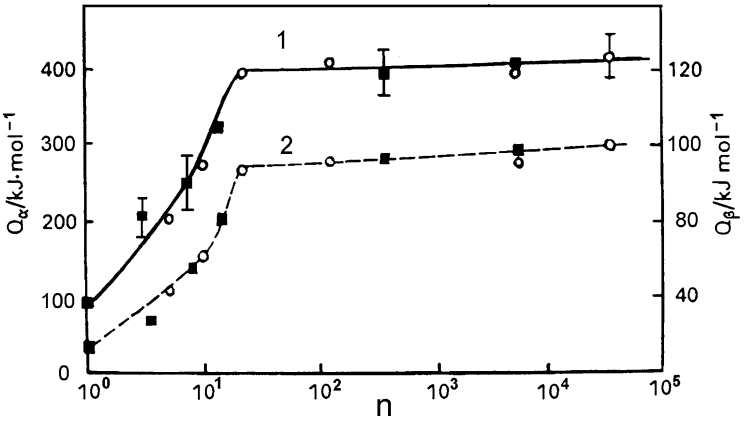

Fig. 19 Activation energies $Q_\alpha(1)$ and $Q_\beta(2)$ vs the average number of monomer units in molecules of PS and PMS, as estimated by DSC [89, 90, 103]

Table 1 Comparison of the shear activation volumes of β- and α-relaxations with the volumes of cooperatively rearranging region (CRR) at T_g (DSC data) and Kuhn segment volumes in glassy polymers [94, 103]

				Kuhn segment size				
Polymer	ν_β/nm^3	ν_α/nm^3	ν_{CRR}/nm^3	(monomer units)	ν_k/nm^3	ν_α/ν_β	ν_α/ν_k	ν_{CRR}/ν_k
PVC	0.9–1.2	2.5–3.0	4.6	12	0.9	∼3	∼3	∼5
PS	1.0–1.3	4.0–4.5	3.3	8	1.3	∼4	∼3	∼3
PMMA	0.8–1.0	2.0–2.5	1.4	6	0.8	∼3	∼3	∼2
PC	0.8–0.9	2.7–3.0	2.4	1–2	0.4–0.8	∼3	4–5	4–5
PVA	–	–	4.4	7	1.2	–	–	3–4

The direct information regarding the molecular nature of β-transition in polymers has been obtained by FIRS [23,100]. First, the estimated potential barriers to skeletal torsional vibrations in chains appeared to be close to the activation energies Q_β, and the values of torsional-vibrational segments approximately coincided with the sizes of Kuhn segments. Second, the temperature measurements of FIR spectra showed that the ratio of T- and G-conformers changed, that is, conformation mobility unfreezed locally starting from temperatures close to T_β values at $\sim 10^{-2}$ Hz [98]. The conclusion that the displacement amplitudes of motional units in the β-relaxation region were as high as to allow conformational transition, was also made from the combined IR and theoretical analysis of breaking/restoring intermolecular hydrogen bonds in model polymers [87].

The above-mentioned studies offered a general mechanism of β-relaxation in flexible-chain polymers [15, 86, 88, 103]. It is considered as a local liquid-like segmental motion that can be realized at the sites of free volume (packing defects) in a solid polymer, in a chain section close in size to a Kuhn segment. Surmounting of basically intermolecular potential barriers, with the participation of a T–G transition,

occurs in each β-relaxation event. The model of conformational isomerization in chains [110–112], with forced twisting of Kuhn segment adjoining to the point of rotation, could be applied best of all to the description of β-relaxation.

Further, the fundamental "genetic" interrelationship of the α- and β-relaxations has been shown experimentally.

Figure 19 shows that the $Q_\alpha(n)$ plot is virtually identical in shape to the $Q_\beta(n)$ plot. Figure 20 and Table 1 show the common relation found for flexible-chain polymers: the low-frequency parameter Z of intermolecular cooperativity of segmental motion in the glass transition [103]:

$$Z = Q_\alpha/Q_\beta \approx \nu_\alpha/\nu_\beta = 4 \pm 1. \tag{19}$$

Parameter Z corresponds to the co-ordination number of the arrangement of segments in the first co-ordination sphere of intermolecular "lattice." The theoretical estimates [113–116] have given the same values of the most probable parameter of cooperativity. Generally, the parameter Z is not a constant. At temperatures over the

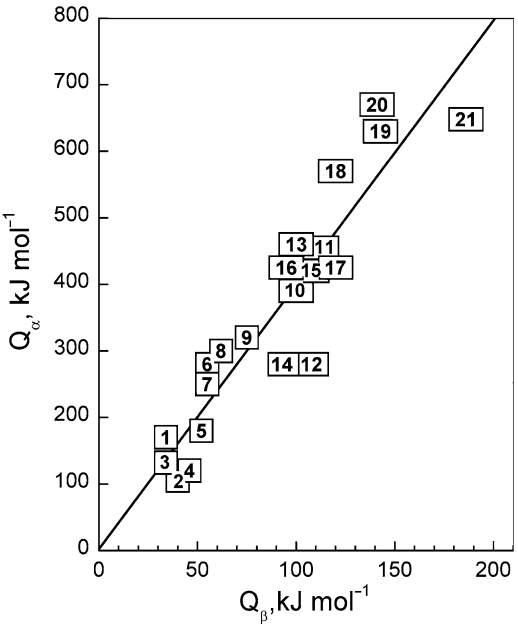

Fig. 20 Apparent activation energy of glass transition (α-relaxation) vs activation energy of β-relaxation dependence obtained at 10-2-1 Hz obtained by DSC or DMA techniques for polymers: (1) polyisoprene; (2) poly(dimethylsiloxane); (3) polyethylene; (4) polypropylene; (5) polyamide-6; (6) poly(ethylene terephthalate); (7) poly(vinyl acetate); (8) poly(vinyl chloride); (9) poly(vinyl alcohol); (10) poly(methyl methacrylate); (11) boron oxide glass; (12) polyacrylonitrile; (13) polycarbonate; (14) poly(cyclohexyl methacrylate); (15) poly(α-methylstyrene); (16) polystyrene; (17) polyarylate; (18) polyimide I; (19) polyimide II; (20) polyimide III; (21) poly(*m*-phenylene isophthalamide)

bifurcation point, Z is close to 1 whereas at strong decreasing temperature $Z \to \infty$. Meanwhile, in the typically studied region of $\nu = 10^{-3}$–10^{3} Hz, $Z \approx 4$ in the glass transition (see a scheme in Fig. 15).

Thus, in these terms the β-relaxation corresponds to the quasi-independent motion of segments ($Z = 1$), whereas the "intermediate" relaxations may be assigned to lower-cooperative segmental motions with $Z = 2$ or 3. From this viewpoint, the course of the $Q(T)$ curve in Fig. 16 is absolutely understandable.

A direct connection between α- and β-relaxations also follows from recently found linear correlation between the logarithm of the β-relaxation time at $T = T_g[\log \tau_\beta(T_g)]$ and the coefficient b in the Kohlrausch α-relaxation correlation function $\exp\,[(-t/\tau_\alpha)^b]$ for dielectric and mechanical relaxations [117]. A simple relaxation process with a single relaxation time corresponds to $b = 1$, and the β-relaxation event was considered by this author as the primary ("primitive") segmental motion in the cooperative α-process.

The far-infrared/Raman spectroscopy data, obtained for PMMA, its oligomers, and plasticized PMMA [106–108], are of interest for the problem being discussed. It was shown that the low-frequency "boson" peak, being characteristic of the solid-state nanoregions with an increased cohesion, turned out to be correlated with vibrational excitations on the scale of a Kuhn segment with intermolecular cooperation of neighboring segments. In fact, this type of motion is a preliminary stage preceding the manifestation of cooperative segmental dynamics.

Table 2 summarizes the results of direct estimation of motional segment lengths in different temperature regions (β-relaxation, glass transition, rubber-like and fluid states), obtained by a few techniques for 14 flexible-chain polymers. A rather satisfactory correspondence of motional segment lengths to the Kuhn segment sizes was observed in all cases, irrespective of the temperature region investigated.

Thus, the size of moving segments remains practically invariable over a wide temperature range, from the β-relaxation region up to polymer melt, being close to the Kuhn segment size; therefore, the β-relaxation process is of special significance. A sharp increase in the scale of motional unit event in the glass transition is not associated with increasing length of intramolecular kinetic unit but is caused by intermolecular cooperativity of segmental motion. The character of segmental motion changes over the indicated temperature range because of (1) variability in a degree of intermolecular cooperativity in a motional event due to the different local densities of segmental packing and (2) the different contributions of cooperative solid-like (α), Arrhenius liquid-like (β) motional events as well as "intermediate relaxations" to segmental dynamics. Only non-cooperative segmental motions occur in a polymer melt having large free volume, but they remain only locally in the β-relaxation region of glassy polymer.

The results discussed provide a distinct understanding of the "anomalous" T_g reduction and its limit: this occurs due to separation of neighboring chains (segments) as a result of loosening molecular packing and rise of free volume points (under nanoconfinement or at free polymer surface), or due to introducing some foreign molecules between chains.

Table 2 Experimental lengths N of kinetic units (segments) of motion in flexible-chain polymers compared to their Kuhn segment lengths N_K [103]

Polymer	Temperature region	Experimental technique	N Monomer units	N_K	References
Polyacrylonitrile	β-relaxation	FIRS	7	9	[23, 95, 100]
Polychlorostyrene	β-relaxation	FIRS	6	8	[23, 95, 100]
Poly(decyl methacrylate)	β-relaxation	FIRS	5	7	[23, 95, 100]
Poly(dimethylsiloxane)	$T \geq T_g$	NMR	5	5	[118]
Poly(ethyl acrylate)	$T \geq T_g$	Photon correlation spectroscopy	4	6	[119]
Polyethylene	β-relaxation	FIRS	7	8	[23, 95, 100]
	β-relaxation	TSDC	8	8	[120]
	$T > T_g$	Diffusion	7	8	[121]
Poly(ethylene glycol)	$T > T_{ll}$(melt)	Paramagnetic probes	5	4–5	[122]
	β-relaxation	FIRS	4	4–5	[23, 95, 100]
	α-relaxation	Light scattering	6	4–5	[123]
Polyisoprene	$T \geq T_g$	Paramagnetic probes	3–4	3–4	[124]
	$T \geq T_g$	Fluorescence depolarization	4–5	3–4	[125]
Poly(methyl acrylate)	β-relaxation	FIRS	4	6	[23, 95, 100]
Poly(methyl methacrylate)	β-relaxation	FIRS	5	6	[23, 95, 100]
Polypropylene	β-relaxation	FIRS	9–10	9	[23, 95, 100]
Polystyrene	β-relaxation	Raman spectra	>3	8	[126]
	β-relaxation	FIRS	7	8	[23, 95, 100]
Poly(vinyl acetate)	β-relaxation	FIRS	6	7	[23, 95, 100]
Poly(vinyl fluoride)	β-relaxation	FIRS	10	11	[23, 95, 100]

Thus, creating the conditions for a decrease in intermolecular cooperativity of segmental motion, down to its total collapsing, is the primary reason for "anomalous" T_g reduction as well as broadening the glass transition range towards lower temperatures, with the manifestation of the dynamic heterogeneity over the $(T_\beta – T_g)$ range. The physical limit for T_g reduction is the attainment of the temperatures of the β-relaxation region.

At the end of this section, we present in Fig. 21a–f several interesting examples of the anomalous glass transition behavior when T_g attained or became very close to the indicated physical limit (T_β). It means that α-relaxation → β-relaxation transformation occurred, and glass transition dynamics was realized via the Arrhenius mechanism. Additionally, the example of the reverse transformation of "anomalous" T_g into "normal" T_g is given.

Figure 21a,b shows how T_g drops to T_β, and the activation energy of basic transition decreases from 400 to 100 kJ mol^{-1} ($Q_\alpha \rightarrow Q_\beta$) in the plasticized

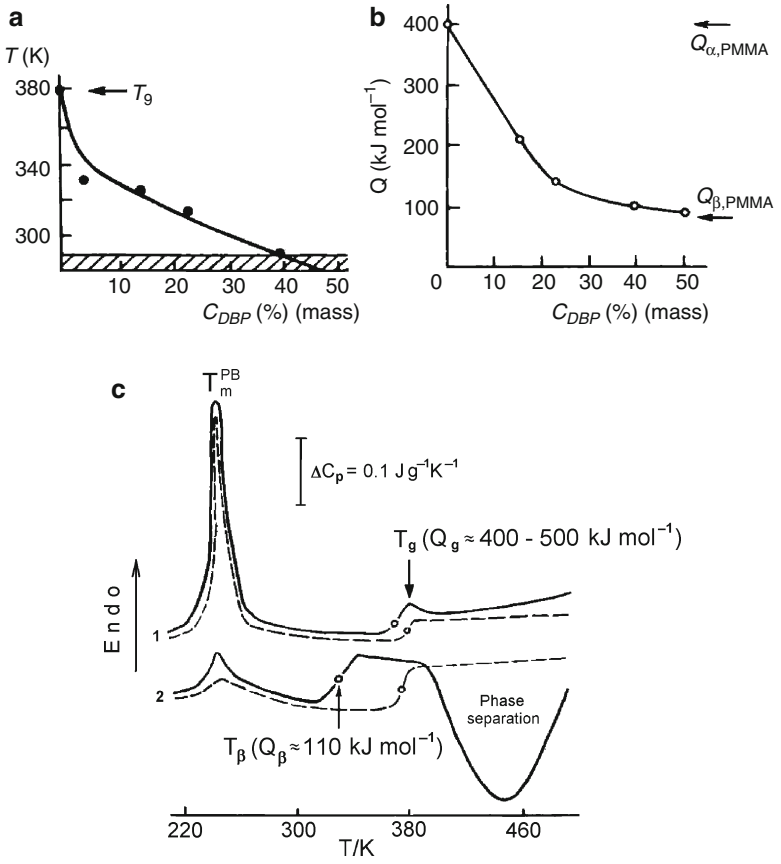

Fig. 21 (**a**–**f**) Examples of collapsing cooperativity in the glass transition dynamics (α-relaxation→ β-relaxation transformation) in flexible-chain polymers. (**a**, **b**) Glass transition temperature and activation energy in PMMA–dibutyl phthalate (DBP) mixtures as a function of DBP content (DSC data [15, 127]). (**c**) DSC curves obtained for PS–PB blend (curves 1) and PS–PB graft copolymer (curves 2) [103]. Heating rate $V = 20\,\mathrm{K\,min^{-1}}$. After scan 1 (*solid lines*) the samples were cooled with $V = 320\,\mathrm{K\,min^{-1}}$ followed by scan 2 (*dashed lines*). Reversal β-relaxation→ α-relaxation transformation may also be seen

PMMA–dibutyl phthalate (DBP) system [127]. A similar effect was observed for the miscible polymer blends (see Sect. 3.5).

Figure 21c compares the DSC curves obtained for the phase-separated polystyrene–polybutadiene (PS/PB) blend and PS–PB graft copolymer with the identical weight ratios of both components (11:89) [103]. For the blend, one can see the melting peak of PB crystallites and ΔC_p step at $T_g^{PS} = 375\,\mathrm{K}$; besides, $Q_\alpha \approx 400\,\mathrm{kJ\ mol^{-1}}$ was obtained. Meanwhile, mixing of both components in the graft copolymer resulted in the manifestation of PS glass transition with T_β and Q_β parameters. At the first scanning the exothermic effect of microphase separation

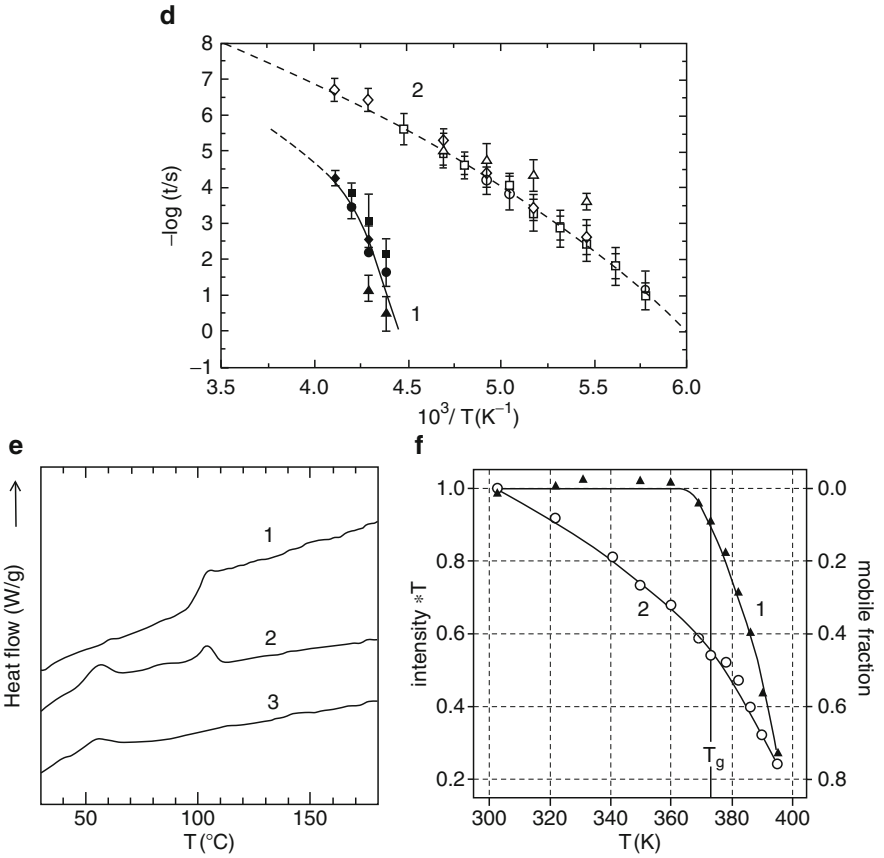

Fig. 21 (continued) (**d**) Arrhenius plot of the relaxation times obtained by dielectric spectroscopy for bulk poly(methylphenylsiloxane) (PMPS) (1) and PMPS intercalated into organically modified layered silicates (1.5–2.0 nm thick polymer films) (2) [41]. (**e**) DSC curves of neat PS (1), physical mixture of PS with the organically modified silicate (2), and PS intercalated (nanoconfined) between silicate nanolayers (3) [40]. (**f**) Unfreezing large-amplitude dynamics in bulk PS (1) and in 2 nm layer of PS confined between the organically modified surfaces of layered fluorohectorite (2): mobile fraction vs temperature plots (^{2}H quadrupole NMR spin-echo experiments [47])

was registered. As a result, the second scanning showed that the "normal" T_g and Q_α values were restored in the glass transition of the phase-separated graft copolymer.

Figure 21d shows the Arrhenius diagram of the relaxation times, obtained by the dielectric relaxation spectroscopy (DRS) for bulk poly(methylphenylsiloxane) (PMPS) and PMPS intercalated as 1.5–2.0 nm films between organically modified silicate layers [41]. Unlike the slow cooperative glass transition dynamics in the bulk PMPS, PMPS confined within the silicate galleries is characterized with very fast, almost Arrhenius segmental dynamics (compare with the "relaxation map" in Fig. 15). The similar result was also obtained for organic molecules located within the well-defined pores and channels with sizes less than 1 nm [39]. As revealed,

six molecules ($Z = 6$) were enough to manifest a cooperative dynamics, whereas the glass transition was transformed into the non-cooperative, Arrhenius dynamic process in the case of a single molecule in a pore ($Z = 1$).

Figure 21e shows the DSC curves obtained for neat PS, PS/silicate mixture, and PS nanolayer intercalated into organically modified layered silicate [40]. One can see the total disappearance of the glass transition at "normal" T_g, and instead the weaker manifestation of this transition at $T_\beta \approx 50°C$ for the intercalated PS.

Figure 21f shows the population of unfrozen segmental dynamics units ("mobile fraction") in the bulk PS and in the intercalated PS as a function of temperature (the spin-echo NMR measurements). The essential unfreezing of segmental dynamics (mobile fraction $c \approx 10\%$) began from $T_g = 373\,K$ for bulk PS but already from $T_\beta \approx 320\,K$ in the 2 nm thickness PS layer [47].

3.1.3 Common Scheme of Possible Glass Transition Anomalies

Based on the above discussion, a common scheme has been offered, illustrating the possible ways for the anomalous behavior of the glass transition as the effective activation energy of segmental dynamics Q vs T plots (Fig. 22). This scheme is applicable to virtually all complex flexible-chain polymer systems or composites, and also to ultra-thin polymer films, freely standing or located on a substrate, and to dynamics in polymers or oligomers under nanoscale confinement conditions. T_g^{free} and T_β^{free} in Fig. 22 relate to the temperatures of α- and β-relaxations in a bulk glassy polymer. In addition, the glass transition widths, ΔT_gs, are indicated at the top of Fig. 22. Six possible kinds of glass transition behaviors can be considered. Additionally, the case of total suppression (disappearance) of the glass transition,

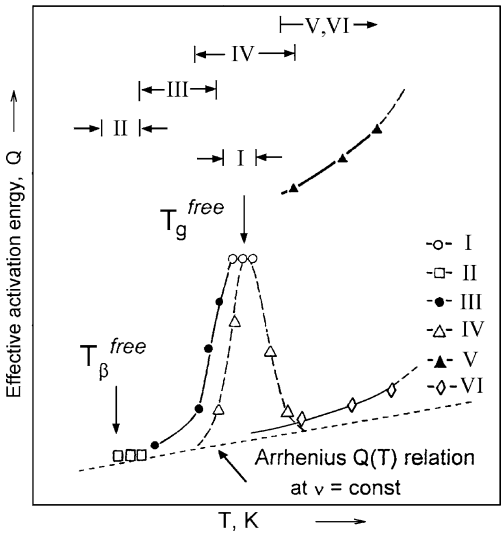

Fig. 22 Activation energy of segmental motion within glass transition vs temperature plots, illustrating schematically the possible dynamic anomalies in different complex polymer systems (see text) [128, 129]. The transition widths are indicated above

due to the pronounced constraining dynamics, is possible as well; this case is not shown in this scheme.

Case I relates to a "normal" glass transition with $T_g \approx T_g^{free}$, a narrow ΔT_g range (typically from 5°C to 20°C, by DSC data), and a high, non-Arrhenius effective activation energy Q. The latter remains invariable within the glass transition range and equal typically to a few hundred kilojoules per mole.

Case II corresponds to a total collapse of intermolecular cooperativity of segmental dynamics in the glass transition. In such a case, the glass transition is realized through the mechanism of non-cooperative Arrhenius β-relaxation. The transition characteristics are displaced to lower values: $T_g \rightarrow T_\beta$, $Q_\alpha \rightarrow Q_\beta$, and $Z \rightarrow 1$.

Case III is characterized by decreasing T_g to different degrees and, therefore, large broadening of the ΔT_g range towards the lower temperatures. This range may extend at the limit to the region of β-relaxation. The glass transition may be represented, due to the different local reduction of motional cooperativity, by a broad $Q(T)$ dispersion.

Case IV corresponds to broadening of the ΔT_g range towards both the lower and higher temperatures, with different Q reductions. This is also caused by a certain reduction of motional cooperativity, but the higher-temperature branch of the $Q(T)$ dispersion arises here being associated with the different constraining impact of a rigid surface or constituent on dynamics of some segments.

Finally, cases V and VI may be related to cooperative or practically non-cooperative segmental dynamics events, respectively, differently constrained by strong interaction of chains with a substrate or rigid constituent.

Some of these variants of the anomalies may manifest themselves simultaneously in a polymer system, e.g., when the constraining effect prevails for some segments, whereas the confinement effect is more pronounced for the other segments. The strong dynamic heterogeneity within the glass transition range (variable Q) may be observed in cases III–VI.

Figure 23 represents the experimental result [130] illustrating the above discussion. In this work, the interfacial interactions and glass transition dynamics were studied for the well-defined silica core-poly(vinyl pyrrolidone) (PVP) shell nanoparticles as model "interface-controlled materials." The PVP shell thickness in these particles varied from 1–2 nm (monomolecular layer in a flattened conformation) up to 10–20 nm. Far- and mid-IR spectra revealed the strong PVP–silica interactions of two kinds: hydrogen bonds and "soft" Lewis acid–base interactions that were maximal for 1–2 nm thick monomolecular PVP shell (20 wt% PVP in the core-shell particles). DSC analysis of the dispersion of activation barriers to segmental motion within the glass transition was performed.

Unlike the transition range $\Delta T_g = 18°C$ ($T_g = 143°C$) for neat PVP, glass transition in the PVP monolayer was sharply broadened in two directions, from ~80°C (β-relaxation region) to 230°C (Fig. 23a). No dynamic heterogeneity within the narrow glass transition range and "normal" cooperative dynamics ($Q = 250\,\text{kJ mol}^{-1}$) were observed for neat PVP (Fig. 23b). In contrast, glass transition dynamics in PVP monolayer dramatically altered: the pronounced dynamic heterogeneity (multi-modal dynamics) was found from the extremely wide Q dispersion. In fact,

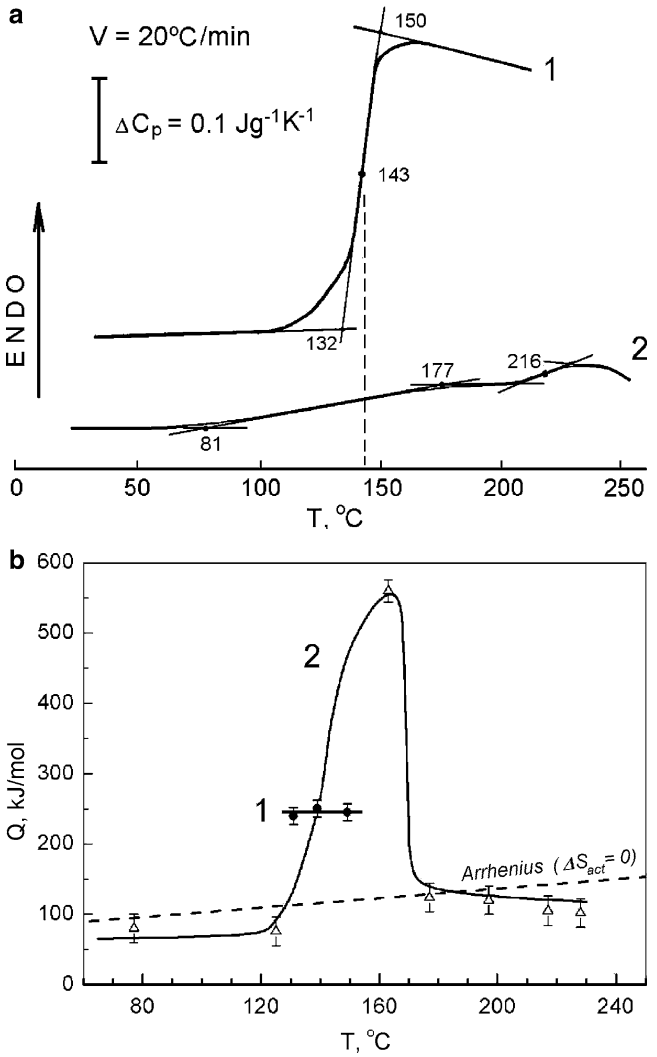

Fig. 23 Neat poly(vinyl pyrrolidone) (PVP) and silica core-PVP shell nanoparticles (20PVP/80SiO_2 composition) with the shell thickness of 1–2 nm (monolayer) [130]. (**a**) DSC curves of PVP (1) and nanoparticles (2) obtained at the heating rate $V = 20°C\,min^{-1}$. (**b**) Dispersions of apparent activation energies Q for segmental motion within waterless PVP glass transition as a function of temperature, as determined by DSC for PVP (1) and 20PVP/80SiO_2 nanoparticles (2)

"normal" cooperative dynamic mode, peculiar to the bulk polymer, was absent in this case at all, and only three "abnormal" (for glass transition) modes were observed. These included: (1) ultra-fast Arrhenius β-relaxation mode at 80–120°C with $Q = 75\,kJ\,mol^{-1}$; (2) constrained cooperative dynamics mode at ~160 °C with $Q = 560\,kJ\,mol^{-1}$; and (3) constrained non-cooperative dynamic mode at 175–230°C with $Q \approx 100\,kJ\,mol^{-1}$.

Similar wide dispersion of the activation energies within the glass transition has been obtained earlier for 4-arm star-like PS where chains were grafted to fullerene (C_{60}) core [131].

3.2 Polymer Networks

Creep rate spectroscopy has been used for the discrete dynamic analysis of polymer networks such as PU network [19]; PU–butyl methacrylate/dimethacrylate triethylene glycol copolymer interpenetrating networks (PU/BMA copolymer IPNs) [132, 133]; commercial epoxy networks [134, 135]; the "model" epoxy-amine networks varying in crosslink density and rigidity [20]; and the cross-linked hyperbranched polyimides [136].

In [19], the PU network was synthesized from poly(oxypropylene glycol) (PPG) with $M_w = 2,000$ g mol^{-1} and adduct of trimethylolpropane (TMP) and toluylene diisocyanate (TDI), and depicted by the formula.

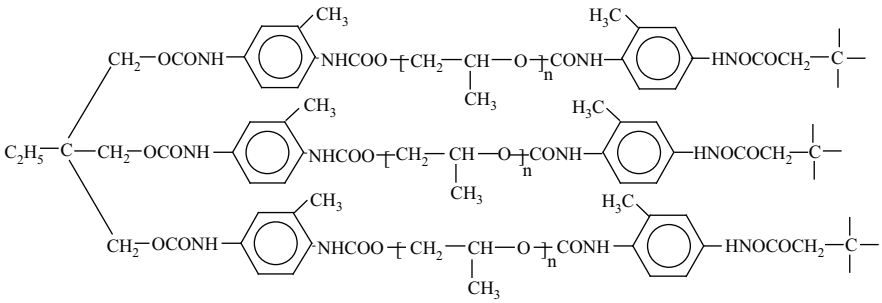

In this PU network relatively rigid nanodomains were incorporated, TMP–TDI adducts, as network junctions chemically connected with flexible PPG chains. Each PPG chain (crosslink) consisted on average of about five Kuhn statistical segments. SAXS measurements indicated Bragg's quasi-periodic distribution of rigid junctions with a characteristic size of 6–9 nm in this network.

Such PU molecular structure assumed, a priori, the possible manifestation of several dynamic modes within the glass transition, in particular, because of the different positions of segments within a PPG crosslink regarding rigid junctions. However, DMA and dielectric relaxation spectrometry (DRS) techniques exhibited only one broad relaxation region for PU glass transition, for instance, the asymmetric mechanical loss peak extending from -60°C to 50°C, with $T_{max} \approx -30$°C (Fig. 9).

In contrast, the discrete CR spectrum was observed for this PU network at low temperatures and tensile stress $\sigma = 0.2$ MPa (Fig. 9). The spectral contour consisted of four partly overlapping peaks: at -50°C to -30°C (I); -20°C to -10°C (II); 0°C to 10°C (III), and 30°C to 40°C (IV). This indicated the distinct heterogeneity in the glass transition dynamics. This heterogeneity was tentatively explained by

different locations of PPG segments regarding network junctions. Creep rate peaks I, II, and III were assigned to unfreezing "undisturbed" dynamics of segments in the middle of PPG crosslink as well as slightly constrained dynamics for two neighboring segments, and to unfreezing dynamics of segments covalently bound to network junctions, respectively. Peak IV may presumably be assigned to motion of network junction.

For the first time, the pronounced heterogeneity of segmental dynamics around T_g, with the discrete manifestation of a number of dynamic modes constituting this relaxation region, together with its origins, were revealed by CRS in the PU/BMA copolymer IPNs [133]. There was no distinct microphase separation in these systems, and DSC, DMA, and DRS techniques were capable of demonstrating a single broad (up to 50–100 K) glass transition only, e.g., the uninterrupted heat capacity step in the DSC curve. For this reason, IPNs are usually considered as the best polymer damping materials.

Meantime, there are a few reasons for assuming, a priori, a large dynamic heterogeneity within or in the vicinity of the glass transition region in these IPNs. Really, the nanoheterogeneous morphology due to incomplete mixing of the constituents, the separate or combined motion of dissimilar segments, and the differences in the segmental packing densities, may contribute to the complicated segmental dynamics.

Basing on the backgrounds described in Sect. 3.1, one could expect up to eight CR peaks (dynamic modes) associated with a Kuhn segment motion, cooperative, partly- or noncooperative, within or around the broad IPN glass transition range. These segmental motions and their approximate parameters, estimated by the other techniques or calculated taking the parameters of solubility of the constituents into account [133], are presented in Table 3. It is evident that segmental motions 1, 3, and 5 are to be peculiar to nanodomains with loosened molecular packing; motions 4 and 8 relate to "normal" glass transition dynamics in neat PU or BMA copolymer nanodomains, and only motions 2, 6, and 7 characterize dynamics in nanodomains with mixed (dissimilar segments) molecular structure.

The creep rate spectra of these IPNs with different compositions exhibited, indeed, the complex structures depending on a weight ratio of the constituent networks [133]. A few discrete or partly overlapping constituents, i.e., CR peaks with the maxima or such contour nonmonotonies as the step or "shoulder" upon the edge of the basic peak, could be seen. Generally, from four to eight constituents were observed in the CR spectra of these IPNs. Their contours turned out to be of peculiar form for each composition, and the relative contributions of the relevant peaks changed regularly with changing PU/BMA copolymer IPN composition. As an example, Fig. 24 shows the CR spectra obtained for the 39PU/61BMA copolymer network at 150–330 K. One can see that the spectra respond in a discrete manner to unfreezing of the different types of segment motions. From comparison of the spectra with expectations (Table 3), it is obvious that (a) the spectra cover just the predicted temperature range, from 170–180 K to 330 K and (b) the peak temperatures satisfactorily coincide with the expected temperatures of unfreezing the predicted motions.

Table 3 Possible kinds of segmental motion within the broadened glass transition in the PU/BMA copolymer IPNs, and their characteristics expected [133]

No	Segmental dynamics mode	T(K) at 10^{-2} Hz	Activation energy Q (kJ mol^{-1})	Cooperativity parameter Z
1	Arrhenius β-relaxation in poly(propylene oxide)-based PU network	170–190	50–55	1
2	Ditto, when contacting PPO segments with PBMA segments	∼200	55–60	1
3	Low-cooperative "intermediate" relaxations in PU network	∼220 ∼250	– –	2 3
4	Cooperative α-transition in PU network	270	220–250	4
5	Arrhenius β-relaxation in BMA copolymer network	270	80–100	1
6	Ditto, when contacting PBMA segments with PPO segments	260	70–80	1
7	Cooperative motion of PBMA and PU neighboring segments	280–290	∼200	3–4
8	Cooperative α-transition in BMA copolymer network	300–330	200–230	∼3

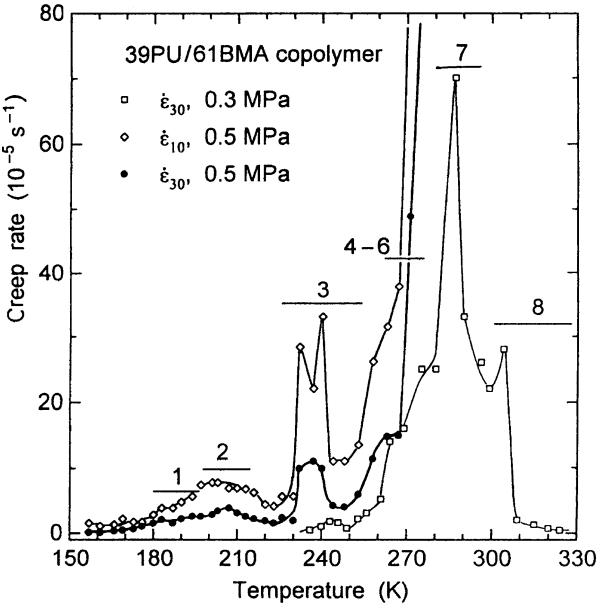

Fig. 24 Creep rate spectra obtained under the tensile stress and indicated experimental conditions for the 39PU/61BMA copolymer interpenetrating network. Temperature ranges 1–8 correspond to the predicted ones for unfreezing different modes of segmental motion indicated in Table 3 [133]

Creep rate spectroscopy allowed us not only to estimate the dynamic heterogeneity but also to probe local (nanoscale) compositional inhomogeneity in the PU–BMA copolymer IPNs. For this purpose, the relative peak contributions to dynamics around T_g as a function of IPN composition were estimated. On this basis, the volume fractions of the nanodomains of neat constituent networks as well as their miscibility degree as a function of IPN composition could be determined, in a semi-quantitative way [133].

Finally, the CRS technique was used for studying molecular motion in the glassy state (sub-T_g relaxations) of a series of model epoxy-amine networks [20]. The experiments were carried out over the temperature range 100–350 K, which covers the regions where the secondary relaxations are basically expected to occur.

The "rigid" and "flexible" epoxy networks, prepared by the reaction of diglycidylether of bisphenol A (DGEBA) with 4,4′-diaminodiphenylmethane (DDM) or hexamethylenediamine (HMDA), respectively, were the subject of this study. In addition, mixtures of these diamines with their homologous monoamines, 4-benzylaniline (BAN) or hexylamine (HA), respectively, were used to vary the crosslink density of the networks without significant modifications in their chemical structure. The fully cross-linked DGEBA-DDM and DGEBA-HMDA networks and loosely cross-linked networks, DGEBA-DDM/xBAN and DGEBA-HMDA/xHA (where x is a figure representing the percentage of N–H reactive functions coming from monoamine), were prepared and studied [20].

The typical feature of the epoxy networks is the occurrence of strong sub-T_g relaxations. On the dynamic mechanical traces (Figs. 10 and 25), the β-relaxation process shows up over a broad temperature region, typically from 150 to 300 K with a maximum at about 200 K at the frequency of 1 Hz; these spectra differ only slightly. The tendency to appear at the lower-temperature γ-relaxation is also observed for the networks with sufficiently long aliphatic sequences (HMDA, HA) (Fig. 25b).

The interpretation of β-relaxation in these epoxy-amine networks with the extraordinarily complicated chemical structure still remains disputable despite many experimental (NMR [137–139] and other) results obtained. Different authors have attributed this relaxation to motion of the hydroxypropylether (HPE) units, the DGEBA ring flips, or their combined motions, as well as to motions in the long enough flexible aliphatic sequences. The γ-relaxation is unambiguously related to localized motion in the aliphatic sequences.

Unlike DMA spectra, the complicated CR spectra of the model epoxy networks, obtained at low compressive stresses, exhibited systematically the multiple peaks, at least four to six ones below T_g, irrespective of the applied stress (20–40 MPa) and the experimental time $t = 10$ or 30 s. Thus, much more informative character of CRS compared to DMA was confirmed in particular in these experiments.

The spectral contours of these model networks were quite different and depended on the network architecture. Nevertheless, a few major CR peaks were reproducible in different compositions, e.g., at 115–130, 190, 200–210, 230, and 270 K; the main effect consisted in redistribution of the amplitudes of spectral components. It is clear

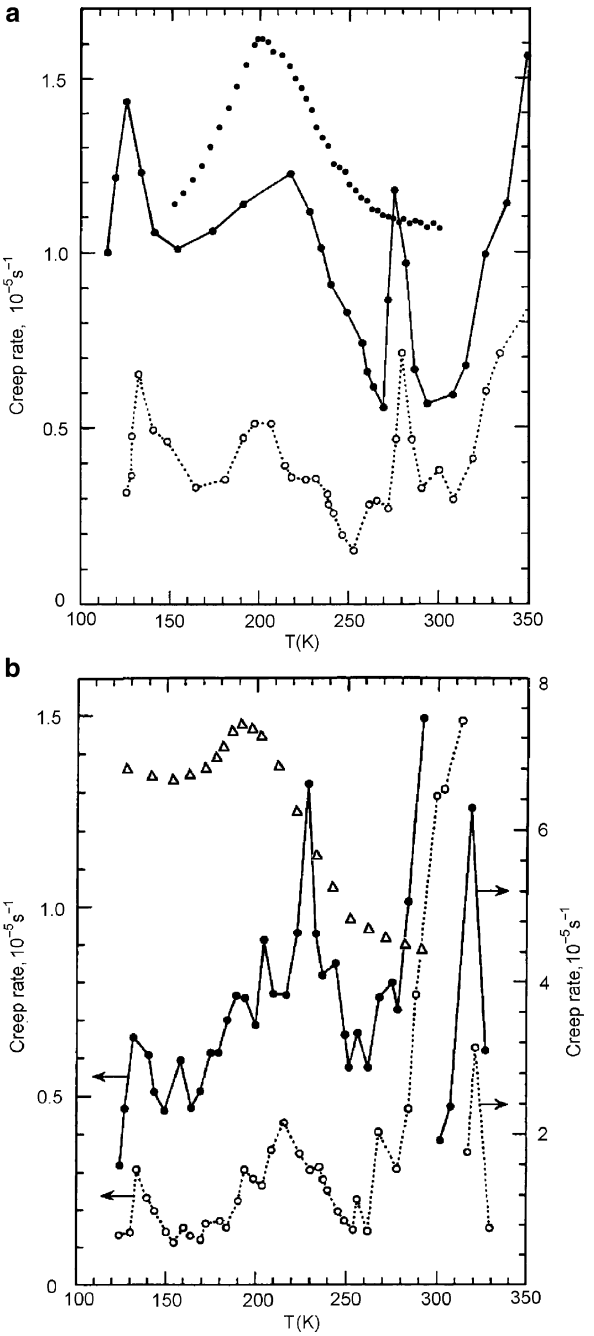

Fig. 25 Creep rate spectra obtained at compressive stress of 20 MPa and $t = 10$ s (*filled circles*) or $t = 30$ s (*open circles*), and E″ dynamic mechanical spectra (1 Hz, *triangle points or dotted contours*) for the model loosely cross-linked DGEBA-DDM/95BAN (**a**) and DGEBA-HMDA/95HA epoxy networks (**b**) [20]

that peak multiplicity might be influenced by a few factors such as differences in local packing density, heterogeneities of crosslink density, the various distances between the motional units and the neighboring junction/next crosslinks, etc. Data analysis was based on the inspection of these peaks without entering much into the details of the fine structure of the spectra.

Figure 25 shows the spectra obtained for the loosely cross-linked aromatic rigid (a) and semi-aliphatic flexible (b) epoxy networks. The substantial difference in these spectra is quite obvious. In particular, over the 120–300 K range at least three main sub-T_g peaks, at 130, 220, and 280 K, may be seen for the rigid network, whereas the highest peak at 230 K and at least five or six slight constituent CR peaks are observed for the flexible network. Additionally, a steep increase in creep rate at 330–350 K for DGEBA-DDM/95BAN network (Fig. 25a) but the narrow CR peak at ~320 K for DGEBA-HMDA/95HA network (Fig. 25b) are observed. The latter effects correspond to the gradual approach to the glass transition of rigid network ($T_g{}^{DMA} = 359$ K) and to the glass transition of flexible network ($T_g{}^{DMA} = 329$ K), respectively.

Analysis of the CRS data, in combination with DMA and NMR data, obtained for the same epoxy networks, allowed the tentative assignments to major CR peaks, that is, to follow up the relations between the CR spectra and molecular mobility [20]. Thus, the basic β-relaxation processes occurred in the temperature range of about 160–260 K where all peaks are supposed to be the reflection of both localized motion of the HPE units and of ring flips of the bisphenol A units. Both rigid and flexible networks exhibited the CR peak at 270 K, which was screened by the constrained β-motion. At last, low-temperature CR peak corresponded to localized γ- or γ′-relaxations in aliphatic sequences, or motion of the DGEBA moieties, respectively [20].

3.3 Polymer–Polymer Hybrid Networks

In recent years considerable attention has been paid to hybrid polymer–polymer networks consisting typically of covalently bound relatively "rigid" and "soft" constituents. Such hybridization of two polymers was aimed at modifying the properties of a basic polymer or combining, to a certain extent, the merits of both constituents within one material. Good examples of such hybrids are three groups of polymer networks based on modified (a) linear polyimide (PI), (b) polycyanurate (PCN), and (c) polyurethane (PU). The improvement of some properties of these polymers was directly associated with complicating segmental dynamics. As shown below, all these systems exhibited a number of "anomalies" in dynamics compared with that for one-component materials. These materials have been successfully characterized by combined use of CRS and a few complementary experimental techniques [19, 129, 140–151], and just CRS turned out to be of special significance for revealing the complexity of glass transition dynamics in hybrid networks.

Linear aromatic PIs are one of the most important high-performance polymeric materials for advanced technologies. Numerous applications of PI in aerospace, microelectronics, membrane technologies, and other fields are due to their excellent thermal stability, chemical resistance, and mechanical, dielectric, and adhesion properties at least up to 250°C. PI membranes show high selectivity for separation of mixtures of air gases but too low permeability for both these gases and organic vapors. Meantime, the industrial importance of membrane technologies has greatly increased in the last few decades, in particular, for separation of volatile organic compounds from air. The membranes prepared from elastomers were successfully tested for this purpose [152–154]. However, for the separation of heat solvent-containing air streams the membrane properties must combine high permeability and good selectivity with the improved thermal, mechanical, and solvent resistance. In this respect, improved membrane properties of PI could be attained by the incorporation of more flexible polymer chains into their structure. Thus, the crosslinked PI-flexible chain or poly(imide-amide) (PIA)-flexible chain hybrid networks, with increased resistance and permeability, turned out to be of special interest. Poly(ether-imide) [155, 156], PIA–poly(ethylene adipate) (PIA–PEA) [129, 143–145, 157], or PIA–poly(ethylene glycol) (PIA–PEG) [149, 150, 158] networks have been studied and successfully used as novel gas-separating membrane materials.

Densely cross-linked PCN networks, synthesized by polymerization, via cyclotrimerization reaction, of dicyanic ester of bisphenol A [159–161], consist of rigid triazine heterocycles as junctions connected with bisphenol A remainders (see a scheme in Fig. 26). At the total conversion of cyanate groups ($X_{CN \rightarrow PCN} \approx 1$), PCN exhibits high $T_g \approx 300$°C and rigidity, good adhesion to different substrates and chemical resistance, as well as low values of dielectric constant and water uptake. This allowed in particular its application as the matrix for glass- and aramid fiber-reinforced plastics in the electronics and aerospace industries.

The major drawback of PCN is the high brittleness restricting the possibilities of its applications. The most perspective route to overcoming this shortage is formation of PCN network in presence of an additive of a flexible-chain linear polymer with terminal groups reacting with cyanate groups. Results concerning modification of brittle PCN with flexible-chain polyurethanes (PUR) [140, 142, 146, 162–166] or hydroxyl-terminated polyethers, such as poly(propylene glycol) (PPG) [162, 167] or poly(tetramethylene glycol) (PTMG) [148, 151, 162, 168], have been reported. The most detailed study of the structure of PCN-flexible chain hybrid networks, containing both “rigid” and “soft” junctions (Fig. 26), and their dynamics has been performed using combined CRS/DSC/TSDC/X-ray analysis [148, 151].

The third group of polymer–polymer hybrid networks, studied with the application of CRS and other techniques, were polyurethane–poly(2-hydroxyethyl methacrylate) (PU–PHEMA) ones [19, 169–171]. Among different applications, PU materials are extensively used for biomedical aims, for instance, in blood contacting apparatus and for organ reconstruction [172–174]. Although PUs are relatively biocompatible materials, they are also known to be prone to biodegradation [175], stress

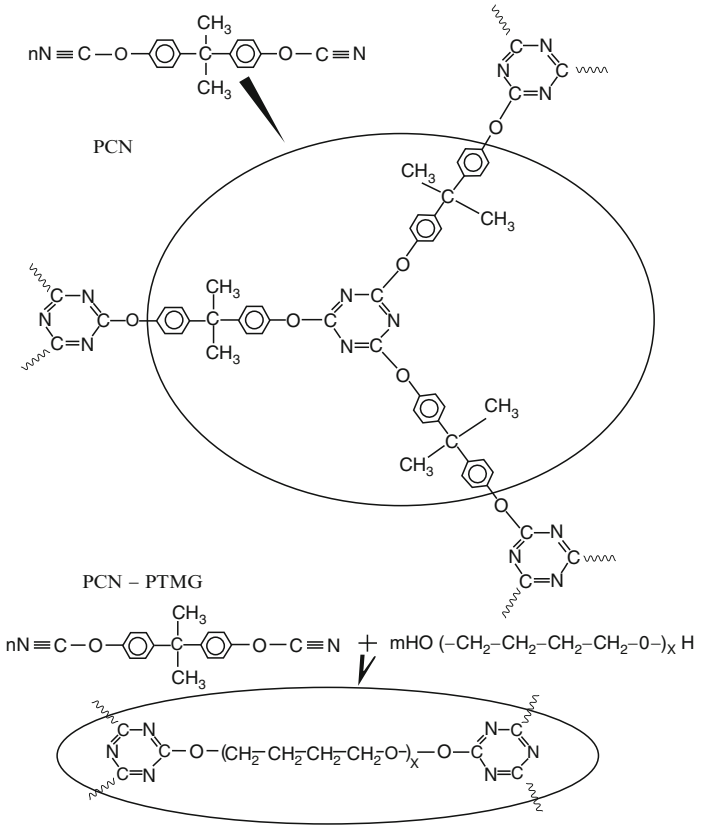

Fig. 26 Schemes of (1) "rigid" triazine ring-aryl junction as the only element of chemical structure in neat PCN networks, and (2) the second, "soft" junction with PTMG crosslink in the PCN–PTMG hybrid networks [148]

induced degradation [176], and surface cracking [177]. One of the most successful approaches that can be used to improve biocompatibility, mechanical properties, and resistance to degradation is creation of PU-containing interpenetrating polymer networks (IPNs). PHEMA is well known as the polymer with good biocompatibility but highly hygroscopic. Hybrid PU–PHEMA semi-IPNs retained PHEMA biocompatibility and acquired better stability and mechanical properties compared with their separate constituents.

The CRS/DSC studies, combined with the structural (SAXS, WAXD) analysis and other techniques, revealed a pronounced heterogeneity of segmental dynamics and structural nanoheterogeneity in all these hybrid networks with basically non-crystalline structures. Of significance are distinct relationships between the peculiarities of dynamics, nanostructure, and properties of hybrid polymer–polymer networks.

3.3.1 Poly(imide-amide)–Poly(ethylene adipate) and Poly(imide-amide)–Poly(ethylene glycol) Hybrid Networks

Poly(imide-amide)–poly(ethylene adipate) networks were synthesized in accordance with the procedures described in [143, 157], via two parallel reactions, of both poly(amic acid) (PAA) imidization and its hybridization (cross-linking) with diisocyanate terminated PEA. PAA was based on pyromellitic dianhydride and 4,4′-oxydianiline. The networks were complicated in their structures, and contained basically imide groups but also amide ones in backbone and ester groups in crosslinks. DSC study of these networks could be performed over the temperature range from 220 to 500 K, only for the PEA component, since the onset of its degradation process at higher temperatures prevented analyzing of the glass transition in PIA component.

Figure 27a shows the DSC curves obtained for the neat PEA network and a series of the PIA–PEA hybrid networks with short PEA crosslinks of about five Kuhn segments (∼10 nm) in length. Unlike one glass transition, with $T_g = 263$ K and the apparent activation energy $Q = 170$ kJ mol^{-1}, for the neat PEA network, two or three glass transitions are observed in the PEA component of the networks with 10–40 wt% PIA, at ∼260–270, 300–320, and 330–340 K. Only one $T_g = 329$ K for the 50PIA–50PEA network, and no transition below 500 K in linear PI were found by DSC. The summary heat capacity step, ΔC_p, in PEA glass transitions decreased with PIA content in a network larger than it might be expected from a change in composition. In addition, the DSC measurements, performed at different heating rates, revealed the wide dispersions of motional activation energy Q, from 100 kJ mol^{-1} to 280 kJ mol^{-1}, for PEA glass transition in the PIA–PEA hybrid networks [143, 145].

These DSC data indicate sharply anomalous glass transition dynamics within rather short PEA crosslinks ($M_n^{PEA} = 1.300$ g mol^{-1}). The displacement of PHEMA glass transition to higher temperatures and the pronounced dynamic heterogeneity could be explained in terms of different constraining impacts of PIA rigid constituents on dynamics of PEA segments; the segments directly anchored to a rigid constraint could be totally immobilized. Threefold Q decreasing indicated the participation of non-cooperative segmental motions in the glass transition dynamics; this effect was more characteristic of the networks with the increased PIA content, i.e., with the larger distances between PEA crosslinks that promoted collapse of intermolecular motional cooperativity due to loosened packing of PEA chains.

The creep rate spectra of the PIA–PEA networks demonstrated distinctly the dynamic heterogeneity in the region of PEA glass transition [143, 145]. Figure 27b shows that the high glass transition peak of neat PEA network with the maximum at ca. 280 K transforms into much less intense but broad, complicated CR spectra for the hybrids with 20–30 wt% PIA. Their contours have a few partly overlapping constituents; up to four to seven spectral components may be discerned in these spectra. The spectrum of the 20PIA–80PEA network exhibits, besides the “usual” glass transition peak remainder at 280 K, the spectral components at about 220, 250, 320, 330, 350, and 390 K. The first two peaks must be attributed to non- and

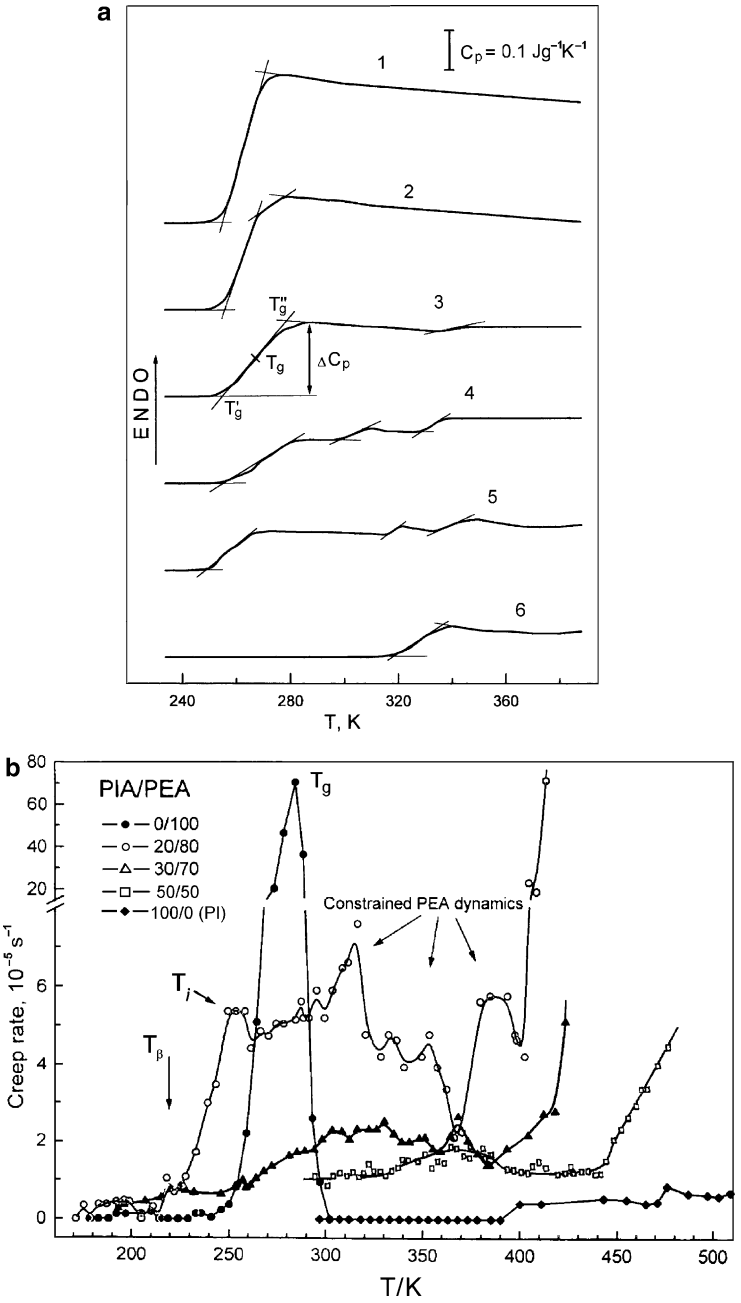

Fig. 27 (**a**) DSC curves obtained at moderate temperatures for the PIA–PEA hybrid networks with $M_n^{PEA} = 1.300\,g\,mol^{-1}$ and PIA/PEA weight ratios: (1) 0/100; (2) 10/90; (3) 20/80; (4) 30/70; (5) 40/60; (6) 50/50. Heating rate $V = 10\,K\,min^{-1}$. Second scans after heating to 500 K with subsequent cooling down to 220 K with $V = 320\,K\,min^{-1}$. (**b**) Creep rate spectra measured at tensile stress of 0.5 MPa for the same hybrid networks with PIA/PEA weight ratios of 0/100; 20/80; 30/70; 50/50, and for linear PI [143, 145]

low-cooperative PEA segmental relaxations at T_β and T_i, respectively, due to loosening of molecular packing of PEA chains. In contrast, the higher-temperature peaks could be explained, again, in terms of PEA dynamic modes differently constrained by rigid PIA chains. A steep increase in creep rates at temperatures over 400 K was associated with the onset of unfreezing segmental mobility in PIA chains.

After introducing 30 wt% PIA into the network, larger reduction of the CR peaks occurred, and strong suppression of segmental dynamics in PEA component at room and moderate temperatures was found for the 50PIA–50PEA network. No distinct CR peaks were observed in the spectra of this network and linear PI (even at elevated stress of 3 MPa) up to 450 and 510 K, respectively. The correlations between the CRS results and the results of DRS measurements, performed for the same hybrid networks and analyzed in terms of morphological characterization [144], were observed. The latter clearly suggested a change in the morphology of these hybrids: the PEA long-range molecular connectivity took place in the hybrids with 70 wt% or more PEA. Since the membrane properties of polymer films are controlled with the enhanced segmental mobility and the long-range connectivity of the "soft" component, it was natural to expect the correlations between the obtained dynamics results and membrane properties (see below).

Another series of hybrids, PIA–PEG networks obtained in a similar way, were subjected to combined CRS/DSC/SAXS/TSDC analysis [149, 150] over the broad temperature range of 160–580 K, covering the regions of both PEG and PIA/PI glass transitions [149]. Depending on their composition, these hybrids were subdivided into (a) the PIA-rich hybrids with spatially isolated PEG domains, strongly suppressed dynamics in the PEG glass transition, and PIA domains with T_g = 520–570 K (group I), and (b) PEG-rich hybrids with a continuous PEG phase (its long-range connectivity was confirmed by the dielectric measurements) and low-temperature glass transition only (group II).

Figure 28a shows the effects of decreasing T_g at 50 or 60 wt% PEG in the networks of group I, due to loosened segmental packing, and total suppression of segmental dynamics in the PEG glass transition by PIA chains in the hybrids of group II with 20 or 40 wt% PEG. Additionally, the weak glass transition at 550–570 K indicating the presence of PIA or PI nanodomains could be discerned for the latter compositions.

The discrete CR spectra provide more detailed information since they reveal the pronounced heterogeneity of segmental dynamics over the temperature range from T_g^{PEG} to T_g^{PI} (Fig. 28b). The peak at 250 K may be assigned to "normal" glass transition in PEG crosslinks. Its intensity decreases with increasing PIA content in a hybrid. This peak is totally suppressed in the 60PIA–40PEG and 80PIA–20PEG compositions. For the latter hybrid a peak at ~560 K, i.e., T_g of PI nanodomains could be revealed. The CR peaks at ~320 and 370 K relate to constrained PEG segmental motions. Low creep resistance at $T > 400$ K is observed only for the 20PIA–80PEG composition. A few peaks in the high-temperature part of the CR spectra, in the region of 420–520 K, are associated with a gradual unfreezing of segmental dynamics in PIA chains.

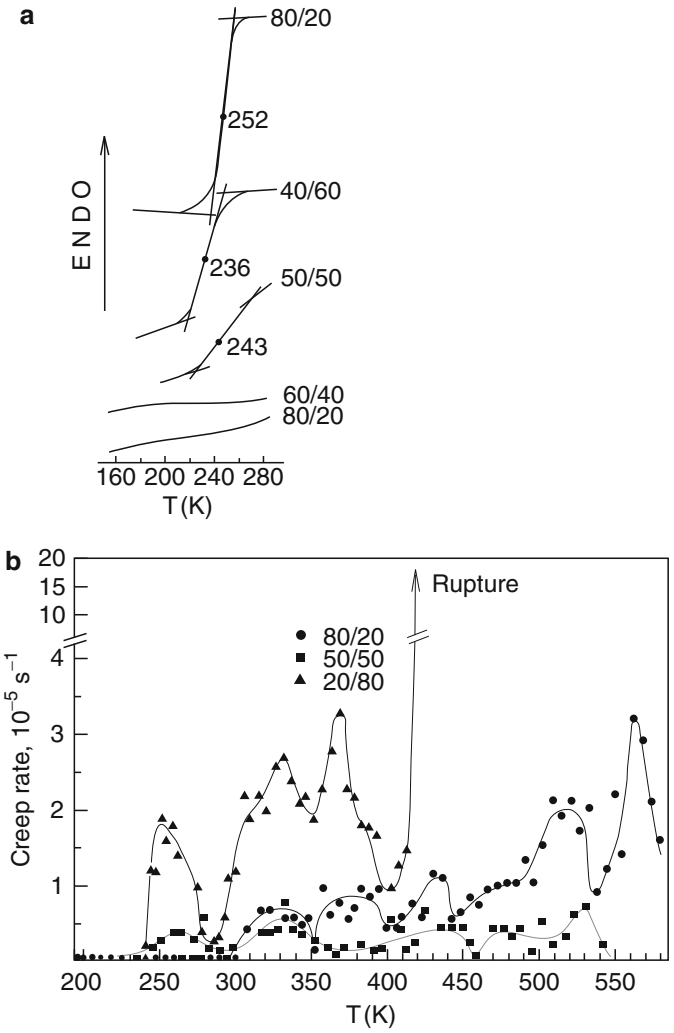

Fig. 28 DSC curves obtained at heating rate of 20 K min^{-1} (**a**), and creep rate spectra measured at tensile stress of 5 MPa (**b**) for the PIA–PEG hybrid networks with $M_n^{PEG} = 1{,}000\,g\,mol^{-1}$ [149]. The PIA/PEG weight ratios in the hybrids are indicated

Of practical importance, some of the indicated PIA-flexible chain hybrid networks turned out to be the promising high-performance membranes for separation of organic vapors from air gases. First, besides the improved thermal/mechanical resistance compared with that for elastomer membranes, the advantage of these hybrid membranes was their resistance to hot organic molecules (penetrants). Second, the distinct correlations between the networks' dynamics and its heterogeneity, as revealed by CRS, and their membrane properties could be followed.

Table 4 Permeability coefficients for organic vapors and air gases in the PIA–PEA and PIA–PEG hybrid networks [129, 149]

Permeability coefficient $P \times 10^{16}$, mol $Pa^{-1}\,m^{-1}\,s^{-1}$							
	PIA/PEA, wt. ratio[a]			PIA/PEG, wt. ratio[b]			
Gas or vapor	40/60	20/80	80/20	60/40	50/50	40/60	20/80
Carbon dioxide	5.6	15.1	5.8	12.3	15.1	25.3	44.6
Oxygen	2.5	3.2	–	–	–	–	–
Nitrogen	0.7	2.1	–	–	–	–	–
Methanol	5,434	18,266	–[c]	155.7	6,282	15,897	50,909
Benzene	2,169	20,578	–	–	–	–	–

[a] $M_n^{PEA} = 1{,}300\,g\,mol^{-1}$
[b] $M_n^{PEG} = 1{,}000\,g\,mol^{-1}$
[c] Non-measurable low

The permeability coefficients for both saturated organic vapors and air gases were dependent on membrane composition. Thus, the membranes with 50 wt% PEA or less showed behavior nearly similar to the neat PI membranes: their permeabilities were too low to be measured. The membranes with 60 or 80 wt% PEA showed much higher permeability coefficients, by three orders of magnitude, for the organic vapors than for air gases (Table 4). Low permeability, e.g., at 20% or 40% PEG in the hybrids was caused by spatially isolated PEG domains and strong suppression of their dynamics. In contrast, with increasing PEG content in the networks, a slight rise in $P(CO_2)$ value and high selectivities $\alpha = P(CH_3OH)/P(CO_2) \approx 400$–$1000$ were reached. High α values at 20°C were associated with unfreezing the glass transition dynamics in continuous PEG phase that provided increased diffusion ability of films.

3.3.2 Polycyanurate–Poly(tetramethylene glycol) Hybrid Networks

Nanostructure and dynamics over the temperature range from −140°C to 300°C have been studied in a few series of the PCN–PTMG hybrid networks by WAXD and SAXS, using synchrotron radiation setup, and by CRS, TSDC and DSC techniques [148, 151]. These networks were synthesized from the dicyanate ester of bisphenol A and hydroxyl-terminated PTMG with molar mass $M_n = 1{,}000$, 2,000, or 5,000 g mol^{-1} [PTMG(1000), PTMG(2000), PTMG(5000)] and weight fraction of 10%, 20%, 30%, or 40%.

Non-crystalline structure and considerable structural nanoheterogeneity of these hybrid networks were shown. A combined analysis revealed their complicated dynamic behavior; moreover, on the basis of CRS data the compositional nanoheterogeneity in these networks could be estimated.

Figure 29 shows the results of SAXS measurements. If the scattering pattern of the pure PCN indicates its homogeneous nature, the nanostructures in the hybrids studied were developed and sensitive to the PTMG chain length and PCN/PTMG ratio. For the hybrids with PTMG(1000), the onset of nanostructurization might

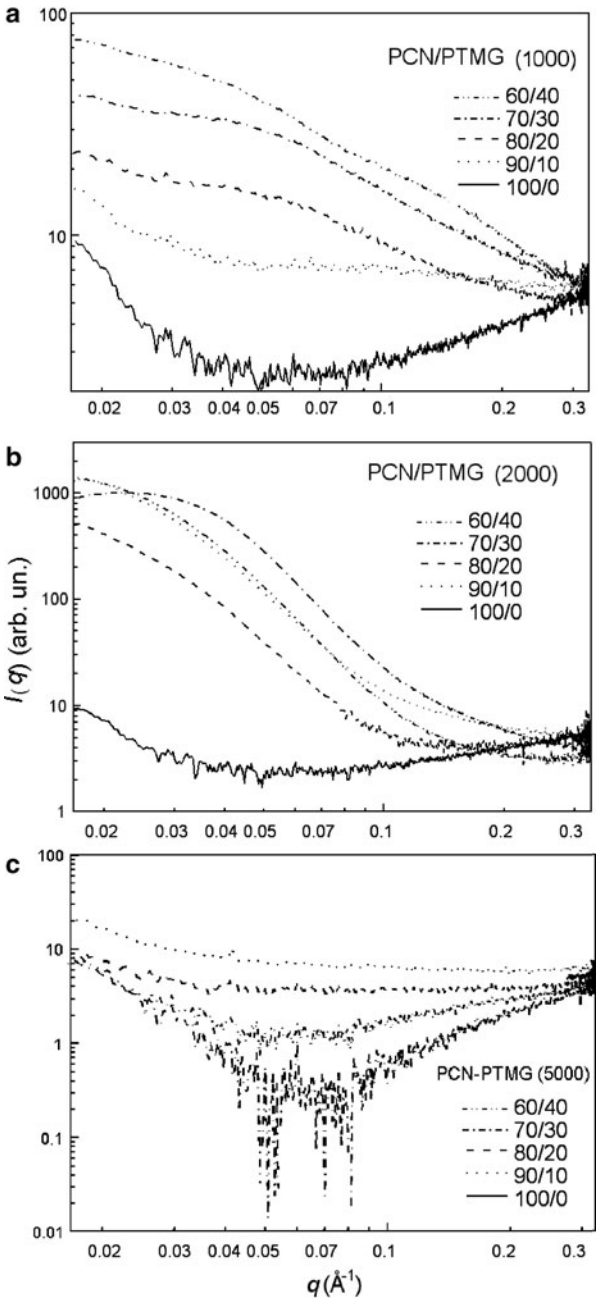

Fig. 29 SAXS patterns obtained with synchrotron radiation for pure PCN and PCN–PTMG hybrid networks differing in composition and molecular weight of PTMG: $M_n = 1.000\,g\,mol^{-1}$ (**a**), $M_n = 2.000\,g\,mol^{-1}$ (**b**), and $M_n = 5.000\,g\,mol^{-1}$ (**c**) [151]. It should be noted that *the first curve*, from below, relates to neat PCN, and *the second curve* to 70/30 and 60/40 compositions in (**c**)

already be assumed in the 90PCN–10PTMG network, and a more considerable scattering was observed with increasing PTMG content in the hybrids, According to the estimates, this indicated the presence of nanoheterogeneities of the order of 10 nm. The PCN–PTMG(2000) systems were very distinctly nanostructured and basically displayed Guinier behavior characteristic of "particle" scattering with gyration radius R_g of about 6.5 nm [151]; the 70/30 composition manifested the broad, well-defined correlation peak (Fig. 29b). In contrast, the PCN–PTMG(5000) networks turned out to be homogeneous in the size window of the analyses performed, and thus could not be considered as nanostructured materials.

Combined CRS/DSC/TSDC analysis revealed a complicated dynamics in these networks as a consequence of their peculiar chemical structure and nanostructure. A dispersion of glass transitions occurring in a wide temperature range was revealed, and some correlations between the structural and CRS data were found. Compositional nanoheterogeneity in these hybrids was estimated by CRS due to the presence of nanodomains with different degrees of rigid cross-linking $X_{CN\rightarrow PCN}$ [148, 151]; to our knowledge, such characteristics were obtained for networks for the first time.

Figure 30 shows typical TSDC thermograms obtained for pure PCN and PCN–PTMG(1000) hybrid networks over the temperature range from −100°C to 300°C. Two peaks, at about 280°C and 230°C, are observed for the neat PCN network, which are assigned to the glass transitions in domains with rather full conversion ($T_g \approx 280$°C) and with about 90% cross-linking density ($T_g \approx 230$°C, see below). TSDC thermograms of the hybrids exhibit, however, a single broad glass transition peak which shifts to lower temperatures with increasing PTMG content. The temperatures of the maxima in TSDC spectra (T_g values) are equal to about 40°C, 100°C, 155°C, and 170°C for the hybrids with 40, 30, 20, or 10 wt% PTMG,

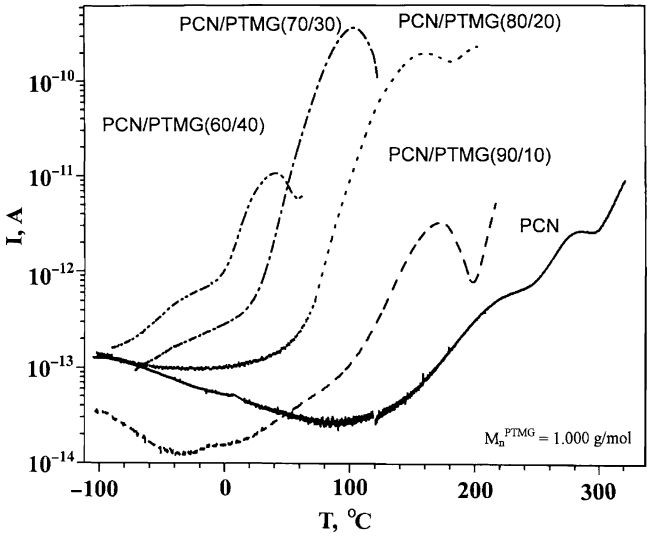

Fig. 30 TSDC thermograms obtained for neat PCN and PCN–PTMG hybrid networks with $M_n^{PTMG} = 1{,}000\,g\,mol^{-1}$ and different compositions [151]

respectively. A single glass transition implies a fairly high degree of "miscibility" of two components in the PCN–PTMG(1000) hybrids over a wide range of compositions, due to chemical incorporation of PTMG chains into the PCN network. TSDC resolution turned out to be insufficient for the estimation of dynamic heterogeneity in these systems.

Figure 31a shows a typical heat capacity $C_p(T)$ curve obtained by DSC for the 80PCN–20PTMG network. This curve is nonmonotonic, and two contributions to heat capacity may be considered. A non-specific C_p rise with temperature is characterized by linear section of the dependence between −150°C and −100°C and its linear extrapolation. Nonmonotonic deviations of heat capacities (ΔC_p) from the straight line are observed at temperatures over −100°C. This second contribution to heat capacity may be considered as the "excess" heat capacity associated with a gradual, step-like unfreezing relaxation dynamics. This occurs presumably in different nanodomains of a hybrid network and in residual "free" PTMG fraction non-incorporated into a network.

Figure 31b shows more distinct $\Delta C_p(T)$ dependence for the same PCN-rich network. The absence of a single glass transition in the PCN–PTMG network and several successive heat capacity steps may be seen in this plot, suggesting the plurality of relaxation transitions. Six ΔC_p steps can be discerned within the range of −100°C to 150°C. DSC could not resolve discrete transitions at $T > 150$°C. The lower-temperature ΔC_p steps correspond to β-relaxation and glass transition in PTMG component, whereas the other ΔC_p steps may be assigned to unfreezing glass transition dynamics in PTMG-enriched nanodomains of modified PCN network, where $X_{CN\rightarrow PCN}$ varies between ∼0.6 and 0.8 (see below).

Creep rate spectroscopy study of the PCN–PTMG hybrid networks [148, 151] demonstrated most distinctly the complicated, heterogeneous nature of glass transition dynamics in these systems providing the detailed information on this problem. Not only the dynamic heterogeneity (T_g plurality) but also the compositional heterogeneity and dynamics/nanostructure interrelationships were found for these amorphous networks.

Analysis of the compositional (chemical) nanoheterogeneity in the PCN–PTMG networks was performed proceeding from (a) the T_g vs $X_{CN\rightarrow PCN}$ dependence found experimentally by Georjon et al. [178, 179] for neat PCN networks with different conversions of monomer into PCN network, that is, different rigid cross-linking degrees (see the inset in Fig. 32), and (b) an assumption of approximate equivalence, with respect to T_g of the network, of unreacted OCN groups in incompletely cross-linked neat PCN to OCN groups chemically connected to PTMG chains, highly mobile at elevated temperatures, in the PCN–PTMG networks (Fig. 26). Therefore, the CR spectra could characterize the dispersions of both T_gs and the approximate rigid cross-linking densities $X_{CN\rightarrow PCN}$ in these hybrid networks (Fig. 32). It was assumed that a partial contribution of each creep rate peak, as estimated by its relative height, $I_i / \sum_{i=1}^{n} I$ (%), to a creep rate spectrum corresponded approximately to a volume fraction occupied by nanodomains with a respective $X_{CN\rightarrow PCN}$ value. The CR spectra of the PCN–PTMG networks allowed us to estimate the volume fractions

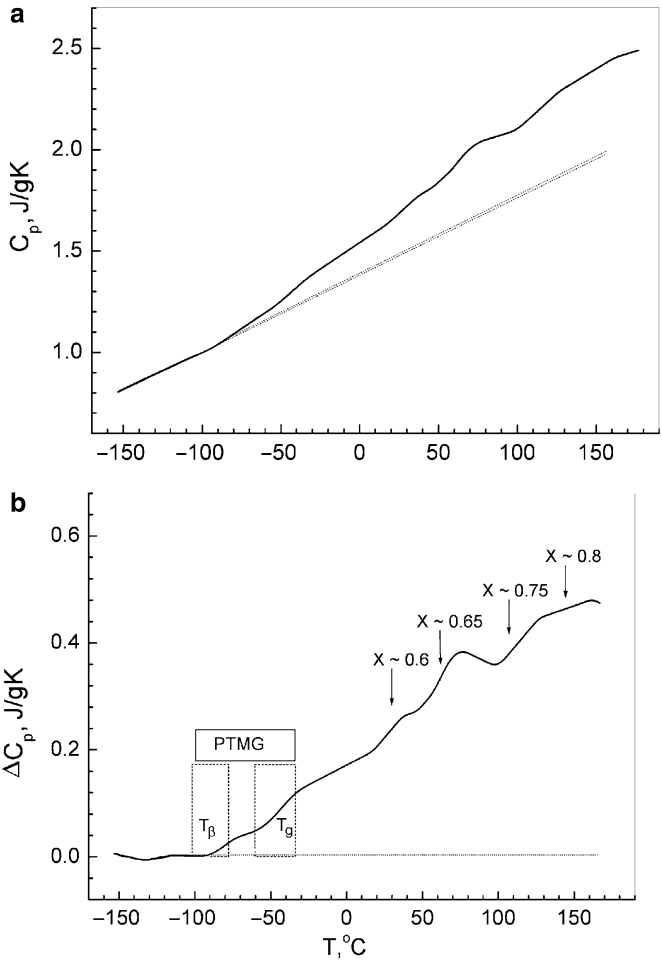

Fig. 31 80PCN–20PTMG hybrid network with $M_n^{PTMG} = 1,000\,g\,mol^{-1}$: total heat capacity (**a**) and relaxation dynamics contribution to heat capacity (**b**) vs temperature plots [148, 151]. Temperature location of β-relaxation and glass transition in PTMG component and rigid cross-linking degrees $X_{CN\rightarrow PCN}$, corresponding to several heat capacity steps (T_gs in modified PCN network domains) are indicated

of nanodomains of different degrees of rigid cross-linking $X_{CN\rightarrow PCN}$. Figures 32 and 33 show the typical CR spectra of the PCN–PTMG networks characterizing both the dynamic and local chemical heterogeneity; some results of such estimates are given for the PCN–PTMG(1000) networks in Table 5.

Figure 32 shows the CR spectra obtained for neat PCN and a series of the PCN–PTMG(1000) networks. A small doublet peak at 280°C and 295°C is observed for PCN. The spectra of the hybrids consist of a few overlapping peaks including the basic glass transition peak and smaller higher-temperature CR ones. Thus, the spectrum of the 80PCN–20PTMG(1000) network exhibits the basic peak with

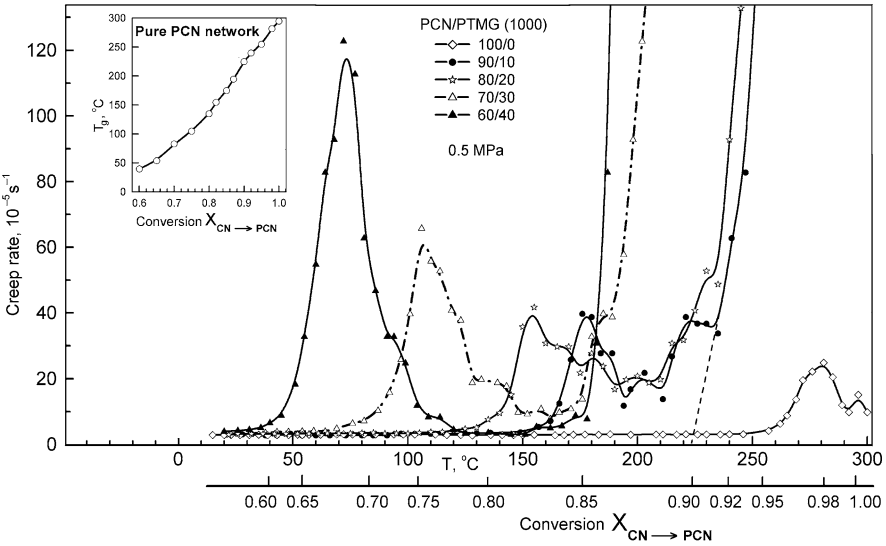

Fig. 32 Creep rate spectra obtained at tensile stress of 0.5 MPa for pure PCN and four PCN–PTMG(1000) hybrid networks with different compositions [148,151]. The inset shows T_g vs cross-linking degree plot found for neat PCN by Georjon et al. [178, 179]. On this basis (see text), *the second abscissa axis* is also given

the maximum at $T_g = 155°C$ and the additional peaks at 170°C, 180°C, 200°C, and 220°C. A steep rise in creep rate is observed for this network only over 230°C. The temperature of the basic T_g peak decreases and its amplitude (height and area) increases with increasing PTMG content in a hybrid. In contrast to the spectrum of neat PCN, sharp unfreezing of molecular dynamics, with a steep rise in creep rate, was always observed for all the hybrids upon their heating up to temperatures exceeding the highest-temperature CR peak. Creep was totally absent in the neat PCN network over the 20–250°C range under the same conditions.

The "over-main T_g" relaxations were attributed to the presence of nanodomains with the higher densities of rigid cross-linking ($X_{CN \rightarrow PCN}$) and T_gs in the molecular structure of the PCN–PTMG networks. Figure 32 shows that neat PCN network is almost completely crosslinked: its two CR peaks correspond to conversions $X_{CN \rightarrow PCN} = 0.98$ and 1.00. At the same time, the compositional nanoheterogeneity, corresponding to the $X_{CN \rightarrow PCN}$ values ranging from ca. 0.8 to 0.9, is observed for the 80PCN–20PTMG(1000) network.

Figure 33a illustrates the correlation between the nanostructures and the CR spectra of the PCN–PTMG networks: it compares three CR spectra of the 90PCN–10PTMG networks with different PTMG chain lengths to their dissimilar nanostructures (Fig. 29). Only one distinct CR peak with a maximum at 180°C is observed for the structurally nanohomogeneous hybrid with PTMG(5000). Increased structural nanoheterogeneity of the network containing PTMG(1000) is displayed in its complicated CR spectrum with the overlapping peaks at about 175°C, 190°C, 200°C, and 220°C. The most distinctly nanostructured hybrid with PTMG(2000)

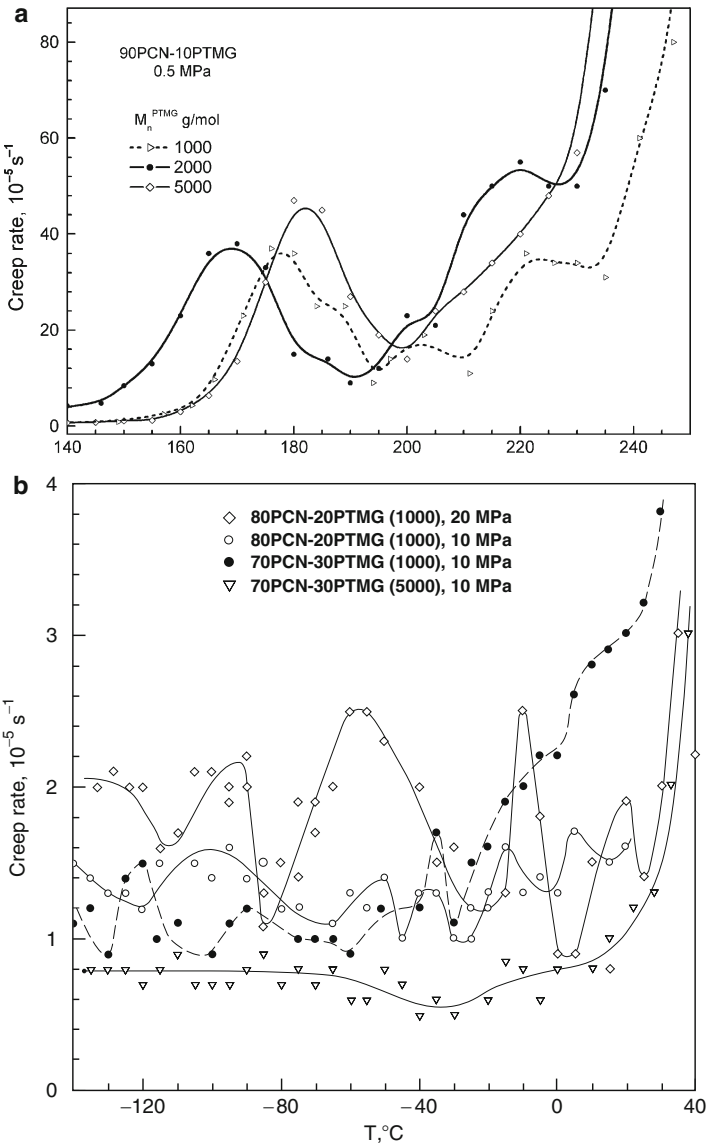

Fig. 33 Creep rate spectra obtained (**a**) for the 90PCN–10PTMG hybrid networks with different PTMG molecular weights, at tensile stress of 0.5 MPa, and (**b**) for the 80PCN–20PTMG(1000), 70PCN–30PTMG(1000), and 70PCN–30PTMG(5000) networks at low temperatures [151]

shows two pronounced peaks located at 165°C and 220°C and corresponding to the conversions $X_{CN \rightarrow PCN} = 0.84$ and 0.90, respectively.

Additional information on dynamic heterogeneity in the PCN–PTMG networks could also be obtained from the CR spectra measured at temperatures much below the main glass transition – at −140°C to 20°C. Figure 33b shows four spectra

Table 5 Plurality of glass transitions and local compositional heterogeneity in the PCN–PTMG hybrid and neat PCN networks, as estimated from the CR spectra obtained at tensile stress of 0.5 MPa [148, 151]

Sample		CRS data		
Composition wt%[a]	PTMG incorporated into network, %[b]	T_g (°C)	$X_{CN\rightarrow PCN}$	$\frac{I_i}{\sum_{i=1}^{n} I}$ (%)[c]
Pure PCN	–	280	0.98	64
		295	1.00	36
90PCN–10PTMG	97.0	175	0.85	32
		185	0.86	21
		200	0.88	16
		220	0.90	31
80PCN–20PTMG	97.0	150	0.82	28
		165	0.84	19
		180	0.86	18
		200	0.88	13
		220	0.90	22
70PCN–30PTMG	85.7	105	0.75	56
		135	0.80	15
		180	0.85	29
60PCN–40PTMG	78.8	70	0.68	72
		90	0.72	18
		110	0.76	5
		170	0.85	5

[a] PTMG with $M_n = 1.000$ g mol^{-1}
[b] Sol–gel analysis
[c] Partial contributions of nanodomains with different $X_{CN\rightarrow PCN}$ conversions

obtained at stresses of 10–20 MPa, high enough for revealing weak relaxations in this temperature region. No CR peak and negligibly small creep rates were observed for nanohomogeneous neat PCN (not shown here) and for the PCN–PTMG(5000) networks at temperatures below 20 °C. In contrast, the dynamic heterogeneity in the nanoheterogenous hybrid networks with PTMG(1000) is distinctly registered. The CR peaks could be attributed to unfreezing segmental dynamics in PTMG chains: segmental β-relaxation and cooperative glass transition, as well as to the constrained dynamics of PTMG segments located close to triazine cycles.

A broad dispersion of the glass transitions in the PCN–PTMG networks is of interest for their applications. A sharp creep acceleration is observed (at low stress) in these networks not at the basic T_g but at much higher temperatures. This means that the low-loaded parts manufactured from PCN–PTMG hybrids with 10 or 20 wt% PTMG may retain some creep resistance up to high temperatures not far from T_g of the neat PCN. On the other hand, the development of microplasticity at low and moderate temperatures due to incorporating PTMG into a network may give rise to some relaxation ability and decreasing (on loading) overstresses around microscopic cracks as stress concentrators. Really, an increase in tensile strength was observed for the PCN–PTMG networks as compared to that of neat PCN. Figure 34 shows

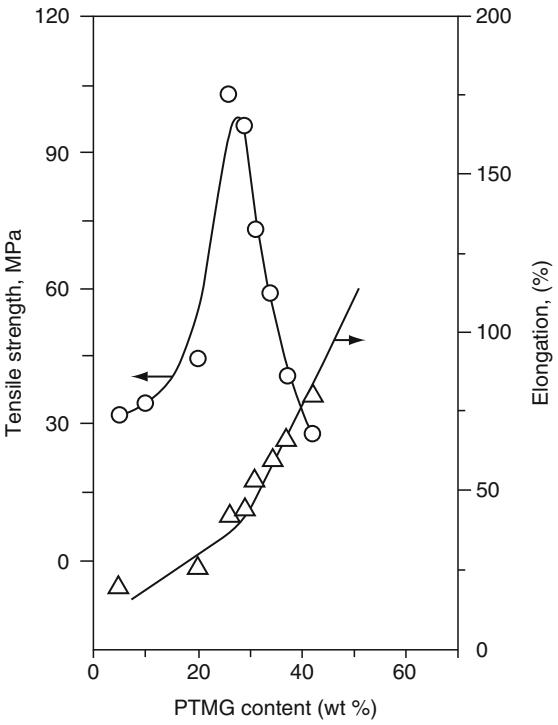

Fig. 34 Tensile strength and elongation at break of the PCN–PTMG hybrid networks at 20°C as a function of PTMG content [180]. $M_n^{PTMG} = 1{,}000\,g\,mol^{-1}$

that PCN–PTMG hybrid tensile strength vs PTMG content plot passes through a maximum, and a threefold increase of the strength at room temperature may be attained at ∼20 wt% PTMG in the network [180].

3.3.3 Polyurethane–Poly(hydroxyethyl methacrylate) Hybrid Networks

These semi-IPNs were synthesized [169] by the sequential method: the PU network was synthesized (Sect. 2.3) and then swollen with 2-hydroxyethyl methacrylate (HEMA) monomer followed by its photopolymerization. The PHEMA content in these semi-IPNs varied from 10 to 57 wt%.

SAXS study of the PU–PHEMA semi-IPNs indicated their nanoheterogeneity. These systems were considered as two-phase ones with incomplete phase separation [171]: two broad mechanical loss peaks related to the glass transitions of constituent components were shown by DMA. The extraordinarily broad PHEMA loss peak covered the temperature range between 50°C and 180–200°C [169]. A two-stage PHEMA glass transition was observed over the range from ∼60°C to 156 °C for the PU–PHEMA networks by DSC [19]; the lower temperature, T_{g1}, was close to T_g of the neat dehydrated PHEMA. The effect of anomalous broadening of the PHEMA glass transition in these networks towards higher temperatures was not expected in view of much lower glass transition temperature of PU constituent. As proved by

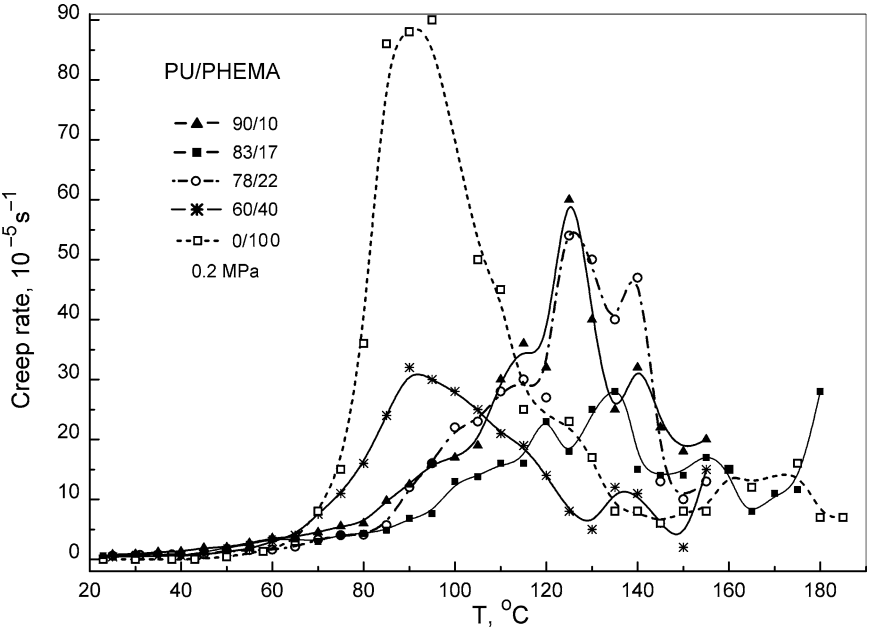

Fig. 35 Creep rate spectra measured at tensile stress of 0.2 MPa in the temperature region of PHEMA glass transition for the stabilized films of neat PHEMA, and the 60PU–40PHEMA, 78PU–22PHEMA, 83PU–17PHEMA, and 90PU–10PHEMA hybrid networks [19]

IR spectra [19], this constrained dynamics effect was caused by chemical bonding of some of PHEMA hydroxyls with unreacted, residual isocyanate groups of PU network, i.e., by some hybridization of the semi-IPN constituents.

The CRS measurements showed the pronounced dynamic heterogeneity as the origin of the extraordinary glass transition breadth in both PHEMA and PU constituents of these hybrid networks [19]. Figure 35 shows the CR spectra obtained for four hybrid PU–PHEMA networks and neat PHEMA in the temperature range of PHEMA glass transition. Strongly modified segmental dynamics is observed when incorporating PHEMA into the semi-IPNs: a very intense peak 1 with $T_{max} = 90°C$ transforms into the complicated spectra. Depending on a network composition, these spectra exhibit different dynamics modes represented by two to five overlapping peaks for the hybrids with 10–40 wt% PHEMA. The residual peak 1, the peaks at 100–115 °C (peak 2), 120–130°C (peak 3), 135–140°C (peak 4), or even at 155°C (peak 5) are observed.

Creep rate peaks 2–5 correspond by their temperature location approximately to the second, higher-temperature stage of PHEMA glass transition in the semi-IPNs studied as measured by DSC [19]. These additional glass transitions may be assigned to unfreezing of differently constrained PHEMA segmental motions, depending on a distance between moving PHEMA segment and PU junction. Some fragments of PU network may also be involved into PHEMA dynamics event. More

pronounced dynamic heterogeneity in the PHEMA glass transition of the networks with 10–22 wt% PHEMA is understandable since the fraction of PHEMA chains chemically attached to PU network is evidently larger when PHEMA content in the semi-IPNs is lower.

Figure 35 indicates the improved creep resistance at low stress of the 83PU–17PHEMA network compared with that for the neat PHEMA or the 60PU–40PHEMA network. This effect is retained up to about 170°C, whereas decreased creep resistance of the neat PHEMA is observed already at 90°C. Segmental dynamics in the PU constituent was suppressed only partly by PHEMA constituent and PU properties were retained at room and low temperatures [19]. Therefore, the large extension of the range of satisfactory performance in the PU–PHEMA networks to higher temperatures is of significance for the different applications.

3.4 Block Copolymers

A precise separation of the components of BCPs into microphases and a "normal" manifestation of two glass transitions, corresponding in characteristics to those in the respective homopolymers or oligomers, are not common phenomena and anomalies in the characteristics of transitions are often observed [15]. This is explained by mixing of the different blocks in the interfacial (transitional) layers or over the entire volume of the microphases. The volume fraction of the interfacial layers in BCP may vary from 1–2% to 30–60%. It increases typically with decreasing difference in the solubility parameters δ_1 and δ_2 of the components [$\delta = (E_{coh}/V_M)^{1/2}$, E_{coh} is the cohesion energy, and V_M is the molar volume] and with decreasing in the block lengths. The mutual influence of dissimilar blocks may contribute to a peculiar dynamics in BCP even at the sharp interfaces.

Anomalous glass transition dynamics was shown and studied in detail for a few groups of BCP with different parameters δ [15, 25, 26, 103, 128, 129, 181, 182]. As an example, Fig. 36 shows the DSC data obtained for the polystyrene–polybutadiene (PS–PB) block copolymers with the identical $\delta = 17$–$18(\mathrm{J\,cm^{-3}})^{1/2}$ [103, 181], and for BCP containing "soft" poly(dimethylsiloxane) (PDMS) blocks with $\delta_{PDMS} = 15(\mathrm{J\,cm^{-3}})^{1/2}$ and "rigid" blocks, PI [128, 129, 182] or poly(phenylsilsesquioxane) (PPSSO) [25] with $\delta \approx 20(\mathrm{J\,cm^{-3}})^{1/2}$; the PDMS-PC block copolymers have also been studied [26]. The activation energies of segmental motion within the glass transitions were determined from the DSC curves measured at different heating rates.

Figure 36a shows the DSC curves obtained in the region of PS glass transition for PS–PB block copolymers with different block lengths but the identical molar masses of dissimilar blocks in an each copolymer. The BCP were amorphous but characterized by a regular micro-domain structure. These curves (and also NMR data [181]) indicate a partial mixing of PS and PB blocks. The degree of mixing increases with decreasing length of blocks. Two steps are seen in the DSC curves over the 300–400 K range: at temperature $T = 380\,\mathrm{K} \approx T_g^{PS}$, at ~330 K, or at ~330 and 358 K. The lower-temperature heat capacity step increases with a decrease in

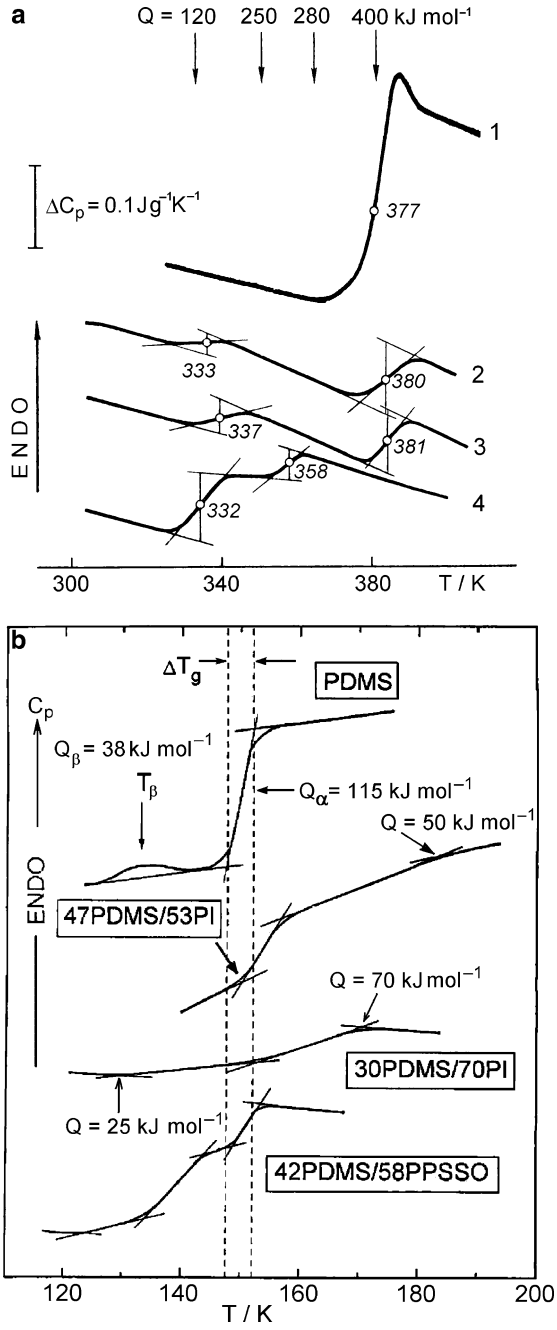

Fig. 36 DSC curves obtained at heating rate 20 K min^{-1} for (**a**) homo PS (1) and PS blocks in the PS–PB block copolymers with the equal M_n values for both blocks, 8×10^4 (2), 3.4×10^4 (3), and 1×10^4 (4) [181] and (**b**) homo PDMS and PDMS blocks in the PDMS-PI and PDMS-PPSSO block copolymers in the temperature region of PDMS glass transition. The activation energies Q obtained at respective temperatures are also indicated [25, 129, 182]

block length, and "normal" T_g disappears for the shortest blocks. It was shown that the degree of mixing PS and PB blocks (volume fraction of interfacial layers) at their molecular masses of $M_n = 8 \times 10^4$, 3.4×10^4, and 1×10^4 was equal to ~20%, 40%, and >70%, respectively [181].

The determination of the effective activation energy Q for transition dynamics showed that the cooperative energy $Q = 400\,\mathrm{kJ\,mol^{-1}}$ for the "normal" transition decreased to lower-cooperative values of 250–280 kJ $\mathrm{mol^{-1}}$ at intermediate temperatures, and to the Arrhenius value of activation energy of the β-transition $Q = 120\,\mathrm{kJ\,mol^{-1}} \approx Q_\beta$ around 330 K. Since $\delta_{PS} \approx \delta_{PB}$, this may be treated as the result of mixing different blocks with a partial or total collapse of intermolecular cooperativity in the PS glass transition dynamics.

Different examples of anomalous dynamics have been obtained for soft PDMS blocks in the BCP containing such rigid blocks as PI [128, 129, 182] or PPSSO [25,129]. The incorporation of flexible PDMS blocks helped to solve the problem of insolubility and lack of processibility of PI in a fully imidized form [183–185]. The perfectly alternating PDMS-PI and PDMS-PPSSO block copolymers manifested a well-defined microphase separation. It might be assumed that the incompatibility of such unlike blocks with strongly different solubility parameters could give rise to a number of microstructural configurations.

Figure 36b shows the DSC curves of homoPDMS and PDMS-containing phase-separated BCP in the temperature range of 120–200 K which covers the regions of the α- and β-relaxations in PDMS. Unlike the narrow range $\Delta T_g = T_g'' - T_g' = 4\,\mathrm{K}$ for homoPDMS (at $T_g = 150\,\mathrm{K}$), multi-fold transition broadening and complex, two- or even four-stage heat capacity steps are typical of the PDMS blocks. Despite the presence of high-T_g rigid blocks in these copolymers, the PDMS glass transition may extend towards both higher and lower temperatures ranging generally from 125 to 185 K. The lower temperature limit for the glass transition onset in the PDMS blocks just corresponds to T_β in homoPDMS, whereas the glass transition completion temperature implies constrained dynamics effects for some of PDMS segments. It should be noted that PDMS blocks only slightly affected the high T_gs of rigid blocks, e.g., $T_g^{PI} \approx 540\,\mathrm{K}$ [182].

This glass transition behavior in the PDMS blocks assumed the pronounced dynamic heterogeneity within this transition. By measuring the DSC curves of the series of well-stabilized samples at different heating rates, the effective activation energy of segmental motion Q vs T dependence was determined (Figs. 36b and 37). A wide Q dispersion, with $Q = Q_\alpha^{PDMS} = 115$–$120\,\mathrm{kJ\,mol^{-1}}$ at "normal" $T_g = 150\,\mathrm{K}$, and decreased Q values, down to ca. 30 kJ $\mathrm{mol^{-1}}$ ($\sim Q_\beta^{PDMS}$) at 130 K and 50 kJ $\mathrm{mol^{-1}}$ at 185 K, is observed. This "peaked" $Q(T)$ plot directly indicates simultaneous participation of cooperative, low-cooperative and non-cooperative segmental motions as well as constrained dynamics modes in the PDMS block glass transition.

Figure 37 and the scheme presented therein show five Q levels for glass transition dynamics in PDMS blocks, corresponding presumably to different conformations of chains between rigid domains (blocks) and different distances between PDMS segments and "rigid walls." The loosened molecular packing in PDMS blocks

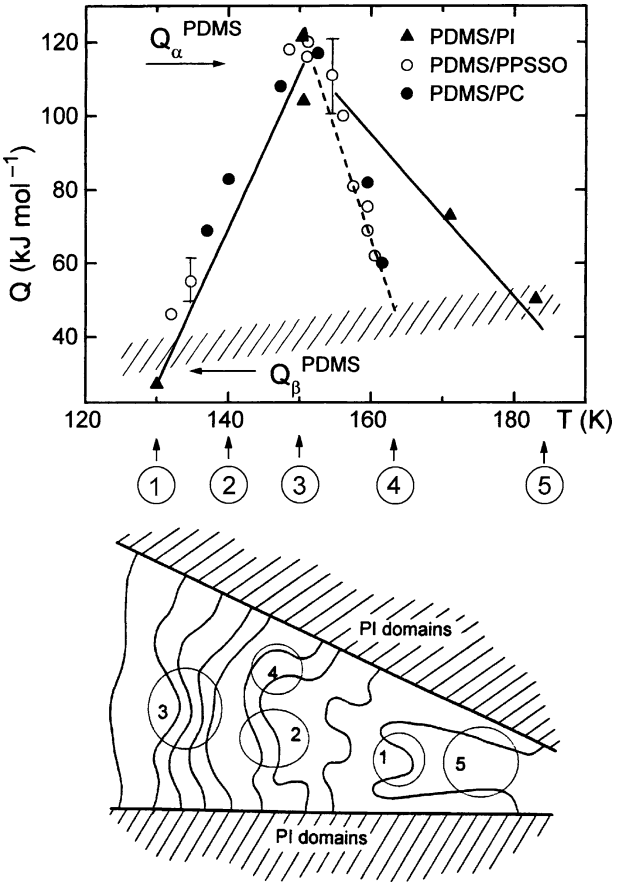

Fig. 37 Activation energy Q vs characteristic glass transition temperature (T_g, T_g', T_g'') dependencies for the PDMS blocks in different types of block copolymers [25, 26, 128, 129]. The *hatched zone* corresponds to the non-cooperative, Arrhenius relaxations at frequencies of ca. 10^{-2} Hz. The numbers 1–5 in *the circles* indicate the Q levels for cooperative, low-cooperative and non-cooperative segmental motion in PDMS blocks with different conformations and locations between rigid domains (*blocks*), shown schematically below

was due to entropy restrictions: X-ray diffractograms confirmed an increase in the PDMS interchain distances [25]. Thus, covalent attachment of PDMS chain ends to rigid blocks contributed to both accelerating and hindering dynamics for different segments.

High-resolution CRS provided discrete information on a special glass transition dynamics in PDMS blocks. Figure 38 shows the CR spectrum obtained for the 70PI–30PDMS block copolymer at low temperatures. In accordance with DSC data, this spectrum confirms a large dynamic heterogeneity within and around the glass transition of PDMS blocks, exhibiting five partly overlapping peaks with the maxima at approximately 130, 150, 170, 190, and 210 K. Three of these peaks practically

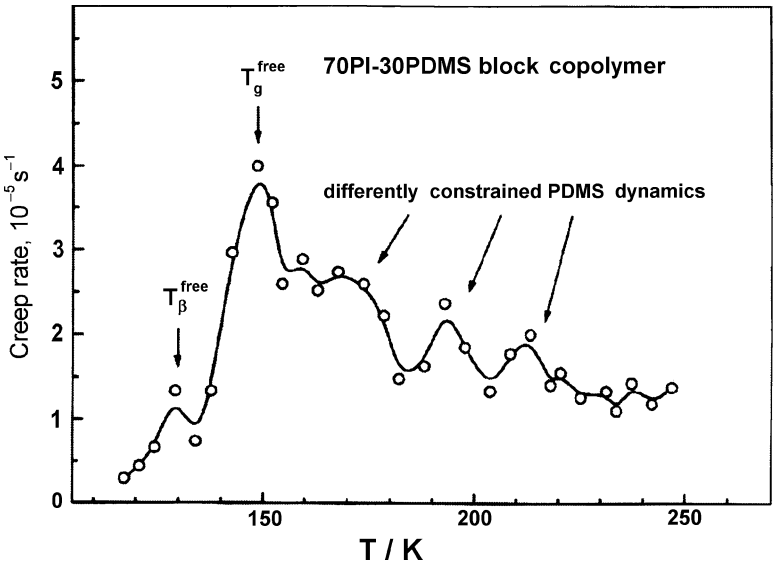

Fig. 38 Creep rate spectrum obtained for the 70PI–30PDMS block copolymer at the tensile stress of 10 MPa [129]. T_g and T_β values denote, respectively, the temperatures of the α- and β-relaxations in linear PDMS

coincide with the characteristic temperatures found by DSC (Fig. 36b) while two latter ones, corresponding to the most strongly constrained dynamics modes, are revealed by CRS only.

3.5 Polymer Blends and Molecular Composites

Glass transition characteristics in miscible polymer blends may also exhibit a special behavior differing considerably from those in neat polymers. Thus, an extraordinarily broad glass transition range, ΔT_g, or the pronounced deviations from the rule of mixtures, or an asymmetry of segmental relaxation dispersion have been observed [186–191]. To account for these anomalies, a few models have been proposed [192–194] in which the heterogeneity of segmental dynamics within a ΔT_g range has been assumed. However, understanding of this phenomenon remained incomplete up to last decade for a lack of direct experimental data. In our opinion, the combined DSC/CRS studies [191, 195–200] filled up this gap.

First of all, two kinds of nanoscale dynamic heterogeneity in the single-phase miscible polymer blends were found. The kinetic and discrete CRS analysis of segmental motion, within and close to the glass transition range, revealed their common origin.

In the studies [191, 195–197], atactic PS ($M_w \approx 10^5$, $M_w/M_n = 1.06$), PMS ($M_w = 2 \times 10^5$, $M_w/M_n = 2.0$), and poly(vinyl methyl ether) (PVME, $M_w = 4 \times 10^4$,

$M_w/M_n = 2.3$) were used for preparing two series of PS/PMS and PS/PVME blends under conditions providing their miscibility. The latter was proved by mid- and far-IR spectroscopy of PS/PMS blends and by NMR measurements for PS/PVME blends.

The first kind of dynamic heterogeneity consisted of a quasi-independent dynamic behavior of PS and PMS segments in their miscible blends, with the manifestation of two rather narrow glass transitions [191, 195, 197]. The T_g values did not change smoothly with composition. They were strongly displaced downwards relative to those for neat polymers; the lower T_gs were close to the temperatures of β-relaxation. Two- or threefold decrease in the activation energy Q values, down to $Q \approx Q_\beta$, was observed, and the degree of intermolecular cooperativity dropped from $Z = 3$–4 in neat polymers down to $Z \approx 1$ in the blends. The simultaneous drop in T_g, Q, and Z values indicated a partial or total collapse of intermolecular cooperativity of segmental motion. Thus, the presence of two T_gs cannot be considered as an undisputable evidence of microphase separation in blends. This is valid only if the transition parameters coincide with, or are close to, those in pure polymers. This means that the separate segmental dynamics of both components in single-phase polymer blends is possible that has also been observed in the NMR experiments [201, 202].

For miscible PS/PVME blends, the heterogeneity of segmental dynamics in the glass transition manifested itself in a quite different way. A single broad transition was observed in their DSC curves (see the insert in Fig. 39). Figure 39 shows the Q vs T dependencies obtained by DSC for the glass transition range in the miscible PS/PVME blends. The wide Q dispersions of different type are seen where the experimental points may differently deviate from the Arrhenius Q vs. T line. Therefore, the cooperativity parameter of segmental motion changed in this case from $Z = 1$, when $Q \approx Q_\beta{}^{PS} \approx 100\,\mathrm{kJ\,mol^{-1}}$, up to $Z = 3$ when $Q \approx 300\,\mathrm{kJ\,mol^{-1}}$. These wide Q dispersions indicate simultaneous participation of cooperative, low-cooperative and non-cooperative segmental motions within the glass transition of the miscible blends.

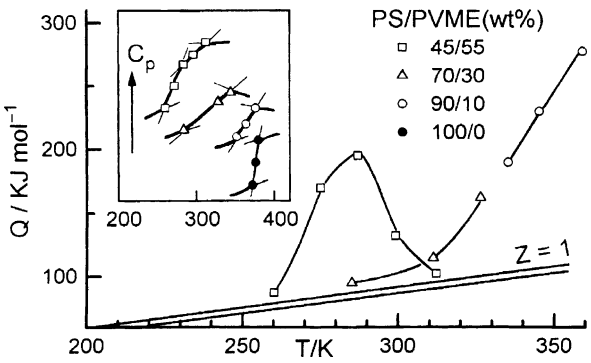

Fig. 39 DSC curves (insert, $V = 20\,\mathrm{K\,min^{-1}}$) and activation energy Q dispersions for segmental motion in the glass transition of the miscible PS/PVME blends. The band $Z = 1$ corresponds to Arrhenius Q vs T relation at 10^{-2} Hz [197]

Table 6 Predicted kinds of possible segmental motions within or close to the glass transition in the PS/PVME miscible blends and their manifestation in the creep rate spectra [197]

No	Motional event	Cooperativity degree Z	Expected T (K) at 10^{-2} Hz	Creep rate peaks at PS/PVME weight ratio		
				45/55	70/30	90/10
1	PVME, β-relaxation	1	170–190	+	+	–
2	PVME, intermediate relaxation	2	200–220	+	+	–
3	PVME, α-relaxation	3	240–250	+	–	–
4	PS, β-relaxation when contacting PS with PVME chains	1	260–270[a]	+	–	–
5	$1\,\mathrm{PS} + (1 \div 3)$ PVME segments cooperation	$2 \div 4$	270–290[a]	+	+	+
6	PS, β-relaxation	1	300–320	–	+	+
7	PS, intermediate relaxations	$2 \div 3$	330–360	–	+	+
8	PS, α-relaxation	4	370–380	–	–	–

[a]The temperatures for relaxations 4 and 5 were predicted with taking their parameters of solubility into account [15]

In the latter blends, one could assume, a priori, the manifestation of up to eight kinds of Kuhn segment motions within or close to the ΔT_g range (Table 6). Really, the CRS measurements allowed recording these predicted kinds of segmental motion. Figure 40 shows the CR spectra for three blends measured over the temperature range of 130–370 K, i.e., from ${T_\beta}^{\mathrm{PVME}}$ to ${T_g}^{\mathrm{PS}}$. This relaxation region could be subdivided by CRS into the multiple constituent relaxations; the CR spectra responded in a discrete manner to unfreezing of each kind of segmental motion. Comparing these spectra with the predictions of Table 6 testifies the validity of our approach since peaks 1–7 correspond by their temperature location to the expectations. Only the cooperative dynamics (peak 8) peculiar to neat PS could not be discerned in these blends. The spectral contours obtained are dependent on blend composition. Thus, only small peaks 5, 6, and the pronounced PS peak 7, constitute the glass transition of the 90PS–10PVME blend. In contrast, PVME peaks 1, 2, and 3, together with peaks 4 and 5 characterizing motion of dissimilar segments constitute a broad ΔT_g range in the 45PS/55PVME blend. Thus, the spectra obtained indicate incomplete mixing in the single-phase PS/PVME blends, obviously on a nanometer-scale level.

One of the exciting concepts in the field of blend/composite materials is the reinforcement of flexible-chain polymers by highly rigid rod-like macromolecules with a persistence length $L_P > 10\,\mathrm{nm}$. The basic principle of these blends, which are known as "molecular composites", is dispersion of rigid-chain polymers in a random coil chain, ductile matrix. The basic principles, advantages, and difficulties of molecular reinforcement, and the available data on this problem were summarized

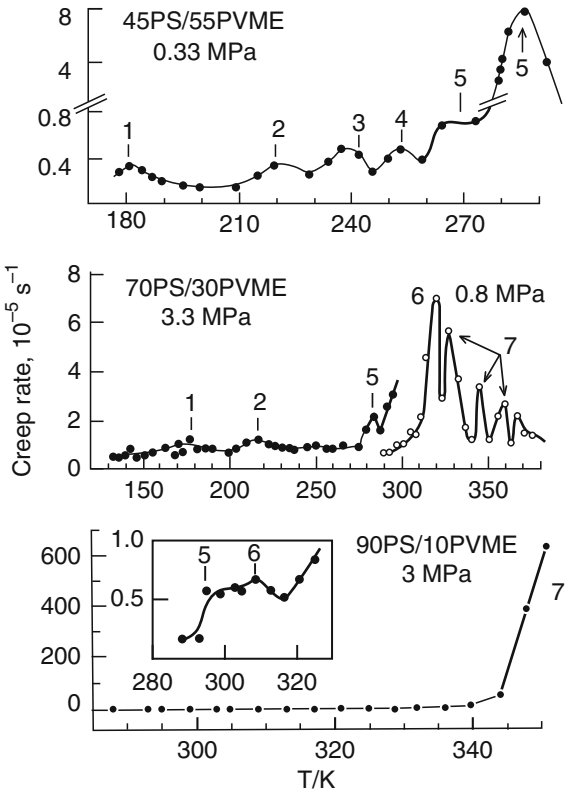

Fig. 40 Creep rate spectra of the miscible PS/PVME blends [197]

in particular in the review [203]. The potential advantages of molecular composites over usual reinforced plastics are determined by the closeness of the coefficients of thermal expansion of their constituents and improved interactions between matrix and reinforcing macromolecules. The indispensable condition of successful molecular reinforcement is the attainment of sufficient structural homogeneity at the submicroscopic level, i.e., preparing composites with molecularly or nanometer-scale dispersed rod-like molecules, best with single molecule fibers in a matrix.

Among the advanced ways of preparation of relatively homogeneous molecular composites are in situ or precursor approaches as applied to PI materials. Poor solubility of the majority of PIs in their fully imidized form makes difficult the experimental determination of their Kuhn segment size. Nevertheless, according to theory [204] and some estimates [203], the rod-like PIs are characterized by Kuhn segment size $A = 25$–30 nm, whereas the PIs with oxygen atoms as the "hinges" in their chains may be considered as relatively flexible ($A \approx 4$–6 nm).

The authors [205–208] reported on rod-like chain PI/ flexible-chain PI (PI_R/PI_F) molecular composite films obtained basically via in situ PI formation by the thermal imidization of a mixture of PAA precursors. Such composite films may exhibit, after only 60% cold drawing before imidization, a large increase in the mechanical properties compared with the properties of isotropic flexible-chain PI_F. Thus, the elastic modulus changed from 5 to 50 GPa, and the tensile strength increased from 0.25 to 1.5 GPa in this case [205]. In our research [198–200], a comprehensive investigation of the nanometer-scale structure and molecular dynamics over a broad temperature range was carried out for a series of PI_R/PI_F composites with 20, 40, 50, 60, and 80 wt% of the rigid component and for the neat components. Six different experimental techniques, including CRS/DSC analysis, were used. Rod-like chain polyimide (PI_R) was synthesized from $3,3',4,4'$-biphenyltetracarboxylic dianhydride (BPDA) and 1,4-phenylenediamine (PPD), whereas PI_F was prepared from the same dianhydride and $4,4'$-oxydianiline (ODA). The starting PAAs and the resulting PI_R and PI_F had the following structures:

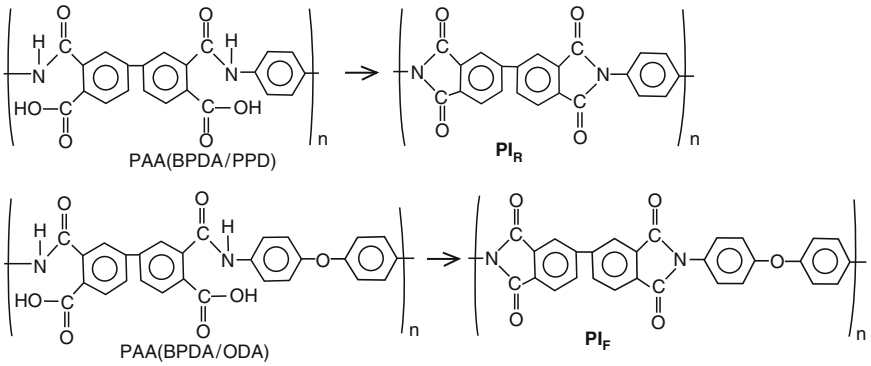

Thus, the blend components, PI_R and PI_F, were rather close in their chemical structure differing, however, by the absence or presence of oxygen "hinges" in the chains. This predetermined the sharply different chain rigidity and allowed one to consider these blends as the PI_R/PI_F molecular composites consisting of molecular reinforcing "fibers" and relatively ductile matrix.

The SAXS patterns of these blends [198] exhibited basically fine nanostructural heterogeneity. The largest nanodomains were observed for pure PI_F (radius of gyration $R_g = 4.5$ nm). Mixing of the PI_F and PI_R components led to smaller nanoscale morphology. The R_g value decreased to 2.0 nm and less. For the $20PI_R/80PI_F$ composition, the scattering was very low and no densely packed domains could be evidenced ($R_g \to 0$). It means that this nanoscale-homogeneous blend could be considered, in the first approximation, as a real molecular composite with molecularly dispersed PI_R rods (single molecule fibers) in the PI_F matrix. The various PI_R/PI_F composite nanostructures turned out to be concordant with their peculiar, non-additive dynamic behavior [198].

Figure 41 shows the DSC curves obtained for the stabilized composite samples, and for neat PI_F and PI_R. Despite some nanostructural heterogeneity, only one glass transition is observed on the DSC curves for neat PI_F and the samples with 20–60 wt% PI_R. For the $80PI_R/20PI_F$ composite, no glass transition could be discerned by DSC, similar to that for neat PI_R, at least up to 630 K.

Figure 42 shows the compositional dependencies obtained by DSC for the glass transition characteristics, T_g, T_g', T_g'', and ΔC_p step. The latter varied with changing

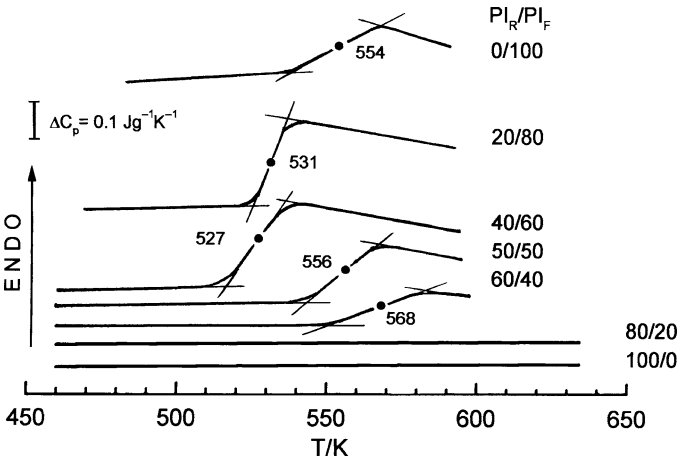

Fig. 41 DSC curves obtained in the glass transition region for pure PI_F and PI_R, and their blends previously stabilized for 10 min at 600 K and cooled with $V = 320\,\mathrm{K\,min^{-1}}$. Heating rate was $20\,\mathrm{K\,min^{-1}}$ [198]

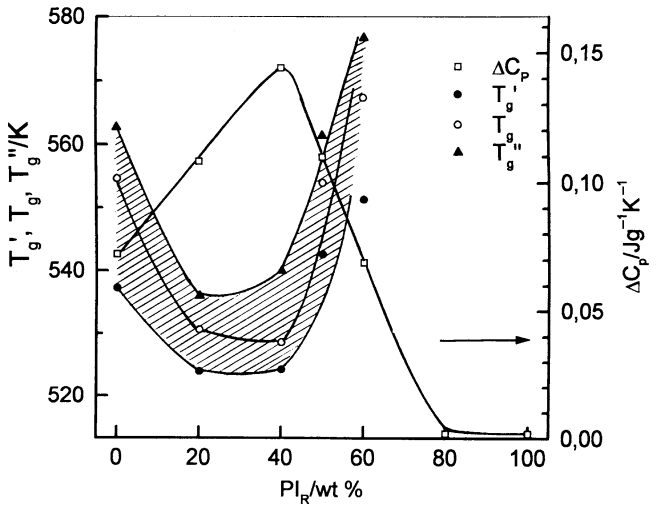

Fig. 42 Compositional dependence of T_g and of the transition onset, T_g', and completion, T_g'' temperatures, as well as of the heat capacity step in the glass transition of the PI_R/PI_F composites [198]

PI_R content in a non-additive way, in particular, did not obey the well-known equations for T_g of miscible blends, e.g., the Flory equation $(1/T_g = w_1/T_{g1} + w_2/T_{g2})$ where w_1 and w_2 are the weight fractions of the blend components. Moreover, the glass transition characteristics changed in two opposite directions. The introduction of 20 or 40 wt% PI_R led to a decrease of T_g and to narrowing of the transition range $\Delta T_g = T_g''–T_g'$. On top of that, 1.5- to 2.0-fold increasing of the ΔC_p step occurred. A further rise of the PI_R content in a composite resulted, contrarily, in T_g increasing, broadening of the transition range, and the sharp decrease in the ΔC_p step, down to its total disappearance for the $80PI_R/20PI_F$ composite.

These "anomalies" reflect the nanostructural changes in the composites and may be treated in terms of (a) the nanoscale confinement of PI_F between the rigid PI_R "walls", leading to the loosened molecular packing in the PI_F matrix due to the entropy hindrances, and (b) the constraining influence of the "rigid walls" on dynamics in PI_F owing to their enhanced interaction. The latter factor resulted in the total suppression of the glass transition in the $80PI_R/20PI_F$ composite.

Figure 43 shows the creep rate spectra obtained for neat PIs and two PI_R/PI_F composites over the temperature range from 300 to 600 K. The insert with the extended ordinate scale makes possible to discern better the heterogeneity within the β- and "intermediate" relaxation regions. In the glass transition region, the CR spectra show the high, narrow α-relaxation peak at 490 K for neat PI_F, and its degeneration for neat PI_R. At the same time, five discrete, partly overlapping CR peaks constitute the spectral contour for the $50PI_R/50PI_F$ composite in the α-relaxation region of 450–600 K. The basic α-peak at 490 K becomes more intense and broadened

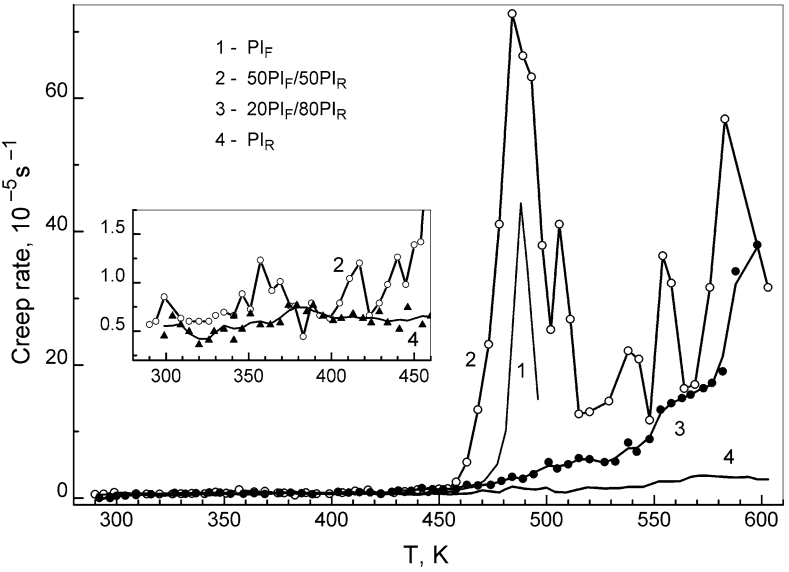

Fig. 43 Creep rate spectra obtained for the $50PI_F/50PI_R$ and the $20PI_F/80PI_R$ composites as compared with the spectra of pure components [198]

to both higher and lower temperatures and, additionally, the peaks at 510, 540, 560, and 580 K appear in the spectrum. With increasing PI_R content in the composite to 80 wt%, only the remnants of these peaks in the CR spectrum could be observed as a gradual, step-like rise of a creep rate with temperature. The glass transition could not be discerned at all in the DSC curve of this composite (Fig. 41). The insert in Fig. 43 emphasizes a few slight CR peaks at ca. 300, 360, 410, and 440 K, that is, the dynamic heterogeneity of sub-T_g relaxations in the $50PI_R/50PI_F$ composite.

Consequently, the CRS data demonstrate a large dynamic heterogeneity around and above the basic T_g. Again, their appearance can be understood in terms of confined geometries/constrained dynamics in PI_F matrix. The facilitation of segmental motion at sites with loosened molecular packing in the PI_F matrix and the different constraining impacts of PI_R rods on the PI_F dynamics may be seen. At 80 wt% PI_R in the composite, when the PI_F chains are "clutched" by PI_R rods or their nanodomains, notable peak remnants may be seen at 560–580 and 590 K only. On the whole, the CR spectra of these molecular composites respond discretely to unfreezing of movement of the PI_F segments differently situated relative to PI_R "rigid walls."

3.6 Disordered Regions of Semi-crystalline Polymers

Linear polymers in the semi-crystalline state are metastable nanostructured systems with the complicated morphology, which are divided into nano-, submicro-, or microphases with crystalline, amorphous, and intermediate (mesophase and other) molecular packing. These different phases are connected in the flexible-chain polymers, such as PE, POM, poly(ethylene terephthalate) (PET), and many others, via strong covalent coupling between crystallites and disordered regions since the typical polymer molecules of 1–100 μm in contour length participate in several nanophases. Due to the multilevel structure, polymers with rather high levels of crystallinity may show up unique dynamics and properties which vary with the thermal and mechanical histories of materials. This has been confirmed by different techniques (DMA, DSC, NMR, DRS, and others) in numerous studies.

One of the main peculiarities of semi-crystalline polymers is the presence of so-called "rigid amorphous fraction" (RAF) [24], along with the rigid crystalline and usual "mobile" amorphous phases; segmental dynamics in RAF typically unfreezes over the temperature range between T_g and melting point T_m. The development of RAF in polymers occurs in parallel with increasing crystallinity. Therefore, at least three types of nanophases are considered in the metastable structure of semi-crystalline polymers that results in strongly modified glass transition dynamics.

We present here some information on the segmental dynamics in semi-crystalline polymers obtained mainly by DSC, NMR, and the combined CRS/DSC analysis [15, 21, 209–214]. These studies have contributed to the detailed characterization of dynamics in the intercrystalline regions.

3.6.1 Flexible-Chain Polymers

Starting from early publications [72] and in subsequent works, three relaxation regions have been observed in PE and similar flexible-chain polymers at low frequencies $f \approx (10^{-3}–1)$ Hz: relaxation I at 150–200 K, relaxation II at 240–270 K, and relaxation III over the broad temperature range, for instance, of 300–370 K for PE or 300–420 K for POM. In addition, rather strong suppression of relaxation II may be observed in high-crystalline polymers (see, e.g., DMA curve presented for POM in Fig. 11).

It has been accepted historically for highly crystalline polymers that the melting point, T_m, was used as the reference temperature whereas the indicated relaxations III, II, and I were designated formally as α, β, and γ ones, respectively [72]. As it has been emphasized earlier [15], use of such designations for relaxations III, II, and I causes some confusion since these relaxations do not correspond, by their physical essence, to the α-, β-, and γ-relaxations in non-crystalline polymers or polymers of low crystallinity. For instance, the α-relaxation means the cooperative glass transition in the latters, whereas the specific relaxation III (in fact corresponds to unfreezing mobility in RAF), associated with the presence of crystallites, is absent in non-crystalline polymers. Relaxation II (or sometimes even relaxation I) have been assigned to the glass transition in PE.

The complicated picture of segmental dynamics in the disordered regions could be expected, a priori, proceeding from the various degrees of chain coiling (conformational states) and various distances between segments and crystallite surface. Figure 44 shows schematically the structure of interlamellar layers in a high-crystalline flexible-chain polymer. Three groups of molecular elements differing in conformational state may be considered [15, 209, 213]:

- Long irregular loops 3, coiled tie chains 4, and long ends of macromolecules 5 protruding from the crystallite cores of lamellae 1
- Slightly bent tie chains 6 and folds 7

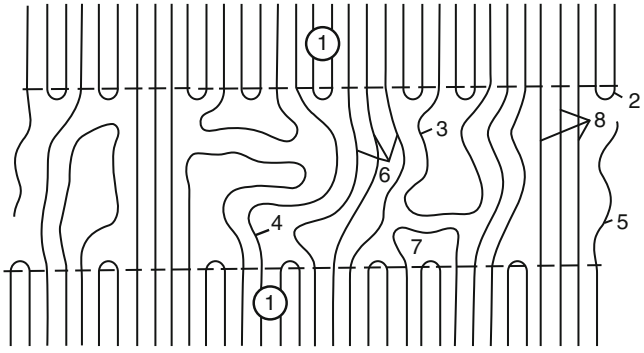

Fig. 44 A scheme of the conformational states for flexible chains located within the disordered interlamellar regions of high-crystalline linear polymers (see text)

- Straightened out tie chains (regular trans- or helix-sections) 8 whose ends are "clamped" in the lamellae, and regular folds 2

Therefore, a highly crystalline linear polymer may be considered as a complex polymer system where chains in the disordered layers are confined to nanometer-scale spaces and, additionally, anchored to the rigid (at $T < T_m$) structural constraints. In this case, the gradual unfreezing of segmental dynamics with temperature in these layers must occur that is determined by (1) different degrees of coiling of tie chains and folds, (2) the difference in packing density of molecular sections located between the crystallites, and (3) the distance between a segment and the point of entering chain into a crystallite.

The complicated segmental dynamics in highly crystalline flexible-chain polymers may be illustrated, for instance, by the results of DSC/NMR/X-ray diffraction studies performed for the well-defined HDPE samples with different crystallinities χ_{DSC}, ranging from 43% to 80% [15,209,213,214], as well as for POM [21,22,210].

Figure 45 shows the temperature dependencies of "mobile fraction" content C_m in HDPE samples determined by the narrow line in the NMR spectra and corresponding to the fraction of segments participating in micro-Brownian motion. A gradual unfreezing of segmental dynamics occurs in the disordered regions, over the range from 160 to 370–380 K, that is, from relaxation I region to the onset of melting of the thinnest lamellae. The C_m values are higher for the quenched and high-molecular-weight samples with the lower crystallinities. The most distinct jumps of C_m are

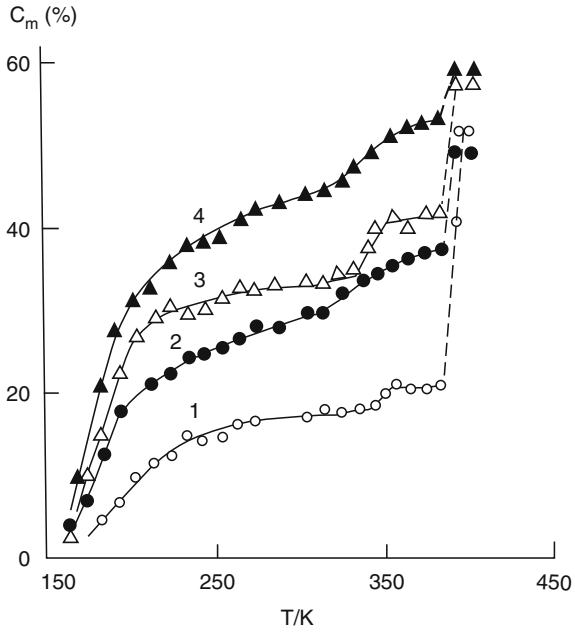

Fig. 45 Temperature dependencies of mobile fraction content C_m in high-density PE (HDPE) samples with $M_w = 7 \times 10^4$ (1, 2) and 1×10^6 g mol^{-1} (3, 4) crystallized from the melt at 393 K (1, 3) or quenched from the melt at 178 K (2, 4), with the crystallinities χ_{DSC} of (1) 80, (2) 52, (3) 51, and (4) 43%. NMR data [213]

observed at ∼160–200, 320–350 K, and beginning from 380 K. Qualitatively the same changes in the heat capacity with temperature were observed for these HDPE samples [15, 209].

From these NMR data [213, 214], the degrees of chain coiling in the disordered regions of HDPE, $y = l/h$, were estimated, where h is a distance between the ends of molecular element in the disordered regions and l is its contour length. The distribution function was calculated for this parameter, and y varied from 1.5 to 4.0 for high-crystalline HDPE [213, 214]. It was concluded that with lower y, the segmental motion unfreezes at the higher temperature; the highest-temperature relaxation must be characteristic of practically straightened out tie chains 8 and regular folds 2 (Fig. 44).

Figure 46 shows the complicated manifestation of the glass transition dynamics in the DSC curves of POM as linear polymer with very high chain flexibility due to a presence of numerous oxygen "hinges" and complex morphology [22]. Depending on the thermal prehistory, the heat capacity steps may be observed at ∼200 K and at different temperatures over the 300–430 K range, including even two or three steps (transitions) for a POM sample with a certain prehistory.

Activation DSC analysis of segmental dynamics in POM [21, 210] and HDPE [15, 209] provided essential information regarding the nature of segmental relaxations constituting, on the whole, glass transition dynamics in the interlamellar disordered regions. It is also noteworthy that these relaxations are related only to the motions outside the crystallites. The theoretical models of segmental motion

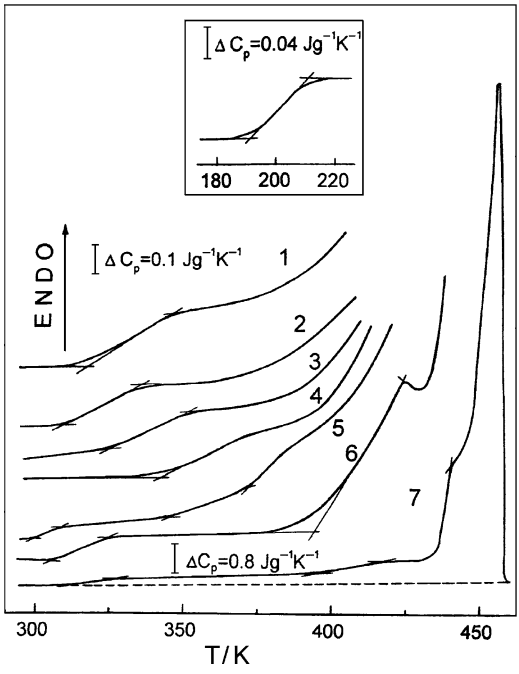

Fig. 46 DSC curves of POM [21, 210] in the initial aged state (1) and after cooling from 300 to 110 K (*the insert*), or after the thermal treatments for (2) 3 h at 310 K after cooling from 500 to 300 K; (3) 2.5 h at 330 K; (4) 0.5 h at 350 K; (5) 1 h at 370 K; (6, 7) 3 h at 433 K plus 24 h storage at 293 K. The heating rate was 10 K min^{-1}. The cooling rate was 320 K min^{-1}

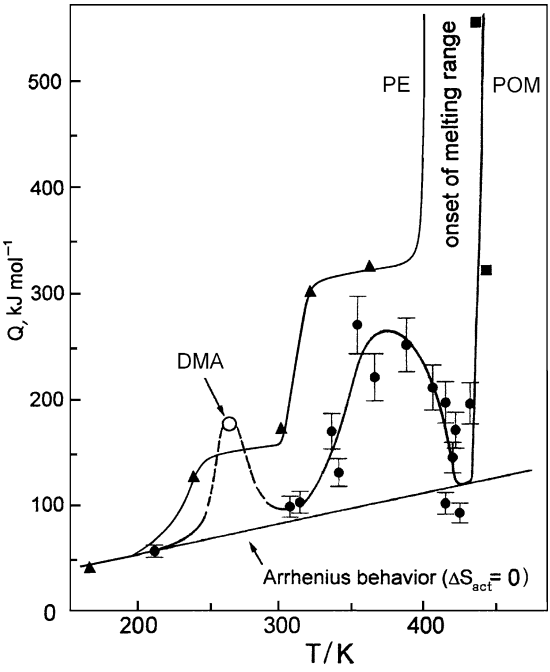

Fig. 47 Activation energy Q of segmental motion as a function of temperature for POM [21, 210] and HDPE [209] as estimated by DSC; one point obtained by DMA is also given. Temperature range covers the regions of relaxations I, II and III. *The straight line* corresponds to the Arrhenius relation between Q and T at frequency of 10^{-2} Hz

within PE crystallites cannot be used for their interpretation. It was confirmed by the DSC experiments performed for the PE lamellar crystalline cores after etching of PE in HNO_3 was done to remove the disordered component [15].

By varying the heating rates, the effective activation energies of segmental motion, Q, in both POM [21, 210] and HDPE [15, 209] were determined as functions of temperature (Fig. 47). One can see that these dependencies are different and are characterized by broad dispersions of Q values varying from ~50–60 to 280–330 kJ mol^{-1}. Three distinct relaxation regions can be seen. These results allowed us to make the undisputable assignments to relaxations I, II, and III.

Relaxations I and II are formed by quasi-independent, non-cooperative ($Q_I \approx 50\,kJ\,mol^{-1}$, 160–200 K) and cooperative ($Q_{II} = 130–180\,kJ\,mol^{-1}$, 230–260 K, cooperativity degree $Z = Q_{II}/Q_I = 3–4$) segmental motions, respectively. It means that relaxation I corresponds to the Arrhenius β-relaxation in non- or low-crystallinity polymers, whereas relaxation II (which was strongly suppressed in PE and POM with high crystallinities) must be related to "usual" cooperative glass transition of amorphous species undisturbed by crystallites.

It can be assumed with a certainty that segmental motions in molecular elements 3, 4, and 5 with the largest y values (Fig. 44) may be responsible for relaxations I and II. Segmental motion in molecular elements 2, 6, 7, and 8 was restricted to different extents by the crystallites, especially strongly for straightened out tie chains and regular folds. Unfreezing of segmental motion in the straightened out tie chains (elements 8) depends on the phase transition of melting and can start only

at temperatures close to melting point T_m for the thinnest lamellae. Therefore, the temperature range of relaxation III is characterized by strongly increased activation energy or large dispersion of activation energies Q_{III} (Fig. 47). High chain flexibility of POM resulted in a peculiar $Q_{III}(T)$ dependence when non-cooperative segmental motion with low Q_{III} value arose, again, at 420 K, due to the onset of softening the lamellae or their surfaces as "rigid constraints."

Dynamics over the extended relaxation region III is the impressive example of anomalies in the glass transition. The presented data show the heterogeneous nature of RAF and its origin in high-crystalline polymers. In fact, differently constrained dynamics modes and collapsing of motional cooperativity may be observed simultaneously in this region.

Finally, high-resolution CRS analysis allowed us to visualize a number of segmental dynamics modes in the disordered regions of POM. Figures 11 and 48 show the CR spectra obtained over the temperature range from 130 to 420 K. The tensile stresses of 20 MPa for the temperatures below 300 K, and 2 MPa for elevated temperatures were chosen. Due to much more malleableness of interlamellar layers as compared to rigid crystallites, the CR peaks could a priori be assigned to unfreezing of segmental dynamics modes in the disordered regions (relaxation regions I, II, and III).

The POM spectral contours consist of three groups of overlapping peaks with various intensities, namely, at approximately 170, 190, 210, and 220 K (relaxation region I); 290, 330, 350, and 380–400 K (relaxation region III), and the complicated spectral line in the relaxation region II, at 230–270 K. A sharp acceleration of creep, by two orders of magnitude, occurs in the vicinity of melting range at 420–430 K,

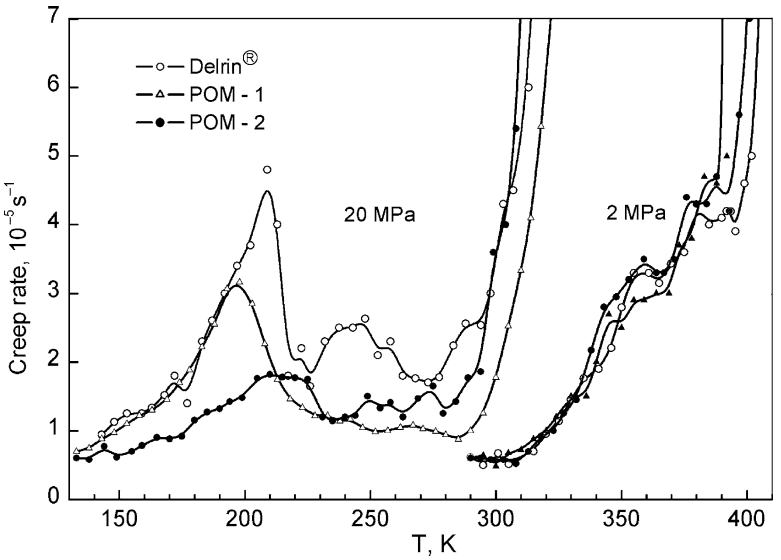

Fig. 48 Comparing the CR spectra obtained at tension for Delrin® and two tentative POM samples (Du Pont) with nucleating agent and different phenol-containing antioxidant additives [21]

even under small tensile stress of 2 MPa (Fig. 11). Thus, the discrete character and superiority of the CR spectra to the DMA spectrum in revealing the dynamic heterogeneity in different relaxation regions can be seen from Figs. 11 and 48.

Figure 48 illustrates a large sensitivity of the CR spectrum to fine structural/dynamic changes in POM caused by introducing of very small quantities (<2%) of the additives of different type, nucleating agent or antioxidant. A certain depression of motion in the regions of relaxations I and II is a common feature for POM samples with additives as compared to the spectrum of commercial Delrin®. For POM-1, the most suppression of cooperative motion at ~230–300 K occurs, whereas the strongest decrease in the height of peak at 210 K (non-cooperative relaxation I) is more pronounced for POM-2. These effects could be explained by localizing the additives at free volume sites (depression of relaxation I) or by a plasticization effect leading to destroying motional cooperativity at ~230–300 K. Small negative impact of the additives on creep resistance at high temperatures may also be discerned. Large changes in the CR spectra of POM, caused by its quenching or pre-straining, are also shown in Sect. 6.1.

The above DSC and other data allowed us to assign tentatively the constituent peaks in the POM creep rate spectra to the certain kinds of relaxation dynamics modes (Table 7).

Table 7 Creep rate peaks in the spectra of POM [21]

Peak no	Temperature (K)	Delrin®	POM-1	POM-2	Tentative assignment of CR peaks characterizing unfreezing of segmental motion within the inter-crystalline regions
1	~160	+	−	+	Non-cooperative relaxation **I:** ($Z = 1$) similar to the β-relaxation in non- or low-crystalline flexible-chain polymers, and its dynamic heterogeneity
2	180–190	+	−	+	
3	200–210	♦	♦	+	
4	220–230	+	−	+	Relaxation region **II:** "intermediate" segmental relaxation ($Z = 2$)
5	250–260	+	−	+	Cooperative glass transition ($Z = 3$)
6	280–290	+	−	+	Relaxation region **III:** differently constrained segmental motions (RAF manifestation and its dynamic heterogeneity)
7	320–340	+	+	+	
8	~360	♦	♦	♦	
9	~380	♦	♦	♦	
10	390–400	♦			

Notes: [1.] Signs −, +, ♦ designate qualitatively the practical absence of peak (−) or very slight peak manifestation (+), or a pronounced peak (♦)

[2.] The discrete or partly overlapping peaks are considered including the maxima or steps, or "shoulders" in a spectral contour

[3.] Tensile stress of 20 MPa below 300 K or 2 MPa above 300 K was applied

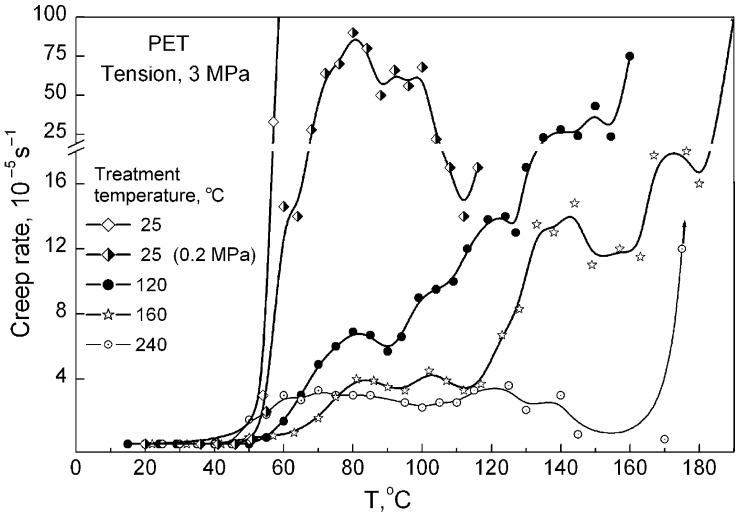

Fig. 49 Creep rate spectra of PET demonstrating the changes in dynamics of initially amorphous polymer in the course of its "cold crystallization" by the thermal treatments for 3 h at indicated temperatures (formation of the peculiar states of inter-crystalline disordered regions)

Another example of the successful application of CRS to revealing a peculiar dynamics in the disordered regions of flexible-chain crystallizable polymer are the spectra of PET subjected to "cold crystallization" (Fig. 49). Isothermal crystallization by annealing at different temperatures above $T_g = 80°C$ resulted in formation of PET samples with different degrees of crystallinity and, consequently, the different states of the disordered regions. As shown [24], the onset of cold crystallization of PET was followed already at prolonged heating at 90°C; the heat capacity measurements suppose increasing RAF content in parallel with increasing crystallinity in PET. On heating, the RAF in PET disappears, with conversion into a mobile amorphous fraction, at a temperatures around 160°C; RAF content in isotropic crystallized PET may attain 30%. It was shown by DSC that the activation energy of relaxations in the broadened PET glass transition may vary (at different crystallinities and draw ratios) from 80 to 350 kJ mol^{-1} [215].

The CR spectra in Fig. 49 show how PET segmental dynamics in the T_g–(T_g + 100°) range is complicated and profoundly changes due to isothermal cold crystallization at different temperatures. For the initial amorphous PET, extra-high creep rates are observed at a tensile stress of 3 MPa already below T_g (at 60–70°C). At 0.2 MPa, glass transition peak is observed at 80°C with a shoulder at ~100°C; the latter arises due to the onset of pre-crystallization period during the CRS experiment. After annealing at temperatures $T_{ann} = 120°C$, 160°C, or 240°C, the large changes in the CR spectra below T_m occur due to cold crystallization. These include increasingly strong suppression of dynamics (multi-fold decreasing creep rates) with increasing T_{ann}, and complicating the spectral contours. The spectra consist of a few overlapping peaks with the maxima at $T_g = 80°C$ and at temperatures of ~100°C, 120°C, 140°C, and 170°C. This indicates the presence of multi-modal dynamics

in the disordered regions of partly crystallized PET over the 80–170°C range, and segmental motion modes undisturbed and differently constrained by the crystallites. Thus, the complicated nature and changeable character of "rigid amorphous phase" is revealed for PET in the CRS experiments.

3.6.2 Polyimides

Creep rate spectroscopy technique turned out to be very useful for comparative estimation high-temperature performance of such valuable polymers with increased chain rigidity such as PI. The bulk of commercial PI materials rely on solvent-based fabrication techniques. However, parts and shapes, formed from dry PI resin such as pyromellitic dianhydride–oxydianiline (PMDA–ODA), have been commercially available in the last few decades from Du Pont (Vespel®). Due to their excellent temperature (up to 300–350°C), mechanical, solvent and wear resistances, these parts have achieved wide acceptance in different demanding technical applications under extremely high temperatures.

PMDA-ODA PIs are not melt-processable, and objects are manufactured using powder metallurgy techniques. Two methods were offered for preparing the initial particulate PI. Gall [216] described the method whereby the PAA imidization occurred in a heated solution, with precipitation of insoluble PI particles. In contrast, Manwiller and Anton [217] offered a sequential method for preparing PI particles: PAA was precipitated from the solution by adding a non-solvent and the solid PAA was then imidized thermally. Processing of such PI particles into monolithic parts requires the application of both high pressure and high temperature. For this purpose, two routes are used: (1) the pressure and heat are applied sequentially, where PI particles are first compacted in a mold and then sintered, or (2) the PI particles are coalesced by applying pressure and heat simultaneously. Figure 50 shows the schemes of preparing PI powder and parts.

The combined WAXD/SAXS/SEM/DSC/CRS study of structure, morphology, dynamics, and properties at 20–470°C was carried out for a large series of PMDA-ODA polyimide samples prepared in the indicated different ways to determine the conditions for optimizing the PI properties at extreme temperatures [211, 212]. As a result, the relationships between the processing conditions, structure, and properties were determined. Of importance, depending on the technology used, totally amorphous or mesomorphic, or semi-crystalline PI samples, with the crystallinity degrees χ of 10–15% or 30%, were obtained; however, the glass transition could be characterized ($T_g \sim 400$°C) by DSC only for the amorphous or low-crystalline PI samples.

Creep rate spectroscopy allowed us to observe and characterize the glass transition in both amorphous and semi-crystalline PI samples. Moreover, a pronounced dynamic heterogeneity within the extremely broad glass transition of semi-crystalline samples and much below T_g could be revealed in a discrete manner by CRS. A considerable difference in the relaxation dynamics and creep resistance of the PI samples prepared in different ways was revealed.

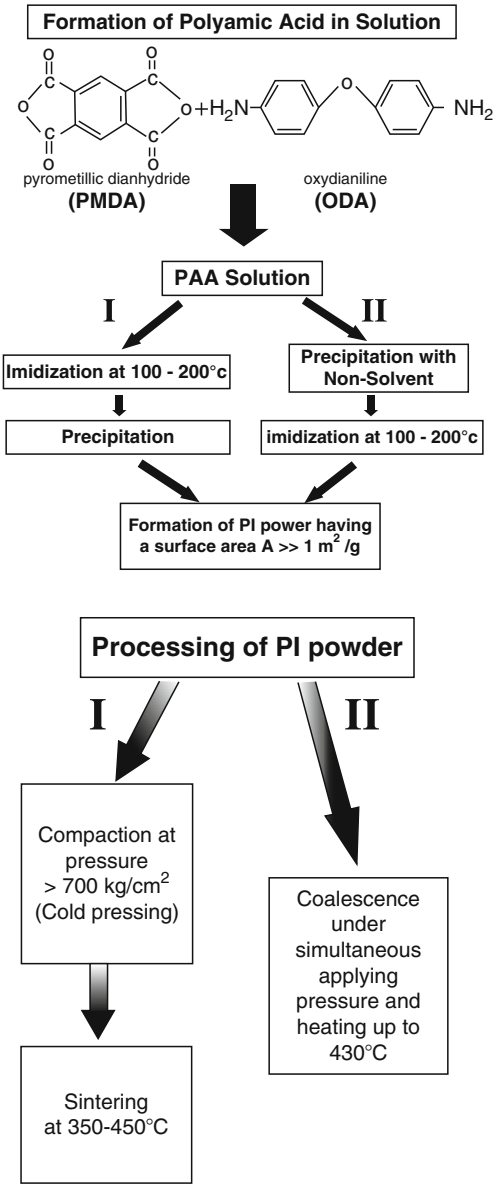

Fig. 50 Schemes of formation of PI powder and its processing into monolithic parts (Vespel®, Du Pont), using two powder metallurgy techniques (sintering or coalescence) [212]

Figure 51 shows the CR spectra obtained over the 200–470°C range under the compressive stress of 20 MPa for amorphous and semi-crystalline PMDA-ODA polyimide samples differing by their preparation technique. Figure 52 shows the CR spectra for some of PI samples in the temperature region of sub-T_g relaxations (20–300°C), including non-cooperative β-relaxation and low-cooperative "intermediate" segmental relaxations (at temperatures T_i where $T_\beta < T_i < T_g$). These spectra

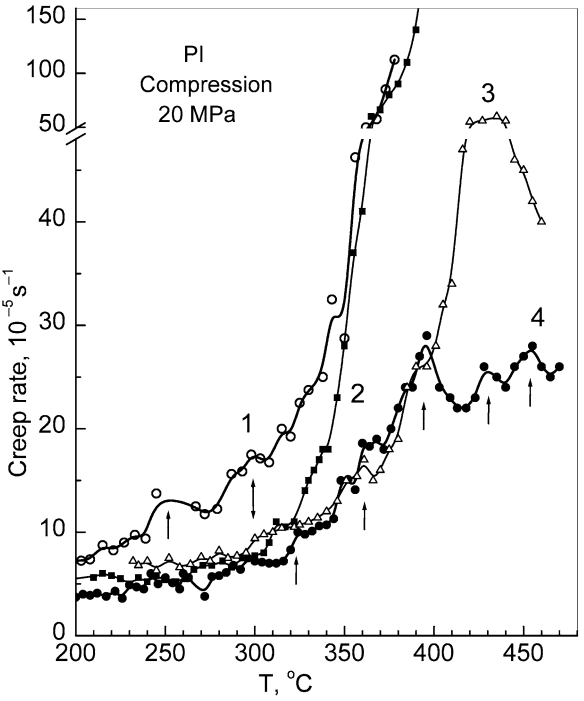

Fig. 51 Creep rate spectra obtained for the amorphous sintered (1), amorphous coalesced (2), semi-crystalline sintered (3), or coalesced (4) PI (Vespel®) samples [212]

indicate the large heterogeneity of segmental dynamics (multi-modal dynamics) within both glass transition and "intermediate" relaxations regions. A gradual unfreezing of segmental dynamics modes is detected over the broad temperature region starting from 40–50°C up to the peak at 460°C. This is observed most distinctly for the semi-crystalline samples, whereas more monotonous curves are observed for the amorphous samples at high temperatures, which characterize basically creep resistance as a function of temperature (Fig. 51).

A few constituents, overlapping peaks with the maxima or "steps" in the spectral contours, can be seen in the broad glass transition of semi-crystalline samples ranging from ~330°C to 470°C. For instance, at least five CR peaks, at temperatures of ~320°C, 360°C, 400°C, 430°C, and 460°C can be identified in the spectrum of coalesced semi-crystalline PI (curve 4 in Fig. 51). Since $T_g \approx 400$°C was observed by DSC for the amorphous Vespel® samples, the CR spectra in the glass transition region of semi-crystalline samples are associated with the complicated morphology in these materials and basically constrained dynamics effects in the disordered regions. The best high-temperature creep resistance of the coalesced semi-crystalline PI (Vespel®) materials was proved by the CRS experiments.

Figure 52 shows the dynamic heterogeneity in the semi-crystalline and amorphous PI samples at 20–300 °C. The distinct β-relaxation in the temperature range

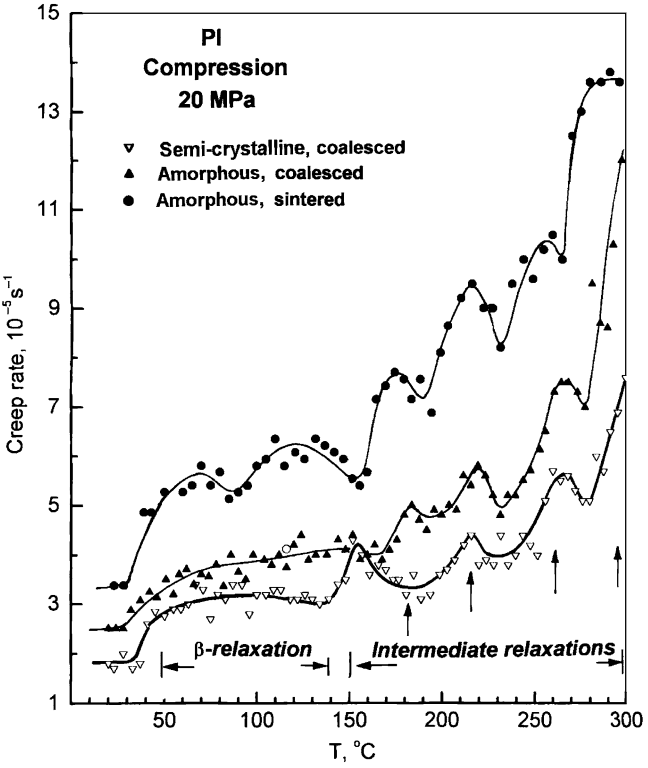

Fig. 52 Creep rate spectra obtained for the indicated PI (Vespel®) samples in the temperature region of sub-T_g relaxations [212]

from 50°C to 140°C and three or four overlapping constituent peaks of the "intermediate" segmental relaxations can be seen. This indicates the presence of a few discrete levels of the molecular packing density in PI micro- or nanodomains. The manifestation of these CR peaks in the Vespel® samples is not incidental: it is associated with the real complicated structure of PI. These peaks are satisfactorily reproduced, by their temperature positions, in differently produced PI samples. Again, one can see the highest creep resistance for the semi-crystalline PI even at moderate temperatures.

Thus, CRS experiments showed the importance of crystalline phase for attaining the best high-temperature performance of Vespel® parts. A high level of creep rates at 20 MPa is observed at temperatures as low as ~350°C for amorphous samples, but such rates cannot be attained even at 470°C for coalesced semi-crystalline PI (Fig. 51) due to constraining dynamics in the disordered regions by crystallites. Thus, the proper choice of the method of PAA imidization played the main role in attaining 30% crystallinity and maximum high-temperature creep resistance. The choice of the coalescence as the processing technique was of lower importance for creep characteristics. Nevertheless, the sintered samples exhibited somewhat weaker

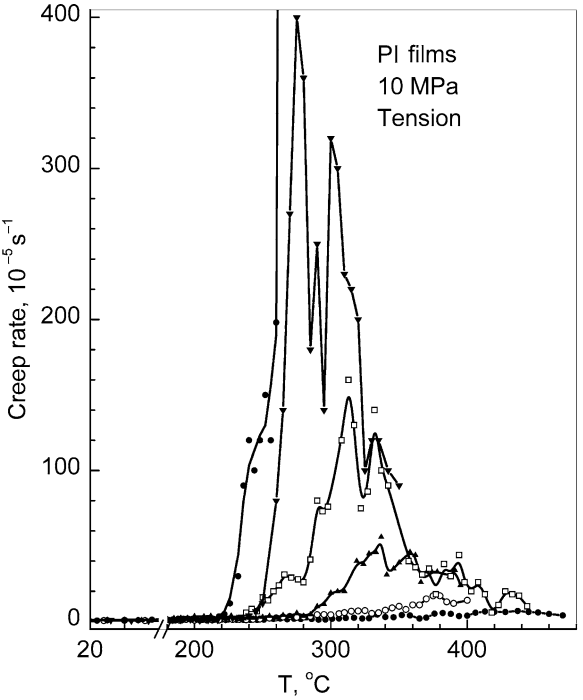

Fig. 53 Creep rate spectra obtained for the commercial Kapton ®, Du Pont (*point-up triangle*) and several tentative samples of PI films

creep resistance (Fig. 51) due to reduced cohesion between PI particles in samples obtained by compaction via cold pressing.

Figure 53 compares the CR spectra obtained for commercial Kapton® (Du Pont) and several tentative compositions of PI films in the temperature region of their glass transition. It illustrates the dynamic heterogeneity in this transition as well as the possibilities for the considerable changing high-temperature creep properties of these films in two opposite directions, including the improvement of creep resistance compared to that for the commercial film.

3.7 Polymer-Layered Silicate Nanocomposites

Polymer composites, containing small amounts of nanofillers, have attracted great attention in the last decade both in industry and academic studies, since a considerable enhancement of mechanical, thermal and other properties may be attained compared with virgin polymers. These nanocomposites can be considered, due to an exceptionally large interfacial area and a very significant role of interfacial layers, as the model systems to study the dynamics of polymers subjected to special

conditions. To date, most studies have focused on polymer nanocomposites containing 2D silicate nanolayers [40, 218, 219] or 1D carbon nanotubes (CNTs) [220]. The key to their enhanced efficiency is achieving a good dispersion, uniform spatial distribution, and alignment of nanoparticles. The role of factors such as a high aspect (e.g., length-to-diameter for CNTs) ratio for a nanofiller, and the necessity of a special chemical functionalization of nanofiller surface, is emphasized to provide its covalent coupling with a polymer matrix. The peculiarities of segmental dynamics in nanocomposites are currently studied experimentally and discussed in the context of polymers located in nanoconfined geometries.

The addition of layered silicate to a polymer can result in three different morphologies: formation of micro- (or even macro-) composites, or nanocomposites with intercalated polymer species (where the polymer is sandwiched between 2D silicate nanolayers) or with exfoliated/delaminated structures. In the last case, the 2D silicate nanolayers are completely separated, at least at distances of a few nanometers from one another.

Recently, a few papers [221–228] on PCN networks, modified by montmorillonite (MMT) silicate nanolayers, were published. Data on structure and mechanical and thermal properties of these nanocomposites were obtained. The 2D shape of MMT nanolayers, the enormous interfacial area, and strong PCN–MMT interactions, due to both covalent bonding between cyanate groups and the functional groups of MMT surface as well as between triazine rings and Al and Si atoms (charge transfer interactions), provided the enhancement of some PCN properties in the nanocomposites. Well-dispersed MMT additive resulted in the substantial increase in fracture toughness and crack resistance of PCN [223, 225], better thermal stability, and reduced coefficient of thermal expansion [221].

In this section, we consider briefly the results [226] where structure–dynamics relationships in the PCN–MMT nanocomposites were studied in detail. Infrared spectroscopy, WAXD, and TEM techniques were applied to study the structure of nanocomposites, whereas their dynamics was studied over the -30°C to 420°C range using CRS and DSC techniques. PCN–MMT nanocomposites were synthesized by polymerization of dicyanate ester of bisphenol A (DCEBA) (see Fig. 26) in the presence of 2 or 5 wt% MMT. Three types of commercial MMT products were used in the experiments: virgin Na-MMT (Cloisite Na) and two types of organically modified MMT – Cloisite 30B and Cloisite 15A. To provide a better dispersion of MMT in the polymer matrix, ultrasonic treatment of the initial mixture was performed, to be indicated as *u.t.* in Figs. 56 and 57. The process of DCEBA polymerization was recorded by the IR spectra. Sol–gel analysis of the samples after their thermal curing indicated incorporation of O–C≡N groups of DCEBA molecules into the PCN network: gel fraction exceeded 99%.

Figure 54 shows the WAXD patterns obtained for neat Cloisite 30B; ground cured PCN/Cloisite 30B mechanical blend, as a model of the PCN/MMT system without interactions between the components, and for one of PCN/Cloisite 30B nanocomposites investigated. The main diffraction peak of neat Cloisite 30B indicates the interlayer spacing of 1.92 nm; the same is observed for the "mechanical blend." The diffraction peak was shifted towards lower angles in the diffractograms

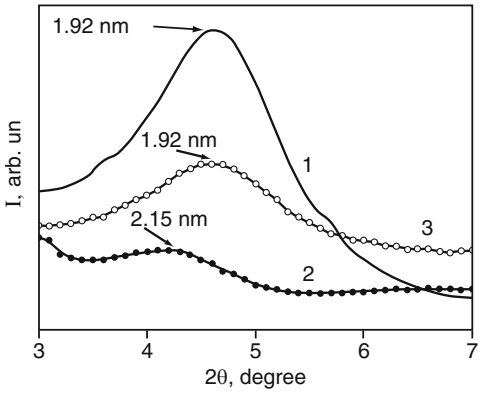

Fig. 54 WAXD patterns of (1) Cloisite 30B, (2) PCN/Cloisite 30B (95/5) nanocomposite, and (3) PCN/Cloisite 30B (95/5) mechanical blends are shown [226]. Interlayer spacings are indicated

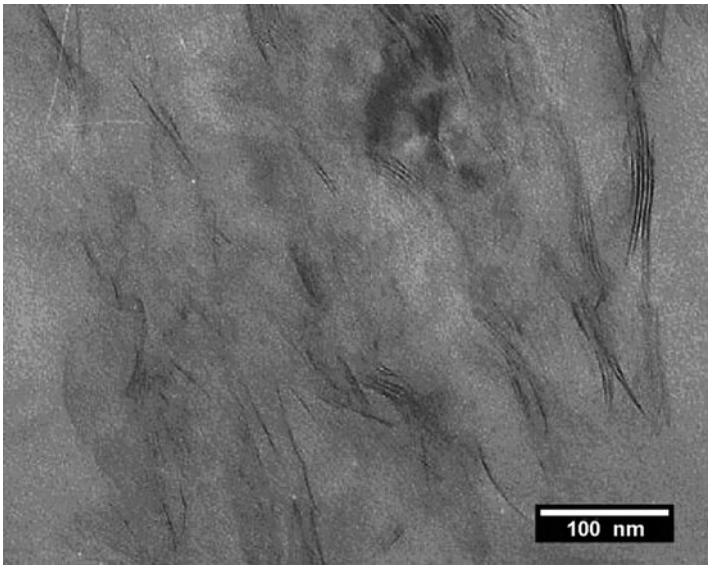

Fig. 55 TEM image of the PCN/Cloisite 30B (95/5) nanocomposite [226]

of the nanocomposites that corresponded to increasing the interlayer spacing to 2.15–2.26 nm [226]. The structure of these nanocomposites may be considered as mixed intercalated/exfoliated one. This was confirmed by the TEM micrographs: Fig. 55 allows discerning simultaneously individual 1 nm thick sheets of Cloisite 30B and well-organized stacks of MMT nanolayers in the PCN matrix.

DSC analysis of glass transition dynamics in these PCN–MMT nanocomposites showed that introduction of 2 or 5 wt% of layered MMT nanofiller into the PCN matrix resulted in the development of a pronounced dynamic heterogeneity and two opposite effects, namely some suppression and the acceleration of dynamics in the nanocomposites. Figure 56a shows that two high-temperature glass

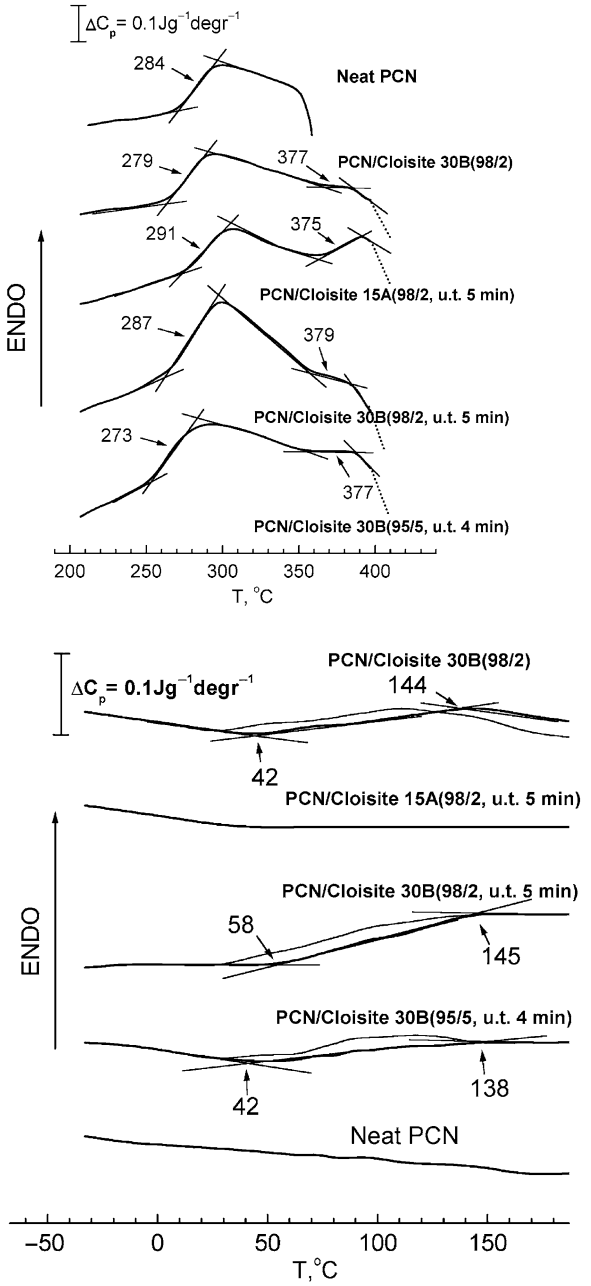

Fig. 56 Stabilized neat PCN and PCN–MMT nanocomposites: DSC curves obtained over the 200°C to 420°C range (**a**) and −30°C to 180°C range (**b**) [226]. Heating rate $V = 20\,\mathrm{K\,min^{-1}}$. (**a**) Stabilization procedure was 20 min holding at 270°C plus scanning to 330°C followed by cooling with the rate of $320\,\mathrm{K\,min^{-1}}$. T_g values in the glass transitions II and III are indicated. (**b**) Scan 1 *thin line*, scan 2 *thick line*. The temperatures of the lower-temperature glass transition I onset, T_g', and completion, T_g'', are indicated

transitions, at about 270–290°C and 375–380°C, are observed in the DSC curves of thermally stabilized PCN–MMT nanocomposites, unlike a single glass transition with $T_g = 284$°C in the neat PCN. In addition, the exothermic process of decomposition started at 350°C for the neat PCN but at ca. 400°C only for the nanocomposites. Increasing thermal stability in the PCN–MMT nanocomposites is in accordance with the results of TGA measurements [223]. On the other hand, DSC curves registered the development of a relatively slight but discernable, very broad glass transition with $T_g \approx 80$–100°C and the ΔT_g range extending from 40–60°C to 140–145°C (Fig. 56b) in the PCN/Cloisite 30B nanocomposites. No transition was discerned, however, in the PCN/Cloisite 15A nanocomposite.

Thus, three glass transitions in the PCN–MMT nanocomposites are located at the same temperature, much below and much higher than T_g of the neat PCN. DMA [223] also showed the development of the higher-temperature and lower-temperature relaxation peaks in the PCN–MMT nanocomposites at 350–400°C and 100–250°C, respectively. The T_g depression down to 140 °C was recently observed in the PCN network when curing dicyanate ester in nanopores of silicate glass [229].

The complicated glass transition dynamics in the PCN–MMT nanocomposites could be interpreted in the following way. The introduction of Cloisite additives into the reaction system, with the formation of intercalated/exfoliated structures, did not affect the part of PCN nanodomains retaining the "usual" T_g. Cloisite nanolayers prevented total CN → PCN conversion in some of the PCN nanodomains, and this resulted in decreased T_gs within the broad (40–140°C) temperature range. Such T_gs indicate the presence of nanodomains with different PCN cross-linking degrees – conversions $X_{CN \rightarrow PCN} \approx (0.65–0.80)$ (see Sect. 3.3.2).

The highest-temperature glass transition characterizes interfacial dynamics in the nanocomposites. This "constrained dynamics" is manifested in PCN nanodomains adjoining to silicate nanolayers, due to strong co-ordinate and covalent bonding between PCN and nanofiller surface. By registering the DSC curves at different heating rates it was shown that, unlike the high apparent (cooperative) activation energies of 700–1100 kJ mol^{-1} for the main glass transition, non-cooperative activation energy of 180 kJ mol^{-1} was obtained for the transition at interfaces in spite of the higher temperatures of this relaxation [226].

To study the heterogeneity of glass transition dynamics in the PCN–MMT nanocomposites in more detail, their CR spectra were measured over the temperature range between 20°C and 330°C. The tensile stress of 10 MPa was chosen for the measurements at moderate temperatures for inducing sufficient creep rates to be measured. At temperatures 200–330 °C, the stress of 0.5 MPa was applied to maintain a high spectral resolution.

Figure 57 shows the CR spectra obtained for the neat PCN and PCN–MMT nanocomposites. One can see that a single CR glass transition peak with maximum at $T_g \approx 280$°C for the neat PCN network transformed for the nanocomposites into the complicated spectra. The spectra were broken off at ca. 300°C for PCN and 330°C for the nanocomposites due to fracture of the samples. These discrete spectra are in accordance with the DSC data and directly confirm the pronounced heterogeneity of glass transition dynamics in the PCN–MMT nanocomposites.

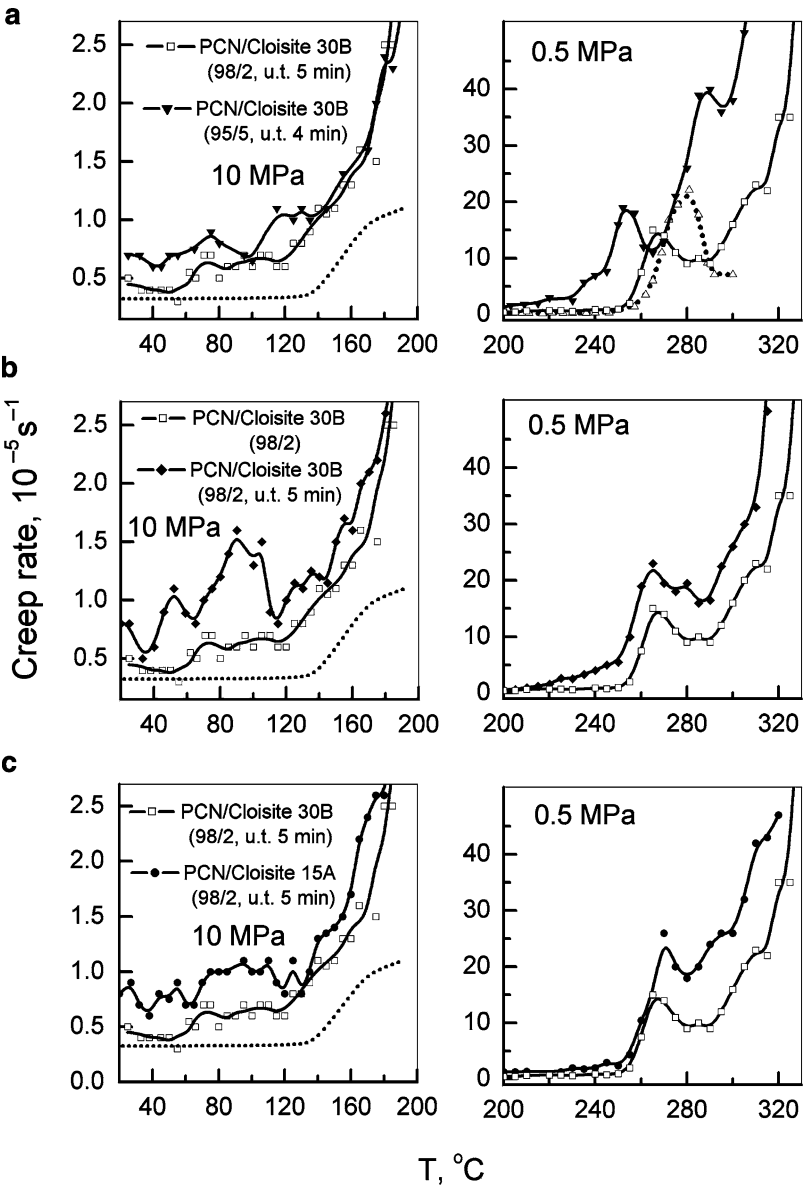

Fig. 57 Creep rate spectra obtained for the PCN–MMT nanocomposites (*solid lines*) and neat PCN (*dotted lines*) under tensile stresses of 10 MPa at moderate temperatures and of 0.5 MPa at higher temperatures [226]. The impacts of (**a**) MMT, (**b**) ultrasonic treatment (u.t.), and (**c**) type of MMT modifier are shown

According to the data [148], $T_g = 260$–$280°C$ corresponds to the glass transition in PCN nanodomains with the degree of cross-linking $X_{CN \rightarrow PCN} = 0.95$–$0.98$. The introduction of MMT with formation of intercalated/exfoliated nanocomposite

structure results in incomplete cross-linking in some of the matrix nanodomains (T_g = 40–140 °C characterizes glass transition corresponding to conversion $X_{CN \rightarrow PCN}$ = 0.65–0.80), and additionally new spectral constituents appear at 290–320 °C. The latter may be assigned to the onset of unfreezing constrained dynamics in the PCN nanolayers at the PCN–MMT interfaces.

Figure 57a–c show separately the influence on dynamics of such factors as different MMT amounts; a role of ultrasonic treatment (*u.t.*) providing the improved dispersion of MMT in the matrix, and comparative efficiency of two types of MMT surface modifiers (Cloisite 30B, Cloisite 15A). The addition of 2% MMT to PCN provides the better thermal stability (creep resistance) than adding of 5% MMT, probably due to the improved dispersion (Fig. 57a). Some increase in mobility, both at moderate and high temperatures, is attained due to using the procedure of ultrasonic treatment of the reaction mixture (Fig. 57b). Some difference in the influence of Cloisite 30B and Cloisite 15A on the glass transition dynamics can also be seen from Fig. 57c.

Of special interest with respect to the applications are that high thermal stability of the PCN matrix is retained and, simultaneously, some microplasticity around room temperature appears in the PCN–MMT nanocomposites. Figure 57 shows the total absence of creep ability of the neat PCN network up to 130 °C, but creep is observed for the nanocomposites in the same temperature range. Much higher creep rates were observed at higher stresses in the latter case. Consequently, MMT additives caused the development of some microplasticity at low temperatures in PCN networks due to locally incomplete cross-linking. Therefore, increasing fracture toughness and crack resistance, observed for the PCN–MMT nanocomposites [223, 225], might be explained by two reasons: (1) crack hindering by 2D silicate nanolayers due to the "pinning" effect, and (2) crack tip blunting. The latter is caused by appearance of some microplasticity in the brittle PCN network leading to a partial relaxation of overstresses near the tips of cracks.

Figure 58 shows the CR spectra of MMT-containing nanocomposites based on the hybrid 90PCN–10PTMG network, in comparison with those of unfilled network and neat PCN. The introduction of 5 wt% of Cloisite 30B results in a decrease of T_g peak with its shift to lower temperatures. A steep rise of creep rates occurs starting already from ca. 230 °C. Unlike that, the introduction of 2 wt% of Cloisite 30B results in a sharp suppression of matrix dynamics at high temperatures, and a steep rise of creep rates only above 270 °C, i.e., not far from T_g of the neat PCN. This assumes simultaneously some microplasticity at moderate temperatures and increased high-temperature performance for this perspective nanocomposite.

3.8 Polymer–Diamond Nanocomposites

Recently, polymer nanocomposites utilizing different carbon nanofillers attracted special attention. The advances in the science and technology of such nanocomposites were reviewed [220, 230–232]. Basic attention was paid to the use of such

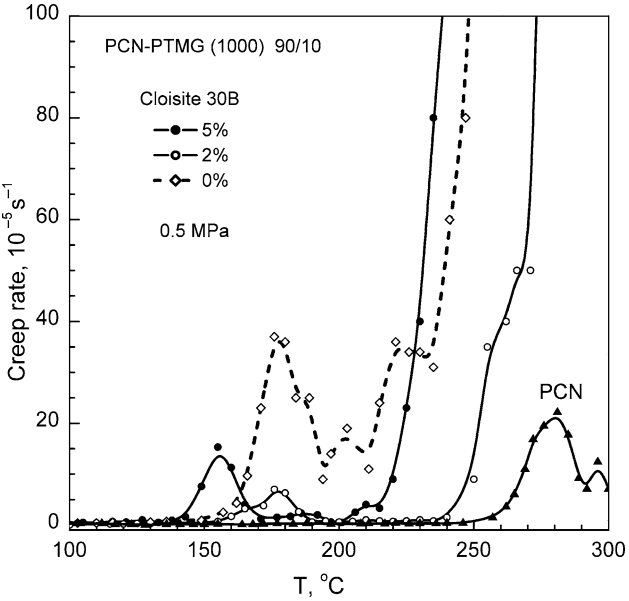

Fig. 58 Creep rate spectra obtained for the hybrid 90PCN–10PTMG network (M_n^{PTMG} = 1000 g mol^{-1}), the nanocomposites with 2 or 5 wt% MMT based thereon, and neat PCN at tensile stress of 0.5 MPa (unpublished data)

1D nanofiller as CNTs; however, among the carbon nanostructures only 3D nanodiamonds (NDs) have been available on a relatively large scale for the last two decades [220].

Successful applications of NDs in polymer nanocomposites for electronics materials [233]; materials having proton conductivity [234] or enhanced thermal conductivity [235]; for selective membranes, sensors, catalytic systems, nonlinear optical materials [230, 236], and elastomers of enhanced strength, wear and heat-ageing resistance [230, 237, 238] can all serve as examples.

In Sect. 3.3.3, a peculiar dynamics in the hybrid PU–PHEMA semi-IPNs was discussed. In the work described in [239, 240], a series of PU–PHEMA–ND nanocomposites with different matrix compositions and ND contents of 0.25, 1, or 3 wt% were studied. Their nanostructure, glass transition dynamics, and elastic properties were investigated in the combined CRS/AFM/DSC experiments. We revealed a possibility of large and specific impact of low content of 3D nanofiller on polymer matrix, without performing a special functionalization of its surface. For preparing nanocomposites, the NDs obtained by the shock-wave method, with the particle sizes of 2–100 nm and specific surface area of 220 m^2 g^{-1}, were used. NDs were introduced into the reaction mixture at the stage of PU synthesis.

Using AFM analysis, three kinds of ND dispersion/distribution in the PU–PHEMA matrices were detected: (1) individual nanoparticles 50–100 nm in size; (2) their agglomerates with the size of 0.2–0.5 μm; and (3) their larger aggregates from 0.6 μm up to several micrometers in size (Fig. 59). Generally, all these

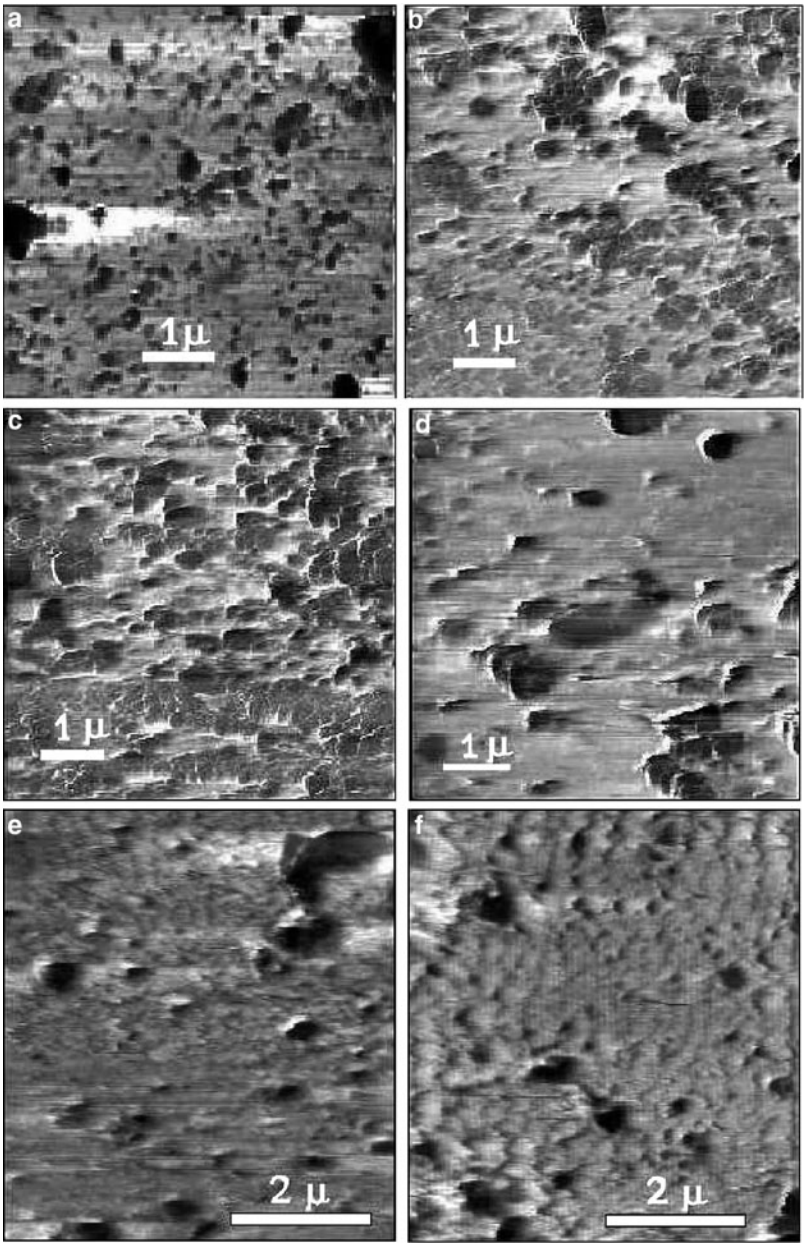

Fig. 59 Deflection AFM images, obtained in contact mode, of the 83PU–17PHEMA–ND (**a–d**) and 63PU–37PHEMA–ND nanocomposites (**e, f**) with 0.25% (**a, e**), 1% (**b**), and 3 wt% NDs (**c, d, f**) [239, 240]

dispersion states were revealed in the composites studied; however, they contributed very differently to the composite structures. Thus, in the 83PU–17PHEMA–ND nanocomposites, after introducing 0.25 wt % NDs, individual nanoparticles, relatively uniformly distributed in the matrix, prevailed in the structure; small ND aggregates were rather sparse (Fig. 59a). However, at 1% and, especially, 3 wt% NDs, such nanoparticles were less discernable (Fig. 59b–d), whereas the dispersion states II and III turned out to be more characteristic of these compositions. The internal structure of the agglomerates consisting of 5–15 particles could be seen. Composites with 3 wt% NDs were characterized not only by the presence of ND agglomerates II and micron aggregates III but also by their sharply non-uniform spatial distribution (Fig. 59c,d).

Somewhat different AFM images were obtained for the 63PU–37PHEMA–ND nanocomposites with the same NDs contents (Fig. 59e,f). In this case, more narrow range of the sizes of ND formations was observed, and agglomeration of NDs did not increase with increasing ND content (from 0.25 to 3 wt%).

Such differences in the dispersion states of NDs in the PU–PHEMA matrices had to provide the respective differences in the interfacial area values. It could be expected that the maximal interfacial area and maximal impact of nanofiller on properties were to be attained at 3 wt% NDs in the 63PU–37PHEMA matrix but the largest impact of NDs on the 83PU–17PHEMA matrix might be at 0.25 wt% NDs.

DSC measurements indicated the substantial changes in the glass transition characteristics of PHEMA constituent in the PU–PHEMA networks after adding NDs. In particular, some suppression of mobility was confirmed by decreasing ΔC_p. The apparent activation energy Q for PHEMA glass transition varied in these nanocomposites from 110 to 250 kJ mol^{-1}, unlike $Q = 160$ kJ mol^{-1} for the neat PHEMA [240]. Nevertheless, only discrete CR spectra represented more detailed dynamic pictures for the glass transition in these nanocomposites. Moreover, distinct correlations between the ND dispersion/distribution and segmental dynamics were found [239, 240].

Figure 60 shows strong changes in the CR spectra caused by the introduction of small ND additives into the 83PU–17PHEMA and 63PU–37PHEMA networks. The main effect here is a sharp suppression of PHEMA dynamics (creep rate reduction) over the temperature range from 90°C to 180 °C. For the 83PU–17PHEMA–ND nanocomposites, the highest creep resistance at 150–180°C is observed at the minimal ND content of 0.25 wt%, whereas the least effect of suppression of dynamics by nanofiller is registered at 3 wt% NDs. In contrast, for the 63PU–37PHEMA–ND nanocomposites, creep resistance at temperatures of 140–180°C increased with increasing ND content in a nanocomposite from 0.25 to 3 wt%. The introduction of small ND additives into neat PU and PHEMA affected only slightly their glass transitions [239]. Much more strong influence of NDs on segmental dynamics in the PU–PHEMA networks implies some synergistic effect in dynamics.

Figure 60 shows that the addition of ND particles also results in the effect of increasing creep rates in the temperature range between 20°C and 70–80°C, i.e., accelerating segmental dynamics in the range between the β- and α-transitions of neat PHEMA ($T_g = 90$°C). This effect was absent, however, at 3 wt% NDs in the 63PU–37PHEMA–ND nanocomposite.

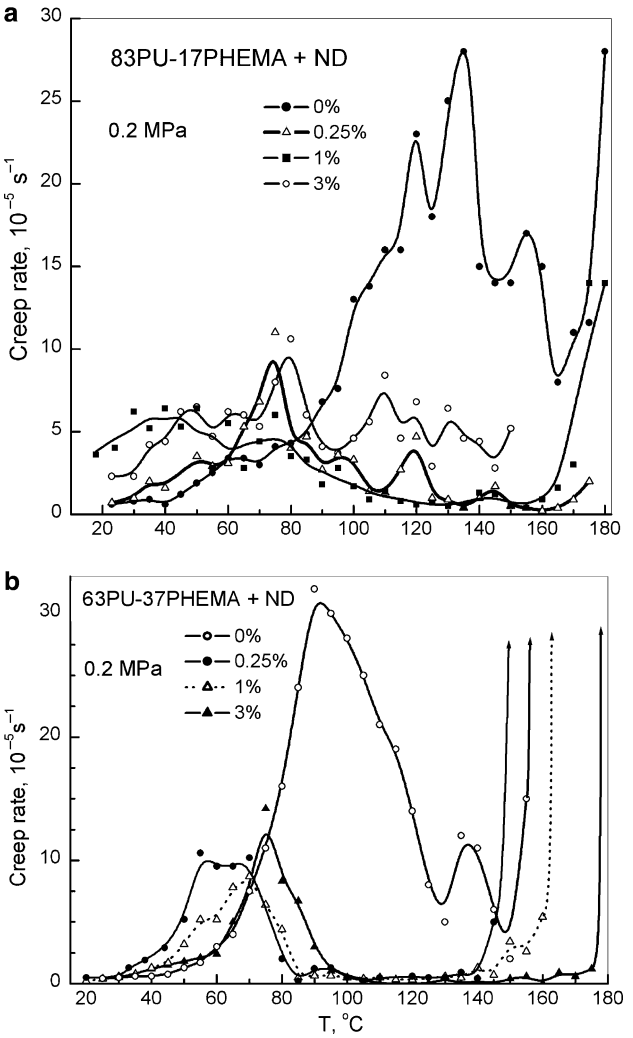

Fig. 60 Creep rate spectra obtained for the 83PU–17PHEMA and 63PU–37PHEMA networks and ND-containing nanocomposites based thereon in the temperature region of PHEMA glass transition, at tensile stress of 0.2 MPa. ND weight contents are indicated [239, 240]

Thus, comparing CRS and AFM data confirms the correlation between the CR spectra and the dispersion state of NDs in nanocomposites, indicating the leading role of the value of interfacial area. The largest effect of changing high-temperature dynamics in the 83PU–17PHEMA–ND nanocomposite was found at 0.25% NDs. Relatively good dispersion and distribution of nanofiller particles promoted their largest influence on the matrix due to a *maximal* interfacial area despite the *very low* ND content. In the case of the similar ND dispersion in the 63PU–37PHEMA–ND composites with 0.25, 1, or 3%NDs, the largest effect was, naturally, at 3% of nanofiller.

Two opposite impacts of NDs on matrix dynamics could be explained, as earlier, in terms of the common notions of constrained dynamics, loosened molecular packing, and a partial or total collapse of intermolecular cooperativity of segmental motion in the glass transition. The large effect of suppression of matrix dynamics at high temperatures and the three- to sixfold increase of modulus of elasticity (see Sect. 6.5) caused by a small additive of 3D nanofiller, in the absence of a special functionalization of its surface are unexpected and remarkable facts.

Really, according to the calculations [220], polymer matrix is considered to be entirely nanoscopically confined by 3D nanofiller only in the case when the average inter-particle distance, L, is close to or less than the dimensions of unperturbed macromolecular random coil; the latter is estimated by radius of gyration R_g. At the same time, in our case $R_g \approx 8$ nm for PHEMA and $L > 300$–500 nm when 0.25% of 3D particles with 50–100 nm size are introduced into the matrix. It means that the PU–PHEMA–ND nanocomposites exhibit an unexpectedly low percolation threshold.

According to the results [239, 240], this large impact of small 3D ND additive could be associated with formation of the peculiarly cross-linked structure in these nanocomposites, due to the effect of double chemical hybridization between three network constituents. A simplified scheme of such a structure is represented in Fig. 61.

PU/PHEMA hybridization was confirmed by IR spectra (Sect. 3.3.3). However, ND particles were also chemically grafted to the network. The surface of NDs produced by a shock-wave method is very active and acquires a "functional cover" (OH, COOH, and other groups) at their high-temperature treatment in air medium before their introduction into a reaction mixture; the presence of such "cover" was shown experimentally in spectroscopic and other studies [241,242]. In view of high reactivity of isocyanate groups towards these surface groups, covalent bonding of forming PU network with ND "functional cover" inevitably occurs. Therefore, the double

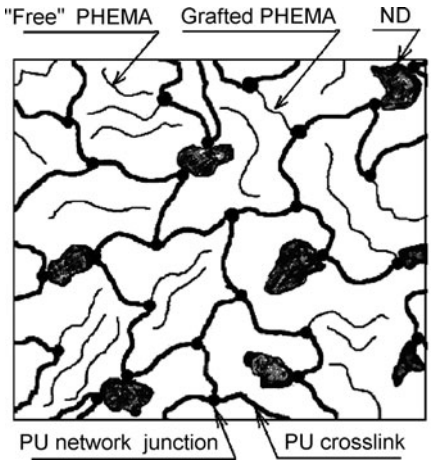

Fig. 61 A scheme of peculiarly cross-linked structure of PU–PHEMA–ND nanocomposite. ND particles are incorporated via covalent bonding into a network [239,240]

hybridization in the hybrid PU–PHEMA–ND nanocomposites may be considered as the second important factor (besides good nanofiller dispersion) resulting in the strong impact of 3D NDs on the matrix dynamics and properties.

3.9 Polymer–Silica Nanocomposites

Considerable attention has also been paid in recent years to hybrid polymer–silica nanocomposites prepared mostly via a sol–gel process [219, 243–254] where 10–100 nm size 3D silica domains (clusters) were covalently bound to the polymer. Polymers deprived of groups reactive in the sol–gel process but prone to hydrogen bonding with silanols of silica nanoparticles have also been successfully incorporated into nanophase-separated hybrid materials [246, 248–252]. Some polymer–silica nanocomposites, in particular silica core-polymer shell nanoparticles [255–258], were prepared using 3D fumed silica nanoparticles.

Since the substantial changes in matrix dynamics were supposed at an average interparticle distance $L \leq R_g$, the impact of 3D particles of ~10 nm in size on the dynamics and properties of polymer matrix are expected at their volume content not below 10–20% [220]. Really, for silica contents of 10–50 wt%, the presence of second glass transition at higher temperatures [259] or increasing glass transition temperature T_g and transition breadth ΔT_g [245, 246, 248, 260–262], or a partial or total suppression of segmental motion [263–265] have been observed. Additionally, the existence of a T_g gradient in the vicinity of silica particles [266] and well-separated bulk and interfacial glass transition dynamics [267] have been shown for elastomer–silica nanocomposites. As recently found for silica core–PVP shell nanoparticles [130], strong interfacial interactions, including hydrogen bonds and Lewis acid–base interactions, resulted in the multi-modal glass transition dynamics in the PVP nanoshells at interfaces (see Sect. 3.1.3 and Fig. 23).

In the research [268], we studied the nanocomposites of potential biomedical and technical applications based on the hybrid PU–PHEMA semi-IPN doped by 3D nanosilica additives. Proceeding from the results, described in the preceding section, only 0.25 or 3 wt% of nanosilica were introduced. The silica dispersion was characterized by AFM, and the combined CRS/DSC approach was used for analysis of glass transition dynamics and measuring the temperature dependencies of the elastic modulus in these materials. Three-dimensional fumed silica nanoparticles of 6–15 nm in size with the specific surface area $S_{BET} = 295\,m^2\,g^{-1}$ were utilized. Three different surface states (functional groups) of silica nanoparticles provided selective bonding with the matrix constituents and allowed us to establish the interrelationship between the interfacial interactions and dynamics/modulus behavior.

The hybrid PU–PHEMA semi-IPNs were prepared as described previously [169]. To prepare the nanocomposites, fumed silica nanoparticles were introduced into the polymer system at the stage of PU synthesis. The silica particles were used (1) without special functionalization of their surface with initial surface silanol groups ("–OH cover"), (2) after their functionalization by

3-aminopropylmethylsilyl groups ("–NH_2 cover"), and (3) after their functionalization by 3-methacryloylpropylsilyl groups ("–$CH = CH_2$ cover"). Functionalization of nanosilica was carried out by 3-aminopropylmethyldiethoxysilane (APMDES) or 3-methacryloyl-oxypropyltrimethoxysilane (MAPTMS).

The presence of different functional covers at silica surface led to selective covalent bonding and different interactions at interfaces. The idea was that highly reactive isocyanate groups of adduct of trimethylol propane and TDI (see Sect. 3.3.3) will provide covalent bonding with silanol or amine groups of silica surface during the process of PU network synthesis. The methacrylic groups of silica surface will participate in copolymerization with hydroxyethyl methacrylate (HEMA). Other "pairs" such as PHEMA/amine, PHEMA/silanol, or PU/methacrylic groups might form only hydrogen bonds at the interfaces.

AFM images showed three kinds of silica dispersion states in the 83PU–17PHEMA matrix: (1) discernable black "points" of about 20–40 nm in size, i.e., close to the size of individual nanoparticles or their very small aggregates; (2) small particle aggregates ~100 nm in size; and (3) sparse aggregates 200–400 nm in size (Fig. 62). Unexpectedly, no substantial changes in silica dispersion after functionalization of its surface were revealed: all three kinds of silica aggregates were detected, irrespective of the type of functionalization. It was a surprising result because the surface functionalization is typically considered as a route to improve the nanofiller dispersion. Nevertheless, this was explainable in the following way. Silica nanoparticles were introduced into the reaction mixture, and composite nanostructure was formed at the initial stage of formation of the PU network, i.e., in the presence of a large quantity of isocyanate groups. The latter are chemically active to both –OH and –NH_2 groups, i.e., both untreated and APMDES-treated silica surfaces. Therefore, it was natural to expect formation of similar nanostructures in the PU–PHEMA-based nanocomposites with no additional impact of functionalization on the filler dispersion. The surface functionalization of silica with –CH=CH_2 groups, which are not capable of reacting with the constituents of the PU-forming reaction mixture (before introducing HEMA), could even enhance silica aggregation to some extent.

Hence, silica dispersion and the value of interfacial area could remain practically unchanged, in the first approximation, in the 83PU–17PHEMA–silica nanocomposites differing by the kind of silica functional cover. This allowed us to estimate the impact of changes in the interfacial interactions on the glass transition dynamics.

Figure 63 shows the DSC curves characterizing the PHEMA glass transition in the stabilized, dehydrated 83PU–17PHEMA network and silica-containing nanocomposites. Glass transition temperature, T_g, at the half-height of a heat capacity step, transition width $\Delta T_g = T_g''–T_g'$ where T_g' and T_g'' are the temperatures of the glass transition onset and completion, respectively, and the values of heat capacity step ΔC_p are indicated. A strongly broadened two-step PHEMA glass transition of the unfilled 83PU–17PHEMA network (curve 1) was discussed in Sect. 3.3.3. Figure 63 depicts a quite different impact of added nanosilica on this transition including the total disappearance of the second ΔC_p step: a sharp narrowing of the glass transition range; a large increase of T_g', a large decrease in the ΔC_p step, and insignificant changes in the matrix glass transition characteristics.

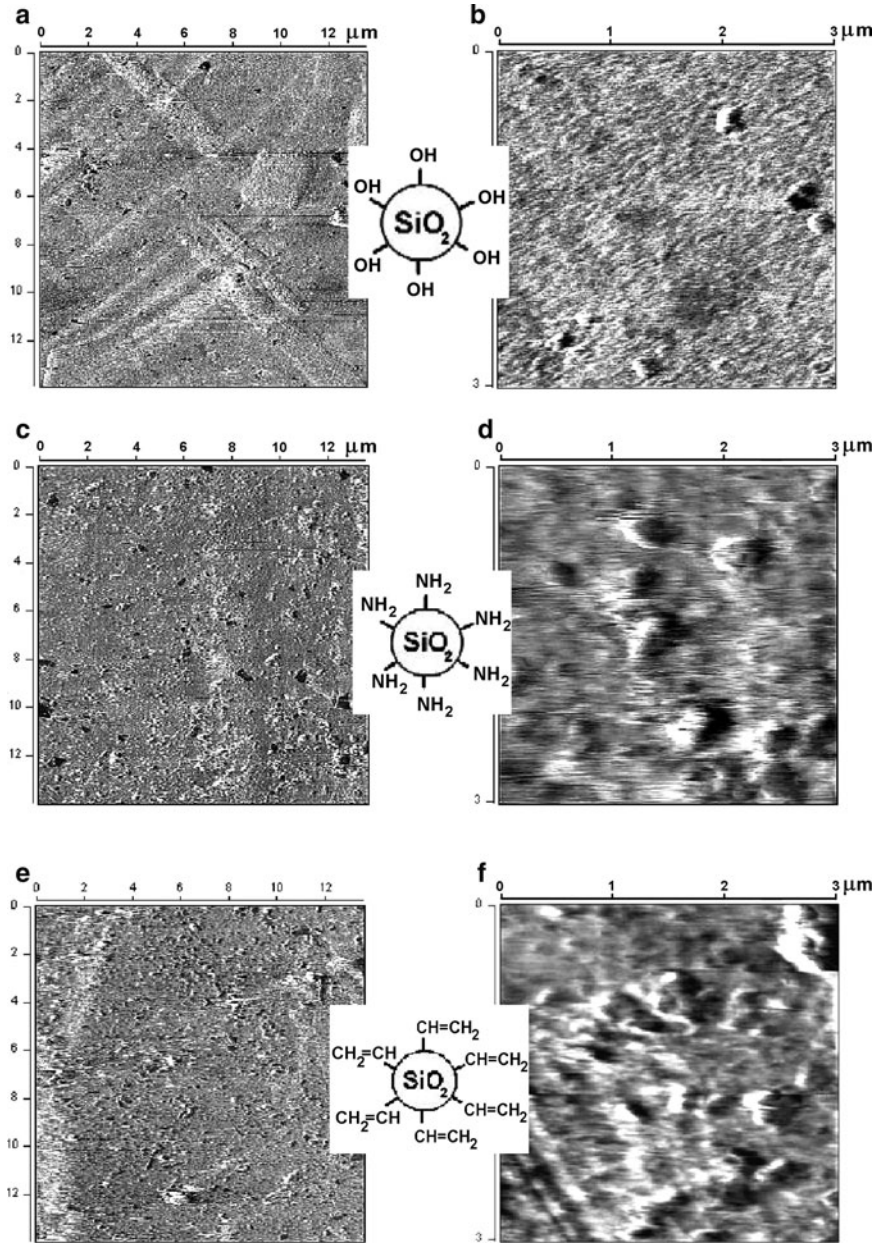

Fig. 62 Deflection AFM images, obtained in a contact mode, for the 83PU–17PHEMA–silica nanocomposites with 3 wt% silica [268]. Samples differed by a type of the functional cover of silica surface: –OH groups (initial cover), $–NH_2$ or $–CH=CH_2$ groups. Most typical and relatively rare nanostructure images are shown on the left and on the right, respectively

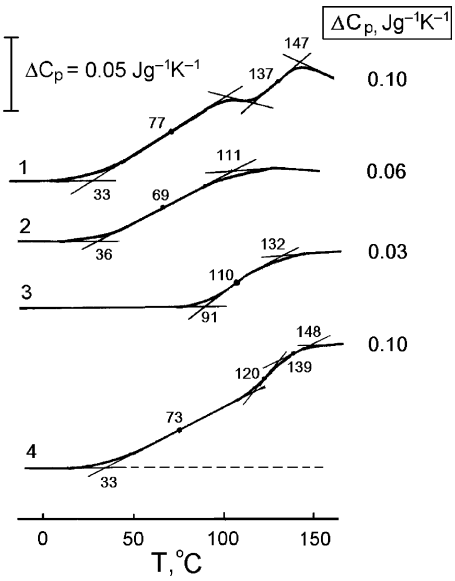

Fig. 63 DSC curves obtained in the temperature region of PHEMA glass transition for the 83PU–17PHEMA network (1) and for the nanocomposites containing 0.25 wt% silica (2–4) [268]. Curve 2 relates to silica surface with –OH groups; curve 3 with $–CH = CH_2$ groups, and curve 4 with $–NH_2$ groups. The *dashed line* designates typical baseline (reference sample was used)

Negligibly small changes in transition temperatures and intensity (ΔC_p) were observed in the case of silica nanoparticles with the $–NH_2$ cover (curve 4). Some suppression of PHEMA dynamics occurred when untreated silica particles with the –OH cover were used (curve 2). The –OH and $–NH_2$ covers provide only hydrogen bonding with PHEMA. Interfacial interactions were more pronounced in the case of the –OH cover since APMDES-modified nanosilica also contained, besides $–NH_2$ groups, non-polar propyl and methyl groups decreasing adhesive interactions at interface. The most pronounced effect was registered by DSC for the nanocomposite with 0.25 wt% silica particles having the $–CH{=}CH_2$ cover (curve 3) when one-step transition as well as threefold reduction of both transition width and intensity were observed. The $–CH{=}CH_2$ groups at silica surface were involved in copolymerization with HEMA monomer. Thus, PHEMA was connected to both PU network junctions and silica surface. This resulted in the strongly constrained dynamics.

Figure 64a,b shows the CR spectra obtained for these materials over the temperature range from 20°C to 160°C. The tensile stress of 0.3 MPa was sufficient to obtain distinct spectra and a satisfactory spectral resolution. The pronounced influence of silica additives on the PHEMA dynamics and its distinct connection with the interfacial interactions (type of silica functionalization) can be seen. First, the complicated spectral contours over the 40–140 °C range are observed; they include a number of overlapping peaks indicating multi-modal dynamics within the glass transition of PHEMA as the constituent of matrix network. This transition covers a temperature range up to ca.100°C. Second, suppression of segmental dynamics depending on the type of surface functional groups is the basic effect of nanosilica on the CR spectrum. Covalent bonding of PHEMA to silica surface ($–CH{=}CH_2$ groups) provided the maximal suppression of dynamics (creep) at 90–160°C. This effect decreased in the case of the untreated silica surface (–OH cover), and especially for the

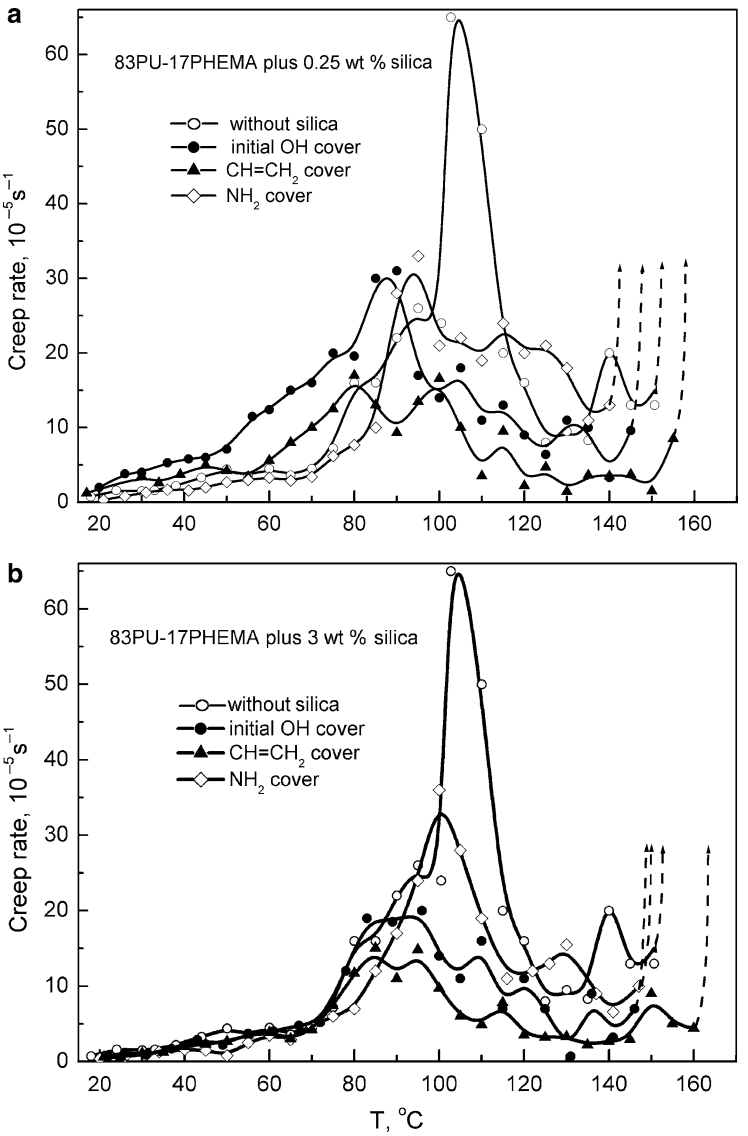

Fig. 64 Creep rate spectra obtained at tensile stress of 0.3 MPa in the temperature region of PHEMA glass transition for the 83PU–17PHEMA network and nanocomposites based thereon, containing 0.25 wt% (**a**) or 3 wt% silica particles (**b**) with different functional groups at their surface [268]

NH_2-functionalized surface, i.e., under conditions of hydrogen bonding only at the silica–PHEMA interfaces. The covalent interfacial interactions (–CH=CH_2 cover) caused the largest displacement of the onset of a sharp acceleration of creep towards higher temperatures, especially at 3 wt% silica (Fig. 64b).

For 0.25 wt% silica, the CR spectra also manifested a less pronounced effect of accelerating segmental dynamics (creep) at ∼ 40–80°C in the temperature region between the β- and α-transitions of PHEMA (Fig. 64a). This was explained as above by a partial or total collapse of intermolecular cooperativity of segmental motions.

Contrary to the majority of papers on polymer–silica nanocomposites, the very low content of 3D nanosilica particles in the polymer matrix in this work resulted in average inter-particle distance L larger by an order of magnitude than the radius of gyration R_G of PHEMA. In spite of that, a considerable impact of small 3D silica additives on matrix dynamics was found due to double PU/PHEMA and silica/matrix hybridization.

4 Comprehensive Analysis of Deformation Kinetics in Polymers

4.1 General Approach: Changeability of Kinetic Parameters as a Common Phenomenon in Polymer Deformation

Descriptions of inelastic deformation of glassy polymers are based on the classical treatments of Frenkel [269] and Eyring with coworkers [109, 270] who have considered an elementary plastic flow event as a transition of a particle from one quasi-equilibrium state to another by means of overcoming a potential barrier under the influence of thermal fluctuations; it is also assumed that its height is lowered by stress. Generally, the polymer deformation rate can be described by the expression

$$\begin{aligned}\dot{\varepsilon} &= \dot{\varepsilon}_0 \exp\left(-\frac{Q_0 - \alpha t_m}{RT}\right) = \dot{\varepsilon}_0 \exp\left(-\frac{Q(t_m)}{RT}\right) \\ &= N\varepsilon_0^* \nu_0 \exp\left(\frac{\Delta S}{R}\right) \exp\left(-\frac{Q(t_m)}{RT}\right), \end{aligned} \tag{20}$$

where $t_m = \sigma/2$ is a maximum tangential stress; Q_0 is an effective activation energy, $Q(t_m)$ is an activation enthalpy, α is an activation volume, ΔS is an activation entropy, N is a number of "flow kinetic units" or elementary shear regions, ε_0^* is the contribution of each of these units to the total strain, R is the gas constant, T is the absolute temperature, $\dot{\varepsilon}_0$ is the pre-exponential factor, and $\nu_0 \approx 10^{13}\,s^{-1}$.

It has also been presumed that the magnitude of the kinetic units corresponds closely to the activation volume of deformation, as well as to the units in different kinds of motion, namely the rotation-translation displacement of a segment or several neighboring segments in a polymer. In addition to the molecular-kinetic model of deformation, the disclination [271], "dislocation analogy" [272, 273], or dislocation-disclination [274, 275] solid-state models of polymer deformation have also been discussed.

Equation (20) assumes the deformation process with constant values of Q_0 and α that are valid, only within a narrow range of varying experimental conditions (see below). In the usual determinations of kinetic parameters of deformation, the values

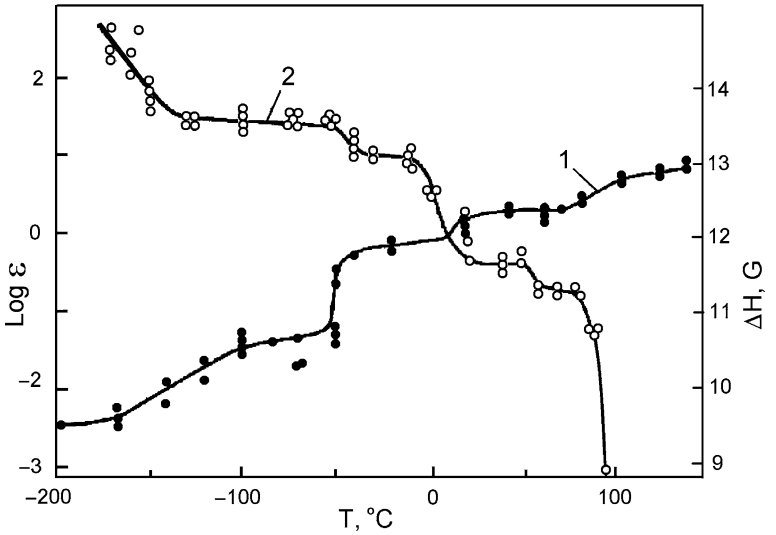

Fig. 65 Correlation between the temperature dependencies of fracture deformation (1) and mobility (NMR line width ΔH) (2) in poly(vinyl formal) [277]

of $Q(t_m)$ and α are found from the slopes of $\ln\dot{\varepsilon}$ against T^{-1} and $\ln\dot{\varepsilon}$ against t_m plots, respectively, which require considerable averaging of the results for the wide ranges of temperatures and stresses; this procedure is unsatisfactory for polymers since it may result in large errors.

The non-constancy of deformation kinetic parameters is expected, a priori, for polymers over the wide ranges of temperatures and stresses (or strains). It has been shown that the diversity of molecular motions inherent to polymers results in a peculiar behavior of their mechanical properties with respect to their relaxation transitions, in particular in non-monotonic temperature dependencies observed for their fracture deformation or stress [276–278]. As an example, Fig. 65 illustrates the typical correlation between change in fracture deformation and step-like "unfreezing" of mobility with temperature, as estimated by the NMR line width, for poly(vinyl formal).

Another difficulty in the correct estimation of the kinetic parameters of deformation is the need to maintain the invariable structure of polymers during measurement, whereas structural changes are inevitable in the process of considerable changes in deformation values for polymers. Therefore, it is impossible to learn deformation kinetics as a function of the magnitude of deformation using the generally accepted techniques for such experiments.

We succeeded in overcoming the above problems by the elaboration of a highly sensitive method for studying deformation kinetics, based on high-precise recording the creep rates by the LICRM setup combined with the Sherby–Dorn method [279] of stress or temperature "jumps" for studying deformation kinetics of solids. The latter method (before using the laser interferometry) showed that the kinetic

parameters of deformation were approximately constant within certain ranges of temperatures or strains only; it allowed only rough estimates of the kinetic parameters due to non-precise measuring of creep rates.

Our laser-interferometric technique made it possible not only to increase dramatically the accuracy of the measurements but also to study the deformation kinetics under formerly inaccessible conditions, namely, to determine activation parameters under the conditions of practically unchangeable polymer structure and mobility. It became possible to obtain precise and complete kinetic information on the process of polymer deformation, in fact at any temperature and at any stage of the deformation process (at different strain and stress values).

The method of ΔT or Δt_m jumps was used to find the values of $Q(t_m)$, Q_0, and α at any "point" along the creep curve using the equations

$$Q(t_m) = R\frac{\ln(\dot{\varepsilon}_2/\dot{\varepsilon}_1)}{1/T_1 - 1/T_2}, \tag{21}$$

$$\alpha = RT\frac{\ln(\dot{\varepsilon}_2/\dot{\varepsilon}_1)}{\Delta t_m} \quad \text{and} \tag{22}$$

$$Q_0 = Q(t_m) + \alpha t_m, \tag{23}$$

where $\dot{\varepsilon}_1$ and $\dot{\varepsilon}_2$ are creep rates before and after a jump in temperature $\Delta T = T_2 - T_1$ (at constant stress) or in stress Δt_m (at constant temperature). Equation (21) is used to determine the parameter $Q(t_m)$, and then (20) yields

$$(\ln \dot{\varepsilon}_0)_{\varepsilon,T} = \ln \dot{\varepsilon} + Q(t_m)/RT. \tag{24}$$

The main point here is the possibility to determine the small changes of creep rate $\dot{\varepsilon}$ using ultra-small changes in the strain (e.g., 0.005–0.01% only) in the jump of $\Delta T = 3$–$5°C$ or $\Delta t_m \ll 0.1 t_m$. It allowed the condition of invariability in polymer structure and dynamics during the test. Under these conditions, the parameters Q_0, α and $\dot{\varepsilon}_0$ in (20) may be regarded as real values inherent to any given "point" of the creep process. The criterion of constancy of the polymer structure during the measurement is the reversibility of creep rate $\dot{\varepsilon}$ after a reverse jump, Δt_m or ΔT. A typical interferogram before and after jump in stress is shown in Fig. 66.

Thus, we assumed that all three kinetic parameters of deformation in (20), Q_0, α, and $\dot{\varepsilon}_0$, are changeable, being the functions of temperature, strain, and stress.

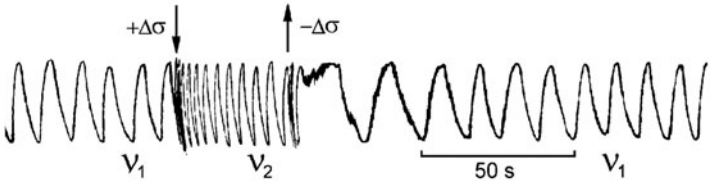

Fig. 66 Typical interferogram of creep recorded during a stress jump $\Delta\sigma$. One oscillation represents the strain of 0.3 μm (0.005%)

However, using the LICRM setup allows them to be constant in each separate measurement due to very small changes in temperature or stress (strain).

Below we consider the results of our systematic research of deformation kinetics for glassy polymers over the wide ranges of temperatures and deformations, using the laser-interferometric technique under consideration [11, 278, 280–287]. This research allowed us (1) to study the dependencies of kinetic parameters of creep on these factors, (2) to reveal the regular relations between the activation parameters of polymer creep, (3) to demonstrate their intimate connection with the parameters of relaxation transitions, and (4) to confirm directly the intermolecular physical nature of potential barriers of polymer "plasticity."

4.2 Activation Parameters of Creep as ÃČ Function of Deformation Value

As was shown schematically in Fig. 5, the precise measurements by the LICRM instrument of $\dot{\varepsilon} = f(\varepsilon)$ dependence at constant t_m and T show that creep rate $\dot{\varepsilon}$ varies continuously with increasing strain; $\dot{\varepsilon}$ is minimum at the deformation ε_y corresponding to the yield stress σ_y in the stress–strain curve. The activation parameters of deformation cited in the literature basically relate only to the region of steady-state creep with a relatively constant rate. Meantime, our studies showed that the values of Q_0, α, and $\dot{\varepsilon}_0$ are not the constants of a polymer material even at constant temperature, changing in the course of the deformation process.

Figure 67 shows the creep rate value and creep kinetic parameters vs total deformation plots obtained for poly(methyl methacrylate) (PMMA) and PVC. For these and other glassy polymers studied, the values of $Q(t_m)$, Q_0, α, and $\dot{\varepsilon}_0$ determined from the various points of the creep curves were found to depend on the strain value in a similar way. At constant stress and temperature, these parameters reach their maximum values at deformation ε_y; thereafter they decrease, and their changes become insignificant at $\varepsilon > 10$–15%. Over the range $\varepsilon = 20$–40%, the value of activation volume α remains constant, while the activation energy Q_0 decreases slightly.

The values of $Q_{0.}$ and α obtained for seven glassy polymers at $\varepsilon = \varepsilon_y$ and $\varepsilon = 20\%$ are given in Table 8. At $\varepsilon \gg \varepsilon_y$, energy $Q_{0.}$ substantially decreases, obviously due to the structural changes and changes in molecular packing in polymers. Figure 67b shows that pre-straining of PVC lowers the "peak" values of $Q_{0.}$ and α at point ε_y, down to the total disappearance of maxima.

Thus, creep of glassy polymers cannot be described by (20) with invariable values of the coefficients Q_0, α, and $\dot{\varepsilon}_0$, but the similarity of the $\alpha(\varepsilon)$, $Q_0(\varepsilon)$ and $\lg\dot{\varepsilon}_0(\varepsilon)$ curves is observed that presumes their interrelationship and the integral nature of the potential barrier $Q_{0.}$

It has been assumed that the barrier Q_0 includes a number of "elementary" energy barriers q_i, overcome by a deformation kinetic unit equal to or at least commensurable with α in its volume. Without considering specific deformation models, we considered a unit event of a creep process as a displacement (transfer)

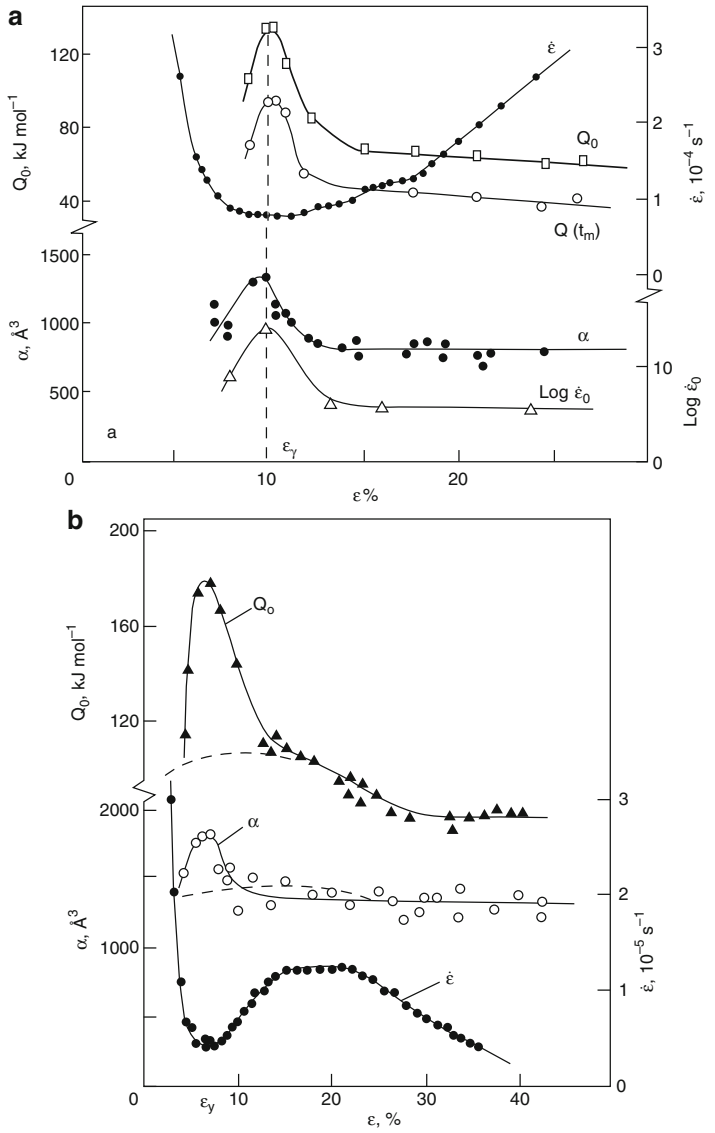

Fig. 67 Strain dependencies of the creep rates and kinetic parameters obtained in compression at 20°C for PMMA, σ=90 MPa (**a**) and at tension for PVC, σ=50 MPa (**b**) [11]. The *dashed curves* relate to pre-strained samples

of a macromolecular segment (or a few neighboring segments), equal in volume to $\alpha = mV$, over the potential barrier $Q_0 = \sum q_i = mq_i$ [281, 282]. Here, $V = M/\rho N_A$ is the volume of one monomer unit, m is the number of monomer units per kinetic unit of deformation, M is the molecular weight of monomer unit, ρ is the density of polymer, and N_A is Avogadro constant, respectively. The energy barrier q_i is a partial contribution to the creep barrier Q_0, being related to one monomer unit.

Table 8 Activation parameters of creep at 20°C and their relationship to the cohesion energy in glassy polymers [11]

Polymer	Activation energy Q_0 (kJ mol^{-1})		Activation volume α, ^{3}		Volume of monomer unit V, A^3	Number of monomer units $m = a/V$		$q_i = Q_0/m$ (kJ mol^{-1})		$E_{coh}/3$ (kJ mol^{-1}) [288–290]
	$\varepsilon = \varepsilon_y$	$\varepsilon = 20\%$	$\varepsilon = \varepsilon_y$	$\varepsilon = 20\%$		$\varepsilon = \varepsilon_y$	$\varepsilon = 20\%$	$\varepsilon = \varepsilon_y$	$\varepsilon = 20\%$	
PVB	143	75	2,240	1,550	163	14	10	10	7.5	9–11
PMMA	134	67	1,340	840	155	9	6	14	11	10–11
PS	134	75	1,400	1,120	166	9	7	15	11	10–13
PVC	167	105	1,800	1,400	73	25	19	7	5	4–7
PC	252	109	2,700	1,680	363	7	5	33	24	21–29
PAN	210	–	1,400	–	75	19	–	11	–	10–11
PET	278	–	2,800	–	240	12	–	23	–	17–24

Table 8 shows, together with the kinetic characteristics, the values of $m = \alpha/V$ and $q_i = Q_0/m$ calculated from the experimental data obtained for glassy polymers at 20°C for the deformation $\varepsilon = \varepsilon_y$, when the initial polymer structure remains basically undamaged by shear, and for $\varepsilon = 20\%$, i.e., in the "cold flow" range. The decreased q_i values are observed in the latter case for all polymers.

If the initial assumptions were correct, the partial barrier q_i should be determined by the chemical structure of a monomer unit and depend on the IMI barriers, that is, the cohesion energy E_{coh} as the characteristics of IMI related to one mole of monomer units. As known, E_{coh} is the energy required to break all intermolecular contacts of a small molecule or chain repeat unit with its environment. According to Eyring [109], for low-molecular weight substances the effective intermolecular barrier to motion (flow) of molecule in the medium of the same molecules is equal to $E_f \cong E_{coh}/3$.

Table 8 shows that for polymers strongly differing in chemical structure the barrier q_i coincides with or is close to the value of $E_{coh}/3$. Inelastic deformation of glassy polymers somewhat reduces the IMI energy (see Sect. 4.4); decreasing barriers q_i at $\varepsilon = 20\%$ reflects this process.

These data indicate some similarity between the processes of creep in glassy polymers and flow. The mechanism of the deformation of solid polymers must be more complicated [271–275]; however, overcoming of IMI barriers is the main point in the different models of deformation processes.

4.3 Temperature Dependencies of Creep Activation Parameters and Their Connection with Relaxation Transitions

The LICRM setups have also been used for studying deformation kinetics of polymers over a wide temperature range [278, 280–287]. Large variability in the kinetic parameters with temperature was observed, although the potential barriers of IMI in every glassy polymer may vary only slightly within the glassy state. Analysis of

these experimental results is of great interest for (1) the q_i problem and (2) studying the connection between deformation kinetics and relaxation transitions in glassy polymers.

Figure 68 shows the experimental Q_0, m, $\log \dot{\varepsilon}_0$, and q_i values vs temperature dependencies obtained for PVC and PC at $\varepsilon = 20\%$, whereas Fig. 69 presents the $Q_0(T)$, $m(T)$, and $q_i(T)$ plots for PMMA.

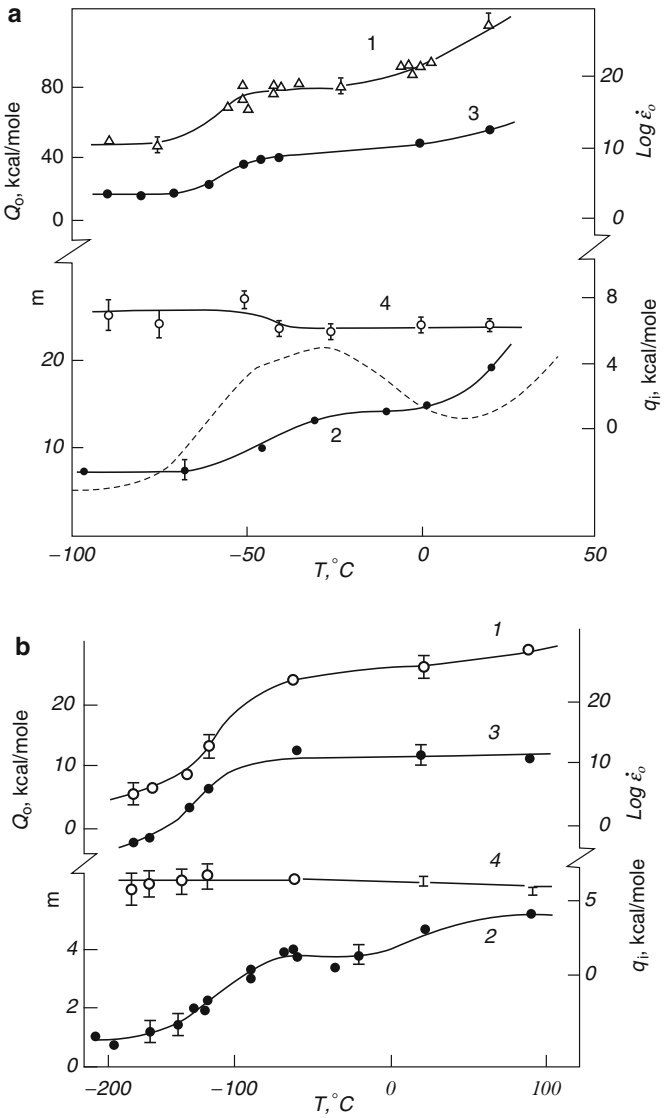

Fig. 68 Temperature dependencies of the creep activation parameters, Q_0 (1), $\mathrm{m} = \alpha/V$ (2), $\log \dot{\varepsilon}_0$ (3), and partial energy barrier q_i (4), obtained at tension for PVC (**a**) and PC (**b**) at $\varepsilon = 20\%$ [11, 282, 283]. *The dashed line* in (**a**) shows the PVC mechanical loss spectral contour (1 Hz)

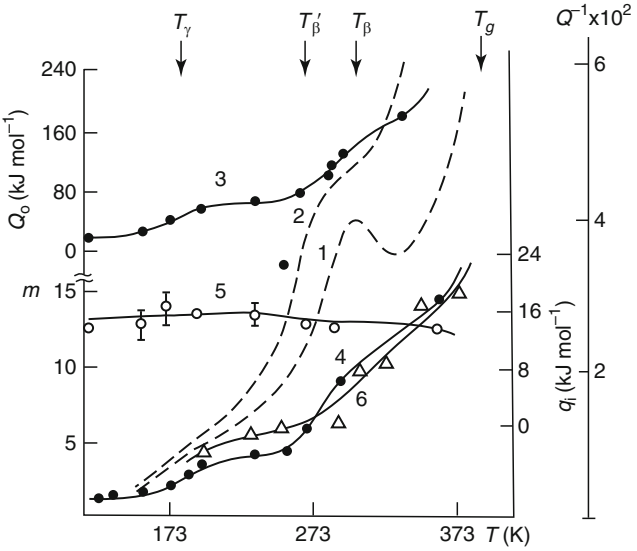

Fig. 69 PMMA: temperature dependencies of the creep activation parameters, Q_0 (3), $\mathrm{m} = \alpha/V$ (4), and partial energy barrier q_i (5) obtained in tension, $\varepsilon = 20\%$. In addition, the mechanical loss spectra (internal friction Q^{-1}, 1 Hz), obtained without (1) and under static shear stress $t_\mathrm{m} = 25\,\mathrm{MPa}$ (2), and the activation volumes of relaxation processes calculated therefrom (6) are shown [11,94]

One can see that kinetic parameters of deformation change strongly with temperature and in a symbatic way. The curves exhibit the regions of slight changes in the parameters and the temperature intervals of their substantial changing. Generally, the parameters increase over the range from 100–120 K to T_g by several times, at the limit by an order of magnitude. Similar regularities were observed also for the other glassy polymers. At the same time, the partial barriers $q_\mathrm{i} \approx E_\mathrm{coh}/3$ remain almost invariable, within the limits of accuracy of their determination of 10–15%, throughout the whole temperature range of the glassy state of polymers (Figs. 68 and 69). Only a small tendency for q_i to decrease with increasing temperature was observed that reflected slight decreasing IMI, as estimated in particular by IR spectroscopy [291].

Figure 70 shows the common relationship between a partial barrier q_i and a cohesion energy E_coh obtained from our creep experiments (at $\varepsilon > \varepsilon_\mathrm{y}$) for 14 polymers with very different chemical structures, when varying E_coh value up to 30 times. One can see that all data fit satisfactorily to a linear dependence between q_i and E_coh:

$$q_\mathrm{i} = (0.3 \div 0.4)\, E_\mathrm{coh}. \tag{25}$$

Remarkably, this relation turned out to be valid for the deformation ("cold flow") of solid amorphous and semi-crystalline polymers, both isotropic and slightly drawn ones, as well as at any temperature below T_g. The values of kinetic parameters,

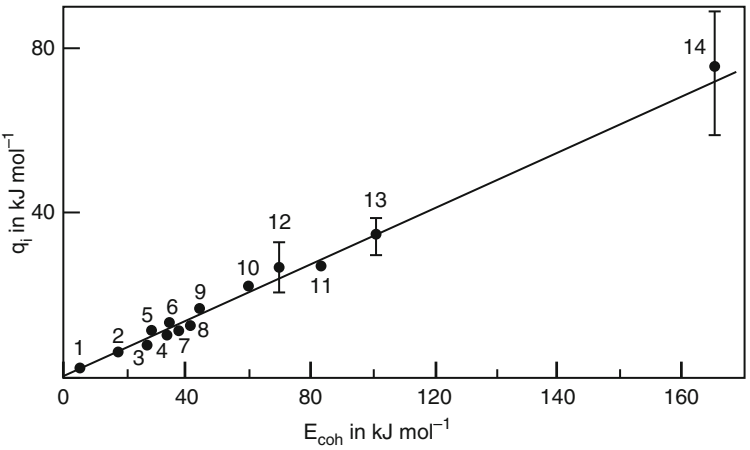

Fig. 70 Relationship between partial energy barrier to creep q_i and the cohesion energy E_{coh} [11]: PE (1); PVC (2); PVB (3); PAN (4); PS (5); PMMA (6); PS-*co*-MAA (84/16) (7); PS-*co*-MAA (67/33) (8); PS-*co*-MAA (40/60) (9); PET (10); PC (11); ebonite (12); epoxy resin I (13); epoxy resin II (14)

found in tension and compression tests, might differ to some extent but the barrier q_i also remained practically invariable over the broad temperature region [11].

This fundamental result certainly indicates the intermolecular nature of the energy barrier to deformation in glassy polymers. An additional experimental corroboration of this viewpoint was obtained in the study of a series of poly(styrene-*co*-methacrylic acid) (PS-*co*-MAA) polymers with regularly varied IMI (Sect. 4.4).

Thus, the above data enable us to conclude that, irrespective of the choice of a specific model for polymer deformation, this process for glassy polymers is associated mainly with surmounting of IMI barriers. The activation barrier of deformation to be overcome is governed by the IMI and the scale of the kinetic units under the given conditions, that is,

$$Q_0 \cong \frac{\alpha(T,\varepsilon)}{V} q_i \cong m(T,\varepsilon)\, E_{coh}/3. \tag{26}$$

As indicated above, the deformability of solid polymers varies with temperature in a step-like manner due to the abrupt changes in the nature of a dominant type of molecular motion in the regions of the relaxation transitions. Similarly, Figs. 68 and 69 show that the most substantial changes in the kinetic parameters of deformation with temperature occur in the temperature regions of sub-T_g (β and γ) relaxations and then in the vicinity of T_g ("intermediate relaxations" region). This is obvious when comparing the kinetic curves obtained for PVC and PMMA with their mechanical loss spectra (see the broad β-peak for PVC, γ and β-relaxations around −100°C and 20 °C for PMMA in Figs. 68a and 69, respectively). For PC, the large step in the plots in Fig. 68b also corresponds to unfreezing mobility within

Table 9 Comparison of activation energies and activation volumes for sub-T_g relaxations (Q_β, Q_γ, m_β, m_γ) and for creep within the same temperature regions (Q_0, m) in glassy polymers

	Kuhn segment size		β-Relaxation region				γ-Relaxation region			
			Q_β	Q_0	m_β	m	Q_γ	Q_0	m_γ	m
Polymer	N_k monomer units	V_k nm^3	kJ mol^{-1}		monomer units		kJ mol^{-1}		monomer units	
PVC	12	0.8	60–65	50–80	12	10–13	–	–	–	–
PC	2	0.7	45–52	42–70	2	2–3	–	–	–	–
PMMA	6	0.9	85	80–120	6	5–8	43	45–70	2–3	2–3

the β-relaxation region extending from about −150°C to −50°C. If the β-transition is associated with the rotational motion within a Kuhn segment, the γ-relaxation in PMMA corresponds to localized torsional motions involving two or three neighboring monomer units in chain [23, 101].

Table 9 demonstrates the "genetic" conformity between the kinetic parameters of sub-T_g relaxations in polymers and the parameters of deformation kinetics within approximately same temperature regions; not only the activation energies but also the activation volumes could be compared. The latter became possible owing to the development of the technique for DMA of statically loaded solids [DMA(σ) method] [91–94]. This allowed us to register the effects of mechanical activation of mobility in glassy polymers (Figs. 17 and 69) and to estimate, on this basis, the effective activation volumes of relaxation processes [92,94]. The latter are represented for three polymers in Table 9 as a number of monomer units (m_β, m_γ) forming these volumes.

Table 9 shows the satisfactory agreement between the activation parameters of deformation and relaxation transitions. Thus, the activation volumes of both processes coincide in the temperature region of β-relaxation with Kuhn segment volume: $m = m_\beta = N_k$. For PMMA, the main contribution to creep kinetics below −100°C is provided by small-scale kinetic units ($m = 1$ and $Q_0 = 10$–$15\,\mathrm{kJ\,mol^{-1}}$) that corresponds to low-temperature δ-relaxation, namely, liberation of a monomer unit in PMMA [23, 99]. At $T > T_\beta$, approaching T_g, the kinetic parameters of deformation increase by a factor of 3. Curves 4 and 6 in Fig. 69 show that an m vs T plot practically repeats the plot of the activation volumes of the relaxation processes over the entire temperature range studied.

Thus, the main contribution to the kinetics of deformation of glassy polymers is provided by molecular motions prevailing in the given temperature region or corresponding to the nearest relaxation transition, due to stress activation of the part of the relaxation time spectrum that is located just above the temperature of the deformation experiment.

Let us stress once more that, irrespective of the specific solid-state deformation model used [271–275, 292], the values of creep activation parameters in polymers are interconnected and depend on the degree of deformation and temperature. Their changes are related in a regular manner to structural alterations in polymers and to their spectra of molecular motions. Due to the changeability of deformation kinetic

parameters, (20) must be represented in the form

$$\dot{\varepsilon} = \dot{\varepsilon}_0(T,\varepsilon)\exp\left[-\frac{Q_0(T,\varepsilon)-\alpha(T,\varepsilon)t_m}{RT}\right]. \quad (27)$$

4.4 Well-defined Changes in Intermolecular Interactions and Potential Barriers to Deformation

As was postulated many years ago [293, 294], deformation of glassy polymers involves overcoming the barriers of inter- and intramolecular interactions; the dominant role of the former has also been assumed in the specific models [271–275,292]. However, the Q_0 values obtained for polymer deformation were typically much higher than the energy of a single "intermolecular bond" or an internal rotation barrier. Moreover, the activation energies of the processes associated with breaking of chemical bonds in chains, namely, of mechanical fracture or thermal degradation, were of the same order of magnitude as for creep processes.

The kinetic data presented above, especially the interrelationship between the deformation kinetic parameters and the approximate equality $q_i \cong E_{coh}/3$, testify in favor of the decisive contribution of IMI to the potential barriers of polymer deformation. Nevertheless, the additional, direct experimental information regarding the connection between IMI behavior and deformation kinetics was needed to come to the final conclusions on the physical nature of Q_0.

This problem has been resolved in two ways.

First, the combined DSC, IRS, and mechanical approaches were employed to study the relation between the resistance to deformation and the changes in a system of intermolecular bonds, energetic state (enthalpy changes), and chain conformation at various stages of deformation in glassy polymers [295–300]. As a result, the direct correlations between the polymer resistance to deformation and the energy of IMI, E_{IMI}, were confirmed.

Second, the study of deformation kinetics was performed, using the LICRM setup, for a series of "model" polymers with the regularly varied and reliably controlled IMI characteristics; that allowed the determination in parallel of the changes in kinetic parameter q_i and energy E_{IMI} [283]. The experiments were performed for PS, PVC, and a series of amorphous copolymers of styrene with different contents of methacrylic acid (PS-*co*-MAA). The latter contained 2, 5, 10, 16, 26, 33, or 60 mol% MAA creating double hydrogen bonds as strong intermolecular crosslinks with the energy $E_H = 38\,\mathrm{kJ\,mol^{-1}}$; their real content and changing with deformation could be determined experimentally.

It was shown that deformations $\varepsilon < 50$–100% led, like an intense quenching, to an increase in the internal energy (enthalpy change $\Delta H > 0$). This "stored energy" was measured by DSC. The values of ΔH themselves, however, did not indicate the basic factor that caused the energy state of the polymers to change. A priori, this could be due to three reasons, namely (1) a change in molecular packing and

E_{IMI}, (2) a change in the intramolecular energy at the expense of conformational trans–gauche (T–G) transitions or distortion of the valence angles and bonds, and (3) because of breaking chemical bonds.

Combined using DSC and IRS for studying changes in PS and PS-*co*-MAA allowed us to estimate these contributions to ΔH and to decipher the nature of the changes in the enthalpy of glassy polymers caused by pre-straining or quenching [295–297]; in particular, the process of mechanical dissociation (breaking) and restoration of hydrogen bonds was revealed and studied in detail. It was shown that the enthalpy change ΔH in pre-strained glassy polymers was associated practically entirely with the changes in IMI, and DSC could serve as the method of quantitative estimation of the character and value of the changes in IMI in glassy polymers [296].

Figure 71 shows the typical changes in resistance to deformation, energetic state, segmental mobility, and conformational characteristics of amorphous PS as a function of its pre-straining on compression at 20°C. The drop in the stress–strain curve for annealed PS begins from the yield point $\varepsilon_y = 5$–7% whereas at $\varepsilon > 15\%$ the resistance to deformation changes only slightly. The conformational composition of PS is barely affected by the transition through yield point (curve 6); a small trend of growth in the *TTTT*-isomer content (542 cm^{-1}) is observed only at $\varepsilon = 40$–60%. At the same time, the shape of the stress–strain curve correlates totally with the changes in enthalpy/IMI: increasing enthalpy (internal energy) (curve 3) and mobility (curve 5) in pre-strained PS are determined by decreasing IMI (curve 4) with deformation.

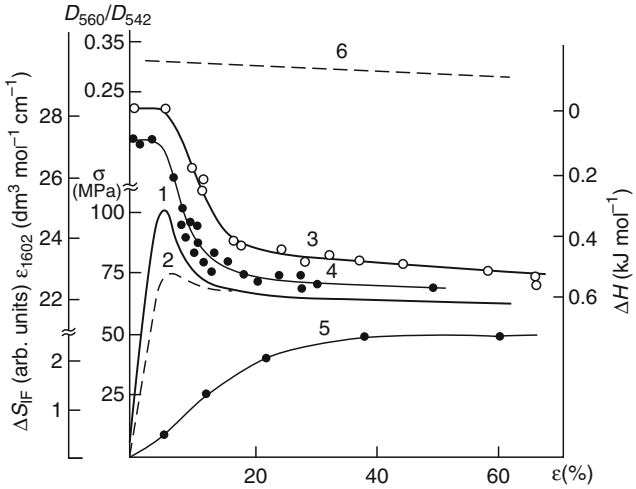

Fig. 71 Polystyrene: the changes in resistance to deformation (σ), energetic state (ΔH) and IR spectral characteristics as a function of pre-straining on compression at 20°C [15]: (1) the stress–strain curve for annealed samples; (2) ditto for quenched samples; (3) enthalpy increment ΔH (DSC); (4) the extinction coefficient ε_{1602} of the IR band of deformation vibrations of the benzene rings at 1,602 cm^{-1} as a measure of universal IMI; (5) increment in mechanical loss (internal friction) ΔS_{IF}; (6) the ratio of optical densities of the IR bands at 560 and 542 cm^{-1} as a criteria of changes in the conformational composition

Consequently, the resistance of PS to deformation at the different stages of this process is controlled, really, with the potential barriers of IMI.

The similar correlations were found also for PS-*co*-MAA samples [298]. The common energy E_{IMI} in these copolymers was estimated as the sum of universal van der Waals, $E_{UN,}$ and specific IMI (hydrogen bonding, E_H) in the initial annealed samples and pre-strained or quenched samples. Total breaking of intermolecular H-bonds or their partial breaking with transformation of double H-bonds into single ones during the deformation process were registered by the IR spectra. On this basis, the specific energy parameter E_H was determined [295, 298] as

$$E_H = 38\omega\beta_2 + 19\omega\beta_1, \tag{28}$$

where ω is the mole fraction of MAA units in these copolymers, while β_2 and β_1 are the relative fractions of MAA units joined by double or single hydrogen bonds with the energies of 38 and 19 kJ mol^{-1}, respectively. The effective energy of universal interactions in the copolymers studied was determined as

$$E_{UN} = E_{coh}^{PS}(1-\omega)/3 + E_{coh}^{PMAA}\omega\beta_0/3, \tag{29}$$

where β_0 is a relative fraction of MAA units free from hydrogen bonding, and $E_{coh}{}^{PS}$ and $E_{coh}{}^{PMAA}$ are the cohesion energies of PS and poly(methacryl acid).

Figure 72 shows the dependence of the yield stress on the common IMI energy (E_{IMI}) in these model polymers (a), and relative decrease in the resistance to

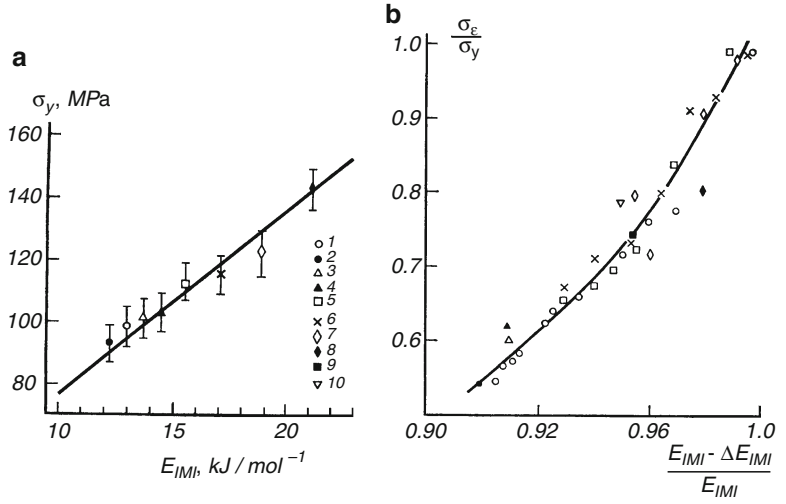

Fig. 72 The dependencies of the yield stress at 20 °C (**a**) and relative decrease in the resistance to deformation due to pre-straining or quenching (**b**) on the effective IMI or its change, respectively, in annealed PS (1), PS-*co*-MAA with 2 (2), 5 (3), 10 (4), 16 (5), 26 (6), 33 (7), 60 mol % MAA (8), and in quenched PS (9) and PS-*co*-MAA with 16 mol% MAA (10) [298]

Table 10 Kinetic parameters of creep and effective energy of intermolecular interactions in PS and PS-co-MAA at 20°C [283]

Polymer	α, [3]	m	Q_0 kJ mol^{-1}	$q_i = Q_0/m$	E_{IMI} [298]	$E_{IMI}m$
PS	1,400/1,120	9/7	130/84	15/12	13/12	117/84
PS-*co*-MAA (95/5)	1,400/1,120	9/7	130/84	15/12	13/12	117/84
PS-*co*-MAA (84/16)	1,820/1,330	11/8	176/92	16/12	15/14	165/112
PS-*co*-MAA (67/33)	1,820/1,120	12/7	200/101	17/14	18/18	216/126
PS-*co*-MAA (40/60)	1,250/950	9/7	164/122	18/18	21/20	189/140

Note: The values of Q_0, α, m, q_i and E_{IMI} are given for $\varepsilon_y = 6$–7% in numerator and for $\varepsilon = 15\%$ in denominator. E_{IMI} and $E_{IMI}m$ values are given in kJ mol^{-1}

deformation for pre-strained or quenched polymers as a function of relative decrease in E_{IMI} (b). Again, a regular growth of the yield stress with increasing E_{IMI} is observed. The distinct correlation between a degree of lowering of both resistance to deformation and IMI energy in the course of deformation is also registered.

Table 10 compares the creep kinetic information and IMI characteristics for PS and several PS-*co*-MAA polymers. Again, increasing IMI (MAA content in copolymers) led, simultaneously, to increasing both the barrier q_i and the energy E_{IMI}. Moreover, the q_i values turned out to be rather close by their magnitudes to the E_{IMI} values, and $Q_0 \cong E_{IMI}m$, with the accuracy of 10–20%.

Thus, all experimental data and relationships, obtained by the laser-interferometric technique combined with DSC and IRS, confirmed the complicated behavior of deformation kinetics in polymers as well as its direct connection with the spectra of molecular motions and the intermolecular potential barriers.

5 Jump-Like Creep on the Submicro-, Micro-, and Meso-scale Levels and Morphology in Polymer Systems

Solids of different classes, including polymers, are characterized typically with a complex non-uniform structure on various morphological levels and the presence of different local defects. The theoretical approaches describe the deformation of solid polymers via local defects in the form of dislocations (or "dislocation analogies") and disclinations, or in terms of dislocation-disclination models even for non-crystalline polymers [271–275, 292]. In principle, this presumes the localized character and jump-like evolution of polymer deformation at various levels. Meantime, the structural heterogeneity and localized microdeformation processes revealed in solids by microscopic or diffraction methods, could not be discerned typically in the mechanical (stress–strain or creep) curves obtained by the traditional techniques. This supports the idea of deformation as a monotonic process with a smoothly varying rate. Creep process has been investigated in the numerous studies in terms of average rates (steady-state creep). For polymers, as the exclusion,

non-monotonic development of deformation was observed for PET crystallizing under stretching [301], or small-scale jumps in stress at deformation of thin polymer films were observed [302]. Additionally, shear bands are typically observed at deformation of glassy polymers.

It may be presumed, a priori, that the above-mentioned contradiction can be resolved and jump-like evolution of polymer deformation may be revealed in the case of (a) sharp improvement of the sensitivity and resolution of the method for creep rate measurements, and (b) coherent occurrence of many elementary micro-shear events (their cooperative or simultaneous manifestation) leading to observable jump-like creep.

In fact, the laser-interferometric technique allowed us to clarify this situation. New possibilities for high-precise measurement of creep rates at any "point" of the process, on the deformation increment of 300 nm (one beat in the interferogram) or even 150 nm (half a beat), made it possible to study creep on the submicro-, micro-, and meso-scale levels. This allowed us to reveal and study in detail the jump-like nature of polymer creep as the general phenomenon [11, 303–321]. The simultaneous development of several jump levels in creep, from submicro- to a hundred micron-scale, was also registered. Some regularities in the characteristics of jump-like creep were found: the amplitude and sharpness of the deformation jumps changed in a regular way in the course of creep. Moreover, the direct connections between the parameters of jumps and the sizes of structural micro-heterogeneities were shown for some polymer systems.

5.1 *Discontinuous Creep of Amorphous Polymers at Different Stages of the Process*

Figure 73 illustrates the jump-like creep process by the interferograms obtained for amorphous polymers and the scheme of stepped deformation. Two parameters were introduced to characterize the stepwise creep: (1) deformation increment L corresponding to the period of creep rate variation (the height of the step in the scheme) and (2) the ratio h of the maximum ($\dot{\varepsilon}_{\max}$) to minimum ($\dot{\varepsilon}_{\min}$) creep rates within the same step L, i.e., jump sharpness. In some cases, the mean value

$$h = \frac{\sum_{i=1}^{n} \dot{\varepsilon}_{\max} / \dot{\varepsilon}_{\min}}{n} \tag{30}$$

was determined, where a number of consecutive periods $n = 5 - 10$ was typically used for a calculation.

It was revealed that both parameters of jump-like creep typically changed with development of the deformation process. The deformation steps L of submicro-, micro-, and meso-scale sizes could be observed in polymers and composites depending on material composition and the deformation stage. It was found that the

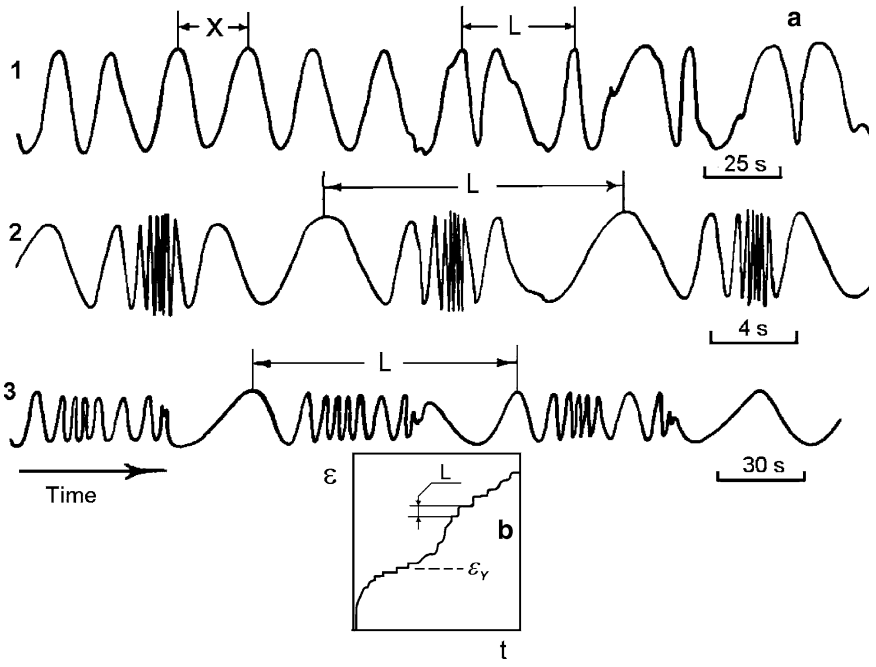

Fig. 73 Typical interferograms (**a**) and a scheme of the stepwise (jump-like) creep (**b**) in amorphous polymers [11, 321]. One oscillation (beat) corresponds to an increase of deformation on compression by 0.3 µm (usually 0.005%), and the creep rate $\dot{\varepsilon}$ is determined by the beat frequency 1/x

strain step L values measured at deformations close to their yield points turned out to be in direct relation to the activation volumes of deformation ($L \sim \alpha$) under the same conditions[321].

Despite some h scattering, the reproducible regularities for the $h(\varepsilon)$ plots were observed. Generally, h value changed with increasing deformation and was maximal (1) at the start of the "flow" stage (destroying the initial structure of the system of intermolecular bonds), i.e., in the vicinity of the yield strain ε_y in isotropic polymers, or (2) prior to fracture in oriented polymers (Figs. 74 and 75). Creep rate variation was observed even at the first stage of creep before reaching the yield point; this shows directly that micro-plasticity contributes to the polymer deformation, even in the quasi-elastic region.

The peculiarities of jump-like creep at different stages of deformation may be illustrated, for instance, for PDMS networks and PDMS–silica nanocomposites with 40 wt% SiO_2 [319] studied at room temperature (above T_g). These nanocomposites were synthesized in situ as described elsewhere [266]. The silica domains formed had a diameter of about 10 nm.

Because of the rubber-like state of the materials studied, the main deformation is developed during loading, and creep rate rapidly decreases. Figure 76 shows the "fragments" of the creep rate vs tension deformation plots obtained for PDMS and

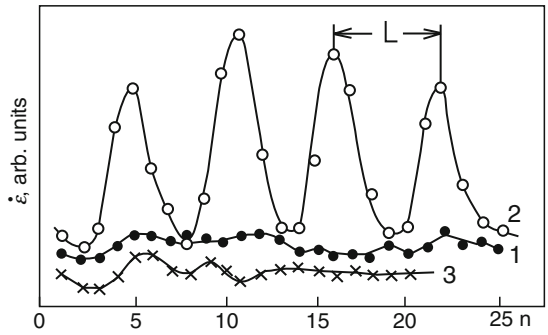

Fig. 74 Variation of the creep rate within the narrow ranges of strains for PC at different stages of deformation process (compression, 20°C) [304]: (1) $\varepsilon = 7.3\%$, (2) yield point $\varepsilon_y = 10.3\%$, and (3) $\varepsilon = 37\%$. Here n is a number of beats in the interferograms where one beat corresponds to strain increment of 0.3 µm

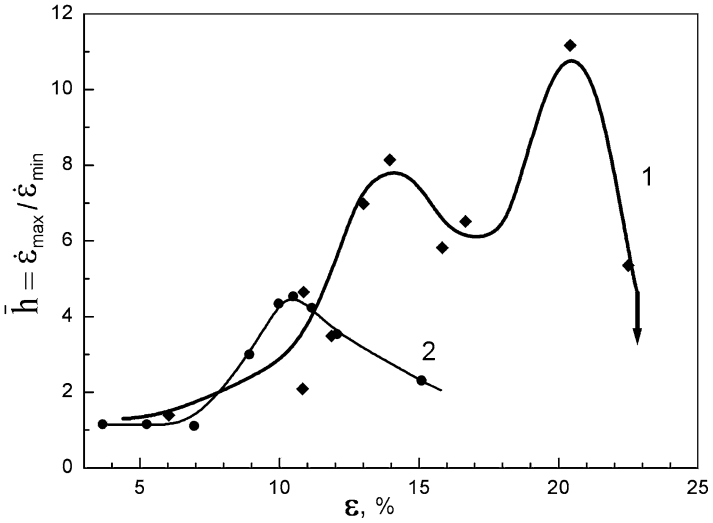

Fig. 75 Strain dependence of jump sharpness parameter h: (1) for isotropic PMMA in the vicinity of the yield point, at compressive stress of 70 MPa, 20°C [309]; (2) for oriented PE monofilaments, at tensile stress of 0.4 GPa, 20°C [316]. The *arrow* indicates the moment of fracture

PDMS–silica nanocomposite within the narrow strain intervals but at different deformation values. Each experimental point in these curves refers to a deformation increment of 0.3 µm. One can see the jump-like development of creep and, simultaneously, very different plots in Fig. 76a–d depending on sample composition and deformation stage.

Figure 76 shows that deformation jumps L can be divided into two groups, L_{min} and L_{max}. Their values and maximal amplitudes of creep rate jumps h_{max} are presented in Table 11. The smallest deformation jumps $L_{min} \sim 1$ µm are typical of both PDMS and nanocomposite being slightly higher only for the larger deformations. The picture changes, however, for the nanocomposite. At first, h_{max} values strongly increase (Fig. 76b), and then, with increasing deformation, the small deformation jumps are united into the coarse ones when L_{max} steps may attain 50 µm (Fig. 76c,d, Table 11). The variety, greater sharpness, and the more complex shape

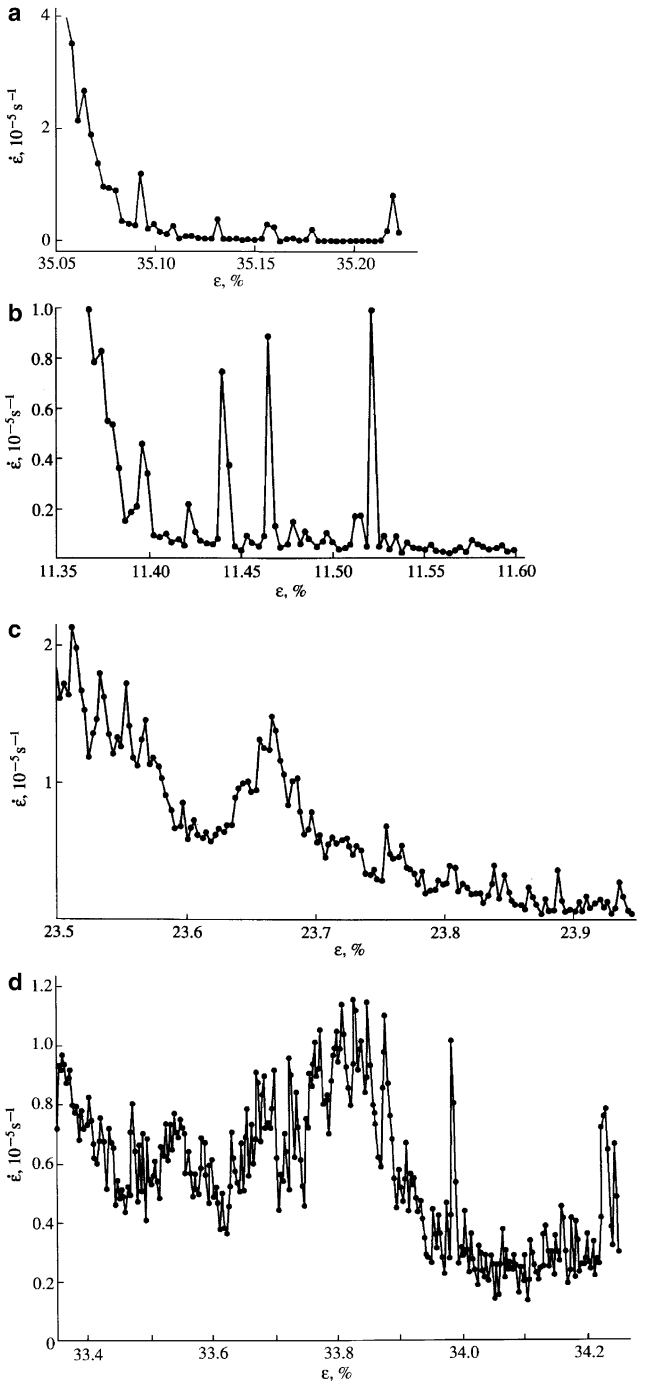

Fig. 76 Variation of the creep rate as a function of tensile strain for (**a**) neat PDMS, $\sigma = 0.15$ MPa, and for (**b–d**) PDMS–silica nanocomposite with 40 wt% SiO_2 at (**b**) $\sigma = 0.2$ MPa, (**c**) $\sigma = 0.35$ MPa, and (**d**) $\sigma = 0.55$ MPa [319]. Each point corresponds to deformation increment of 0.3 μm

Table 11 Parameters of creep jumps at different stages of the process (upon tension at 20°C) for PDMS network and PDMS-silica nanocomposite [319]

Sample	σ (MPa)	ε (%)	Average values of L_{min} (μm)	L_{max} (μm)	h_{max}
PDMS	0.15	35	0.9	1.2	3
PDMS–silica composite	0.20	11.3	1.0	1.5	10
	0.35	23.4	1.25	9	3
	0.55	33.6	1.8	50	7

of deformation jumps of micro- and meso-scale sizes in the nanocomposite could be attributed to shears not only in polymer matrix but also (perhaps basically) at polymer–silica interfaces, i.e., in the interfacial nanolayers manifesting the restricted mobility [266]. The formation of microcracks at interfaces could also contribute, to some extent, to the complication of jump-like creep picture. Anyway, the data obtained for the nanocomposite reflected, obviously, the morphological and dynamic heterogeneities in this system.

The interesting result of changing the activation parameters of creep within a micro-scale deformation jump in glassy polymers is noteworthy [12]. It was supposed that the variation of creep rate over the deformation step L in the jump-like creep process was determined by changing the activation barriers within microvolumes, and it is the cause of the stepped character of deformation. The high accuracy of the laser-interferometric method allowed us to estimate the parameters Q_0, α and q in two points of a deformation jump (period L). It was revealed that the potential barriers to creep changed within a micro-scale deformation increment. The higher creep rates in a deformation jump corresponded to the lower values of activation energy Q_0 but to the larger activation volumes α. As a result, parameter q, characterizing the IMI energy per one monomer unit, substantially decreased in a step L. Additionally, it turned out that parameter q for the macroprocess of steady-state creep was close by its magnitude to the q value for the stage of the easiest slip with increased rate in a deformation jump [12].

5.2 Creep Rate Variability and Interfibrillar Slippage in Oriented Polymers

Highly oriented flexible-chain polymers, in particular ultrahigh-molecular-weight polyethylene (UHMWPE) fibers prepared by gel spinning process, as suggested by Smith and Lemstra [322], exhibit the extremely high mechanical strength and modulus of elasticity rather close to the theoretical estimates. At the same time, these fibers reveal decreased creep resistance which substantially restricts their application potential.

When using gel spinning and other techniques for preparing fibers, a very complicated hierarchy of their supermolecular structures is generated. First, microfibrillar

units are typical of oriented materials. They consist of crystalline and disordered regions alternating along their long axes. Microfibrils are connected by tie molecules and, as a rule, aggregate into macrofibrils. Such complicated morphology implies inevitably the manifestation of a few deformation modes operating simultaneously in a mechanical field. The most frequently considered modes of inelastic deformation of oriented polymers are intracrystalline slip, conformational *gauche–trans* (*G–T*) transitions, or chain scissions. At the same time, the interfibrillar slippage is rarely taken into account, although it was shown that this process occurs, being most pronounced in gel-spun UHMWPE fibers, owing to a weak connection between fibrillar units [323, 324].

In the series of publications [312–318], the laser-interferometric method has been successfully used for oriented polymers (basically PE), and it has been shown that creep developed non-uniformly in oriented PE. These studies were aimed at (a) gaining new information on establishing the true creep mechanism of highly oriented fibers and films, (b) revealing the correlations between creep at micro/meso-scale levels and fibrillar structure, and (c) searching a proper route for enhancing such long-term mechanical property of highly oriented fibers as creep resistance.

In study [316], a series of the gel-spun UHMWPE fibers of the various draw ratios, with crystallinities of 55–81% and modulus varying from 38 to 131 GPa, were investigated. Three typical levels of deformation jumps could be distinguished: of 2–10 μm (L_1), a few tens of microns (L_2), and of about 100 μm (L_3) in size. The deformation steps of various magnitudes were observed for all filaments tested but more clearly for those of higher draw ratio. The larger deformation jumps were formed from micro-scale jumps. Creep rate variability parameter h, characterizing the creep jump sharpness, increased with strain and then decreased again before fiber rupture (Fig. 75).

This phenomenon was discussed in terms of the possible direct correlations between stepwise creep and fiber morphology, namely, of micro-shear displacements of various fibrillar elements in a stick-slip mode. It was shown that the fibrillar units were weakly connected and loosely packed in these fibers; interfibrillar regions contained pores and a small number of tie molecules. The length of microfibrils has been estimated to be microns, whereas the length of macrofibrils reached 100 μm and more. These sizes correlate satisfactorily with the observed deformation steps. Of course, this approach (slippage of fibrils upon creep) did not exclude the participation of the intracrystalline slip events and the process of scission of overstressed interfibrillar tie molecules in jump-like creep. Submicro- and microcrack formation could also contribute, to some extent, to creep heterogeneity and the total deformation of fibers [314].

To obtain further information on the role of interfibrillar slippage in creep of oriented polymers, LI technique was used in studying of oriented UHMWPE samples with various connectedness of fibrils, namely, of melt-crystallized and solution-cast films drawn to various degrees, as well as of modified samples [313, 315]. The fibrils in melt-crystallized films were interconnected by a larger amount of molecules. In addition, increasing the interfibrillar interaction was attained using two methods: (1) removing low molecular weight fractions and (2) chemical cross-linking.

It was found that the jumps of creep rate strongly depended on the type of oriented UHMWPE sample. Again, the deformation jumps of various values (microns, tens and hundred microns) were observed, and the large jumps were formed from the smaller ones. Both procedures, increasing the interfibrillar interactions, resulted in reduction of creep rate variability. Moreover, the number of large deformation jumps L_3 reduced with increasing interfibrillar interactions. Thus, it was shown that the size distribution of the deformation jumps appeared to be controlled by the structure of interfibrillar regions, and interfibrillar slippage contribution was indeed predominant. The deformation jumps come, obviously, from a coherent (cooperative or simultaneous) slippage of individual microfibrils, their aggregates, or microfibrillar layers.

Figure 77 demonstrates different creep behavior in the narrow deformation intervals for ultimately drawn flexible-chain and rigid-chain polymers, melt-crystallized and gel-cast UHMWPE films, and poly(paraphenylene terephthalamide) (PPTA) fibers (Kevlar 49, DuPont). Tensile stresses equal to a half of fracture stress σ_F were applied. Total deformation to break was equal to 25%, 13%, and 1.32%, respectively, in these samples. To see better a difference in the development of creep process in the investigated polymers, the inserts in Fig. 77 are presented for very narrow deformation intervals.

Creep of UHMWPE occurs in a jump-like manner, accelerating and decelerating periodically. The deviations from the average creep rates may be as large as an order of magnitude and more frequent and impressive for melt-crystallized films than for gel-cast UHMWPE films. The small- and intermediate-scale deformation periods (creep jumps) of about 10 and 50–70 μm were typically revealed in both melt-crystallized and gel-cast films; however, the largest creep jumps of 100 μm and more in size occurred only in the melt-crystallized oriented films. The difference in creep behavior of these UHMWPE films was explained in terms of different internal structure of the microfibrils and, especially, their connectivity with each other. The stepwise creep in the UHMWPE samples was attributed to stick-slip displacement of fibrils along each other (interfibrillar slippage). In addition, separate molecules and even whole fibrils could be ruptured in the course of creep; this could be derived from the SEM observation of kink band generation.

Unlike UHMWPE, creep in Kevlar 49 occurred monotonically (Fig. 77c). No marked inhomogeneity in a creep rate is detected in this case. The average level of creep rates is less by two orders of magnitude than that in UHMWPE (see insert). Strong interactions between rigid chain macromolecules and formation of ribbon-shape, very densely packed fibrils in these fibers prevented, obviously, interfibrillar slippage and, therefore, creep jumps were absent in this case. No kinks were generated also during creep experiments in Kevlar fibers [318]. The absence of jump-like creep for rigid-chain polymer evidences, additionally, that the creep rate variation is not caused by the methodological reasons (scattering, noise, etc.).

The above experimental data, including the established correlation between creep rate variations and structural heterogeneity, gave a better insight into the creep mechanism in highly oriented flexible-chain semi-crystalline polymers and allowed to propose a route for improving UHMWPE creep resistance. Generally, creep of these

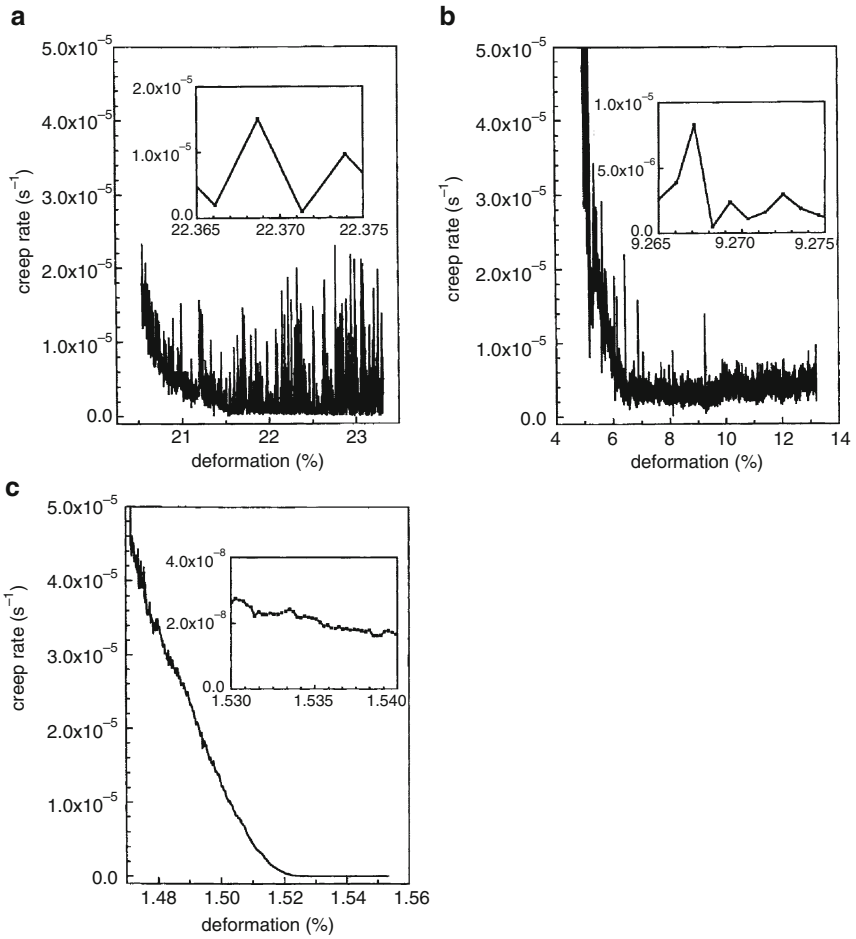

Fig. 77 Creep rate vs deformation for (**a**) UHMWPE melt-crystallized film (draw ratio $\lambda = 7.3$, $\sigma = 0.5\,\sigma_F = 0.32\,\text{GPa}$), (**b**) UHMWPE gel-cast film ($\lambda = 119, \sigma = 0.5\,\sigma_F = 1.58\,\text{GPa}$), and (**c**) Kevlar 49 fiber ($\sigma = 0.5\,\sigma_F = 3.15\,\text{GPa}$) [318]

fibers may be controlled, presumably, by slip motion of separate macromolecules through the crystallites and via slippage of microfibrils along one another. If the second mechanism more contributes to slip, interfibrillar chemical crosslinks should be generated to increase a creep resistance. Really, the experiments with cross-linked PE show their smallest variability in creep rates and the improved creep resistance.

Highly oriented gel-crystallized UHMWPE fibers contain macrofibrils whose length reaches tens and hundreds of microns as aggregates of microfibrils of micrometer length; macrofibrilles form layers separated by longitudinal voids of submicron and micron scale [312]. Figure 78a shows that the creep jumps with deformation steps of 1–10 and about 100 microns are observed in this case. In fact, meso-jumps are formed from micro-jumps similar to formation of macrofibrils from

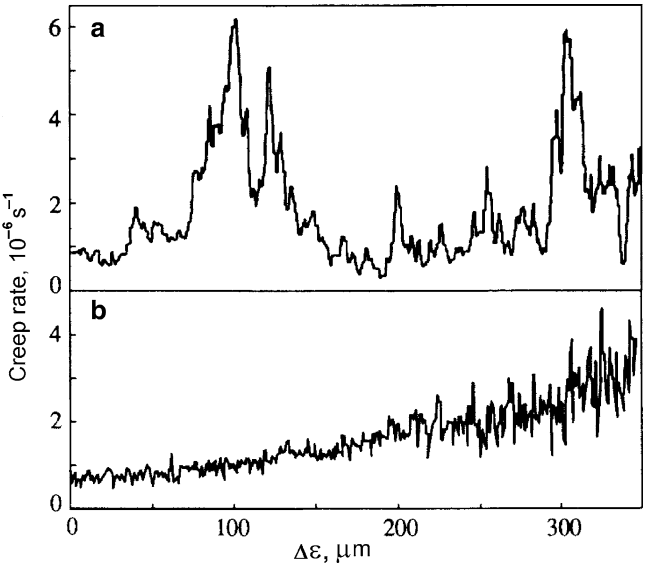

Fig. 78 Dependence of the creep rate (at $\varepsilon \sim 2\%$ on the creep increment: (**a**) for oriented gel-crystallized UHMWPE fibers with draw ratio $\lambda = 45$ (creep rate jumps of large strain periods $L \sim 100\mu m$ are observed), and (**b**) for the same fibers chemically modified for generating crosslinks between fibrils (the large strain periods are absent) [313]

microfibrils. In the work [313], the same fibers were impregnated with the special agent (trichloroethylene) followed by UV irradiation for generating crosslinks between the fibrils. Agent molecules could not penetrate inside the fibrils for steric reasons. This means that crosslinks could be formed only between the molecular segments located on the surface of neighboring fibrils; the grafting also occurred there. Figure 78b shows that cross-linking resulted in suppression of intermacrofibrillar slippage since large deformation steps disappeared. In addition, the deformation, which may be as high as 15% in non-crosslinked fibers, sharply decreased after cross-linking.

Jump-like creep was also studied for UHMWPE films with intentionally varied structural organization of interfaces between fibrils at the expense of their different preparation (gel-casting, crystallization from the melt), various draw ratios λ (from 7 to 119), and the special cross-linking of fibrils [315,317]. The fibrils were weakly connected and loosely packed, weakly tied but closely packed, or cross-linked by long molecular segments or connected by short crosslinks, in these samples. As a result, absolutely different jump-like creep rate vs deformation curves and jump sharpness parameter h vs strain dependencies were obtained for these "model" samples with different interfacial structures. Short interfibrillar crosslinks provided the largest effect on creep behavior. Creep occurred basically through shear of fibrillar structural units relative to one another in an "acceleration-deceleration" way; deceleration was due to slip resistance by some "stoppers."

The above results evidence the controlling role of interfibrillar slippage for creep properties of UHMWPE fibers.

5.3 *Controlled Structural Heterogeneities of Micro-scale Sizes in Polymers vs Micro-plasticity Jumps Correlations*

Of special interest are the results of studying jump-like creep on the micro-scale level when the controlled structural heterogeneities of the same sizes are present in polymers, namely, for epoxy networks with a globular structure [311], for epoxy composites containing diabase microparticles [310], for POM plastics with different spherulite sizes [320], and for PI–graphite composites [320]. These materials can be considered as models for checking up the micro-plasticity vs structure correlations. It was possible to compare directly the sizes of heterogeneities (solid microparticles or densely packed micro-domains of polymers) with the creep micro-jumps, and to draw the conclusions about their interrelationship.

In [320], jump-like creep was studied for two POM semi-crystalline polymers. Analysis of their polarizing microscope images showed that homoPOM contained predominantly spherulites 1–5 μm in diameter, whereas poly(oxymethylene-*co*-oxyethylene) (95POM/5POE) sample contained both the same small spherulites and larger ones, up to 25 μm in diameter. It might be supposed that the size of these more dense structural units will be reflected in the character of variation of the creep rate and the values of deformation jumps L. Then the loosely packed inter-spherulite boundaries could be considered presumably as the most probable points for local shear displacements (micro-plasticity).

The results obtained are given in Fig. 79 and Table 12 where the sizes of deformation jumps, including the smallest jumps L_{min}, the moderate jumps L_m, and the largest jumps L_{max}, are presented for several macro-strains; the latter were chosen to prevent essential distortions (breaking) of the initial structure of samples. The L_{min}

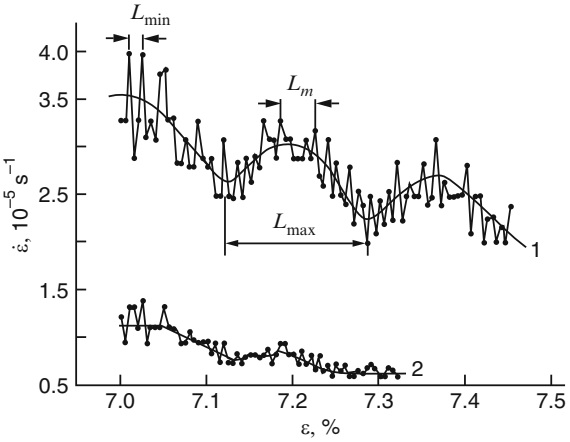

Fig. 79 Variation of creep rate within the narrow range of strains for poly(oxymethylene-*co*-oxyethylene) (95POM/5POE) (1) and homoPOM (2) [320]. Points were registered in 0.3μm deformation increments. $T = 20°C$, compressive stress $\sigma = 70$ MPa

Table 12 The values of micro-scale creep jumps L at different deformations ε for two semi-crystalline samples with different spherulite sizes ($T = 20°C$, compressive stress $\sigma = 70$ MPa) [320]

Poly(oxymethylene) (POM) (spherulite size of 1–5 μm)				Poly(oxymethylene-*co*-oxyethylene) (95POM/5POE) (spherulite size of 1–25 μm)			
ε (%)	L_{min} (μm)	L_m (μm)	L_{max} (μm)	ε (%)	L_{min} (μm)	L_m (μm)	L_{max} (μm)
2	0.77	1.5	3.3	2.5	1.0	1.8	3.9
		1.5	3.9			2.1	4.8
							6.6
5.6	0.82	2.7	3.9	4.2	0.85	3.3	12
		2.7	3.9			3.9	5.7
		2.1				3.0	6.0
		1.8				4.8	
7.0	1.0	1.8	4.8	8.5	1.0	3.6	7.8
		1.8	5.7			4.5	11.1
		2.7	5.7			4.5	10.8
		2.7					
12	0.93	1.5	5.7	10.5	1.23	4.5	15.6
		1.8	4.8			4.5	9.6
		1.8	4.3			3.6	25.5
		3.6	5.7			4.8	7.2
						4.8	8.4

values were determined as mean of the seven creep rate periods, whereas L_m, and L_{max} values corresponded to single deformation jumps. Figure 79 shows that small-scale periodic variations are combined into the larger deformation jumps, and the largest ones are composed of the smallest and moderate jumps. More pronounced variation of the creep rate is observed for the copolymer.

It follows from Table 12 that the smallest deformation jumps L_{min} are approximately equal to each other for both polymers ($\sim$1 μm) but the deformation jumps L_m and L_{max} for the copolymer are larger, on average, than those for homopolymer. The jumps L_m and L_{max} also exhibit a tendency towards an increase as the creep strain increases. For homopolymer, the L_m and L_{max} values were less than 6 μm, i.e., the deformation jumps of $\sim$1–5 μm corresponded to spherulite sizes in this polymer. The larger jumps $L_{max} = 6$–25 μm were observed for copolymer, and their appearance corresponded, obviously, to the presence of spherulites of the same scale in this sample.

The found coincidence of deformation micro-jumps in creep with the sizes of spherulites may be associated with the fact that creep occurs initially preferably through micro-shears along the boundaries of spherulites. Of course, at larger strains the transformation of the structure can result in the manifestation of new structural units and another deformation jumps on the meso-scale level.

Similar structure vs jump-like creep correlations were revealed for neat epoxy network [310, 311] and for the composite based thereon and filled with diabase particles of 5–10 μm size (weight ratio of both components was 1:1) [310]. Electron

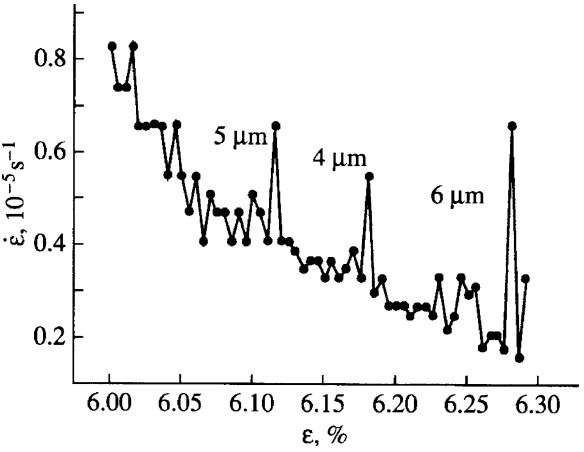

Fig. 80 Variation of creep rate within the narrow range of strains for the epoxy composite with diabase particles of 5–10 μm in size (weight ratio of 1:1). $T = 20°C$, compressive stress $\sigma = 60$ MPa. The values of large period L of creep rate variation are indicated [310]

microscope images showed that the epoxy network had the globular structure, and more densely packed globules with different sizes, from 0.2 to about 1 μm, could be discerned. Variation in creep rate at the submicro- and micro-scale levels was observed, and the deformation jumps L varied from 0.4 to 1.6 μm, i.e., practically coincided with globular sizes.

The other information was obtained for the epoxy-diabase composite. Figure 80 shows that, together with the small deformation jumps equal to 0.6–1.2 μm in size, peculiar to neat epoxy matrix, the larger periodic variations of creep rate arose with $L = 4$–6 μm. These deformation jumps were associated, undoubtedly, with the diabase particles of the same size. The presence of solid diabase micro-particles introduced a new heterogeneity level into the structure. The increased microshears could occur due to weaker interfacial polymer layers and breaking adhesion between polymer and diabase.

The most remarkable result has been obtained when comparing the plots for creep rate in the narrow ranges of deformation for amorphous PI and graphite-containing composite based thereon [320]. These high-performance materials with $T_g = 400°C$ (Vespel®, DuPont) were produced by powder metallurgy techniques (see Sect. 3.6.2). Figure 81c shows the SEM micrograph of this composite with graphite particles 5–10 μm in size. Rather good mixing of PI and graphite powders might be attained during preparation of the composite.

Figure 81 demonstrates variation of creep rate within the narrow ranges of strains for neat PI and its composite. For neat PI with the complicated supermolecular structure (different local molecular packing, the presence of mesophases, etc.) the periods and amplitudes of creep rate variations (L and h parameters) are changeable (Fig. 81a); creep rate jumps h did not exceed mainly 2–3. The microregions of $\sim$0.6–1.0 μm size with different molecular packing densities may result in such creep rate–strain plots.

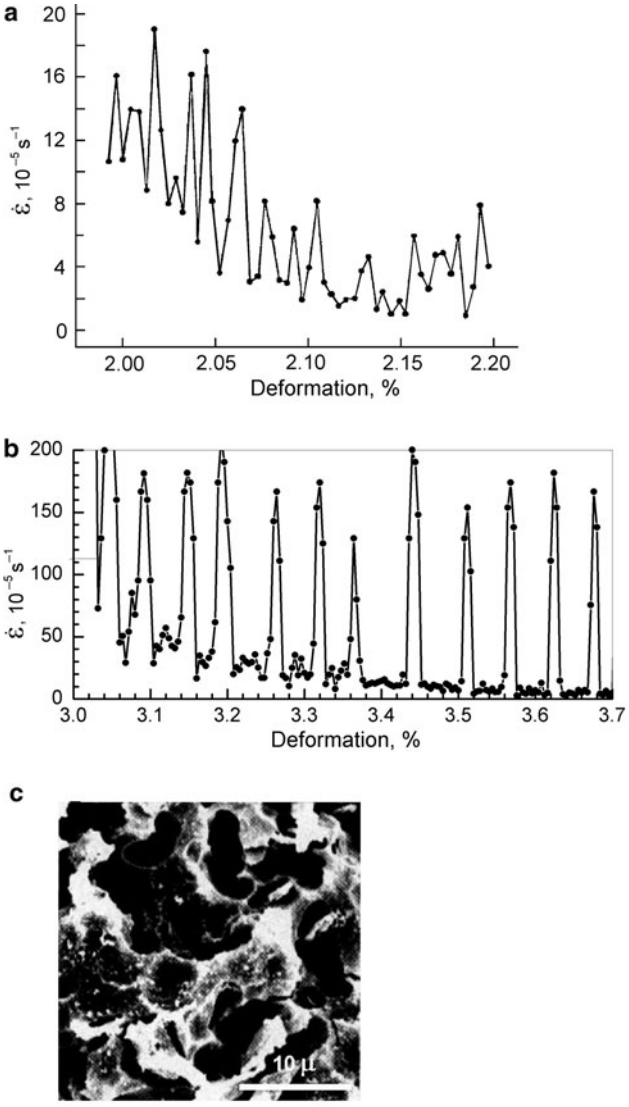

Fig. 81 Variation of creep rate within the narrow range of strains for the neat amorphous polyimide (Vespel ®, DuPont) (**a**) and for the same polyimide filled with graphite micro-particles (**b**) [320]. $T = 327°C$, compressive stress $\sigma = 20$ MPa. In (**c**), SEM micrograph of the etched cut surface of graphite-containing sample is shown. Black graphite particles of about 5 ± 2 μm in size are seen

The plot dramatically changes for PI–graphite composite. This composite can be considered as the model material in which crystalline graphite particles of approximately the same size with the sharp boundaries (interfaces) were relatively regularly distributed throughout the matrix. Figure 81b shows two peculiarities of the plot

obtained for this composite. First, in addition to small creep rate jumps, very strong jumps are observed where creep rate changes (increases and then again decreases) by many times, e.g., from 5–10 to $200 \times 10^{-5}\,s^{-1}$. Second, under these experimental conditions (the temperature 327°C was not far from the onset of PI glass transition), periodical variations of creep rate with large amplitude became regular: the value of deformation step in each jump was practically invariable and equal to about 4 μm, being close to the size of graphite particles. It was concluded that these steps and the relevant large jumps in creep rate could be caused by overcoming the barriers to adhesive PI–graphite interactions.

Thus, the experiments with model polymer materials confirm the idea that the deformation jumps in creep on the micro- or meso-levels are controlled, to a large extent, by material structure and correspond approximately, by their magnitudes, to the sizes of structural heterogeneities.

6 Other CRS Applications

6.1 Detection of Fine Changes in Relaxation Dynamics of Polymers Caused by Different Treatments

High CRS sensitivity allowed registering not only the essential but also fine changes in the structure and dynamics of materials caused by any external influences.

Figure 8 (Sect. 2.2) illustrated the CRS superiority in resolution to the DMA and TSDC techniques for characterization of low-temperature dynamics in PC. Additionally, this figure showed that the cyclic thermal treatment of PC at low temperatures resulted in the substantial changes in the CR spectrum. These changes included the overall increasing of creep rates, displacement of the peaks to lower temperatures, and the redistribution of their intensities.

Another example of high sensitivity and discrete character of CR spectra in the characterization of fine changes in a polymer material is the impact of slight pre-straining or quenching on semi-crystalline POM. Figure 82 shows the spectra obtained under compression, demonstrating the influence of such treatments. Due to very complex morphology of POM [22], the complicated CR spectra are characteristic of this polymer. The better separation of CR peaks is observed under compression in this case than in the spectra obtained under tension (compare with Fig. 11). Peak displacements by 5–20 K and some redistribution of the peak intensities take place with the substitution of tension by compression. In addition, peaks at 120 and 420 K appear in the compression experiments. The peak at 120 K may be related to small-angle torsion vibrations of short chain sections typical of γ-relaxation [23]. The CR peak at 420 K, located close to the onset of the melting range, is associated with unfreezing the most constrained dynamics modes in the disordered regions, due to the onset of softening of rigid constraints (lamellae surface or the thinnest crystallites). Nevertheless, the spectra, obtained under compression, manifest nearly the same set

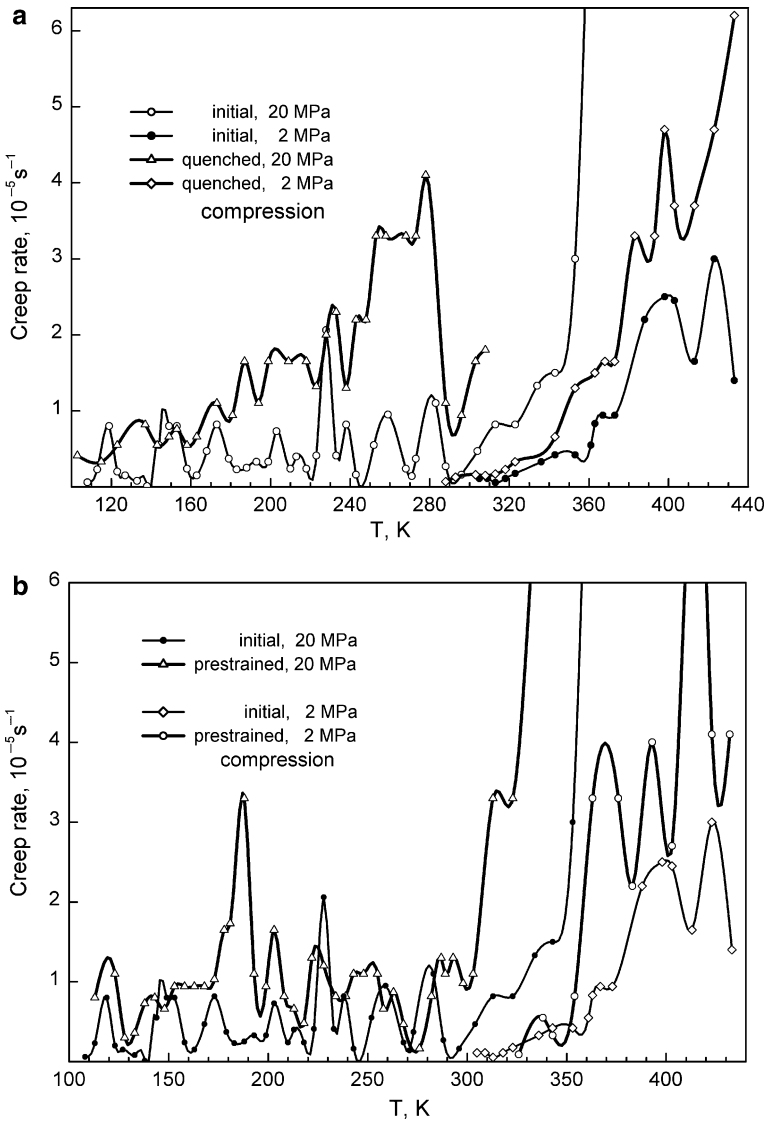

Fig. 82 Creep rate spectra of POM obtained under compression for the samples in the initial aged state and after their quenching from 423 K into liquid nitrogen before the measurements (**a**), or after compressive pre-straining at 20°C with immediate cooling down to 110 K with the rate of 2.5 K min^{-1} (total deformation 17%, residual deformation 8%) (**b**) [21]

of peaks as found in the tension tests, namely, at 150–160, 170–180, 200, 230, 260, 280, 320–340, ∼370, and 400 K. Thus, changing the kind of loading affects the resultant CR spectrum to some extent; however, the basic features of a CR spectrum remain.

Figure 82a shows large changes in the POM spectrum caused by quenching of solid polymer from 423 K into liquid nitrogen. One can see a general rise of mobility when the majority of peaks above 160 K increased in height, but the most pronounced changes occurred at 250–280 K. This implies a more distinct manifestation of cooperative glass transition (T_g).

Figure 82b shows the considerable influence of small compressive pre-straining of POM (residual deformation 8% only) on the CR spectrum. Pre-straining resulted, obviously, in a certain disturbance of initial structure, with loosening segmental packing, since an increase in the intensities of a few peaks, especially of the peak at 180–190 K and the basic peaks above 300 K, is observed.

Creep rate spectroscopy technique was successfully applied also to the study of changes in creep characteristics of polymers being subjected, preliminarily, to small doses of γ-irradiation [325, 326].

6.2 *Impact of a Static Magnetic Field on Creep in Diamagnetic Glassy Polymers*

The effect of constant magnetic field on the properties of diamagnetic polymer materials is well-known as the factor resulting in the orientation of molecules due to the anisotropy of the diamagnetic susceptibility χ of polymer chains. However, the magnetic treatment is performed typically for polymers in the liquid state or in the softening region. It has been assumed that the effects of magnetic field are absent or negligibly small for glassy polymers due to much longer relaxation times of segmental motion in polymers at temperatures $T \ll T_g$.

In [305, 306, 311, 327], the effects of a static magnetic field (2 or 4 kOe) on creep processes at room temperature in linear and cross-linked glassy polymers (basically within or close to the β-relaxation region) were revealed and studied on the microscopic level. This became possible owing to using the LICRM setup and decrease in the relaxation times of dynamic processes in solid polymers under the action of mechanical forces.

The moderate magnetic fields affected creep differently, basically increasing mobility and accelerating creep, presumably due to the change in the potentials of IMI. The changes in polymer mobility were caused by action of the magnetic field similarly to that after slight mechanical orientation at temperatures much below T_g. In both cases, some loosening of molecular packing took place. Additionally, creep characteristics of glassy polymers could be modified by their prolonged holding in the constant magnetic field, e.g., at 4 kOe for 30 days; this effect retained to some extent even after removal of the field. Interestingly, for glassy PMMA the optical anisotropy was manifested in the magnetic field; this effect varied with the time of action of the magnetic field and gradually decreased and disappeared after its removal [307].

The constant magnetic field affected not only the mean creep rate but also the jump-like character of deformation on the micro-scale level. It was shown

[305,306,311,327] that the parameters of periodic variations in the deformation and creep rate (parameters h and L) substantially decreased at deformation in a magnetic field. The reaction of discontinuous creep in glassy polymers to a magnetic field (h changing) was in the satisfactory correspondence with their magnetic susceptibilities [307]. Taking into account that the jump size in creep on the micron-scale level is associated with the size of structural inhomogeneities (Sect. 5.3), the conclusion was drawn that the magnetic field destroyed, to some extent, the structural aggregates (e.g., globules in epoxy and polyester networks) with their transformation into the smaller units in the course of deformation on the micro-scale level.

6.3 *Non-destructive Tool for the Prediction of Temperature Anomalies in the Mechanical Behavior of Polymeric Materials*

Since CR spectra respond in a discrete manner to unfreezing of different segmental motion modes, the correlations between the spectrum and temperature peculiarities ("anomalies") in the mechanical behavior of polymers could be expected. CRS can be the non-destructive method for the prediction of temperature points of changing in the mechanical property-temperature plots. Such points were revealed for the mechanical strength of polymers (PVB, PVC, PMMA, PS, epoxy networks, and others) [328].

Two samples of such correlations are presented in Fig. 83 for PVC and poly(vinyl butyral) (PVB). One or a few bends in the fracture stress σ_F vs T plots are observed at low temperatures $T \ll T_g$ for these polymers. A single CR peak at ~180 K in PVB corresponds to the onset of a much more intense drop in fracture stress with temperature. More complex CR spectrum in the temperature region of β-relaxation and, simultaneously, three bends in the σ_F vs T plot may be seen for PVC. In this case, a pair of the neighboring creep rate peaks at ~200 and 220 K, and the onset of a new peak form ~250 K are observed instead of a broad β-relaxation mechanical loss peak with maximum at ca. 240 K. The changes in the slope of the σ_F vs T plot occur just at the characteristic temperatures in the CR spectrum of PVC. Similar correlations were also found for PMMA [11], PS [13], and epoxy networks [328].

Consequently, the temperature "anomalies" in strength may be predicted more distinctly from the CRS data than from the DMA ones.

6.4 *Revealing Micro-plasticity and Analysis of Transitions in Brittle Materials*

Unlike the traditional methods of studying plasticity, CRS technique provided the unique possibility to carry out micro-plasticity investigations, with revealing transitions and measuring creep rate spectra, for materials in their brittle and super-brittle states such as ceramics and silicone nitride [329–335], silicate glasses [286], brittle

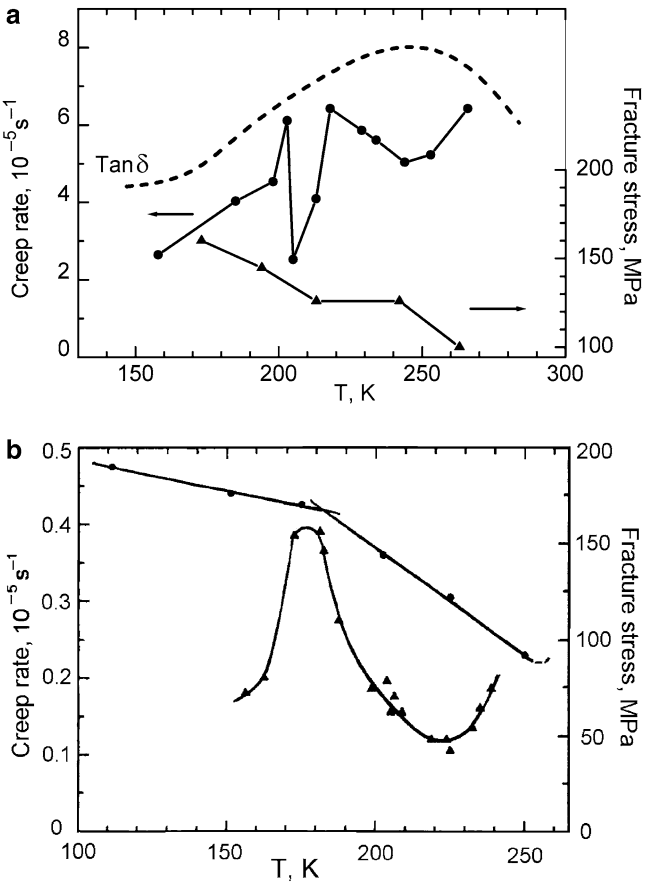

Fig. 83 Creep rate spectra at low temperatures and tensile fracture stress σ_F vs temperature dependencies obtained for PVC (**a**) and PVB (**b**) [328]. The spectra were measured at compressive stress of 23 MPa (**a**) or tensile stress of 28 MPa (**b**). *Dotted line* is a contour of mechanical loss spectrum of PVC at 1 Hz in the β-relaxation region

crystals at moderate and low temperatures [333, 334], or metals at low temperatures [333,336]. Two examples of CRS applications to brittle ceramics are presented below.

In [329, 330], CRS was applied to $YBa_2Cu_30_{7-x}$ ceramics, single-phase and multi-phase, with different grain sizes and oxygen contents. At the maximal oxygen content, ceramics manifested superconducting properties at temperatures below the superconducting transition temperature $T_S = 93$ K. Figure 84 shows the CR spectra over the temperature range from 80 to 300 K for three types of multi-phase ceramics with different oxygen content. Their spectra differ from one another but five peaks are observed in all cases, one of which corresponds to T_S. The peak at room temperature corresponds to antiferromagnetic transition. The T_S peak has the most stable position in the spectra of the ceramics studied, while the temperature positions of the other peaks varied depending on their structure.

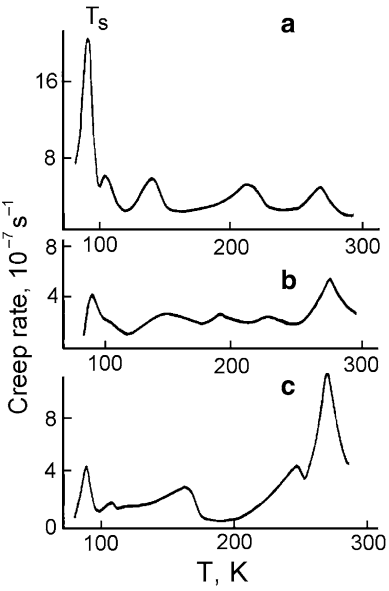

Fig. 84 Creep rate spectra of the Y–Ba_2–Cu_3–O_{7-x} superconducting (**a**) and non-superconducting ceramics (**b, c**) with different oxygen deficit: $O_{6.95}$ (**a**), $O_{6.70}$ (**b**), and $O_{6.20}$ (**c**). Compressive stress 30 MPa [329, 330]

The most remarkable fact is that the highest CR peak at $T_S \sim 90$ K was observed for the superconducting ceramics with the high oxygen content; when the latter decreased, superconducting effect disappeared, and this CR peak sharply reduced as well. In contrast, the CR peak corresponding to antiferromagnetic transition, typical of oxygen deficit in the crystalline lattice [337], became much more intense. Consequently, an electronic state of ceramics affected the creep rate, i.e., CRS allowed one to observe the distinct correlation between electronic processes and micro-plasticity.

Figure 85 shows the CR spectrum (micro-plasticity) of brittle porcelain at low temperatures compared with its fracture stress σ_F vs temperature dependence. One can see that the increased micro-plasticity (creep rates) arising at ca. 200 K in porcelain corresponds to a bend in the $\sigma_F(T)$ plot towards the higher strength values. Such an effect is in accordance with a physical model for brittle fracture [278, 338, 339] that takes the role of micro-plasticity (local shear strains in the loaded brittle solid) into account. The latter results in some relaxation of dangerous local overstresses and, therefore, increasing the strength.

Creep rate spectroscopy was also successfully used as the method allowing one to estimate the ability of steels to be inclined to brittle fracture. The temperature position and height of the CR peak within the range between -60°C and 20 °C was the distinct characteristics of their comparative tendency towards the brittle fracture and was of use for prediction of the critical brittle–ductile transition temperature [336].

At last, for the first time the total kinetic analysis of micro-plasticity ($\varepsilon \sim 0.01\%$) could be performed by means of CRS for silicate glasses over the temperature range from -120°C to 350°C [286].

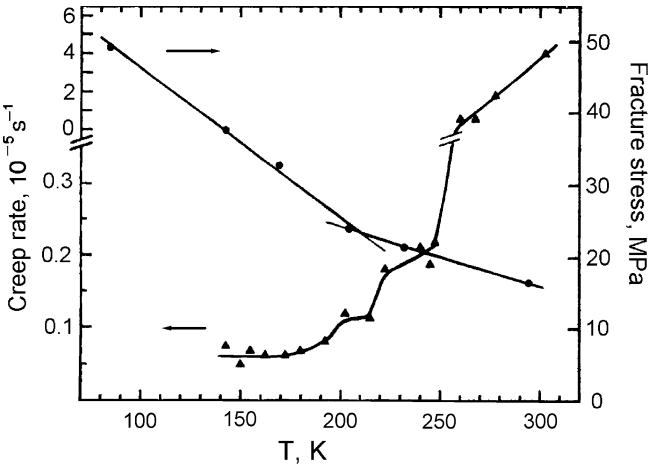

Fig. 85 Porcelain: the creep rate spectrum (compression, $\sigma = 9$ MPa), and fracture stress vs temperature dependence [331]

6.5 Precise Measuring of the Elastic Properties as a Function of Temperature

The laser-interferometric technique provided a convenient route for the precise determination, simultaneously with the measurements of creep rates, of a modulus of elasticity E as a function of temperature T. Such dependencies can be determined directly from the number of oscillations in the interferograms characterizing the deformation value obtained for 1–2 s after loading and using (10).

As an example, Fig. 86 shows the tensile modulus of elasticity E vs temperature T plots, as measured for the 83PU–17PHEMA network and ND-containing composites based thereon (their CR spectra were described in Sects. 3.2 and 3.8). One can see a considerable and various (by a sign and magnitude) influence of small ND additives on the elastic properties of polymer matrix; additionally, these changes are different in the different temperature regions.

The largest effect of increasing nanocomposite modulus is observed in the broad temperature region of PHEMA glass transition, when the E_n/E_0 ratio reaches 3. The modulus changes very differently depending on ND content: the *maximal* effect of increasing modulus is observed at the *minimal* ND content of 0.25 wt%; the effect strongly decreases at introducing 1% and especially 3% NDs. Moreover, in the latter case the modulus became much lower than that of unfilled polymer matrix.

This result became understandable after the AFM analysis of nanocomposites since modulus changes turned out to be in a good accordance with the dispersion state of NDs in the matrix. As indicated in Sect. 3.8, three kinds of ND dispersion/distribution were revealed in this matrix but individual ND particles with 50–100 nm size prevailed and were relatively uniformly distributed only in

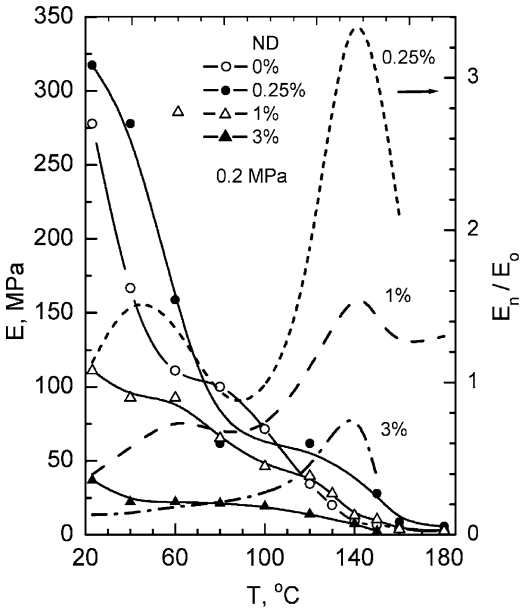

Fig. 86 Modulus of elasticity vs temperature plots obtained using the laser interferometer for the 83PU–17PHEMA hybrid network (E_0) and its nanodiamond (ND)-containing composites (E_n) with 0.25, 1, or 3 wt% ND in the temperature region of PHEMA glass transition [240]. The *interrupted lines* show E_n/E_0 ratios

the nanocomposite with 0.25 wt% NDs. For this reason, the minimal ND content resulted in the largest interfacial area in the composite, increased contribution of interfacial layers and maximal influence of NDs on the matrix modulus.

Acknowledgements The authors gratefully acknowledge the significant contributions which a number of our colleagues from the Ioffe Institute made to the study of the problems considered in this survey. We are grateful to the late Dr. G.S. Pugachev for his leading role in the development of the first LICRM setup. We would also like to express our deep gratitude to Dr. N.N. Peschanskaya, the author of numerous important studies in this field performed for over 30 years. We thank also our other co-authors in some of the CRS studies, Drs. A.B. Sinani, V.A. Marikhin, L.P. Myasnikova, and V.V. Shpeizman. Finally, we are grateful to Dr. V.M. Egorov and Mrs. L.M. Egorova for their long-time fruitful participation in the combined CRS/DSC studies.

References

1. Ready J (1997) Industrial applications of lasers. Academic, New York
2. Halsey D, Raynor W (eds) (2009) Handbook of interferometers: research, technology and applications. Nova Science, Hauppauge, NY
3. Barker LM (1968) In: Berger J (ed) Behavior of dense media under high dynamics pressures. Gordon and Breach, New York
4. Barker LM (1972) Exper Mech 12:209
5. Barker LM, Hollenbach RE (1972) J Appl Phys 43:4669
6. Zlatin NA, Mochalov SM, Pugachev GS, Bragov AM (1974) Phys Solid State 16:1752
7. Zlatin NA, Mochalov SM, Pugachev GS, Bragov AM (1975) Phys Solid State 17:2599
8. Peschanskaya NN, Pugachev GS, Yakushev PN (1977) Polym Mech 2:357

9. Yakushev PN (1980) Mech Compos Mater 1:167
10. Peschanskaya NN, Yakushev PN, Stepanov VA (1984) Phys Solid State 26:729
11. Peschanskaya NN, Yakushev PN, Sinani AB, Bershtein VA (1994) Thermochim Acta 238:429
12. Peschanskaya NN, Yakushev PN (1998) Phys Solid State 40:1486
13. Peschanskaya NN, Yakushev PN, Sinani AB, Bershtein VA (1997) Macromol Symp 119:79
14. Hong J, Brittain JO (1981) J Appl Polym Sci 28:2471
15. Bershtein VA, Egorov VM (1990) Differential scanning calorimetry in physical chemistry of polymers (in Russian). Khimia, Leningrad. Translation: (1994) Differential scanning calorimetry of polymers: physics, chemistry, analysis, technology. Ellis Horwood, New York
16. Graf R, Ewen B, Spiess HW (2007) J Chem Phys 126:041104
17. Arrese-Igor S, Arbe A, Alegria A, Colmenero J, Frick B (2005) J Chem Phys 123:1
18. Fan CF, Cagin T, Shi W, Smith KA (1997) Macromol Theory Simul 6:83
19. Karabanova LV, Sergeeva LM, Svyatyna AV, Yakushev PN, Egorova LM, Ryzhov VA, Bershtein VA (2007) J Polym Sci B Polym Phys 45:963
20. Bershtein VA, Peschanskaya NN, Halary JL, Monnerie L (1999) Polymer 40:6687
21. Bershtein VA, Egorov VM, Egorova LM, Peschanskaya NN, Yakushev PN, Keating MY, Flexman EA, Kassal RJ, Schodt KP (2002) J Macromol Sci Phys 41:797
22. Sukhanova TE, Bershtein VA, Keating MY, Matveeva GN, Vylegzhanina ME, Egorov VM, Peschanskaya NN, Yakushev PN, Flexman E, Greulich S, Sauer B, Schodt K (2004) Macromol Symp 214:135
23. Bershtein VA, Ryzhov VA (1994) Adv Polym Sci 114:43
24. Wunderlich B (2003) Progr Polym Sci 28:383
25. Bershtein VA, Levin VY, Egorova LM, Egorov VM, Zhdanov AA, Slonimsky GL, Rabkina AY, Zavin BG, Gritsenko OI (1987) Vysokomol Soedin A 29:2360
26. Bershtein VA, Levin VY, Egorova LM, Egorov VM, Zhdanov AA, Slonimsky GL, Makarova LL, Martirosov VA (1987) Vysokomol Soedin A 29:2553
27. Bershtein VA, Egorova LM, Ginsburg LI, Kleptsova IT, Egorova EI (1987) Vysokomol Soedin A 29:2564
28. Jackson CL, McKenna GB (1991) J Non-Cryst Solids 131/133:221
29. Jackson CL, McKenna GB (1996) Chem Mater 8:2128
30. Keddie JL, Jones RAL, Cory RA (1994) Europhys Lett 27:59
31. Keddie JL, Jones RAL, Cory RA (1994) Faraday Disc 98:219
32. Wallace WE, van Zanten JH, Wu WL (1995) Phys Rev E 52:R3329
33. Orts WJ, van Zanten JH, Wu WL, Satija SK (1993) Phys Rev Lett 71:867
34. Van Zanten JH, Wallace WE, Wu WL (1996) Phys Rev E 53:R2053
35. Forrest JA, Dalnoki-Verres K, Stevens JR, Dutcher JR (1996) Phys Rev Lett 77:2002
36. Forrest JA, Dalnoki-Veress K, Dutcher JR (1997) Phys Rev E 56:5705
37. Dalnoki-Verres K, Forrest JA, Murray C, Gigault C, Dutcher JA (2001) Phys Rev E 63:031801
38. Pissis P, Daoukakis-Diamanti D, Apekis L, Christodoulides C (1994) J Phys Condens Mater 16:L325
39. Huwe A, Kremer F, Behrens P, Schweiger W (1999) Phys Rev Lett 82:2338
40. Giannelis EP, Krishnamoorti R, Manias E (1999) Adv Polym Sci 138:107
41. Anastaisiadis SH, Karatasos K, Viachos G, Manias E, Giannelis EP (2000) Phys Rev Lett 84:915
42. Vaia RA, Giannelis EP (2001) MRS Bull 26:394
43. Tien YI, Wei KH (2002) J Appl Polym Sci 86:1741
44. Schonhals A, Goering H, Schick Ch (2002) J Non-Cryst Solids 305:140
45. Kuppa V, Manias E (2003) J Chem Phys 118:3421
46. Manias E, Kuppa V (2002) Eur Polym J 8:193
47. Zax DB, Yang DK, Santos RA, Hegemann H, Giannelis EP, Manias E (2000) J Chem Phys 112:2945
48. Kuppa V, Foley TMD, Manias E (2003) Eur Phys J E 12:159
49. Lu H, Nutt S (2003) Macromolecules 36:4010
50. Ellison CJ, Torkelson JM (2003) Nat Mater 2:695

51. De Gennes PG (2000) Eur Phys J E 2:201
52. Alcoutlabi M, McKenna GB (2005) J Phys Condens Matter 17:R461
53. Forrest JA, Dalnoki-Verres K (2001) Adv Colloid Interface Sci 94:161
54. Hrobaricova J, Robert JL, Calberg C, Jerome R, Grandjean J (2004) Langmuir 20:9828
55. Urbanczyk L, Hrobaricova J, Calberg C, Jerome R, Grandjean J (2006) Langmuir 22:4818
56. Xiong J, Zheng Z, Jiang H, Ye S, Wang X (2007) Composites A Appl Sci Manufact 38:132
57. Rittigstein P, Priestley RD, Broadbelt LJ, Torkelson JM (2007) Nat Mater 6:278
58. Blum FD, Young EN, Smith G, Sitton OC (2006) Langmuir 22:4741
59. Metin B, Blum FD (2006) J Chem Phys 125:054707
60. Vignaud G, Bardeau JF, Gibaud A, Grohens Y (2005) Langmuir 21:8601
61. Melnichenko YB, Schuller J, Richert R, Ewen B (1995) J Chem Phys 103:2016
62. Gorbatschow W, Arndt M, Stannarius R, Kremer F (1996) Europhys Lett 35:719
63. Reiter G (1993) Europhys Lett 23:579
64. Jean YC, Zhang R, Cao H, Yuan JP, Huang CM, Nielsen B, Asoka-Kumar P (1997) Phys Rev B 56:R8459
65. DiMaggio GB, Frieze WE, Gidley DW, Zhu M, Hristov HA, Yee AF (1997) Phys Rev Lett 78:1524
66. Milchev A, Binder K (1996) Macromolecules 29:343
67. Starr FW, Schroder TB, Glotzer SC (2002) Macromolecules 35:4481
68. Desai T, Keblinski P, Kumar SK (2007) Polymer 47:722
69. Douglas JF, Schneider HM, Franz P, Lipman R, Granick S (1997) J Phys Condens Matter 9:7699
70. Jones RL, Kumar SK, Ho DL, Briber RM, Russel TP (2001) Macromolecules 34:559
71. Boiko YM, Prud'homme RE (1997) Macromolecules 30:3708
72. McCrum N, Read B, Williams G (1967) Anelastic and dielectric effects in polymeric solids. Wiley, London
73. Johari G (1976) Ann NY Acad Sci 279:117
74. Donth E (1992) Relaxation and thermodynamics in polymers. Glass transition. Academic, Berlin
75. Williams G (1979) Adv Polym Sci 33:59
76. Goldstein M, Johari G (1970) J Phys Chem 74:2034
77. Heijboer J (1977) Int J Polym Mater 6:11
78. Bershtein VA, Egorova LM, Egorov VM, Sinani AB (1989) Vysokomol Soedin B 31:457
79. Gotze W (1991) In: Hansen JP, Levesque D, Zinn-Justin J (eds) Liquids, freezing and the glass transition. North Holland, Amsterdam
80. Sjorgan L, Gotze W (1991) J Non-Cryst Solids 131/133:153
81. Boyer R (1966) (ed) Transitions and relaxations in polymers, Wiley, New York
82. Boyer R (1976) Polymer 17:996
83. Boyer R (1980) J Macromol Sci Phys 18:461
84. Pschorn V, Rossler E, Silescu H, Kaufman S, Schaefer D, Spiess H (1991) Macromolecules 24:398
85. Bershtein VA, Egorov VM, Stepanov VA (1983) Dokl Akad Nauk SSSR 269:627
86. Bershtein VA, Egorov VM, Emelyanov YA, Stepanov VA (1983) Polym Bull 9:98
87. Bershtein VA, Pertsev NA (1984) Acta Polym 35:575
88. Bershtein VA, Egorov VM (1985) Vysokomol Soedin A 27:2440
89. Bershtein VA, Egorov VM, Podolsky AF, Stepanov VA (1985) J Polym Sci Polym Lett 23:371
90. Bershtein VA, Egorov VM, Emelyanov YA (1985) Vysokomol Soedin A 27:2451
91. Bershtein VA, Emelyanov YA, Stepanov VA (1980) Fiz Tverd Tela 22:399
92. Bershtein VA, Emelyanov YA, Stepanov VA (1981) Mekh Compoz Mater 1:9
93. Bershtein VA, Emelyanov YA, Stepanov VA (1983) Glastechn Ber K 56:1142
94. Bershtein VA, Emelyanov YA, Stepanov VA (1984) Vysokomol Soedin A 26:2272
95. Bershtein VA, Ryzhov VA (1985) Dokl Akad Nauk SSSR 284:890
96. Bershtein VA, Ryzhov VA (1984) J Macromol Sci Phys 23:271
97. Bershtein VA, Ryzhov VA, Ganicheva SI, Ginsburg LI (1983) Vysokomol Soedin A 25:1385
98. Ryzhov VA, Bershtein VA (1987) Vysokomol Soedin A 29:1852

99. Ryzhov VA, Bershtein VA (1989) Vysokomol Soedin A 31:451
100. Ryzhov VA, Bershtein VA (1989) Vysokomol Soedin A 31:458
101. Ryzhov VA, Bershtein VA, Sinani AB (1990) Vysokomol Soedin A 32:1385
102. Nikitin VV, Bershtein VA (1990) Vysokomol Soedin A 32:325
103. Bershtein VA, Egorov VM, Egorova LM, Ryzhov VA (1994) Thermochim Acta 238:41
104. Moynihan CT, Easteal AJ, DeBolt MA (1976) J Am Ceram Soc 59:12
105. Donth E (1982) J Non-Cryst Solids 53:325
106. Bershtein VA, Ryzhov VA, Egorova LM, Kober EV (1997) In: Third Intern Disc Meeting on Relaxations in Complex Systems, P IV-4, Vigo, Spain
107. Ryzhov VA (2002) Phys Solid State 44:2336
108. Ryzhov VA, Bershtein VA (2008) Phys Solid State 50:1985
109. Glasstone M, Laidler K, Eyring H (1941) The theory of rate processes. McGraw-Hill, New York
110. Gotlib YY, Darinskii AA (1970) Vysokomol Soedin A 12:2263
111. Helfand E, Wasseman Z, Weber T (1979) J Chem Phys 70:2016
112. Skolnick J, Helfand E (1980) J Chem Phys 72:5489
113. Bueche E (1956) J Chem Phys 24:418
114. Shakhparonov MI, Durov VA (1979) Zh Fiz Khim 53:2451
115. Havlicek J, Nikolais L (1982) Polymer 27:921
116. Emelyanov YA, Bershtein VA (1985) Fiz Chim Stekla 11:429
117. Ngai KL (1998) Phys Rev E 57:7346
118. Litvinov VM, Lavrukhin BD, Zhdanov AA, Andrianov KA (1977) Vysokomol Soedin A 19:2031
119. Fytas G, Patkovski A, Meier G, Dorfmuller T (1982) Macromolecules 15:870
120. Audren P, Konarch D (1986) J Appl Phys 60:946
121. Chang S (1984) Polymer 25:209
122. Kovarskii AL (1986) Vysokomol Soedin A 28:1347
123. Jacobsson P, Borjesson L, Torell L (1991) J Non-Cryst Solids 131/133:104
124. Barashkova II, Kovarskii AL, Vasserman AM (1982) Vysokomol Soedin A 24:91
125. Jarry J, Monnerie L (1980) J Macromol Sci Phys 18:637
126. Wendorff J (1977) In: Proc 4th Intern Conf Phys Non-Cryst Solids, Aedermannsdorf
127. Bershtein VA, Egorova LM, Egorov VM, Sinani AB (1989) Vysokomol Soedin A 31:12
128. Bershtein VA, Egorov VM, Egorova LM, Sysel P, Zgonnik VN (1998) J Non-Cryst Solids 235/237:476
129. Bershtein VA, David L, Egorov VM, Pissis P, Sysel P, Yakushev PN (2005) In: Mittal KL (ed) Polyimides and other high temperature polymers, vol 3. VSP, Utrecht-Boston
130. Bershtein VA, Gun'ko VM, Egorova LM, Guzenko N, Pakhlov E, Ryzhov V, Zarko V (2009) Polymer 50:860
131. Bershtein VA, Egorov VM, Zgonnik VN, Melenevskaya EY, Vinogradova LV (2000) J Therm Anal Calorim 59:23
132. Bershtein VA, Yakushev PN, Peschanskaya NN, Sinani AB, Pissis P (1998) J Non-Cryst Solids 235/237:584
133. Bershtein VA, Yakushev PN, Karabanova LV, Sergeeva LM, Pissis P (1999) J Polym Sci Polym Phys Ed 37:429
134. Peschanskaya NN, Yakushev PN, Khristova Y, Topliiiska A (1993) Polym Sci A 35:1491
135. Peschanskaya NN, Yakushev PN, Surovova VI (1995) Phys Solid State 37:1429
136. Bershtein VA, Egorova LM, Yakushev PN, Sysel P, Hobzova R, Kotek J, Pissis P, Kripotou S, Maroulas P (2006) Polymer 47:6765
137. Heux L, Halary JL, Laupretre F, Monnerie L (1997) Polymer 38:1767
138. Garroway AN, Ritchy MR, Moniz WB (1982) Macromolecules 15:1051
139. Shi JF, Inglefield PT, Jones AA, Meadows MD (1996) Macromolecules 29:605
140. Bershtein VA, Egorova LM, Ryzhov VA, Yakushev PN, Fainleib AM, Shantalii TA, Pissis P (2001) J Macromol Sci Phys 40:109
141. Bershtein VA, Egorov VM, Egorova LM, Yakushev PN, Fainleib AM, Pissis P, Sysel P (2000) In: NATAS 2000 Proc, Orlando

142. Georgoussis G, Kyritsis A, Bershtein VA, Fainleib AM, Pissis P (2000) J Polym Sci Polym Phys Ed 38:3070
143. Bershtein VA, David L, Egorov VM, Egorova LM, Yakushev PN, Pissis P, Sysel P, Sindelar V (2002) Polymer 43:6943
144. Kanapitsas A, Pissis P, Delides CG, Sysel P, Sindelar V, Bershtein VA (2002) Polymer 43:6955
145. Bershtein VA, Egorov VM, Yakushev PN, David L, Sysel P, Sindelar V, Pissis P (2003) In: Abadie MJM, Sillion B (eds) Polyimides and high performance polymers. University Montpellier, Montpellier
146. Pissis P, Georgoussis G, Bershtein VA, Neagu E, Fainleib AM (2002) J Non-Cryst Solids 305:150
147. Kripotou S, Pissis P, Bershtein VA, Sysel P, Hobzova R (2003) Polymer 44:2781
148. Bershtein VA, David L, Egorov VM, Fainleib AM, Grigorieva O, Bey I, Yakushev PN (2005) J Polym Sci Polym Phys 43:3261
149. Bershtein VA, Egorova LM, Yakushev PN, Sindelar V, Sysel P, Sukhanova TE, Dobrovolskaya IP, Grigoriev AI, Kripotou S, Pissis P (2007) Polym Bull 58:65
150. Kripotou S, Pissis P, Sysel P, Sindelar V, Bershtein VA (2006) Polymer 47:357
151. Bershtein VA, Egorov VM, Yakushev PN, David L, Fainleib AM, Grigorieva OP, Bei I, Kripotou S, Pissis P (2007) J Macromol Sci Phys 46:207
152. Kimmerle K, Bell CM, Gudernatsch W (1988) J Membr Sci 36:477
153. Baker RW, Yioshioka N, Mohr JM, Khan AJ (1987) J Membr Sci 31:259
154. Matsumoto K, Ishii K, Kuroda T, Inoue K, Iwama A (1991) Polym J 23:491
155. Feng X, Sourirajan S, Tezel H, Matsuura T (1991) J Appl Polym Sci 43:1071
156. Deng S, Tremblay A, Matsuura T (1998) J Appl Polym Sci 69:371
157. Sindelar V, Sysel P, Hynek V, Friess K, Sipek M, Castaneda N (2001) Collect Czech Chem Commun 66:533
158. Sysel P, Sindelar V, Hobzova R, Nejedla S, Frycova M (2003) Plasty a Kaucuk 40:292
159. Pogosyan M, Pankratov VA, Zaplyshny VN, Matsyan S (1987) Polytriazines. Armenian Acad Sci Publ, Erevan
160. Hamerton I (ed) (1994) Chemistry and technology of cyanate ester resins. Chapman and Hall, Glasgow
161. Hamerton I, Hay JN (1998) High Perform Polym 10:163
162. Fainleib AM, Grigoryeva OP, Pissis P (2006) In: Vasile C, Zaikov GE (eds) Focus on natural and synthetic polymer science. Nova Science, New York
163. Fainleib AM, Sergeeva LM, Novikova TI, Shantalii TA (1992) Polym Mater Sci Eng 66:131
164. Fainleib AM, Novikova TI, Shantalii TA, Sergeeva LM (1992) Vysokomol Soedin B 33:60
165. Bartolotta A, DiMarco G, Carini G, D'Angelo G, Tripodo G, Fainleib AM, Privalko VP (1998) J Non-Cryst Solids 235/237:600
166. Bartolotta A, DiMarco G, Lanza M, Carini G, D'Angelo G, Tripodo G, Fainleib AM, Slinchenko EA, Shtompel VI, Privalko VP (1999) Polym Eng Sci 39:549
167. Fainleib AM, Grigoryeva OP, Hourston D (2001) Macromol Symp 164:429
168. Fainleib AM, Grigoryeva OP, Hourston D (2001) Int J Polym Mater 51:57
169. Karabanova LV, Boiteux G, Gain O, Seytre G, Sergeeva LM, Lutsyk ED (2004) Polym Int 53:2051
170. Karabanova LV, Mikhalovsky SV, Sergeeva LM, Meikle ST, Helias M, Lloyd AW (2004) Polym Eng Sci 44:940
171. Shilov VV, Karabanova LV, David L, Boiteux G, Seytre G, Gomza YP, Nesin SD, Sergeeva LM, Lutsyk ED, Svyatyna AV (2005) Polimerniy Zhurnal (Kyiv) 27:255
172. Lehah MD, Cooper SL (eds) (1986) Polyurethane in medicine and surgery. CRC, Boca Raton, FL
173. Lloyd AW, Faragher RGA, Denyer SP (2001) Biomaterials 22:769
174. Lowe AB, Vamvakaki M, Wassall MA, Wong L, Billingham NC, Armes SP, Lloyd AW (2000) J Biomed Mater Res 52:88
175. Paynter RW, Martz H, Guidoin R (1987) Biomaterials 8:94

176. Thoma RJ, Phillips RE (1987) J Biomed Mater Res 21:525
177. Szycher M, Poirier VL, Dempsey D (1983) Elastomerics 115:11
178. Georjon O, Galy J, Pascault JP (1993) J Appl Polym Sci 49:1441
179. Georjon O, Galy J (1998) Polymer 39:339
180. Fainleib AM, Hourston DJ, Grigoryeva OP, Shantalii TA, Sergeeva LM (2001) Polymer 42:8361
181. Bershtein VA, Vilesov AD, Vinogradova LV, Volodin VP, Gotlib YY (1990) Vysokomol Soedin A 32:2324
182. Bershtein VA, Egorova LM, Sysel P (1998) J Macromol Sci Phys 37:747
183. Rogers ME, Rodrigues D, Wilks GL, McGrath JE (1991) Polym Prepr 32:176
184. Schauer J, Sysel P, Marousek V, Pientka Z, Pokorny J, Bleha M (1996) J Appl Polym Sci 61:1333
185. Sysel P, Qupicky D (1996) Polym Int 40:275
186. Saeki S, Cowie JMG, McEwen IJ (1983) Polymer 24:60
187. Yang H, Shibayama M, Stein RS, Shimizu N, Hashimoto T (1986) Macromolecules 19:1667
188. Aubin M, Prud'homme RE (1988) Polym Eng Sci 28:1355
189. Roovers J, Toporowski P (1992) Macromolecules 25:3454
190. Alegria A, Colmenero J, Ngai KL (1994) Macromolecules 27:4486
191. Bershtein VA, Egorova LM, Prud'homme RE (1997) J Macromol Sci Phys 36:513
192. Roland CM, Ngai KL (1992) Macromolecules 25:363
193. Fischer EW, Zetsche A (1992) Polym Prepr 33:78
194. Jones AA, Inglefeld PT, Liu Y, Roy AK, Cauley BJJ (1991) J Non-Cryst Solids 131/133:556
195. Bershtein VA, Egorova LM, Ryzhov VA (1997) Polym Sci A 39:1107
196. Bershtein VA; Egorova LM, Peschanskaya NN, Yakushev PN (1997) Polym Sci A 39:173
197. Bershtein VA, Egorova LM, Ryzhov VA, Yakushev PN (2000) Macromol Symp 149:87
198. Bershtein VA, Egorova LM, David L, Kanapitsas A, Meszaros O, Pissis P, Sysel P, Yakushev PN (2002) J Macromol Sci Phys 41:419
199. Bershtein VA, David L, Egorova LM, Kanapitsas T, Meszaros O, Pissis P, Sysel P, Yakushev PN (2002) Mater Research Innov 5:230
200. Pissis P, Kanapitsas A, Georgoussis G, Bershtein VA, Sysel P (2002) Adv Compos Lett 11:49
201. Takegoshi K, Hikichi J (1991) J Chem Phys 94:3200
202. LeMenestrel C, Kenwright AM, Sergot P, Laupretre F, Monnerie L (1992) Macromolecules 25:3020
203. Schartel B, Wendorff JH (1999) Polym Eng Sci 39:128
204. Birshtein TM, Goryunov AN (1979) Vysokomol Soedin A 21:1990
205. Yokota R, Horiuchi R, Kochi M, Soma H, Mita I (1988) J Polym Sci Polym Lett 26:215
206. Ree M, Yoon DY, Volksen W (1990) Polym Prepr 31:613
207. Rojstaczer S, Ree M, Yoon DY, Volksen WJ (1992) J Polym Sci Polym Phys 30:133
208. Campbell JA, Goodwin AA, Mercer FW, Reddy V (1997) High Perform Polym 9:263
209. Bershtein VA, Egorov VM, Marikhin VA, Myasnikova LP (1985) Vysokomol Soedin A 27:77
210. Bershtein VA, Egorov VM, Egorova LM, Peschanskaya NN, Yakushev PN, Keating MY, Flexman EA, Kassal RJ, Schodt KP (2002) Thermochim Acta 391:227
211. Krizan TD, Bershtein VA, Sukhanova TE, Keating MY, Grigoriev AI, Egorov VM, Vylegzhanina ME, Yakushev PN, Bursian AE (2005) In: Mittal KL (ed) Polyimides and other high temperature polymers, vol 3. VSP, Utrecht-Boston
212. Bershtein VA, Sukhanova TE, Krizan TD, Keating MY, Grigoriev AI, Egorov VM, Yakushev PN, Peschanskaya NN, Vylegzhanina ME, Bursian AE (2005) J Macromol Sci Phys 44:613
213. Egorov EA, Zhizhenkov VV, Marikhin VA, Myasnikova LP, Popov A (1983) Vysokomol Soedin A 25:693
214. Egorov EA, Zhizhenkov VV, Zakrevskii VA (1993) Macromol Chem Macromol Symp 72:47
215. Okazaki I, Wunderlich B (1996) J Polym Sci Polym Phys 34:2941
216. Gall WG (1966) US Patent 3.249.588
217. Manwiller CH, Anton WL (1988) US Patent 4.755.555
218. Ray SS, Okamoto M (2003) Progr Polym Sci 28:1539

219. Ke YG, Stroeve P (2005) Polymer-layered silicate and silica nanocomposites. Elsevier, Amsterdam
220. Hu Y, Shenderova OA, Hu Z, Padgett CW, Brenner DW (2006) Rep Progr Phys 69:1847
221. Ganguli S, Dean D, Jordan K, Price G, Vaia R (2003) Polymer 44:6901
222. Wooster TJ, Abrol S, MacFarlane DR (2004) Polymer 45:7845
223. Ganguli S, Dean D, Jordan K, Price G, Vaia R (2003) Polymer 44:1315
224. Kim DS, Lee KM (2003) J Appl Polym Sci 90:2629
225. Wooster TJ, Abrol S, MacFarlane DR (2005) Polymer 46:8011
226. Bershtein VA, Fainleib AM, Pissis P, Bei I, Dalmas F, Egorova LM, Gomza YP, Kripotou S, Maroulos P, Yakushev PN (2008) J Macromol Sci Phys 47:555
227. Fainleib AM, Bei I, Maroulas P, Kripotou S, Pissis P, Bershtein VA, Gomza YP, Yakushev PN (2007) In: Proc 16th Intern Conf Compos Mater (ICCM-16), Kyoto, Japan
228. Maroulas P, Kripotou S, Pissis P, Fainleib A, Bei I, Bershtein V, Gomza Y (2007) In: Proc 6th Intern Symp Adv Compos, Corfu, Greece
229. Li Q, Simon S (2008) Macromolecules 41:1310
230. Dolmatov VY (2001) Russian Chem Rev 70:687
231. Moniruzzaman M, Winey KI (2006) Macromolecules 39:5194
232. Shaffer MSP, Sandler JKW (2006) In: Advani S (ed) Processing and properties of nanocomposites, chap 1. World Scientific, Singapore
233. Dolmatov VYu (2006) In: Shenderova OA, Gruen DM (eds) Ultrananocrystalline diamond: synthesis, properties and applications. William-Andrew, Norwich, NY
234. Williams OA, Zimmermann T, Kubovic M, Denisenko A, Kohn E, Jackman RB, Gruen DM (2005) In: Gruen DM, Shenderova OA, Vul' AY (eds) Synthesis, properties and applications of ultrananocrystalline diamond. Springer, Amsterdam
235. Shilov VV, Gomza YP, Shilova OA, Padalko VI, Efimova LN, Nesin SD (2005) In: Gruen DM, Shenderova OA, Vul' AY (eds) Synthesis, properties and applications of ultrananocrystalline diamond. Springer, Amsterdam
236. Davidson JL, Kang WP (2005) In: Gruen DM, Shenderova OA, Vul' AY (eds) Synthesis, properties and applications of ultrananocrystalline diamond. Springer, Amsterdam
237. Voznyakovskii AP (2004) Phys Solid State 46:644
238. Ghosh A, Sciamanna SF, Dahl JE, Shenggao L, Carson MK, Schiraldi DA (2007) J Polym Sci Polym Phys 45:1077
239. Bershtein VA, Karabanova LV, Sukhanova TE, Yakushev PN, Egorova LM, Lutsyk ED, Svyatyna AV, Vylegzhanina ME (2008) Polymer 49:836
240. Karabanova LV, Bershtein VA, Sukhanova TE, Yakushev PN, Egorova LM, Lutsyk ED, Svyatyna AV, Vylegzhanina ME (2008) J Polym Sci Polym Phys 46:1696
241. Korobko AP, Krasheninnikov SV, Levakova IV, Ozerina LA, Chvalun SN (2001) Polym Sci A 43:1163
242. Kulakova II (2004) Phys Solid State 46:636
243. Mark YE, Lee CYC, Bianconi PA (eds) (1995) Hybrid organic–inorganic composites, ACS Symp Ser 585. American Chemical Society, Washington
244. Noell JLW, Wilkes DL, Mohanty DK, McGrath JE (1990) J Appl Polym Sci 40:1177
245. Huang ZH, Qiu KY, Wei Y (1997) J Polym Sci Polym Chem 35:2403
246. Tian D, Dubois PH, Jerome K (1997) J Polym Sci Polym Chem 35:2295
247. Sysel P, Pulec R, Maryska M (1997) Polym J 29:607
248. Suizdak DA, Mauritz KA (1999) J Polym Sci Polym Phys 37:143
249. Hu Q, Marand E (1999) Polymer 40:4833
250. Iyoki Y, Kakimoto M, Imai Y (1994) High Perform Polym 6:43
251. Tamaki R, Naka K, Chujo Y (1998) Polym J 30:60
252. Matejka L, Dusek K, Plestil J, Kriz J, Lednicky F (1998) Polymer 40:171
253. Hajji P, David L, Gerard JF, Pascault JP, Vigier G (1999) J Polym Sci Polym Phys 37:3172
254. Yang F, Nelson GL (2006) Polym Adv Technol 17:320
255. Gun'ko VM, Zarko VI, Leboda R, Chibowski E (2001) Adv Colloid Interface Sci 91:1
256. Gun'ko VM, Voronin EF, Zarko VI, Goncharuk EV, Turov VV (2004) Colloids Surfaces A 233;63

257. Gun'ko VM, Voronin EF, Nosach LV, Pakhlov EM, Guzenko NV (2006) Adsorp Sci Technol 24:143
258. Gun'ko VM, Voronin EF, Nosach LV, Pakhlov EM, Voronina OE (2006) Appl Surf Sci 253:2801
259. Tsagaropoulos G, Eisenberg A (1995) Macromolecules 28:396
260. Jin SW, Keunok HY, Kim HI (2004) Polymer 28:487
261. Berriot J, Montes H, Lequeux F, Long D, Sotta P (2002) Macromolecules 35:9756
262. Théneau C, Salmerón SM, Rodriguez Hernández JC, Monleón Pradas M, Saiter JM, Gómez Ribelles JL (2007) Eur Phys J E 24:69
263. Bershtein VA, Egorova LM, Yakushev PN, Pissis P, Sysel P, Brozova L (2002) J Polym Sci Polym Phys 40:1056
264. Bershtein VA, Egorova LM, Sysel P, Yakushev PN (2000) Polym Sci 42:788
265. Bershtein VA, Egorova LM, Yakushev PN, Georgoussis G, Kyritsis A, Pissis P, Sysel P, Brozova L (1999) Macromol Symp 146:9
266. Fradiadakis D, Pissis P, Bokobza L (2005) Polymer 46:6001
267. Arrighi V, McEwen IJ, Qian H, Serrano Prieto MB (2003) Polymer 44:6259
268. Bershtein VA, Gun'ko VM, Karabanova LV, Sukhanova TE, Yakushev PN, Egorova LM, Glievyy OB, Lutsyk ED, Pakhlov EM, Turova AA, Zarko VI, Vylegzhanina ME (2010) J Macromol Sci Phys 49, 18 (2010)
269. Frenkel YI (1946) Kinetic theory of liquids. Oxford University Press, Oxford; reprinted (1954) by Dover, New York
270. Krausz AS, Eyring H (1975) Deformation kinetics. Wiley, New York
271. Argon AS (1973) Phil Mag 28:839
272. Bowden PB, Raha S (1974) Phil Mag 29:149
273. Sinani AB, Peschanskaya NN, Stepanov VA (1982) Phys Solid State 24:775
274. Pertsev NA (1982) Thesis, Polytechn Inst, Leningrad
275. Pertsev NA (1992) Progr Colloid Polym Sci 92:52
276. Peschanskaya NN, Stepanov VA (1966) Phys Solid State 7:2402
277. Egorov EA, Peschanskaya NN, Stepanov VA (1969) Phys Solid State 11:1073
278. Stepanov VA, Peschanskaya NN, Shpeizman VV (1984) Strength and relaxation phenomena in solids (in Russian). Nauka, Leningrad
279. Sherby OD, Dorn IE (1958) J Mech Phys Solids 6:145
280. Peschanskaya NN, Stepanov VA (1978) Phys Solid State 20:1157
281. Peschanskaya NN, Bershtein VA, Stepanov VA (1978) Phys Solid State 20:1945
282. Bershtein VA, Peschanskaya NN, Sinani AB, Stepanov VA (1980) Phys Solid State 22:448
283. Bershtein VA, Peschanskaya NN, Stepanov VA (1980) Vysokomol Soedin A 22:2246
284. Peschanskaya NN, Stepanov VA, Yakushev PN (1981) Phys Solid State 23:2078
285. Peschanskaya NN, Stepanov VA, Filyanov EM (1982) Phys Solid State 24:1851
286. Bershtein VA, Peschanskaya NN, Emelyanov YA, Stepanov VA (1982) Fiz Khim Stekla 8:552
287. Stepanov VA, Bershtein VA, Peschanskaya NN (1980) In: Proc VIII Intern Congr Rheol, Plenum, New York
288. Van Krevelen DW (1972) Properties of polymers. Correlations with chemical structure. Elsevier, Amsterdam
289. Askadskii AA, Kolmakova LK, Tager AA, Slonimskii GL, Korshak VV (1977) Vysokomol Soedin A 19:1004
290. Lee C, Sewell J (1968) J Appl Polym Sci 12:1397
291. Bershtein VA, Petkevich MZ, Razgulyaeva LG, Stepanov VA (1978) Vysokomol Soedin A 20:2681
292. Li JCM, Gilman JJ (1970) J Appl Phys 41:4248
293. Lazurkin YS, Fogelson RL (1951) J Tech Phys 21:267
294. Kobeko PP (1952) Amorphous substances (in Russian). Izd AN SSSR, Moscow
295. Bershtein VA, Razgulyaeva LG, Sinani AB, Stepanov VA (1976) Phys Solid State 18:1758

296. Bershtein VA, Egorov VM, Razgulyaeva LG, Stepanov VA (1978) Vysokomol Soedin A 20:2278
297. Bershtein VA, Egorov VM, Ryzhov VA, Sinani AB, Stepanov VA (1981) Phys Solid State 23:941
298. Anischuk TA, Bershtein VA, Galperin VM, Egorov VM, Kolosova TA (1981) Vysokomol Soedin A 23:963
299. Bershtein VA, Pertzev NA (1984) Acta Polym 35:575
300. Bershtein VA, Egorov VM (1984) Phys. Solid State 26:1987
301. Kechekyan AD, Andrianova GP, Kargin VA (1970) Vysokomol Soedin A 12:2424
302. Gee ML, McGuiggan PM, Israelishvili JN, Homola AM (1990) J Chem Phys 93:1895
303. Peschanskaya NN, Yakushev PN (1988) Phys Solid State 30:1264
304. Peschanskaya NN (1989) Vysokomol Soedin A 31:1181
305. Peschanskaya NN, Surovova VY, Yakushev PN (1992) Phys Solid State 34:1127
306. Peschanskaya NN, Yakushev PN, Sinani AB (1998) Phys Solid State 40:626
307. Peschanskaya NN, Yakushev PN (1997) Phys Solid State 39:1509
308. Peschanskaya NN, Hristova J, Yakushev PN (2001) Polymer 42:7101
309. Peschanskaya NN (2001) Phys Solid State 43:1478
310. Peschanskaya NN, Hristova J (2006) Phys Solid State 48:1896
311. Peschanskaya NN, Sinani AB (2008) Phys Solid State 50:182
312. Peschanskaya NN, Myasnikova LP, Sinani AB (1991) Phys Solid State 33:1665
313. Peschanskaya NN, Yakushev PN, Myasnikova LP, Marikhin VA, Sinani AB, Jakobs MJ (1996) Phys Solid State 38:1416
314. Peschanskaya NN, Yakushev PN, Myasnikova LP, Marikhin VA, Sinani AB, Jakobs MJ (1997) Phys Solid State 39:505
315. Myasnikova LP, Marikhin VA, Ivan'kova EM, Yakushev PN (1999) J Macromol Sci Phys 38:859
316. Yakushev PN, Peschanskaya NN, Marikhin VA, Myasnikova LP, Jacobs MJ (1997) Polym Eng Sci 37:1286
317. Ivan'kova EM, Marikhin VA, Myasnikova LP, Peschanskaya NN, Yakushev PN (1999) Phys Solid State 41:1641
318. Myasnikova LP, Marikhin VA, Ivan'kova EM, Yakushev PN (2001) J Macromol Sci Phys 40:473
319. Peschanskaya NN, Yakushev PN, Egorov VM, Bershtein VA, Bokobza L (2002) Phys Solid State 44:1684
320. Peschanskaya NN, Yakushev PN, Bershtein VA, Keating MY, Krizan TD (2005) Phys Solid State 47:949
321. Peschanskaya NN (1993) Phys Solid State 35:1484
322. Smith P, Lemstra P (1980) J Mater Sci 15:505
323. Marikhin VA, Myasnikova LP (1991) Macromol Chem Macromol Symp 41:209
324. Krisyuk BE, Marikhin VA, Myasnikova LP, Zaalishvili NL (1993) Int J Polym Mater 22:181
325. Peschanskaya NN, Smolyanskii AS, Surovova VY (1992) Vysokomol Soedin B 34:3
326. Peschanskaya NN, Smolyanskii AS, Surovova VY (1993) Phys Solid State 35:1222
327. Peschanskaya NN, Yakushev PN (2003) Phys Solid State 45:1185
328. Bershtein VA, Yakushev PN, Peschanskaya NN (1999) Macromol Symp 147:73
329. Peschanskaya NN, Smirnov BI, Stepanov YP, Shpeizman VV, Yakushev PN (1989) Phys Solid State 31:703
330. Shpeizman VV, Peschanskaya NN, Smirnov BI, Stepanov YP (1989) Phys Solid State 31:2084
331. Zlatin NA, Peschanskaya NN, Yakushev PN (1987) J Tech Phys 32:1419
332. Bershtein VA, Peschanskaya NN, Yakushev PN (2000) In: NATAS 2000 Proc, Orlando
333. Shpeizman VV, Peschanskaya NN (1989) In: Physical aspects of predicting fracture and deformation in heterogeneous materials. Leningrad

334. Peschanskaya NN, Yakushev PN, Shpeizman VV, Sinani AB, Bershtein VA (1999) Phys Solid State 41:767
335. Yakushev PN, Peschanskaya NN, Shpeizman VV (1993) Int J Polym Mater 20:245
336. Peschanskaya NN, Shpeizman VV, Andreev AK, Kodzhaspirov GE, Solnzev IP, Yakushev PN (1987) Strength Problems 7:115
337. Bershtein VA, Guryanov AA, Egorov VM (1989) Phys Solid State 31:1402
338. Stepanov VA, Peschanskaya NN, Shpeizman VV, Nikonov GA (1975) Int J Fracture 11:851
339. Stepanov VA, Shpeizman VV (1981) Mater Sci Eng 49:195

Editor: K. Dušek

Adv Polym Sci (2010) 230: 221–282
DOI:10.1007/12_2010_49

Published online: 27 April 2010

Polymer Nanocomposites for Electro-Optics: Perspectives on Processing Technologies, Material Characterization, and Future Application

Katarzyna Matras-Postolek and Dariusz Bogdal

Abstract This review concentrates on semiconductors and carbon nanotubes as the inorganic component of organic–inorganic nanomaterials. One of the cornerstones of the current push towards future improvements in electronics and in optics technology is the decrease in size of the various components used for device manufacture. This paper discusses the character of nanocomposites for optics and electronics, their preparation, and the properties of semiconductor nanoparticles such as ZnS, ZnO, ZnS:Mn, TiO_2, CdSe, and CdS. Research in this area has shown the great potential advantages of novel materials composed of semiconductor nanocrystals and a polymer matrix. A short characterization of the nature of carbon-based materials (i.e., fullerenes and nanotubes) is given to provide a brief review of these materials. Then, the characterization of non-conjugated (PMMA, PS, and PVDF) and conjugated (PT, PVK, PPV, and PANI) polymer matrices and nanocomposites is described. Finally, the most advanced applications of the nanocomposites are presented.

Keywords Conjugated polymer · Fullerene · Nanocomposites · Nanocrystals · Nanotube · Non-conjugated · Polymer semiconductor

K. Matras-Postolek (✉)
Faculty of Chemical Engineering and Technology, Cracow University of Technology,
ul. Warszawska 24, 31–155 Krakow, Poland
and
Department of Chemical Engineering, Fachhochschule Münster, University of Applied Sciences,
Stegerwaldstraße 39, 48565 Steinfurt, Germany
e-mail: matras@fh-muenster.de

D. Bogdal
Faculty of Chemical Engineering and Technology, Cracow University of Technology,
ul. Warszawska 24, 31–155 Krakow, Poland
e-mail: pcbogdal@cyf-kr.edu.pl

Contents

Abbreviations

AA	Acrylic acid
AAO	Anodic aluminum oxide
AC EL	Alternating current electroluminescence
AIBN	2,2-Azobis(isobutyronitrile)
AKY	Polyoxyethylene(4..5)laurylether acetic acid

Alq_3	Tris(8-hydroxyquinolinato)aluminium(III)
AM	Air mass
BHJ	Bulk heterojunctions
CB	Conduction band
CNT	Carbon nanotube
CPDHFPV	Poly(9,9′-dihexylfluorene-2,7-divinylene-*m*-phenylenevinylene-*stat*-*p*-phenylenevinylene)
C60	[60] Fullerene or buckminsterfullerene
CVD	Chemical vapor deposition
DBSNa	Sodium dodecylbenzene sulfonate
DC EL	Direct current electroluminescence
DCM	4-(Dicyanomethylene)-2-methyl-6-(*p*-dimethylaminostyryl)-4H-pyran
DMF	*N*,*N*-dimethylformamide
DPA	Dodecylphosphonic acid
DSC	Dye-sensitized solar cell
EBE	Electron beam evaporation
E_C	Energy of an electron in the conduction band
E_F	Fermi level
E_g	Energy band gap
E_v	Energy of an electron at the top of the valence band
EL	Electroluminescence
EQE	External quantum efficiency
ER	Electrorheological properties
eV	Electron fill factor volt
FCC	Face-centered cubic
o-FET	Field effect transistors
FF	Fill factor
FT-IR	Fourier transform infrared spectroscopy
HOMO	Highest occupied molecular orbital
HDA	Hexadecylamine
I_{mpp}	Current in the maximum power point
I_{sc}	Short circuit current
ITO	Indium tin oxide
IUPAC	International Union of Pure and Applied Chemistry
k	Wavevector
LAVD	Laser-assisted vapor deposition
LB	Langmuir–Blodgett technique
LED	Light-emitting diode
LUMO	Lowest unoccupied molecular orbital
MA	Methacrylic acid
MDDA	Didecylamine-solubilized carbon nanotubes
MEH-PPV	Poly[2-methoxy-5(2-ethyl-hexyloxyl)-*p*-phenylene vinylene]
MBE	Molecular beam epitaxy
MMA	Methyl methacrylate

MOCVD	Metal–organic chemical vapor deposition
MPA	3-Mercaptopropionic acid
MPTMS	γ-Ethacryloxypropyltrimethoxysilane
MWCNT	Multiwall carbon nanotube
p-MWCNT	Purified multiwall carbon nanotube
n	Refractive index of the matrix
n'	Refractive index of the particles
NaAOT	Sodium bis(2-ethylhexyl)sulfosuccinate
NC	Nanocrystal
OLED	Organic light-emitting diode
PAA	Poly(acrylic acid)
PANI	Polyaniline
PCBM	[6,6]-Phenyl-C_{61}-butyric acid methyl ester
PC	Photonic crystal
PCE	Power conversion efficiency
PCO	Photocatalytic oxidation
PEDOT	Poly(3,4-ethylenedioxythiophene)
PHOS	Polyoxyethylene(1)laurylether phosphoric acid
P3HT	Poly(3-hexylthiophene)
P3OT	Poly(3-octylthiophene)
P_{light}	Incident solar radiation
PL	Photoluminescence
PLD	Pulsed laser deposition
PMMA	Poly(methyl methacrylate)
PmPV	Poly(*m*-pheneylenevinylene-co-2,5-dioctoxy-*p*-phenylene)
P_o	Incident power
PPV	Poly(*p*-phenylene vinylene)
PPy	Polypyrrole
PS	Polystyrene
PSS	Polystyrene sulfonic acid
PT	Polythiophene
PTU	Polythiourethane
PU	Polyurethane
PUMM	Poly(urethane-methacrylate macromer)
PV	Photovoltaic
PVA	Poly(vinyl alcohol)
PVB	Poly(vinyl butyral)
PVDF	Poly(vinylidene fluoride)
PVK	Poly(*N*-vinylcarbazole)
PVP	Poly(vinylpyrrolidone)
QD	Quantum dot
QY	Quantum yield
SAM	Self-assembled monolayer
SC	Semiconductor
SSG	Solution–sol–gel

SWCNT	Single-wall carbon nanotube
SQ	Size quantization
TDPA	Tetradecylphosphonic acid
TFEL	Thin-film electroluminescence
Th	Thorium
TOPO	Tri-*n*-octylphosphine oxide
TPDA	N,N'-Diphenyl-N,N'-bis(3-methylphenyl)-1,1′-biphenyl-4-4′-diamine
TTAB	Tetradecyltrimethylammonium bromide
Tween 20	Poly(oxyethylene) (20) sorbitan monolaurate
W	Wurtzite structure
UMM	Urethane-methacrylate macromer
UV	Ultraviolet
V	Volume of single particles
VB	Valence band
V_{oc}	Open circuit voltage
V_{mpp}	Voltage in the maximum power point
ZB	Zinc blende
ΔW_f	Work functions of electrodes
ε	Dielectric constant
ε_r	Relative dielectric constant
λ	Wavelength of light
δ_d	Dispersive contribution
δ_p	Polar contribution
δ_h	Hydrogen bonding contribution
η_{eff}	Overall efficiency of a solar cell
ρ	Density dimensions of quantities of particles

1 Introduction

In recent years, great progress has been achieved in the preparation of various types of polymer nanocomposites and in understanding the basic principles that determine their optical, electronic, and magnetic properties. As a result, nanocomposite-based devices such as light-emitting diodes (LEDs), photodiodes, and photovoltaic (PV) solar cells have been fabricated and their properties characterized.

Composites are defined in a IUPAC (International Union of Pure and Applied Chemistry) technical report as "multicomponent materials comprising multiple different (non-gaseous) phase domains in which at least one type of phase domain is a continuous phase" [1], whereas elsewhere the notation "the components as well as the interface between them can be physically identified" is added [2]. Polymer nanocomposites are a group of materials defined as polymers in which a small amount (i.e., a few wt%) of nanofillers (1–100 nm in size) are homogeneously distributed. Hybrid materials consist of both organic and inorganic components;

however, they are not easy to classify because of the large variety of different types of hybrids. Thus, inorganic–organic hybrid materials are divided into two major classes [3]. In class I materials, the inorganic and organic components interact only weakly through hydrogen bonding or van der Waals interactions. In class II materials, the organic and inorganic building blocks are strongly linked through the formation of covalent or ionic bonds [4].

The idea of an improvement in conventional materials through the formation of multiphase composites is not an invention of the last few decades. Materials possessing such structural complexity are very common in nature; for example, bones [5], the enamel of the mature human tooth (composed of hydroxyapatite and proteins) [6], and the aragonitic nacreous layers of the abalone shell [7]. Biological systems can create these materials at ambient temperature and aqueous environments, whereas most synthetic protocols need high temperature or pressure and very reactive chemicals. At present, it still remains an exciting challenge to find novel methods for the preparation of synthetic nanocomposites that have properties comparable to materials found in biological systems.

Nanoparticles can posses a variety of sizes and morphologies (amorphous, crystalline, spherical, needles, etc.) and different kinds of nanofillers are classified depending on size and shape. Nanofillers are grouped into four categories: zero-dimensional (e.g., embedded clusters), one-dimensional (e.g., nanowires), two-dimensional (nanoscale coatings, layered materials such as clays, metal oxides, metal phosphates), and three-dimensional (framework system such as zeolites). Nowadays, semiconductor nanocrystals (NCs) dispersed into a polymeric matrix, thus forming an inorganic–organic nanocomposite, are of great interest due to their unique electronic and optical properties. Organic–inorganic nanocomposite structures have been used to develop optically functional materials; for example, to enhance the photoconductivity of host polymers by charge and energy transfer or to modify their refractive index. Due to these physical properties, the nanocomposites can be viewed as promising materials for many applications such as LEDs, PV devices, sensors, and catalysts.

A number of books and review articles cover selective aspects of nanocomposite preparation and properties [8–12], trying to answer the fundamental questions: What is so special about polymer nanocomposites? What is the motivation for using polymer nanocomposites in optics and electronics? What kind of devices would benefit from having polymer nanocomposites as the active components? What are the advantages of the nanocomposite-based devices that have attracted so much interest from the fields of electronics and optics?

These are a few of the important issues that are discussed in this paper. A comprehensive review is presented of current research activities that concentrate on polymer nanocomposites based on conducting and non-conducting polymers and semiconductor NCs like ZnS, ZnO, TiO_2, CdSe, and CdS and their doped variants. Carbon-based materials such as fullerene are also shortly described. The review is divided into ten parts, with the introduction as the first. In the second and third parts, the fabrication methods and types of semiconductor-based nanocomposites are reported. In the fourth part, we characterize the nanocomposites on the basis

of their optical and electronic properties, while in the fifth part, we describe semiconductor NCs. The sixth part discusses carbon-based materials as nanofillers. In the seventh and eight parts, conjugated and non-conjugated polymers as a base for nanocomposites are discussed in detail. In the final sections, we present nanocomposite applications in optics and electronics, and outline prospects for the future.

2 Fabrication of Polymer Nanocomposites

There are four common approaches for the synthesis of polymer nanocomposites that have been adopted so far. The first approach is an in-situ polymerization of various monomers in the presence of nanoparticles, which are dispersed in a monomer or monomer solution. The advantages of this technique are subtle dispersion of the filler in formed polymer matrix and the potential to graft the polymer onto the particle surface, which often requires a modification of the particle surface. Moreover, a modification the surface of nanoparticles prior to polymerization makes them more dispersible in organic solution. The second approach involves both in-situ formation of the nanoparticles and in-situ monomer polymerization. This method is very often used for the manufacture of polymers filled with metal nanoparticles. The formation of metal particles from suitable metal precursors occurs in the presence of a protective polymer, which limits the size of the particles. Then, the composite can be cast together with a monomer of the same or a different polymer type and polymerize. The third method, so-called direct mixing, involves dissolving a polymer in solvent and then mixing with nanoparticles in dispersion. The fourth approach is melt intercalation, i.e., heating a polymer above its glass transition temperature and then mixing it with nanoparticles. Some of the limitations of melt intercalation can be overcome if both polymer and nanoparticles are dissolved or dispersed in solution. This allows modification of the particle surface without drying, which reduces particle agglomeration [11].

3 Types of Semiconductor-Based Composites

The electrical and optical properties of polymer–inorganic nanocomposites depend on the characteristics of the semiconductor NCs and degree of interaction between the nanofillers and polymer matrix. To obtain desirable properties, organic–inorganic nanocomposites usually require fine-tuning of the size, topology, and spatial assembly of individual domains and their interfaces.

Rajeshwar et al. have classified nanocomposites based on semiconductors (SCs) into four groups, in which the SC phase is the key building block in nanocomposite structure (Fig. 1) [12].

The SC nanoparticles can be dispersed directly in a continuous matrix as schematized in Fig. 1a. Alternatively, the composite could consist of stacked layers of

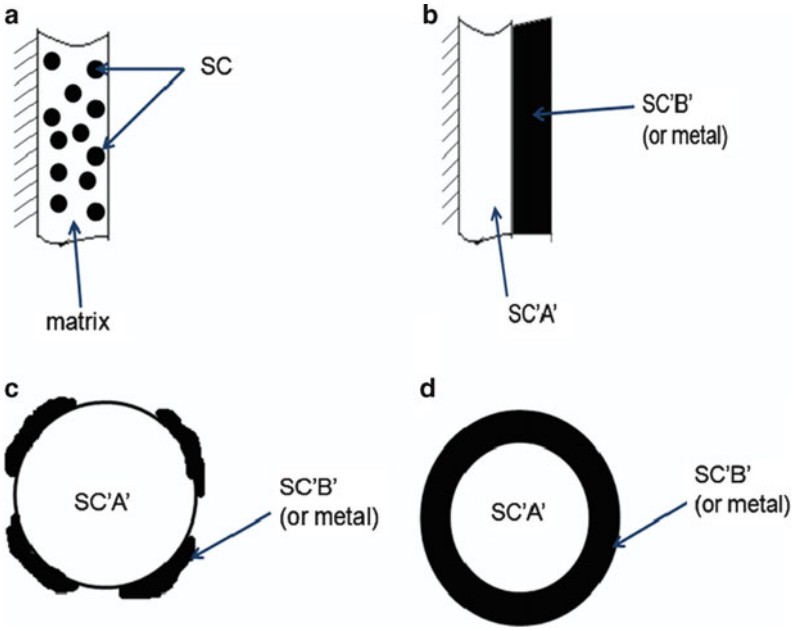

Fig. 1 Four types of semiconductor-based composite architectures: (**a**) semiconductor/matrix; (**b**) layered configuration of two semiconductors, A and B; (**c**) coupled semiconductors; (**d**) core–shell geometry; *SC* denotes the semiconductor [12]

various components (Fig. 1b). Layer-by-layer assembled polyelectrolyte and inorganic SC "sandwich" films belong to this group of composites. In other instances, the SC might be simply in physical contact with another particle in a "coupled" geometry (Fig. 1c, d). Obviously, the distinction between the two configurations in Fig. 1c, d is the degree of coating, i.e., whether the second phase partially or completely engulfs the other SC. An interesting aspect of composite systems such as those depicted in Fig. 1c, d is that photogenerated electrons and holes may be spatially confined in either the same particle or in different particles, depending on the interfacial energetics. Alternatively, the hole might be confined to the core, while the electron is delocalized throughout the (core) shell structure. The two types of semiconductor NC assembly depicted in Fig. 1c, d can be dispersed in a suitable matrix (e.g., polymer) to form the final composite. Often, the SC nanoparticles are coated with another (nominally wider band gap) SC in a core–shell geometry (Fig. 1d). This is done for passivating the initial nanoparticle surface and enhancing its light-emissive properties [13–17].

4 Optical and Electronic Characteristics of Nanocomposites

The term "nanocomposites" was used by Roy et al. during the period 1982–1983 to describe the major conceptual redirection of the sol–gel process to the solution–sol–gel (SSG) process for preparation of maximally heterogeneous instead of homogeneous materials [18]. Nowadays, nanocomposite refers to composites of more than one solid phase, where at least one dimension of solid is in the nanometer range, i.e., 1–100 nm. The solid phase can be crystalline, semicrystalline, amorphous, or a combination thereof.

One of the most important advantages of the polymer nanocomposite-based devices is the relatively low cost of preparation of materials used for the device fabrication and the availability of totally new material morphologies and device geometries, unattainable by traditional electro-optic technology and methods. Moreover, it is possible to realize a nanoscale size for the device structural elements without significant effort, especially when using self-assembly techniques. Another advantage of polymer nanocomposites is the creation of p–n heterojunctions; in particular, junctions with highly doped SC particles, interpenetrating networks of nanoparticles and other valuable properties for device operation, and peculiar material morphologies. In addition, due to the change in the size of nanoparticles, one has the opportunity to tailor the band gap and its positions, which leads to such physical objects as quantum dots (QDs). Furthermore, polymer nanocomposites can be transparent because the size of nanoparticles can be much smaller than the wavelength of visible light. As a result, scattering can be very low (in the Rayleigh regime), leading to virtually completely transparent objects [11]. Thus, a wide range of polymer nanocomposite devices have been developed and intensively studied [19].

4.1 Nanofiller–Polymer Interface

One of the most important features of nanocomposites is the large interfacial area between nanofillers and polymer. The interfacial area can be defined as the zone between nanofillers and polymer, characterized by altered chemistry, altered polymer chain mobility, altered degree of cure, and altered crystallinity [11]. In comparison with conventional micrometer-sized fillers, the same volume fraction of nanofillers contains a billion-fold number of nanoparticles [9], and the surface-to-volume ratio of nanoparticle atoms can increase up to 90% [20]. The interface controls the degree of interaction between the nanofillers and polymer and thus determines many of the properties of nanocomposites. Therefore, a huge challenge in developing polymer nanocomposites is to have control over the interface [11]. The synergistic combination of nanoparticles and polymers can lead to the sum of the properties of organic and inorganic materials, but also to creation of new functionalities that do not exist for either material alone.

A further difference between nanocomposites and conventionally filled polymers is the amount of filler. Conventionally filled polymers usually contain a large

amount of filler, sometimes more than 50 wt%, whereas the nanocomposites typically include less than 10 wt% of nanoparticles. In the case of nanofillers, only a small amount of filler is required to obtain an improvement in the physical and chemical properties of the material, e.g., to increases the yield stress, tensile strength, Young's modulus, or chemical resistivity as compared to pure polymer. Another interesting difference originating from the size of particle and nanoparticle is the distance between neighboring fillers. In the absence of ordering or segregation, the distance between neighboring fillers is larger in nanocomposites than in conventionally filled polymers [9].

4.2 Nanocomposites Can be Optically Transparent

Since small nanoparticles cannot scatter light significantly, it is possible to make nanocomposites with improved electrical or mechanical properties that retain their optical transparency. Usually, for a transparent polymer, modification of the matrix by dispersing an inorganic component into the polymer results in a significant loss of transparency due to scattering from large particles or agglomerates. A novel approach for the functionalization of transparent plastics is the use of nanoparticles. The scattering power for light propagation through a collection of very small isotropic scatterers can be predicted by Rayleigh scattering (1) [21]:

$$P_{\text{scat}} = 24\pi^4 P_o \rho (n' - n/n^2)(V^2/\lambda^4) \tag{1}$$

where P_o is the incident power, ρ is the density dimension of quantities of particles, n' is the refractive index of the particles, n is the refractive index of the matrix, V is the volume of single particles, and λ is the wavelength of light [21]. Therefore, to minimize scattering, the particles must be as small as possible with an index of refraction as close as possible to that of the matrix material [11]. However, a challenge is to avoid agglomeration inside the matrix, which would result in turbid composites, and thus techniques need to be developed that allow for the integration of particles with a high external surface area into polymers [16]. The small size of nanofillers can also lead to unique properties of the particles themselves. Good optical clarity has been obtained in many nanocomposites, particularly with poly(methyl methacrylate) (PMMA) [16] and polythiourethane (PTU) [22].

In contrast to homogenous materials, the optical properties (e.g., refractive index) of nanocomposites can be tailored simply by changing the concentration of nanoparticles in the polymer matrix. It is possible to prepare transparent nanocomposites with refractive indices over the entire range of about 1 to >3.9, which are by far the lowest and highest ever achieved for any polymer system [11]. These materials have attracted considerable attention for their potential applications in optical filters, lenses, reflectors, optical waveguides, and antireflective films [22]. Among SC nanoparticles, TiO_2 is especially known as a material of high refractive index, so it was most often used to increase the refractive index of a system.

4.3 *Electrical Properties of Nanocomposites*

Understanding of electronic properties is necessary for selection of suitable polymer matrix and nanofillers for the fabrication of electronic devices. In many cases, p–n heterojunctions play an important role both in modern electronic applications and in understanding of other SC devices.

Two regions of p- and n-type SC materials that are uniformly doped and physically separated before the junction is formed are shown in Fig. 2. Note that Fermi level (E_F) is near the valence band (VB) edge in the p-type material and near the conduction band (CB) edge in the n-type material. Consequently, a negative space charge forms near the p-side of the junction and a positive space charge forms near the n-side. This space charge region creates an electric field that is directed from the positive charge toward the negative charge [23]. Such an effect is observed in PV solar cells as well as in emitting light devices, when, for example, conjugated polymers contact nanocrystal SCs. Light emission from the forward-biased SC p–n heterojunction is a result of electronic injection from the n-region into the p-region, where electrons recombine with their counterparts and generate light-emitting excited states [24].

4.3.1 Photoluminescence and Electroluminescence Effects in Polymer Nanocomposites

The electroluminescence (EL) process is defined as light generation by an application of an electric field. Two types of EL behavior can be distinguished according to the voltage applied: low-field EL, called direct current electroluminescence (DC EL), and high-field EL, called alternating current electroluminescence (AC EL) [19].

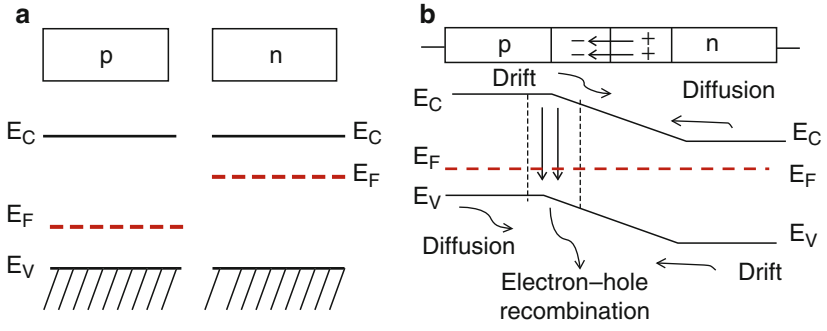

Fig. 2 Energy-band diagram of p–n heterojunction. (**a**) Uniformly doped p-type and n-type semiconductors before junction is formed. (**b**) The energy-band diagram of p-n heterojuntion in the equilibrium, after merging the n-type and p-type regions [23]

The high-field EL is realized under the action of strong electric fields ($\sim 10^6\,\mathrm{V\,cm^{-1}}$) and is further divided into two types: powder (phosphor) EL and thin-film EL (TFEL). The active layer can consist of a doped SC of II–VI groups and an organic or inorganic thin film [25]. Typical AC TFEL devices are made by encapsulating large band gap SCs such as ZnS:Mn by two insulating layers, typically yttrium oxide (Y_2O_3), on both sides of the SC layers [26].

Nowadays, organic light-emitting diodes (OLEDs) based on charge-transporting organic molecules or polymers have gained much attention, in both academic and commercial fields, because they are potential candidates for the next generation of flat panel color displays [27]. The typical OLED consists of two electrodes and an active layer sandwiched between the electrodes. The active layer is composed of conducting polymer, e.g., poly(*p*-phenylene vinylene) (PPV), polythiophenes (PTs), poly(*N*-vinylcarbazole) (PVK), or polyaniline (PANI). For the standard device structure, one of the electrodes needs to be transparent, and indium tin oxide (ITO) is usually used as transparent anode. A great effort has been made to modify the ITO surface to improve hole injection from its side, and it was found that the deposition of very thin buffer layers such as poly(3,4-ethylenedioxythiophene):polystyrene sulfonic acid (PEDOT:PSS) between the ITO and the hole transport layer significantly enhanced OLED performance. At present, this field is rapidly progressing, so that the currently available OLEDs for color application are highly advanced in terms of lifetime (100,000 h), operation voltage (below 5 V) and efficiency (above $20\,\mathrm{lm\,W^{-1}}$), and most of these record performances have been reported by commercial companies [28, 29].

Preparing polymer nanocomposite OLED devices containing semiconductor NCs still remains a challenge. However, a few EL devices have been fabricated successfully [30–38]. For instance, Liu et al. investigated the properties of diode structures fabricated from PVK conducting polymer and luminescent Au-CdSe/ZnS core–shell nanocrystals. A series of double-layered EL devices with structures as represented in Fig. 3 were designed and fabricated [30].

The active layer of three of these devices contained orange-emitting iridium(III) triplet emitter and green-emitting Au-CdSe/ZnS nanocrystals in the molar ratios

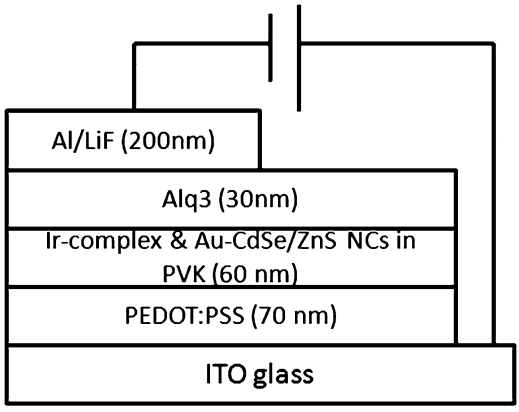

Fig. 3 EL device structure with Au-CdSe/ZnS NCs and Ir-complex in PVK matrix as emitting material [30]

1:0 (blank), 1:1, and 1:3 in PVK. The emitting components were spin-cast onto PEDOT:PSS-coated ITO. Tris(8-hydroxyquinolinato)aluminium(III) (Alq_3) was subsequently spin-cast onto the emitting layers and LiF/Al cathode was vacuum-deposited. Dependence of the intensity of PL and EL on the molar ratio of the Ir complex to Au-CdSe/ZnS nanocrystals in the polymer matrix was observed. PL intensity emission was at maximum when the molar ratio of Ir complex to Au-CdSe/ZnS was 1:3 and was approximately ten times greater than that of the blank. EL performance was found to be maximal in the device that contained Ir complex and Au-CdSe/ZnS nanocrystals in the ratio of 1:1. At a fixed current density ($44.5\,mA\,cm^{-2}$) and applied voltage (5.9 V), EL was found to be $521\,cd\,m^{-2}$; this was the best device. When the ratio of Ir complex to Au-CdSe/ZnS was 1:3, EL decreased, which was attributed to quenching in the device with a higher concentration [30].

QD nanocrystals, CdSe/ZnS and PEDOT:PSS have been used by Hikmet et al. to produce EL devices [31]. The diodes were produced by depositing a layer of QDs on top of a layer of conducting polymer, PEDOT:PSS, followed by the deposition of a metal electrode. Light emission was induced at about 5 V of applied voltage when PEDOT was at positive bias, and 7 V when it was at negative bias. However, all the devices showed very low efficiencies [31].

In turn, Yang et al. demonstrated DC EL from a hybrid CdS:Mn/ZnS and conjugated polymer [32]. EL devices were prepared from multilayer structures of ITO/PEDOT:PSS/conjugated polymer/CdS:Mn/ZnS NCs/Al, using two different conjugated polymers (PVK and PPV). Nanocrystal hybrid EL devices with PVK and PPV are characterized by orange and green EL emission, respectively, which means that electron–hole recombination is confined to the CdS:Mn/ZnS nanocrystalline layer in PVK-based devices, but occurs in the PPV layer in PPV-based devices [32].

Elsewhere, Manzoor et al. reported AC EL devices based on ZnS nanocrystals doped with Cu^{+} and Al^{3+} or with Cu^{+}, Al^{3+}, and Mn^{2+}, which emit in blue, green, and orange-red [35]. The uniform layer of highly packed nanocrystals (emissive layer) was spray-coated over ITO/Y_2O_3 substrate and over-coated with a high-dielectric cyano resin. Finally, an aluminium back electrode was formed by e-beam evaporation. EL emission was observed from the nanocrystal layer at low voltages of $\sim$10 V AC at 100 Hz. Current–voltage characteristics showed a proportional increase in current density with the applied voltage. The mechanism of ACEL in ZnS nanocrystals has been explained, and the excitation was attributed to the electric-field-assisted injection of electron–hole pairs from the surface regions into the interiors and their subsequent recombination therein causing emission [35].

EL emission from ZnO nanoparticles/*N*,*N*′-diphenyl-*N*,*N*′-bis(3-methylphenyl)-1,1′-biphenyl-4–4′-diamine (TPD):PMMA nanocomposite devices was also investigated by Lee et al. [36]. For fabrication of the ZnO–organic nanocomposite EL devices, the phase-segregation method was used, and the ZnO NCs and TPD:PMMA were separated into two layers. The method improved the probability of recombination of electrons and holes within the ZnO nanoparticles. Maximum EL emission peak was observed at 392 nm, which corresponded to the band-gap energy of ZnO nanocrystals at a drive voltage of 7 V [36].

Recently, the synthesis of polymer nanocomposite OLEDs based on a new series of sulfide-containing polyfluorene homopolymers and copolymers and CdSe/ZnS nanocrystals was described by Yang et al. [38]. CdSe/ZnS nanoparticles were grafted to sulfur atoms by a ligand-exchanging reaction. The EL efficiency of nanocomposite OLEDs was effectively improved by QD nanocrystals incorporated in the polymers [38].

More examples of the application of polymer nanocomposite for the fabrication of OLEDs are presented in Chaps. 7 and 8.

4.3.2 Photovoltaic Effect in Polymer Nanocomposites

Composites of semiconductor NCs with conjugated polymers are promising candidates as active "bulk heterojunction" (BHJ) layers in organic PV cells [23]. During last decade, there has been an explosion of academic and industrial interest in the photovoltaic application of molecular thin films [39–54]. A subclass of BHJ is formed by hybrid cells, using semiconducting polymers like regioregular poly-3-hexylthiophene (P3HT) as hole-conducting component and a small molecule such as phenyl-C_{61}-butyric acid methyl ester (PCBM) [39–44] or inorganic semiconductor NCs (e.g., ZnO, CdSe, TiO_2, carbon nanotubes) [45–54] as an electron acceptor. The main advantage of hybrid nanocrystal–polymer blend PV devices is the ease of fabricating a highly interpenetrating network of donor and acceptor materials from solution. For soluble media, the large interfacial area is achieved spontaneously by blending the acceptor and donor components together in a solution, which is then cast into thin films [55].

A typical hybrid nanocrystal–polymer blend PV device is composed of one active layer deposited usually onto ITO anode and covered with a material with comparable low work function (e.g., Al cathode). The structure of hybrid nanocrystals–polymer blend PV devices, essentially a single layer device, is shown in Fig. 4.

The conversion of solar light into electric power requires the generation of both negative and positive charges as well as a driving force that can push these charges

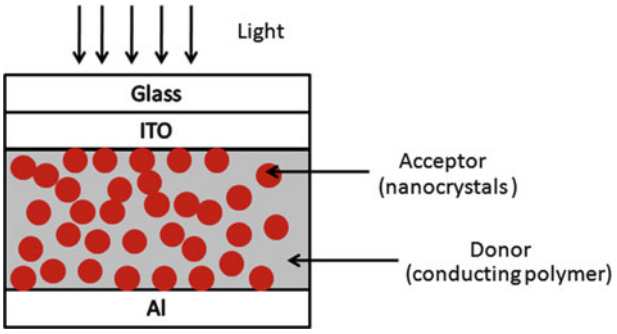

Fig. 4 Typical structure of hybrid nanocrystal–polymer blend photovoltaic devices

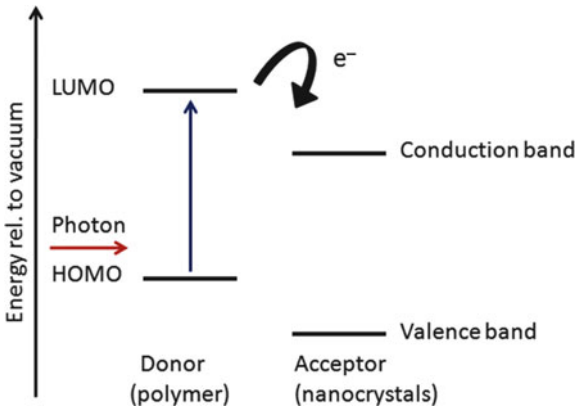

Fig. 5 Energy-level diagram of photoinduced electron transfer at a polymer–nanocrystal interface [56]

through an external electric circuit. Crystalline and nanocrystalline inorganic SCs have several advantages as electron acceptors, including relatively high electron mobility, high electron affinities, and good physical and chemical stability [56].

Under illumination, charges are separated between the two components at the internal interface of the BHJ and collected on asymmetric electrodes. In organic SCs, absorption of photons leads to the creation of bound electron hole pairs (excitons) rather than free charges. In turn, excitons can subsequently diffuse to dissociation sites where their charges can be separated. In the case of organic solar cells, the process can be divided into following stages (Fig. 5) [56]:

- Excitation of the light absorber, i.e., transference of an electron from the highest occupied molecular orbital (HOMO) to its lowest unoccupied molecular orbital (LUMO)
- Formation of an exciton
- Exciton diffusion
- Charge separation at the donor–acceptor interface
- Selective charge transport through the composite layer to the appropriate electrodes [electrons to the cathode (Al) and holes to the anode (ITO)]
- Charge collection

A simple model of band location in polymer solar cells is shown in Fig. 6. The term Fermi level (E_F) is used as synonym for the chemical potential of the electrons. Since this level, even as a virtual one, is defined only for an equilibrium situation in the dark, the term quasi-Fermi level is used to describe the situation under illumination. On illumination, and if no current flows, the light-induced carriers split the quasi-Fermi levels, where the electron E_F, $E_{F,n}$, is essentially that in the polymer, while the hole E_F, $E_{F,p}$, is in the semiconductor NCs. If the system is short-circuited, there will be a gradual variation in $E_{F,p}$, and $E_{F,n}$ across the absorber (blend layer) [57].

The electrical behavior of a solar cell can be seen in the fourth quadrant of the current–voltage curve presented in Fig. 7.

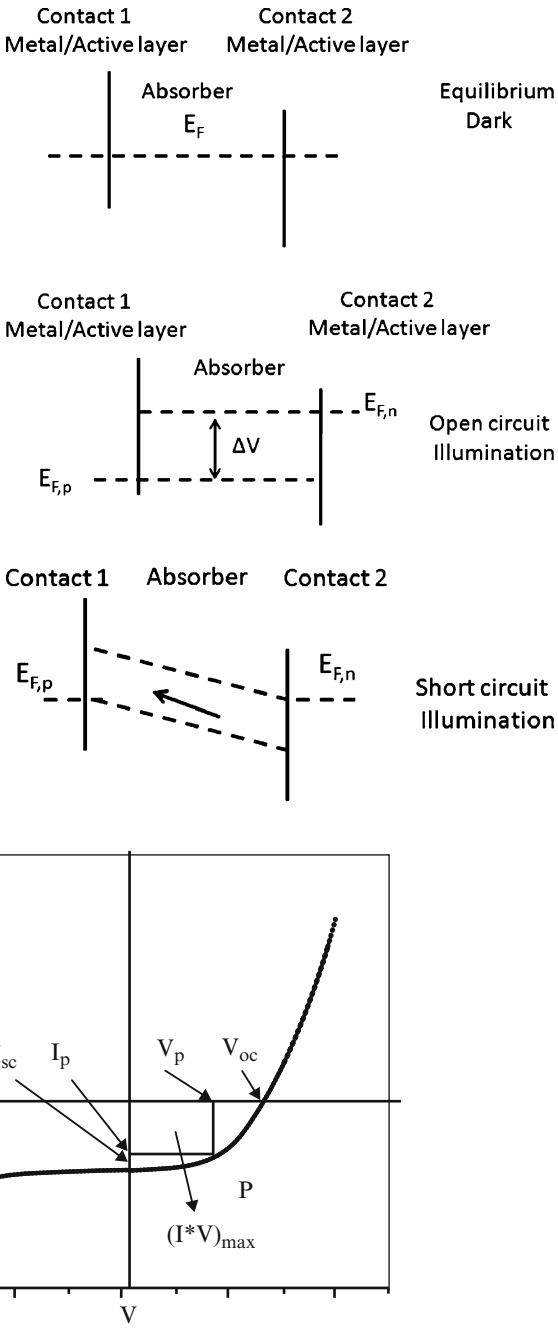

Fig. 6 Simplified schematic of the Fermi level (E_F) positions of photovoltaic devices at equilibrium in the dark and under illumination at open circuit and short circuit [57]

Fig. 7 Current versus applied voltage of a solar cell. The fourth quadrant (negative current) represents the voltage and current that is generated by the cell [55]. V_{oc}, open circuit voltage; I_{sc}, short circuit current density descriptions of I_p, V_p and P

The overall power efficiency η_{eff} of a solar cell is calculated by the following formula (2):

$$\eta_{\text{eff}} = V_{\text{oc}} I_{\text{sc}} \text{FF} / P_{\text{light}}. \tag{2}$$

where V_{oc} is the open circuit voltage in V, I_{sc} the short circuit current density in A m^{-2}, FF is the fill factor and P_{light} is the incident solar radiation in W m^{-2}. The FF of solar cells is defined(3):

$$\text{FF} = I_{\text{mpp}} V_{\text{mpp}} / (I_{\text{sc}} V_{\text{oc}}). \tag{3}$$

with I_{mpp} and V_{mpp} as the current and the voltage in the maximum power point of the I/V curve in the 4th quadrant (Fig. 7).

One of the highest power conversion efficiencies in hybrid cells (up to 5%) under air mass (AM) 1.5 simulated solar light illumination ($80\,\text{mW cm}^{-2}$) were recently reported for BHJ organic solar cells made of blends of P3HT and a substituted fullerene, PCBM [43]. A number of studies have focused on the use of fullerene derivatives as acceptors, because of the high e^- mobilities in these materials and their high electron affinities compared to other molecular acceptors. In particular, the combination with poly(3-hexylthiophene) (P3HT), as a good h-transporter, was successful [39–44]. For instance, Wong et al. studied solar cells composed of P3HT/fullerene derivatives and platinum/conjugated polymer/fullerene derivatives. The cells reached efficiencies in the range of 4.4–5.0% under AM 1.5 simulated solar light illumination ($100\,\text{mW cm}^{-2}$) [39]. Alternatively, conjugated polymers have been combined with n-type inorganic SCs such as ZnO, TiO_2, and CdSe. A number of hybrid polymer solar cells with such semiconductor NCs and conjugated polymers have been reported recently [45–50, 52–54]. More details on the application of polymer nanocomposites for the fabrication of PV cells are reported in the Chaps. 7 and 8.

5 Semiconductor Nanocrystals for Optics and Electronics

5.1 Introduction

In this chapter, we present a background and overview of semiconductor NCs, which have been used as nanofillers for the formation of nanocomposites for optics and electronics. However, it is difficult to discuss all nanocrystals that are currently being investigated. Thus, we decided to focus only on the most important that are most frequently met in the literature, i.e., ZnS and ZnS:Mn, ZnO, CdSe, CdS, and TiO_2. Such compounds, with band-gap energies as large as 2 eV, are the best candidate materials for phosphors that emit visible luminescence, and ZnS is among the most important in this context. In fact, electron affinity and, in turn, emission color can be finely controlled within a single synthetic route, not only by the choice of material, but also by size of nanocrystal [58].

5.2 *Physical and Electrical Properties of Semiconductor Nanoparticles*

The optical response of an SC is critically controlled by its energy band gap (E_g), which gives the threshold energy for an electronic transition from the VB to the CB [59], which in molecular terms can be consider as a transition from HOMO to LUMO [60]. The values of E_g and the corresponding wavelength cutoff limits for the SCs under consideration in this article are listed in Table 1.

On the other hand, SCs are divided into two types, depending on the kind of band gap: direct-gap materials and indirect-gap materials (Fig. 8). Direct-gap materials

Table 1 Some elemental and compound semiconductors and their optical characteristics

Type of semiconductor	Band-gap energy (289 K) (eV)	Approximate threshold, wavelength (nm)	Refractive index	References
Elemental				
Si	1.12	1107	3.52	[61]
Oxides				
TiO_2 (rutile)	3.00	413	3.87	[11, 62]
TiO_2 (anatase)	3.5	394	2.5–3.0	[11, 62]
ZnO	3.35	370	2.0	[63]
Chalcogenides				
CdS	2.5	512	2.35	[64]
CdSe	1.7	729	2.56	[65]
ZnS	3.68	388	2.36	[66]
ZnSe	2.71	481	2.6	[67]

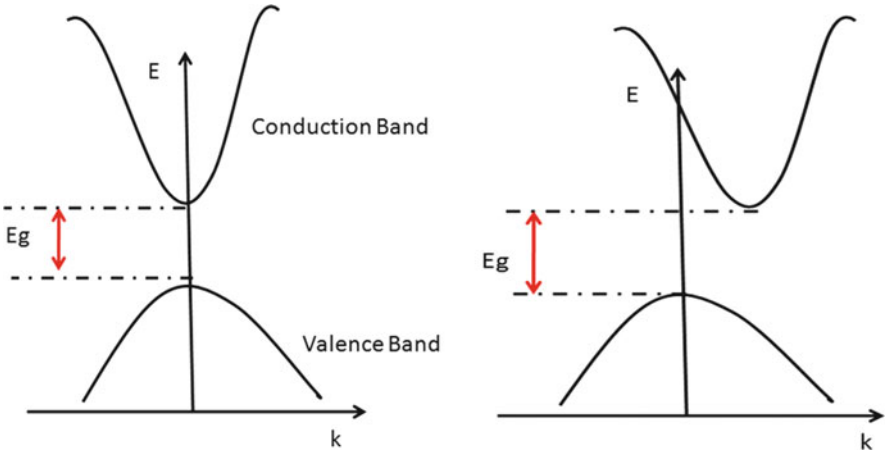

Fig. 8 Electron energy (E) in (*left*) direct band gap (e.g., GaAs, InP, CdS, ZnS) and (*right*) indirect band gap (e.g., Si, Ge, GaP) [68]. E_g, energy band gap; k, propagation vector

are materials for which the top of the VB and the bottom of the CB are at the same value of k (e.g., GaAs, InP, or CdS). In free space, both electrons and photons are described by a propagating plane wave whose amplitude is constant throughout space, and by a propagation vector, k, which describes the direction of the propagation; the magnitude of k is related to the momentum.

Indirect-gap materials are the materials for which the top of the VB and the bottom of the CB are not the same value of k (e.g., Si, Ge, GaP). In the case of an indirect-gap SC, the transition of an electron between the VB and CB involves a substantial change in the momentum of the electron. Therefore, silicon, for instance, in the bulk form is not a luminescent light emitter, in contrast to direct-gap materials, which are mostly efficient emitters [68]. This difference between direct and indirect band structures is very important for LEDs, SC lasers, and PV cells.

SCs with delocalized electrons and holes, as well as conjugated organic molecules containing delocalized π electrons, exhibit strong effects on optical properties at the nanoscale. When particles such as electrons and holes are constrained by potential barriers to regions of space that are comparable or smaller than their de Broglie wavelength, energy states become discrete (i.e., quantized) rather than continuous. This manifests itself in absorption (or emission) spectra as discrete lines that are reminiscent of atomic (line) transitions; these sharper features often appear superimposed on a broader envelope. Another manifestation for SCs is that E_g increases or, equivalently, the absorption threshold exhibits a blue shift. The critical dimension for size quantization (SQ) effects to appear in SCs depends on the effective mass of the electronic charge carriers. In general, charge carriers in SCs can be confined in one, two, or three spatial dimensions, giving rise to QDs, quantum wires, or quantum wells, respectively. There is much scientific and technological interest in SQ effects in SCs. One underlying reason is that the optical, electrical, and redox properties of SCs can be tuned simply by manipulating their physically dimensions rather than their chemical composition [60].

5.3 ZnS Nanocrystals

ZnS, an SC with large E_g of 3.68 eV at 25°C (Table 1), possesses a direct-band gap, which makes optical transitions very probable. Pure ZnS is characterized byn-type conductivity. ZnS is chemically more stable and thus technologically easier to manipulate than other compound SC materials [69]. ZnS is a luminescent material well known for its PL, EL, and cathodoluminescence. ZnS-based phosphors exhibit excellent conversion efficiencies for fast electrons into electron–hole pairs and are, therefore, among materials with the highest overall cathodoluminescence efficiency [70]. Because of its wide-band gap, ZnS has become one of the most applied active layers in TFEL devices [26].

ZnS crystallizes either in the cubic zinc blende (ZB) structure (traditionally called α-ZnS) or the hexagonal wurtzite (W) structure (traditional called β-ZnS). The ZB structure corresponds to the low-temperature phase; it transforms into W structure with a transition temperature of about 1020°C [58]. In both structures, each anion

is surrounded by four cations at the corners of a tetrahedron, and vice versa. This tetrahedral coordination is typical of sp^3 covalent bonding, but these materials also have a substantial ionic character.

Nanoparticles of ZnS activated by a metal ion form a special class of luminescent materials. The incorporation of impurities or defects into SC lattices is the primary means of controlling electrical conductivity and may also have an immense effect on the optical, luminescent, magnetic, or other physical properties of the SC [71]. Usually, most of the doped ZnS nanocrystals reported have a low luminescence quantum yield (QY), especially those synthesized in aqueous solution, compared with microcrystals. A number of papers have reported on the luminescence of nanocrystalline ZnS doped with different ions, such as ZnS:Mn [72–75], ZnS:Eu, ZnS:Er and ZnS:Tb [76, 77], ZnS:Ag [78, 79], ZnS:Au [80], ZnS:Cu [81–83], ZnS:Sm and ZnS:Pb [84, 85].

5.3.1 Structure and Properties of ZnS:Mn

The orange emission of ZnS:Mn crystal has been known since the early days of luminescence research because of its high quantum efficiency at room temperature and chemical stability. The highest value of quantum efficiency, ca. 38% for isolated ZnS:Mn nanopowder stabilized by acrylic acid (AA), has been reported by Althues et al. [16].

The radiative lifetime of ZnS:Mn depends on the crystal structure and its value is approximately equal to 1.5 ms. ZnS:Mn possesses deep-lying levels that can be approximately described by the states of the free divalent ion [85]. The valence electrons ($3d^5$) of Mn^{2+} in ZnS remain at their ion in the highest fields encountered, without shifting spectrally or changing their transition probabilities. Therefore, they appear to be ideal centers for EL. Since both zinc and manganese ions are isovalent and are of comparable ionic radii, manganese is very soluble in ZnS, and Mn^{2+} does not change the electrical properties of the host lattice significantly, even at concentrations of several percent. The emission corresponds to the $^4T_1 \rightarrow {}^6A_1$ transition that explains all the spectral properties: broad band due to different slopes of the energy levels; a long decay time due to the spin selection rule; and dependence of the emission color on the host lattice due to the dependence on crystal field [86].

The luminescence properties of ZnS:Mn nanocrystals have attracted a great deal of interest for a number of years [71]. However, the luminescence spectroscopy is complicated by energy transfer and nonradiative relaxation processes, which might lead to selective observation of a subset of dopant ions that are capable of emitting light.

5.3.2 Preparation and Surface Chemistry of ZnS:Mn

Nowadays, there are many methodologies available for the synthesis of nanostructures, such as molecular beam epitaxy (MBE) [87], metal–organic chemical vapor

deposition (MOCVD) [88], laser-assisted vapor deposition (LAVD) [89], certain physical methods (e.g., solution growth), and chemical techniques. For example, due to the development in the cluster source technologies in chemical vapor deposition (CVD), it is now possible to produce intense beams of virtually any material for a wide range of sizes from a few atoms to a few thousand atoms [90]. All these methods are reviewed elsewhere in detail [68, 91].

Another useful, synthetic technique for nanomaterials is the chemical approach using wet chemistry. This group of methods has been used not only for growing nanostructured inorganic SCs but also to produce core–shell-type nanoparticles (ZnS:Mn/ZnS [92]), and organic–inorganic hybrid systems [93]. The advantage of these methods is that surface-functionalized nanoparticles and nanorods of inorganic SCs, dispersible in a wide variety of media (e.g., water, alcohols, polymer, biological fluids), can be easily prepared. To achieve the fabrication of nanostructures, wet chemistry is performed in a number of ways, such as chemistry in nanoconfined geometries (as in micelles and reverse micelles) or termination of reaction at a precise point of growth by chemical capping (arrested precipitation). Reverse micelles are often called "microemulsions" or "nanoreactors". This system is composed of two immiscible liquids, (water and oil), where the aqueous phase is dispersed as nanosized water droplets by a monolayer film of surfactant molecules in a continuous nonpolar organic solvent [68, 94].

The first report on the luminescence properties of Mn-doped ZnS nanocrystals prepared at room temperature by a chemical process was given by Bhargava et al. [84, 95]. Precipitation of ZnS in the presence of Mn^{2+} can result in incorporation of Mn^{2+} in the ZnS structure. Mn^{2+} substitutes the Zn^{2+} ion and is tetrahedrally coordinated by the S^{2-} ion. One can observe that the precipitation rates of ZnS and MnS are different and that the Mn^{2+} ionic radius (91 pm) is slightly bigger than the radius of the Zn^{2+} ion (83 pm). Most reports on nanocrystalline ZnS:Mn describe Mn^{2+} incorporation at levels of up to 5–15% at most [96, 98]. Peng et al. reported that nanocrystalline powder of ZnS:Mn with an average size of about 3 nm was synthesized using a co-precipitation method with different Mn^{2+} concentrations (Mn:Zn = 5, 10 and 15% in atom ratio). The increase of Mn^{2+} concentration has resulted in the luminescence enhancement of such two emission bands and a red shift of the ZnS emission band [97].

Different kinds of surfactants have been used in the preparation of ZnS:Mn; both long-chain organic molecules with functional groups such as –SH, –CN, –COOH, $–NH_2$, and polymer ligands. ZnS:Mn nanoparticles are prepared by mixing aqueous solutions of metallic salts and sodium sulfide, which leads to co-precipitation. The process is carried out in the presence of a surface modifier with a functional group, e.g., carboxylic acid, acrylic acid (AA) and methacrylic acid (MA) [99–101], poly(vinyl alcohol) (PVA) [102], poly(vinyl butyral) (PVB) [103, 104], poly(vinylpyrrolidone) (PVP) [105], 1-dodecanethiol in the presence of sodium hydroxide [104], 3-mercaptopropionic acid (MPA) [106], sodium hexametaphosphate [107], and thioglycerol [108]. In particular, the PL intensity of the ZnS:Mn nanocrystals increases remarkably using a capping agent with carboxyl or phosphate

groups. Toyoda et al. compared PL signal intensities of ZnS:Mn nanocrystals with and without AA. Due to addition of surface passivators such as AA, the PL signal intensity significantly increases [101].

In turn, Konishi et al. [100] showed that using either poly(acrylic acid) (PAA) polymer or AA monomer as a starting material, differences in optical and chemical properties of hybrid nanocrystals could be observed. The enhancement of PL at 580 nm is larger for ZnS:Mn nanocrystals modified by monomer AA and then in situ polymerization, than for those modified by PAA. The carboxyl groups (C=O) were simultaneously excited by light of 350 nm together with ZnS, followed by energy transfer to Mn^{2+} ions. Further, the authors explained how energy transfer from C=O groups to Mn^{2+} ions depends on the degree of polymerization and the chemical states of carboxyl groups. In the case of the sample modified by AA, oxygen atoms of C=O groups form –S–O–C(=O) bonds and the valence number of sulfur increases from −2 to +6. As a result, electrons of sulfur atoms are pushed towards C=O groups to enhance the emissions. By contrast, the sample modified by polymer PAA exhibits predominant interaction of C=O groups with metallic ions to form –C–O–Me– bonds. This decrease in the amount of C=O groups reduces energy transfer to Mn^{2+} ions [100]. In both cases, the co-precipitation method has been used for the synthesis of ZnS:Mn nanocrystals [100, 101].

Recently, Kubo et al. reported that nanocrystal powder of ZnS:Mn was synthesized in sodium bis(2-ethylhexyl)sulfosuccinate (NaAOT) reverse micelles modified by surfactants based on phosphates [polyoxyethylene(1)laurylether phosphoric acid (PHOS)] or carboxyl groups [polyoxyethylene(4..5)laurylether acetic acid) (AKY)] [109]. In consequence, the modification of ZnS:Mn nanocrystal suspension by a surfactant containing carboxyl groups brings about similar effects to modification by a surfactant containing phosphate groups, i.e., an increase in emission and quantum efficiency (from 1.7 to 8.1%). However, a larger amount of AKY (by one order of magnitude) is required to increase the emission intensity, as compared with PHOS. Therefore, PHOS is more effective for increasing emission intensity and quantum efficiency than AKY [109].

5.4 ZnO Nanocrystals: Synthesis, Structure and Properties

Zinc oxide (ZnO), similarly to ZnS, is well known to the SC field, with studies of its lattice parameter dating back to 1935 [110]. ZnO is a direct semiconducting oxide with a wide E_g of 3.35 eV (Table 1) at room temperature and a large exciton binding energy of 60 meV. Some optoelectronic applications of ZnO are similar to those of GaN, another wide-gap SC with E_g of 3.42 eV at 18°C (Table 1). GaN is widely used for the production of green, blue-ultraviolet, and white light-emitting devices. However, ZnO has some advantages over GaN, among which are the availability of fairly high quality ZnO bulk single crystals and a large exciton binding energy. ZnO also needs much simpler crystal-growth technology, resulting in a potentially lower cost for ZnO-based devices [111].

ZnO, like most of the group II–VI SCs, crystallizes in either a cubic ZB or hexagonal W structure. In addition to these structures, one more crystallographic phase for ZnO is known: the rock salt (NaCl) structure, which is formed as a result of transformation of the W structure at high external hydrostatic pressures. At ambient conditions, the thermodynamically stable phase is W. The ZB ZnO structure can be stabilized only by growth on cubic substrates. ZnO is generally an n-type SC because oxygen vacancies or non-stoichiometric Zn ions serve as donor states. In consequence, the electrical properties of ZnO can be changed from insulator, through n-type SC, to metal by controlling the doping level. Pure stoichiometric ZnO is an insulator; the conductivity of ZnO can be tuned over ten orders of magnitude with only relatively small changes in the concentrations of native or non-native defects such as interstitial zinc or aluminum [71].

ZnO is an efficient phosphor and nanocrystals emit light in the visible (trap emission) and UV ranges (exciton emission).Thus, ZnO exhibits UV, blue, green, yellow, and red color emissions and therefore could be a good candidate for the next generation of laser diodes and LEDs [112, 113]. A green band in the luminescence of ZnO appearing at about 2.5 eV has been observed in nearly all samples, regardless of growth conditions, and has also been obtained in undoped ZnO due to copper impurities. Schirmer et al. have prepared doped ZnO with Li acceptor, resulting in a yellow luminescence band with a peak at about 2.2 eV [114]. In contrast to the green band, the yellow band decays very slowly after switching off the excitation source and can also be observed in the thermoluminescence spectrum. A red luminescence band emerged at ca. 1.75 eV in the PL spectrum of undoped bulk ZnO after it was annealed in air at 700°C [111].

Other important properties of ZnO that make it preferable over other wide-band-gap materials are: high catalytic activity, effective antibacterial and bactericide action, stability and amenability to wet chemical etching [115], and resistance to high-energy radiation, which make it a very suitable candidate for applications in the space industry [116]. ZnO can find potential application in devices such as resonators, chemical absorbents [117], gas and pressure sensors [118], transparent thin-film transistors [119, 120], and as catalysts for photocatalytic degradation [121]. Piezoelectric ZnO can be used to build surface and bulk acoustic wave devices. Transparent and conductive ZnO thin films are finding application in solar cells and energy-efficient windows [112]. In particular, ZnO has been widely studied for organic–inorganic solar cells because of its very high electron mobility and high electron affinity [122, 123].

Many techniques have been used to prepare ZnO-based thin films and nanostructures, such as CVD, electron beam evaporation (EBE), MBE, pulsed laser deposition (PLD), sol–gel, spray pyrolysis, sputtering, and vapor phase growth. To prepare ZnO films or nanostructures, thermal oxidation of Zn and ZnS in air has also been used [124]. However, as for ZnS nanocrystals, wet methods, in this case wet oxidation, are still important techniques for SC processing [112].

5.5 TiO_2 Nanocrystals: Synthesis, Structure and Properties

Titanium dioxide (TiO_2) is an n-type SC with a wide E_g of 3.0–3.5 eV, it is well-known for its potential applications in the field of photocatalysis and photoelectrochemistry because of its excellent optical transmittance and high refractive index (2.5–3.87) (Table 1) [11]. TiO_2 is of outstanding importance as a white pigment because of its scattering properties, chemical stability, biological inertness, and lack of toxicity. Applications are found in paints, papers, fibers, cosmetics, sunscreen products, toothpaste etc.

TiO_2 exists in three crystallographic forms, namely anatase, rutile, and brookite, but the first two are the most important. However, the optical and electrical properties of anatase and rutile are different. Rutile is the most thermodynamically stable, and exhibits the highest refractive index. Nevertheless, the lattice energies of the other phases are similar and hence metastable over long periods of time. Rutile and anatase are produced industrially in large quantities and used as pigments and catalysts, and in the production of ceramic materials [125].

In addition, in recent years TiO_2, like ZnO, has been highly interesting for hybrid organic–inorganic PV devices and dye-sensitized solar cells (DSCs) [56]. Nanosized TiO_2 has been studied as a photovoltaic material since the 1980s, when the first observations of efficient photoinduced charge injection from dyes into TiO_2 were reported [126]. The voltage generated under illumination corresponds to the difference between the E_F of the electron in the SC electrode and the redox potential of the electrolyte. Along with these processes, electrons in the CB of the SC can recombine with the oxidized dye sensitizer or other electron-acceptor species in the electrolyte solution [127]. The highest conversion efficiency reported so far for this kind of device is about 10% under AM 1.5 (100 mWcm^{-2}) irradiation when liquid electrolytes containing I^-/I_3^- redox couples were used as conjunction [128].

During the last decade, a number of reports have been published on PV devices based on conjugated polymer and SC TiO_2 nanocrystals [129,130]. Compared to DSCs, solid nanostructured polymer–TiO_2 solar cells offer the potential advantage of useful photocurrents at much smaller device thicknesses because the entire polymer-filled pore volume is available for exciton generation, rather than only a dye monolayer at TiO_2 [56].

Kumazawa et al. used TiO_2 as an SC gas sensor that was able to distinguish alcohol and benzene compounds at low concentrations. It was found that the sensitivity of the sensor increased almost one order of magnitude under monochromatic light (at 700 nm) at an intensity of 50 mWcm^{-2} [130].

Many efforts have been made to develop and use TiO_2 as photocatalyst in heterogeneous photocatalytic oxidation (PCO) processes [130–132]. Gogate et al. defined PCO as a photocatalytic process that generates hydroxyl radicals for the degradation of organic chemicals present in water [133]. In the anatase and rutile crystalline form, TiO_2 behaves as a classic photocatalyst in which illumination of less than 385 nm promotes a redox environment. In turn, redox reaction takes place due to the presence of positive holes at the VB and negative electrons at the CB. These charge carriers might recombine, but if not, they diffuse rapidly to the surface for reduction or oxidation processes [131].

Different methods have been used for the preparation of TiO_2, such as hydrothermal methods [134], sol–gel processes [135], emulsion precipitation [136], and solvothermal methods [137, 138].

5.6 *CdSe, CdS, and CdSe/ZnS Quantum Dots: Synthesis, Structure and Properties*

Cadmium-based systems (CdSe, CdTe, and CdS) with direct-band gap have been extensively investigated during the last decade due to their nanocrystallites (QDs) and potential application in nonlinear optics, biological labeling and diagnostics, EL and PV devices, and sensors. SC QDs are nanocrystals that exhibit radii smaller than the bulk exciton Bohr radius, and they constitute a class of materials intermediate between molecular and bulk forms of matter. Recently, a number reviews concerning selective aspects of CdSe, CdS, and CdSe/ZnS QDs were published [139–141]. In the early 1980s, the blue shift of the band gap and a strong nonlinear response of nanoparticles of CdS and CdSe in glass samples was reported for the first time [140]. The representative samples of CdSe nanocrystals under room lights and UV illumination are presented in Fig. 9 [139]. The CdSe nanocrystals have been synthesized in TOPO/HDA/DPA (tri-*n*-octylphosphine oxide, hexadecylamine and dodecylphosphonic acid).

The structure of CdSe and CdS nanocrystals exhibits a phase transition of wurtzite to rock salt structures [141]. During illumination with UV light, the color of emission varies according to nanocrystal size with a complete color spectrum from blue to red. CdSe, CdTe, and CdS systems have drawn much attention as a consequence of the development of several synthetic methods for the preparation

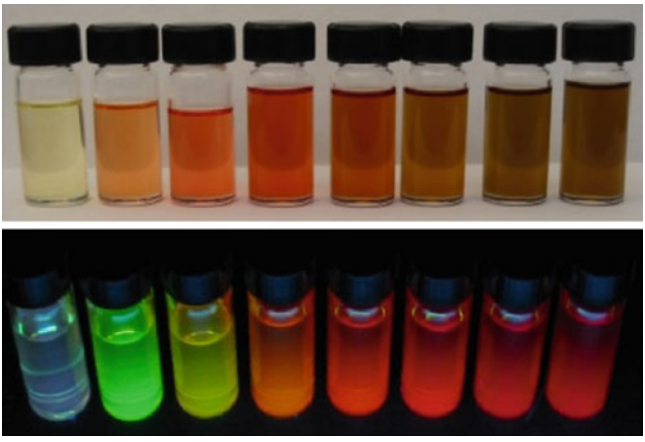

Fig. 9 Series of highly fluorescent CdSe nanocrystals synthesized in TOPO/HDA/DPA. CdSe nanocrystals under room light (*top*) and under UV illumination (*bottom*). The emission can be tuned from blue to red depending on the size of the CdSe nanocrystal [139]

of monodispersed samples. Nowadays, by using modern methods it is possible to synthesize gram quantities of nanocrystals with exquisite control of size ($\pm 20\,A^{\circ}$) [142]. Originally, the synthesis of nanoparticles relied on salts as precursors and micellar methods to attempt to control the size. Murray et al. reported for the first time a quantum leap in the quality and size control of CdSe nanocrystals with the development of high-temperature pyrolysis of organometallic precursors in a surfactant (i.e., dimethylcadmium $(CH_3)_2Cd$ in, TOPO) [143]. Further, TOPO on the surface allows the nanocrystals to be soluble in organic solvents or dispersed in a polymer film. Ligand exchange reactions can be performed to put polar groups on the surface of the nanocrystals and enable their dispersion in polar solvents [144]. Because $(CH_3)_2Cd$ has some disadvantages, such as toxicity and the need for airless techniques, Qu et al. elaborated a new procedure of synthesizing QDs using cadmium acetate $Cd(CH_3CO_2)_2$ as the precursor [145]. In this technique, a stock selenium solution of TOPO:Se is added to a mixture of TOPO/HDA/TDPA (tetradecylphosphonic acid) at 120°C. Then, the mixture was heated to 300°C and a stock solution of cadmium acetate in TOPO rapidly injected. In order to improve the yield and quality of the nanocrystals, co-solvents such as DPA and HDA have been added to TOPO. Typical PL QYs of CdSe nanocrystals were reported in the range 1–15% [145].

Overcoating nanocrystallites with higher-band-gap inorganic materials (e.g., ZnS, ZnSe, CdS) has been shown to improve PL QYs by a passivation of the surface against nonradiative recombination sites [146]. In the case of the core–shell QD nanocrystals such as CdSe/CdS or CdSe/ZnSe, they can show high fluorescence QYs in the range of 68–85% with initial surface ligands [147, 148]. In many cases, ZnS is the most important shell material because both photogenerated electrons and holes are efficiently confined in the nanocrystal core. The benefit of such QD-based OLEDs is that each recombination of a hole and an electron generates a photon, resulting in a possible 100% quantum efficiency at any visible wavelength [149].

6 Characterization of Carbon-Based Nanomaterials

6.1 Introduction

A great number of reviews concerning selective aspects of fullerenes and carbon nanotube (CNT) chemistry and physics have been published. The fundamentals of carbon nanostructures connected with fullerenes and CNTs were summarized by Kratschmer [150], Dresselhaus et al. [151] and Bernholc et al. [152]. The electronic and structural properties of CNTs were described by Mintmre et al. [153]. An overview of the synthesis and application of CNT–polymer nanocomposites can be found in recently published reviews [154–162] and in a comprehensive review with over 250 references cited in a tabular format [158]. Recent results on electrochemical formation of polymers containing fullerenes, and studies of their

properties and applications were critically reviewed by Winkler et al. [163]. Also, a review that summarized the latest theories of geological fullerenes was published by Buseck et al. [164]. In turn, important issues from the point of view of the preparation of polymer nanocomposites, such as functionalization reactions of fullerene (C60) with aliphatic amines and acenes as well as Diels–Alder cycloaddition reactions, have been summarized by Miller [165] and Briggs et al. [166], respectively.

In this chapter, we present a very short background and overview of carbon-based nanomaterials such as fullerenes and CNTs that have been used as nanofillers for the formation of nanocomposites for optics and electronics. However, their functional incorporation and utilization have been limited due to some processing difficulties. In general, there are two ways to incorporate CNTs into such a device configuration: layered assembly at desired locations or as a blend with the organic species. The success of the latter approach depends on appropriate chemical functionalization, individualization, and length-shortening of tubes, in addition to optimization of their concentration in organic composites [51].

6.2 Fullerenes

Various kinds of polymeric fullerenes can be prepared by using functional polymers to react with fullerenes, or by synthesizing polymers in the presence of fullerenes. From a structural point of view, these polymer are divided into four main categories: (1) polymers with fullerenes physically incorporated into the foreign polymeric network without forming covalent bonds, (2) fullerene homopolymers formed via [2 + 2] cycloaddition, (3) "pearl necklace" polymers with fullerenes mutually linked covalently to form polymer chains, and (4) "charm bracelet" polymers containing pendant fullerene substitutes. All these polymers have been critically reviewed by Winkler et al. [163].

Doping of polymeric systems with fullerenes is also a very important research area, especially for preparation of PV and EL devices. Since C60 is an electron transport material with high carrier mobility, which is a good electron acceptor capable of accepting as many as six electrons [167], a promising approach consists of blends of strongly light-absorbing conjugated polymers and soluble C60 derivatives deposited on transparent conductive substrate by a simple solution processing technique [168–170]. Fullerenes are hardly soluble in ordinary solvents; however, derivatives such as [6, 6]-phenyl-C_{61}-butyric methyl ester (PCBM) are soluble in common organic solvents such as chloroform, chlorobenzene, and 1,2-dichlorobenzene. The most commonly used semiconducting polymer for the fabrication of BHJ PV devices is regioregular P3HT. With optimized device structure and fabrication conditions, P3HT/PCBM BHJ solar cells can reach efficiencies as high as 4.4–5.0%, which is one of the highest efficiencies for blend organic solar cells [39,171]. On the other hand, Hutchison et al. used C60 for fabrication of LEDs with white emission, which were prepared from a blended film of the C60 adduct Th-hexapyrrolidin (PVK) and 2,5-bis-(4-naphthyl)-1,3,4-oxadiazole [172].

6.3 Nanotubes

CNTs are characterized by extraordinary mechanical, thermal and electronic properties, and CNT–polymer composites possess a broad range of potential applications such as digital data storage, PV cells, field emission displays, photodiodes, batteries, and sensors [156]. A number of reviews have been published on the synthesis and application of CNTs and their polymer composites [154–162]. CNTs are predicted to have high stiffness and axial strength as a result of the carbon–carbon sp^2 bonding. There are two main types of nanotubes available today. Single-wall carbon nanotubes (SWCNTs) consist of a single sheet of graphene rolled seamlessly to form a cylinder with diameter in the order of 1 nm and length of up to centimeters. Multiwall carbon nanotubes (MWCNTs) consist of an array of such cylinders formed concentrically and separated by 0.35 nm, similar to the basal plane separation in graphite [154]. Nowadays, MWCNTs are more than 500 times cheaper than SWCNTs at a similar purity (>95%). The electronic properties of perfect MWCNTs are known to be similar to those of SWCNTs owing to the one-dimensional electronic structure and electronic transport characteristics [173]. For example, their capacity to carry an electrical current is 1000 times higher than that of copper wires [174]. The electronic properties have proved to be especially unique, with capabilities of acting as either metal or SC, depending on the tubule diameter and chiral angle [155].

Recently, various methods used to produce CNTs, i.e., condensation–vaporization densation (CVD), a thermal chemical vapor deposition, and an arc method have been summarized by Paradise et al. [155]. It has been reported that the strength and thermal conductivity of polymers increase by about 3.5 and two times when 1–2% of CNTs is added in a conducting polymer matrix [175]. In this context, special attention has been paid to the following conducting organic polymers: PANI, polypyrrole (PPy), PTs, PEDOT, PPV and poly(*m*-pheneylenevinylene-co-2,5-dioctoxy-*p*-phenylene) (PmPV). Furthermore, the diameter of CNTs at nanoscale enables these nanocomposites to be transparent when the CNTs are well dispersed. Usually, CNTs are very difficult to disperse in a polymeric matrix because they possess a large surface area and have large van der Waals forces between tubules; due to this effect they can create strongly bound aggregates. In order to solve this problem, Liu et al. thoroughly investigated the dispersibility of SWCNTs in PMMA in eight different solvents by varying solubility parameters in three dimensions such as dispersive contribution (δ_d), polar contribution (δ_p), and hydrogen bonding contribution (δ_h) [176]. The results showed that for achieving good dispersion, the polar component (δ_p) of the solubility is very important, whereas the other components were less critical. The best SWCNT/PMMA dispersion was achieved in nitromethane, the most polar solvent used in this study [176].

7 Inorganic Nanoparticles in Non-conjugated Polymer Matrices for Optics and Electronics

7.1 Introduction

In this chapter, we describe nanocomposites based on non-conjugated polymers and the SC nanoparticles characterized in previous chapters. Recently, much effort has been devoted to the development of novel flexible and high dielectric constant (ε) dielectric materials that are processable and amenable to printing techniques. Polymers, however, posses relatively low dielectric constants; e.g., polystyrene (PS) and PMMA have relative dielectric constants (ε_r) of 2.6 and 3.5, respectively (Table 2). In turn, ceramics such as inorganic oxides are well known for their high dielectric constants; for instance, TiO_2 can have a dielectric constant of up to 330. Thus, polymer–inorganic nanocomposites are promising materials that can combine the high dielectric constant of the inorganic component with the processability and flexibility of polymers [179].

Inorganic–polymer nanocomposites characterized by exceptional dielectric constant are often called "artificial dielectrics". Artificial dielectrics are created when isolated particles become polarized due to the presence of an applied electric field. These novel nanocomposite artificial dielectrics have the potential to posses high dielectric constants (>100) at high frequencies and the low processing temperature associated with polymers. Such a combination of properties is not found in other capacitor materials [180]. Polymer matrices like PMMA, poly(vinylidene fluoride) (PVDF), PS, and polyurethane (PU) have been used. Owing to their physicochemical properties, they represent suitable polymer components for embedding nanoscopic functional inorganic fillers (Table 2).

Table 2 Non-conjugated polymers and their physical characteristics

Type of polymer	Dielectric constant (frequency)[1]	Refractive index	Glass transition temperature (K)	Specific electrical resistivity (Ω cm)
Poly(methyl methacrylate) (PMMA)	3.5 (50) [177]	1.49 [177]	379 [177]	10^{14} [177]
Poly(vinylidene fluoride) (Kynar) (PVDF)	8.4 (10^2) [178] 7.7 (10^3) [178]	1.46 [177]	337 [177]	2×10^{15} [178]
Polystyrene (PS)	2.6 (10^2–10^6) [178]	1.59–1.6 [177]	373 [177]	$>10^{17}$ [178]
Polyurethane (PU)	4.2 (60) [178] 2.75 (110) [178]	1.879 [177]	295 [177]	7×10^{13}–1×10^{15} [178]

[1]Frequency in Hz is given in parentheses
Relevant references for each entry are shown

7.2 Poly(methyl methacrylate)

Poly(methyl methacrylate) (PMMA) has been one of the most widely studied non-conducting polymers during recent decades due to its unique combination of good mechanical properties with excellent optical properties such as clarity and transparency from the near UV to the near IR. The fundamental electrical properties of PMMA and hybrid organic–inorganic composites of this polymer have been summarized by Gross et al. [4]. PMMA shows specific electrical resistivity that makes it an appealing starting material for the development of dielectric films. In turn, high resistance has resulted in its use in high voltage applications.

A further advantage of PMMA relies on its availability. Uniformly sized PMMA spheres are prepared by polymerization of methyl methacrylate (MMA) in water. The product of the polymerization then takes the form of a colloidal suspension of solid particles that are so small that they tend not to settle. By centrifugation, the PMMA particles are forced to settle and pack into a solid, often called a colloidal crystal. In such colloidal crystals, the PMMA spheres are arranged in a close-packed fashion in the same manner as the silica spheres that make up natural opal [178]. Therefore, these materials can be referred to as synthetic opals. Several textbooks cover selective aspects of the physicochemical properties of PMMA [181, 182].

7.3 Poly(methyl methacrylate) Nanocomposites

In this section, organic–inorganic nanocomposite materials in which PMMA is used as matrix are surveyed. Some reasons exist for the choice of PMMA as host matrix: PMMA can be easily obtained starting from a liquid low-cost monomer. The use of a liquid precursor allows molecular mixing with the inorganic nanoparticles already in the starting solution, thus ensuring a uniform distribution of the filler in the organic backbone. A further advantage of using PMMA as matrix polymer is that PMMA can be easily polymerized by means of a wide range of photoinitiators. Its use is thus encouraged by the most recent evolution of the coating industry, which is moving towards UV curing as a more flexible and energetically efficient technique. In addition, PMMA can be easily cast into film, thus allowing the final material to be shaped according to device requirements [4].

PMMA modified by inorganic nanoparticles such as TiO_2, ZnS:Mn, CdSe, CdSe/ZnS, ZnO, and CNTs has led to enhanced optical [16], thermal [149], and electrical properties, as compared to pure polymer. For example, Althues et al. [16] reported an efficient method for generation of completely transparent and strongly luminescent ZnS:Mn/PMMA nanocomposites. They used in-situ bulk polymerization of transparent dispersions containing ZnS:Mn nanoparticles in a mixture of MMA and AA; the effective diameter of nanoparticles in the monomer dispersion was 22 nm. Two factors were responsible for the stability of the ZnS:Mn/monomer dispersion, i.e., coordination of AA, which modified the surface of the nanoparticles and led to hydrophobization, and adsorption of ions leading to a surface charge

causing electrostatic repulsion. As mentioned before, adsorbed AA molecules are known to increase the PL intensity of ZnS:Mn nanoparticles. Therefore, ZnS:Mn/PMMA nanocomposites are characterized by strong luminescence with an emission maximum at 590 nm and a QY of 29.8%, one of the highest reported [16].

In turn, Pedone et al. [183] fabricated CdS/PMMA nanocomposites by a photocuring process. CdS nanoparticles capped with NaAOT and synthesized by using water-in-oil microemulsions were embedded in PMMA matrix. As a result, transparent yellow, solid nanocomposites of CdS/PMMA were obtained. It was found that during the embedding process, CdS nanoparticles were homogeneously dispersed in the polymer matrix and did not change their size [183].

In recent decades, PMMA has been used for modification of the optical properties of semiconductor NCs by using gamma (γ) radiation [184]. For instance, Wang et al. reported that the surfaces of TiO_2, ZnO, $Al2O_3$, and SiO_2 nanoparticles were modified by PMMA through γ irradiation [184–186]. The treated nanocrystals were mixed with MMA monomer solution and were put into an ampoule, and then sealed. The samples were irradiated with a dose of 10, 20, 30, 50, 70, or 90 kGy by radiation from a ^{60}Co source. The Fourier transform infrared spectroscopy (FT-IR) spectrum showed strong interactions between PMMA and nanoparticles. It was suggested that strong PL was caused by the carbonyl adjacent to the surface of the nanoparticles. Moreover, the nanocrystals modified by polymers showed changes in the PL spectra; for instance, ZnO exhibited strong blue luminescence (420 nm) [184], whereas emissions usually reported by many researches were at about 550 nm.

The example of PMMA-grafted nanoparticles was reported by Hong et al. [187]. First, ZnO nanoparticles were synthesized by homogeneous precipitation. In order to reduce the agglomeration of ZnO nanoparticles, the surface of ZnO nanoparticles was initially treated with the silane coupling agent γ-methacryloxypropyltrimethoxysilane (MPTMS), which introduces functional double bonds onto the surface of ZnO nanoparticles. The introduction of reactive groups onto the surface of ZnO nanoparticles was achieved through the reaction between the silane coupling agent and the hydroxyl groups on the nanoparticle surface, which was followed by radical polymerization in a non-aqueous system whereby PMMA chains were grafted onto the surface of ZnO nanoparticles. Finally, the modified ZnO nanoparticles were used as nanofiller for preparations of PS nanocomposites. The ZnO/PS nanocomposite was prepared by adding PMMA-grafted ZnO into styrene monomer, followed by radial grafting polymerization. The grafting polymerization did not change the crystalline structure of ZnO nanoparticles. Due to the grafting process, the dispersibility of ZnO nanoparticles remarkably improved in organic medium and aggregation was reduced [187].

Next, nano-ZnO/PMMA composite latex microspheres were fabricated by in-situ emulsion polymerization [188]. In order to avoid the aggregation of ZnO nanoparticles in the polymerization and to ensure effective encapsulation, nano-ZnO was also treated with a silane coupling agent, MPTMS, before the polymerization. MPTMS, which offers steric hindrance between inorganic nanoparticles and prevents their aggregation, was grafted to the surface of nano-ZnO by reaction with hydroxide groups and later copolymerized with MMA monomer. Transmission electron microscopy images indicated that ZnO nanoparticles (20–70 nm in size) were present in the

sphere and were completely encapsulated in the PMMA phase. The absorbance spectrum of the nanocomposite polymer suggested that increasing the amount of ZnO nanoparticles in composite particles could enhance the UV-shielding properties of the polymers [188].

The interest in using CNTs as nanofillers in a PMMA matrix is increasing [188–193]. For instance, Jin et al. reported on the electrical conductivity and electrorheological (ER) properties of MWCNT-adsorbed PS and PMMA microspheres prepared by a simple and potentially scalable process [191]. First, homogeneous aqueous dispersions of MWCNTs were obtained with various surfactants and then dispersions of PS and PMMA microspheres were dropped into a beaker containing the nanotube dispersions. The PS and PMMA microspheres with adsorbed nanotubes underwent slow sedimentation. Adhesion of the nanotubes to the PS and PMMA microsphere surfaces was believed to be related to the hydrophobic interaction. The electrical conductivity of these nanotube-adsorbed microspheres was investigated; the DC conductivity of samples was in the range of 1.9×10^{-4} to $6.2 \times 10^{-5}\,\mathrm{S\,cm^{-1}}$ at room temperature, based on the cross-sectional area, whereas the electron conductivity of the pure MWCNTs was $2.3 \times 10^{-1}\,\mathrm{S\,cm^{-1}}$. Next, ER fluids were prepared by sonication using the dried nanotube-adsorbed microspheres dispersed in silicone oil. The behavior of the particle chain in silicone oil was demonstrated under an applied electric field of $1.4\,\mathrm{kV\,mm^{-1}}$. The nanotube-adsorbed PMMA microspheres formed thin chains of particles under the applied electric field within 1 s, and the structure remained stable as long as the field was applied. ER fluids have been used in many fields using electromechanical devices, including engine mounts, shock absorbers, clutches and so on [191].

Park et al. [144] conducted a study in which PMMA/MWCNT nanocomposites were prepared via both in-situ bulk polymerization and suspension polymerization, using the radical initiator 2,2-azobis(isobutyronitrile) (AIBN). The electrical and electrorheological (ER) properties of the nanocomposites were investigated. The conductivity of pure PMMA and MWCNT/PMMA nanocomposites were measured, and it was shown that the conductivity of MWCNT/PMMA composites rapidly increased when MWCNTs were added to the PMMA matrix, i.e., 3.192×10^{-4}, 2.163×10^{-2}, and $1.693 \times 10^{-1}\,\mathrm{S\,cm^{-1}}$ for 1.5, 5 and 10 wt% of MWCNT in the composites, respectively. The conductivity of insulating PMMA was about $1 \times 10^{-13}\,\mathrm{S\,cm^{-1}}$ [144].

Recently, the thermal and mechanical properties of MWCNT/PMMA or SWCNT/PMMA nanocomposites have been thoroughly investigated [145, 146]. For instance, Lee et al. [146] reported the fabrication and characterization of MWCNT/PMMA by using both injection molding and film-casting processes. The tensile strength of the MWCNT/PMMA nanocomposite increased by more than 15% and tensile stiffness also increased by about 17.5%, compared to pure PMMA. It was confirmed that a combined fabrication process efficiently dispersed MWCNTs in the PMMA matrix and also maintained the well-dispersed state more effectively [146].

Similarly, Dai et al. reported on the electrical conductivity and mechanical properties of SWCNT/PMMA composites fabricated in a stretching process. The composite films showed higher conductivity and higher mechanical draw ratios

along the stretched direction than perpendicular to it. Compared to pure PMMA, the electrical conductivity of nanocomposite containing 3 wt% aligned SWCNTs increased by nine orders of magnitude, up to $10^{-3}\,S\,cm^{-1}$, and the maximum draw ratio was higher (up to 5000) than that of pure PMMA (3500). The authors also observed improved thermal stability of nanocomposites compared to a PMMA matrix [193]. Also, the dielectric properties of PMMA nanocomposites were thoroughly investigated. Clayton et al. reported that the dielectric constant increased in the composite samples as compared with the pure PMMA samples prepared by the same methods. SWCNT/PMMA composites were fabricated via in-situ polymerization induced by heat, UV light, or ionizing (γ) radiation [194].

PMMA nanocomposites were used to fabricate vertical microcavities having a well-defined resonance wavelength. However, in all these samples, the active layer of the NCs was deposited by spin-coating, without any control on the in-plane positioning. The possibility of selectively localizing the NCs on a substrate is a very challenging task, because it can lead to fabrication of two-dimensional active photonic crystals (PC). For instance, Martiradonna et al. [195] reported the successful and precise localization of colloidal nanocrystals (CdSe/ZnS) through the nanopatterning of colloidal nanocrystals dispersed in a PMMA matrix. To enable the fabrication of active PMMA-based optical devices embedding localized colloidal nanocrystals as the gain medium, a blend of PMMA and nanocrystals was directly exposed by means of an electron beam lithography process. Monodimensional periodic stripes and bidimensional periodic pillars were patterned on a thin film of CdSe/ZnS/PMMA nanocomposite deposited on a silica substrate. The investigation of PL properties of the patterned samples showed a complete removal of active material from the regions exposed to the electron beam without affecting the emission spectrum of nanocrystals in unexposed regions [195].

CdSe/PMMA nanocomposites have also been used as chemical sensor for detection of aromatic hydrocarbons [196]. In that study, a series of surface-modified QDs, which utilized both TOPO and carboxylic acids attached to the surface of CdSe SC QDs, were developed. Unmodified QDs and surface-modified nanocrystals were incorporated into PMMA matrices, and the PL of nanocomposites was studied as a function of a series of exposures to toluene and xylene vapors ranging in concentration from ppm to percent levels. It was reported that reversible enhancement and quenching of the PL on film exposure to toluene and xylene vapors were both observed for the QDs modified by carboxylic acid systems. PL enhancement was observed at low target gas concentrations, with the onset of the quenching process for each of the films being dependent on the target gas type and its concentration [196].

7.4 Polystyrene

PS is an important non-conducting polymer that belongs to the most common polymer matrix used for the synthesis of inorganic–organic nanocomposites. The dispersion of SC QDs within the polymer can be achieved by both ex-situ and in-situ methodologies. Monolithic spherical colloids from PS were self-assembled

into high-order face-centered cubic (FCC) PCs. Both theoretical and experimental work indicates that homogeneous spheres assembled into traditional FCC lattices yield incomplete photonic band gaps, or stopgaps, regardless of high dielectric contrast. However, coated spheres or core–shell colloids in a simple FCC lattice were calculated to exhibit a significantly enhanced L-stopgap width, by as much as 50% over their monolithic counterparts [197].

7.5 Polystyrene Nanocomposites

Recently, PS nanocomposites have been extensively reported and various inorganic nanomaterials including C60, nanotubes, CdS, CdSe/ZnS, and ZnS have been used as nanofillers [197–206]. For instance, the structure and electrical transport properties of C60 PS structures were investigated by Adamopoulos et al. [198]. The C60-containing PS materials were prepared by cycloaddition reaction of azidomethyl-substituted polystyrene with C60. The values of the dielectric constant of the nanocomposite increased with increasing the content of C60 from 2.4 for pure PS up to 2.7 for a C60 content of 60 wt%. The PS–C60 organic SC was used as an electron acceptor in PV systems [198].

Modification of the electrical properties of PS by the introduction of SWCNTs was described by Wang et al. [199]. The SWCNT/PS nanocomposites with 0–1.0 wt% content of SWCNTs were successfully fabricated by an in-situ suspension polymerization method. DC resistivity and AC impedance measurements performed on the nanocomposites showed that the presence of SWCNTs significantly modifies the electrical impedance of the composites. For instance, for a loading of 1.0 wt% CNT, the resistivity value dropped by over ten orders of magnitude [199].

Several reports related to CdS nanocrystals incorporated in PS matrix have been reported in the literature [200–202]. Zhao et al. described preparation of small nanoparticles of CdS by a hydrothermal procedure in an aqueous solution that yields transparent CdS/PS nanocomposite films [200]. CdS/PS nanocomposites were also prepared successfully using in-situ thermolysis synthesis of a cadmium thiolate precursor dispersed in the polymer [201, 202]. The preparation of CdS/PS via a thermolysis method has several interesting advantages with respect to the common methods of precipitation; for example, the CdS precursor is easy to prepare and is stable under normal conditions. The thermal and structural properties of CdS/PS nanocomposites also were broadly investigated [201, 202].

Antolini et al. found that CdS nanocrystals could be obtained by regioselective thermal decomposition of metal alkanethiolates in a PS matrix by selective heating of a polymer foil filled with the cadmium-(bis)-thiolate precursor by means of focused laser beam irradiation. The nanocomposites were characterized by strong PL with an emission maximum at 535 nm, which confirms the presence of CdS nanocrystals. These materials can be use for preparation of nanoelectronic devices or conductive plastics [203].

Submicrometer fluorescent colloidal PS beads have been used in medical and biotechnological fields, where they are utilized as fluorescent probes for diagnosis,

imaging, and optical tracking, making them very valuable tools. The preparation of fluorescence submicrometer polymer particles exhibiting a narrow particle size distribution (the emission wavelength being size-dependent) improved the photostability. Some of the most frequently studied systems are composed of CdSe, or of a CdSe core passivated with ZnS, and great progress in this field has been observed in the last decade [204–206]. For instance, Riegler et al. reported a facile and fast method of fabricating CdSe/ZnS/PS nanocomposite beads [204]. The nanocrystals were immobilized within the PS beads by demixing two nonmiscible solvents. In this method, nanocrystalline CdSe/ZnS stabilized by TOPO was dissolved in a substance (toluene) that dissolves PS beads, and then added to beads dispersed in an nonmiscible solvent (water). The solvent and nanoparticles were quickly transferred to the polymer phase (demixing). Next, all solvents were removed. Finally, it was observed that the CdSe/ZnS/PS nanocomposite beads exhibited strong and differently colored luminescence. CdSe/ZnS/PS nanocomposite beads found an application as a model sterptavidin–biotin binding system and demonstrate the applicability of this technique to enzyme-linked assays [204].

Another synthetic method for submicrometer fluorescence CdSe/ZnS/PS nanocomposite particles was developed by Joumaa et al. [205]. Submicrometer-sized particles were synthesized via a mini-emulsion PS process and CdSe/ZnS was coated by PS. Styrene emulsion and mini-emulsion polymerizations were performed in the presence of either TOPO-coated or vinyl-functionalized CdSe/ZnS nanocrystals. Both emulsion and mini-emulsion processes were first applied to the incorporation of TOPO-coated CdSe/ZnS nanoparticles. Then, the concentration and type of QD as well as the surfactant concentration were varied in order to investigate the influence of these parameters on the mini-emulsion polymerization kinetics and PL properties of the final particles. The final particle size could be tuned between 100 and 350 nm by varying the initial surfactant concentration. The intensity of luminescence properties increased with the number of incorporated TOPO-coated CdSe/ZnS nanoparticles, and the slight red shift of the emission maximum, induced by the polymerization, was correlated with modification of the medium surrounding the nanoparticles. TOPO-coated CdSe/ZnS nanoparticles showed higher fluorescence intensity than those with a vinyl moiety [205].

Sherman et al. fabricated CdS and CdSe/CdS nanoparticles/PS latex composite materials [206]. The nanocrystals were stabilized with poly(cysteine acrylamide) and then bound to polystyrene latex by two different methods. First, anionic 5-nm diameter CdS particles were electrostatically attached to 130-nm surfactant-free cationic PS latexes to fabricate stable dispersions. The PL spectrum showed that the luminescence properties of the latex composite did not depend on the amount of CdS nanoparticles, and that the emission did not change. Another approach to forming CdS and CdSe/CdS nanoparticles/PS latex composites was performed in surfactant-free PS latexes by in-situ polymerization in the presence of nanocrystals. This method was simple and effective, and the size of the latexes was easily tunable. All of these nanocomposite particles were dispersed in water and have a potential application as colloidal crystals for photonic band-gap materials, biological labeling, and optical tracking [206].

More recently, ZnS-coated PS nanocomposite colloids were synthesized by the chemical bath deposition technique of thioacetamide in the presence of PS seed particles and metal salt [197]. It allowed deposition of high refractive index ZnS shells of controlled thickness onto sulfate-modified and plain PS cores of size of about 200–500 nm. In order to prevent aggregations of PS particles, PVP was added during the reaction. The effective refractive index of the ZnS shell–PS core (PS/ZnS) composite particles varied between 1.73 and 1.98 at wavelengths above the optical absorption edge of ZnS. The porosity of the shells was between 12 and 19%, and the core–shell colloids served as building blocks for self-assembly at the submicron length scale [197].

7.6 Poly(vinylidene fluoride)

Poly(vinylidene fluoride) (PVDF) is a semicrystalline commercially available polymer with outstanding electrical properties. The dielectric constant is unusually high compared with other polymers, i.e., 7.7–8.4 (Table 2). The glass transition temperature is typically ca. 40°C, so the polymer is glassy with good mechanical properties at room temperature [177, 207]. Usually, PVDF is synthesized by radical polymerization in an emulsion or suspension of the gaseous monomer ($CH_2 = CF_2$). The reaction has been preferentially performed in water at elevated temperatures (up to 150°C) and pressures (1–100 MPa) with organic peroxides (e.g., benzoyl peroxide or diisopropyl peroxidicarbonate) as initiators [208, 209].

PVDF has a complex crystalline polymorphism not observed in other synthetic polymers. It has four known polymorphs, called α, β, γ, and δ. The most common form and most thermodynamically stable form of PVDF is obtained from melt with α-polymorph monoclinic unit cell. The β-phase is usually used in pyro- and piezoelectric applications because of the chain structure of the polymer, which consists of all the fluorine atoms on one side of the chain and the hydrogen atoms on the other side ("zigzag" chain structure). This structure is the key to high piezo- and pyro-activity because the net dipole momentum is very high and perpendicular to the chain direction. The β-phase is generally obtained by drawing PVDF α-phase films at a temperature of 70–87°C [210]. The γ-phase is obtained by high temperature melt crystallization. The δ-phase is obtained by a distortion of one of the other phases under high electric fields [207].

7.7 Poly(vinylidene fluoride) Nanocomposites

In contrast to studies on PMMA and PS nanocomposites, limited information has been available concerning the fabrication of PVDF nanocomposites. PVDF has been used as a solid polymer electrolyte for attaining high solar energy conversion in DSCs [132, 211, 212]. Moreover, PVDF has become a favorable choice as the

polymer matrix for solid polymer electrolytes due to its appealing properties, such as a high dielectric constant and strongly electron-withdrawing fluorine atoms.

Anandan et al. reported that PVDF was used as a component in fabrication of DSCs [211]. For such a purpose, heteropolyacid was impregnated in PVDF polymer with iodine/iodide as a solid polymer electrolyte for DSCs in order to effectively decrease the back-electron transfer reaction; TiO_2 nanoparticles were used as dye-adsorbants. The solar cell, composed of new polymer electrolyte (PVDF), TiO_2 nanoparticles (photoanode) and conducting carbon cement, was cemented on conducting glass (photocathode). An overall energy conversion efficiency of up to 8% was reported [211].

In turn, nanocomposite polymer electrolytes composed of PVDF, lithium perchlorate ($LiClO_4$), and TiO_2 nanoparticles were fabricated by a solution-cast method. TiO_2 nanoparticles were synthesized in situ within the polymer host by a sol–gel process. The analysis of mechanical properties showed that the Young's modulus of the PVDF/$LiClO_4$/TiO_2 nanocomposites increased with an increasing amount of TiO_2 nanoparticles. The ionic conductivity of the solid polyelectrolyte system PVDF/$LiClO_4$/TiO_2 was strongly related to the TiO_2 content. The maximum conductivity was observed for nanocomposites containing 10 wt% of TiO_2 nanoparticles and the optimal value was $7.1 \times 10^{-4}\,S\,cm^{-1}$. For a wet system of PVDF/$LiClO_4$/TiO_2 nanocomposites, conductivity was increased more than twofold to $1.8 \times 10^{-3}\,S\,cm^{-1}$. This kind of nanocomposite can be used to create a new generation of rechargeable solid-state lithium batteries [213].

Losit et al. reported the preparation and characterization of the TiO_2/PVDF nanocomposite films by X-ray photoelectron spectroscopy. TiO_2/PVDF nanocomposites were deposited on glass by the spin-coating method and by casting. The optimized TiO_2/PVDF composite was adopted successfully in a preliminary photocatalytic test on the phenylurea herbicide known as isoproturon, and showed a significant increase in its degradation rate, compared to simple photolysis under the same conditions. The TiO_2/PVDF nanocomposites appeared promising substrates for pesticide degradation under solar UV radiation [132].

Recently, PVDF has been intensively studied by many authors as a polymer matrix for ceramic nanopowders such as $BaTiO_3$ [212, 214–216], $PbTiO_3$ [217], $CaCO_3$ [218], and $Pb(Zr_{0.5}Ti_{0.5})O_3$ [215] because they combine the excellent ferroelectric properties of ceramics with the flexible mechanical properties of the polymer. The PVDF polymer composites with electroactive ceramic nanoparticles were prepared by sol–gel processes [214, 217], a natural adsorption action between the nanosized $BaTiO_3$ and PVDF particles, and then a hot press process [216].

Lijie et al. reported the fabrication and characterization of $BaTiO_3$/PVDF nanocomposites via the sol–gel method, in which nanosized $BaTiO_3$ particles with an average size of 50–100 nm were grown in situ in the PVDF matrix. $BaTiO_3$ is a ferroelectric ceramic widely used in capacitors and ultrasonic transducers. It was observed that the relative dielectric constant of nanocomposites increased in the frequency range of 5×10^4 to 3×10^6 Hz with increasing weight fraction of nanosized ceramic in the polymer matrix [214].

Yan et al. used $CaCO_3$/PVDF nanocomposites for the fabrication of superhydrophobic coatings for water-repellent application [218]. In the last decade,

there has been a continuous demand for water-repellent coatings in industry, and especially for super-hydrophobic coatings that present water contact angles greater than 150°. A simple mixing method for the preparation of $CaCO_3$/PVDF nanocomposite solutions was used, and then coatings were obtained by casting of the resulting solution on clean glass substrates. The obtained $CaCO_3$/PVDF nanocomposite coatings were extremely hydrophobic. Water droplets were unstable on these surfaces and were observed to be constantly rotating while resting on the stable horizontal coating surface. The contact angle of water on these surfaces was ca. 153° whereas the contact angle of water on pure PVDF is 108° [218].

7.8 Other Non-conducting Polymer Nanocomposites

There have been only a few reports on the fabrication of PU or PU copolymers nanocomposites with SCs inorganic nanoparticles [22, 215, 219].

Lu et al. studied the optical properties of ZnS/poly(urethane-methacrylate macromer) (PUMM) [219]. First, ZnS nanoparticles were synthesized using thiophenol-4-thiomethylstyrene as capping agent. Next, nanoparticles were dissolved in DMF and then a UV-curable urethane-methacrylate macromer (UMM) macromer was introduced in the nano-ZnS solution. The ZnS nanoparticles were immobilized into the polymer matrix via copolymerization of the macromer with 4-thiometylstyrene bound on the surface of ZnS particles. The ZnS/PUMM nanocomposites were characterized by high optical transparency, good distribution of ZnS nanoparticles in polymer matrix, a relatively smooth surface of nanocomposite films, and high refractive index (ranging from 1.645 to 1.796 at 632.8 nm as the content of ZnS nanoparticles increased from 0 to 86 wt%). This material can be successfully used for producing highly refractive optical coatings for such applications as lenses and antireflective films [219].

In a subsequent study, PTU was used as a polymer matrix and ZnS nanoparticles were stabilized by thiophenol/mercaptoethanol [22]. Like in the previous report [219], the investigated ZnS/PTU nanocomposites exhibited good thermal stability, well-dispersed ZnS nanoparticles in the polymer matrix, high optical transparency, and a high refractive index in the range 1.574–1.848 at 632.8 nm, which linearly increased with the content of ZnS nanoparticles from 0 to 97 wt% [22].

8 Inorganic Nanoparticles in Conjugated Polymer Matrices for Optics and Electronics

8.1 Introduction

The conjugated polymers discussed in this paper have a bonding pattern consisting of alternating single and double carbon bonds along the backbone of the chain. After 30 years of maturation, the world of conjugated polymers and oligomers has become

Table 3 Conjugated polymers and their physical characteristics

Type of polymer	Dielectric constant (frequency)	Refractive index	Glass transition temperature (K)	Specific electrical resistivity (Ωcm)
Poly(3-hexyl-thiophene) (P3HT)	2.6 (1) [238]	1.7 [239]	370 [240]	3.7×10^5 [238]
Poly(*N*-vinyl-carbazole) (PVK)	3 (1) [241]	1.69 [177]	423 [241]	10^{12} [241]
Poly(*p*-phenylene vinylene) (PPV)	3.2 (0.5) [177]	2.1 ± 0.2 [177]	423 [242]	10^2–10^3 [243]
Polyaniline (PANI)	8.9 (1) [244]	1.85 [177]	474 [177]	10^3 [245]

[1]Frequency in MHz is given in parentheses
Relevant references for each entry are shown

established as an important branch of materials science with many opportunities for applications in electronics and photonics [220]. In recent years, a number of reviews on application of conjugated and conductive polymers have been published [221–230]; however, in this paper we concentrate on the application of conjugated polymers for the preparation of polymer nanocomposites and their applications.

In contrast to inorganic SCs, photoexitation of organic SCs results in a strongly bound electron–hole pair, called exciton. An important consequence is that for photovoltaic p–n junctions, such bound electron–hole pairs in organic SCs are only effectively separated at an interface between a p-type (electron-donating) and n-type (electron-accepting) material. In general, the exciton life time and mobility within organic SCs are limited by radiative and nonradiative decay, which results in short exciton diffusion lengths (10 nm) in these polymeric materials. Further challenges in achieving an optimized phase separation for an improved exciton-dissociation limit the thickness of the active layer in a number of applications [231]. Only excitons generated in close vicinity of a p–n interface will give rise to separated charges. In BHJ solar cells this limitation is circumvented by intimately mixing the p- and n-type materials, thus creating junctions throughout the bulk of the material and ensuring quantitative charge generation from photogenerated excitons [232].

High performance electrical or optoelectrical devices, such as LEDs, field effect transistors (o-FET), and PV cells, fabricated from conjugated polymers have been demonstrated [233–236]. Also, a number of important prototypes have been demonstrated in this emerging "plastic electronics" technology such as multi- and full-color displays and radio-frequency transponders [237]. The properties of the conjugated polymers discussed in this chapter are presented in Table 3.

8.2 Polythiophenes

Among conducting polymers, various derivatives of polythiophenes (PTs) have been investigated extensively because of their interesting semiconducting, electronic,

and optical properties, combined with processing advantages and good mechanical characteristics [246]. A number of comprehensive reviews have been published on PTs; for example, Roncali surveyed electrochemical synthesis and the electronic properties of substituted PTs [247], while McCullough focused on chemical synthesis of conducting PTs [248]. Compared with other conjugated polymers, PTs show sufficient stability for practical applications [46, 249].

To improve the solubility of PTs, many different R groups have been explored, ranging from alkyl, alkoxy, acid, ester, and phenyl groups. For such applications, the most important group is P3HT. For instance, as an electron donor in solar cells, P3HT can be blended with many acceptors such as fullerene derivatives and inorganic nanocrystals. For this reason, P3HT is one of the most-studied conjugated polymers, with the low band gap of 1.9 eV (650 nm) [227].

8.3 Polythiophene Nanocomposites

Solar cells based on P3HT : TiO_2 nanocomposite films were investigated by Kwong et al. [47]. The device structure was ITO/PEDOT : PSS/P3HT : TiO_2/Al. For low nanoparticle concentrations (20–30%), the device performance was worse than that of pure P3HT, whereas for higher concentrations (50 and 60%) significant improvements were obtained. The best result was for 60% TiO_2, with open circuit voltage (V_{oc}) of 0.44 V, short circuit current density (I_{sc}) of 2.76 mA cm^{-2}, FF of 0.36, quantum efficiency up to 15%, and power conversion efficiency (PCE, η) of 0.42%. Recently, P3HT/titanium hybrids were also synthesized by the sol–gel process using titanium(IV) isopropoxide as a precursor in the presence of silane-bearing P3HT [250]. It was demonstrated that the presence of the silane group effectively prevents the macroscopic aggregation of TiO_2 during sol–gel reaction, and that the effectiveness of photoinduced charge transfer from polymer to titanium in $Si-P3HT/TiO_2$ is approximately twice that of $P3HT/TiO_2$.

In turn, a composite of PTs and nanoscopic TiO_2, possessing a core–shell structure, was prepared via Sugimoto's oxidative polymerization of thiophene by iron(III) chloride in the presence of TiO_2 particles [251]. It was found that electrophoretic deposition was a feasible method for the preparation of thin nanocomposite layers, with highly porous structure, on various conductive substrates (e.g., Pt, ITO). Thin layers prepared in such a way were applicable for the investigation of electrochemical and photoelectrochemical properties of the nanocomposites. Cyclic voltammetry confirmed that the PT was still electrochemically active after electrophoretic deposition, showing the oxidation potential of the PT to be $+0.8\,V_{SCE}$. Finally, a direct transition (with band-gap energy of 1.95 eV) and a flat band potential ($0.6\,V_{SCE}$) were obtained via photocurrent measurements [251].

Blending inorganic nanorods with polymers has the potential of bridging the efficiency gap between organic and inorganic photovoltaic materials in the performance of solar cells [252]. Shape control of nanocrystals from spherical to rod-like forms allows for efficient one-dimensional electrical transport that can reach carrier

mobilities comparable to those of bulk inorganic SCs [253]. For instance, charge transport in composites of inorganic nanorods and a conjugated polymer was investigated using a PV device structure [254]. PV devices were fabricated by spin-casting a solution of CdSe nanocrystals and P3HT in a pyridine and chloroform solvent mixture onto an ITO or PEDOT layer with PSS on ITO-coated glass substrate in an inert atmosphere. By improving the efficiency of 7×60-nm CdSe nanorods, polymer blend devices at high intensity and achieving the same external quantum efficiency (EQE) and FF as at low intensity (54% and 0.62, respectively) a PCE of 3.6% can be reached under AM 1.5G illumination, which is about double the value that is currently achieved. Moreover, replacement of CdSe with CdTe to absorb a higher amount of solar radiation would enable these hybrid devices to reach a solar PCE beyond 5%.

In another paper, it was demonstrated that CdSe nanocrystals can be dispersed efficiently in P3HT matrix by the use of binary solvent mixtures, in which one of the components is a ligand for the nanocrystals [255]. Optimization of the morphology of nanocrystal–polymer blends with solvent mixtures and thermal treatment to remove interfacial and excess of the solvents yielded high efficiency PV devices. A device fabricated from 90 wt% $(7 \times 60\,\text{nm})$ nanorods of CdSe in P3HT spin-cast from 4 vol% pyridine in chloroform and thermally treated at 120°C achieved a maximum EQE of 59% under 450 nm illumination at an intensity of approximately $0.1\,\text{mWcm}^{-2}$, which is one of the highest EQEs observed in polymer blend PV devices [255].

Recently, nanorod–polymer composites consisting of intimately connected regioregular P3HT and CdSe nanorods also showed promise for applications in PV devices [48]. A synthetic route to chemically attach P3HT to CdSe nanorods was elaborated, and transmission electron microscopy of the P3HT-functionalized CdSe nanorods showed excellent nanorod dispersion in the P3HT matrix. The solid-state PL emission of thiophene-covered CdSe nanorods (8 nm in diameter and 40 nm in length) was centered at 660 nm, with peak width at half-height of 35 nm. It was noted that PL from the CdSe nanorods is relatively weak compared to that from P3HT, and that PL spectra of the nanorods and P3HT overlap. Thus, PL characterization performed on thin films of the P3HT-covered nanorods showed PL quenching of P3HT, making these hybrid materials good candidates for PV applications [48].

By controlling the size, shape, and distribution of nanoparticles, control of the efficiency of optical excitation to create electron–hole pairs as well as consequent radiative decay is possible due to the quantum size effect [252]. Combining electron-transporting nanocrystals with a good hole-transporting polymer, such as P3HT, enables the good transport characteristics of inorganic SCs to be exploited without sacrificing the solution processability of organic materials [256]. In order to compare the behavior of CdS and CdSe, QDs in P3HT-based nanocomposites were prepared [50]. Morphological studies showed that nanocomposites with ordered QDs having an average particle size of 3–5 nm were formed. UV results suggested that the conjugation present in the polymer matrix causes increased overlapping between electron–hole pair wave functions, while comparison of cyclic

voltammograms for pure polymer, CdS/P3HT, and CdSe/P3HT nanocomposites in the presence and absence of light showed that QDs immobilized in polymer can trap the intermediate radical cation at a given potential.

In turn, the Langmuir–Blodgett (LB) technique was used to deposit composite multilayers of poly(3-octylthiophene) (P3OT) with cadmium arachnidate (P3OT-CdA), zinc arachnidate (P3OT-ZnA) and copper arachnidate (P3OT-CuA). These composite multilayers were used as precursors to develop the respective semiconducting CdS, ZnS, and Cu_2S nanoclusters in the P3OT-arachnidic acid matrix. The formation of sulfide nanoclusters in the multilayer was determined, and X-ray reflectivity measurements showed a drastic reduction in the layered structural order on sulfide formation. Single-layer LED structures were fabricated using P3OT-CdA, CdS-P3OT-arachnidic acid, and ZnS-P3OT-arachnidic acid composites as active layers. The EL peaks from these structures are attributed to P3OT and nanoclusters of CdS and ZnS, respectively. The electroluminescent devices with nanoclusters containing emitter layers exhibited low turn-on voltages of ca. 5 V. Finally, blue EL was observed at room temperature from ITO/ZnS-P3OT- arachnidic acid/Al devices [257].

Blends of nanocrystalline ZnO nanoparticles and regioregular P3HT were used to construct hybrid polymer metal-oxide solar cells [53]. These PV devices provide an estimated AM 1.5 G energy conversion efficiency of 0.9% and an EQE of 27% at 480 nm. However, it was found that the charge recombination in the structure containing vertically aligned ZnO nanorods treated with an amphiphilic molecular interface layer is remarkably slow, with a half-life of ca. 6 ms and is over two orders of magnitude slower than that for similar structures based on randomly oriented ZnO nanoparticles [54]. The best ZnO nanorod:P3HT device using the molecular interface layer yields a I_{sc} density of $2\,mA\,cm^{-2}$ under AM 1.5 G illumination $(100\,mW cm^{-2})$ and a peak EQE of over 14%, resulting in a PCE of 0.2%.

Another alternative approach in the direction of introducing nanoscale structures into a polymer matrix is the addition of nanostructures like C60 and CNTs, which hold promise as exciton-dissociating centers and ballistically conductive agents with high carrier mobilities, in addition to being optically transparent, flexible, and environmentally resistant [258].

The properties of a device structured of SWCNTs and P3OT composites were investigated by Kymakis et al. [259]. Composite films were dropped or spin-cast from solution onto ITO and quartz substrates and studied using absorption spectroscopy and electrical characterization methods. It was found that diodes of Al/polymer–nanotube composite/ITO with a low nanotube concentration (1%) showed photovoltaic behavior, with an open circuit voltage (V_{oc}) of 0.7–0.9 V. The I_{sc} increased by two orders of magnitude compared with the pristine polymer diodes and the FF also increased from 0.3 to 0.4 for the nanotube–polymer cells. It is proposed that the main reason for this increase is the photoinduced electron transfer at the polymer–nanotube interface. Thus, the conjugated polymer–SWCNT composite represents an alternative class of organic semiconducting material. However, in a subsequent paper, it was shown that I_{sc} increased with light intensity, while V_{oc} remained constant at 0.75 V, which is larger than the theoretical limit calculated by

the metal–insulator–metal model [260]. Moreover, high V_{oc} is weakly dependent on the negative electrode work function, which suggested that E_F pinning between the negative electrode and the C60 could be the origin of the ohmic-like behavior of the C60-negative electrode contact [261].

Later, the interaction between SWCNTs and P3HT was investigated, and formation of P3HT microcrystals on the sidewall of CNTs was observed. SWCNTs were dispersed in the active layer homogeneously, which resulted in a large interface for photoinduced exciton formation and exciton dissociation. In addition, SWCNTs served as an additive reagent to elevate the crystallinity for P3HT based on local order of the polymer chain along the sidewall of CNTs, which accounts for the performance improvement of PV devices. The work-function-modulated reduction of the HOMO level for SWCNTs based on electron transfer from sulfur atoms on the polymer chain to SWCNTs explains the occurrence of high open circuit voltage. Sulfurs in the thiophene ring on the polymer chain are electron-rich due to the lone electrons. Therefore, strong interaction exists between thiophene segments of the polymer chain and pentagon defects on the CNTs. A similar binding was reported between an alkoxy phenylene segment on a PmPV chain and a pentagonal defect on CNTs [262].

In turn, the realization of controlled placement of a SWCNT monolayer network at four different positions in polymer–C60 BHJ solar cells was demonstrated, and their optoelectronic performance was investigated. Several devices were fabricated by precisely placing SWCNTs at different hierarchical levels in the device with structure P3HT/PEDOT/ITO. Dip-coating from an additive-free suspension of mildly purified SWCNTs in DMF was utilized for this purpose. It was found that SWCNTs on the cathodic side of the active layer lead to increased PCE from 4 to 4.9% under AM 1.5 G illumination; this being the highest value achieved for polymer-based solar cells incorporating CNTs [51].

Recently, a new method for the preparation of active layers of polymeric solar cells without the need for thermal post-treatment to obtain optimal performance was presented by Berson et al. [263]. P3HT nanofibers were obtained in highly concentrated solutions, which enabled the fabrication of nanostructured films on various substrates. By mixing the nanofibers with a molecular acceptor such as PCBM in solution, it was possible to obtain in a simple process a highly efficient active layer for organic solar cells with a demonstrated PCE of up to 3.6%, which was achieved with an optimum composition of 75 wt% nanofibers and 25 wt% P3HT.

8.4 Poly(N-vinylcarbazole) Nanocomposites

Since the photoconductive properties of poly(*N*-vinylcarbazole) (PVK) were revealed, carbazole-based polymeric materials have been extensively studied [264–266]. Recently, there has been a renewed interest in the study of photoconductive polymer composites. Photoactive dopants capable of charge injection into the polymer matrix are normally employed. Of these photoactive dopants, C60 and CNTs as well as inorganic SCs have been shown to be among the most efficient to date [267].

Because hole mobility is larger than that of electrons in most organic materials, some attempts have been made to fabricate organic–inorganic heterostructures, in which electrons have higher mobility than that of holes. For instance, the influence of PVK on the emission properties of ZnSe thin film in heterostructure devices was investigated by Yu et al. [268]. To obtain a hybrid device, PVK was spin-coated onto ITO to give a layer with thickness of about 130 nm. ZnSe film was then deposited by electron-beam evaporation at a rate of 1 Å s^{-1} under high vacuum, with the thickness of the ZnSe layer at ca. 100 nm. Next, it was found that the EL emission at 466 nm came from the ZnSe layer. The threshold voltage was about 10 V, and a brightness of 12 cd m^{-2} was obtained at 17 V. In a subsequent paper, the roles of ZnSe sandwiched between organic layers (i.e., organic/ZnSe/Alq_3) were studied by varying the device structure [269]. A broad band emission peaking at 443 nm with shoulders at 520 and 595 nm was observed from the device under electric fields; these corresponded to emissions from PVK, ZnSe, and Alq_3 layers. Finally, it was concluded that holes can transport through ZnSe into the Alq_3 layer and that electrons transport through ZnSe into the PVK layer. Oppositely charged carriers were encountered in ZnSe bulk and recombined to emit light [270].

The EL properties of PVK multilayered EL devices doped with ZnS:Mn and based on nanocrystalline particles were also investigated and compared with bulk thin film materials [271]. The PVK double layer was fabricated by successive spin-coating of PVK and PVK:NCs, and the film thickness of each layer was about 100 nm. It was found that multilayer EL devices that exhibited luminance up to thousands of cd m^{-2} [272] in the case of the application of nanocrystalline particles only reached a luminance of the order of 0.1 cd m^{-2}, probably due to an aggregation of nanoparticles. In turn, the properties of ZnS:PVK nanocomposites confined in the MCM-41 silicate were studied [273]. To prepare PVK:ZnS nanocomposites confined in the silicate, MCM-41 was modified with ethylenediamine followed by introduction of ZnS into their mesopores. Finally, N-vinylcarbazole was mixed with the obtained ZnS/MCM-41 and polymerized at 85°C for 6.5 h. In the PL spectra, an emission peak at 468 nm was observed. Further analysis indicated that the emission could be attributed to the exciplex of excited-state PVK molecules and ground-state ZnS clusters [272].

Furthermore, PVK:ZnS and PVK:CdS nanocomposites were synthesized via an in-situ microwave irradiation method [274], and their PL spectra studied by He et al. [275]. As many publications previously reported, these nanocomposites showed a strong emission from PVK and a weak one from metal sulfide nanoparticles. However, if ethylenediamine was employed as solvent to prepare the nanocomposites, two emission peaks attributed to PVK and exciplex could be observed when the nanocomposites were irradiated by light with wavelength of 355 nm. The existence of the emission from PVK should be assigned to the poorly mixed PVK matrix. Additional experiments indicated that no exciplex emission could be observed in the absence of any component of the ethylenediamine-modified nanocomposites.

A subsequent paper described the photoconductive characteristics of an inorganic–organic hybrid composite, in which PVK serves as a polymeric charge-transporting matrix, and in which QDs composed of surface-passivated cadmium sulfide serve as

a charge-generating sensitizer [267]. The PVK:CdS nanocomposites were directly compared with a similar composite composed of PVK and C60. The PVK:CdS-nanocrystal composite exhibited the greatest value for primary quantum efficiency ($\Phi_0 = 0.60$) at 514.5 nm and likewise exhibited the maximum achievable photocharge generation efficiency under conditions of high electric field ($>80\,\mathrm{V\,\mu m^{-1}}$). Similarly, the PVK:C60 composite showed the greatest photocharge generation efficiency below $80\,\mathrm{V\,\mu m^{-1}}$. From the comparison of the magnitudes of the dark current densities associated with the PVK:C60 composite and the PVK:CdS-nanocrystal composite, it was evident that they are of almost identical magnitude for the entire range of electric field that was studied, which is an important parameter for practical applications such as photorefractivity [267].

In turn, the interfacial charge separation process in these chemically hybridized CdS:PVK nanocomposites by steady-state and picosecond time-resolved PL and photoconductivity measurements was investigated by Cheng et al. [276]. The molar ratio of CdS to PVK was 1:80 and 1:34 for the PVK-10-CdS and PVK-15-CdS samples, respectively. The average particle size of Q-CdS was estimated to be ca. 3.0 nm for PVK-10-CdS and 3.8 nm for PVK-15-CdS. The photoconductivity was evaluated by the ratio of $\delta\sigma/\sigma_0$; where $\delta\sigma$ is the difference of the photocurrent of the device upon white light irradiation (σ) and the photocurrent of the same device without irradiation (σ_0). It was found that the samples doped with CdS nanoparticles exhibited photoconductivity enhancement and shorter response time than pure PVK. Moreover, PVK-10-CdS showed a higher photoconductivity than PVK-15-CdS although it contains less CdS.

Recently, cadmium selenium (CdSe) nanocrystals in aqueous system were synthesized after addition of mercaptoacetic acid as a stabilizer [277]. Then, a film of PEDOT:PSS was spin-coated on ITO glass and dried at 80°C for 10 min. Emitting materials, CdSe:PVK at a ratio of 2:1 by weight, were dissolved in chloroform and spin-coated onto the substrates. A surfactant was used to transfer the nanocrystals from the aqueous solution to organic solvent so that both CdSe and PVK were able to mix sufficiently in organic solvent. The thickness was about 50 nm. The organic films were grown in a high vacuum in the following sequence: a 10 nm thick film of bathocuproine, followed by a 10 nm thick film of Alq_3. In EL spectra, there were emission peaks at 405 and 560 nm,which came from PVK and CdSe QDs, respectively. Compared with the PL spectra, PVK emission was restrained in the EL spectra, and a strong EL band from CdSe QDs was observed. In the PL process, the incident light excites both PVK and CdSe QDs. Therefore, the PL spectra show characteristic features of both PVK and CdSe nanocrystals. The strong CdSe QD emission in the EL spectra indicates that the direct charge injection and formation of exciton on the CdSe QDs is the dominant excitation process in EL [277]. In a similar paper, it was shown that the doping of PVK with organic dyes (DCJTB) at 1 wt% and ZnO nanorods enhanced hole current density, which made EL devices more efficient [278].

As stated in the Chap. 7, manipulation and processing of CNTs have been blocked by their insolubility in most common solvents and by their tendency to aggregate. It has been found that one of the most promising approaches to effectively

resolve these problems is the covalent functionalization of CNTs with polymer. For this reason, PVK-grafted MWCNTs were synthesized via free-radical reaction in the presence of AIBN as an initiator [279]. The final product, in the form of a grey powder, was soluble in common organic solvents like chloroform and dichlorobenzene. The optical limiting properties were quantitatively compared by the measuring the limiting threshold, defined as the input fluence at which the transmittance falls to 50% of the linear transmittance. The limiting thresholds of all PVK-grafted MWCNT samples were about $1\,J\,cm^{-2}$.

Blends of PVK and CNTs were investigated as well. For example, the photoconductivity of PVK–CNTs blends was studied by Wu et al. [280]. To prepare PVK (1.6 wt%) blends with purified MWCNTs (p-MWCNTs) or didecylamine-solubilized CNTs (MDDA) for the photoconductivity measurements, a predetermined amount of p-MWCNTs or MDDA was added into a chloroform solution of PVK (25 mg/ml) and sonicated. The resulting mixture was spin-coated onto aluminum substrates covered with a thin layer of nylon film to ensure a full charge for the sample film. Both samples showed significant dark discharges, indicating a good dark conductivity [280].

The irradiation effect on the PL spectrum of PVK–C60 form nanocomposite films was also studied [281]. The physical jet deposition technique [282] was applied to fabricate the PVK–C60 form composite films, including multilayer and mixed films. Multilayer PVK–C60 form films were fabricated by alternatively depositing PVK and C60 materials on the fused silica substrate with nearly equal layer thickness. It was found that lengthy irradiation with a 532 nm picoseconds laser beam steadily increased the intensity of PL emission of PVK at 630 nm in the mixed film, reflecting that the population of the triplet state of the C60 molecule has a great effect on the excitation transfer process in the nanocomposite films.

Recently, the PL and EL properties of a polymer LED containing PVK–C60 form nanocomposite was described by Park et al. [283]. The device with ITO/PVK-C60/PVK/CPDHFPV/LiF/Al structure was fabricated as follows: a 40 nm-thick PVK-C60 film was spin-cast from chlorobenzene solution onto ITO. On top of the PVK-C60 layer, a PVK layer of ca. 10 nm thickness and an emitting CPDHFPV layer of 40 nm thickness were successively deposited by spin-casting from cyclohexanone and trichloroethylene solutions, respectively; finally, a 1 nm-thick LiF layer was vacuum-deposited. The properties of such a diode were compared with the diode without a PVK-C60 layer. The EL spectrum of the former diode showed a blue-shift compared with the diode without PVK-C60. The diodes with the PVK-C60 and PVK layers for hole transport gave a much stronger optical output than other diodes. Compared with the diode of ITO/PVK/CPDHFPV/LiF/Al structure, the diode with a PVK-C60 layer produced approximately threefold stronger optical output. Finally, it was concluded that PVK and C60 can form a group-state charge-transfer complex that provides improved balancing of electron and hole currents, resulting in an increase in EL efficiency.

SWCNTs were also used for the construction of OLEDs with the structure ITO-coated glass/PEDOT:PSS/SWCNT–PVK nanocomposites/DCM-doped Alq3/Li:Al [284]. The SWCNT–PVK nanocomposite was spin-coated onto the

PEDOT:PSS/ITO-coated glass and then DCM-doped Alq3 was deposited using cluster beam deposition methods [285]. Studies of PL, EL, and device characteristics demonstrated that whereas the EL of the devices with SWCNTs show the same characteristic emission as those without SWCNTs, the device qualities such as EQE were improved two- to threefold for SWCNT concentrations up to 0.2 wt% [284].

Finally, PV cells containing PVK and C60 built by using the physical jet deposition technique [282] were prepared and investigated [286]. The steady and transient photovoltage data were obtained for five kinds of photocells formed between ITO and aluminum electrodes. From the steady photovoltaic data, it was found that the PV signal of two-layer composite film structures was significantly enhanced compared with those of single-layer and multilayer films. The steady photovoltaic quantum efficiency of this photocell of two-layer composite structure, at $50\,\mathrm{mW\,cm^{-2}}$, $V_{oc} = 5.7\,\mathrm{mV}$ and $I_{sc} = 2 \times 10^{-6}\,\mathrm{A\,cm^{-2}}$ was evaluated to be about 0.5% electron/photon. Moreover, it was found that the PV signal of PVK/C60 two-layer composite is enhanced by five orders of magnitude compared to that of a single layer of pure PVK or its mixed (with C60) films. The experiments demonstrated that the significant enhancement of PV signal in two-layer composite films is attributed to the efficient charge separation at the PVK–C60 interface, which results from photoinduced electron transfer from PVK to C60. It was shown that there are two parts to the photovoltage contribution to the transient photovoltaic response of the two-layer composite films: the faster contribution is from the PVK–C60 interface and the slower is from the C60–Al interface. The time constants of these two response mechanisms correspond to 20 and 480 ns, respectively [286].

8.5 Poly(p-phenylene vinylene)

PPV and its derivatives are known to exhibit excellent PL and EL (green–yellow region) and nonlinear optical properties as well a high electrical conductivity ($10^{-4}\,\mathrm{S\,cm^{-1}}$). Thus, PPV is one of the most investigated organic materials and is favorable for application in EL and laser materials, solar energy cells and photoconductors. Due to its electrical properties (Table 3) and high thermal stability, PPV is still one of the most attractive materials for OLEDs [287]. The optical and electrical properties of PPV can still be improved by combination of this polymer with different inorganic SCs nanoparticles.

PPV can be prepared using standard electrochemical oxidation and simultaneous polymerization of monomers, which react at the anode of an electrochemical cell. An electrochemical synthesis of *p*-PPV and *o*-PPV has been reported by Peres et al. [288], who obtained thin polymer films on Au electrodes, by the cathodic reduction of $\alpha,\alpha,\alpha'\alpha'$-tetrabromo-*p*-xylene and $\alpha,\alpha,\alpha'\alpha'$-tetrabromo-*o*-xylene.

Like most conjugated polymers, PPV exhibits poor solubility, and its decomposition before melting makes it difficult to be processed, which can limit the applications. One strategy for solving this problem is to process the soluble sulfonium precursor of PPV and then convert it into the conjugated form by a thermal

elimination reaction. This provides easy processability and a pure material with high molar mass. Another way to solve this problem is an application of substituted derivatives PPV, e.g., poly[2-methoxy-5(2-ethyl-hexyloxyl)-*p*-phenylene vinylene] (MEH-PPV); such derivatives are soluble in common organic solvents and can be processed from solution into a uniform large area [288, 289].

8.6 Poly(p-phenylene vinylene) Nanocomposites

PPV is currently intensely studied by many authors as a polymer matrix for the preparation of hybrid inorganic–organic nanocomposites, and various inorganic SCs nanomaterials have been used as nanofillers, such as TiO_2 [290–295], SiO_2 [289, 296], CdSe [297–299], and fullerenes [300, 301].

Zhang et al. studied the relationship between the confined environments of the TiO_2 matrix and the optical properties of PPV/TiO_2 nanocomposites, prepared from mixtures of PPV precursor and titanium butoxide ethanol solution in a sol–gel process [292, 293]. It was found that the emitted light of the PPV/TiO_2 nanocomposites was blue-shifted without fine structure, and the PL intensity enhanced, when the TiO_2 network formed. These phenomena suggested that the optical properties of the PPV/TiO_2 nanocomposites were dependent on the interfacial structure between PPV and the TiO_2 nanocrystals [293]. In recent years, it was observed that TiO_2, CdSe, and C60 nanocomposite blends with PPV and MEH-PPV could result in improving PV efficiency [295, 297, 301, 302]. For instance, Salafsky et al. showed that in a nanocrystalline TiO_2/PPV composite, excitons photogenerated in the polymer can be dissociated at the interface between the components, with the electrons transferred to the nanocrystals [291].

Gao et al. reported the fabrication and characterization of photodetectors and PV cells from conjugated polymer MEH-PPV (donor) and C60 (acceptor) blend [301]. As solvent for both components, 1,2-dichlorobenzene has been used to prepare ITO/MEH-PPV:C60/Ca PV cells by spin-coating. By optimizing the donor–acceptor ratio, a PCE of 2.5% and a collection efficiency of 26% were achieved for solar cells. Under reverse bias, a photosensitivity of approximately 0.26 A W^{-1} has been achieved at 430 nm. The excellent photoresponse has been attributed to efficient charge separation and collection by the donor–acceptor BHJ of the composite films [301]. Similarly, the photovoltaic effect of photodiodes based on nanocomposites of water-soluble CdSe nanocrystals and MEH-PPV was studied by Tang et al. [297]. They observed that the intensity of PL of the nanocomposite decreased with an increasing weight ratio of CdSe nanoparticles to MEH-PPV. By comparing the photocurrent action spectra of the nanocomposite device and pristine MEH-PPV device, it was found that the nanocomposite device exhibited a wider photocurrent action range [297].

PPV nanocomposites have also received attention as EL materials, and there are several reports in the literature [294, 298, 299]. For instance, Yang et al. investigated the optical and electrical properties of PPV/SiO_2 and PPV/TiO_2 nanomaterials,

made by incorporation of SiO_2 or TiO_2 nanoparticles of different concentrations and sizes into PPV [294]. The absorption and PL spectra showed a large blue-shift trend with SiO_2 nanoparticles, but only a small difference with TiO_2 nanocrystals. Additionally, the intensity of PL spectra for PPV/SiO_2 exhibited an increase in intensity of the high-energy shoulder (515 nm) when the concentration of nanocrystals increased. Results of the investigation suggested that, in contrast to TiO_2 nanoparticles, SiO_2 nanoparticles reduced the PPV conjugation length. Finally, EL cells were prepared by depositing the active layer (PPV/SiO_2 and PPV/TiO_2) thin film onto ITO glass, followed by thermal evaporation of Mg/Ag cathode. For devices using PPV/SiO_2 composites, different current variations depending on the particles size were observed. The conductivity of the composites for small particles (20 nm) decreased with increasing concentration, whereas for larger particles (100 nm), it increased with the concentration [294].

Taylor et al. used the hybrid organic–inorganic CdSe/MEH-PPV nanocomposite as an efficient lumophore layer in order to tune the color emission in alternating current TFEL displays [298]. The flexible TFEL devices were composed of a plastic substrate (Mylar)/ITO//CdSe/MEH-PPV//phosphors (ZnS)//Ag layers. It was observed that CdSe nanocrystals can effectively absorb blue-green light produced by ZnS phosphors and re-emit the light in the red spectrum. The emission wavelength of the display was found to be directly related to the emission of CdSe QDs. A device emitted light when an AC voltage of approximately 100 V in a frequency range of 60–20,000 Hz was applied. In contrast to DC TFEL, AC TFEL devices do not need electrodes with different work functions and can be fabricated with chemically and physically stable electrodes. In recent work, ITO and Ag have been used to construct the devices. These devices were stable for six months at room temperature and ambient conditions [298].

In turn, Gao et al. studied thin films of CdSe/PPV nanocomposites that were prepared from a water-soluble precursor of pre-PPV and CdSe nanoparticles using a self-assembly deposition method [299]. The pre-PPV was converted to PPV by heating the whole sample at 130°C under 10^{-5} bar for at least 10 h. EL diodes were prepared from 20 double layers of PPV/CdSe deposited onto ITO glass and covered by Al electrodes. EL devices exhibited stable EL with a turn-on voltage below 5 V, and the emission of EL was only from CdSe nanoparticles. The current–voltage curves show inversion symmetry, but light emission was observed only under forward bias. The broad emission spectra are related to exciton trapping at the particle surface, which was confirmed by temperature-dependent measurements of PL [299].

8.7 Polyaniline

PANI has been applied for many practical fields such as energy storage, alternative energy sources, nonlinear optics, shielding of electromagnetic interference, antistatic coating, catalysts, indicators, sensors, corrosion protection, supercapacitors, etc. A number of articles and reviews covering selective aspects of PANI synthesis, properties and application were published recently [296, 302–312].

PANI and its derivatives can be synthesized by the electrochemical polymerization or chemical polymerization of aniline; although some other approaches have also been reported such as solid-state polymerization [313], electroless polymerization [314], plasma polymerization [315], and emulsion polymerization [307]. Various oxidants were used for oxidation of aniline monomer, such as ammonium peroxydisulfate, sodium peroxydisulfate, potassium bichromate, and hydrogen peroxide.

The processability of PANI is relatively poor because it is infusible and insoluble in common solvents. In order to improve processability, an alternative approach is to prepare PANI nanoparticles and disperse them uniformly in a mixture of aqueous and organic solvents. The PANI nanoparticles have been synthesized using polymer surfactant, and the diameter of the PANI was controlled by using different surfactants [303]. The preparation of PANI dispersions is one of the methods for increasing the processability. Preparing the polymer in the dispersion form has many attractive features. For example, the dispersion can be spread over surfaces to help dissipation of static charge. The dispersion can be blended with latexes or solutions of commodity polymers to yield conducting composites that can be easily processed [304,309].

8.8 Polyaniline Nanocomposites

PANI nanocomposites have been extensively reported in the literature [316–337]. In the case of nanocomposites of inorganic nanoparticles and conducting polymer, various inorganic nanomaterials including TiO_2 [316–321], CdS [322–324], Au [325], Fe_3O_4 [326], ZnSe [327], ZnO [328], and CNTs [329–337], have been formed via inclusion techniques using both chemical and electrochemical approaches. In general, the key issue for preparation of PANI nanocomposites is the good dispersion of nanoparticles in the PANI matrix, which is difficult to obtained with conventional methods due to the agglomeration caused by the high surface energy of the nanoparticles.

At the present time, several approaches to preparing PANI/TiO_2 nanocomposites have been reported. For instance, metal oxide (TiO_2) particles were encapsulated into a shell of PANI, giving rise to a host of nanocomposites. Li et al. prepared a hybrid nanocomposite of PANI with a self-assembled monolayer (SAM) of aminopropylsilane (PANI/SAM-TiO_2) that possessed better thermal stability, chemical stability, and photocatalytic activity in photodegradation of methyl orange under sunlight than neat TiO_2 nanoparticles without any surface modification [316]. In order to prepare hybrid PANI/SAM-TiO_2 composites, γ-aminopropyltriethoxysilane was used as a coupling agent to form a dense aminopropylsilane SAM with active sites for the graft polymerization of aniline. After TiO_2 nanoparticles were surface-modified, the conductive PANI layer was chemically grafted onto the surface of the SAM-coated TiO_2 nanoparticles, resulting in PANI/SAM-TiO_2 composites [316]. A similar method for preparation of PANI/TiO_2 nanocomposites was also presented in another paper [319].

Another interesting fabrication method of PANI/TiO_2 hybrid microwire nanocomposites in the microchannels of a template has been developed by Xiong et al. [320]. Hybrid PANI/TiO_2 microwires with diameter of 160–180 nm were successfully prepared via sol–gel process of TiO_2 and in-situ polymerization of aniline in the microchannels of anodic aluminium oxide (AAO) template. The PL characterization of PANI/TiO_2 microwires exhibited a blue shift of the emission peaks of hybrid microwires due to the quantum effects of TiO_2, and an energy band between PANI and TiO_2 [320].

Yavuz et al. reported the in-situ polymerization and characterization of PANI/TiO_2 nanocomposites in the presence of TiO_2 nanoparticles and three different surfactants: anionic sodium dodecylbenzenesulfonate (DBSNa), cationic tetradecyltrimethylammonium bromide (TTAB), and the nonionic surfactant poly(oxyethylene) (20) sorbitan monolaurate (Tween 20) [321]. All the composites were characterized by different thermal, electrical, and morphological properties. Electrical conductivity measurements indicated that the conductivity of PANI/TiO_2 synthesized in the presence of the cationic surfactant had the highest conductivity ($2.27\,S\,cm^{-1}$), whereas that in the presence of the anionic DBSNa had the lowest ($0.14\,S\,cm^{-1}$). All the composites showed negative mass magnetic susceptibility values. Moreover, the nanocomposites exhibited different morphological structure with changing type of surfactant, and the strongest interaction with composite matrix was with TTAB cationic surfactant [321].

Elsewhere, Tai et al. used PANI/TiO_2 nanocomposites prepared by in-situ chemical oxidation polymerization synthesis in the presence of TiO_2 nanoparticles to fabricate a gas sensor [317]. The responses of the PANI/TiO_2 nanocomposite thin film to toxic NH_3 and CO gas were investigated. It was found that the response, reproducibility, and stability of nanocomposite thin film to NH_3 were superior those for CO gas. The gas-sensing properties of the PANI/TiO_2 thin film to NH_3 and CO indicated that the PANI/TiO_2 thin film was an excellent candidate for NH_3 detection, but not for the fabrication of a CO gas sensor [317].

PANI/TiO_2 nanocomposites have been also used by Sathiyanarayanan et al. to protect magnesium alloy from corrosion [318]. The ability of the PANI/TiO_2 nanocomposite coating to protect against corrosion was found to be more than that of the pure PANI coating, because the uniform distribution of PANI can protect the metal surface more uniformly [318].

In recent decades, there have been many attempts to fabricate CNT/PANI composites [329–337]. The incorporation of nanotubes into PANI can result in novel composite materials with enhanced electrical, electrochemical, and mechanical properties. For example, Yu et al. prepared MWCNT/PANI nanocomposites through in situ inverse microemulsion synthesis [334]. Such nanocomposites are characterized by very strong interaction between MWCNTs and conducting polymers. Moreover, MWCNT/PANI core–shell nanowires exhibited better thermal stability and electrical conductivity than the pure PANI. The electrical conductivity of MWCNT/PANI composite containing 1 wt% of MWCNTs increased by one order of magnitude (pure PANI$\sim 0.02\,S\,cm^{-1}$, MWCNT/PANI composite $\sim 0.20\,S\,cm^{-1}$) [334].

In turn, Konyushenko et al. obtained MWCNT/PANI composites during in-situ polymerization in the presence of MWCNTs, which were uniformly coated with protonated PANI [330]. The electrical properties of nanocomposites were investigated, and similar effects as in previous work [334] were observed, i.e., the electrical conductivity increased with increased concentration of nanotubes in composite materials. The maximum conductivity, $25.4\,\mathrm{S\,cm^{-1}}$, was recorded for composites containing 70 wt% of MWCNTs [330]. Likewise, Wu et al. reported the increase of electrical conductivity for MWCNT/PANI composites [329]. The electrical conductivities of MWCNT/PANI composites containing 0.5 wt% functionalized MWCNTs are about 60–70% higher than of net-PANI [329].

Due to the outstanding electrical and electrochemical properties of CNT/PANI, composite materials have also been applied as anode for a microbial fuel cell [335], high performance supercapacitors [333, 336, 337], and as modified electrode for the reduction of nitrite [331].

9 Application of Nanocomposites

In this survey, we are focusing particularly on organic–inorganic hybrid nanocomposites applied in electro-optic devices as photovoltaic and light-emitting materials. Therefore, the state of the art concerning the PV, PL, and EL properties of inorganic–organic nanocomposites has been outlined. Other applications of polymer hybrid nanocomposites have also been broadly reviewed in the literature [10, 28, 56, 156].

In recent decades, many examples of heterojunction organic–inorganic PV devices have been studied [39–54, 254, 255, 259–263, 291, 295, 297]. BHJ polymer PV devices and photodiodes have been constructed with composite films of conducting polymers as electron donors, and semiconductor NCs or carbon compounds as electron acceptors. The most common compounds used to fabricate such solar cells are the semiconducting polymer P3HT and functionalized fullerene (PCBM) as electron acceptor. These devices show the highest PCE ($\sim$4.4–5.0%), which has been recently reported for BHJ organic solar cells. The main step in these devices is an ultrafast photoinduced electron transfer reaction at the donor–acceptor interface, which results in a metastable charge-separated state. However, the overall conversion efficiency of these devices is limited by the collection efficiency, which is greatly influenced by the morphology of the active film. Other advantages of hybrid nanocrystal–polymer blend PV solar cells are: easy and fast production at room temperature and mild conditions, low material cost, large interfacial area between acceptor and donor compound, and flexibility.

Nowadays, hybrid organic–inorganic polymer nanocomposites with luminescent semiconductor NCs are also of interest for their potential applications in electronic devices such as OLEDs. Unfortunately, polymer nanocomposite EL LEDs containing semiconductor NCs have remained a challenge. Only a few EL devices have been so far fabricated successfully [30–38, 294, 297–299]. Common EL devices are composed from a few layers, with one of them containing SC nanoparticles.

Usually, an addition of semiconductor NCs into conducting polymer ensures improvement of charge transport, stability characteristics, and EL efficiency of these devices as compared to pure conducting polymer.

Organic–inorganic nanocomposites can also be used for the preparation of electrochemical capacitors, also known as supercapacitors. They are important devices in energy storage and conversion systems, and are considered for a variety of applications such as in electric vehicles, support for fuel cells, uninterruptible power supplies, memory protection computer electronics, and cellular devices. The most widely used material for supercapacitors are nanocomposites of CNTs and a conducting polymer, especially composites based on MWCNTs and PPy, PANI, or PVK [333,336–338]. The introduction of CNTs into a polymer matrix improves the electric conductivity as well as the mechanical properties of the original polymer matrix, while possibly providing active material for capacitive energy storage.

Recently, gas sensors based on organic–inorganic nanocomposite materials have also been investigated [196,317]. The gas-sensing properties of the PANI/TiO_2 thin film to NH_3 and CO indicated that PANI/TiO_2 thin film was an excellent candidate for NH_3 detection, but not for the fabrication of a CO gas sensor [276]. CdSe/PMMA nanocomposites have been also used as a chemical sensor for detection of aromatic hydrocarbons [196].

Nanocomposite polymer electrolytes composed of PVDF, lithium perchlorate ($LiClO_4$), and TiO_2 nanoparticles have been used to create a new generation of rechargeable solid-state lithium batteries [213]. Also, the electrochemical preparation of PVK-functionalized CNT composites for rechargeable lithium batteries has been described [339]. Using the PVK/CNT composite as a positive electrode and an electrolytic solution containing $LiPF_6$ during the 20th charge-discharge cycle, higher specific discharge capacities of the rechargeable lithium cells (ca. 45 and 115 $mA\,h\,g^{-1}$) were reported for PVK-functionalized SWCNTs and MWCNTs, respectively.

10 Conclusions

In this review, a great number of aspects and examples that apply to the preparation and utilization of organic–inorganic hybrid nanocomposites have been raised. Among other things, the methods and properties of inorganic SC nanoparticles and carbon-based materials (fullerenes and nanotubes), stressing the surface chemistry of those compounds, have been presented. Also, characterization of non-conducting and conducting polymer matrices and their nanocomposites have been described. Finally, we have reported some of the applications of the hybrid inorganic–organic nanocomposites in optics and electronics, which have been demonstrated in many successful laboratory-scale applications.

It can be seen that there are many factors influencing the synthesis and application of hybrid organic–inorganic polymer nanocomposites. Nanocomposites containing semiconductor NCs dispersed into a polymeric matrix can greatly

benefit from new properties such as unique large organic–inorganic interfacial area, optically transparency, possibility of controlling the refractive index, better electric conductivity, and obtaining p–n heterojunctions and, in particular, junctions with highly doped SC particles. Another advantage is the possibility of realizing a nanoscale size for the device structural elements without significant effort, especially when using self-assembly techniques. In addition, due to the possibility of changing the size of nanoparticles, nanomaterials have the opportunity to tailor the band gap and positions, leading to such physical objects as QDs. Moreover, hybrid polymer nanocomposites have been shown to possess exceptional mechanical and thermal properties, while the inherent advantages of organic technology (i.e., low cost production, low cost of the materials used, and the possibility of fabrication of large area devices) are preserved.

In the past few years, it has been demonstrated that vast potential exists for the discovery of novel nanocomposite materials as well as for the development of new technology centered on functional nanocomposites, which can result in fast progress of these materials on the consumer market. Nowadays, our ability to control the structures and properties of nanocomposites is limited only by our knowledge of manipulation of these nanoscale structures. This area of research will clearly lead to further commercial applications with meaningful economic effect driven by materials with new combinations of properties.

References

1. Work WJ, Horie K, Hess M, Stepto RFT (2004) Pure Appl Chem 76:1985
2. Sanchez C, Romero P (2004) Functional hybrid materials. Wiley, Weinheim
3. Judenstein P, Sanchez C (1996) J Mater Chem 6:511
4. Gross S, Camozzo D, Noto VD, Armelao L, Tondello E (2007) Eur Polym J 43:673
5. Weiner S, Wagner HD (1998) Rev Mater Sci 28:271
6. Fong H, Sarikaya M, White SN, Snead ML (2000) Mater Sci Eng C 7:119
7. Zaremba CM, Morse DE, Mann S, Hansma PK, Stucky GD (1998) Chem Mater 10:3813
8. Gacitua WE, Ballerini AA, Zhang J (2005) Maderas Cienc Tecnol 7:159
9. Tanka T, Montanari GC, Mulhaup R (2004) IEEE Trans Dielectr Electr Insul 11:763
10. Jang J (2006) Adv Polym Sci 199:189
11. Ajayan PM, Schadler LS, Braun PV (2003), Nanocomposite science and technology. Wiley, Weinheim
12. de Tacconi NR, Wenren H, Rajeshwar K (1997) J Electrochem Soc 144:3159
13. Lee BH, Kwon KW, Shim M (2007) J Mater Chem 17:1284
14. Ghosh PK, Mitra MK, Chattopadhyay KK (2005) Nanotechnology 16:107
15. Tanaka M, Qi J, Masumoto Y (2000) J Cryst Growth 214:410
16. Althues H, Palkovits R, Rumplecker A, Simon P, Sigle W, Bredol M, Kynast U, Kaskel S (2006) Chem Mater 18:1068
17. Adachi D, Hasui S, Toyama T, Okamoto H (2000) Appl Phys Lett 77:1301
18. Komarneni S (2005) Chemical processing of ceramics, 2nd edn. CRC, New York
19. Godovsky DY (2000) Adv Polym Sci 153:163
20. Sugunan A, Dutta J (2004) J Phys Sci I 4:5
21. Kerker M (1969) The scattering of light. Academic, New York
22. Lu C, Cui Z, Li Z, Yang B, Shen J (2003) J Mater Chem 13:526
23. Sze SM (1985) Semiconductor devices. Wiley, New York

24. Kalinowski J (1997) In: Miyata S (ed) Organic electroluminescent materials and devices. CRC, Boca Raton
25. Vij DR (2004) Handbook of luminescence materials, Institute of Physics (Great Britain). CRC, Boca Raton
26. Abou El-Ela FM (2000) Egypt J Sol 23:27
27. Fahlman M, Salaneck WR (2002) Surf Sci 500:904
28. Holder E, Tessler N, Rogach AL (2008) J Mater Chem 18:1064
29. Oey CC, Djurisic AB, Kwong CY, Cheung CH, Chan WK, Nunzi JM, Chui PC (2005) Thin Solid Films 492:253
30. Liu HW, Laskar IR, Huang CP, Cheng JA, Cheng SS, Luo LY, Wang HR, Chen TM (2005) Thin Solid Films 489:296
31. Hikmet RAM, Talapin DV, Weller H (2003) J Appl Phys 93:3509
32. Yang H, Hollowy PH (2003) J Phys Chem B 107:9705
33. Park JH, Park SI, Kim TH, Park OO (2007) Thin Solid Films 515:3085
34. Lee KW, Lee SP, Choi H, Mo KH, Jang JW (2007) J Appl Phys 91:023110
35. Manzoor K, Vadera SR, Kumar N (2004) Appl Phys Lett 84:284
36. Lee CY, Haung YT, Su WF, Lin CF (2006) Appl Phys Lett 89:231116
37. Yang Y, Huang J, Yang B, Liu S, Shen J (1997) Synth Met 91:347
38. Yang CH, Bhongale CJ, Chou CH, Yang SH, Lo CN, Chen TM, Hsu CS (2007) Polymer 48:116
39. Wong WY, Wang XZ, He Z, Djurisic AB, Yip CT, Cheung KY, Wang H, Wang H, Mak CSK, Chan WK (2007) Nat Mater 6:521
40. Shrotriya V, Ouyang J, Tseng RJ, Yang GL, Yang Y (2005) Chem Phys Lett 411:138
41. Kim Y, Cook S, Kirkpatrick J, Nelson J, Durrant JR, Bradley DDC, Giles M, Heeney M, Hamilton R, McCulloch I (2007) Phys Chem Lett C 111:8137
42. Kim Y, Choulis SA, Nelson J, Bradley DDC (2005) J Mater Sci 40:1371
43. Wong WY, Wang XZ, He Z, Djurisic AB, Yip CT, Cheung KY, Wang H, Wang H, Mak CSK, Chan WK (2007) Nat Mater 6:521
44. Al-Ibrahim M, Sensfuss S, Uziel J, Ecke G, Ambacher O (2005) Sol Energ Mater Sol Cell 85:277
45. Kwong CY, Choy WCH, Djurisic AB, Chui PC, Cheng KW, Chan WK (2004) Nanotechnology 15:1156
46. Vu QT, Pavlik M, Hebestrei N, Rammelt U, Plieth W, Pfleger J (2005) React Funct Polym 65:69
47. Kwong CY, Djurisic AB, Chui PC, Cheng KW (2004) Chem Phys Lett 384:372
48. Zhang Q, Russell TP, Emrick T (2007) Chem Mater 19:3712
49. De Girolamo J, Reiss P, Pron A (2007) J Phys Chem C 111:14681
50. Sonar P, Sreenivasan KP, Madddanimath T, Vijayamohanan K (2006) Mater Res Bull 41:198
51. Chaudhary S, Lu H, Muller AM, Bardeen CJ, Ozkan M (2007) Nano Lett 7:1973
52. Geng J, Zeng T (2006) J Am Chem Soc 128:16827
53. Beek WJE, Wienk MM, Janssen RAJ (2006) Adv Funct Mater 16:1112
54. Ravirajan P, Peiro AM, Nazeeruddin MK, Graetzel M, Bradley DDC, Durrant JR, Nelson J (2006) J Phys Chem B 110:7635
55. Jaglarz J, Kassiba A, Armatys P, Pokladko M, Gondek E, Sanetra J (2004) Mater Sci 22:389
56. Boucle J, Ravirajan P, Nelson J (2007) J Mater Chem 17:3141
57. Hodes G (2001) Electrochemistry of nanomaterials. Wiley, Weinheim
58. Shionoya S, Yen W (1998) Phosphors handbook. Hardcover, CRC, New York
59. Smith RA (1964) Semiconductors. Cambridge University Press, Cambridge
60. Rajeshwar K, Tacconi NR, Chenthamarakshan CR (2001) Chem Mater 13:2765
61. Geusic JE, Singh S, Tipping DW, Rich TC (1967) Phys Rev Lett 19:1126
62. Penzkofer A, Falkenstein W (1976) Opt Commun 17:1
63. Staginus G, Frohlich D, Gaps T (1968) Rev Sci Instrum 39:1129
64. van der Ziel JP (1977) Phys Rev B 16:2775
65. Basov NG, Grasyuk AZ, Efimov VF, Zubarev IG, Katulin VA, Popov JM (1966) J Phys Soc Jpn Suppl 21:276

66. Panizza E (1967) Appl Phys Lett 10:265
67. Arsen'ev VV, Dneprovskii VS, Klyshko DN, Penin AN (1969) Sov Phys Dokl 12:4
68. Prasad PN (2004) Nanophotonics. Wiley, New Jersey
69. Peng WQ, Cong GW, Qu SC, Wang ZG (2006) Opt Mater 29:313
70. Nalwa HS, Rohwer LS (2003) Handbook of luminescence display materials & devices. American Scientific Publishers, Stevenson Ranch, CA
71. Bryan JD, Gamelin DR (2005) Prog Inorg Chem 54:47
72. Yang H, Holloway PH (2002) J Appl Phys 93:586
73. Hawang J, Oh MO, Kim I, Lee JK, Ha ChS (2005) Curr Appl Phys 5:31
74. Manzoor K, Vadera SR, Kumar N (2004) Appl Phys Lett 84:284
75. Yang H, Han S, Cui Y, Liang Y (2004) Mater Lett 58:2087
76. Toyama T, Yoshimura K, Fujii M, Haze H, Okamoto H (2005) Appl Surf Sci 244:524
77. Bol AA, van Beek R, Meijerink A (2002) Chem Mater 4:1121
78. Jian W, Zhuang J, Zhang D, Dai J, Yang W, Bai Y (2006) Mater Chem Phys 99:497
79. Swart HC, Greeff AP, Holloway PH, Berning GLP (1999) Appl Surf Sci 140:63
80. Raevskaya AE, Korzhak AV, Stroyuk AL, Kuchmii SY (2005) Theor Exp Chem 41:359
81. Kushida T, Kurita A, Watanabe M, Kanematsu Y, Hirata K, Okubo N, Kanemitsu Y (2000) J Lumin 87:466
82. Peng WQ, Cong GW, Qu SC, Wang ZG (2006) Opt Mater 29:313
83. Yang P, Lu M, Zhou G, Yuan DR, Xu D (2001) Inorg Chem Commun 4:734
84. Bhargava RN, Gallagher D, Welker T (1994) J Lumin 60:275
85. Kitai AH (1993) Solid state luminescence: theory, materials, and devices. Chapman & Hall, New York
86. Blasse GB, Grabmaier BC (1994) Luminescence materials. Springer, Berlin
87. McClean IP, Thomas CB (1992) Semicond Sci Technol 7:1394
88. Hirabayashi K, Kozawaguchi H (1986) Jpn J Appl Phys 25:711
89. Ozawa M, Satoh T, Hirate T (2008) E-MRS Fall Meeting 2007, Acta Materialia Gold Medal Workshop, Warsaw, Poland, September 17–21, http://www.science24.com/paper/11683 (14.02.2008)
90. Dutta J, Hofmann H (2003) In: Nalwa HS (ed) Encyclopaedia of nanoscience and nanotechnology, vol. 10. American Scientific Publishers, Stevenson Ranch, CA, pp 1–23
91. McHardy J, Ludwig F (1992), Electrochemistry of semiconductors and electronics. Noyes, Park Ridge, NJ
92. Cao L, Zhang J, Ren S, Huang S (2002) Appl Phys Lett 80:23
93. Yang H, Han S, Cui Y, Liang Y (2004) Mater Lett 58:2087
94. Sugunan A, Warad HC, Thanachayanont C, Dutta J (2005) In: 2nd ECTI annual conference proceedings, Pattaya, Thailand, 12–13 May 2005
95. Bhargava RN, Gallagher D, Hong X, Nurmiko A (1994) Phys Rev Lett 72:416
96. Maity R, Chattopadhyay KK (2004) Nanotechnology 15:812
97. Peng WQ, Qu SC, Cong GW, Zhang XQ, Wang ZG (2005) J Crys Growth 282:179
98. Martinez-Castanon GA, Martinez-Mendoza JR, Ruiz F, Gonzalez- Hernandez J (2007) Inorg Chem Commun 10:531
99. Kane RS, Cohen RE, Silbey R (1999) Chem Mater 11:90
100. Konishi M, Isobe T, Senna M (2001) J Lumin 93:1
101. Toyoda T, Cruz AB (2003) Thin Solid Films 438:132
102. Bol AA, Meijerink A (2001) J Phys Chem B 105:10197
103. Yu J, Liu H, Wang Y, Fernandez FE, Jia W (1997) J Lumin 75:252
104. Zhao K, Dai J, Zhuang J, Li J, Yang W (2007) Colloids Surf A 296:154
105. Karar N, Singh F, Mehta BR (2004) J Appl Phys 95:656
106. Zhuang J, Zhang X, Wang G, Li D, Yang W (2003) J Mater Chem 13:1853
107. Warad HC, Ghosh SC, Hemtanon B, Thanachayanont C, Dutta J (2005) Sci Technol Adv Mater 6:296–301
108. Bredol M, Althues H (2004) Solid State Phenomena 99:19
109. Kubo T, Isobe T, Senna M (2002) J Lumin 99:39
110. Bunn CW (1935) Proc Phys Soc London 47:836

111. Ozgur U, Alivov YI, Liu C, Teke A, Reshchikov MA, Dogan S, Avrutin V, Cho SJ, Morko H (2005) J Appl Phys 98:041301
112. Li ZW, Gao W (2007) Thin Solid Films 515:3323
113. Chakrabarti S, Das D, Ganguli D, Chaudhuri S (2003) Thin Solid Films 441:228
114. Schirmer F, Zwingle D (1970) Solid State Commun 8:1559
115. Look DC (2001) Mater Sci Eng B 80:381
116. Kucheyev O, Williams JS, Jagadish C, Zou J, Evans C, Nelson AJ, Hamza AV (2003) Phys Rev B 67:094115
117. Turton R, Berry DA, Gardner TH, Miltz A (2004) Ind Eng Chem Res 43:1235
118. Xu JQ, Pan QY, Shun YA, Tian ZZ (2000) Sens Actuaators B Chem 66:2000
119. Hoffman L, Norris BJ, Wager JF (2003) Appl Phys Lett 82:733
120. Hoffman L (2004) J Appl Phys 95:5813
121. Curridal ML, Comparelli R, Cozzli PD, Mascolo G, Agostiano A (2003) Mater Sci Eng C 23:285
122. Peiro AM, Ravirajan P, Govender K, Boyle DS, Brien PO, Bradley DDC, Nelson J, Durrant JR (2005) Organic photovoltaic VI, Proc SPIE 5938:191
123. Beek WJE, Wienk MM, Janssen RAJ (2006) Adv Funct Mater 16:1112
124. Li ZW, Gao W, Reeves R (2005) Surf Coat Technol 198:319
125. Chichina M, Tichy M, Churpita Hubicka Z (2005) 14th Annual Conference of Doctoral Student. Prauge, Czech Republic, WDS'05 Proceedings of Contributed Papers, Part II, 325–331, 2005 (03.03.2008) WDS 2005 - Proceedings of Contributed Papers Proceedings of the 14th Annual Conference of Doctoral Students - WDS 2005 Prague, 7th June - 10th June, 2005 www.mff.cuni.cz/veda/konference/wds/contents/wds05.htm
126. Vlachopoulos N, Liska P, Augustynski J, Gratzel M (1988) J Am Chem Soc 110:1216
127. Kong FT, Dai SY, Wang KJ (2007) Adv Opt Electron 1155:75384
128. Nazeeruddin MK, Kay A, Rodicio I, Humphry-Baker R, Mueller E, Liska P, Vlachopoulos N, Gratzel M (1993) J Am Chem Soc 115:6382
129. Salafsky JS (1999) Phys Rev B 59:10885
130. Kumazawa N, Rafiqul Islam M, Takeuchi M (1999) J Electroanal Chem 472:137
131. Chin SS, Chiang K, Gordon Fane A (2006) J Membr Sci 275:202
132. Losito I, Amorisco A, Palmisano F, Zambonin PG (2005) Appl Surf Sci 240:180
133. Gogate PR, Pandit AB (2004) Adv Environ Res 8:501
134. Cozzoli PD, Kornowski A, Weller H (2003) J Am Chem Soc 125:14539
135. Zhang Q, Gao L (2003) Langumir 19:967
136. Ramakrishna G, Ghosh HN (2003) Langumir 19:505
137. Kim CS, Moon BK, Park JH, Choi BC, Seo HJ (2003) J Cryst Growth 257:309
138. Hsu WP, Yu R, Matijevic E (1993) J Colloid Interface Sci 156:56
139. Rosenthal SJ, McBride J, Pennycook SJ, Feldman LC (2007) Surf Sci Rep 62:111
140. Nirmal M, Brus L (1999) Acc Chem Res 32: 407
141. El-Sayed MA (2001) Acc Chem Res 34:257
142. Dabbousi BO, Rodriguez-Viejo J, Mikulec V, Heine JR, Mattoussi H, Ober R, Jensen KF, Bawendii MG (1997) J Phys Chem B 101:9463
143. Murray CB, Norris DJ, Bawendi MG (1993) J Am Chem Soc 115:8706
144. Kippeny TC, Swafford LA, Rosenthal SJ (2002) J Chem Educ 79:1094
145. Qu L, Peng AZ, Peng X (2001) Nano Lett 1:333
146. Wang CC, Chen AL, Chen IH (2006) Polym Adv Technol 17:598
147. Murcia MJ, Shaw DL, Woodruff H, Naumann CA, Young BA, Long EC (2006) Chem Mater 18:2219–2225
148. Reiss P, Bleuse J, Pron A (2002) Nano Lett 781:2
149. Liu HW, Laskar IR, Huang CP, Cheng JA, Cheng SS, Luo LY, Wang HR, Chen TM (2005) Thin Solid Films 489:296
150. Kratschmer W (1995) Nanostruct Mater 6:65
151. Dresselhaus MS, Dresselhaus G (1997) Nanostruct Mater 9:33
152. Bernholc J, Roland Ch, Yakobson B (1997) Curr Opin Solid State Mater 2:706
153. Mintmire JW, White CT (1995) Carbon 33:893

154. Coleman JN, Khan U, Blau WJ, Gun'ko YK (2006) Carbon 44:1624
155. Paradise M, Goswami T (2007) Mater Des 28:1477
156. Baibarac M, Gomez-Romero P (2006) J Nanosci Nanotechnol 6:1
157. Xie XL, Mai YW, Zhou XP (2005) Mater Sci Eng R 49:89
158. Breuret O, Sundararaj U (2004) Polym Compos 25:630
159. Desai AV, Haque MA (2005) Thin Wall Struct 43:1787
160. Lau KT, Chipara M, Ling HY, Hui D (2004) Composites B 35:95
161. Lau KT, Hui D (2002) Composites B 33:263
162. Thostenson ET, Ren Z, Chou TW (2001) Compos Sci Technol 61:1899
163. Winkler K, Balch AL, Kutner W (2006) J Solid State Electrochem 10:761
164. Buseck PR (2002) Earth Planet Sci Lett 203:781
165. Miller GP (2006) C R Chimie 9:952
166. Briggs JB, Miller GP (2006) C R Chim 9:916
167. Adamopoulos G, Heiser T, Giovanella U, Ould-Saad S, van de Wetering KI, Brochon C, Zorba T, Paraskevopoulos KM, Hadziioannou G (2006) Thin Solid Films 511:371
168. Camaioni N, Ridolfi G, Casalbore-Miceli G, Possamai G, Garlaschelli L, Maggini M (2002) Sol Energ Mater Sol Cell 76:107
169. Al-Ibrahim M, Sensfuss S, Uziel J, Ecke G, Ambacher O (2005) Sol Energ Mater Sol Cell 85:277
170. Kim Y, Nelson J, Durrant J, Bradley DD, Heo K, Park J, Kim H, McCulloch I, Heeney M, Ree M, Ha ChS (2006) Soft Matter 3:117
171. Wang C, Guo ZX, Fu S, Wu W, Zhu D (2004) Prog Polym Sci 29:1079
172. Hutchison KLG, Schick G, Rubin Y, Wudl F (1999) J Am Chem Soc 121:5611
173. Protiere M, Reiss P (2006) Nanoscale Res Lett 1:62
174. Collins PG, Avouris P (2000) Sci Am 283:62
175. Kim P, Shi L, Majumdar A, McEuen PL (2001) Phys Rev Lett 87:215502
176. Liu J, Liu T, Kumar S (2005) Polymer 46:3419
177. Mark JE (1999) Polymer data handbook Oxford University Press, New York
178. Howard M (1980) Plastics desk top data bank, Book B, 5th edn. International Plastics Selector, San Diego
179. Reichmanis E, Katz H, Kloc Ch, Maliakal A (2005) Bell Labs Tech J 10:87
180. Hunt AT (2006) Technical report. nGimat TM Co. Atlanta, USA http://www.ngimat.com/pdfs/Nanocomposites_Metal_Ceramic_Polymer.pdf (20.08.2008)
181. Ward IM, Sweeney J (2004) An introduction to the mechanical properties of solid polymers. Wiley, Chichester
182. Brandrup J, Immergut EH, Grulke EA (1999) Polymer handbook 4th edn. Wiley, New York
183. Pedone L, Caponetti E, Leone M, Militello V, Panto V, Polizzi S, Saladino ML (2005) J Colloid Interface Sci 284:495
184. Wang ZG, Zu XT, Yu HJ, He X, Zhu S, Wei QM, Wang LM (2006) Nucl Instrum Methods Phys Res Sect B 250:196
185. Wang ZG, Zu S, Xiang X, Fang LM, Wang LM (2006) Phys Lett 359:252
186. Wang ZG, Zu XT, Yu HJ (2006) J Nanopart Res 8:137
187. Hong RY, Qian JZ, Cao JX (2006) Powder Technol 163:160
188. Park SJ, Lim ST, Cho MS, Kim HM, Joo J, Choi HJ (2005) Curr Appl Phys 5:302
189. Lee WJ, Lee SE, Kim ChG (2006) Compos Struct 76:406
190. Wang M, Pramoda KP, Goh SH (2006) Carbon 44:613
191. Jin HJ, Choi HJ, Yoon SH, Myung SJ, Shim SE (2005) Chem Mater 17:4034
192. Zeng J, Saltysiak B, Johnson WS, Schiraldi DA, Kumar S (2004) Composites B 35:173
193. Dai J, Wang Q, Li W, Wei Z, Xu G (2007) Mater Lett 61:27
194. Tang E, Cheng G, Pang G, Ma X, Xing F (2006) Colloid Polym Sci 284:422
195. Martiradonna L, Stomeo T, De Giorgi M, Cingolani R, De Vittorio M (2006) Microelectron Eng 83:1478
196. Vassiltsova OV, Zhao Z, Petrukhina MA, Carpenter MA (2007) Sens Actuators B 123:522
197. Huang KJ, Rajendran P, Liddell CM (2007) J Colloid Interface Sci 308:112

198. Adamopoulos G, Heiser T, Giovanella U, Ould-Saad S, van de Wetering KI, Brochon C, Zorba T, Paraskevopoulos KM, Hadziioannou G (2006) Thin Solid Films 511:371
199. Wang Z, Lu M, Li HL, Guo XY (2006) Mater Chem Phys 100:77
200. Zhao PQ, Wu XL, Fan JY, Chu PK, Siu GG (2006) Scr Mater 55:1123
201. Pentimalli M, Antolini F, Bauer EM, Capitani D, Luccio TD, Viel S (2006) Mater Lett 60:2657
202. Antolini F, Pentimalli M, Luccio TD, Terzi R, Schioppa M, Re M, Mirenghi L, Tapfer L (2005) Mater Lett 59:3181
203. Antolini F, Ghezelbash C, Esposito C, Trave E, Tapfer L, Korgel BA (2006) Mater Lett 60:1095
204. Riegler J, Ehler O, Nann T (2006) Anal Bioanal Chem 384:645
205. Joumaa N, Lansalot M, Theretz A, Elaissari A (2006) Langumir 22:1810
206. Sherman RL, Ford J, Ford WT (2005) 21:5218
207. Iezzi RA (1998) Technical report 11-18-04. Elf Atochem North America Inc., Research Center, King of Prussia, Pa., Philadelphia, USA http://www.arkema-inc.com/pdf/techpoly/Iezzi_Article_From_PCI%20Mag.pdf (25.03.2008)
208. Jugnickel BJ (1996) The polymeric materials encyclopaedia. CRC, Boca Raton
209. Dohany JE (1981) US Patent 4360652
210. Hsu CC, Geil PH (1989) J Mater Sci 24:1219
211. Anandan S, Pitchumani S, Muthuraaman B, Maruthamuthu P (2006) Sol Energy Mater Sol Cells 90:1715
212. Hilczer B, Kulek J, Polomska M, Glinchuk MD, Ragulya AV, Pietraszko A (2005) Ferroelectr 316:31
213. Wang YJ, Kim D (2007) Electrochim Acta 52:3181
214. Lijie D, Chuanxi X, Juan Ch, Cewen N (2004) J Wuhan Univ Technol Mater Sci Ed 19:9
215. Gallagher SJ, Norton B, Eames PC (2007) Sol Energy 81:813
216. Dang ZM, Wang HY, Zhang YH, Qi JQ (2005) Macromol Rapid Commun 26:1185
217. Hongying Q, Chuanxi X, Lijie D, Guanghui Z (2006) J Wuhan Univ Technol Mater Sci Ed 21:133
218. Yan L, Wang K, Ye L (2003) J Mater Sci Lett 22:1713
219. Lu Ch, Cui Z, Wang Y, Li Z, Guan Ch, Yang B, Shen J (2003) J Mater Chem 13:2189
220. Shirakawa H, Louis EJ, MacDiarmid AG, Chiang CK, Heeger AJ (1977) J Chem Soc Chem Commun 16:578
221. Strenger-Smith JD (1998) Prog Polym Sci 23:57
222. Chan HSO, Ng SC (1998) Prog Polym Sci 23:1167
223. Kim DY, Cho HN, Kim CY (2000) Prog Polym Sci 25:1089
224. Pron A, Rannou P (2002) Polym Sci 27:135
225. Winder C, Sariciftci NS (2004) J Mater Chem 14:1077
226. Jang J (2006) Adv Polym Sci 199:189
227. Bundgaard E, Krebs FC (2007) Sol Energy Mater Sol Cells 91:954
228. Fahlman M, Salaneck WR (2002) Surf Sci 500:904
229. Reddinger JL, Reynolds JR (1999) Adv Polym Sci 145:57
230. McQuade DT, Pullen AE, Swager TM (2000) Chem Rev 100:2537
231. Kim Y, Cook S, Choulis SA, Nelson J, Durrant JR, Bradley DC (2005) Synth Met 152:105
232. Beek WJE, Wienk MM, Janssen RA (2004) Adv Mater 16:1009
233. Shon JH, Dodabalapur A, Bao Z, Kloe C, Schenker G, Batlogg B (2001) Nature 410:189
234. Spannggasrd H, Krebs FC (2004) Sol Energy Mater Sol Cells 83:125
235. Grimsdale AC, Mullen K (2006) Adv Polym Sci 199:1
236. Kim DY, Cho HN, Kim CY (2000) Prog Polym Sci 25:1089
237. Ho PKH, Friend RH (2002) J Chem Phys 116:6782
238. Estrada M, Mejia I, Cerdeira A, Iniguez B (2008) Solid State Electron 52:53
239. Estrada M, Mejia I, Cerdeira A, Pallares J, Marsal LF, Iniguez B (2008) Solid State Electron 52:787
240. Werzer O, Matoy K, Strohriegl P, Resel R (2007) Thin Solid Films 515:5601

241. Cotts DB, Reyes Z (1987) Electrically conductive organic polymers for advanced applications. SRI International, Menlo Park, CA
242. Bertho S, Haeldermans I, Swinnen A, Moons W, Martens T, Lutsen L, Vanderzande D, Manca J, Senes A, Bonfiglio A (2007) Sol Energy Mater Sol Cells 91:385
243. Ghosh M, Barman A, De SK, Chatterjee S (1998) Synt Met 97:23
244. Mo TC, Wang HW, Chen SY, Yeh YC (2008) Ceram Int 34:1767
245. Ahlskog M, Reghu M, Noguchi T, Ohnishi T (1997) Synt Met 89:11
246. Bhatia V, Gupta D, Kabra D, Narayan KS (2007) J Mater Sci Mater Electron 18:925
247. Roncali J (1997) Chem Rev 97:173
248. McCullough RD (1998) Adv Mater 10:9
249. Tan Z, Zhou E, Yang Y, He Y, Yang C, Li Y (2007) Eur Polym J 43:855
250. Ji JS, Lin YJ, Lu HP, Wang L, Rwei SP (2006) Thin Solids Film 511–512:182
251. Vu QT, Pavlik M, Hebestreit N, Rammelt U, Plieth W, Pfleger J (2005) React Funct Polym 65:69
252. Huynh WU, Dittmer JJ, Alivisatos AP (2002) Science 295:2427
253. Cui Y, Duan XF, Hu JT, Lieber CM (2000) J Phys Chem 104:5213
254. Huynh WU, Dittmer JJ, Teclemariam N, Milliron DJ, Alivisatos AP, Barnham KW (2003) Phys Rev B 67:115326
255. Huynh WU, Dittmer JJ, Libby WC, Whiting GL, Alivisatos AP (2003) Adv Funct Mater 13:73
256. Huynh WU, Peng X, Alivisatos AP (1999) Adv Mater 11:923
257. Vidya V, Ambily S, Narang SN, Major S, Talwar SS (2002) Colloids Surf 198:383
258. Pradhan B, Batabyal SK, Pal A (2006) J Appl Phys Lett 88:093106
259. Kymakis E, Amaratunga GAJ (2002) Appl Phys Lett 80:112
260. Parke ID (1994) J Appl Phys 75:1656
261. Kymakis E, Alexandrou I, Amaratunga GAJ (2003) J Appl Phys 93:1764
262. McCarthy B, Coleman JN, Curran SA, Dalton AB, Davey AP, Konya Z, Fonseca A, Nagy JB, Blau WJ (2000) J Mater Sci Lett 19:2239
263. Berson S, Bettignies R, Bailly S, Guillerez S (2007) Adv Funct Mater 17:1377
264. Zhang Y, Wada T, Sasabe H (1998) J Mat Chem 8:809
265. Kippelen B, Peyghambarian N (2003) Adv Polym Sci 161:87
266. Pielichowski J, Bogdal D (2004) Nonlinear Opt Quantum Opt 32:59
267. Winiarz JG, Zhang L, Lal M, Friend CS, Prasad PN (1999) Chem Phys 245:417
268. Yu W, Xu Z, Teng F, Yang S, Hou Y, Qian L, Qu C, Quan S, Xu X (2005) Phys Lett A 338:402
269. Yang S, Jiang Y, Teng F, Xu Z, Hou Y, Xu X (2006) Solid State Commun 139:415
270. Jiang Y, Yang S, Teng F, Xu Z, Hou Y, Xu X (2007) J Lumin 122:617
271. Horii Y, Kitagawa M, Taneoka H, Kusano H, Murakami T, Hino Y, Kobayashi H (2001) Mater Sci Eng B 85:92
272. Kawakami S, Kitagawa M, Kusano H, Morita D, Horii Y, Hirooka Y, Hatano K, Sawada T, Tsushima T, Kobayashi H (2000) Thin Solid Films 363:17
273. Xi H, Qian X, Yin J, Bian L, He R, Zhu Z (2003) Mater Lett 57:2657
274. Bogdal D, Prociak A (2007) Microwave-enhanced polymer chemistry and technology. Blackwell-Wiley, Oxford
275. He R, Qian X, Yin J, Bian L, Xi H, Zhu Z (2003) Mater Lett 57:1351
276. Cheng J, Wang S, Li XY, Yan Y, Yang S, Yang CL, Wang JN, Ge WK (2001) Chem Phys Lett 333:375
277. Gao Y, Liang C, Tang A, Teng F, Li D, Deng Z, Huang S (2007) J Lumin 122:646
278. Zhang T, Xu Z, Qian L, Tao DL, Teng F, Xu XR (2006) Opt Mater 29:216
279. Wu HX, Qiu XQ, Cai RF, Qian SX (2007) App Surf Sci 253:5122
280. Wu W, Li J, Liu L, Yanga L, Guo ZX, Dai L, Zhu D (2002) Chem Phys Lett 364:196
281. Qian J, Qian S, Cai Z (1999) Solid State Commun 109:371
282. Wang D, Ke G, Qian S (1995) Phys Lett 12:717
283. Park JH, Park OO, Kim J, Yu JW, Kim JK, Kim YC (2004) Curr Appl Phys 4:659
284. Kim JY, Kim M, Kim H, Joo J, Choi JH (2002) Opt Mater 21:147
285. Kim JY, Kim ES, Choi JH (2002) J Appl Phys 91:1944

286. Wang G, Qian S, Xu J, Wang W, Liu X, Lu X, Li F (2000) Physica B 279:116
287. Gurunathan K, Vadivel Murugan A, Marimuthu R, Mulik UP, Amalnerkar DP (1999) Mater Chem Phys 61:173
288. Peres LO, Varela H, Garcia JR, Fernandes MR, Torresi RM, Nart FC, Gruber J (2001) Synth Met 118:65
289. Xin Y, Huang Z, Chen J, Wang C, Tong Y, Liu S (2008) Mater Lett 62:991
290. Yang BD, Yoon KH, Chung KW (2004) Synth Met 143:25
291. Salafsky JS, Lubberhuizen WH, Schropp REI (1998) Chem Phys Lett 290:297
292. Zhang J, Wang B, Ju X, Liu T, Hu T (2001) Polymer 42:3697
293. Zhang J, Ju X, Wang B, Li Q, Liu T, Hu T (2001) Synth Met 118:181
294. Yang SH, Nguyen TP, Rendu PL, Hsu CS (2005) Composites A 36:509
295. Sirimanne PM, Premalal EVA, Pitigala PKDDP, Tennakone K (2006) Sol Energy Mater Sol Cells
296. Su SJ, Kuramoto N (2000) Synth Met 108:121
297. Tang A, Teng F, Jin H, Gao Y, Hou Y, Liang C, Wang Y (2007) Mater Lett 61:2178
298. Taylor RM, Church KH, Sluch MI (2007) Displays 28:92
299. Gao M, Richter B, Kirsein S (1999) Synth Met 102:1213
300. Chen Y, Midorikawa T, Bai J, Liu Y, Araki Y, Ito O (2005) Polymer 46:9803
301. Gao J, Hide F, Wang H (1997) Synth Met 84:979
302. Gospodinova N, Terlemezyan (1998) Prog Polym Sci 23:1443
303. Zhang D, Wang Y (2006) Mater Sci Eng B 134:9
304. Somani PR (2002) Mater Chem Phys 77:81
305. Araujo WS, Margarit ICP, Ferreira M, Mattos OR, Neto PL (2001) Electrochim Acta 46:1307
306. Vaschetto ME, Monkman AP, Springborg M (1999) J Mol Struct 468:181
307. Palaniappan S, Amarnath CA (2006) React Funct Polym 66:1741
308. Zhou S, Wu T, Kan J (2007) Eur Polym J 43:395
309. Yoshikawa H, Hino T, Kuramoto N (2006) Synth Met 156:1187
310. Troitsky VI, Berzina TS, Fontana MP (2002) Synth Met 129:39
311. Malinauskas A (2001) Polymer 42:3957
312. Goel S, Gupta A, Singh KP, Mehrotra R, Kandpal HC (2007) Mater Sci Eng A 443:71
313. Huang JX, Moore JA, Acquaye JH, Kaner RB (2005) Macromolecules 38:317
314. Liao C, Gu M (2002) Thin Solid Films 408:37
315. Paterno LG, Manolache S, Denes F (2002) Synth Met 130:85
316. Li J, Zhu L, Wu Y, Harima Y, Zhang A, Tang H (2006) Polymer 47:7361
317. Tai H, Jiang Y, Xie G, Yu G, Chen X (2007) Sens Actuators B 125:644
318. Sathiyanarayanan S, Syed Azim S, Venkatachari G (2007) Prog Org Coat 59:291
319. Li X, Wang G, Li X, Lu D (2004) Appl Surf Sci 229:395
320. Xiong S, Wang Q, Chen Y (2007) Mater Chem Phys 103:450
321. Yavuz AG, Gok A (2007) Synth Met 157:235
322. Yan B, Chen D, Jiao X (2004) Mater Res Bull 39:1655
323. Khanna PK, Kulkarni MV, Singh N, Lonkar SP, Subbarao VVVS, Viswanath AK (2006) Mater Chem Phys 95:24
324. Khanna PK, Lonkar SP, Subbarao VVVS, Jun KW (2004) 87:49
325. Lee KP, Gopalan AI, Santhosh P, Lee SH, Nho YC (2007) Compos Sci Technol 67:811
326. Long Y, Chen Z, Duvail JL, Zhang Z, Wan M (2005) Physica B 370:121
327. Kaushik D, Sharma M, Singh RR, Gupta DK, Pandey RK (2006) Mater Lett 60:2994
328. He Y (2004) Powder Technol 147:59
329. Wu TM, Lin YW (2006) Polymer 47:3576
330. Konyushenko EN, Stejskal J, Trchova M, Hradil J, Kovarova J, Prokes J, Cieslar M, Hwang JY, Chen KH, Sapurina I (2006) Polymer 47:5715
331. Mottaghitalb V, Xi B, Spinks GM, Wallace GG (2006) Synth Met 156:796
332. Guo M, Chen J, Li J, Tao B, Yao S (2005) Anal Chim Acta 532:71
333. Zhou Y, He B, Zhou W, Huang J, Li X, Wu B, Li H (2004) Electrochim Acta 49:257
334. Yu Y, Che B, Si Z, Li L, Chen W, Xue G (2005) Synth Met 150:271
335. Qiao Y, Li CM, Bao SJ, Bao QL (2007) J Power Sources 170:79

336. Gupta V, Miura N (2006) Electrochim Acta 52:1721
337. Gupta V, Miura N (2006) J Power Sources 157:616
338. Baibarac M, Gomez-Romero P, Lira-Cantu M, Casan-Pastor N, Mestres N, Lefrant S (2006) Eur Polym J 42:2302
339. Baibarac M, Lira-Cantu M, Oro Sol J, Baltog I, Casan-Pastor N, Gomez-Romero P (2007) Compos Sci Technol 67:2556

Editor: K. Dušek

Index